AMINE-CONTAINING ANTHRACYCLINES COVALENTLY BIND AP SITES IN DNA CREATED BY NITROGEN MUSTARDS, RESULTING IN REDUCED CELL VIABILITY AND LEADING TO RAPID STRAND SCISSION VIA β-/δ-ELIMINATION

By

John Treadwell Terrell

Dissertation
Submitted to the Faculty of the
Graduate School of Vanderbilt University
in partial fulfillment of the requirements
for the degree of

DOCTOR OF PHILOSOPHY
in
Chemistry

December 16, 2023
Nashville, TN

Approved:

Carmelo J. Rizzo, Ph.D.

Michael P. Stone, Ph.D.

Gary A. Sulikowski, Ph.D.

Martin Egli, Ph.D.

To my parents, Martha and William Terrell, who made many sacrifices of their own to visit me, support me, and keep me healthy these last 7 years and beyond. Dedicated also to my Gaga and Papa, whom I strive every day to be more like in mind and spirit and who I am glad were able to watch and share in this final step.

Acknowledgements

My time at Vanderbilt University has been a journey of many parts during a stage in my life where self-discovery was paramount. Through relationships made and lost, focuses on my own personal and mental well-being, the natural struggles of research, and much more, I could not have done any of it without support along the way. Coming out of it all I find myself a different person than when I entered, more aware and prepared for the next stages of my scientific career.

I would first like to express my utmost thanks to Dr. Carmelo Rizzo, without whom any of the work presented here would not have been possible. In the years since taking me into his research group, Dr. Rizzo has been a wonderful advisor in more than just academics, pushing me to advance myself in all ways while also supporting me when personal needs came first. Thank you for your guidance when I strayed too far from my own work and for the independence you allowed me as a researcher to pursue some ideas anyway.

I would also like to thank the members of my Ph.D. committee, all of whom either worked directly as a part of the bigger picture of this project or taught the courses that constituted my first two years in the graduate school. Dr. Michael Stone, Dr. Gary Sulikowski, and Dr. Martin Egli have provided invaluable guidance through knowledge imparted and questions asked in my many exams to help me better develop as a chemist. I appreciate the time each of you has taken from your busy schedules, whether in official capacity or for individual meetings, to answer my own questions and discuss academic curiosities.

Thank you also to Dr. Amanda Wolfe at the University of North Carolina at Asheville, my research advisor from my time as an undergraduate. The research experience I gained under her was important, but she also provided significant support in my transition to graduate school and guided me along a path that was most appropriate for my interests and abilities.

Many thanks go to Dr. Plamen Christov, a former member of the Rizzo Lab who provided me with significant technical instruction and experimental guidance with aspects of old projects he had once worked on. As lab personnel turned over early in my graduate career, Plamen was able to teach me many of the less intuitive aspects of lab work and help me keep things running smoothly.

I would also like to thank current and past members of the lab: Dr. Francesca Gruppi, Dr. Chanchal Malik, Dr. Joshua Elder, Dr. Jotirling Mali, Dr. Arjun Kaffle, Benjamin Sexton, and Thomas Raymond. Francesca, Chanchal, and Jotirling provided much of my initial lab instruction over the first 2-3 years as I grew acclimated to the experimental work required, and Francesca especially started me on the path of the project which I have ended up publishing and defending today. Josh, as my graduate cohort and longest-serving lab mate, along with Ben oftentimes provided emotional support when experimental progress was slow or frustrating and I thank him for that. Arjun joined the lab at a time when I had really transitioned from trainee to teacher in our project and I appreciate our extensive conversations about all things research and life in general on slow lab days. Finally, I owe Thomas some of the most significant thanks for doing the most lab work of late as I have been writing this dissertation. He has been invaluable to keeping the research progress going while my focus has mostly been elsewhere.

I would also like to express my greatest appreciation for the friends and support systems I have made in graduate school outside of the lab. Dr. Caleb Jones and Dr. Carson Reed were some of the first close friends I had through our classes together and I still reminisce about the Friday lunch hours and occasional coffee breaks over the years. Dr. Caleb Fast provided some much-needed steady ground over the years and I thank him for the occasional dinner invitation and “backyard” chats. Dr. Benjamin Mueller has always been a welcome presence in the lab to talk about sports of any kind, and more recently weather of any kind, and I am glad to have stayed close to him and Dr. Jenna DeSousa as their lives together progress. I could not have done any of this without non-graduate school friends either and my special thanks go to Sophia Pannullo and Bowie, with whom I spent many wonderful afternoons and got more exercise than I could have hoped for.

Most of all, I would like to thank my family for all their support throughout this process and my whole life. I am lucky to have never been far from home and have my mother and father both be able to visit when wanted or needed. Graduate school has been a stressful time, but they have been there for me through it all, expressing their support and concern and never questioning my decisions or desires. I never thought an apartment would be a good place for Thanksgiving, but much thanks goes to my brother for suggesting it and being willing to sleep on the couch just to see me. I must thank my more extended family and Erick Backus as well for their support in all aspects to lift me up through the past seven years and push toward the next chapter of my life.

Table of Contents

List of Figures

List of Tables

List of Equations

List of Abbreviations

12mer	12-base pair DNA oligonucleotide
AP-12mer	12-base pair DNA oligonucleotide containing an internal AP site
A_x/λ_x	absorbance measurement at wavelength *x* nm
AU	absorbance units
A	adenine
A/C	Adriamycin/Cyclophosphamide
ARP	aldehyde reactive probe
AGT	alkylguanine DNA transferase
THF-12mer	analog of the AP-12mer with a stable tetrahydrofuran (THF) in place of the AP site
AP	apurinic or apyrimidinic
API	atmospheric pressure ionization
BER	base excision repair
HN2	bis(2-chloroethyl)methylamine (mechlorethamine; nitrogen mustard)
CT-DNA	calf thymus DNA
G-12mer	canonical sequence of the modified uracil-containing 12mer
ΔAbs	change in absorbance for T_m studies
ΔT_m	change in melting temperature
CID	collision-induced dissociation

t_0	control sample or “zero” time-point for reactions
COSY	correlation spectroscopy
C	cytosine
DAU	Daunorubicin
dA	2’-deoxyadenosine
dC	2’-deoxycytidine
dG	2’-deoxyguanosine
dR	2’-deoxy-D-ribose
dT	2’-deoxythymidine
DNA	deoxyribonucleic acid
dsDNA	double-stranded DNA
DOX	Doxorubicin (Adriamycin)
DOXol	Doxorubicinol
EC_{50}	effective concentration of drug required to induce scission in 50% of the AP-12mer oligonucleotide (10 µM)
ESI	electrospray ionization
ELISA	enzyme-linked immunosorbent assay
EPI	Epirubicin
EPIol	Epirubicinol
EDTA	ethylenediaminetetraacetic acid
FAPY	formamidopyrimidine
FA	formic acid
G	guanine

HSQC	heteronuclear single quantum coherence
HPLC	high performance liquid chromatography
hOGG1	human 8-oxoguanine DNA N-glycosylase 1
hNEIL1	human endonuclease VIII-like 1
HEPES	4-(2-hydroxyethyl)-1-piperazineethanesulfonic acid
HMCES	hydroxymethylcytosine-binding protein
LC	liquid chromatography
ICL	inter- or intra-strand crosslink
$^{13}C_5$-dR	2-deoxy-D-ribose isotopically enriched with ^{13}C at all five Carbons
MS	mass spectrometry
m/z	mass-to-charge ratio
MTX	Mitoxantrone
mwc	molecular weight cutoff
NM	nitrogen mustard
NNM	nor-nitrogen mustard
idSp	notation for the THF spacer in the THF-12mer
NMR	nuclear magnetic resonance
nt	nucleotide
NER	nucleotide excision repair
pDNA/DNAp	oligonucleotide sequences with terminal phosphates at the noted positions
8-oxo-dG	8-oxo-2’-deoxyguanosine

[M]	parent compound for MS CID fragmentation
PIX	Pixantrone
PMOA	*o*-(pyridin-3-ylmethyl)hydroxylamine
RNS	reactive nitrogen species
ROS	reactive oxygen species
$1e^-$	single-electron oxidation
$1H^+$	single-proton reduction
ssDNA	single-stranded DNA
SPE	solid phase extraction
T_m	temperature at which the rate of change in absorbance for a dsDNA oligonucleotide is the greatest (melting temperature); also used to denote thermal melting analysis
THF	tetrahydrofuran
T	thymine
Tris	tris(hydroxymethyl)aminomethane
$2e^-$	two-electron oxidation
$2H^+$	two-proton reduction
UPLC	ultra performance liquid chromatography
UV	ultraviolet
U/mU	units/milliunits based on enzyme specifications
U	uracil
UDG	uracil DNA glycosylase
λ_{max}	wavelength of maximum absorbance values

Chapter I

Introduction

Background

Cancer as a research topic is difficult to define due to the broad spectrum of understood causes, effects, and interactions in today's scientific sphere. The NCI[1] defines cancer as "[…] a disease in which some of the body's cells grow uncontrollably and spread to other parts of the body," while the WHO[2] defines it as "[…] a large group of diseases that can start in almost any organ or tissue of the body when cells grow uncontrollably, go beyond their usual boundaries to invade adjoining parts of the body and/or spread to other organs." These definitions lack any mention of causes or biological indicators other than those that can be directly observed because there is no true commonality among diagnoses. The irregularities that lead to uncontrolled cell proliferation are typically understood to be genetic mutations that permanently turn "on" cell replication processes or turn "off" the processes that terminate them, but genetic abnormalities are caused by any number of biochemical factors all along the DNA replication, transcription, and translation processes as well as by outside influence through epigenetic modification. One can dive into ever-narrowing definitions that seek to isolate the root causes of cancer, but we ultimately reach the simplest basis of cell biology wherein biochemical damage to DNA at the structural level affects all subsequent pathways.

The simplest forms of structural damage to DNA are typically those arising from intrinsic errors during DNA replication and repair whereby incorrect base pairings or ribonucleotides are inserted and allowed to persist within the genetic structure. Chemically, DNA can be modified in a multitude of ways ranging from simple alkylation or oxidation to complete loss of the bases (C, T, A, and G) that make up the nucleic acid structure. This is usually a result of interactions of healthy DNA with endogenous or exogenous reactive species. Many forms of damage due to this reactivity are more dangerous to the overall health of cells because enzymes are not typically encoded to recognize the modifications in question. Repair of DNA affected in this way is a significantly less targeted process and tends to be much more error-prone as a result, leading to a buildup of degradation within the overall genetic structure.

The highly chemical environment in which we live today causes us to be exposed to an ever-increasing variety of damaging toxicants, and the practical irreversibility of cancer induction means that we are more susceptible than ever to the effects of such processes. Our main courses of action in treatment involve either excising the affected cells before they can permeate other systems or attempting to kill them more rapidly than they can replicate. For nearly a century now, the latter method has been dominated by the field of “chemotherapy”, or chemically induced cell death. This is a relatively untargeted process where the chemicals in question are administered directly to surface tumors if possible, or more generally throughout the body if not. The hope is that there is an effective dose where healthy cells will be able to correctly repair a significant portion of the induced damage, but cancerous cells will lack the necessary mechanisms to do so, thus eliminating them from the body and allowing the patient to recover over time.

Historically, chemotherapy has been used in combination with other forms of treatment due to the extreme physical toll on the human body. Solid tumors in particular are most easily treated by chemotherapy to reduce their size before surgically removing the remainder of the tumor cells, both avoiding extended chemical treatment and minimizing organ or tissue loss from surgery. Due to the untargeted nature of most chemotherapeutic drugs, they are unlikely to kill tumor growths completely on their own because their mechanisms of action cannot take into account all methods of cancer induction. As research methods improved along with understanding of biochemical processes, the details of antineoplastic drugs' interactions with cellular mechanisms were rapidly elucidated, allowing for more intentionally designed treatment regimens. With a growing number of compounds showing clinical use in tumor treatment through a variety of methods, combination chemotherapies utilizing two or more effective drugs in limited doses emerged as more effective, lower risk protocols than single-drug treatments.

Of all the potential combinations of compounds, one of the first to see clinical success is still a commonly used chemotherapeutic regimen to this day. The co-treatment of Doxorubicin (also known as Adriamycin) and Cyclophosphamide, called A/C chemotherapy, is specifically used in patients with primary breast cancer and in some cases those with slightly more advanced stages of the disease. The compounds comprising this treatment regimen are well-studied and thought to function through independent biochemical mechanisms. However, interactions of the two compounds with biological damage profiles created by the other are relatively under-studied, and additional mechanisms of action could contribute to the efficacy of modifications to this treatment regimen.

Antineoplastic Chemicals and their DNA Damage Profiles

Nitrogen Mustards form N^7-dG Adducts that Result in Various DNA Crosslinks

The discovery that mustard gases used as chemical weapons during World War I exhibited therapeutic potential against leukemias gave rise to studies in treating cancer chemically[3]. Although mustard gas, bis(2-chloroethyl)sulfide, proved too toxic to be used as a clinical treatment, the related derivative nitrogen mustard, bis(2-chloroethyl)methylamine (mechlorethamine, **HN2**), was developed as the first chemotherapy drug and underwent initial trials beginning in 1942[4,5]. Mechlorethamine itself has since been discontinued as a treatment option due to high levels of toxicity, but many alternatives, such as those shown in **Figure 1-01**, were developed in successive years and are still widely used in cancer treatment[6,7].

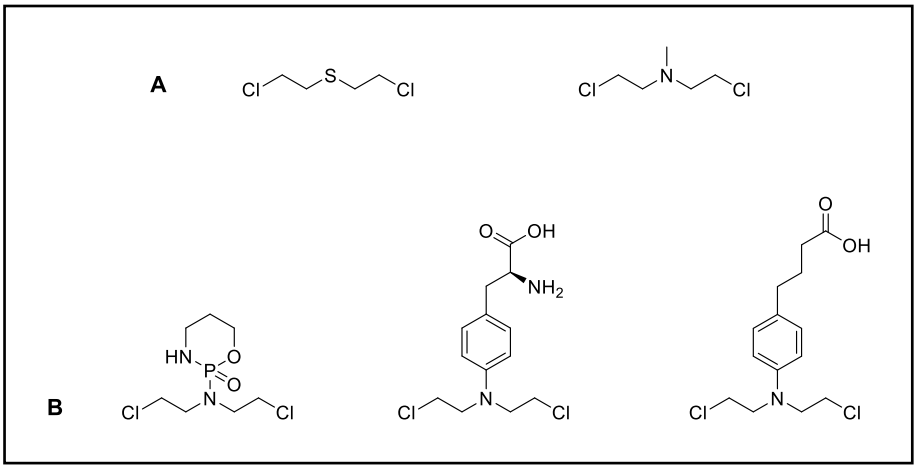

Figure 1-01. (A) Initial mustards used in clinical trials: mustard gas (left) and mechlorethamine (right). (**B**) Currently used nitrogen mustard derivatives (from left to right) Cyclophosphamide, Melphalan, and Chlorambucil.

The class of compounds known as nitrogen mustards are characterized as bis- or tris-electrophiles (typically [2-chloroethyl]amines) and are known to nonspecifically alkylate DNA at its various nucleophilic sites. It was shown early on that their reactivity was dependent on self-cyclization to form reactive aziridinium species before further reaction with nucleophiles[3–5,8,9]. These nearly planar, highly electrophilic small molecules are optimal for reaction with the structurally constrained amines that compose nucleic acids. The most common products of mustard reactions with DNA are cationic N^7-dG adducts due to the relative nucleophilicity of the N^7 position of guanine[5,8]. Such reactions result in a variety of lesions (**Fig. 1-02**) including, but not limited to, deglycosylation, inter-/intra-strand crosslinks (ICLs), and N^7-formamidopyrimidine (FAPY) adducts[5,8,10–16]. Each of these products has been studied extensively and linked to cytotoxicity in proliferating cell lines through independent mechanisms.

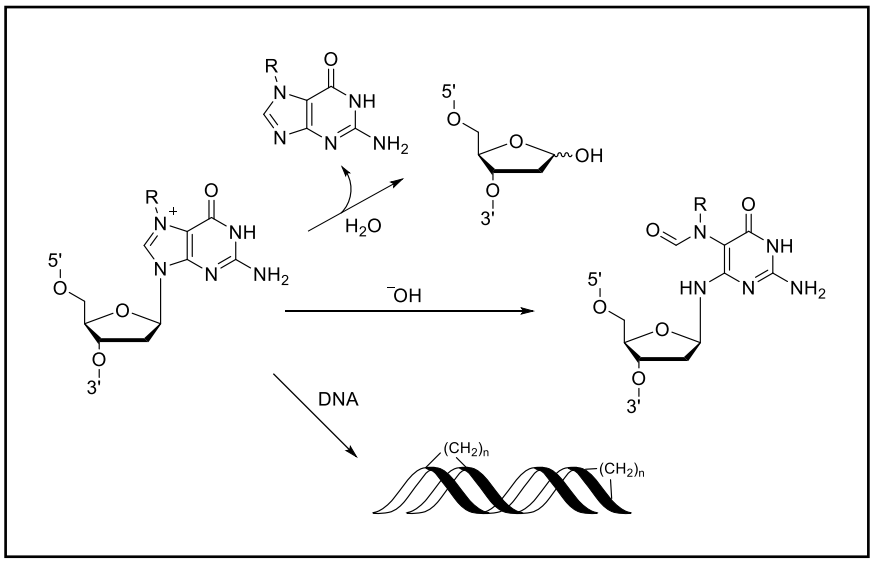

Figure 1-02. Secondary products of DNA alkylation damage (top to bottom); AP site formation from deglycosylation, N^7-FAPY-dG, and inter-/intra-strand DNA crosslinking.

The most prevalent of these lesions, but the ones largely assumed to be the least toxic, are the cationic N^7-dG adducts. These are known to form via reactions with a variety of DNA alkylating agents such as aflatoxin, butadiene, and ethylene oxide (**Fig. 1-03**), but are unstable and prone to hydrolysis involving loss of the modified base[17–19]. This process (also referred to as deglycosylation) results in relatively non-toxic free N^7-G residues that are processed and excreted by the body while leaving an apurinic/apyrimidinic (AP) site within the DNA. AP sites are a naturally occurring result of ongoing DNA replication and repair and are perhaps the most common form of DNA damage[20–22]. There are highly efficient enzymatic processes to repair AP sites by inserting the correct nucleotide in healthy cells via both BER and NER pathways, thus the long-standing consensus that hydrolytically unstable N^7-dG adducts are relatively non-toxic in the absence of high levels of alkylating agents[21,23,24]. This is likely one reason that the nitrogen mustards have seen broad use as chemotherapeutic agents. As with many antineoplastic chemicals, the mustards do not specifically target tumor cells, but the induction of AP sites and inter-strand crosslinks (as well as some of the more minor byproducts of DNA alkylation) at high levels in cells lacking the necessary repair mechanisms is much more cytotoxic than it would be in healthy cells. This induced damage leads to rapid cell death, whereas in healthier lines the cells that survive can gradually repair the damage done with relatively little error.

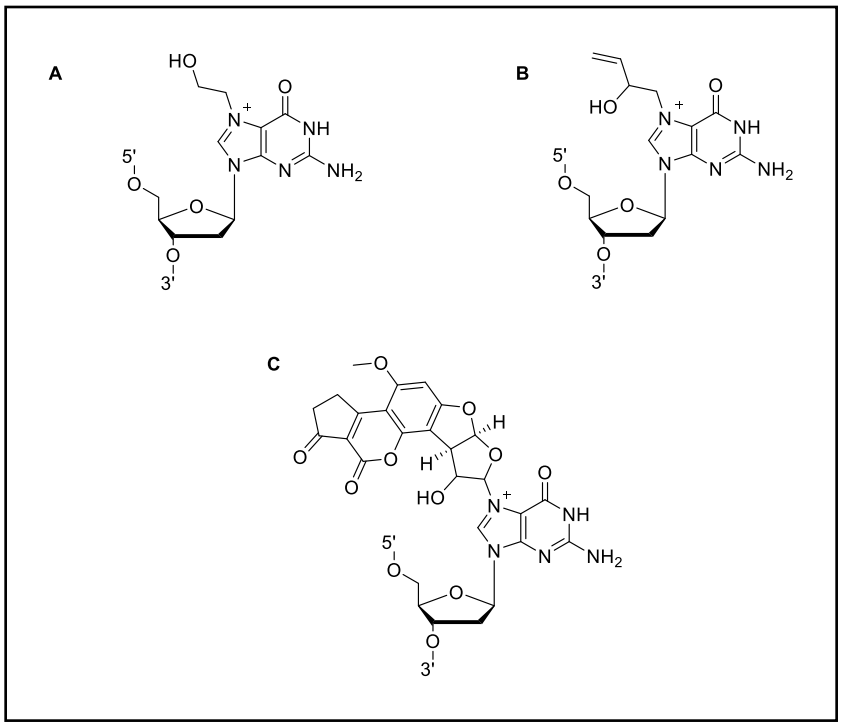

Figure 1-03. Common N^7-dG adducts resulting from exposure to environmental toxins **(A)** ethylene oxide, **(B)** 1,4-butadiene, and **(C)** aflatoxin.

Methods have been developed over the years seeking to quantify the levels of AP sites present naturally and through chemical induction. Many of these seem to involve isotope- or radio-labeling for secondary identification of modified aldehydes, but such methods are expensive for any sort of high throughput experimentation. The most common methods for many years were colorimetric ELISA-type assays utilizing biotin modifications for pull-down isolation[20,25]. This aldehyde reactive probe (ARP) is commercially available, but is non-specific to AP sites and not significantly sensitive for analytical quantitation. Shown in **Figure 1-04**, modification of the ARP theory by the Turesky lab to utilize a small molecule that is highly reactive toward AP sites as a sort of "label" coupled with LC/MS^2 analysis of post-reaction DNA digestion products allowed for both detection and quantitation of steady-state AP site levels with high sensitivity[22]. Recent improvements upon this methodology have further increased the sensitivity of detection while minimizing artifactual generation of "labeled" AP sites during sample processing[26]. The most recent assessment of background levels of AP sites in rat liver gave values of <1 in 10^7 nts, a significant decrease from estimates of 8-9 per 10^6 nts produced by the ARP method. This level rose to about 6.5 AP sites per 10^7 nts under conditions used for neutral hydrolysis experiments, which is still significantly low to be of any concern biologically. This methodology proved effective at measuring induced AP sites as well, as testing with nor-nitrogen mustard (NNM) in rat liver yielded a linear dose-dependent increase over a concentration range of 3-100 μM drug, peaking at ~200 sites per 10^6 nts. This both provided further confirmation of the main DNA damage product of NM treatment and allowed for much more accurate identification of the extent of this damage at various dose levels.

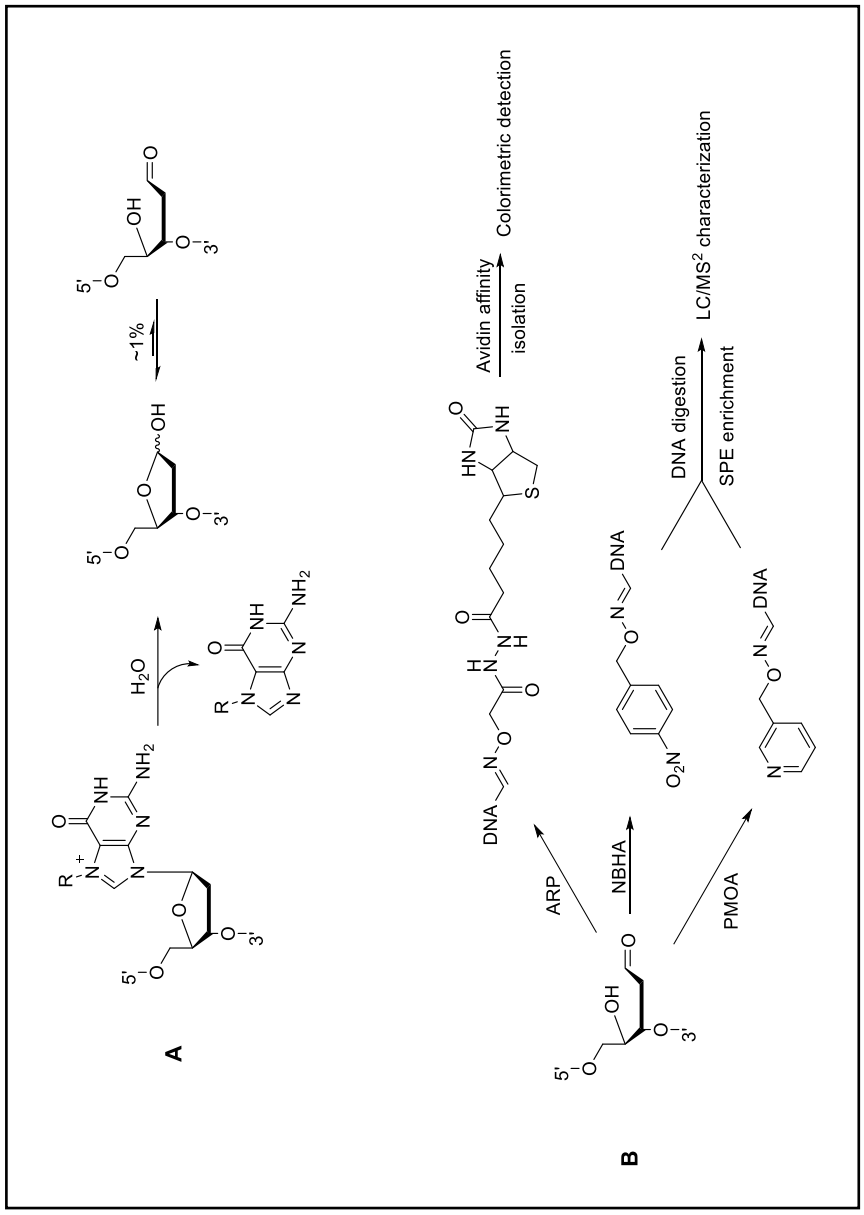

Figure 1-04. (A) AP sites exist in a natural equilibrium between the ring-closed hydroxy-furan (~99%) and the ring-opened aldehyde (~1%). **(B)** Quantitative analysis of AP sites is performed via formation of stable covalent adducts upon reaction with strongly nucleophilic compounds optimized for isolation and detection.

AP Sites are Susceptible to Further Reactivity that is More Damaging than their Presence Alone

One aspect of AP site generation that has been relatively under-explored in terms of its effect from chemotherapeutic treatment is their potential stability and reactivity. As mentioned, there are normally highly efficient repair processes to recognize and remediate damage from DNA alkylation. In instances where this is not the case or the damage is for some reason bypassed by repair enzymes, AP sites that persist can interact with any number of reactive nucleophiles. The ring-opened aldehydic form of the sugar only exists at about 1% abundance in equilibrium with the ring-closed form but is a reactive electrophilic species, something that is not typically found among the many biomolecules that make up our cells. In fact, many of the reactive sites on DNA, proteins, and other cellular components are actually *nucleophilic*, raising the possibility that they will covalently bind to persistent AP sites if allowed to interact.

In 2014, the Gates group at the University of Missouri provided evidence that dA residues opposing AP sites (offset one nt to the 3'-terminus) formed a stable covalent adduct through formation of an imine bond with the exocyclic N^6-amine[27,28] (**Fig. 1-05 A**). Three years later, Admiraal and O'Brien[29] reported similar observations with AP sites present at the 5'-terminus of "nicked" DNA, an intermediate of the BER pathway. These more translationally and rotationally free versions were able to form adducts with free nucleophiles and amines on the adjacent nucleotide of the fragmented oligonucleotide as well as those on the opposing strand, but these products were significantly less stable than those formed with an internal AP site. In 2019, two independent studies[30,31] reported the discovery that protein sequences containing terminal cysteine residues were able to

covalently bind AP sites, forming semi-stable thiazolidine functionalities (**Fig. 1-05 B**). This DNA protein crosslink was actually found to be protective against further DNA damage by preventing reactions that would normally cleave the DNA strand in two. Such interactions were subsequently shown to occur at non-terminal cysteine residues through formation of a stable thioacetal[32], suggesting a prominent form of both DNA and protein damage that is yet unstudied.

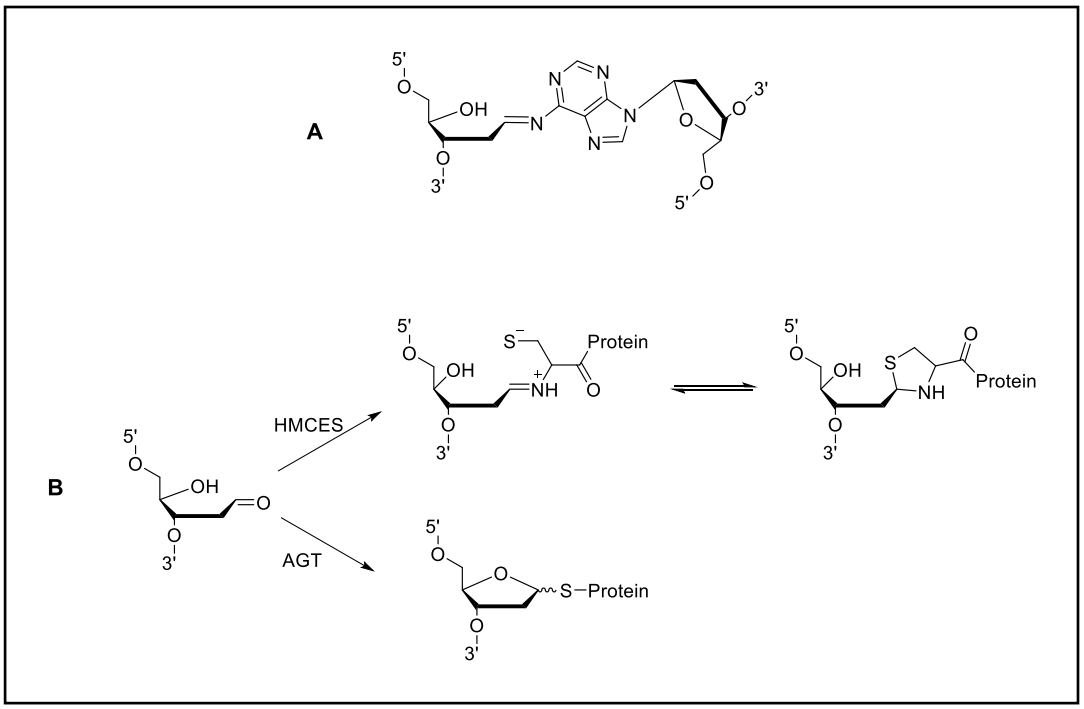

Figure 1-05. (A) Structure of the naturally forming AP-dA DNA inter-strand crosslink. **(B)** Recently discovered DNA-protein crosslinks between 5-hydroxymethylcytosine-binding protein (HMCES) and alkylguanine DNA-transferase (AGT) arising from interactions of AP sites with cysteine residues.

As mentioned, 3'-terminal AP sites are known intermediates of the BER pathway through breakage of the phosphate backbone. This DNA scission can occur both enzymatically and chemically, but failure to re-anneal the broken strand correctly can result in DNA single- or double-strand breaks which are subject to highly inefficient repair processes and can quickly result in cell death. Enzymatic processes that incise DNA strands are part of normal regulatory function and can occur both with healthy DNA and to excise damaged bases as is seen with AP sites. Chemically-induced DNA scission, however, is a wholly unregulated process that occurs largely at AP sites. Formation of the hydrolytically unstable Schiff base intermediate seen in all previously outlined examples also increases the acidity of the hydrogens at the 2'-position of the sugar. Elimination of the 3' section of the DNA to form an α/β-unsaturated iminium species, termed β-elimination, is thus highly favored and results in a 3'-terminal unsaturated AP site that is not readily recognized or repaired. This species can undergo further δ-elimination to release the fully unsaturated deoxyribose analog and two fragmented strands of DNA separated by a one nucleotide gap. This process is outlined in **Figure 1-06**, and these strand breaks are highly cytotoxic forms of damage and a chemical overload of species that can take advantage of this reactivity would cause irreparable damage via DNA strand scission.

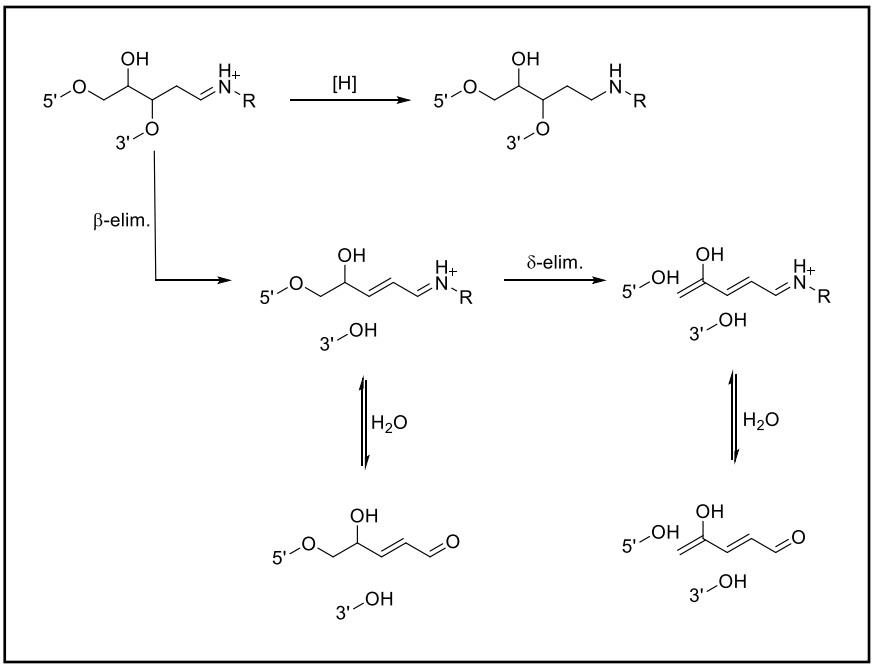

Figure 1-06. Progressive reactions of Schiff bases formed at AP sites upon reduction to the stable amine (top) or scission via β- and δ-elimination on extended existence in solution (bottom).

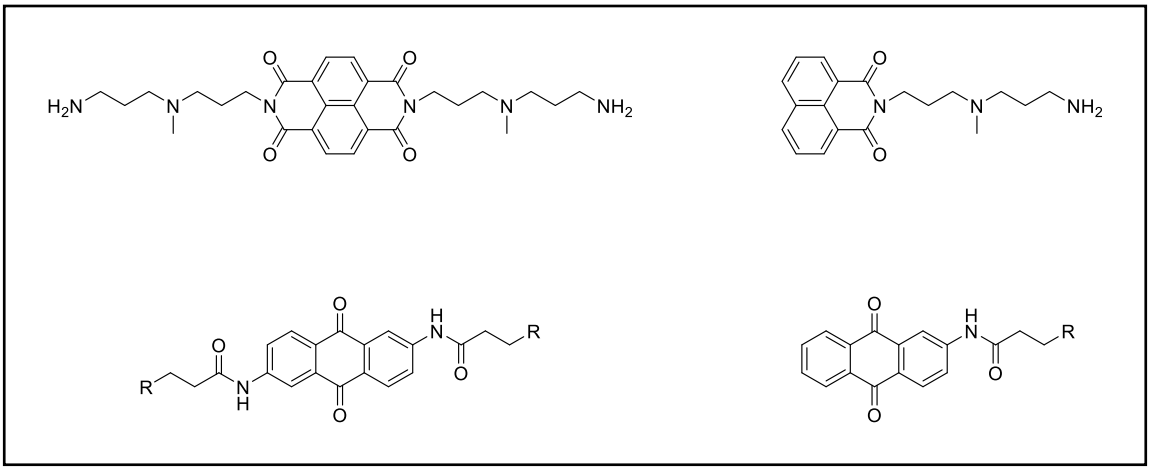

Figure 1-07. General structure of intercalating amines studied by the Dixon group for their ability to induce DNA scission via β- and δ-elimination at AP sites.

Again, this reactivity has been observed with a wide variety of amines with minimal structural requirements in model systems and in cell culture. The Dixon group at Georgia State University published an initial compilation of various polyamine species (**Fig. 1-07**) and their abilities to cleave plasmid DNA at induced AP sites in 1999[33]. This study concluded that while intercalation and a three-carbon spacing between nitrogen atoms most benefitted DNA scission efficiency, the only true requirement for molecules to induce this reactivity is the presence of a second "basic" atom to abstract the α-proton. In an isolated system of simple amines and plasmid DNA, this required the compounds themselves to contain multiple amino groups either on a singular or on separate flexible arms. Biologically, this catalytic activity could be performed by a variety of species with sufficient proton-abstracting ability. A study published by our lab in conjunction with the Lloyd and McCullough groups in 2016[34] found that a series of compounds containing a single nucleophilic amine was able to catalyze the DNA scission. Experiments comparing DNA scission products from this reaction to those of hOGG1 and hNEIL1 (**Fig. 1-08**), human enzymes that specifically catalyze β- and β-/δ-elimination reactions at AP sites, also confirmed that these small molecules produced both products with the β-elimination reaction being favored. Taken together, all of these studies would indicate that induction of an extreme level of AP sites seen from treatment with drugs like nitrogen mustards causes increased susceptibility to secondary reactions that are far more deleterious to DNA but have not been studied in full.

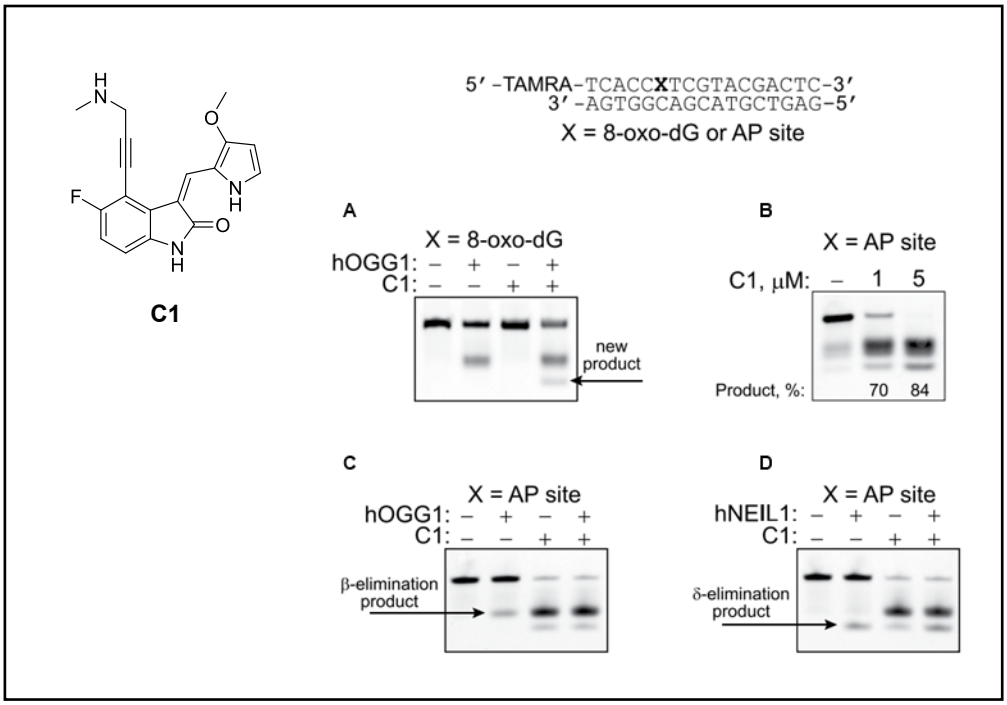

Figure 1-08. Minko et al. observed that amine-containing small molecules induced β- and δ-elimination at AP sites in the DNA oligonucleotide sequence shown above, the most efficient of which was termed **C1**. The enzymes hOGG1 (gels **A/C**; DNA = 250 nM) and hNEIL1 (gel **D**; DNA = 250 nM) are known DNA repair proteins; hOGG1 is a bifunctional enzyme that removes by-products of oxidative damage such as 8-oxo-dG to leave an AP site, then removes the AP site by catalyzing β-elimination whereas hNEIL1 specifically removes AP sites primarily via δ-elimination. Compound **C1** catalyzed both reactions with significant efficiency (gel **B**; DNA = 2 μM) in an enzyme-independent manner (AP sites were generated by reacting DNA with UDG when **X** = uracil).

Anthracyclines are Known Intercalators and Topoisomerase II Inhibitors

In contrast to nitrogen mustards, anthracyclines are understood to cause DNA damage through more indirect interactions. First isolated as natural products in 1964[35] under the category of “Rhodomycins”, certain of the brightly colored compounds were quickly shown to have significant activity against solid tumors. Shown in **Figure 1-09**, Daunorubicin and its 14-hydroxy analog, Doxorubicin[36], were among the earliest group of those identified and were swiftly approved for clinical use. Similar to previously known DNA-interacting chemicals though, the true mechanism of action for the drugs was not clearly elucidated until much later. Early indications were that all of the anthracyclines interacted strongly with nuclear DNA and localized almost exclusively within it, an observation that was not surprising due to the planar, aromatic structure of the compounds that is characteristic of DNA intercalators. The primary assumption for years was that the apparent strength of this interaction likely interfered with DNA processing by preventing the separation of duplex strands, thus inhibiting replication and cell proliferation. It was not until nearly two decades after their initial discovery that the broader scope of this process was elucidated with the advancement of biochemical knowledge and techniques.

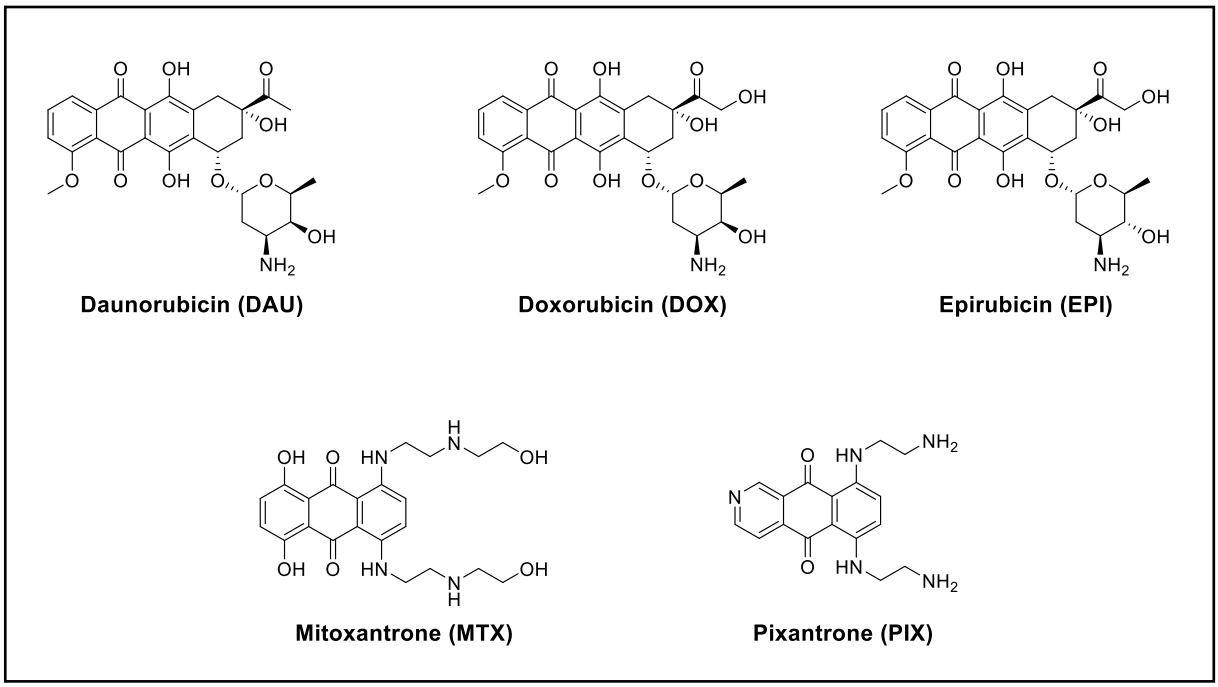

Figure 1-09. Natural and synthetic anthracyclines with significant clinical relevance.

With the mechanistic elucidation of Topoisomerase II and its role in DNA processing in 1983[37], many known DNA-interfering molecules were immediately tested as inhibitors of the enzyme. The function of mammalian DNA Topoisomerase II is to relieve stress built up by DNA supercoiling. As replication enzymes straighten out the double helix structure, tension builds at the processing end of the DNA as the coils tighten. Topoisomerase II relieves this strain by creating transient double strand breaks to allow duplex DNA to “pass through” another portion of the strand, then re-ligation of the strands as they existed before[37–40] (**Fig. 1-10**). A number of follow-up studies in 1984[41,42] found that many DNA intercalating molecules, including the anthracyclines, interfered with this process by inhibiting re-ligation of the transient double strand break. In such cases, a stabilizing effect causes the enzyme to remain covalently bound to the DNA fragments (a trimolecular interaction known as the “cleavable complex”) before dissociating without performing the repair step, leaving a permanent double strand break behind. As outlined with the dangers of AP sites, this type of damage is nearly irreparable on a large scale and highly cytotoxic. This functionally explains why the anthracyclines are optimal chemotherapeutic agents since they will have the greatest impact on highly proliferative cell lines where Topoisomerase II is most active.

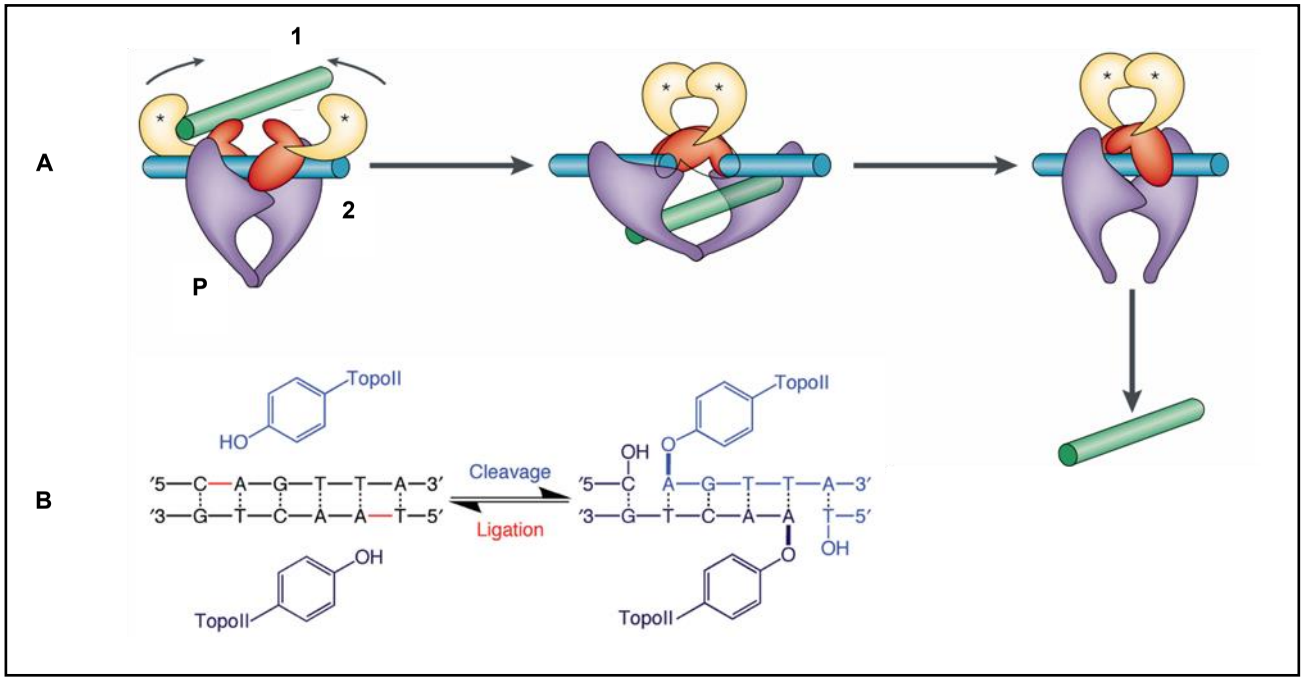

Figure 1-10. Generalized depictions of the mechanism by which Topoisomerase II creates transient double strand breaks within DNA to relieve supercoiling during replication. (**A**) Protein **P** binds two duplexes of DNA (**1** and **2**), nicking duplex **2** to allow duplex **1** to pass through before re-ligating duplex **1** and releasing the DNA as it existed previously. (**B**) The chemical equilibrium between ligated and nicked duplex DNA that exists as it interacts with the active site of Topoisomerase II. The presence of Doxorubicin and other anthracyclines significantly stabilizes the “cleavable complex” to the right of this equilibrium, preventing re-ligation of the duplex and eventually resulting in permanent double strand breaks. Images taken from (**A**) Wang, J.C. (2002) and (**B**) Deweese and Osheroff (2009).

Anthracyclines: Problems and Improvements

Anthracycline Treatment Results in an Increased Chance of Cardiomyopathy

One of the first realizations made upon treating patients with Daunorubicin and Doxorubicin was the visible and highly prevalent cardiac damage in patients over 50 years of age[43,44]. Onset of symptoms was apparently rapid and unexpected, and death occurred within 24 hours of said onset. Originally this was thought to be an acute dosage effect due to the rapidity and surprising nature of the problem, but it is now known that the overall cardiotoxicity of anthracycline-class compounds is due to a lifetime cumulative dose effect. Some symptoms related to this, such as an increased heart rate, express in an acute manner during the course of treatment but stop once the treatment regimen is concluded. This likely contributed to the initial designation as an acute effect, as the treatment schedule for the drug had not been optimized yet and a daily introduction of anthracyclines to the body would have had an extreme effect on those with weaker hearts. Even with a more spaced-out dosing routine, the cumulative effects of the drug on cardiac tissue are permanent and limit the utility of one of the most commonly used chemotherapeutic agents on the market.

Unfortunately, the cause of this deleterious relationship is still not well understood. Unlike the cells that make up tumors, cardiac cells do not replicate and should not be overly sensitive to the DNA-replicative inhibition that these molecules are known to induce. Metabolism of Doxorubicin and other anthracyclines does, however, produce a number of reactive species that could affect cardiac tissue more severely than other organs. Most notably, redox cycling of the anthraquinone core structure that defines these

molecules is known to produce elevated levels of reactive oxygen and reactive nitrogen species (ROS and RNS)[45–47]. These radical molecules are highly reactive and extremely damaging to anything with which they may come into contact, the effects of which may be exacerbated by qualities specific to cardiac function. Additionally, there is strong evidence that anthracyclines localize significantly within cardiac tissue, which serves to further amplify such problems.

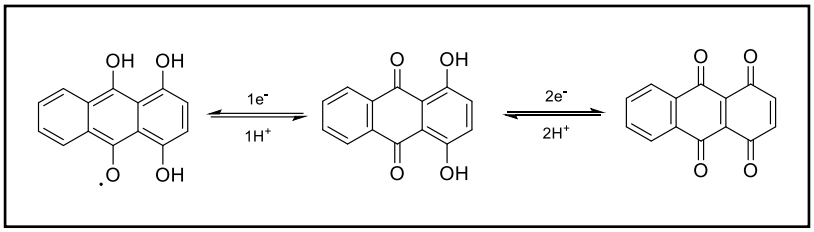

Figure 1-11. Redox cycling of the dihydroxy-anthraquinone core results in increased production of radical species that are highly damaging within cellular environments.

Because many of these factors are, as far as we know, general to all anthracyclines with no clear structural or chemical specificity, focused drug design with the intention of mitigating cardiotoxicity is not feasible. Even though Doxorubicin exhibits some of the highest levels of this, its chemotherapeutic potential has kept it as the main line of treatment for various cancers for 50 years. Current protocols limit patients to a cumulative lifetime dose of the drug above which the risk of cardiomyopathy increases exponentially. Once this dose is reached, nearly all anthracycline derivatives are excluded from further treatment and a new regimen must be found to carry forward, severely limiting the utility of the compounds relative to their potential. The advent of combination chemotherapies in the mid-1970s was of great benefit to Doxorubicin in particular, allowing for the co-treatment with nitrogen mustards via A/C chemotherapy and significantly lowering the required dose for comparable chemotherapeutic effects[48,49]. For now, other methods of improving the efficacy of treatment and lowering necessary dosage amounts appear to be the only method of mitigating the dangerous offsite cardiotoxicity of antineoplastic anthracyclines.

Synthetic Development of new Anthracycline Analogs

Slightly before the groundbreaking discovery of the function of Topoisomerase II, research involving synthetic modification or development of new anthracycline derivatives was accelerating as it does with all medically relevant compounds. The original assumption that the natural product anthracyclines functioned primarily through their intercalative nature provided a baseline for drug design, and nearly all synthetic derivatives developed to this day are structured around an anthraquinone core. The four-ring structure common to the natural product class of anthracyclines was abandoned relatively early for the production of purely synthetic compounds in an attempt to minimize structures to the strictly necessary components, resulting in a new class of 9,10-anthracenediones as a basis for modification as seen in **Figure 1-12**. This scaffold provided for much more straightforward synthetic methodology as exemplified by the abundance of work published by Paul Krapcho from the mid-80s to the mid-90s[50–55]. Identification of the Topoisomerase-dependent mechanism of action for the original anthracyclines allowed for a more guided approach to drug development and led to confirmation that the structurally simplified compounds acted in the same manner.

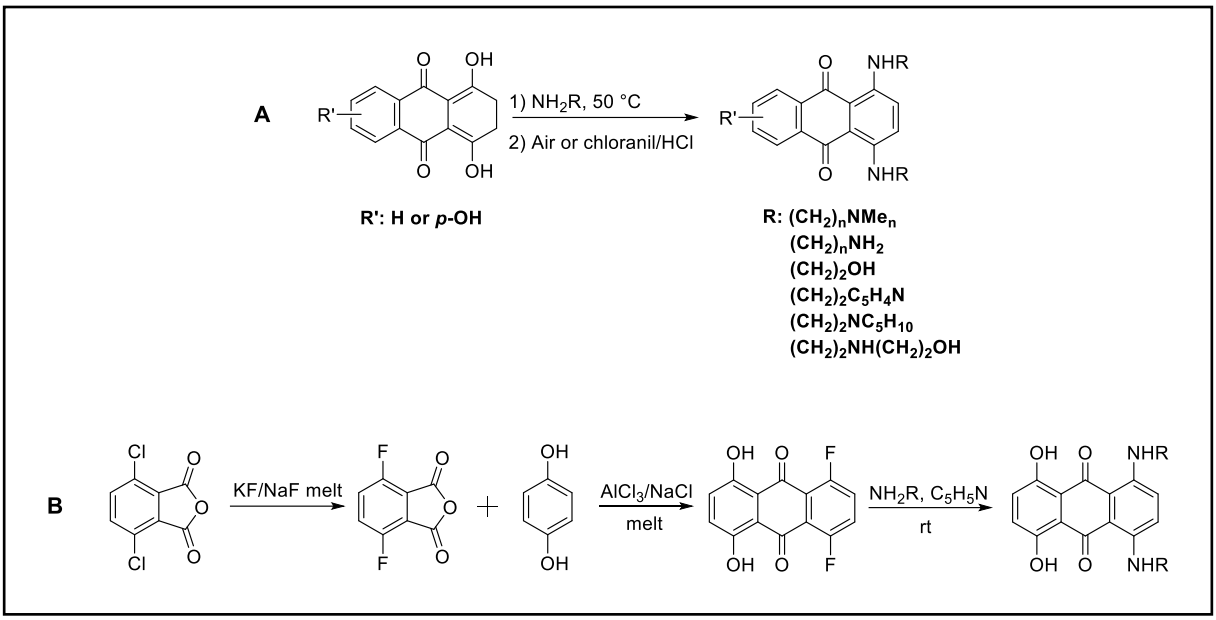

Figure 1-12. Conditions developed by Murdock **(A)** and Krapcho **(B)** for the synthesis of symmetrically and unsymmetrically substituted amino-anthraquinones.

Some of the synthetic derivatives exhibited similar cytotoxic profiles to Doxorubicin and were tested for clinical viability; two of the more promising derivatives became subsequently known as Mitoxantrone (MTX) and Pixantrone (PIX) (**Fig. 1-09**). These compounds are similar in structure, consisting of slightly different variations on the anthraquinone core structure and *para*-substituted alkyl-amine arms on the C ring. Mitoxantrone was among the first 9,10-anthracenedione analogs synthesized and the only one that exhibited significant anti-tumor activity against a wide range of leukemias[56,57]. The early discovery of MTX as an effective Topoisomerase inhibitor was promising for the prospects of replacing Doxorubicin with synthetic analogs due to its apparently less significant induction of cardiomyopathy, but further efforts did not produce a variant with both further reduction of this offsite effect and significant chemotherapeutic potential. MTX itself does not reduce tumor levels as effectively as DOX, and thus was not considered a viable replacement.

Pixantrone was synthesized nearly 10 years later as an investigation into A-ring modifications to the anthraquinone core, particularly creation of the aza-anthracenediones outlined in **Figure 1-13**[52]. This analog exhibited significant activity against L1210 leukemia (nearly equivalent to that of MTX), human colon adenocarcinoma, and P388 murine leukemia, but did not stand out among its class as MTX had in this regard. Where PIX showed promise was in the fact that it appeared to have a much higher lethal dose than other compounds of its class, with significantly elevated survival rates in treated rats than any comparable analog. Additionally, later studies showed much higher tolerable doses of PIX with regards to cardiomyopathic induction compared to DOX or MTX. Intriguingly, Pixantrone also seems to be a relatively

weak inhibitor of Topoisomerase II activity, suggesting an alternative mechanism of action for its chemotherapeutic activity. The details of this are not well understood, which is likely a reason it is not currently approved for clinical use in the US. In Europe, it is used sparingly as a last course of action for non-Hodgkin's lymphoma relapse patients who have already been treated with significant amounts of other anthracyclines[58]. These three compounds more or less embody the sphere of anthracycline-derived drugs that show significant clinical promise with progressive improvement toward mitigating cardiotoxicity.

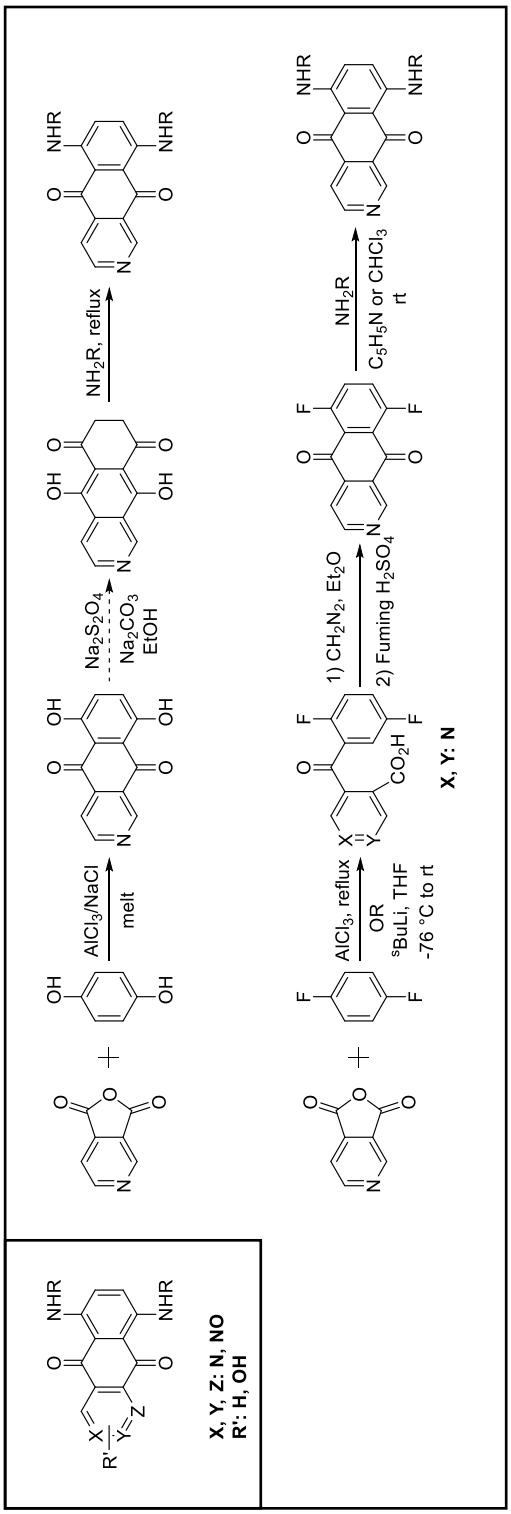

Figure 1-13. Conditions developed by the Krapcho group for the synthesis of isoquinoline amino-anthraquinone analogs.

A Formaldehyde-mediated Covalent Adduct of DOX with DNA shows Improved Efficacy in DOX-resistant cell lines

During structural studies on the interactions of a Daunorubicin analog known simply as MAR70 with DNA, contamination of the crystallization solvent used for X-ray studies with trace amounts of formaldehyde resulted in the fortuitous discovery that a covalent bond formed between the two structures[59]. As shown in **Figure 1-14**, the reactive aldehyde was able to facilitate an interaction between the 3'-amino group on the daunosamine sugar and the exocyclic N^2-amine of a dG residue within the DNA strand. This interaction was subsequently reproduced with both Daunorubicin and Doxorubicin[60], potentially showing the first indications of anthracyclines causing direct DNA damage. The discovery kicked off a new era of research around the amino-glycoside anthracyclines in search of incorporating this new reactivity into drug design. The Koch lab was able to perform experiments with so-called "activated" versions of DAU and DOX, called Daunoform and Doxoform (**Fig. 1-15**), that mimicked this reactivity in a cellular environment and showed that each exhibited improved cytotoxicity over their parent compounds, particularly in Adriamycin-resistant cell lines[61].

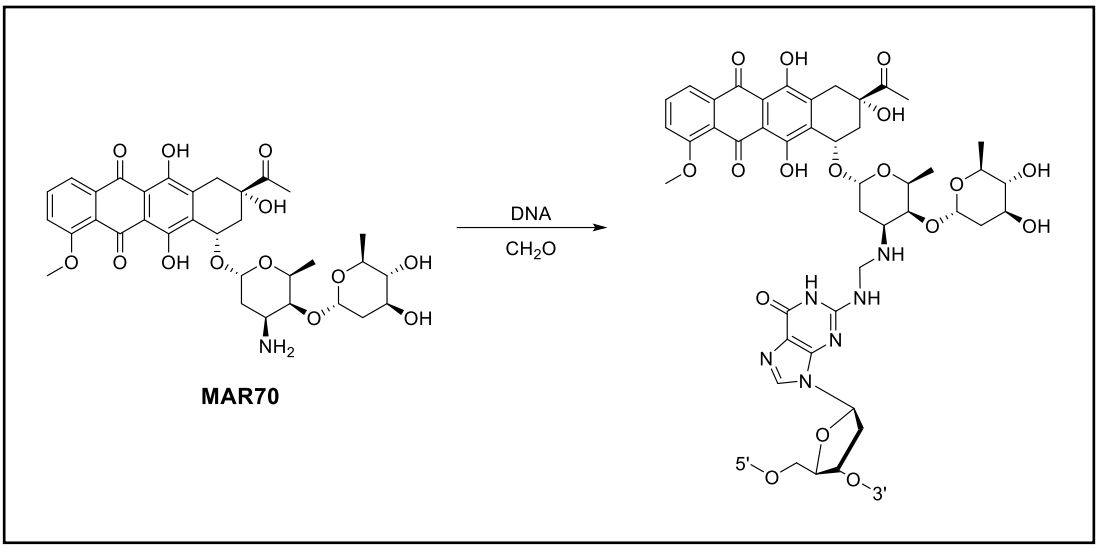

Figure 1-14. The synthetic Doxorubicin derivative **MAR70** forms a semi-stable covalent adduct with N^2-dG via a methylene bridge when crystallized in solvent contaminated with trace amounts of formaldehyde.

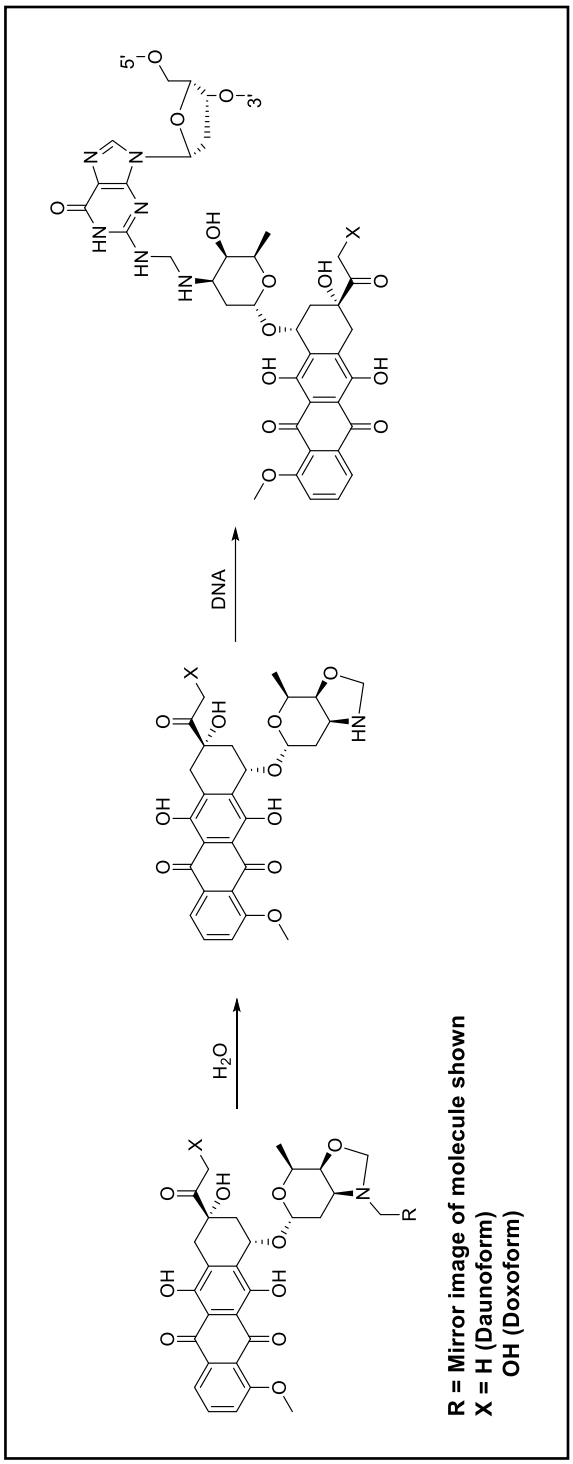

Figure 1-15. *in vitro* reaction of Daunoform and Doxoform to form a covalent N^2-dG adduct identical to the one seen by Gao et al. upon introduction of trace formaldehyde.

It is still unclear whether this reactivity is in any way responsible for the cytotoxicity observed for the parent compounds as the methylene bridge formed by this interaction is readily hydrolyzed and not easily isolated. Modifications to existing compounds that can replicate this, either through direct interactions or cellular activation of a reactive species, could greatly improve upon existing treatment methods and provide an alternative mechanism of cell death. This idea was quickly latched upon and a new portfolio of synthetic analogs (**Fig. 1-16**) was produced. Most of these new analogs contained "masked aldehydes"[61], electrophilic sites that would bind the exocyclic amine of dG without formaldehyde or being susceptible to hydrolytic deactivation. While they are able to readily bind DNA and block transcription, Koch notes that the lability of the methylene bridge is important for the protection of healthy cells since they can slow their growth process and allow the highly toxic lesion to dissociate without resulting DNA damage. The absence of this ability for the other compounds ultimately results in them being non-viable as treatment options due to being overly cytotoxic. Even Daunoform and Doxoform themselves are not true clinical candidates due to the rapid release of formaldehyde, itself a toxic chemical at high cellular concentrations.

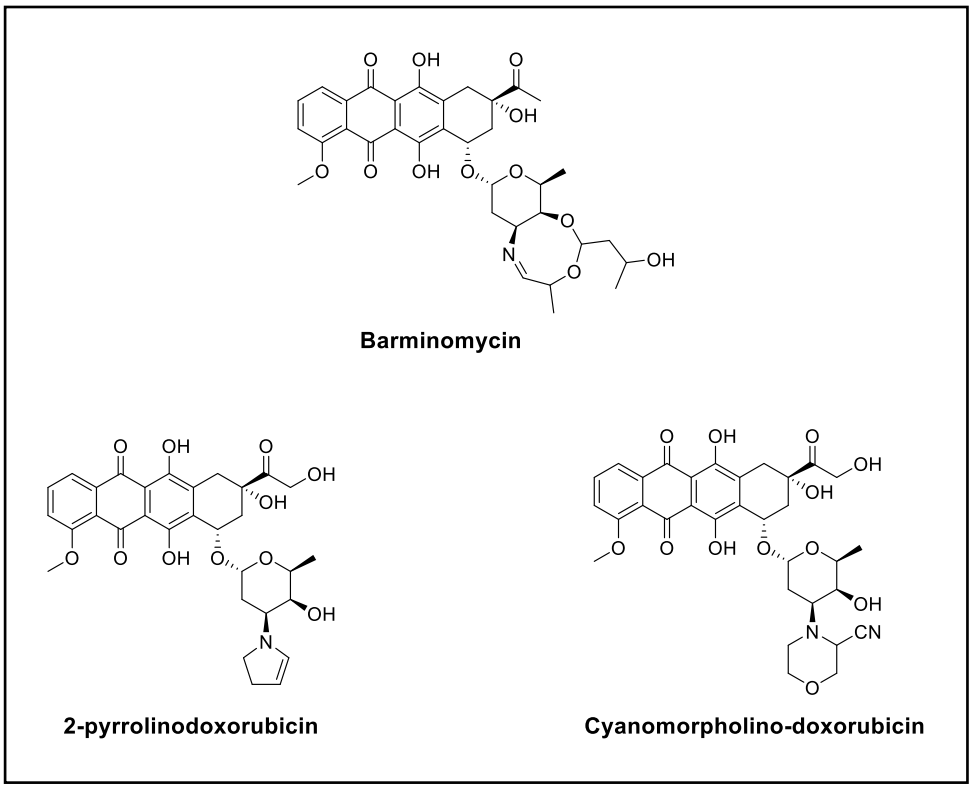

Figure 1-16. Synthetic analogs of Doxorubicin produced with the intention of mimicking the formaldehyde-mediated reactivity that creates a methylene-bridged DOX-dG adduct.

What these studies ultimately provided was evidence that covalent interactions between the anthracyclines and DNA can produce enhanced cytotoxicity at low doses without the need for enzymatic mediation. The problem with accessing this reactivity, as was experienced in the formaldehyde-activation experiments, is that cellular environments are inherently nucleophilic and introduction of nonnatural electrophiles as mediators could result in toxic side effects. However, one of the few persistent biological electrophiles is produced at greatly elevated levels during the course of A/C chemotherapy and is only present within DNA. The realization that AP sites formed through NM treatment are a prime handle for anthracycline alkylation led us to hypothesize that this interaction likely already occurs and could be a significant contributor to the efficacy of this treatment regimen. Due to the lack of significant analytical study around AP sites and a nominal focus on the anthraquinone core of anthracyclines rather than other reactive portions of the molecules, this reactivity has gone unstudied for nearly half a century. Additionally, the structural characteristics of the synthetic analogs MTX and PIX match almost perfectly with those found to be ideal for catalyzing DNA strand scission through β- or β-/δ-elimination at AP sites. If this covalent binding interaction is shown to be a natural product of combinatorial drug treatment and has a measurable impact on non-enzymatic DNA damage, it opens a world of possibility into clinical modification and drug design.

References

(1) *What Is Cancer? - NCI*. https://www.cancer.gov/about-cancer/understanding/what-is-cancer (accessed 2023-07-23).

(2) *Cancer*. https://www.who.int/health-topics/cancer#tab=tab_1 (accessed 2023-07-23).

(3) Gilman, A.; Philips, F. S. The Biological Actions and Therapeutic Applications of the B-Chloroethyl Amines and Sulfides. *Science* **1946**, *103* (2675), 409–415.

(4) Gilman, A. The Initial Clinical Trial of Nitrogen Mustard. *Am. J. Surg.* **1963**, *105*, 574–578.

(5) Brookes, P.; Lawley, P. D. The Reaction of Mono- and Di-functional Alkylating Agents with Nucleic Acids. *Biochem. J.* **1961**, *80*, 496–503.

(6) Antoni, F.; Bernhardt, G. Derivatives of Nitrogen Mustard Anticancer Agents with Improved Cytotoxicity. *Arch. Pharm.* **2021**, *354*.

(7) Singh, R. K.; Kumar, S.; Prasad, D. N.; Bhardwaj, T. R. Therapeutic Journey of Nitrogen Mustard as Alkylating Anticancer Agents: Historic to Future Perspectives. *Eur. J. Med. Chem.* **2018**, *151*, 401–433.

(8) Hemminki, K. DNA-Binding Products of Nornitrogen Mustard, a Metabolite of Cyclophosphamide. *Chem.-Biol. Interactions* **1987**, *61*, 75–88.

(9) Polavarapu, A.; Stillabower, J. A.; Stubblefield, S. G. W.; Taylor, W. M.; Baik, M.-H. The Mechanism of Guanine Alkylation by Nitrogen Mustards: A Computational Study. *J. Org. Chem.* **2012**, *77*, 5914-5921.

(10) Masta, A.; Gray, P. J.; Phillips, D. R. Molecular Basis of Nitrogen Mustard Effects on Transcription Processes: Role of Depurination. *Nucleic Acids Res.* **1994**, *22* (19), 3880–3886.

(11) Cushnir, J. R.; Naylor, S.; Lamb, J. H.; Farmer, P. B.; Brown, N. A.; Mirkes, P. E. Identification of Phosphoramide Mustard/DNA Adducts Using Tandem Mass Spectrometry. *Rapid Communications in Mass Spectrometry* **1990**, *4* (10), 410–414.

(12) Rink, S. M.; Solomon, M. S.; Taylor, M. J.; Rajur, S. B.; Mclaughlin, L. W.; Hopkins, P. B. Covalent Structure of a Nitrogen Mustard-Induced DNA Interstrand Cross-Link: An N^7-to-N^7 Linkage of Deoxyguanosine Residues at the Duplex Sequence 5'-d(GNC). *JACS* **1993**, *115* (7), 2551–2557.

(13) Christov, P. P.; Brown, K. L.; Kozekov, I. D.; Stone, M. P.; Harris, T. M.; Rizzo, C. J. Site-Specific Synthesis and Characterization of Oligonucleotides Containing an N ^{6}-(2-Deoxy-D-*erythro*-pentofuranosyl)-2,6-diamino-3,4-dihydro-4-oxo-5-N-methylformamidopyrimidine Lesion, the Ring-Opened Product from N^7-Methylation of Deoxyguanosine. *Chem. Res. Toxicol.* **2008**, *21* (12), 2324–2333.

(14) Christov, P. P.; Son, K.-J.; Rizzo, C. J. Synthesis and Characterization of Oligonucleotides Containing a Nitrogen Mustard Formamidopyrimidine Monoadduct of Deoxyguanosine. *Chem. Res. Toxicol,* **2014**, *27*, 1610-1618.

(15) Gruppi, F.; Hejazi, L.; Christov, P. P.; Krishnamachari, S.; Turesky, R. J.; Rizzo, C. J. Characterization of Nitrogen Mustard Formamidopyrimidine Adduct Formation of Bis(2-chloroethyl)ethylamine with Calf Thymus DNA and a Human Mammary Cancer Cell Line. *Chem. Res. Toxicol.* **2015**, *28*, 1850–1860.

(16) Gates, K. S. The Chemical Reactions of DNA Damage and Degradation. Chapter 8 in *Reviews of Reactive Intermediate Chemistry*; **2007**; pp 333–378.

(17) Gates, K. S.; Nooner, T.; Dutta, S. Biologically Relevant Chemical Reactions of N^7-Alkylguanine Residues in DNA. *Chem. Res. Toxicol.* **2004**, *17* (7), 840–856.

(18) Alekseyev, Y. O.; Hamm, M. L.; Essigmann, J. M. Aflatoxin B_1 Formamidopyrimidine Adducts Are Preferentially Repaired by the Nucleotide Excision Repair Pathway *in vivo*. *Carcinogenesis* **2004**, *25* (6), 1045–1051.

(19) Boysen, G.; Pachkowski, B. F.; Nakamura, J.; Swenberg, J. A. The Formation and Biological Significance of N^7-Guanine Adducts. *Mutation Res.* **2009**, *678*, 76–94.

(20) Atamna, H.; Cheung, I.; Ames, B. N. A Method for Detecting Abasic Sites in Living Cells: Age-Dependent Changes in Base Excision Repair. *PNAS* **2000**, *97* (2), 686-691.

(21) Boiteux, S.; Guillet, M. Abasic Sites in DNA: Repair and Biological Consequences in *Saccharomyces cerevisiae*. *DNA Repair* **2004**, *3*, 1–12.

(22) Roberts, K. P.; Sobrino, J. A.; Payton, J.; Mason, L. B.; Turesky, R. J. Determination of Apurinic/Apyrimidinic Lesions in DNA with High-Performance Liquid Chromatography and Tandem Mass Spectrometry. *Chem. Res. Toxicol.* **2006**, *19*, 300–309.

(23) Mccullough, A. K.; Sanchez, A.; Dodson, M. L.; Marapaka, P.; Taylor, J.-S.; Lloyd, R. S. The Reaction Mechanism of DNA Glycosylase/AP Lyases at Abasic Sites. *Biochemistry* **2001**, *40* (2), 561–568.

(24) Esadze, A.; Rodriguez, G.; Cravens, S. L.; Stivers, J. T. AP-Endonuclease 1 Accelerates Turnover of Human 8-Oxoguanine DNA Glycosylase by Preventing Retrograde Binding to the Abasic-Site Product. *Biochemistry* **2017**, *56*, 1974–1986.

(25) Kubo, K.; Ide, H.; Wallace, S. S.; Kow, Y. W. A Novel, Sensitive, and Specific Assay for Abasic Sites, the Most Commonly Produced DNA Lesion. *Biochemistry* **1992**, *31* (14), 3703–3708.

(26) Chen, H.; Yao, L.; Brown, C.; Rizzo, C. J.; Turesky, R. J. Quantitation of Apurinic/Apyrimidinic Sites in Isolated DNA and in Mammalian Tissue with a Reduced Level of Artifacts. *Anal. Chem.* **2019**, *91*, 7403–7410.

(27) Nejad, M. I.; Johnson, K. M.; Price, N. E.; Gates, K. S. A New Cross-Link for an Old Cross-Linking Drug: The Nitrogen Mustard Anticancer Agent Mechlorethamine Generates Cross-Links Derived from Abasic Sites in Addition to the Expected Drug-Bridged Cross-Links. *Biochemistry* **2016**, *55*, 7033–7041.

(28) Price, N. E.; Catalano, M. J.; Liu, S.; Wang, Y.; Gates, K. S. Chemical and Structural Characterization of Interstrand Cross-Links Formed between Abasic Sites and Adenine Residues in Duplex DNA. *Nucleic Acids Res.* **2015**, *43* (7), 3434–3441.

(29) Admiraal, S. J.; O'Brien, P. J. Reactivity and Cross-Linking of 5′-Terminal Abasic Sites within DNA. *Chem. Res. Toxicol.* **2017**, *30*, 1317–1326.

(30) Chan, W.; Ham, Y.-H.; Jin, L.; Wai Chan, H.; Wong, Y.-L.; Chan, C.-K.; Chung, P.-Y. Quantification of a Novel DNA−Protein Cross-Link Product Formed by Reacting Apurinic/Apyrimidinic Sites in DNA with Cysteine Residues in Protein by Liquid Chromatography-Tandem Mass Spectrometry Coupled with the Stable Isotope-Dilution Method. *Anal. Chem.* **2019**, *91*, 4987–4994.

(31) Thompson, P. S.; Amidon, K. M.; Mohni, K. N.; Cortez, D.; Eichman, B. F. Protection of Abasic Sites during DNA Replication by a Stable Thiazolidine Protein-DNA Cross-Link. *Nat. Struct. Mol. Biol.* **2019**, *26*, 613–618.

(32) Ghodke, P. P.; Matse, J. H.; Dawson, S.; Guengerich, F. P. Nucleophilic Thiol Proteins Bind Covalently to Abasic Sites in DNA. *Chem. Res. Toxicol.* **2022**, *35*, 1805-1808.

(33) Steullet, V.; Edwards-Bennett, S.; Dixon, D. W. Cleavage of Abasic Sites in DNA by Intercalator-Amines. *Bioorg. Med. Chem.* **1999**, *7*, 2531–2540.

(34) Minko, I. G.; Jacobs, A. C.; de Leon, A. R.; Gruppi, F.; Donley, N.; Harris, T. M.; Rizzo, C. J.; Mccullough, A. K.; Lloyd, R. S. Catalysts of DNA Strand Cleavage at Apurinic / Apyrimidinic Sites. *Scientific Reports* **2016**, *6*, 28894.

(35) Di Marco, A.; Gaetani, M.; Orezzi, P.; Scarpinato, B. M.; Silvestrini, R.; Soldati, M.; Dasdia, T.; Valentini, L. 'Daunomycin', a New Antibiotic of the Rhodomycin Group. *Nature* **1964**, *201*, 706–707.

(36) Di Marco, A.; Gaetani, M.; Scarpinato, B. Adriamycin; Antibiotic with Antitumor Activity. *Cancer Chemotherapy Rep.* **1969**, *53* (1), 33–37.

(37) Liu, L. F.; Rowe, T. C.; Yang, L.; Tewey, K. M.; Chen, G. L. Cleavage of DNA by Mammalian DNA Topoisomerase II*. *J. Biol. Chem.* **1983**, *258* (24), 15365–15370.

(38) Berger, J. M.; Gamblin, S. J.; Harrison, S. C.; Wang, J. C. Structure and Mechanism of DNA Topoisomerase II. *Nature* **1996**, *379*, 225–232.

(39) Wang, J. C. Cellular Roles of DNA Topoisomerases: A Molecular Perspective. *Nature Reviews* **2002**, *3*, 430–440.

(40) Deweese, J. E.; Osheroff, N. The DNA Cleavage Reaction of Topoisomerase II: Wolf in Sheep's Clothing. *Nucleic Acids Res.* **2009**, *37* (3), 738–748.

(41) Tewey, K. M.; Chenb, G. L.; Nelsonf, E. M.; Lius, L. F. Intercalative Antitumor Drugs Interfere with the Breakage-Reunion Reaction of Mammalian DNA Topoisomerase II*. *J. Biol. Chem.* **1984**, *259* (14), 9182–9187.

(42) Tewey, K. M.; Rowe, T. C.; Yang, L.; Halligan, B. D.; Liu, L. F. Adriamycin-Induced DNA Damage Mediated by Mammalian DNA Topoisomerase II. *Science* **1984**, *226*, 466–468.

(43) Smith, B. Damage to the Intrinsic Cardiac Neurones by Rubidomycin (Daunorubicin). *Brit. Heart J.* **1969**, *31*, 607–609.

(44) Bonadonna, G.; Monfardini, S. Cardiac Toxicity of Daunorubicin. *The Lancet* **1969**, 837–838.

(45) Peters, J. H.; Gordon, G. R.; Kashiwase, D.; Lown, J. W.; Yen, S-F.; Plambeck, J. A. Redox Activities of Antitumor Anthracyclines Determined by Microsomal Oxygen Consumption and Assays for Superoxide Anion and Hydroxyl Radical Generation. *Biochem. Pharmacol.* **1986**, *35* (8), 1309–1323.

(46) Ma, W.; Wei, S.; Zhang, B.; Li, W. Molecular Mechanisms of Cardiomyocyte Death in Drug-Induced Cardiotoxicity. *Front. Cell Dev. Biol.* **2020**, *8*, (434).

(47) Šimùnek, T.; Štìrba, M.; Popelová, O.; Adamcová, M.; Hrdina, R.; Geršl, V. Anthracycline-Induced Cardiotoxicity: Overview of Studies Examining the Roles of Oxidative Stress and Free Cellular Iron. *Pharmacological Reports* **2009**, *61*, 151–171.

(48) Corbett, T. H.; Griswold, D. P.; Mayo, J. G.; Laster, W. R.; Schabel Jr., F. M. Cyclophosphamide-Adriamycin Combination Chemotherapy of Transplantable Murine Tumors. *Cancer Res.* **1975**, *35*, 1568–1573.

(49) Jones, N. E.; Durie, B. G. M.; Salmon, S. E.; Jones, S. E. Combination Chemotherapy with Adriamycin and Cyclophosphamide for Advanced Breast Cancer. *Cancer* **1975**, *36*, 90–97.

(50) Krapcho, A. P.; Landi, Jr., J. J.; Shaw, K. J.; Phinney, D. G.; Hacker, M. P.; McCormack, J. J. Synthesis and Antitumor Activities of Unsymmetrically Substituted l, 4-Bis[(aminoalkyl)amino]anthracene-9,10-diones and Related Systems. *J. Med. Chem.* **1986**, *29* (8), 1370–1373.

(51) Krapcho, A. P.; Getahun, Z.; Avery, Jr., K. L.; Vargas, K. J.; Hacker, M. P.; Spinelli, S.; Pezzoni, G.; Manzotti, C. Synthesis and Antitumor Evaluations of Symmetrically and Unsymmetrically Substituted 1,4-bis[(aminoalkyl)amino]anthracene-9,10-diones and 1,4-bis[(aminoalkyl)amino]-5,8-dihydroxyanthracene-9,10-diones. *J. Med. Chem.* **1991**, *34* (8), 2373–2380.

(52) Krapcho, A. P.; Petry, M. E.; Getahun, Z.; Landi, Jr., J. J.; Stallman, J.; Polsenberg, J. F.; Gallagher, C. E.; Maresch, M. J.; Hacker, M. P.; Giuliani, F. C.; Beggiolin, G.; Pezzoni, G.; Menta, E.; Manzotti, C.; Oliva, A.; Spinelli, S.; Tognella, S. 6,9-Bis[(aminoalkyl)amino]benzo[*g*]isoquinoline-5,10-diones. A Novel Class of Chromophore-Modified Antitumor Anthracene-9,10-diones: Synthesis and Antitumor Evaluations. *J. Med. Chem.* **1994**, *37* (6), 828–837.

(53) Krapcho, A. P.; Maresch, M. J.; Hacker, M. P.; Menta, E.; Oliva, A.; Giuliani, F. C.; Spinelli, S. Aza and Diaza Bioisosteric Anthracene-9,10-diones as Antitumor Agents. *Acta Biochim. Pol.* **1995**, *42* (4), 427–432.

(54) Krapcho, A. P.; Maresch, M. J.; Hacker, M. P.; Hazelhurst, L.; Menta, E.; Oliva, A.; Spinelli, S.; Beggiolin, G.; Giuliani, F. C.; Pezzoni, G.; Tognella, S. Anthracene-9,10-diones and Aza Bioisosteres as Antitumor Agents. *Curr. Med. Chem.* **1995**, *2*, 803–824.

(55) De Isabella, P.; Palumbo, M.; Sissi, C.; Capranico, G.; Carenini, N.; Menta, E.; Oliva, A.; Spinelli, S.; Krapcho, A. P.; Giuliani, F. C.; Zunino, F. Topoisomerase II DNA Cleavage Stimulation, DNA Binding Activity, Cytotoxicity, and Physico-Chemical Properties of 2-Aza-and 2-Aza-oxide-anthracenedione Derivatives. *Mol. Pharmacol.* **1995**, *30*, 30–38.

(56) Murdock, K. C.; Child, R. G.; Fabio, P. F.; Angier, R. B.; Wallace, R. E.; Durr, F. E.; Citarella, R. V. Antitumor Agents. 1. 1,4-Bis[(aminoalkyl)amino]-9,10-anthracenediones. *J. Med. Chem.* **1979**, *22* (9), 1024–1030.

(57) Thomas, X.; Archimbaud, E. Mitoxantrone in the Treatment of Acute Myelogenous Leukemia: A Review. *Hematol. Cell Ther.* **1997**, *39* (4), 163–174.

(58) Minotti, G.; Han, H.; Cattan, V.; Egorov, A.; Bertoni, F. Pixantrone: Novel Mode of Action and Clinical Readouts. *Expert Rev. Hematol.* **2018**, *11* (7), 587–596.

(59) Gao, Y.-G.; Liaw, Y.; Li, Y.-C.; Van der Marel, G. A.; Van Boom, J. H.; Wang, A. H.-J. Facile Formation of a Crosslinked Adduct between DNA and the Daunorubicin Derivative MAR70 Mediated by Formaldehyde: Molecular Structure of the MAR70-d(CGTnACG) Covalent Adduct. *Proc. Natl. Acad. Sci. USA* **1991**, *88*, 4845–4849.

(60) Wang, A. H.-J.; Gao, Y.-G.; Liaw, Y.-C.; Li, Y. Formaldehyde Cross-Links Daunorubicin and DNA Efficiently: HPLC and X-Ray Diffraction Studies. *Biochemistry* **1991**, *30* (16), 3812–3815.

(61) Fenick, D. J.; Taatjes, D. J.; Koch, T. H. Doxoform and Daunoform: Anthracycline-Formaldehyde Conjugates Toxic to Resistant Tumor Cells. *J. Med. Chem.* **1997**, *40* (16), 2452–2461.

Chapter II

Detection, Identification, and Quantitation of Anthracycline Interactions with AP sites in DNA via Adduct Trapping through Reductive Amination

Anthracyclines can Covalently bind Apurinic/Apyrimidinic (AP) Sites in DNA

We first set out to prove that our hypothesized reactivity occurred and was measurable. By utilizing model systems with increasing levels of complexity, we should be able to develop a method to detect and analyze anthracycline-DNA covalent conjugates. Due to the hydrolytic instability of the Schiff base this reaction forms, the C=N double bond must be reduced to form a stable compound for isolation and characterization. For our studies on this reactivity, we chose to work with four anthracyclines shown in **Figure 2-01** that are either commonly used as antineoplastics or well-studied as potential replacements. Doxorubicin, as outlined before, is still the most commonly used chemotherapeutic agent for a wide variety of solid tumors and breast cancers, while Epirubicin (EPI) is simply a derivative with inverted stereochemistry at the 2'-hydroxyl of the daunosamine sugar. We did not expect significant differences in reactivity between these two compounds, but the stereochemical differences have the potential to effect structural relationships between the reactive portions of the two molecules that could improve one mechanism of action over another.

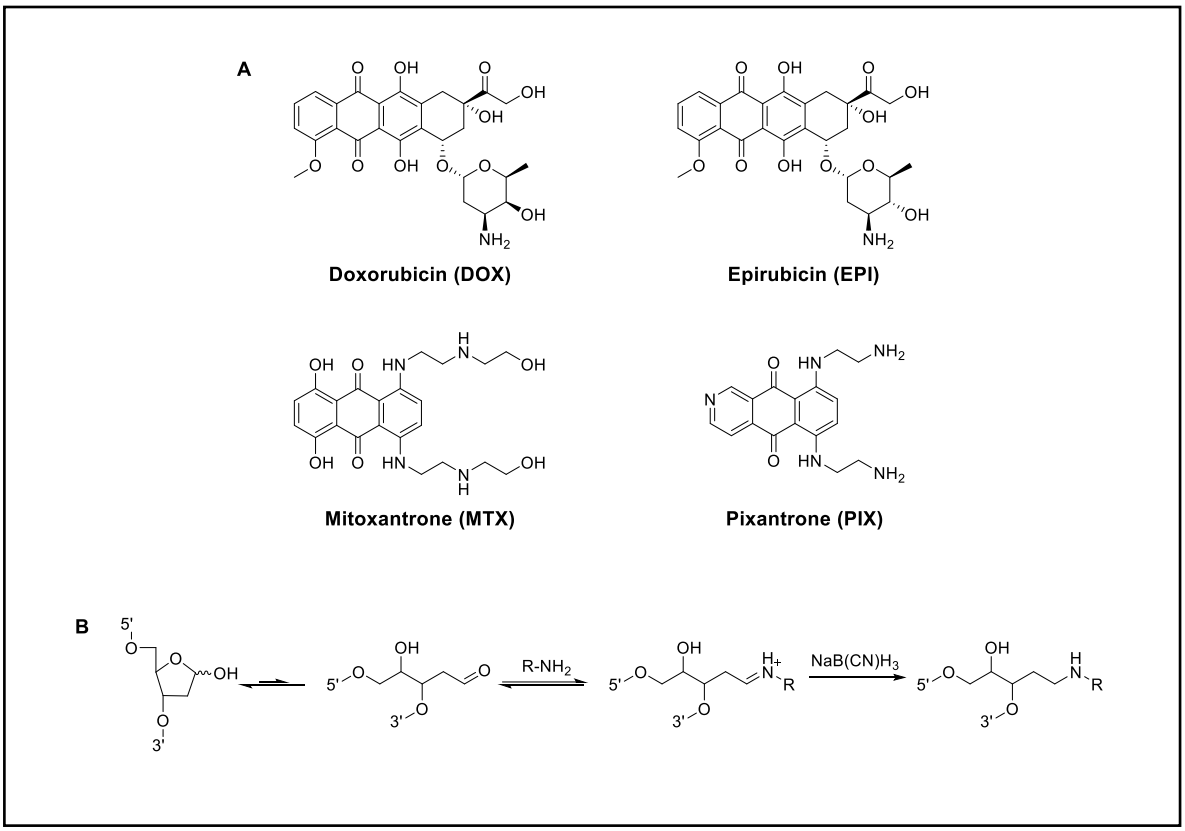

Figure 2-01. (A) Clinically significant anthracyclines chosen for study. **(B)** Equilibrium of AP sites allows for formation of a Schiff base upon interaction with amines present in these anthracyclines that can be subsequently trapped via reductive amination.

Two other compounds we selected for testing fall into the class of compounds known as anthracenediones, a structural derivative of anthracyclines with a planar core structure consisting of three rings rather than four and no sugar substituent. Mitoxantrone (MTX) is approved for treatment of non-Hodgkin's lymphoma, but is more commonly used to treat multiple sclerosis[1]. Pixantrone (PIX), a compound where the A-ring consists of an unsubstituted pyridine ring rather than the *para*-hydroxyl substituted benzene, is not currently approved for any treatments in the US but has exhibited significantly reduced cardiotoxic effects compared to DOX or MTX[2]. All four compounds show promise for expanded use as chemotherapeutics, and further understanding of their interactions with DNA during such treatment regimens will promote investigations into their clinical utility beyond the current scope. DOX, MTX, and PIX were selected because they were previously shown to form formaldehyde-mediated covalent cross-links with DNA[3–7] as discussed in **Chapter I**.

As proof of concept, we first synthesized a stable covalent adduct of the four anthracyclines with specifically generated AP site in a 12-base pair oligonucleotide (sequence 5'-GTT GC**U** CGT ATG-3'). The AP site was induced through enzymatic deglycosylation of the internal uracil residue by Uracil DNA Glycosylase (UDG). Anthracyclines were then introduced in 1.6-fold excess in the presence of sodium cyanoborohydride ($NaB(CN)H_3$) in order to reductively trap the Schiff base as a stable C-N bound adduct. We found a significant difference in reactivity between the compounds in the order of PIX > MTX > DOX/EPI, with both the PIX and MTX reductions proceeding to completion within 8 hours while the DOX/EPI reductions required more than 24 hours of incubation.

The crude reactions were analyzed by HPLC with UV detection at both 260 nm and the visible absorption wavelengths of the anthracycline compounds. Analysis at 260 nm showed both DNA products from the reactions (**Fig. 2-02**) and residual anthracycline byproducts since both absorb in that range, while analysis at 595 nm for MTX, 320 nm for PIX, and 480 nm for DOX/EPI allowed us to visualize incorporation of the compounds into the DNA strands. HPLC peaks that exhibited both absorbance profiles were collected and analyzed by ESI-LC/MS^2 to confirm the identity of the reduced covalent conjugates. CID fragmentation patterns were also analyzed as a further confirmation of sequence identity and anthracycline incorporation at the AP site.

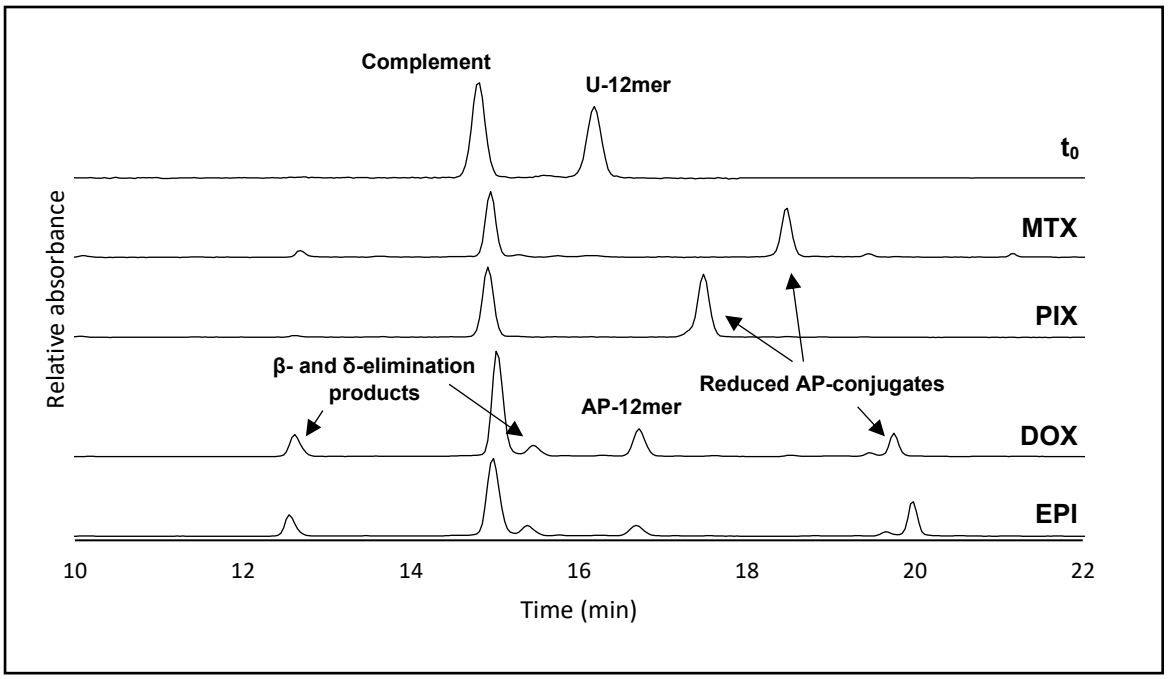

Figure 2-02. HPLC traces of the crude reaction mixture from reductive amination of the four anthracyclines with the AP-12mer after 24 hours. $NaB(CN)H_3$ was added simultaneously with MTX and PIX, but 3 hours after incubation of the DNA with DOX/EPI in these experiments.

HPLC and Mass Spectrometric Identification of the Partially Reduced DOX/EPI Covalent Adducts

One difficulty that arose in the isolation and identification of the anthracycline-12mer adducts was that the ketone at the C-13 position of DOX and EPI was partially reduced to the racemic alcohol by $NaB(CN)H_3$, giving a mixture of products for these reactions. Doxorubicinol (DOXol) is known to be a primary metabolite of DOX during treatment[8,9], so formation of this adduct is still biologically relevant if difficult to control in terms of production. In this sense, Epirubicnol (EPIol) is also expected to be a major metabolite, and thus relevant to our studies as well. HPLC (**Fig. 2-03**) and ESI-LC/MS^2 separation and identification of these variants was hindered by the fact that the (-3) charge state of the DNA was favored by ESI-MS, causing them to fall within the same mass window for detection. Injection as a crude mixture identified both adducts as present due to slight differences in total ion mass detection and mass differences from selected ion fragmentation. **Figures 2-04** and **2-05** outline this slight mass difference for the 12mer adducts of the parent and reduced compounds and how they match the calculated masses for each.

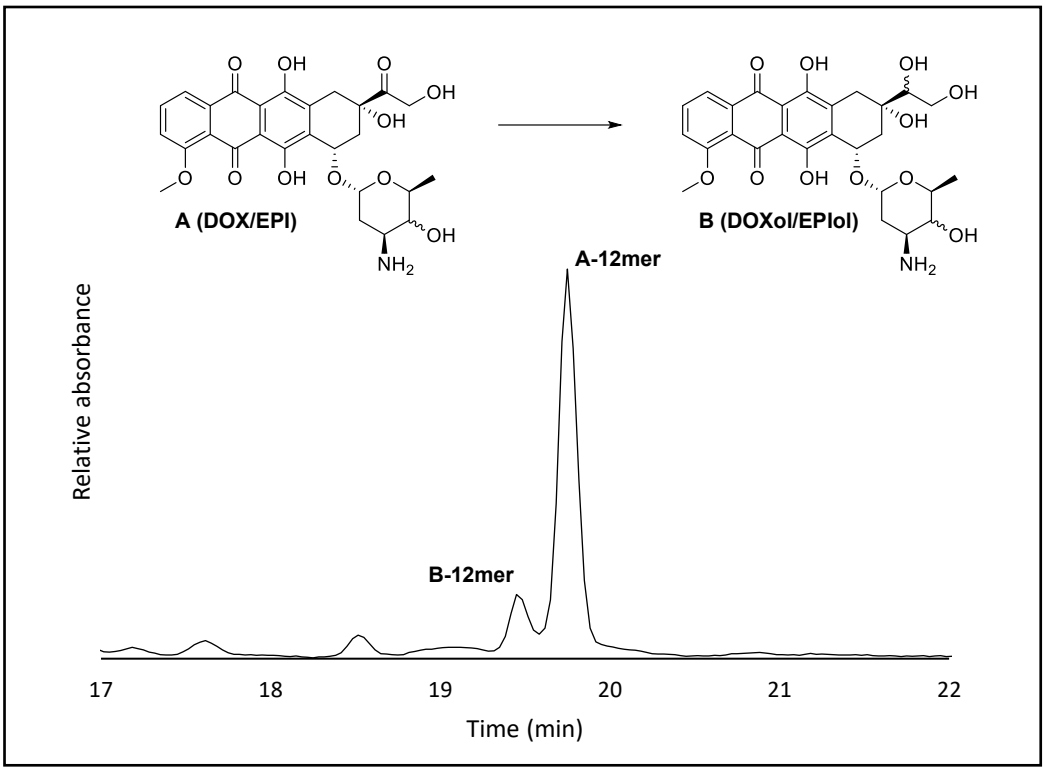

Figure 2-03. Mixture of products for the DOX/EPI-12mer reduced conjugates observed by HPLC resulting from partial reduction of the ketone at C-13.

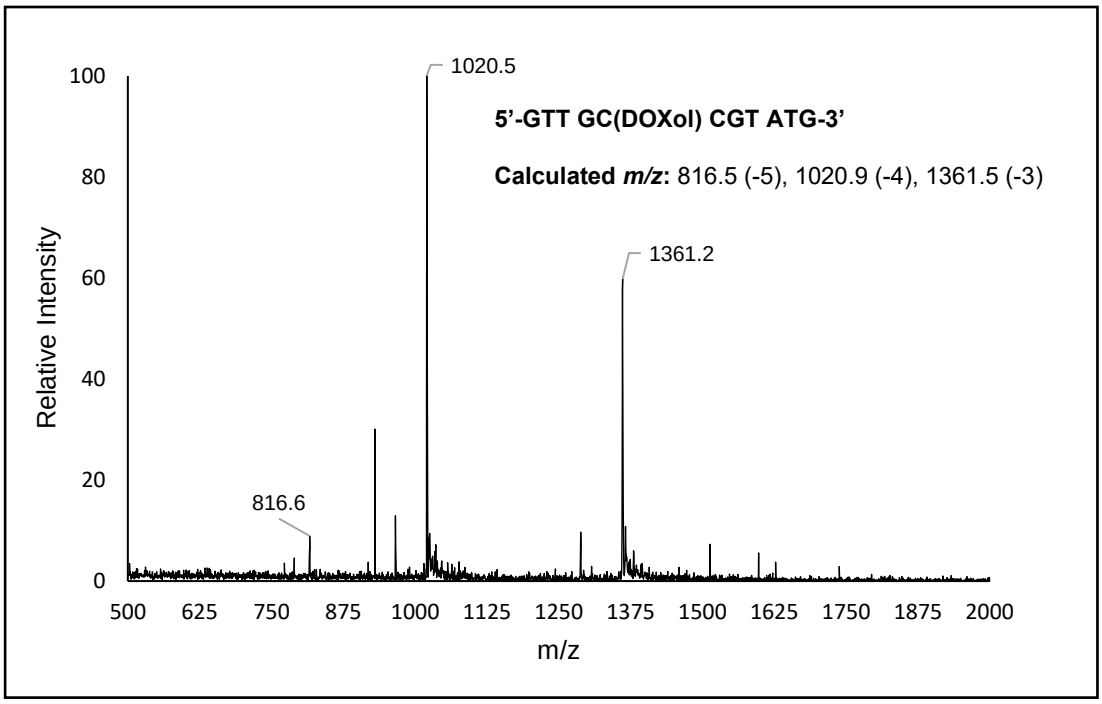

Figure 2-04. ESI-LC/MS total ion spectrum characterization of the purified **B-12mer** product observed in **Fig. 2-03**.

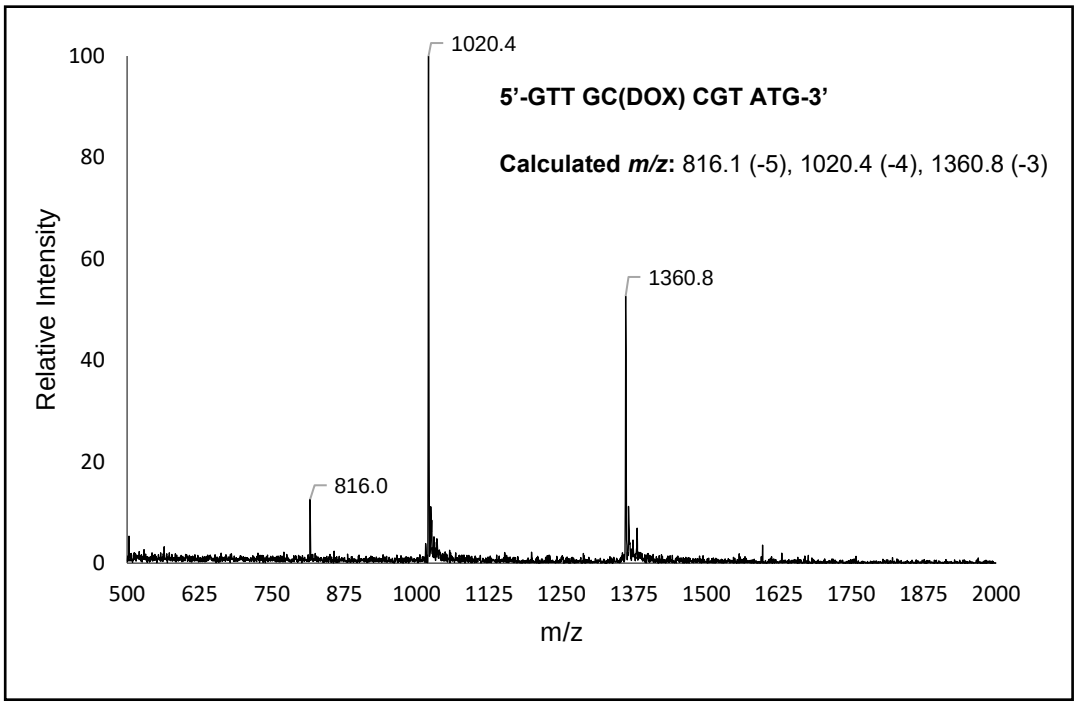

Figure 2-05. ESI-LC/MS total ion spectrum characterization of the purified **A-12mer** product observed in **Fig. 2-03**.

Synthesis of Anthracycline-dR Reduced Covalent Adducts

Detection and isolation of the anthracycline-12mer covalent adducts provided evidence that the Schiff base forms readily for this class of drug, particularly the anthracenedione compounds, and likely contributes to interactions between the chemotherapeutic drugs and DNA. We planned to employ mass spectrometry to detect and quantify the reduced Schiff base of the monomeric anthracycline-deoxyribose conjugate. Enzymatic digestion of DNA is a common method to break down the DNA into its constituent nucleotide or nucleoside building blocks alongside any products of base damage. By subjecting the purified anthracycline-12mer adducts to an enzyme cocktail composed of DNAse I, phosphodiesterase I, nuclease P1, alkaline phosphatase, and (optionally) adenosine deaminase, we expected to obtain a solution containing unmodified nucleosides and the anthracycline-dR covalent conjugate. This would provide us with a common reaction product that could be analyzed from our various model systems as well as from cell culture and biological samples, but one who's identity would need to be independently confirmed by comparing ESI-LC/MS^2 patterns to those of synthetically prepared authentic standards.

The synthetic standards were prepared via reductive amination of the Schiff base formed between the anthracyclines and commercially purchased 2-deoxy-D-ribose (dR) with $NaB(CN)H_3$ in methanol (**Fig. 2-07**). The reactions proceeded easily enough, but controlling the production of various products and purification proved much more difficult than expected. As was seen with the DOX/EPI reductive aminations with 12mer oligonucleotides, the reaction with dR also resulted in the DOXol/EPIol conjugates being produced. This was accounted for by subjecting the precursor anthracyclines to an initial

reduction with sodium borohydride ($NaBH_4$) followed by simple workup to isolate the alcohols. This process gave full conversion of DOX/EPI to DOXol/EPIol but could not be replicated in reactions with DNA due to the significant increase in pH that results from reaction of $NaBH_4$ in water and inability to truly control reaction equivalents due to rapid degradation of the reducing agent. In fact, when this reaction was attempted on a solution of DNA, the normally red color due to DOX/EPI was immediately bleached upon addition of $NaBH_4$ and HPLC analysis showed a multitude of extra peaks that did not correspond to the 12mer oligonucleotide. The change in color was attributed to borate-ester complexes of the anthraquinone core that have been reported through NMR studies previously[10] and were evident in the larger scale reductions by a shift in solution color from red to green which matched UV analysis from the same reports. Because of this, we proceeded with $NaB(CN)H_3$ reductions for all reductive aminations and performed ESI-LC/MS^2 analysis of the DOX/EPI reactions with DNA on a mixture of the reduced and non-reduced compounds. Analysis of the synthetic standards by ESI-LC/MS^2 and NMR was performed solely on the reduced DOXol/EPIol forms. Reaction of DOXol/EPIol with an excess of dR provided the synthetic standards in good conversion but still required purification by reversed phase semi-preparative HPLC. Pure DOXol/EPIol-dR were isolated as relatively narrow peaks with ~1 minute of separation from the unmodified anthracyclines (**Fig. 2-06**).

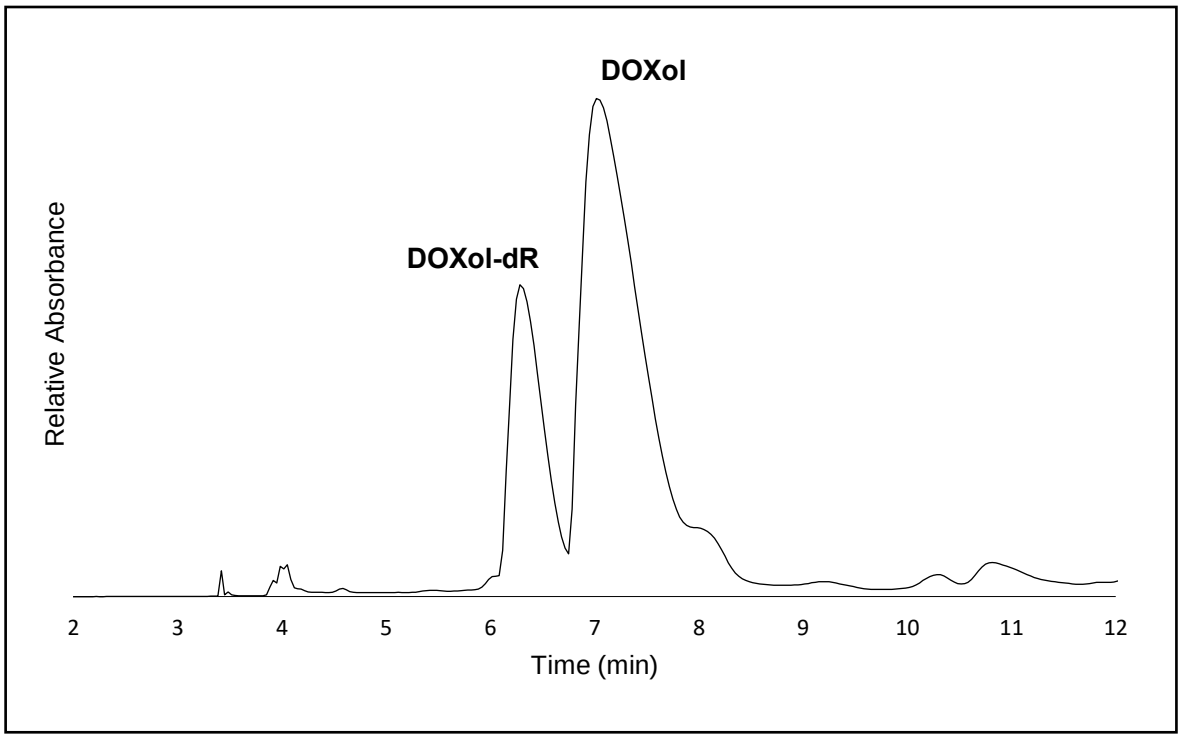

Figure 2-06. HPLC chromatogram of the crude reaction mixture between DOXol and 2-deoxy-D-ribose.

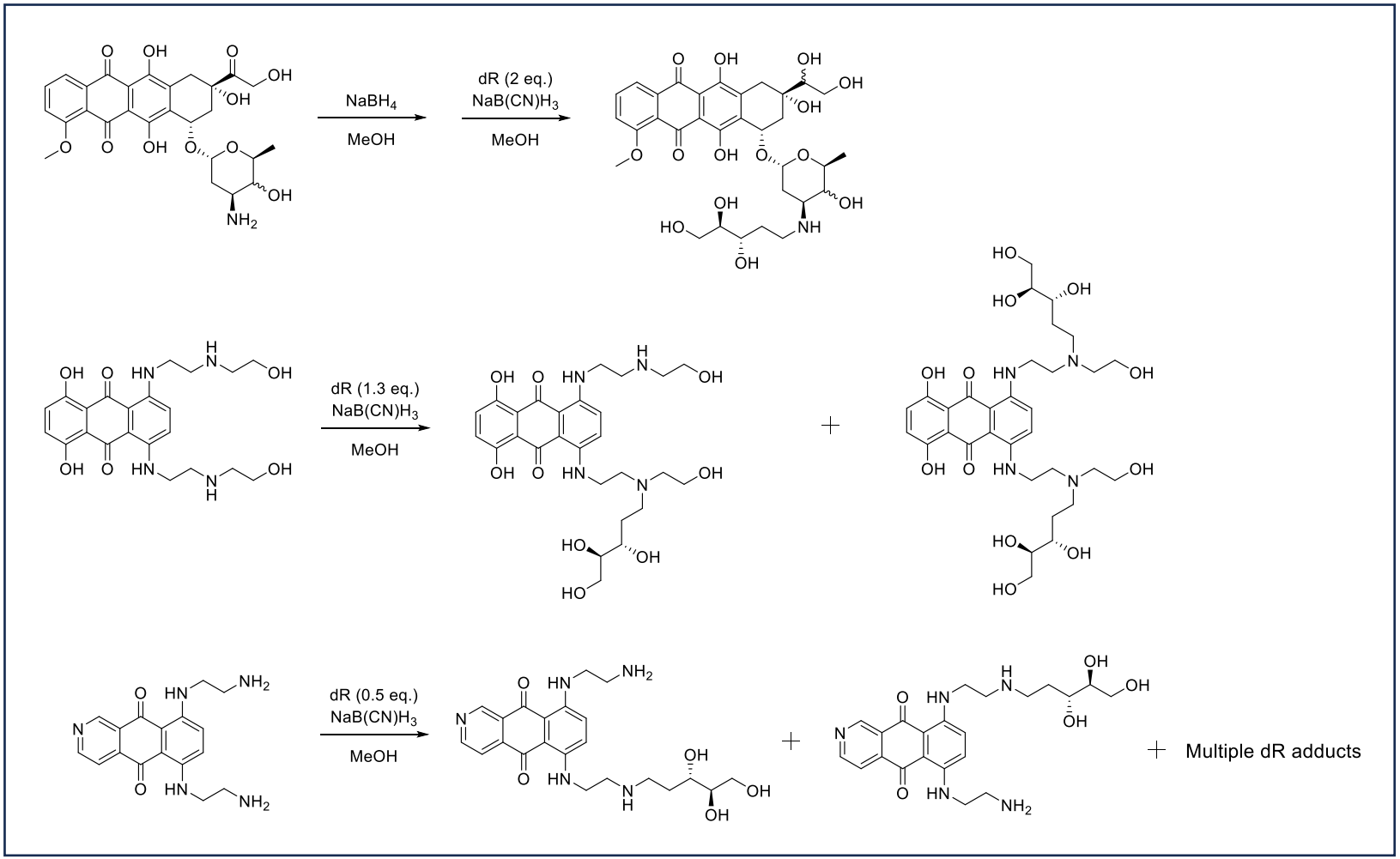

Figure 2-07. Summary of reductive amination conditions for each of the studied anthracyclines and the resulting products.

Synthesis and purification of the MTX and PIX covalent conjugates proved significantly more difficult. Unlike DOX/EPI, these compounds have two equally reactive amines toward reductive amination with dR. Due to this, controlling for reaction with a single equivalent of dR was not possible, and the desired compounds had to be isolated from a mixture of mono- and bis-dR products. In addition to this, the anthracenediones purified from HPLC as significantly broader peaks due to retention on the column and had much poorer peak separation for the same reason. Isolation of both the MTX-dR and PIX-dR adducts from their crude reaction mixtures required sequential purification by HPLC with injection of minimal amounts of material to provide optimal initial purity. PIX had an added difficulty due to the unsymmetric nature of the molecule, resulting in an isomeric mixture of the mono- and bis-reductive amination products. These isomers were identifiable as separate, overlapping peaks, but were purified as a mixture for analysis to mimic the products that would form biologically. Retention of these compounds on the stationary phase during HPLC resulted in significant loss of product with each successive round of purification, meaning significant amounts of time and material were required to obtain enough sample for analysis.

Several common protection/deprotection procedures were attempted to either control product formation or improve purification methods, but none proved useful due to the large amount of identical reactive sites in our compounds. For example, attempted silylation or trifluoroacetylation of the complex MTX-dR_n mixture (**Fig. 2-08**) would result in numerous products if the reactions were incomplete, and a lack of solubility for the MTX-derived compounds in any appropriate solvents made this a significant possibility. Attempts to protect one of the reactive amines would have fared no better than the

reductive amination of MTX with dR due to the reactivity of the second amine not being impacted by chemical changes to the first, and purification of all products would still have been required before further reactions. Protection of the multiple alcohols present in dR prior to reductive amination was a promising route since the aldehyde necessary for this step could be shielded as a dithioester[11] or stable aniline-imine[12,13] (**Fig. 2-09**), but incomplete reaction with the need for purification again proved non-ideal and time consuming. Due to a later need for synthesis of isotopically labeled versions of the compounds, multi-step reactions with significant material loss were discarded as viable pathways and work was carried forward with the one-step process.

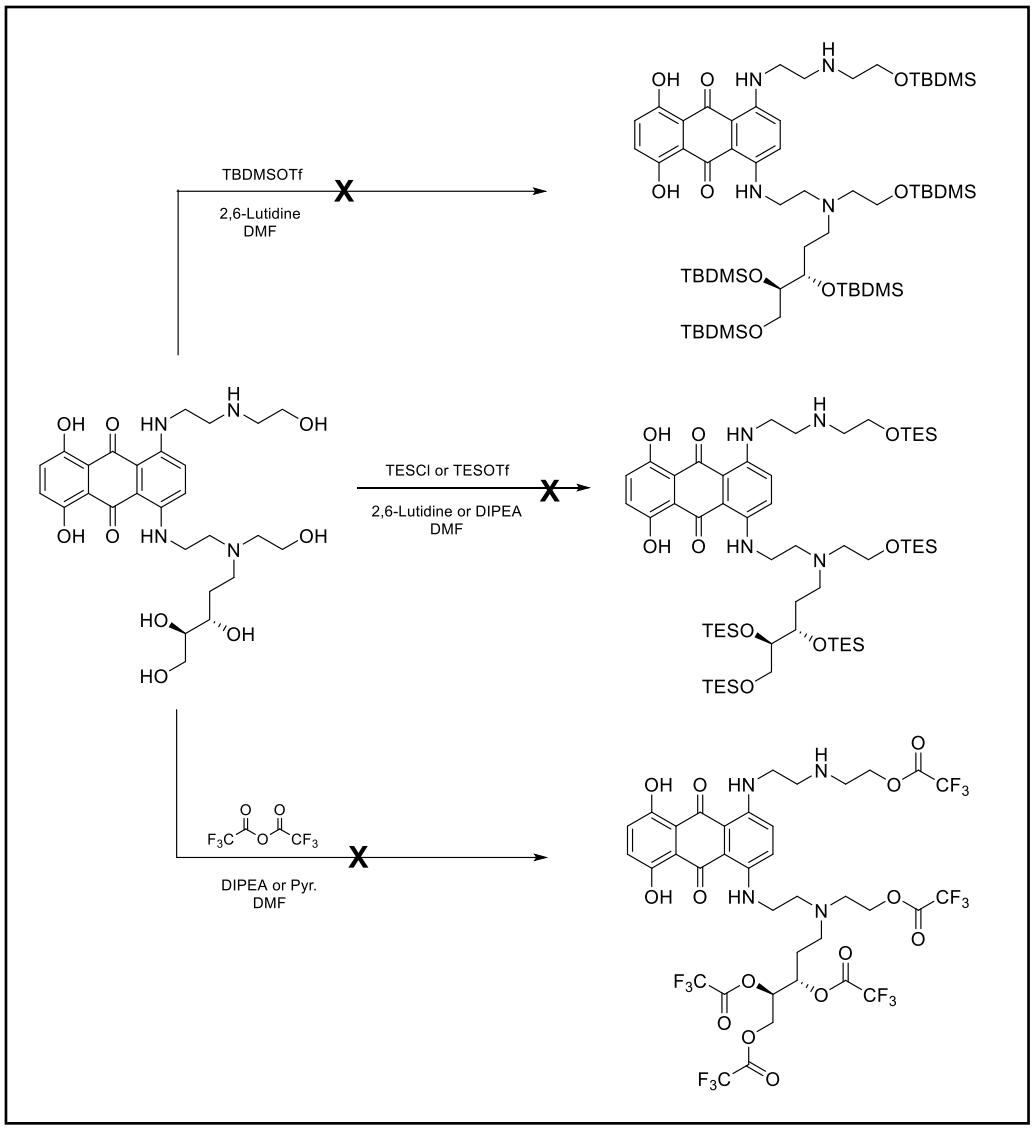

Figure 2-08. Attempted MTX-dR protection pathways to improve purification efficiency.

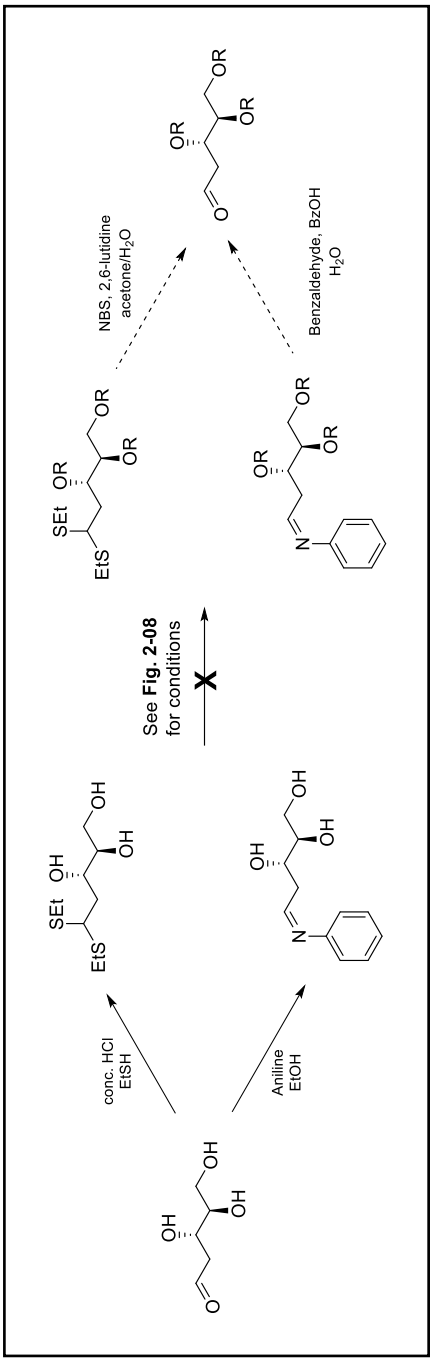

Figure 2-09. Attempted 2-deoxy-D-ribose protection pathways to improve purification efficiency after reductive amination with MTX and PIX.

Qualitative Analysis of the Anthracycline-dR Synthetic Standards and Conjugates Isolated from Enzymatic Digestion of Modified DNA

Each of the four anthracycline-dR adducts (as well as the doubly reacted MTX-dR_2 adduct) were characterized by NMR (^{1}H NMR, COSY, and HSQC) and ESI-LC/MS^2 via our enzymatic digestion LC method. Solubility and solvent choice for NMR of the anthracenediones at relevant concentrations again proved problematic due to overlap of the water signal from common solvents with many of the dR proton signals. Ultimately, the PIX-dR synthetic standard proved soluble in a solution of 0.1% formic acid-d_2 in D_2O with minimal signal overlap, while the MTX-dR synthetic standard was only soluble in pyridine-d_5 at low concentrations. DOXol-dR and EPIol-dR were characterized as mixtures of diastereomers at the 13-OH position, while the isomeric forms of PIX-dR could not be fully independently characterized. ESI-LC/MS^2 analysis of the four compounds in solutions spiked with the four unmodified nucleosides (dC, dT, dA, and dG) isolated the products well for improved ion detection. This method also allowed for enhanced signal detection by isolating the selected fragment ions identified from direct injection of the purified compounds.

The purified anthracycline-12mer reduced covalent conjugates were subjected to enzymatic digestion following established protocol that hydrolyzed the short DNA strands down into their constituent nucleosides and modified AP site conjugates identical to our synthesized analytical standards. ESI-LC/MS^2 analysis of the crude hydrolysate provided chromatograms and fragment ion spectra consistent with those of the previous controls for each compound. The total ion scan at the appropriate retention times also showed detection of the representative parent ions as seen in **Figure 2-10**, further confirming the

efficiency of reaction. The ability to readily detect the reduced anthracycline-dR adducts in reaction solution after enzymatic digestion was not expected to carry over to more complex model systems due to the controlled method of generating AP sites and their relative abundance in the 12mer oligonucleotides. As a more representative model system, we also performed these reactions with calf thymus DNA (CT-DNA). AP sites were generated nonspecifically by suspending the DNA in pH = 6.5 citrate buffer and heating to 65 °C. The DNA was isolated by ethanolic precipitation and the covalent adducts were then generated in a similar manner as before. The DNA was again precipitated and washed to remove excess reactants and the now colored pellet of DNA was re-suspended in digest buffer and subjected to enzymatic digestion for analysis.

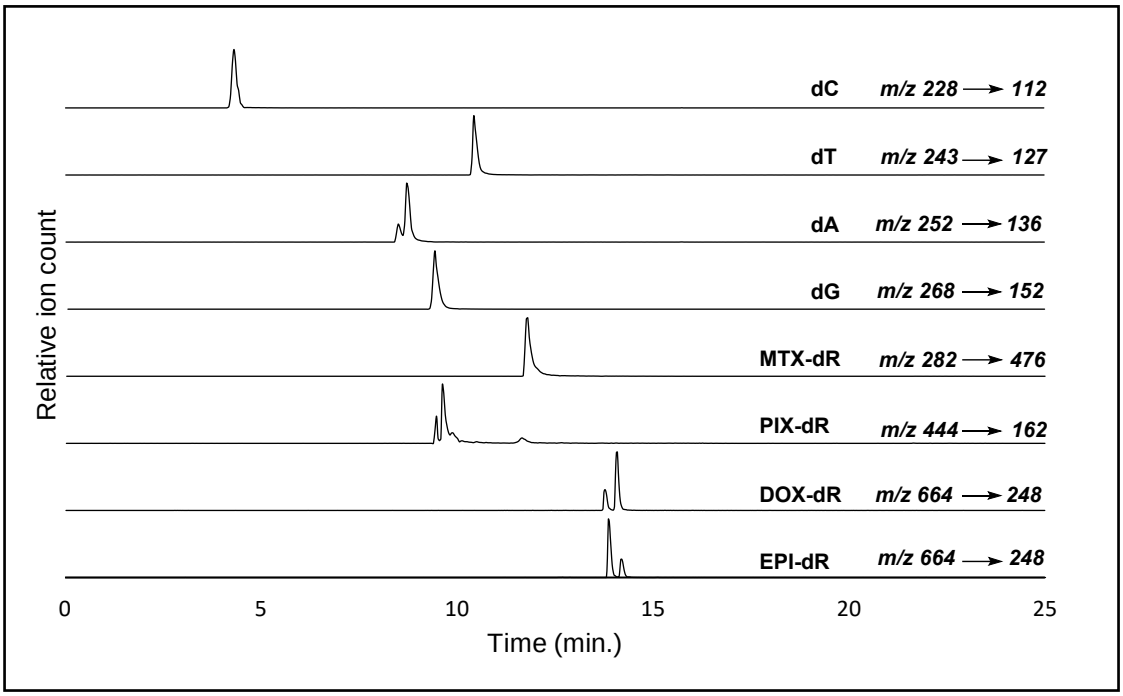

Figure 2-10. ESI-LC/MS chromatograms for the elution and detection of products from enzymatic digestion of reduced anthracycline-DNA adducts. Product peaks were isolated by MS^2 selected ion detection of the fragment *m/z* shown for each compound.

Due to the large excess of unmodified nucleosides present in the hydrolysate mixture when compared to our 12mer model system, enrichment of the reduced anthracycline-dR adducts was necessary for LC/MS detection. For this, an SPE method was developed to wash a majority of the unmodified nucleosides from a reverse phase cartridge before eluting the desired analyte. LC/MS identification of the anthracycline adducts from this process was performed by MS^2 detection of the selected fragment ions identified previously. In this manner we reported an efficient method of synthesizing and isolating adducts of anthracyclines with AP sites in DNA for detection and analytical analysis by ESI-LC/MS^2.

All further experiments were conducted solely on MTX due to a combination of factors, including its reactivity toward AP sites, ease of analysis compared to the other anthracyclines, and its clinical relevance. Utilizing the initial reaction, purification, and analysis protocol developed to this point, the Turesky lab at the University of Minnesota moved forward with detection and quantitation of the MTX-DNA adducts in CT-DNA and cultured human breast cancer (MDA-MB-231) cells. We provided them the purified MTX-dR synthetic standard for use as an analytical reference, and the $^{13}C_5$-dR isotopically labeled analog was independently synthesized, purified, and provided as an internal standard for analytical quantitation by the stable isotope dilution method.

Detection and Quantitative Analysis of MTX-DNA Adducts at AP Sites by the Turesky Lab

Continuation of the initial experiments in CT-DNA confirmed that over a period of 3 hours, MTX reacts with AP sites at a similar efficiency to *o*-(pyridin-3-ylmethyl)hydroxylamine (PMOA), a molecule studied previously by the lab that is highly reactive toward aldehydes and forms a stable covalent oxime conjugate with all available AP sites as shown in **Figure 1-04**. Although this indicates a high occurrence of reaction, it is important to note that $NaB(CN)H_3$ selectively reduces the reversible Schiff base formed between MTX and the AP site but reacts slowly with the free aldehyde itself. This likely pushes the reaction equilibrium toward the covalent adduct rather than indicating a steady state of formation, as evidenced by the rate of increased adduct formation over time for MTX while the levels of PMOA-DNA adducts (represented as “AP sites” in **Figure 2-11 B**) remain consistent. Indeed, reactions using a freshly prepared solution of $NaBH_4$ in water as the reducing agent exhibited the same reactivity as with $NaB(CN)H_3$ for the first 5 minutes but plateaued from that point forward due to full reduction of the free aldehyde and degradation of the reducing agent. The level of adducts measured within this time period was thus viewed as a more accurate representation of the steady state for MTX-DNA Schiff base formation. Unfortunately, $NaBH_4$ reduction of nuclear DNA from MDA-MB-231 cells treated with NNM and MTX (performed by Kyle Brandt in the Turesky lab) gave an unextractable precipitate, and no reduced MTX-dR was detected.

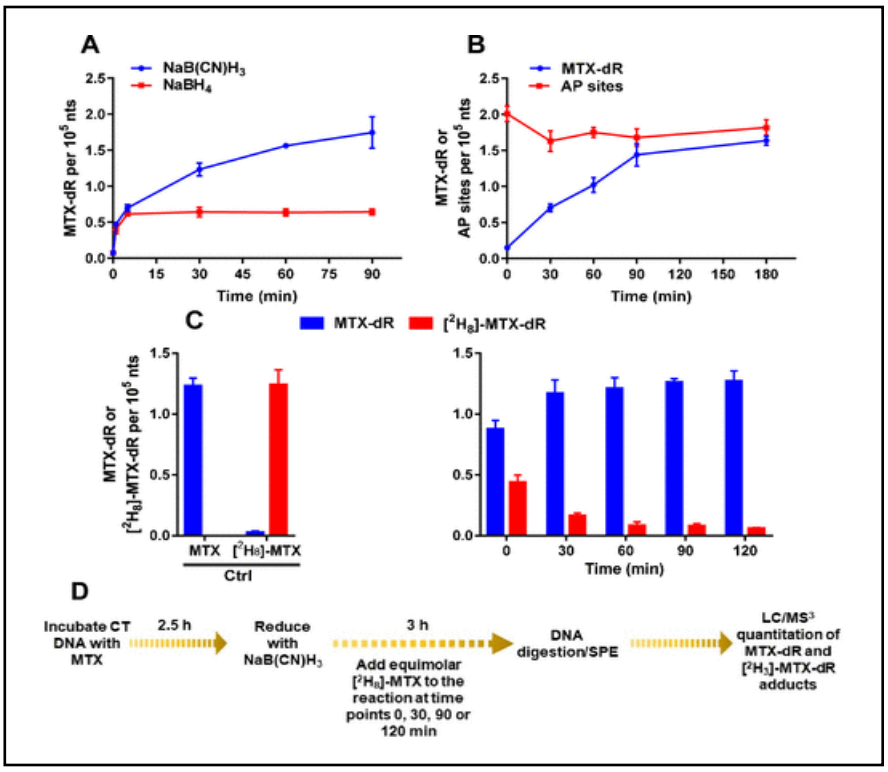

Figure 2-11. Analysis of MTX reactivity with existing AP sites in CT DNA. (**A**) Reductive amination with $NaBH_4$ terminates rapidly with no further reaction seen after 5 minutes whereas $NaB(CN)H_3$ reduction continues to occur over a period of 1.5h. (**B**) MTX reacts with nearly 100% of the existing AP sites in CT DNA (0.1 *μg/μL* DNA, 5 μM MTX) over 3h as the Schiff base is continuously reduced by $NaB(CN)H_3$. (**C**) Deuterium-labeled MTX reacts with AP sites identically to the unlabeled compound and displaces ~35% of the unlabeled adduct in the first 30 minutes, confirming the instability of the unreduced adduct and the necessity of reduction for isolation and detection.

Experiments in cell culture were performed by Medjda Bellamri and Kyle Brandt of the Turesky lab using MDA-MB-231 cells to observe cell viability and measure MTX-DNA adducts from co-treatment of NNM and MTX (**Fig. 2-12**). Breast cancer treatment regimens using similar combination therapies are well-known, but the drugs are thought to function independently. We set out here to test whether there is improved cytotoxicity from this method over treatment with each of the compounds individually and whether formation of the previously observed MTX-DNA covalent interaction at AP sites does occur biologically. Individual treatment of the cells for 24-96 hours with each compound showed that NNM is not cytotoxic itself below doses of 100 μM while MTX significantly reduced cell viability at concentrations as low as 40 nM. Co-treatment for 24-48 hours with 1 mM NNM and varying concentrations of MTX (0.04-0.63 μM) caused an observable decrease in cell viability over that seen with either compound on its own, indicating an enhanced cytotoxicity not intensively studied before.

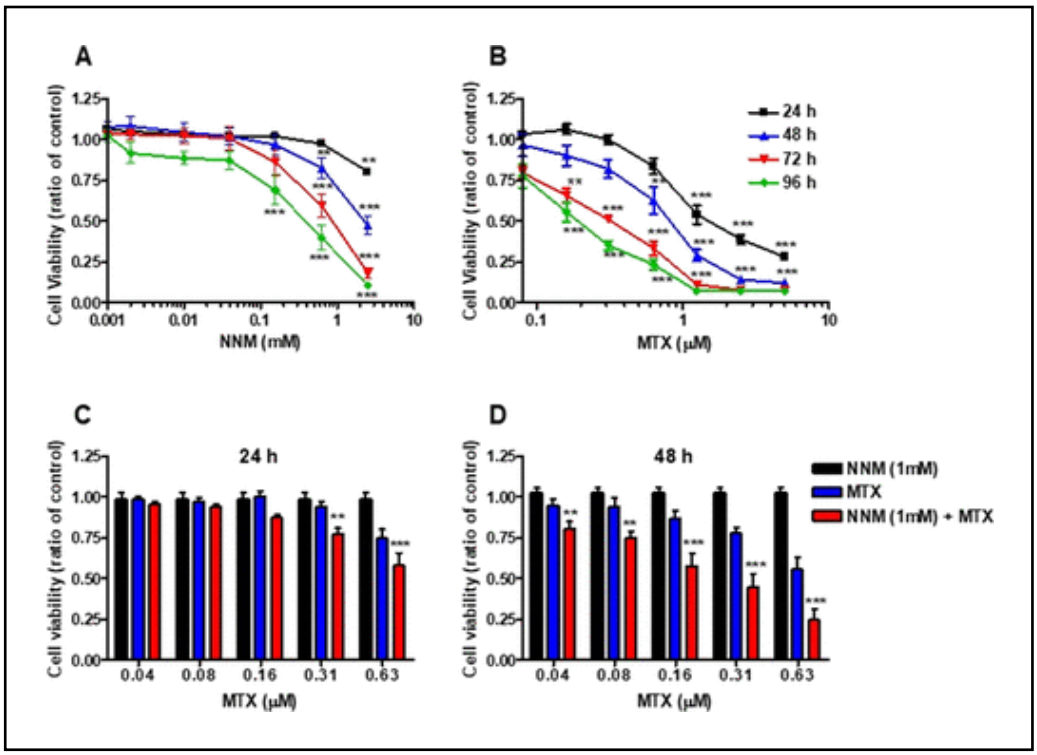

Figure 2-12. Measurement of cell death as a result of co-treatment with NNM and MTX by MTT assay. (**A/B**) Cell viability with varying concentration of each drug individually over four days; NNM alone is relatively non-toxic up to doses of 1 mM over 48 hours of treatment. (**C**/**D**) Simultaneous dosing of 1 mM NNM with MTX results in a significant increase in cell death over controls within 48 hours of treatment (0.04-0.63 μM MTX).

Although not necessarily cytotoxic within a 24-hour period, NNM was shown to induce AP sites in a concentration-dependent manner in both dividing and confluent cells. Treatment of cells in log phase division exhibited a marked increase in levels of AP sites, supporting our theory that interactions between this type of damage and anthracyclines would be enhanced in proliferating cells. Following treatment with both NNM and MTX, the nuclei were isolated and treated with $NaB(CN)H_3$ to trap the transient MTX-DNA adducts as we had done in our model systems. The DNA was subsequently isolated, digested, and subjected to our SPE procedures to enrich the resulting MTX-dR reduced conjugates for LC/MS^3 detection and quantitation. Outlined in **Figure 2-13**, the level of adducts increased with reduction times ranging from 1.5-18 hours with no further increase seen after that, reaching a maximum of 1.50 ± 0.40 adducts per 10^5 nts. This matched well with the measured level of AP sites initially present after NNM treatment (1.16 ± 0.15 per 10^5 nts), indicating a high reaction efficiency for the Schiff base formation between MTX and damaged DNA. A decrease in the amount of AP sites was seen over 18 hours in cells treated only with NNM, and this was attributed to natural repair processes. However, formation of the MTX-DNA adduct was not apparently influenced by this, suggesting that the Schiff base forms quickly and has some stability in order to be bypassed by repair enzymes.

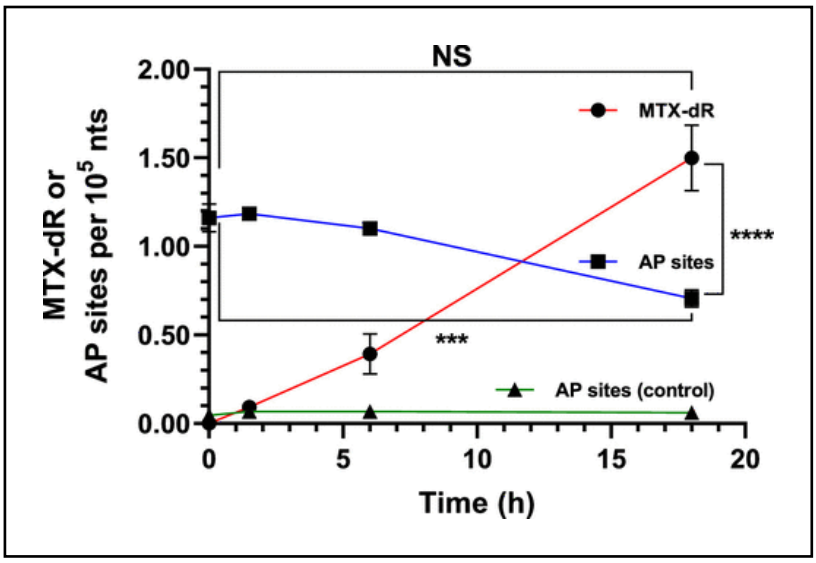

Figure 2-13. Rate of MTX-AP adduct formation in MDA-MB-231 cells co-treated with 1 mM NNM and 0.6 μM MTX. The level of MTX-dR adducts observed after 18 hours was not significantly different than the background level of AP sites initially present. The gradual decrease of AP sites present without MTX dosing is attributed to natural DNA repair that is unable to occur when MTX is present.

Through these experiments we have developed a method for synthesizing, detecting, and quantifying products of covalent interactions between anthracycline-derived chemotherapeutic drugs and AP sites in DNA. In collaboration with the Turesky lab, we have shown that these interactions occur readily in cells and can be captured as stable adducts through post-lysis reduction with $NaB(CN)H_3$ followed by digestion and ESI-LC/MS^3 detection. Co-treatment of MTX with NNM, a variation on already used clinical practices, enhances cytotoxicity over treatment with either drug individually. This effect can be interpreted as a product of the interactions studied here due in part to the concentration- and time-dependent increases in quantifiable MTX-dR adducts from isolated DNA that follows the trends in cell viability. Such results suggest a potentially cooperative effect between nitrogen mustards and amine-containing anthracyclines, supporting our hypothesis that covalent interactions between induced AP sites and the anthracycline compounds provide a significant but understudied contribution to the damage profile of this chemotherapeutic regimen. Further investigations into this enzyme-independent function of anthracyclines could lead to the development of compounds that better take advantage of such reactivity, further enhancing the combinatorial benefit. Additionally, improvements to the cytotoxic effects through improved drug design could in turn lead to lower necessary doses and a reduction in the off-site cardiotoxic induction that currently limits the utility of A/C chemotherapy.

Experimental Procedures

Chemicals and Reagents

Mitoxantrone was purchased from Toronto Research Chemicals (Ontario, Canada). Doxorubicin hydrochloride and Pixantrone dimaleate were purchased from Carbosynth (Biosynth International). Epirubicin hydrochloride was purchased from LC Laboratories (Woburn, MA). 2-deoxy-D-ribose was purchased from Oakwood Chemical (Estill, SC). Oligonucleotides (12bp sequences) were purchased with prior HPLC purification from Integrated DNA Technologies (Coralville, IA). $^{13}C_5$-deoxyribose (98.9% isotopic purity) was purchased from Santa Cruz Biotechnology (Dallas, TX, USA). 4-(2-hydroxyethyl)-1-piperazineethanesulfonic acid (HEPES), 98% aqueous formic acid, calf thymus (CT) DNA, DNase I (type IV, bovine pancreas), alkaline phosphatase (*Escherichia coli*), and nuclease P1 (*Penicillium citrinum*) were purchased from Sigma Aldrich (St. Louis, MO, USA). Phosphodiesterase I (*Crotalus adamanteus* venom) and adenosine deaminase (calf spleen) were purchased from Worthington Biochemical Corp (Newark, NJ). UDG (*Escerichia coli*) was purchased from New England Biolabs (Ipswich, MA). Ammonium formate (solid, 97% for buffers), sodium cyanoborohydride, sodium borohydride, ethanol (95%), Sola HRP Polymeric Reversed Phase 10 and 30 mg SPE cartridges, Optima LC/MS grade water, acetonitrile, and methanol were purchased from Thermo Fisher Scientific. Ultrafree®-MC-HV Durapore®-PVDF 0.45 µm centrifugal filters were purchased from Millipore Sigma.

Buffer Compositions

HEPES buffer: 0.1 M HEPES free-base, 0.1 M NaCl, pH = 7.40

Digest buffer: 5 mM Bis-Tris, 0.01 M MgCl, pH = 7.10

Chromatography

HPLC analysis was carried out on a gradient HPLC (Beckman Instruments; System Gold Software) equipped with pump module 126 and photodiode array detector module 168. Reduced anthracycline-dR synthetic standards were purified using a C-8 reversed phase column (Phenomenex Luna, 250 x 10 mm, flow rate 5.0 mL/min) with the effluent monitored at 260 nm. Oligonucleotide reactions were monitored and purified using a proprietary reversed phased column (Phenomenex Luna: Clarity, 250 x 4.6 mm, flow rate 1.5 mL/min) with the effluent monitored at 260 nm and either 595 nm (MTX), 320 nm (PIX), or 480 nm (DOX/EPI) when necessary. All analyses and purifications were performed with 0.1 M aqueous ammonium formate buffer (**A**) and acetonitrile (**B**).

Gradient 1: Isocratic at 18% **B** for 22min; 2 min linear gradient to 25% **B**; isocratic at 25% **B** for 6 min; 2 min linear gradient to 80% **B**; isocratic at 80% **B** for 3 min; 2 min linear gradient to 0% **B**; isocratic at 0% **B** for 3 min.

Gradient 2: Isocratic at 14% **B** for 15 min; 2 min linear gradient to 80% **B**; isocratic at 80% **B** for 3 min; 2 min linear gradient to 0% **B**; isocratic at 0% **B** for 3 min.

Gradient 3: Isocratic at 8% **B** for 40 min; 2 min linear gradient to 80% **B**; isocratic at 80% **B** for 3 min; 2 min linear gradient to 0% **B**; isocratic at 0% **B** for 3 min.

Gradient 4: Isocratic at 23% **B** for 15 min; 2 min linear gradient to 80% **B**; isocratic at 80% **B** for 3 min; 2 min linear gradient to 0% **B**; isocratic at 0% **B** for 3 min.

Gradient 5: Initially 1% **B**; 15 min linear gradient to 10% **B**; 5 min linear gradient to 20% **B**; 2 min linear gradient to 80% **B**; isocratic at 80% **B** for 3 min; 2 min linear gradient to 0% **B**; isocratic at 0% **B** for 3 min.

NMR Spectra

^{1}H NMR spectra were recorded at 600 MHz in D_2O containing 0.1% CD_2O_2, pyridine-d_5, or CD_3OD. The two-dimensional ^{1}H-^{1}H correlation spectroscopy (COSY) and heteronuclear single quantum coherence (HSQC) experiments were performed on a 600 MHz spectrometer. ^{1}H NMR, COSY, and HSQC spectra were collected using 64, 4, and 8 total scans respectively with a pre-acquisition delay of 10 µs. ^{1}H NMR spectral width was set to 20.00 ppm with an O1P of 5.000 ppm. Acquisition times were 1.092 seconds for ^{1}H NMR, 21.3 µs (F1) and 85.2 µs (F2) for COSY, and 4.71 µs (F1) and 42.6 µs (F2) for HSQC.

Mass Spectrometry

LC-ESI/MS^2 and MS^3 was performed on two instruments. Low resolution spectra were obtained using Waters Acquity UPLC system (Waters, Milford, MA) connected to a Finnigan LTQ ion trap mass spectrometer (Thermo Electron, San Jose, CA) equipped with an *Ion Max* API source and a standard electrospray probe. High resolution spectra

were obtained using and Orbitrap XL ion trap mass spectrometer (Thermo Electron, San Jose, CA) equipped with an *Ion Max* API source and a standard electrospray probe with auxiliary gas heating capabilities. For detection of compounds without in-line separation, samples were injected directly to the ion source at a flow rate of 0.25 mL/min in a 50% solvent A/B mixture. Analysis of compounds utilizing in-line purification was performed with a Phenomenex Luna 3-micron C-18 reversed phase column (2 x 150 mm; Torrance, CA) at a flow rate of 0.125 mL/min using the appropriate elution gradient. Data acquisition and spectral analysis were done using Thermo-Finnigan Xcalibur version 2.0.7 SP1.

All oligonucleotide samples were purified using a buffer system consisting of 1% acetonitrile in water containing 0.01 M ammonium acetate (**A**) and 90% acetonitrile in water containing 0.1 M ammonium acetate (**B**) along the following gradient: isocratic at 1% **B** for 1 min; 3 min linear gradient to 5% **B**; 2 min linear gradient to 20% **B**; 1 min linear gradient to 40% **B**; 2 min linear gradient to 50% **B**; 1 min linear gradient to 100% **B**; isocratic at 100% **B** for 1 min; 1 min linear gradient to 0% **B;** isocratic at 0% **B** for 6 min. Analysis was conducted in negative ion mode using the following ESI conditions: N_2 sheath gas pressure was 36 psi; N_2 auxiliary gas pressure was 37 psi; source voltage was 5.0 kV; tube lens voltage was -85 V; capillary voltage was -37.0 V; capillary temperature was 300 °C; the normalized capillary-induced dissociation was 35% for MS^2; activation Q was 0.25; 1 microscan, AGC max injection time was 100 ms; the isolation width was *m/z* 3.0 for MS^2. The Mongo Oligo Mass Calculator (v.2.06, http://ma.rega.kuleuven.be/masspec/mongo.htm) was used to calculate the theoretical electrospray mass series and the a-b, w, and y fragment ions. The theoretical *m/z* values

were compared to the experimental spectra. **Figure 2-14** outlines the DNA fragment ion nomenclature used.

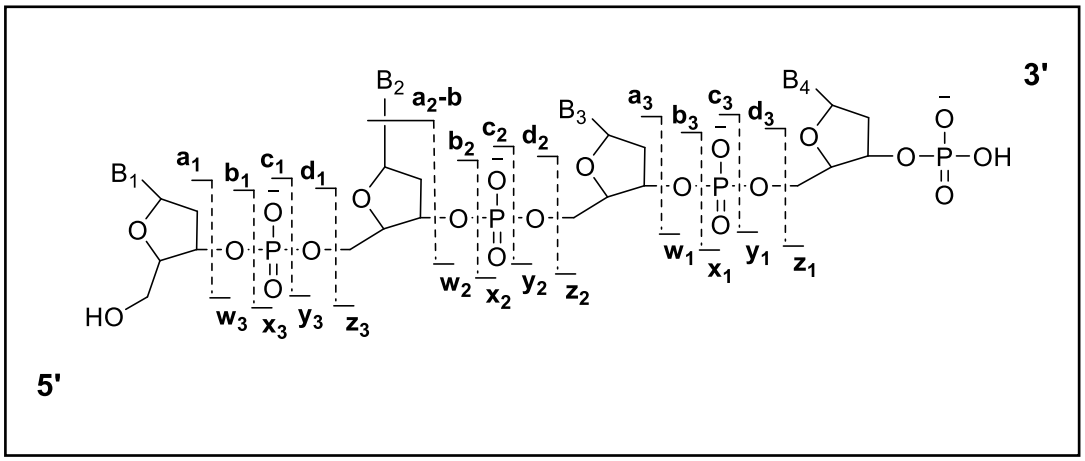

Figure 2-14. Typical CID fragmentation pattern of DNA oligonucleotides from ESI-MS^2 analysis.

The anthracycline-dR synthetic standards and products of DNA enzymatic digestion were purified using a buffer system consisting of 0.05% formic acid in water (**A**) and 95% acetonitrile in water containing 0.05% formic acid (**B**) along the following gradient: isocratic at 2% **B** for 2.5 min; 6 min linear gradient to 15% **B**; 4 min linear gradient to 40% **B**; 5 min linear gradient to 100% **B**; isocratic at 100% **B** for 5 min; 1 min linear gradient to 0% **B;** isocratic at 0% **B** for 6 min. Analysis was conducted in positive ion mode using the following ESI conditions for adducts of MTX and PIX: N_2 sheath gas pressure was 44 psi; N_2 auxiliary gas pressure was 21 psi; source voltage was 5.0 kV; tube lens voltage was 55 V; capillary voltage was 28.5 V; capillary temperature was 300 °C; the normalized capillary-induced dissociation was 35% for MS^2; activation Q was 0.25; 3 microscans, AGC max injection time was 10 ms; the isolation width was *m/z* 3.0

for MS^2. *ESI conditions for analysis of DOX and EPI adducts contained the following modifications*: N_2 sheath gas pressure was 36 psi; N_2 auxiliary gas pressure was 37 psi; tube lens voltage was 30 V; capillary voltage was 10 V; 1 microscan, the isolation width was *m/z* 2.0 for MS^2. The MS^2 transition parameters for unmodified deoxynucleosides ($[M + H - 116\ Da]^+$) are as follows:

dC: *m/z* 228.1 → 112.1; **dT**: *m/z* 243.0 → 127.2; **dA**: *m/z* 252.1 → 136.1; **dG**; *m/z* 268.1 → 152.1.

The MS^2 and MS^3 transitions for the reduced anthracycline-dR conjugates are as follows:

MTX-dR $[M + H]^+$: MS^2 *m/z* 563.3 → 476.3, 206.2;

MS^3 $[M + 2H]^{2+}$; *m/z* 282.2 → 476.3 → 297.1, 206.2.

PIX-dR $[M + H]^+$: MS^2 *m/z* 444.2 → 427.2, 384.2, 309.2, 292.2, 266.2, 179.2, 162.2, 136.2

DOXol-dR $[M + H]^+$: MS^2 *m/z* 664.1 → 248.2

EPIol-dR $[M + H]^+$: MS^2 *m/z* 664.1 → 248.2

Synthesis of the reduced MTX-dR covalent adducts

Mitoxantrone (50 mg, 0.113 mmol) was mixed with 2-deoxy-D-ribose (18 mg, 0.135 mmol) in methanol (4.5 mL, 0.025 M) and stirred for 1 hour at rt under an argon atmosphere. $NaB(CN)H_3$ (35 mg, 0.563 mmol) was added and the reaction stirred at rt for 12 hours. The solvent was removed under reduced pressure on a rotary evaporator

and the crude product was dissolved in water (5 mL). Initial purification was performed by SPE elution (0.25 mL sample loading in LC/MS-grade water) on a vacuum manifold (Supelco, Visiprep™ 12). Cartridges were preconditioned with 3 mL methanol followed by 3 mL water. After sample loading, elution was performed by washing with 4 mL water followed by 4 mL of 0.05% FA. All fractions were collected, dried, and further purified by reversed phase HPLC following **Gradient 1**. MTX-dR was collected as the second major peak eluting at 19 minutes while MTX-dR_2 was collected as the third major peak eluting at 25 minutes. After successive rounds of lyophilization with water to remove excess ammonium formate, the identity of both compounds was confirmed by low resolution ESI-MS^2 via direct sample (dissolved in 0.05% FA) injection with a mobile phase solvent mixture of 50% methanol/H_2O. See **Appendix III** figures for NMR labeling. MTX-dR ^1H NMR (600 MHz; pyridine-d_5): δ 10.97, (t, 1H, J = 5.2 Hz, **Ar-NH**), 10.92 (t, 1H, J = 5.0 Hz, **Ar-NH**), 7.40 (s, 2H, **2,3**), 7.31 (s, 2H, **6,7**), 4.44 (dd, 1H, J = 3.9, 10.4 Hz, **5'**), 4.38 (td, 1H, J = 2.3, 8.1 Hz, **3'**), 4.32 (dd, 1H, J = 6.2, 10.3 Hz, **5'**), 4.23 (dd, 1H, J = 5.8, 10.1 Hz, **4'**), 4.05 (t, 2H, J = 5.8 Hz, **15**), 4.01 (t, 2H, J = 5.0 Hz, **11**), 3.63 (m, 2H, **18**), 3.56 (q, 2H, J = 5.8 Hz, **14**), 3.18 (m, 1H, **1'**), 3.11 (m, 1H, **1'**), 3.05 (t, 2H, J = 6.0 Hz, **13**), 3.01 (m, 2H, **12**), 2.99 (m, 2H, **17**), 2.96 (m, 2H, **16**), 2.47 (m, 1H, **2'**), 2.18 (m, 1H, **2'**). $LRMS^2$ (ESI^+) $[M + H]^+$ calc'd *m/z* 563.3, found *m/z* 563.3 → 545.3, 476.4, 384.2, 323.1, 297.1, 206.1; $[M + 2H]^{2+}$ calc'd *m/z* 282.1, found *m/z* 282.2 → 502.2, 476.3, 358.1, 251.7, 206.3, 88.1. UV (1% FA) λ_{max} 610 and 660 nm.

MTX-dR_2 ^1H NMR (600 MHz, pyridine-d_5): δ 10.90 (t, 2H, J = 5.1 Hz, **Ar-NH**), 7.38 (s, 2H, **2, 3**), 7.29 (s, 2H, **6, 7**), 4.44 (dd, 2H, J = 4.1, 10.9 Hz, **5'**), 4.37 (ddd, 2H, J = 2.7, 6.8 Hz, **3'**), 4.31 (dd, 2H, J = 6.5, 10.9 Hz, **5'**), 4.23 (ddd, 2H, J = 4.4, 6.5 Hz, **4'**), 4.04 (t, 4H, J =

5.9 Hz, **14**), 3.61 (dq, 4H, J = 2.0, 6.5 Hz, **11**), 3.18 (m, 2H, J = 6.1, 7.8 Hz, **1'**), 3.10 (m, 2H, J = 6.9 Hz, **1'**), 2.98 (t, 4H, J = 6.5 Hz, **12**), 2.95 (m, 4H, **13**), 2.46 (m, 2H, **2'**), 2.17 (m, 2H, **2'**). $LRMS^2$ (ESI^+) $[M + H]^+$ calc'd *m/z* 681.3, found *m/z* 681.4 → 663.4, 502.3, 323.3, 206.2; $[M + 2H]^{2+}$ calc'd *m/z* 341.2, found *m/z* 341.3. UV (1% FA) λ_{max} 610 and 660 nm.

Isotopically-labeled MTX-[$^{13}C_5$]dR was synthesized by the same method and purified using a sample-isolated HPLC column and injection port. Its identity was confirmed by LC/MS^3 fragmentation patterns of the doubly charged species. $LRMS^2$ (ESI^+) $[M + H]^+$ calc'd *m/z* 568.3, found *m/z* 568.3 → 550.3, 507.2, 481.2, 384.2, 323.1, 297.1, 211.2. $LRMS^3$ (ESI^+) $[M + 2H]^{2+}$ calc'd *m/z* 284.7, found *m/z* 284.6 → 507.2, 481.3 → 211.2, 445.4, 358.1, 275.8, 267.2, 254.0, 223.1, 211.3, 88.1.

Synthesis of the reduced PIX-dR covalent adduct

Synthesized as a mixture of regioisomers using the procedure described above with the following modifications. After evaporation of the reaction, the crude product was dissolved in water and insoluble materials were removed by centrifuge filtration (Ultrafree®-MC-HV centrifugal filters; Durapore®-PVDF 0.45 µm). Initial HPLC purification performed using **Gradient 2**. The product eluting at 8 min was dried by lyophilization and further purified using a smaller column (250 x 4.6 mm) of the same specifications by **Gradient 3**. The PIX-dR adduct eluted as a broad peak between 20-25 minutes and was dried and characterized as described for the MTX-dR conjugate. See **Appendix III** figures for NMR labeling. ^1H NMR (600 MHz; 0.1% CD_2O_2 in D_2O): δ 9.04 (bs, 1H, **1**), 8.90 (bs,

1H, **2**), 7.84 (d, 1H, J = 4.0 Hz, **3**), 6.97 (ds, 2H, **7, 8**), 3.77 (m, 1H, **3'**), 3.73 (m, 1H, J = 2.4, 11.0 Hz, **5'**), 3.56 (bs, 2H), 3.52 (bs, 2H), 3.45 (t, 2H, J = 5.4 Hz), 3.36 (t, 2H, J = 5.8 Hz), 3.33 (m, 2H, **1'**), 2.09 (m, 1H, **2'**), 1.91 (m, 1H, J = 8.45 Hz, **2'**). $LRMS^2$ (ESI^+) $[M + H]^+$ calc'd *m/z* 444.2, found *m/z* 444.3 → 427.2, 401.3, 384.2, 309.2, 292.2, 283.2, 266.2, 179.2, 162.2, 136.2. UV (H_2O) λ_{max} 317 nm.

Synthesis of the reduced DOXol-dR covalent adduct

To a stirred solution of Doxorubicin hydrochloride (100 mg, 0.172 mmol) in methanol (3.5 mL, 0.05 M) was added excess $NaBH_4$ (32.6 mg, 0.862 mmol) under an argon atmosphere. The reaction proceeded at rt with vigorous bubbling and a rapid color change from bright red to a dark green. Once the color had returned to an orange/red color indicating dissolution of the borate-ester salts and full degradation of the reducing agent, the reaction solution was diluted to 20 mL with H_2O and slowly neutralized with 1N HCl (must be very careful not to over-acidify and degrade the glycosyl bond). The reaction mixture was then filtered through celite and washed with methanol (MeOH), and the filtrate was removed under reduced pressure by rotary evaporation. The bright orange film was taken up in H_2O and appeared as one peak by HPLC **Gradient 4**. The resulting product was confirmed to be the 13-OH reduced form of Doxorubicin by ^1H NMR and LRMS and carried forward. The DOXol-dR covalent conjugate was then synthesized as a mixture of diastereomers at C-13 as described above and eluted as the first major peak appearing at 8 minutes by HPLC following **Gradient 4**. See **Appendix III** figures for NMR labeling. ^1H NMR (600 MHz; CD_3OD) mixture of diastereomers: δ 8.00 (d, 1H, J = 7.6 Hz, **1**), 7.86 (t, 1H, J = 8.2 Hz, **2**), 7.59 (d, 1H, J = 8.5 Hz, **3**), 5.49 (bs, 0.5H, **1'**), 5.48 (bs ,

0.5H, **1'**), 5.15 (bs, 0.5H, **7**), 5.13 (bs, 0.5H, **7**), 4.26 (q, 1H, J = 6.6 Hz, **5'**), 4.04 (s, 3H, **4-OCH$_3$**), 3.96 (dd, 1H, J = 3.6, 11.2 Hz, **14**), 3.75 (m, 1H, **4'**), 3.74 (m, 1H, **14**), 3.64 (dd, 1H, J = 4.2, 11.2 Hz, **5''**), 3.61 (m, 1H, **3''**), 3.57 (dd, 1H, J = 3.5, 7.3 Hz, **13**), 3.53 (dd, 1H, J = 6.1, 11.2 Hz, **5''**), 3.44 (m, 1H, J = 4.4, 6.3 Hz, **4''**), 3.34 (m, 1H, **3'**), 3.10 (d, 0.5H, J = 20.6 Hz, **10**), 3.07 (d, 0.5H, J = 18.7 Hz, **10**), 3.03 (m, 2H, **1''**), 2.88 (d, 0.5H, J = 18.7 Hz, **10**), 2.84 (d, 0.5H, J = 20.4 Hz, **10**), 2.49 (d, 0.5H, J = 14.7 Hz, **8**), 2.29 (d, 0.5H, J = 14.0 Hz, **8**), 2.17 (d, 0.5H, J = 14.0 Hz, **8**), 2.01 (dd, 0.5H, J = 4.6, 14.7 Hz, **8**), 1.93 (m, 2H, **2'**), 1.91 (m, 1H, **2''**), 1.75 (m, 1H, J = 7.4 Hz, **2''**), 1.31 (d, 3H, J = 6.4 Hz, **6'**). LRMS^2 (ESI$^+$) $[M + H]^+$ calc'd *m/z* 664.3, found *m/z* 664.1 → 646.2, 399.0, 363.2, 248.2. UV (H_2O) λ_{max} 480, 500 nm.

Synthesis of the reduced EPIol-dR covalent adduct

The reduced EPIol-dR conjugate was synthesized, purified, and analyzed as a mixture of diastereomers at the C-13 hydroxyl group using the procedure described above for the reduced DOXol-dR covalent conjugate. ^{1}H NMR (600 MHz; CD_3OD) mixture of diastereomers: δ 7.95 (d, 1H, J = 7.6 Hz, **1**), 7.84 (t, 1H, J = 8.1 Hz, **2**), 7.56 (d, 1H, J = 8.4 Hz, **3**), 5.49 (d, 0.5H, J = 3.2 Hz, **1'**), 5.47 (d , 0.5H, J = 3.2 Hz, **1'**), 5.11 (bs, 0.5H, **7**), 5.09 (bs, 0.5H, **7**), 4.04 (m, 1H, **5'**), 4.03 (s, 3H, **4-OCH$_3$**), 3.96 (m, 1H, J = 3.7 Hz, **14**), 3.74 (m, 1H, J = 7.5, 10.9 Hz, **14**), 3.63 (m, 1H, **3''**), 3.60 (m, 1H, **5''**), 3.57 (dd, 1H, J = 3.4, 7.3 Hz, **13**), 3.51 (dd, 1H, J = 6.0, 11.2 Hz, **5''**), 3.44 (m, 1H, J = 4.4, 6.2 Hz, **4''**), 3.27 (m, 1H, **3'**), 3.22 (m, 1H, **4'**), 3.18 (m, 1H, **1''**), 3.08 (d, 0.5H, J = 18.5 Hz, **10**), 3.04 (d, 0.5H, J = 18.5 Hz, **10**), 3.03 (m, 1H, **1''**), 2.85 (d, 0.5H, J = 18.5 Hz, **10**), 2.82 (d, 0.5H, J = 18.5 Hz, **10**), 2.47 (d, 0.5H, J = 14.7 Hz, **8**), 2.33 (m, 1H, **2'**), 2.29 (d, 0.5H, J = 14.8 Hz,

8), 2.18 (d, 0.5H, J = 4.8, 14.7 Hz, **8**), 2.02 (dd, 0.5H, J = 4.4, 14.7 Hz, **8**), 1.94 (m, 1H, **2”**), 1.80 (m, 1H, **2’**), 1.79 (m, 1H, **2”**), 1.35 (d, 3H, J = 6.2 Hz, **6’**). LRMS^2 (ESI$^+$) $[M + H]^+$ calc’d *m/z* 664.3, found *m/z* 664.1 → 646.1, 399.0, 363.1, 266.2, 248.2. UV (H_2O) λ_{max} 480, 500 nm.

Synthesis of reduced covalent adducts of anthracyclines with an AP-containing double-stranded 12mer oligonucleotide

A typical procedure is given for the reaction of MTX with the AP-containing 12mer duplex. The uracil-containing 12mer oligonucleotide (10 nmol, 5’-GTT GC**U** CGT ATG-3’) was combined with its complement oligonucleotide (10 nmol, 5’-CAT ACG CGC AAC-3’) in HEPES buffer (total volume was 0.5 mL). The solution was heated to 90 °C for 5 minutes and the strands were annealed by allowing the solution to cool slowly to ambient temperature. UDG (0.25 units/μL) was added and the mixture heated to 37 °C for 1 hour. MTX (0.011 mL of a 0.002 M stock solution, 0.04 mM final concentration) and $NaB(CN)H_3$ (0.028 mL of a freshly prepared 1 M solution in water, 50 mM final concentration) were mixed and added to the DNA solution. The reaction was allowed to incubate at 37 °C for 3 hours, then purified by reversed-phase HPLC according to **Gradient 5**.

Enzymatic digestion of DNA containing reduced anthracycline-AP covalent adducts

DNA (10 μg) was suspended in digest buffer. To this solution was added DNase 1 (5 μg) and nuclease P1 (0.5 μg) at 37 °C. After 3 hours, phosphodiesterase 1 (24 mU)

and alkaline phosphatase (40 mU) were added and incubation continued for 15 hours. Optionally (for improved SPE enrichment when needed), adenosine deaminase (12.5 mU) was added at ambient temperature for 2 hours, after which digest solutions were then placed on ice for 5 minutes and 3 volumes of ice-chilled ethanol was added. The samples were stored at -20 °C for 1 hour after which they were centrifuged at 21,000 x g for 10 min. Supernatants were collected and vacuum centrifuged to dryness, then resuspended in LC/MS grade water (1 mL) for SPE encrichment.

SPE enrichment of the reduced MTX-dR covalent conjugate

The MTX-dR resulting from modified DNA digestion was enriched by SPE employing a Sola HRP cartridge (10 mg, 1 mL). The cartridge was preconditioned with methanol containing 0.1% FA (2 mL) followed by 0.1% aqueous FA (2 mL). Samples were then loaded and washed with 0.1% aqueous FA containing 6% methanol (2 mL). MTX-dR was eluted from the cartridge with 50% methanol/0.05% FA. Samples were dried by vacuum centrifugation at room temperature, reconstituted in 0.1% aqueous FA containing 10% acetonitrile (20 µL), sonicated, and transferred to polypropylene autosampler vials for LC/MS analysis.

Formulas used to condense data for generation of figures in Excel

HPLC chromatograms were plotted using every second data point from the exported analysis. Absorbance values were modified by dividing the raw data values by 1,000 for singular plots and by 5,000 for comparisons.

Retention time offset x = OFFSET(A2, (ROW(D[*N*])*2)-1, 0) (**Eq. 2-01**)

Absorbance offset y = OFFSET(C2, (ROW(E[*N*])*2)-1, 0) (**Eq. 2-02**)

where A was the column containing raw time values, B was the column containing raw absorbance values, C was the column containing modified absorbance values, D was the column containing offset time calculations, E was the column containing offset absorbance calculations, *N* was the number corresponding to the row for each calculated value, and 1 was the row containing column labels.

The DOX-dR and EPI-dR chromatograms for ESI-LC/MS analysis of the digest hydrolysates for the reduced 12mer covalent conjugates (**Fig. 2-10**) were plotted as a combination of the maximum ion counts for the *m/z 662* and *664* ions to represent total product formation according to the equations below:

Chromatogram intensity modifier

Intensity = (E[*N*]/MAX(E:E))*100 (**Eq. 2-03**)

Maximum intensity value selection

y(E) = INDEX(C[*N*]:D[*N*], 0, MATCH(MAX(C[*N*]:D[*N*]), C[*N*]:D[*N*], 0)) (**Eq. 2-04**)

Time value selection for selected maximum intensity value

x(F) = IF(E[*N*]=C[*N*], A[*N*], B[*N*]) (**Eq. 2-05**)

where A was the column containing raw time values for *m/z 662*, B was the column containing raw time values for *m/z 664*, C was the column containing raw intensity values for *m/z 662*, D was the column containing raw intensity values for *m/z 664*, E was the column containing selected maximum intensity values, F was the column containing selected time values correlating to selected maximum intensity values, G was the column

containing modified maximum intensity values, and *N* was the number corresponding to the row for each calculated value. Chromatograms for the unmodified nucleosides, MTX-dR, and PIX-dR were plotted only using the intensity modifier.

Mass spectra were plotted using every fifth data point from the exported analysis according to the equations below. Relevant values for labeled data points were selected manually according to maximum intensity values and added to the modified data set. Ion count intensities were modified to fit a scale of 1-100%.

Mass value offset x = OFFSET(A2, (ROW(D[*N*]*5)-1, 0) (**Eq. 2-06**)

Ion count intensity modifier Intensity = (B[*N*]/MAX(B:B))*100 (**Eq. 2-07**)

Relative intensity offset y = OFFSET(C2, (ROW(E[*N*]*5)-1, 0) (**Eq. 2-08**)

where A was the column containing raw *m/z* values, B was the column containing raw intensity values, C was the column containing ion intensity modifier calculations, D was the column containing *m/z* value offset calculations, E was the column containing modified ion intensity value offset calculations, *N* was the number corresponding to the row for each calculated value, and 1 was the row containing column labels.

References

(1) *Mitoxantrone Injection: MedlinePlus Drug Information*. https://medlineplus.gov/druginfo/meds/a608019.html (accessed 2023-07-30).

(2) Jezeršek, B.; Lučka, N.; Novaković, A. Current Opinion on Pixantrone in the Treatment of Non-Hodgkin B-Cell Lymphoma. *Therapeutics and Clinical Risk Management* **2021**, *17*, 183-192.

(3) Parker, B. S.; Cullinane, C.; Phillips, D. R. Formation of DNA Adducts by Formaldehyde-Activated Mitoxantrone. *Nucleic Acids Res.* **1999**, *27* (14), 2918–2923.

(4) Parker, B. S.; Cutts, S. M.; Cullinane, C.; Phillips, D. R. Formaldehyde Activation of Mitoxantrone Yields CpG and CpA Specific DNA Adducts. *Nucleic Acids Res.* **2000**, *28* (4), 982-990.

(5) Evison, B. J.; Mansour, O. C.; Menta, E.; Phillips, D. R.; Cutts, S. M. Pixantrone Can Be Activated by Formaldehyde to Generate a Potent DNA Adduct Forming Agent. *Nucleic Acids Res.* **2007**, *35* (11), 3581–3589.

(6) Evison, B. J.; Chiu, F.; Pezzoni, G.; Phillips, D. R.; Cutts, S. M. Formaldehyde-Activated Pixantrone Is a Monofunctional DNA Alkylator That Binds Selectively to CpG and CpA Doublets. *Mol. Pharmacol.* **2008**, *74* (1), 184-194.

(7) Mansour, O. C.; Evison, B. J.; Sleebs, B. E.; Watson, K. G.; Nudelman, A.; Rephaeli, A.; Buck, D. P.; Collins, J. G.; Bilardi, R. A.; Phillips, D. R.; Cutts, S. M. New Anthracenedione Derivatives with Improved Biological Activity by Virtue of Stable Drug-DNA Adduct Formation. *J. Med. Chem.* **2010**, *53* (19), 6851–6866.

(8) Cummings, J.; Stuart, J. F. B.; Calman, K. C. Determination of Adriamycin, Adriamycinol, and their 7-Deoxyaglycones in Human Serum by High-Performance Liquid Chromatography. *J. Chromatogr.* **1984**, *311*, 125–133.

(9) Beijnen, J. H.; Meenhorst, P. L.; Van Gijn, R.; Fromme, M.; Rosing, H.; Underbergii, W. J. M. HPLC Determination of Doxorubicin, Doxorubicinol and Four Aglycone Metabolites in Plasma of AIDS Patients*. *J. Pharm. Biomed. Anal.* **1991**, *9* (10-12), 995–1002.

(10) Schweitzer, B. A.; Egholm, M.; Koch, T. H. Mechanistic Studies of the Reduction of Daunomycin with Sodium Borohydride. Formation and Reaction of Borate Esters. *JACS* **1992**, *114* (1), 242–248.

(11) Tungen, J. E.; Gerstmann, L.; Vik, A.; De Matteis, R.; Colas, R. A.; Dalli, J.; Chiang, N.; Serhan, C. N.; Kalesse, M.; Hansen, T. V. Resolving Inflammation: Synthesis, Configurational Assignment, and Biological Evaluations of RvD1$_{n-3\,DPA}$. *Chem. Eur. J.* **2019**, *25* (6), 1476–1480.

(12) Kent, P. W.; Stacey, M.; Wiggins, L. F. Deoxy-Sugars. Part II. Synthesis of 2-Deoxy-D-Ribose and 3-Deoxy-D-Xylose from D-Arabinose. *J. Chem. Soc.* **1949**, 1232–1235.

(13) Sowden, J. C. A Convenient Method of Preparing 2-Deoxy-D-Ribose. *JACS* **1954**, *76* (13), 3541–3542.

Chapter III

Unreduced Interactions of MTX, PIX, DOX, and EPI with AP Sites Contribute to DNA Damage

Background

During our method development for the reductive amination between anthracyclines and AP sites in 12mer oligonucleotides, we noticed an unintended, competing reactivity between MTX and the AP site. Our initial reaction protocol was to incubate the anthracycline with the AP-12mer for 1-3 hours to maximize formation of the Schiff base before reduction, but this led to incomplete conversion to the MTX-12mer as well as several new products in the HPLC analysis (see **Fig. 2-02**). PIX produced less of these new products under the same reaction conditions, and they were not observed with DOX/EPI. The immediate solution was to co-treat the AP-12mer with MTX and $NaB(CN)H_3$ that was freshly prepared from a solid rather than a pre-made solution in THF, which prevented this side reaction in full and was also adopted for the PIX-12mer reduction protocol.

When a control reaction was performed by incubating MTX with the AP-12mer without $NaB(CN)H_3$, we found that AP-12mer was still consumed over the course of a day while the new products increased at the same rate. It was hypothesized that the oligonucleotide was undergoing fragmentation around the AP site via β- and/or β-/δ-elimination, a reactivity that we had predicted due to formation of the Schiff base but occurring much more rapidly than expected. Purification of the various new peaks and

analysis by ESI-LC/MS confirmed this hypothesis, showing masses that matched those expected from both β- and β-/δ-elimination as well as partial hydrolysis of the terminal phosphate of the same fragments.

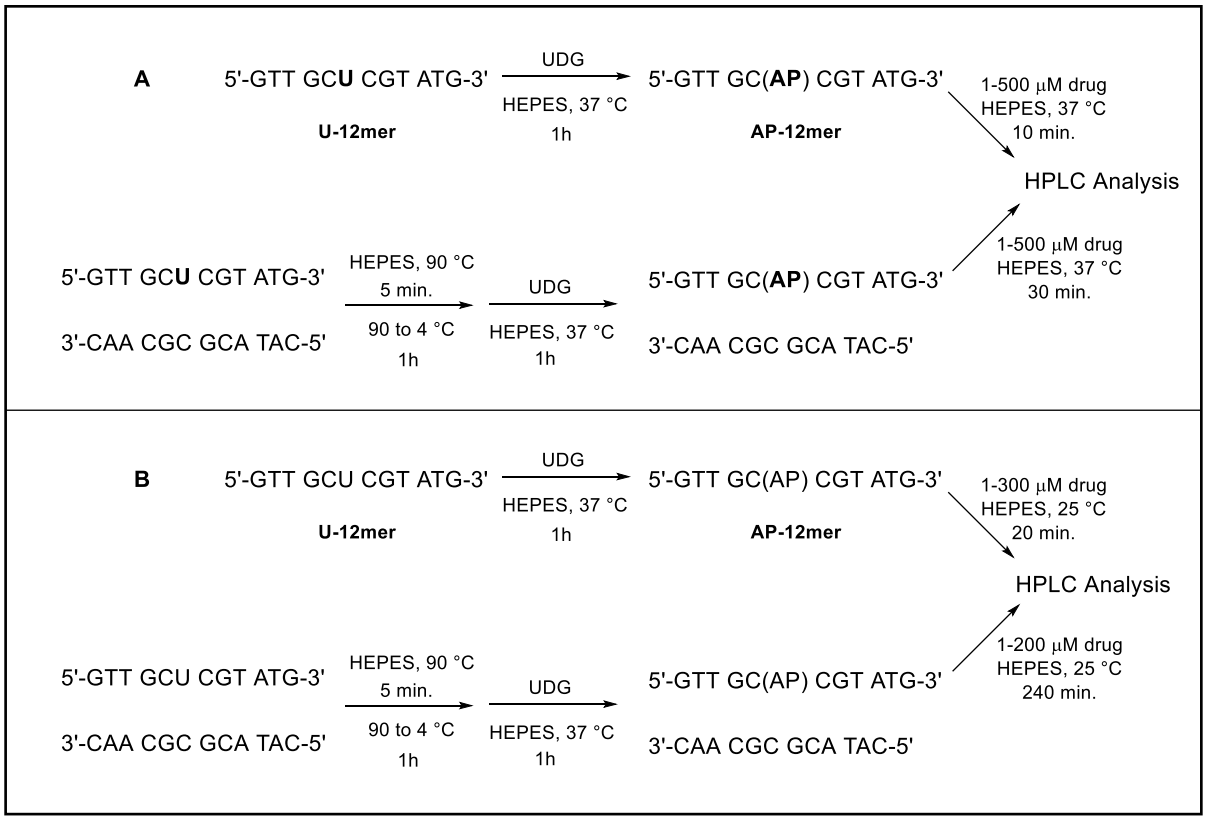

Figure 3-01. Reaction schemes for ssDNA and dsDNA scission reactions by anthracyclines. Initial conditions with scission performed at 37 °C (**A**) provided EC_{50} curves outlined in **Figures 3-07 A** and **3-08 A**. *HPLC conditions to prevent complement strand peak overlap were not yet developed for this*. $ssEC_{50}$ curves for **B** conditions with updated HPLC elution methods are shown in **Figure 3-07 B** and the $dsEC_{50}$ curves for **B** conditions with MTX and PIX via updated HPLC elution methods is shown in Figure **3-08 B**.

Anthracyclines Incise DNA at AP Sites with Varying Efficiencies

HPLC Analysis of 12mer Oligonucleotide Scission by MTX, PIX, and DOX

Repeating this reaction with the other three anthracyclines on longer time scales and elevated drug concentrations by the methods outlined in **Figure 3-01** showed that this reactivity is exhibited by all of them at varying efficiencies which paralleled the relative reductive amination reactivity (MTX > PIX > DOX). Each produced the same DNA fragment products in similar ratios over the course of the full reaction, albeit at slightly different rates, as seen in **Figure 3-02**. Observation of this reactivity was extremely promising for our overall goals as it provides further evidence that formation of the Schiff base between certain anthracyclines and AP sites is favorable and contributes to previously unrecognized DNA damage in a Topoisomerase-independent manner.

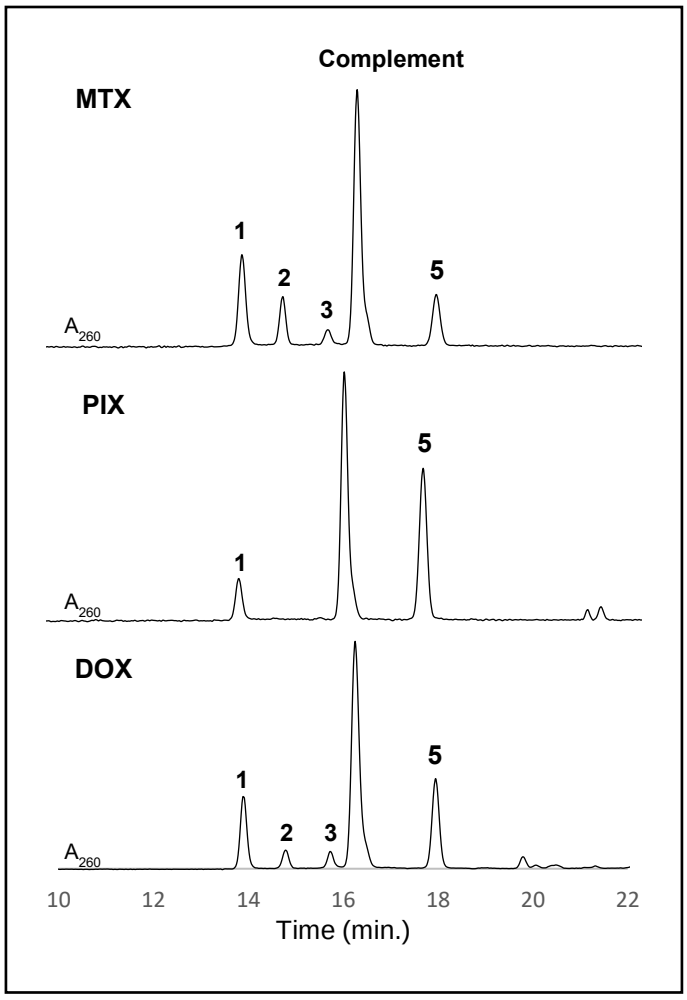

Figure 3-02. HPLC chromatogram of double-stranded scission reaction mixtures (10 μM DNA) for MTX (150 μM, 30min.), PIX (150 μM, 30min.), and DOX (200 μM, 7h) with peaks labeled according to **Fig. 3-03**.

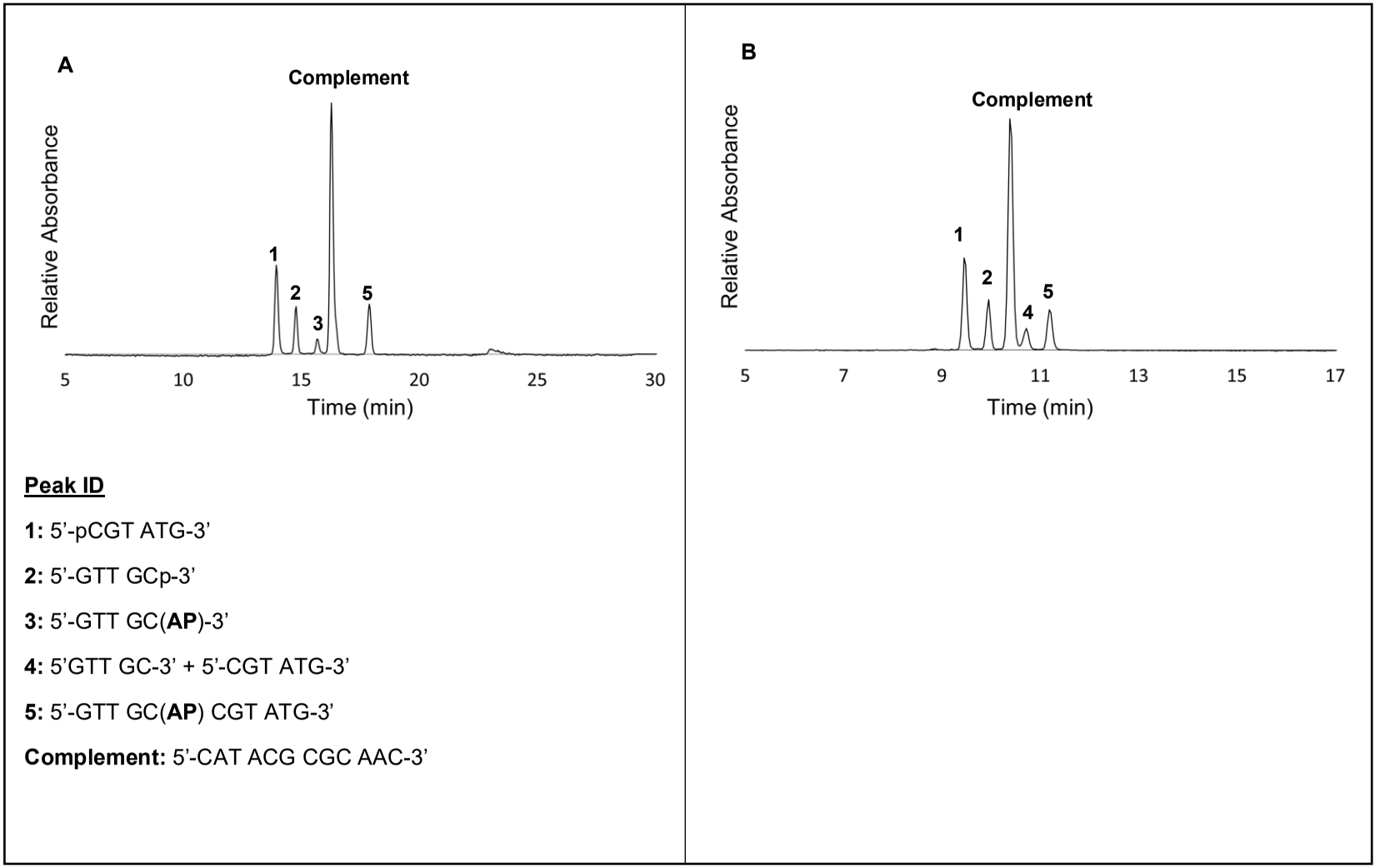

Figure 3-03. HPLC chromatograms of the double stranded MTX-12mer scission crude reaction mixture (10 μM DNA, 150 μM MTX, 37 °C) by Gradient 3 (**A**) and Gradient 1 (**B**). Peaks that could be isolated were purified and characterized by ESI-LC/MS resulting in the identities shown.

After seeing this reactivity in MTX at low drug concentration, we wanted to examine the efficiency of each compound to induce strand scission in our 12mer oligonucleotide in a more quantifiable manner. Initially, we hoped to be able to quench the reaction by adding excess methoxyamine since it is known to form stable covalent adducts at AP sites. However, due to how quickly MTX was able to cause strand scission, any quenching with known AP site binders was ruled out as an experimental method since it likely would not truly outcompete the anthracycline to give us an instantaneous snapshot of reaction progress. Quenching the reaction could alternatively be accomplished by flash-freezing small-scale reaction aliquots at -80 °C and storing for future analysis. Optimally, this analysis would be performed via gel electrophoresis with quantitation by fluorescence or ^{32}P-radioactivity of 5'-labeled DNA strands. However, the 3'-fragment of the substrate strand is invisible in such experiments. We chose to qualitatively analyze the nicking reactions by LC/MS because this method will detect all fragment products and can give structural/sequence information.

For calculation of reaction efficiencies, we opted to use HPLC as a method to separate, identify, and quantify the products from anthracycline-induced DNA scission. Samples did not require further processing or cleanup and could be directly injected onto the column for analysis upon thawing. This prevented re-induction of the reaction process by initial separation of the reaction components on the solid phase before the solution could warm to room temperature. Additional reactions to label the DNA strands for detection were also avoided as UV detection through HPLC identified all fragments produced. The corresponding chromatographic peaks were quantified by peak areas for calculation of reaction efficiency. In ssDNA, efficiency was calculated by simply

comparing the ratio of fragment peaks to remaining AP-12mer. There were additional difficulties when attempting to quantify dsDNA products due to overlap of the complement strand with one of the fragment products via any number of similar elution methods (**Fig. 3-03**). Extended elution methods were developed to more optimally isolate individual fragment peaks, but it appears that significantly high concentrations of MTX stabilize interactions between some of the fragments and the complement strand, causing them to co-elute as a broad mixture of products when analyzing these samples. Isolation of the DNA from the anthracyclines by passing the crude reaction through a polyacrylamide-based spin column proved useful for LC/MS analysis but appears to suffer from similar binding interactions as recovery of DNA drops from ~85% to 10-15% at high concentrations of MTX. This strong binding interaction reflects the significant DNA stabilization by MTX reported later herein and was prevented by heating the HPLC column to 65 °C during purification via another extended elution method.

Mass Spectrometric Analysis of the 12mer Oligonucleotide Scission Products

As mentioned before, hydrolysis of the terminal phosphates as a DNA scission product was confirmed by ESI-LC/MS analysis (**Figures 3-04** and **3-05**). This is an atypical reaction for DNA scission at AP sites and caused concern that some reactivity was occurring with the HPLC buffer or on the column itself. A second indication for this was the presence of two peaks by HPLC when running pure commercial standards of the phosphorylated fragment products, but observing only mass peaks corresponding to the precursor oligonucleotide by ESI-MS. Crude analysis of the reaction mixture by ESI-LC/MS still showed significant presence of both phosphorylated and dephosphorylated fragments, suggesting this reactivity to either be occurring in solution or on the column used for tandem MS purification, although the former was unlikely due to the lack of dephosphorylation seen from the commercial standard via direct sample injection for ESI-MS. Analysis of the crude reaction mixture without column separation was performed by passing the sample through a polyacrylamide-based size exclusion gel column to isolate the DNA from anthracyclines or buffer. Direct injection of this sample into the ESI-MS source showed significantly lower levels of dephosphorylated DNA fragments, shown in **Figure 3-06**. Although this reactivity does appear to be primarily due to column interactions rather than *in situ* processes, it can only occur upon scission of the DNA strand into these constituent fragments and thus does not affect our calculations for reaction efficiency as long as all fragments are identified and accounted for.

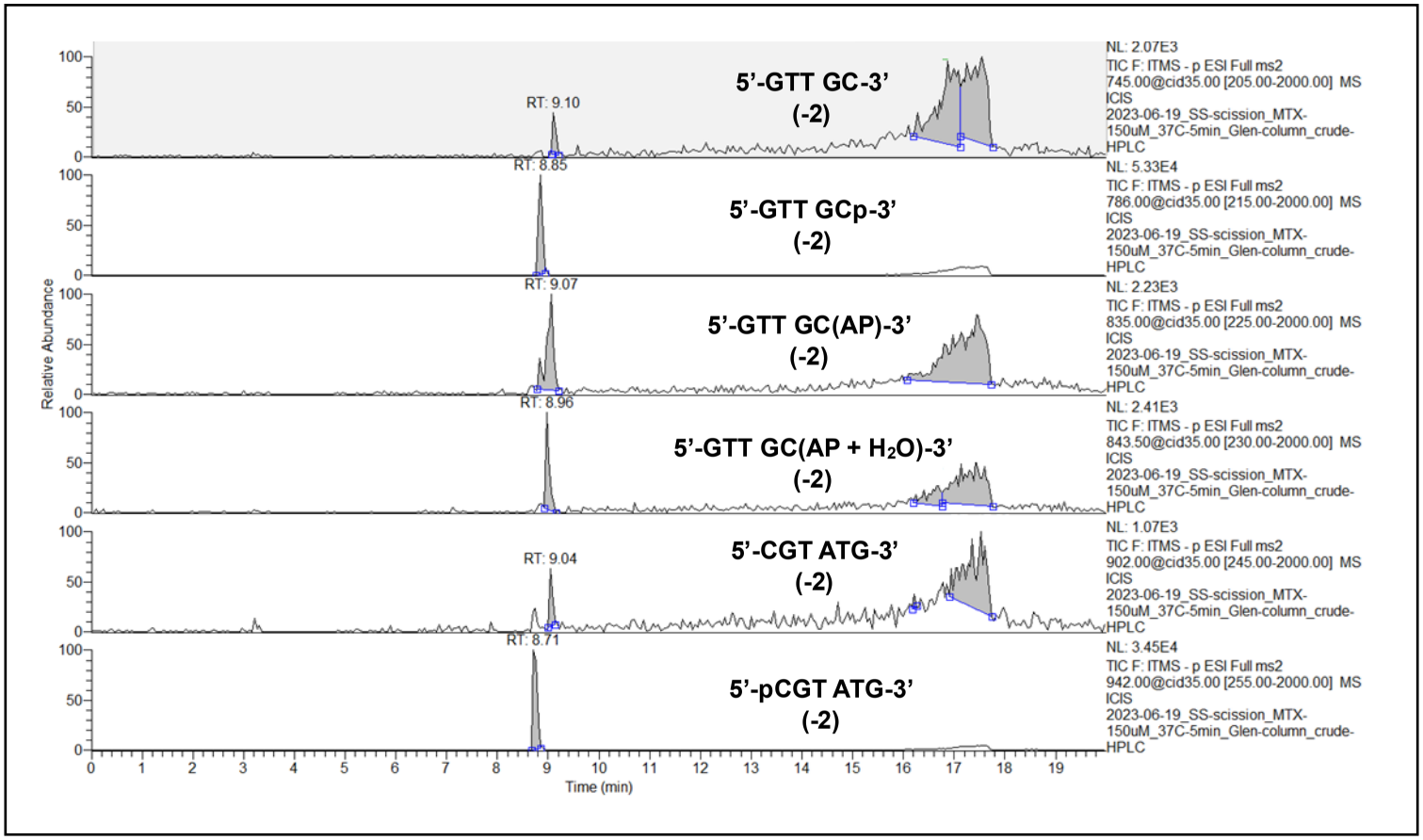

Figure 3-04. ESI-LC/MS chromatogram of the single stranded MTX-12mer scission crude reaction analysis with detection for selected ion *m/z* corresponding to expected 12mer β- and δ-elimination oligonucleotide products.

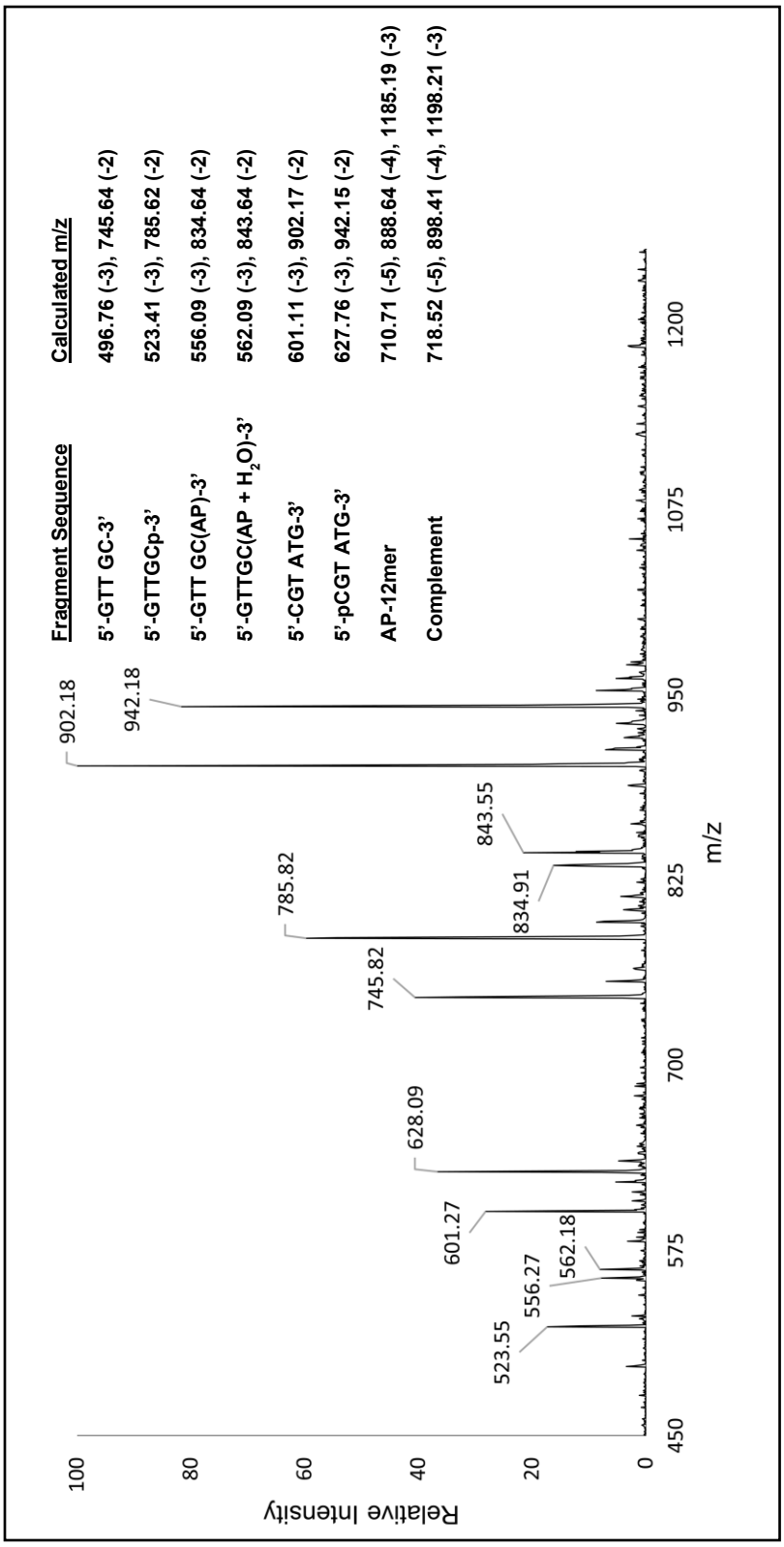

Figure 3-05. ESI-LC/MS total ion scan mass spectrum of the MTX + ssAP-12mer scission crude reaction mixture after 5 minutes (10 μM DNA, 150 μM MTX, 37 °C).

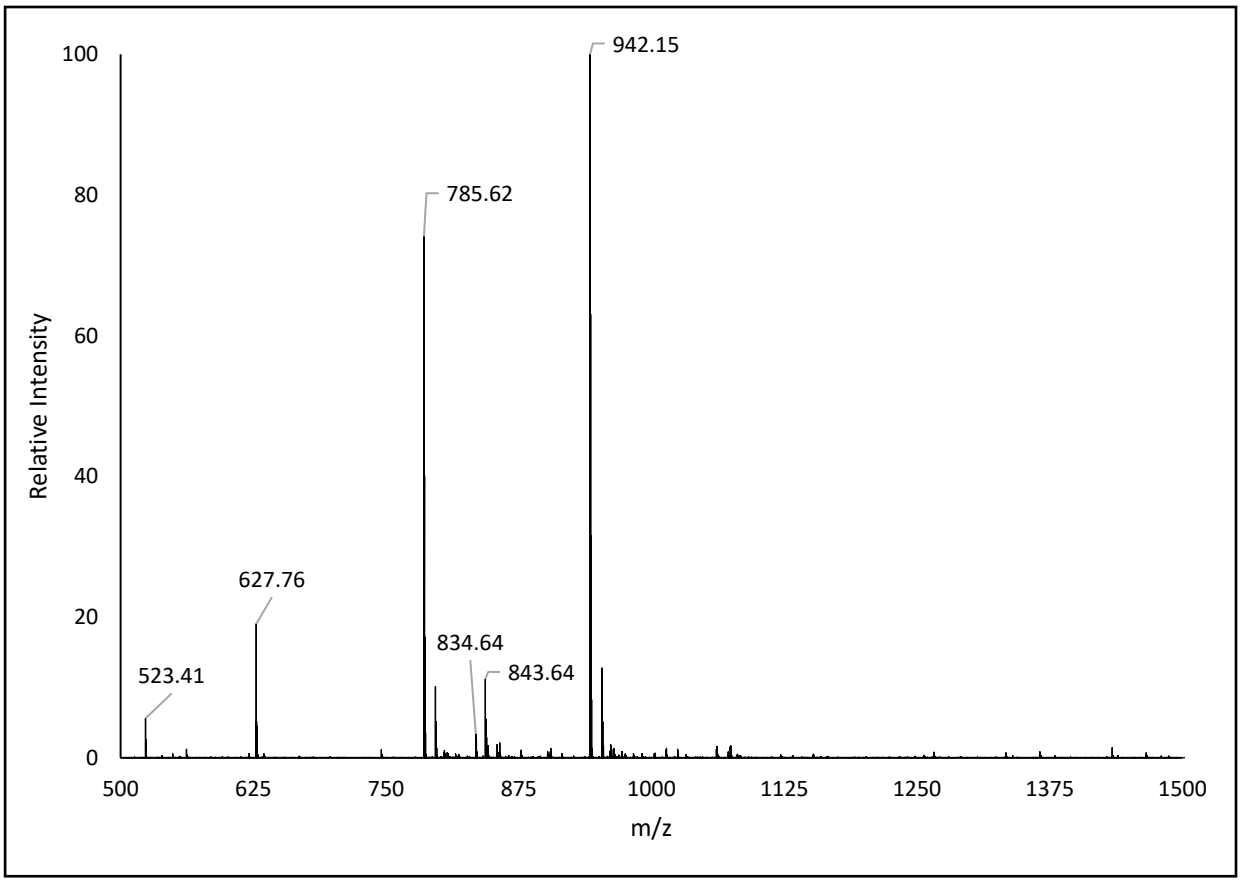

Figure 3-06. ESI-MS total ion scan mass spectrum of the MTX + ssAP-12mer scission crude reaction mixture (10 μM DNA, 150 μM MTX, 37 °C, 10 min.) via direct injection after desalting with Bio-Spin® gel columns. Calculated fragment *m/z* shown in **Figure 3-05**.

Calculation of Differential Scission Efficiencies for MTX, PIX, and DOX in both the Single- and Double-stranded 12mer Oligonucleotides

Reaction efficiency by HPLC analysis could be calculated by comparing the ratio of fragment products to remaining AP-12mer as described above for both ssDNA and dsDNA. Alternatively, efficiency for the duplex reactions could be calculated using the complement strand as an internal reference and monitoring the depletion of the AP-12mer:complement ratio when compared to that of the t_0 measurement before the addition of any anthracycline. This method was preferred when possible as it allowed us a static reference point for quantitative measurement. By this method, peak areas also had to be corrected for differences in absorbance by dividing each by their calculated extinction coefficient. Initially, reactions were performed by incubating 10 μM DNA with drug concentrations ranging from 0.001-1 mM at 37 °C. Results were plotted as log[Anthracycline] vs fraction of DNA cleaved after 10 minutes for ssDNA and 30 minutes for dsDNA (**Fig. 3-07**). EC_{50} values were determined for each compound based on the sigmoidal fit equation generated by the KaleidaGraph® software.

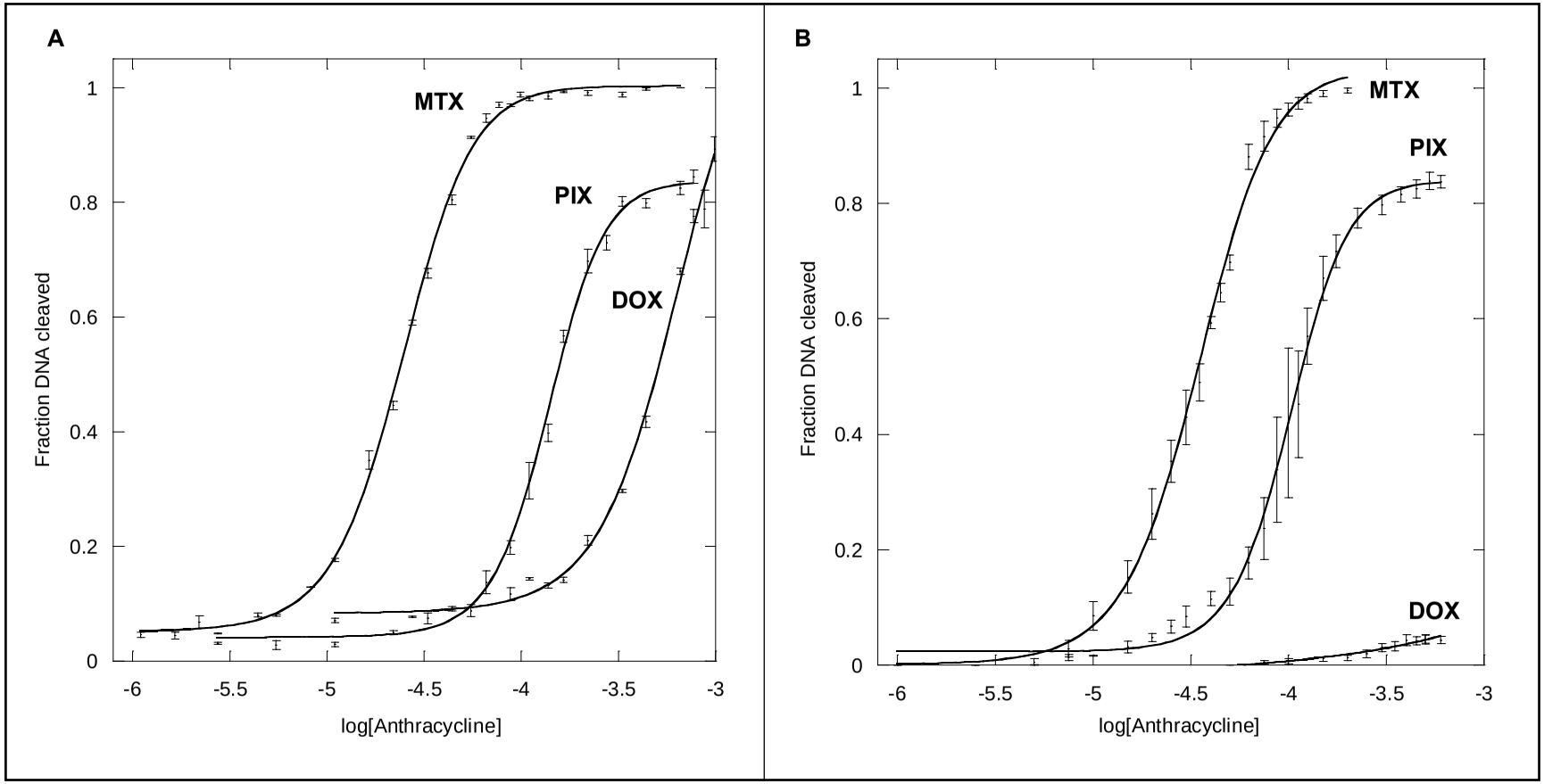

Figure 3-07. ssAP-12mer (10 μM) scission efficiency curves for MTX, PIX, and DOX/EPI after (**A**) 10 minutes at 37 °C and after (**B**) 20 minutes at 25 °C.

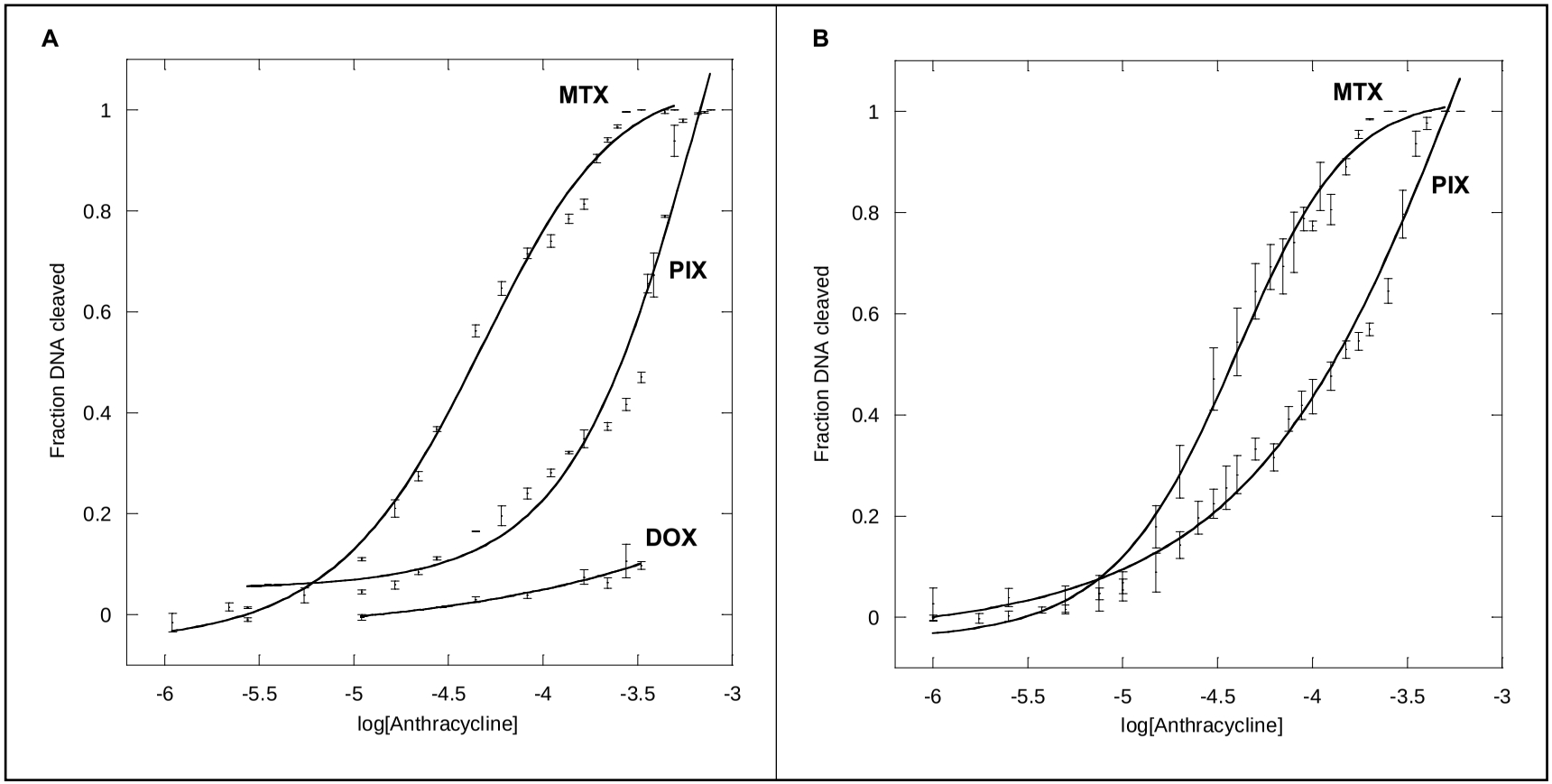

Figure 3-08. dsAP-12mer (10 μM) scission efficiency curves for MTX, PIX, and DOX after (**A**) 30 minutes at 37 °C and for MTX and PIX after (**B**) 240 minutes at 25 °C.

An interesting observation was the significant difference in reactivity between DOX and the anthracenediones similar to that seen in the reductive amination reaction to form the reduced 12mer adducts. MTX exhibited the greatest reaction efficiency of the compounds (**Fig. 3-07**), followed by PIX, then DOX/EPI which both required extreme concentrations of drug to effect similar levels of strand scission in ssDNA over the same time period and showed little reaction at all at lower temperatures. These results indicate a structural inhibition to the interactions of the glycosyl amines of DOX and EPI with AP sites in our DNA sequence. Both classes of compounds are known to preferentially intercalate at GC sequences of DNA, and the significantly higher reactivity shown by the anthracenediones may be attributed to the greater conformational freedom of the hydrocarbon chains allowing more frequent interactions between amines and AP sites in this particular sequence. These reactivity differences in ssDNA initially suggested a chemical perspective for interpreting such trends rather than a structural one since intercalation would not play a role, but studies have shown the ability of DOX to still interact strongly with GC sequences in ssDNA as well as weaker electrostatic interactions with AT sequences along the phosphodiester backbone that do not require intercalation[1,2]. Both types of interactions would inhibit the amine-AP site interactions in a similar manner to dsDNA, potentially explaining the equivalent trend for both in our model system.

Although the relative trends between the different drugs were similar in both dsDNA and ssDNA, there was also a significant difference in reactivity observed for each compound between the two systems. As can be seen in **Figures 3-07 A** and **3-08 A**, achieving the same reaction efficiency for MTX in dsDNA as in ssDNA required about 3x

the reaction time at 37 °C. This observation of the difference between single-stranded and double-stranded reactivities was actually underestimated due to the later realization that the strands of the dsAP-12mer dissociate at much lower temperatures than its undamaged counterpart. The T_m of the AP-12mer is only 33 °C, meaning that under our reaction conditions the so-called duplex DNA was ~80% single-stranded. Recent revisions of these experiments at 25 °C suggest an even more drastic reactivity difference for MTX and PIX with dsDNA, requiring nearly 12x as long to achieve the same scission levels as with ssDNA (**Fig. 3-08**).

While the ssDNA reaction itself appears to follow simple temperature:rate convention (where the reaction efficiency doubles with a 10 °C increase), dsDNA clearly does not. Our current investigations do not provide an explanation for this, but it is likely a stability phenomenon wherein intercalation of the anthracyclines prevents the catalysis of β- and β-/δ-elimination even when formation of the Schiff base may be rapid. A summary of the EC_{50} values, defined as the concentration of drug at which half of the original amount of AP-12mer has been cleaved, can be found in **Table 3-01** more clearly delineating the differences in reactivity between these systems.

	37 °C		**25 °C**	
	$ssEC_{50}$ (mM) 10 minutes	$dsEC_{50}$ (mM) 30 minutes	$ssEC_{50}$ (mM) 20 minutes	$dsEC_{50}$ (mM) 240 minutes
MTX	0.024	0.043	0.035	0.037
PIX	0.138	0.561*	0.102	0.438*
DOX	0.606*	Minimal rxn.	Minimal rxn.	N/A

Table 3-01. Summary of reaction efficiencies for scission of the AP-12mer (0.01 mM) with MTX, PIX, and DOX. EC_{50} values were calculated using sigmoidal curve fit equations generated by KaleidaGraph® software and outlined in the **Experimental Procedures**.

**Likely overestimates due to non-Sigmoidal nature of data set at relevant concentrations*.

Identification of a Long-lived, Stable Covalent Adduct Between PIX and the AP-Containing DNA Scission Product

Our combined HPLC-MS approach also allowed us to identify a long-lived PIX-AP site covalent adduct of a β-elimination fragment without the need for reduction. While the Schiff base itself is unstable to hydrolysis, the characteristic primary amine of Pixantrone that creates it likely allows for greater stability of the hemiaminal formed upon ring closure of the PIX-AP site adduct (**Fig. 3-09**). This is supported by the fact that we have not seen evidence of a stable adduct resulting from reaction of PIX with dR alone, suggesting the necessity of an α/β-unsaturated aldehyde for this stability. Thus, it is unlikely that we will be able to isolate and characterize PIX-DNA adducts within the full oligonucleotide without further reduction of the Schiff base as performed before. The major adduct we see by ESI-LC/MS in **Figure 3-10** is the hydrated form [5'-GTT GC(**AP + PIX + H2O**)-3' from **Fig. 3-09**] that we predict to form at C-3' of the sugar and be stabilized by tautomerization of the resulting alkene to the imine and further cyclization to the hemiaminal, a process that is unlikely with MTX due to its Schiff base forming from a secondary amine. We performed basic NMR, ESI-MS, and UV experiments to determine if this stable adduct was potentially formed by MTX as well at previously undetectable levels, but no evidence was seen by any method that would be representative of biological reactivity.

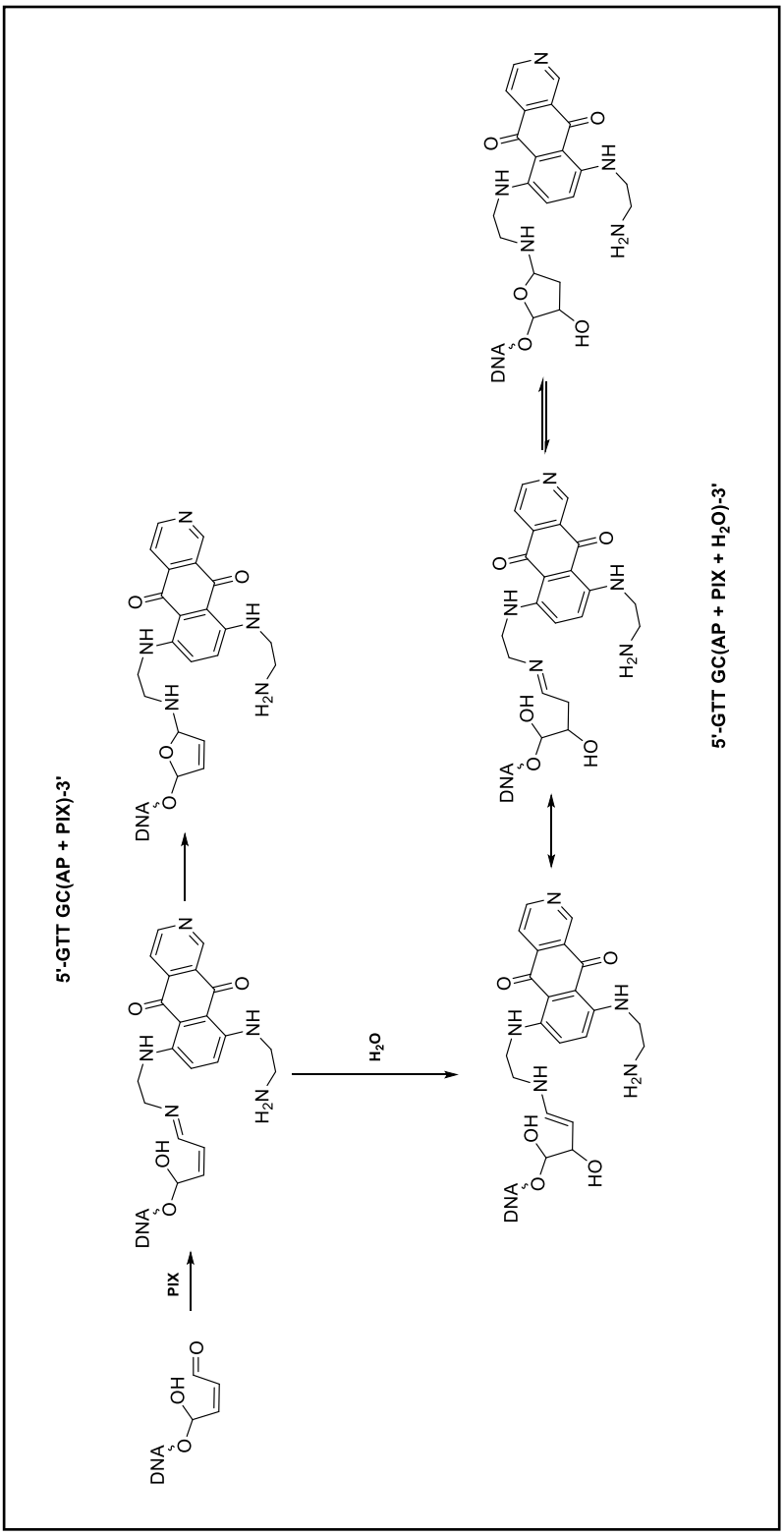

Figure 3-09. Proposed mechanism for the formation of a stable PIX-DNA adduct at the AP site of the fragment resulting from β-elimination of the AP-12mer.

Fragment analysis by ESI-LC/MS^2/MS^3 methodology further confirmed the identity of these products as meta-stable covalent adducts between PIX and the fragment sequence 5'-GTT GC(**AP**)-3'. Shown in **Figure 3-11**, the major fragments at *m/z 785.50* and *m/z 834.42* resulting from MS^2 analysis of the major peak at *m/z 997.18* correspond to the DNA sequences 5'-GTT GCp-3' and 5'-GTT GC(**AP**)-3' as identified in **Figure 3-05**. These characterizations were further confirmed by MS^3 analysis of the corresponding peaks and comparison of the selected ion CID spectrum to that of both the purchased standards and previously analyzed fragments from the reaction with MTX outlined in **Appendix V**. Although stable enough to allow for adduct purification and characterization, the unreduced bond between PIX and the AP site is clearly not as stable as the reduced form since the PIX-12mer reduced covalent conjugate reported in **Chapter II** does not exhibit the same ESI-LC/MS^2 fragmentation pattern. The CID spectrum for the latter, shown in **Appendix II**, does not contain any peak corresponding to the parent AP-12mer as would be expected if the compounds were of similar stability. This is unsurprising from a chemical perspective as the non-reduced C-N bond is still relatively weak in any of its equilibrium congeners when compared to the reduced structure and would be labile to both hydrolysis and energetic dissociation.

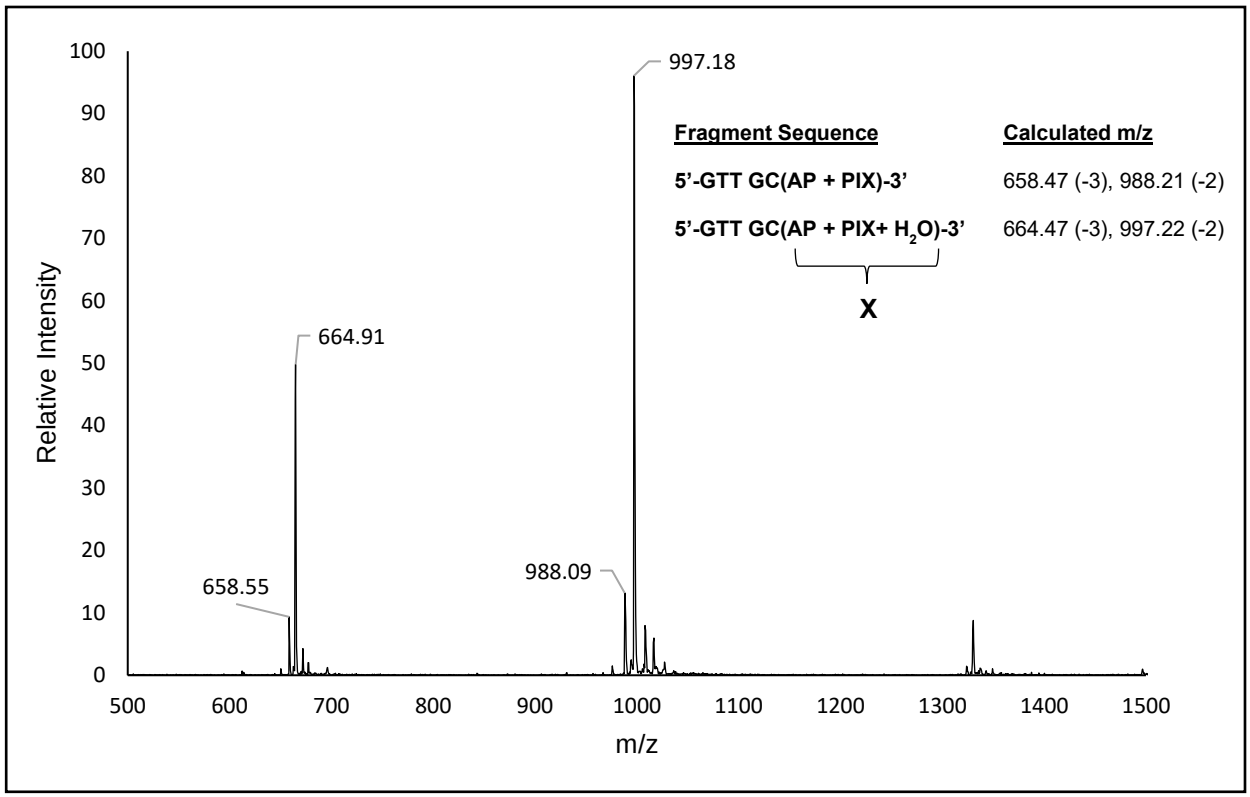

Figure 3-10. ESI-LC/MS total ion scan mass spectrum of the purified PIX-DNA fragment adduct sequence 5'-GTT GC**X**-3' resulting from β-elimination of the AP-12mer (structure shown in **Fig. 3-09**).

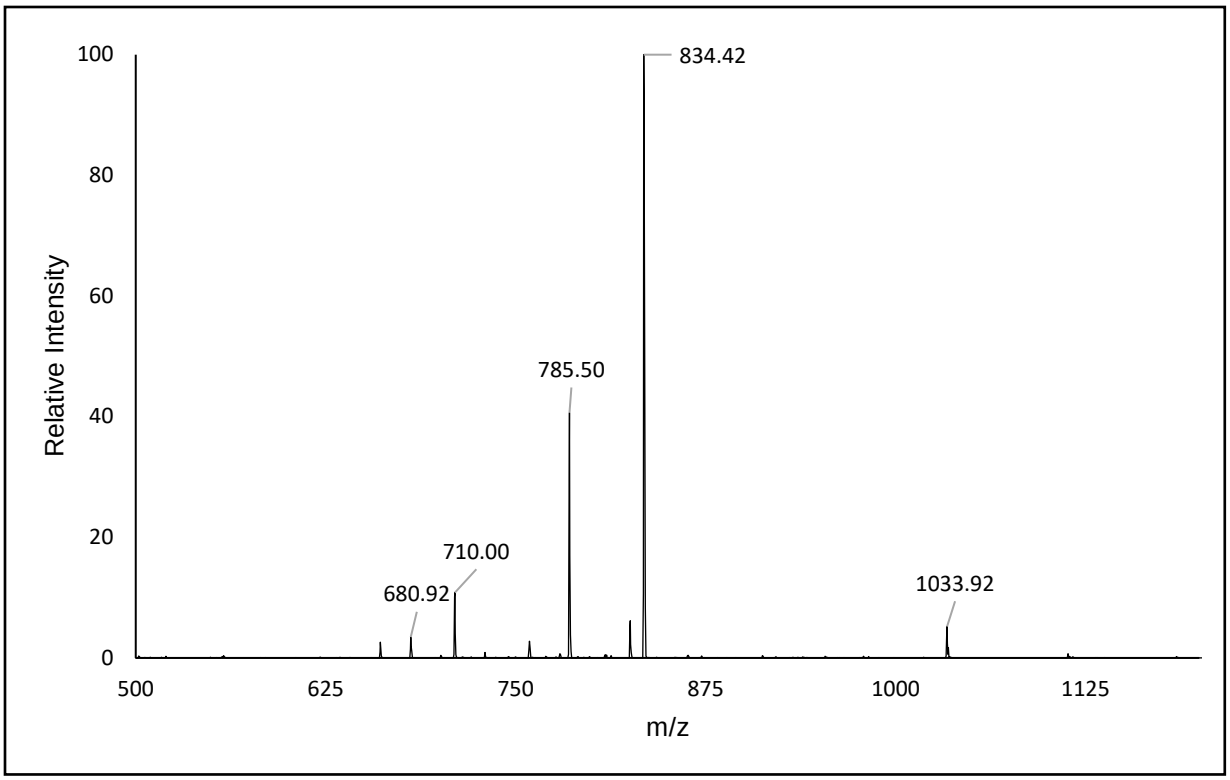

Figure 3-11. *m/z 997* selected ion ESI/LC-MS^2 spectrum with CID fragmentation for the 5'-GTT GC(**AP + PIX + H_2O**)-3' unreduced adduct after purification by HPLC.

Although clearly less stable in this non-reduced form, the fragment adducts observed form extremely quickly and persist over the course of multiple days in reaction solution, long after the parent AP-12mer has been degraded. HPLC chromatograms for the full reaction between 10 μM ssAP-12mer and 250 μM PIX at 25 °C after 5, 30, 90 minutes and 24 hours are shown in **Figure 3-12** where the meta-stable fragment adducts appear with retention times between 17-18 minutes. These peaks reach a maximum after ~60 minutes, tracking with the disappearance of the AP-12mer peak that elutes at 11.2 minutes. However, they remain present in measurable quantities for about five days thereafter with their gradual reduction corresponding to the subsequent growth of peaks containing the 5'-fragments observed much sooner with MTX-induced scission. While PIX does not react as efficiently as MTX with AP sites in our oligonucleotide, its ability to form these long-lived covalent adducts is nonetheless intriguing if the drug has a sustained nuclear presence over the course of treatment and warrants further investigation. With the knowledge that 3'-terminal AP sites are a common intermediate of the natural BER pathway as mentioned in **Chapter I**, adducts of this sort could present yet another target for enhancement of chemotherapeutic cytotoxicity.

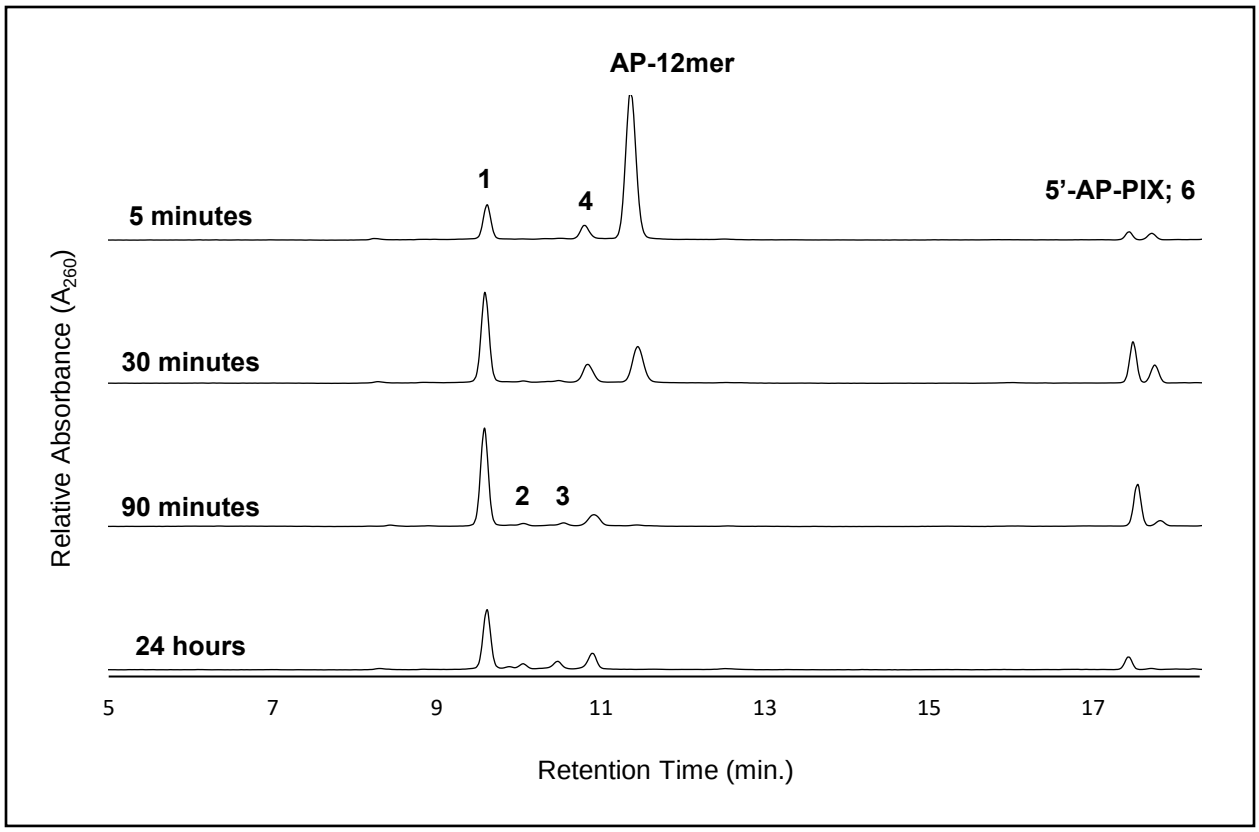

Figure 3-12. HPLC chromatograms of the crude reaction mixture for the ssAP-12mer (10 μM) with PIX (250 μM) at 25 °C without reduction after 5, 30, 90 minutes, and 24 hours.

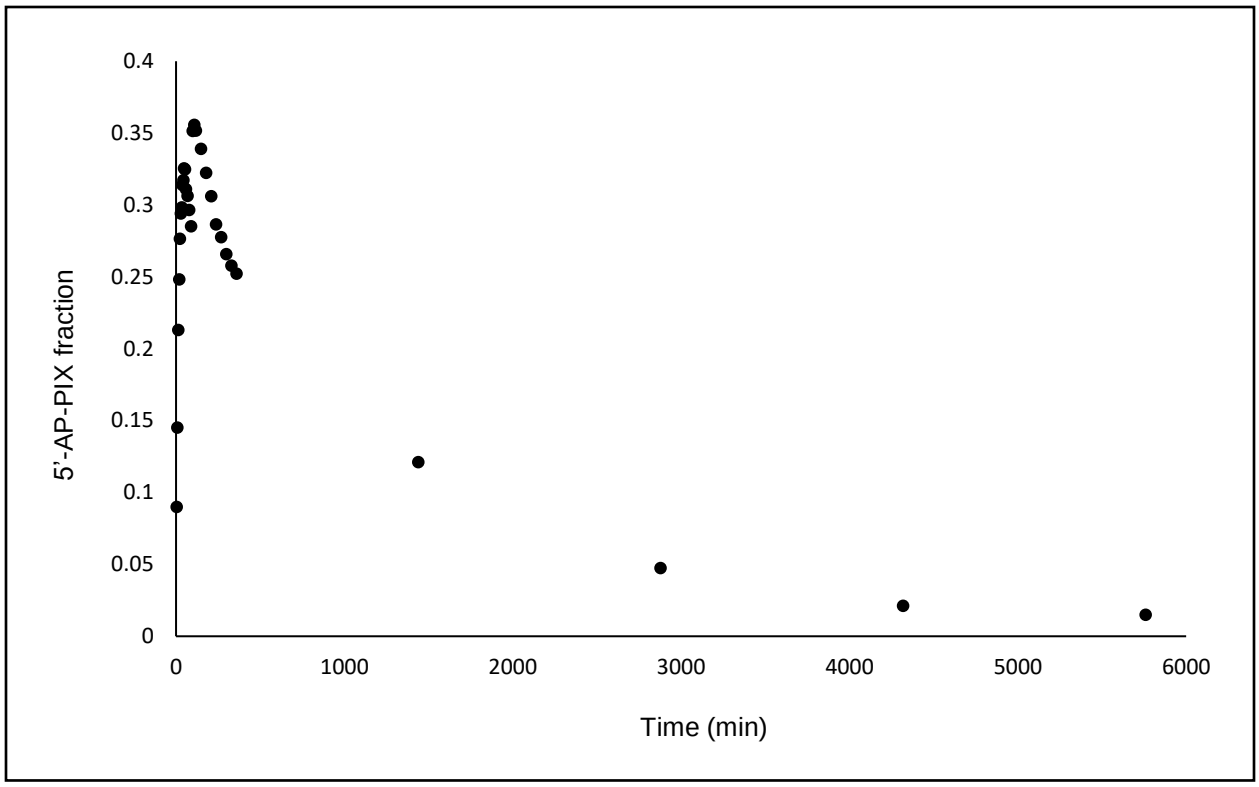

Figure 3-13. Measure of the 5'-GTT GC(**AP+PIX**)-3' unreduced covalent adduct peak areas in reaction solution (0.01 mM ssAP-12mer, 0.25 mM PIX, 25 °C) as a fraction of total DNA peak area by HPLC from 5 minutes to 96 hours.

Structural analysis of the reduced 12mer conjugates through NMR or crystallography may provide better insight into the mechanism of these reactions, detailing what molecule acts as the catalytic base for elimination and how it is affected by overall DNA structure. Such studies could also provide significant detail as to the positioning of reactive elements of the anthracenediones and anthracyclines within our DNA sequence, helping to improve experiment design to better study this type of reactivity for more structurally confined compounds. This data could also help in development of structural analogs to better take advantage of the positioning of individual reactive elements.

Changes in the Thermal Stability of Duplex DNA Oligonucleotides due to Interactions with Anthracyclines

Thermal melting (T_m) analysis of MTX with the dsAP-12mer confirmed that anthracycline-induced DNA scission was occurring *in situ* and not due to interactions during purification. The presence of an AP site greatly reduces the duplex stability, represented by a decrease in T_m to 29 °C for the representative THF analog (THF-12mer) from 55 °C for the canonical duplex (G-12mer). Significant stabilization was re-introduced upon incubation of the THF-12mer with one equivalent of MTX as seen in **Figure 3-14**. This was expected as a common effect from DNA intercalators and replicated to a lesser degree with both PIX and DOX, and the same experiment was then run with the AP-12mer.

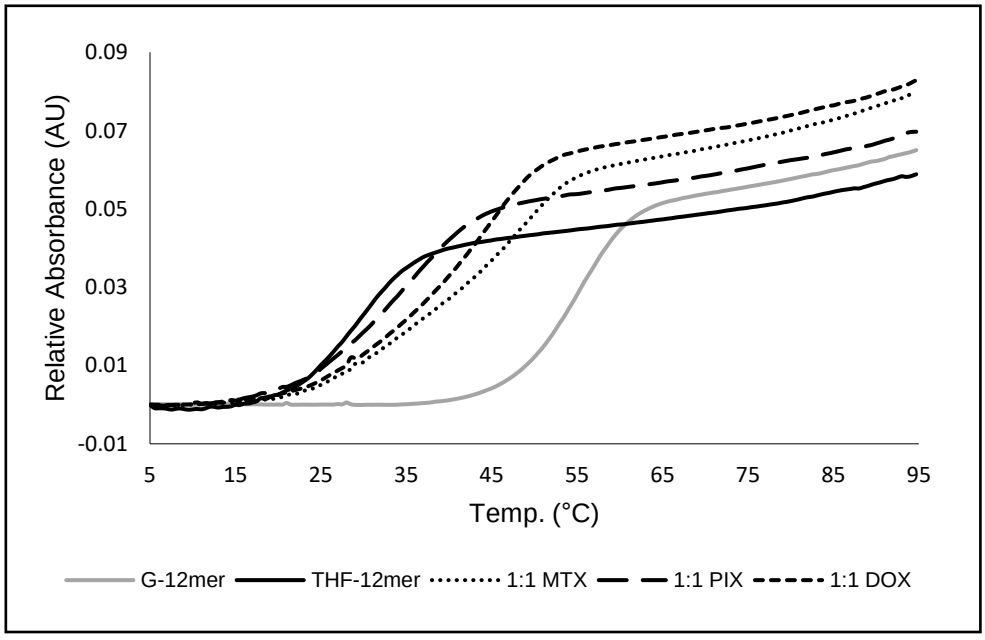

Figure 3-14. Anthracyclines differentially stabilize the THF-12mer by T_m analysis with MTX having the largest effect and PIX having the smallest.

Evidence of Anthracycline-induced Scission from a Progressive Decrease in Stability of the AP-containing Oligonucleotide

Over the course of two melting and re-annealing runs for a 1:1 mixture of MTX and the dsAP-12mer, the slightly lower melting temperature (**Fig. 3-15**) for run 2 indicated destabilization of the DNA duplex, suggesting some fraction of fragmented DNA. This shift was also seen in the re-annealing curves both within a single run and between runs, providing further confirmation that the reaction was continuous in solution. Upon repeating this experiment with a 2.5-fold excess of MTX, the destabilizing shift was more pronounced within a single run as shown in **Figure 3-16**. The more amorphous character of the re-annealing curve is representative of a large amount of fragmented AP-12mer with extremely low thermal stability while there is still some evidence of the undamaged duplex from the sharp absorbance decrease around 50 °C. These shifts were not seen with either the canonical duplex or the THF-12mer analog, further confirming that scission was due solely to the interaction between MTX and the AP site in a concentration-dependent manner.

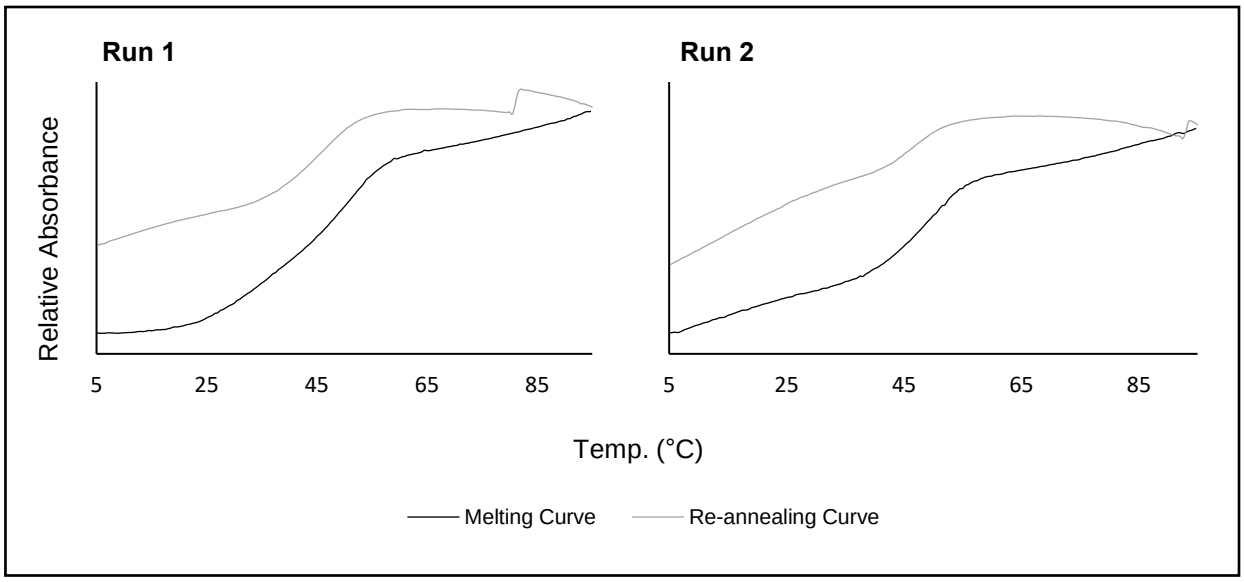

Figure 3-15. Changes to thermal stability of the AP-12mer duplex over the course of two runs (5-95 °C, 1 °C/min.) upon incubation with one equivalent of MTX. The leftward shift of the ΔAbs_{Max} and amorphous nature of the curve indicate a growing abundance of DNA fragments from β- and δ-elimination at the AP site.

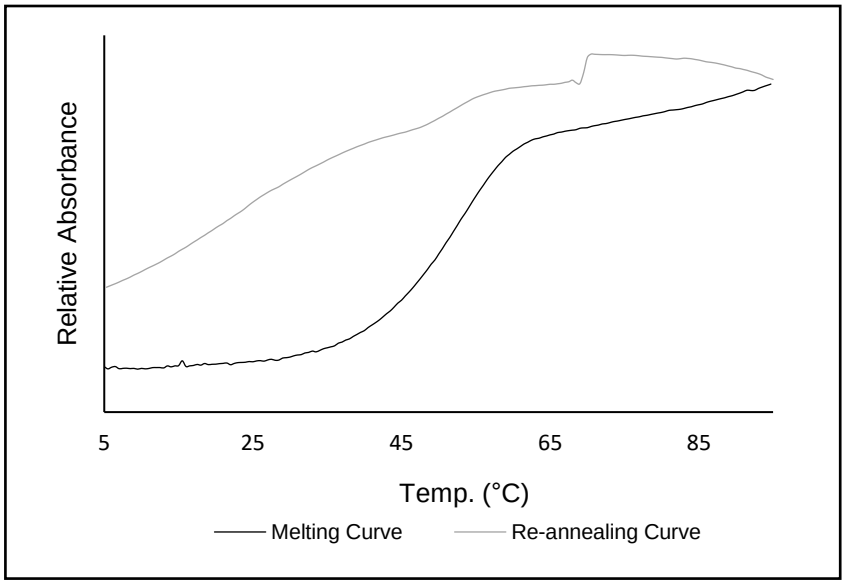

Figure 3-16. Changes to thermal stability of the AP-12mer duplex upon incubation with 2.5 equivalents of MTX (5-95 °C, 1 °C/min).

Increases in Stability of the THF-12mer AP-analog Conferred by Increasing Ratios of MTX, PIX, and DOX

In addition to confirming that the scission reaction occurs in solution, these T_m studies also showed the significant stabilizing effect that MTX has on the damaged DNA duplex. As mentioned, introduction of one equivalent of MTX to the THF-12mer raises the T_m value to 50 °C from 29 °C, nearly matching that of the canonical duplex (G-12mer). As outlined in **Figure 3-17** and **Table 3-02**, this trend is detectable at lower MTX:DNA ratios as a biphasic T_m curve with two inflection points in the calculated first derivative. These maxima likely corresponded to the unbound duplex THF-12mer (29 °C) and the intercalation of one equivalent of MTX into the duplex structure (~48 °C). Further stabilization at higher concentrations of MTX is observed and prescribed to either secondary intercalation points or electrostatic interactions between the drug and the DNA phosphate backbone that have been previously reported with DOX[1,3]. Thermal melting stabilization is also exhibited in the canonical duplex as a slight increase in T_m from 55 °C to 60 °C upon incorporation of one equivalent of MTX (**Fig. 3-18**). This data matched well with preliminary results from Andrew Kellum[4] of the Stone lab at Vanderbilt University, giving similar T_m values for the unmodified duplex and THF analog while the reduced MTX-12mer duplex had a T_m of 50 °C according to their reports.

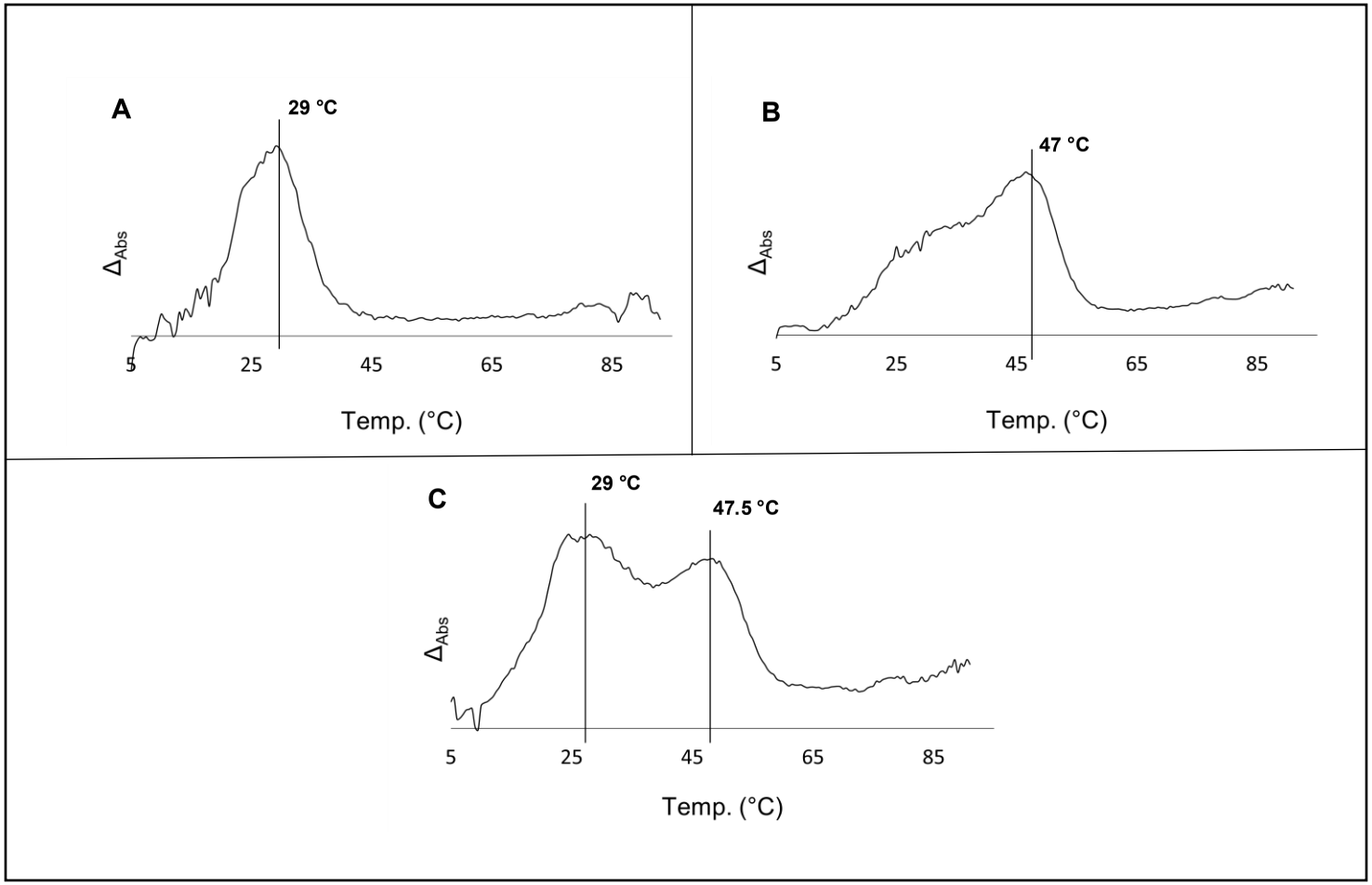

Figure 3-17. Calculated first derivatives of the thermal stability curves for **(A)** the THF-12mer, **(B)** a 1:1 ratio of the THF-12mer and MTX, and **(C)** a 2:1 ratio of the THF-12mer and MTX.

The Stone group also measured the T_m of the PIX-12mer reduced covalent adduct and determined it to be 43 °C in the same DNA sequence, which is significantly higher than that of the purely intercalative effect seen with a 1:1 ratio of PIX and the THF-12mer (T_m = 35 °C, **Table 3-02**). While the stabilizing effect of PIX intercalation does not appear to be significant up to one equivalent, the T_m increases much more (as much as 13 °C) in the presence of 2-5 equivalents of drug in much the same manner as MTX. The thermal melting properties of the DOX-12mer reduced covalent adduct have not yet been experimentally determined, but we do observe the same pattern of stabilizing effects from intercalation with the duplex THF-12mer. DOX appears to do this with an efficiency between that of MTX and PIX with a 1:1 ratio of drug to DNA raising the T_m back to 45 °C, and higher ratios (up to a 5-fold excess of DOX) shifting this as high as 49 °C.

Drug Equivalents	MTX T_m (°C)	PIX T_m (°C)	DOX T_m (°C)
0	29	29	29
0.25	29	29	29
0.5	29, 50	29	29
0.75	29, 50	32	29, 41
1	50	35	45
1.6	53	38	45
2	55	38	46
5	58	42	49

Table 3-02. Comparison of thermal melting stabilization for the duplex THF-12mer (5'-GTT GC(**idSp**) CGT ATG-3') with increasing ratios of MTX, PIX, and DOX. T_m with "0 equivalents" represents the measured melting temperature of the parent THF-12mer.

Anthracyclines also Stabilize Undamaged DNA via the Canonical 12mer Duplex

The trend in relative stabilizing effects (MTX > DOX > PIX) was also seen in 1:1 ratios with the canonical duplex as represented in **Figure 3-18**. Structurally, we can thus assume that presence of the AP site is not a requirement for this pattern in the DNA sequence used even though the effect is drastically reduced with the G-12mer. Intriguingly, this does not match the trend we see in reactivity for either the reductive aminations or the strand scission. The trends seen in thermal stabilization also do not match those seen in various calculations of anthracycline-DNA binding affinity[5–8]. Although no singular report compares these three compounds by the same experimental methods, a general order of K_A values in CT-DNA can be extrapolated as PIX > DOX > MTX. This can be attributed to the importance of secondary interactions due to conformational changes in CT-DNA that are not present in our 12-base pair oligonucleotide. Electrostatic interactions with the DNA backbone[1,3], sequence specificity[5,9,10], and even molecular self-aggregation[11] have all been shown to impact binding affinity calculations and likely have varying impacts in the experiments reported here as we change drug-DNA ratios. It is also possible that the space generated by the presence of an AP site changes the manner of intercalation for the different types of molecules and allows for new structural interactions that could either enhance or inhibit stability. In contrast to DOX where the anthracycline core is intercalated and the glycosidic portion is formed to the minor groove of DNA[7], the structure of MTX and PIX actually prevents incorporation of the full molecule[5], and MTX and its analogs have even been shown to induce DNA condensation initiated by secondary structure destabilization[11]. This effect could be negated by the induction of an AP site, allowing the typically non-

interacting hydrocarbon arms to fit more neatly into the overall DNA structure and consequently placing the reactive amines in closer proximity to the aldehydic carbon.

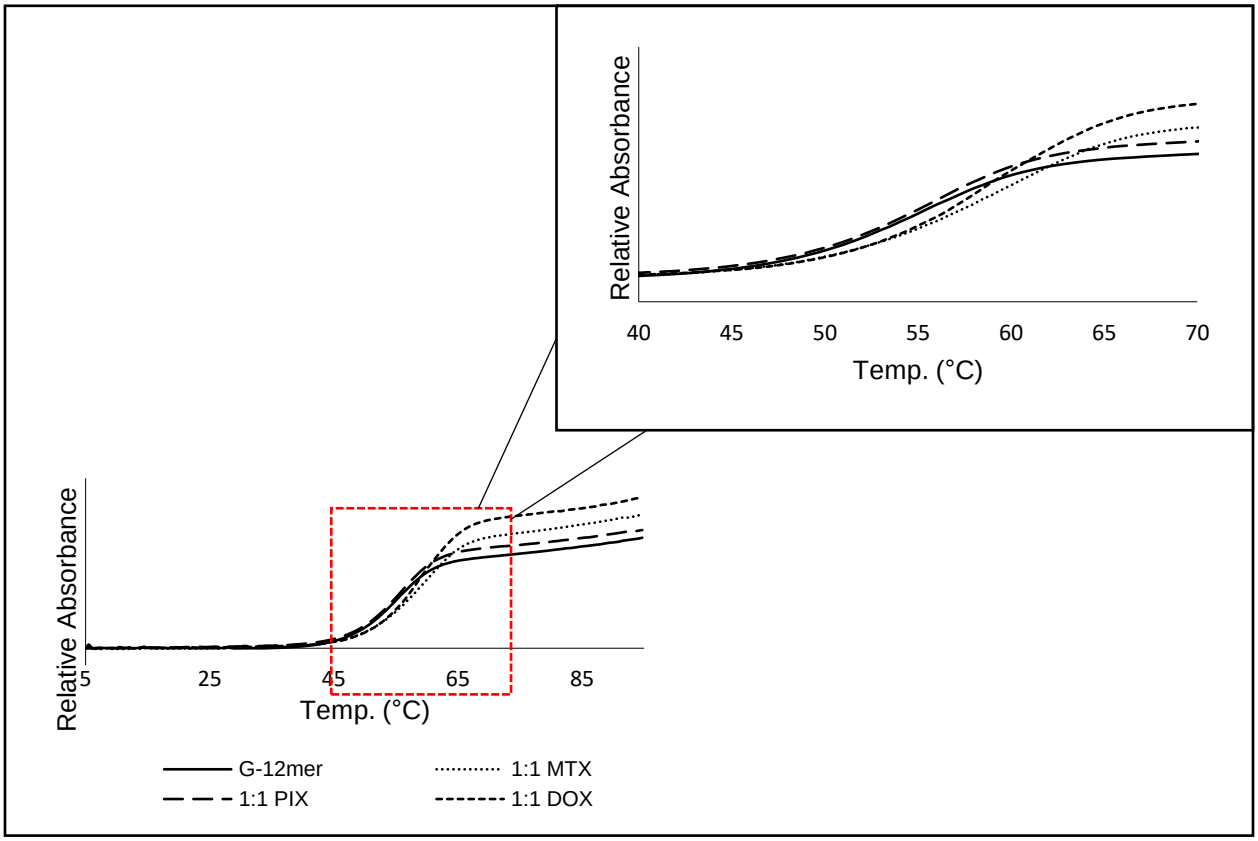

Figure 3-18. Stabilization of the canonical duplex (5'-GTT GC**G** CGT ATG-3'; G-12mer) upon introduction of one equivalent of MTX, PIX, and DOX.

Thermal melting stability of duplex DNA with non-covalently bound intercalators has not been reported in great detail, but Akhter et al. reported a ΔT_m of +10 °C for the interaction of DOX with a 24-base pair duplex oligonucleotide containing a GC-rich internal sequence in a 0.9:1 drug/DNA ratio[12]. A more common practice seems to be measuring the thermal stability induced by covalently binding intercalators to the terminus of an oligo as is reported by Garbesi et al. wherein DOX induced a +10-15 °C ΔT_m in a triplex oligo when attached at various positions[13]. These values are more significant than those that we see in either the duplex AP-12mer or the canonical duplex with a similar ratio of DOX to DNA, differences that are most likely due to the length and sequence of the oligos in question. The effect on trends in stability incurred by the presence of the AP site cannot be overlooked, and the correlation between the structural characteristics that cause this and the trends in reactivity for both reductive amination and DNA scission should be studied in much greater detail.

Experimental Procedures

Chemicals and Reagents

Oligonucleotide sequence 5'-GTT GCp-3' was purchased without additional purification from Bio-Synthesis Inc. (Lewisville, TX). All other oligonucleotide sequences were purchased with prior HPLC purification from Integrated DNA Technologies (Coralville, IA). $Na_2EDTA \cdot 2H_2O$ was purchased as a solid from Sigma Aldrich (St. Louis, MO). NaH_2PO_4 was purchased as a solid from Thermo Fisher Scientific. Pierce™ Concentrator, PES, 10 kDa mwc filters were purchased from Thermo Scientific. Bio-Spin® 30 Tris gel columns were purchased from Bio-Rad Laboratories (Hercules, CA). KaleidaGraph® software Version 4.0 developed by Synergy Software (Reading, PA).

Buffer Compositions

HEPES buffer: 0.1 M HEPES free-base, 0.1 M NaCl, pH = 7.40

***T_m* buffer**: 0.01 M NaH_2PO_4, 0.1 M NaCl, 0.05 mM Na_2EDTA, pH = 7.10

UV Spectroscopy

UV analysis was performed using a Cary 3500 Compact Peltier UV-Vis spectrophotometer with heating capability purchased from Agilent Technologies. Analysis of anthracycline standards was performed using 500 µL black-walled quartz cuvettes (1 cm path length) purchased from Fisher Scientific. Analysis of oligonucleotide samples

was performed using 1 mL clear quartz cuvettes (1 cm path length). All single scan measurements were done over a range of 225-800 nm with an averaging time of 0.048 seconds, a data interval of 0.5 nm, and a spectral bandwidth of 2.00 nm (scan rate 625 nm/min). Variable temperature studies were conducted with detection at 260 nm over a range of 5-95 °C at a rate of 1 °C/min (followed by the reverse process after a 1-minute hold at 95 °C) with an averaging time of 2.000 seconds and a spectral bandwidth of 2.00 nm. A continuous flow of industrial-grade compressed nitrogen gas was introduced to the sample chamber for all variable temperature studies to prevent condensation.

Chromatography

Oligonucleotide reaction solutions were monitored and analyzed utilizing HPLC instrumentation, mobile phases, and columns identical to those for oligonucleotide analysis outlined in **Chapter II**.

Gradient 1: Initially 0% **B**; 8 min linear gradient to 10% **B**; isocratic at 10% **B** for 7 min; 2 min linear gradient to 80% **B**; isocratic at 80% **B** for 3 min; 2 min linear gradient to 0% **B**; isocratic at 0% **B** for 3 min.

Gradient 2: Initially 0% **B**; 8 min linear gradient to 10% **B**; isocratic at 10% **B** for 4 min; 5 min linear gradient to 20% **B**; isocratic at 20% **B** for 3 min; 2 min linear gradient to 80% **B**; isocratic at 80% **B** for 3 min; 2 min linear gradient to 0% **B**; isocratic at 0% **B** for 3 min.

Gradient 3: Initially 0% **B**; 15 min linear gradient to 10% **B**; 5 min linear gradient to 20% **B**; isocratic at 20% **B** for 5 min; 2 min linear gradient to 80% **B**; isocratic at 80% **B** for 3 min; 2 min linear gradient to 0% **B**; isocratic at 0% **B** for 3 min.

Gradient 4: Column heated to 65 °C. Initially 0% **B**; 10 min linear gradient to 5% **B**; isocratic at 5% **B** for 5 min; 7 min linear gradient to 7% **B**; isocratic at 7% **B** for 0.5 min; 2.5 min linear gradient to 10% **B**; isocratic at 10% **B** for 10 min; 2 min linear gradient to 80% **B**; isocratic at 80% **B** for 3 min; 2 min linear gradient to 0% **B**; isocratic at 0% **B** for 3 min.

Gradient 5: Column heated to 65 °C. Initially 0% **B**; 10 min linear gradient to 5% **B**; isocratic at 5% **B** for 5 min; 7 min linear gradient to 7% **B**; isocratic at 7% **B** for 0.25 min; 2.5 min linear gradient to 10% **B**; isocratic at 10% **B** for 2.25 min; 2 min linear gradient to 20% **B**; isocratic at 20% **B** for 6 min; 2 min linear gradient to 80% **B**; isocratic at 80% **B** for 3 min; 2 min linear gradient to 0% **B**; isocratic at 0% **B** for 3 min.

Mass Spectrometry

All oligonucleotides and resulting fragments were analyzed by high resolution MS according to ESI-LC/MS^2 procedures outlined in **Chapter II**. For crude analysis of oligonucleotide scission without in-line purification, reaction solutions were de-salted by passing twice through Bio-Spin® 6 gel columns containing Tris buffer according to provided procedures for buffer exchange to elute the samples in LC/MS grade water. Samples were immediately analyzed by ESI-MS without further preparation to prevent further reaction.

General method for the reaction of anthracyclines with AP-containing single-stranded 12mer oligonucleotides

A generalized method is given for the reaction of varying concentrations of anthracycline compounds with 12mer oligonucleotides containing a single AP site. Total volumes and amounts of DNA and UDG used will vary based on the number of samples required for each drug. Each set of reactions was run in triplicate for all compounds.

37 °C

To a 25 μM solution of the uracil-containing 12mer oligonucleotide (5'-GTT GC**U** CGT ATG-3') in HEPES buffer was added 0.25 units/μL of UDG and the solutions were incubated at 37 °C for 1 hour. The solution was then portioned out into 80 μL aliquots, to which an appropriate amount of HEPES buffer was added to bring the volume of each sample to 200 μL upon further addition of anthracycline stock solutions. These new DNA solutions (10 μM at final volume) were placed back at 37 °C and brought to temperature before adding the necessary volume of anthracycline solution from 0.1, 1, and 5 mM stock solutions in HEPES buffer. Reaction mixtures were vortexed and incubated for 10 minutes at 37 °C, then 60 μL aliquots of each were taken and all samples were immediately stored at -80 °C. These aliquots were thawed at ambient temperature 5 minutes prior to HPLC analysis and run via **Gradient 1**.

Table 3-03. Anthracycline concentrations used (μM) in the ssAP-12mer scission reactions performed at 37 °C.

MTX	PIX	DOX
1.096	2.740	10.96
1.644	5.480	27.41
2.193	10.96	54.81
2.740	21.93	87.7
4.390	32.89	109.6
5.480	43.85	137.0
8.220	65.76	164.4
10.96	87.7	219.3
16.44	109.6	328.9
21.93	137.0	438.5
27.41	164.4	657.8
32.89	219.3	767.4
43.85	274.1	877.0
54.81	328.9	986.6
65.76	438.5	
76.74	657.8	
87.70	767.4	
98.66		
109.6		
137.0		
164.4		
219.3		
328.9		
438.5		
657.8		

25 °C

To a 25 μM solution of the uracil-containing 12mer oligonucleotide (5'-GTT GC**U** CGT ATG-3') in HEPES buffer was added 0.25 units/μL of UDG and the solutions were incubated at 37 °C for 1 hour. The solution was allowed to cool to ambient temperature then portioned out into 80 μL aliquots, to which an appropriate amount of HEPES buffer was added to bring the volume of each sample to 200 μL upon further addition of anthracycline stock solutions. These new DNA solutions (10 μM at final volume) were incubated at 25 °C and brought to temperature before adding the necessary volume of anthracycline solution from 0.1, 1, and 5 mM stock solutions in HEPES buffer (also incubated at 25 °C prior to addition). Reaction mixtures were vortexed and incubated for 20 minutes at 25 °C, then 60 μL aliquots of each were taken and all samples were immediately stored at -80 °C. These aliquots were thawed at ambient temperature 5 minutes prior to HPLC analysis and run via **Gradient 1** for MTX and DOX or **Gradient 2** for PIX.

Table 3-04. Anthracycline concentrations used (μM) in the ssAP-12mer scission reactions performed at 25 °C.

MTX	PIX	DOX
1.000	1.000	50.00
2.500	2.500	75.00
5.000	5.000	100.0
7.500	7.500	150.0
10.00	10.00	200.0
15.00	15.00	250.0
20.00	20.00	300.0
25.00	25.00	350.0
30.00	30.00	400.0
35.00	40.00	450.0
40.00	50.00	500.0
45.00	62.50	550.0
50.00	75.00	600.0
62.50	87.50	
75.00	100.0	
87.50	112.5	
100.0	125.0	
112.5	150.0	
125.0	175.0	
150.0	225.0	
200.0	300.0	
	375.0	
	450.0	
	525.0	
	600.0	

General method for the reaction of anthracyclines with AP-containing double-stranded 12mer oligonucleotides

A generalized method is given for the reaction of varying concentrations of anthracycline compounds with duplex 12mer oligonucleotides containing a single AP site. Total volumes and amounts of DNA and UDG used will vary based on the number of samples required for each drug. Each set of reactions was run in triplicate for all compounds.

37 °C

The uracil-containing 12mer oligonucleotide (5'-GTT GC**U** CGT ATG-3') was combined with its complement oligonucleotide (5'-CAT ACG CGC AAC-3') in HEPES buffer (25 μM of each oligonucleotide). The solution was heated to 90 °C for 5 minutes and the strands were annealed by allowing the solution to cool slowly to ambient temperature. UDG (0.25 units/μL) was added and the solutions were incubated at 37 °C for 1 hour. The solution was then portioned out into 80 μL aliquots, to which an appropriate amount of HEPES buffer was added to bring the volume of each sample to 200 μL upon further addition of anthracycline stock solutions and an additional dilution made as a control sample for t_0 analysis. These new DNA solutions (10 μM at final volume) were placed back at 37 °C and brought to temperature before adding the necessary volume of anthracycline solution from 0.1, 1, and 5 mM stock solutions in HEPES buffer. Reaction mixtures were vortexed and incubated for 30 minutes at 37 °C, then 60 μL aliquots of each were taken and all samples were immediately stored at -80 °C. These aliquots were thawed at ambient temperature 5 minutes prior to HPLC analysis and run via **Gradient 3**.

Table 3-05. Anthracycline concentrations used (μM) in the dsAP-12mer scission reactions performed at 37 °C.

MTX	PIX	DOX
1.096	2.740	10.96
2.190	5.480	43.85
2.740	10.96	82.22
5.480	16.44	164.4
10.96	21.93	219.3
16.44	27.41	274.1
21.93	43.85	328.9
27.41	60.29	
43.85	82.22	
60.29	109.6	
82.22	137.0	
109.6	164.4	
137.0	219.3	
164.4	274.1	
191.8	328.9	
219.3	356.3	
246.7	383.7	
274.1	438.5	
328.9	493.3	
438.5	548.1	
493.3	602.9	
	657.8	
	712.6	
	767.4	

25 °C

The uracil-containing 12mer oligonucleotide (5'-GTT GC**U** CGT ATG-3') was combined with its complement oligonucleotide (5'-CAT ACG CGC AAC-3') in HEPES buffer (25 μM of each oligonucleotide). The solution was heated to 90 °C for 5 minutes and the strands were annealed by allowing the solution to cool slowly to ambient temperature. UDG (0.25 units/μL) was added and the solutions were incubated at 37 °C for 1 hour. The solution was then allowed to cool to ambient temperature, then further to 4 °C to ensure re-annealing of the DNA strands. This DNA sample was portioned out into 80 μL aliquots, to which an appropriate amount of HEPES buffer was added to bring the volume of each sample to 200 μL upon further addition of anthracycline stock solutions and an additional dilution made as a control sample for t_0 analysis. These new DNA solutions (10 μM at final volume) were incubated at 25 °C and brought to temperature before adding the necessary volume of anthracycline solution from 0.1, 1, and 5 mM stock solutions in HEPES buffer (also incubated at 25 °C prior to addition). Reaction mixtures were vortexed and incubated for 4 hours at 25 °C, then 60 μL aliquots of each were taken and all samples were immediately stored at -80 °C. These aliquots were thawed at ambient temperature 5 minutes prior to HPLC analysis and run via **Gradient 4** for MTX or **Gradient 5** for PIX.

Table 3-06. Anthracycline concentrations used (μM) in the dsAP-12mer scission reactions performed at 25 °C.

MTX		**PIX**		**DOX**
1.000	110.0	1.000	150.0	N/A
1.750	125.0	2.500	175.0	
2.500	150.0	5.000	200.0	
3.750	175.0	7.500	250.0	
5.000	200.0	10.00	300.0	
7.500	250.0	15.00	350.0	
10.00	300.0	20.00	400.0	
15.00	400.0	25.00	500.0	
20.00	500.0	30.00	600.0	
30.00		35.00		
40.00		40.00		
50.00		50.00		
60.00		62.50		
70.00		75.00		
80.00		87.50		
90.00		100.0		
100.0		125.0		

Calculation of reaction efficiency in ss12mer oligonucleotides from HPLC peak areas

Chromatographic peaks detected at λ_{260} were defined manually according to known DNA products and total peak areas were taken from System Gold Software analysis. For reactions with MTX and DOX, reaction efficiency for each sample was calculated as the sum of the fragment peak areas divided by the peak area of the remaining AP-12mer. For reactions with PIX, the added absorbance due to PIX incorporation in some fragment strands was taken into account by dividing all peak areas by the corresponding extinction coefficients based on peak identification with purchased oligonucleotide standards. Reaction efficiency was thus calculated as follows:

$$\text{Fraction DNA cleaved} = \frac{\left(\frac{A1 + A4}{58900}\right) + \left(\frac{A2 + A3}{44500}\right) + \left(\frac{A6}{44500 + 10000}\right)}{\left(\frac{AP}{103200}\right)} \qquad \textbf{(Eq. 3-01)}$$

where *A1-A6* are the peak areas associated with peaks 1, 2, 3, 4, and 6 as assigned in **Figure 3-12** and *AP* is the peak area of the unreacted AP-12mer. Extinction coefficients for the fragmented DNA strands and AP-12mer were calculated using the OligoAnalyzer™ Tool provided by IDT's website and the extinction coefficient for Pixantrone was calculated by UV analysis.

Calculation of reaction efficiency in ds12mer oligonucleotides from HPLC peak areas

Chromatographic peaks detected at λ_{260} were defined manually according to known DNA products and total peak areas were taken from System Gold Software

analysis. Reaction efficiency for each sample was calculated as the change in the ratio of AP-12mer to its complement strand with correction for extinction coefficients according to **Equation 3-03** as follows:

$$A/C = \frac{\left(\frac{AP}{103200}\right)}{\left(\frac{Comp.}{114100}\right)} \qquad (\textbf{Eq. 3-02})$$

$$\text{Fraction DNA cleaved} = 1 - \frac{A/C_R}{A/C_0} \qquad (\textbf{Eq. 3-03})$$

where AP is the peak area of the unreacted AP-12mer, Comp. is the peak area of the complement oligonucleotide strand, “R” denotes the peak area ratio of the reaction, and “0” denotes the peak area ratio of the control sample.

The resulting data from these calculations was transferred to a KaleidaGraph® spreadsheet and used to plot EC_{50} curves with line fitting for sigmoidal functionality. For data averaging purposes, the software’s statistical analysis was used to calculate mean values and standard error for each data set. Sigmoidal curves were fit based on **Equation 3-04** with estimates made for each variable based on the data generated.

$$y = m1 + \frac{m2 - m1}{1 + \left(\frac{x}{m3}\right)^{m4}} \qquad (\textbf{Eq. 3-04})$$

Values for m1 and m2 were taken directly from the data sets in question while m3 was estimated visually and values for m4 were calculated by deriving the slope between the two points adjacent to 50% reaction completion based on maximum reaction efficiency. The EC_{50} values for MTX, PIX, and DOX in each reaction system was taken as log(m3) from the post-fit generated equation.

Monitoring the reaction between PIX and the ssAP-12mer.

In order to monitor the appearance/depletion of the 5'-AP-PIX covalent fragment adduct at 25 °C, the uracil-containing 12mer oligonucleotide identified above (10 nmol) was combined with UDG (0.25 units/μL) in HEPES buffer (0.4 mL total volume) and the mixture incubated at 37 °C for 1 hour. After cooling to room temperature, additional HEPES buffer was added (0.55 mL, 0.01 mM DNA) and the diluted solution incubated at 25 °C for 15 minutes, after which 50 μL of a 5 mM stock solution of PIX was added (0.25 mM reaction concentration). The solution was vortexed and incubated at 25 °C, and 60 μL aliquots were taken at various time points from 5 minutes to 7 days and stored at -80 °C with additional reactions prepared as necessary for extended sampling. Aliquots were analyzed by HPLC according to **Gradient 2** and peak areas were recorded for reaction efficiency calculations as described above. The fraction of the 5'-AP-PIX adduct present in reaction solution was calculated according to **Equation 3-05**.

$$\text{Fraction 5'-AP-PIX} = \frac{\left(\frac{A6}{44500 + 10000}\right)}{\left(\frac{A1 + A4}{58900}\right) + \left(\frac{A2 + A3}{44500}\right) + \left(\frac{AP}{103200}\right)} \qquad (\textbf{Eq. 3-05})$$

where *A1-A6* and *AP* follow the labeling convention outlined for **Equation 3-01**.

Thermal melting analysis of unmodified duplex 12mer oligonucleotides with non-covalent anthracycline interactions

Either the constituent 12mer oligonucleotide (5'-GTT GC**G** CGT ATG-3', 1.69 nmol) or the THF-12mer AP-analog (5'-GTT GC(**idSp**) CGT ATG-3', 1.69 nmol) was annealed with its complementary oligonucleotide (5'-CAT ACG CGC AAC-3', 1.69 nmol)

in T_m buffer (25 μM) according to established protocol, allowing the samples to cool to 4 °C rather than ambient temperature. Baseline absorbance at λ_{260} was measured using T_m buffer at 5 °C, then the DNA sample and an appropriate volume of anthracycline stock solution (0.5 mM) were added to a final cuvette volume of 1.3 mL (1.3 μM DNA). The sample was mixed well and allowed to stand for 5 minutes while equilibrating to 5 °C. Absorbance readings were taken at 260 nm every 30 seconds with temperature ramping from 5-95 °C at a rate of 1 °C/min. The temperature was held at 95 °C for 1 minute, then the reverse process was performed to analyze oligonucleotide reannealing.

Thermal melting analysis of duplex 12mer oligonucleotides containing an AP site reacting with MTX

The uracil-containing 12mer oligonucleotide (5'-GTT GC**U** CGT ATG-3', 5 nmol) was annealed with its complementary oligonucleotide (5'-CAT ACG CGC AAC-3', 5 nmol) in T_m buffer (25 μM) according to established protocol. Once cooled to ambient temperature, UDG (0.25 units/μL) was added and the DNA solution was incubated at 37 °C for 1 hour. The reaction mixture was immediately passed through a 10 kDa mwc filter with centrifugation at 15,000 x g for 5 minutes to remove the UDG and the collected filtrate was cooled to 4 °C. The duplex oligonucleotide concentration was re-calculated by UV measurement based on absorbance values from a known concentration of duplex THF-12mer. Baseline absorbance at λ_{260} was measured using T_m buffer at 5 °C, then the DNA sample and an appropriate volume of anthracycline stock solution (0.5 mM) were added to a final cuvette volume of 1.3 mL (1.3 μM DNA). The sample was mixed well and UV analysis was immediately begun. Absorbance readings were taken at 260 nm every 30

seconds with temperature ramping from 5-95 °C at a rate of 1 °C/min. The temperature was held at 95 °C for 1 minute, then the reverse process was performed to analyze oligonucleotide reannealing. Where necessary, a second round of UV analysis was immediately begun upon the first run reaching 5 °C.

Formulas used to plot data in Excel

HPLC chromatograms and ESI-LC/MS spectra were plotted as described in **Chapter II**. The first derivatives of the melting curves for T_m analysis were calculated as follows:

$$\Delta Abs_{260} = (B[N]-B[N+8])/4 \qquad (\textbf{Eq. 3-06})$$

where B was the column containing raw absorbance values and *N* was the number corresponding to the row for each calculated value.

References

(1) Pérez-Arnaiz, C.; Busto, N.; Leal, J. M.; García, B. New Insights into the Mechanism of the DNA/Doxorubicin Interaction. *Journal of Physical Chemistry B* **2014**, *118* (5), 1288–1295.

(2) Airoldi, M.; Barone, G.; Gennaro, G.; Giuliani, A. M.; Giustini, M. Interaction of Doxorubicin with Polynucleotides. A Spectroscopic Study. *Biochemistry* **2014**, *53*, 2197-2207.

(3) Ijäs, H.; Ijäs, I.; Shen, B.; Heuer-Jungemann, A.; Keller, A.; Kostiainen, M. A.; Liedl, T.; Ihalainen, J. A.; Linko, V. Unraveling the Interaction between Doxorubicin and DNA Origami Nanostructures for Customizable Chemotherapeutic Drug Release. *Nucleic Acids Res.* **2021**, *49* (6), 3048–3062.

(4) Andrew Howard Kellum Jr. Structural Effects of Secondary DNA Damage Products, Vanderbilt University, Nashville, TN, 2020.

(5) Lown, J. W.; Morgan, A. R.; Yen, S.-F.; Wang, Y.-H.; Wilson, W. D. Characteristics of the Binding of the Anticancer Agents Mitoxantrone and Ametantrone and Related Structures to Deoxyribonucleic Acids. *Biochemistry* **1985**, *24* (15), 4028–4035.

(6) Hasinoff, B. B.; Wu, X.; Patel, D.; Kanagasabai, R.; Karmahapatra, S.; Yalowich, J. C. Mechanisms of Action and Reduced Cardiotoxicity of Pixantrone; a Topoisomerase II Targeting Agent with Cellular Selectivity for the Topoisomerase IIα Isoform. *J. Pharmacol. Exp. Ther.* **2016**, *356*, 397–409.

(7) Chaires, J. B.; Satyanarayana, S.; Suh, D.; Fokt, I.; Przewloka, T.; Priebe, W. Parsing the Free Energy of Anthracycline Antibiotic Binding to DNA. *Biochemistry* **1996**, *35* (7), 2047–2053.

(8) Kapuscinski, J.; Darzynkiewicz, Z.; Traganos, F.; Melamed, M. R. Interactions of a New Antitumor Agent, 1,4-dihydroxy-5,8-bis[[2-[(2-hydroxyethyl)amino]-ethyl]amino]-9,10-anthracenedione, with Nucleic Acids. *Biochem. Pharmacol.* **1981**, *30*, 231–240.

(9) S. Rosenberg, L.; J. Carvlin, M.; R. Krugh, T. The Antitumor Agent Mitoxantrone Binds Cooperatively to DNA: Evidence for Heterogeneity in DNA Conformation. *Biochemistry* **2002**, *25* (5), 1002–1008.

(10) Cutts, S. M.; Parker, B. S.; Lonnie, P.; Kimura, K.; Phillips, D. R. Structural Requirements for the Formation of Anthracycline – DNA Adducts. *Anticancer Drug Design* **2001**, *15*, 373–386.

(11) Kapuscinski, J.; Darzynkiewicz, Z. Interactions of Antitumor Agents Ametantrone and Mitoxantrone (Novantrone) with Double-Stranded DNA. *Biochem. Pharmacol.* **1985**, *34* (24), 4203–4213.

(12) Akhter, M. Z.; Rajeswari, M. R. Interaction of Doxorubicin with a Regulatory Element of *hmga1* and Its *in vitro* Anti-Cancer Activity Associated with Decreased HMGA1 Expression. *J. Photochem. and Photobiol. B: Biology* **2014**, *141*, 36-46.

(13) Garbesi, A.; Bonazzi, S.; Zanella, S.; Capobianco, M. L.; Giannini, G.; Arcamone, F. Synthesis and Binding Properties of Conjugates between Oligodeoxynucleotides and Daunorubicin Derivatives. *Nucleic Acids Res.* **1997**, *25* (11), 2121-2128.

Appendix I:

UV Analysis of MTX, PIX, and DOX for Analytical Applications; HPLC and ESI-LC/MS^2 Characterization for Anthracycline-dR Synthetic Standards in Chapter II

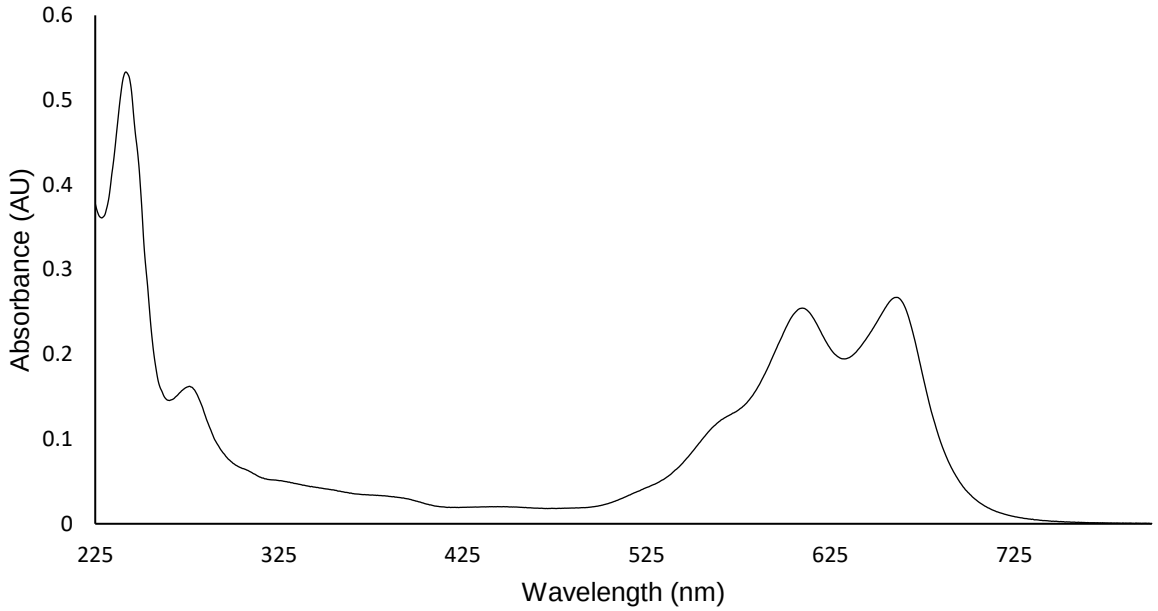

Representative UV spectrum of 20 μM MTX in water from 225-800 nm.

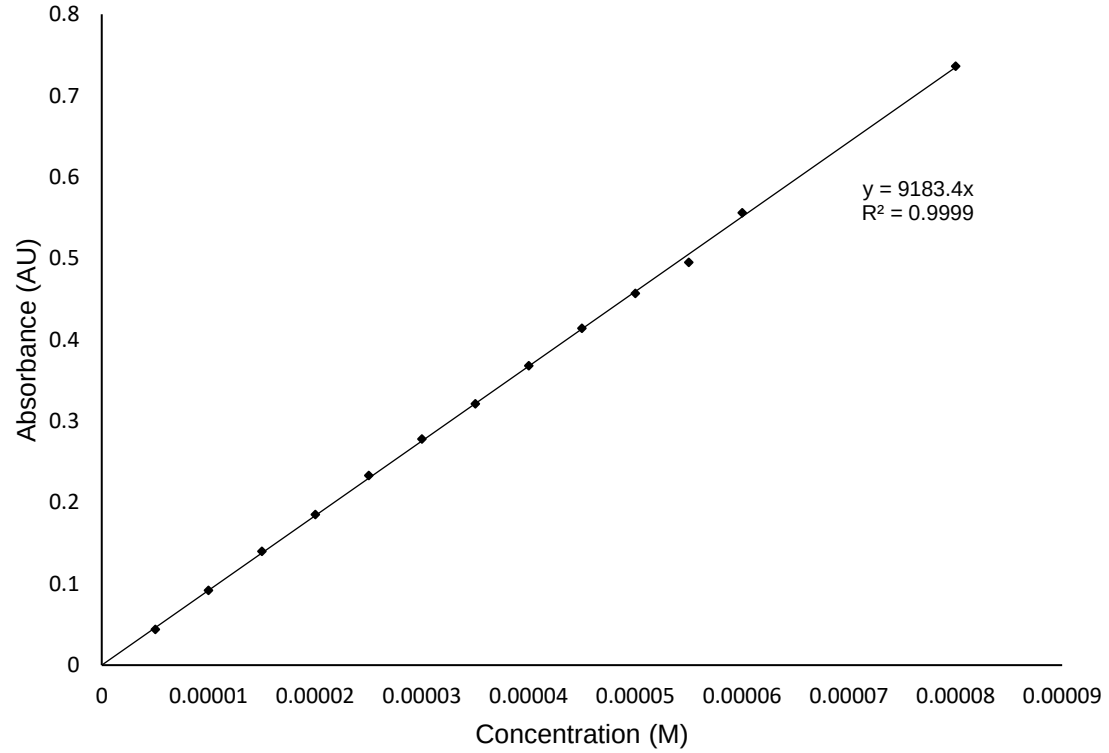

Calibration curve for MTX generated from UV absorbances at λ = 678 nm for 5-80 μM solutions in 0.1% formic acid with calculated extinction coefficient of ~9180 $M^{-1}cm^{-1}$.

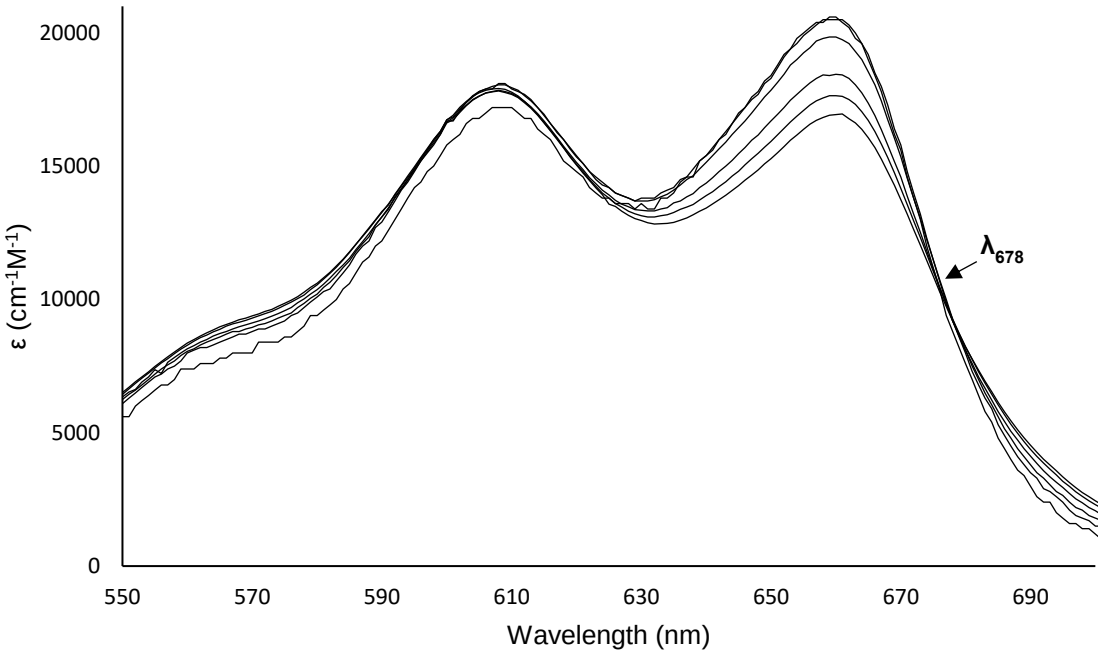

Overlaid graph of calculated extinction coefficients for 5-80 µM solutions of MTX in 0.1% formic acid shows the isosbestic point to be 678 nm.

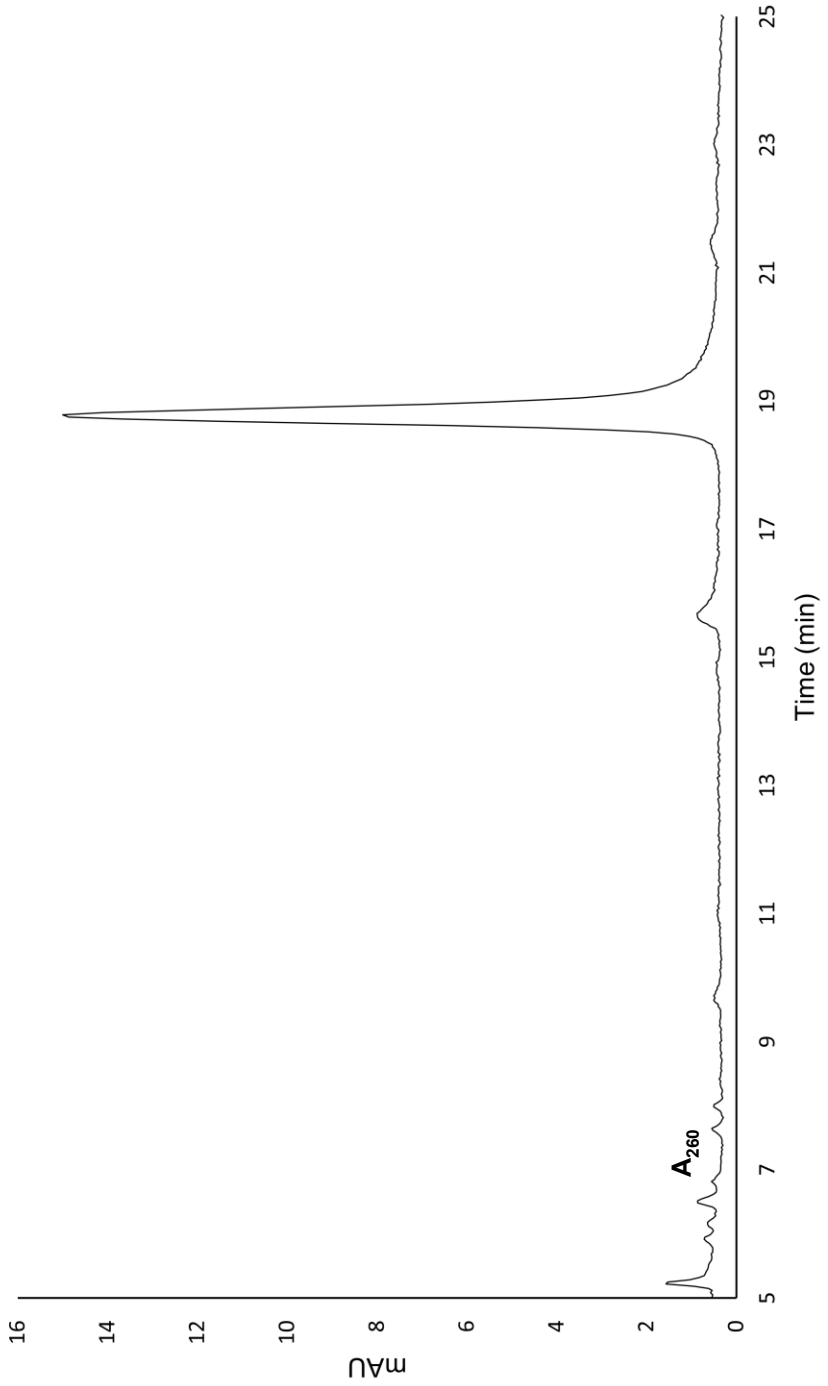

HPLC trace of the purified MTX-dR synthetic standard.

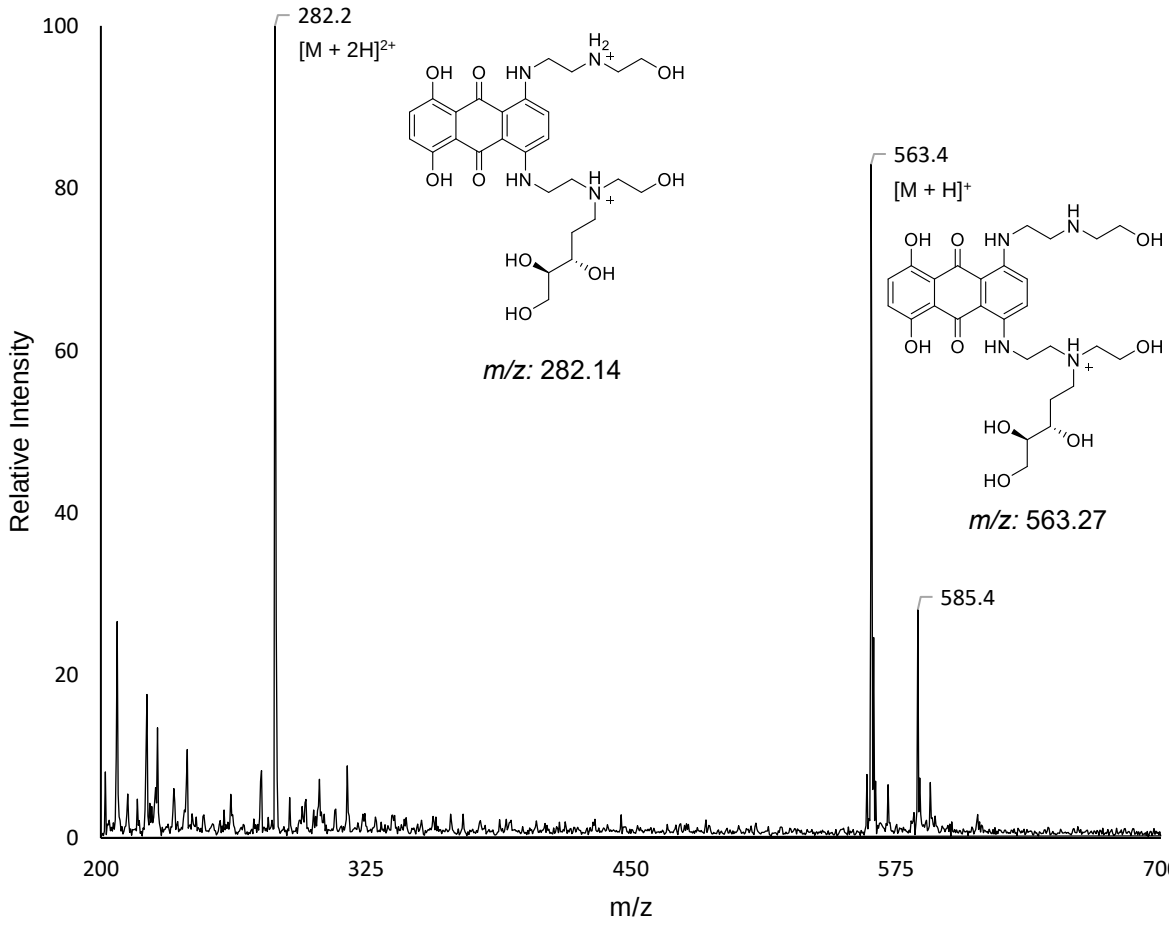

ESI-MS total ion mass spectrum of the MTX-dR synthetic standard.

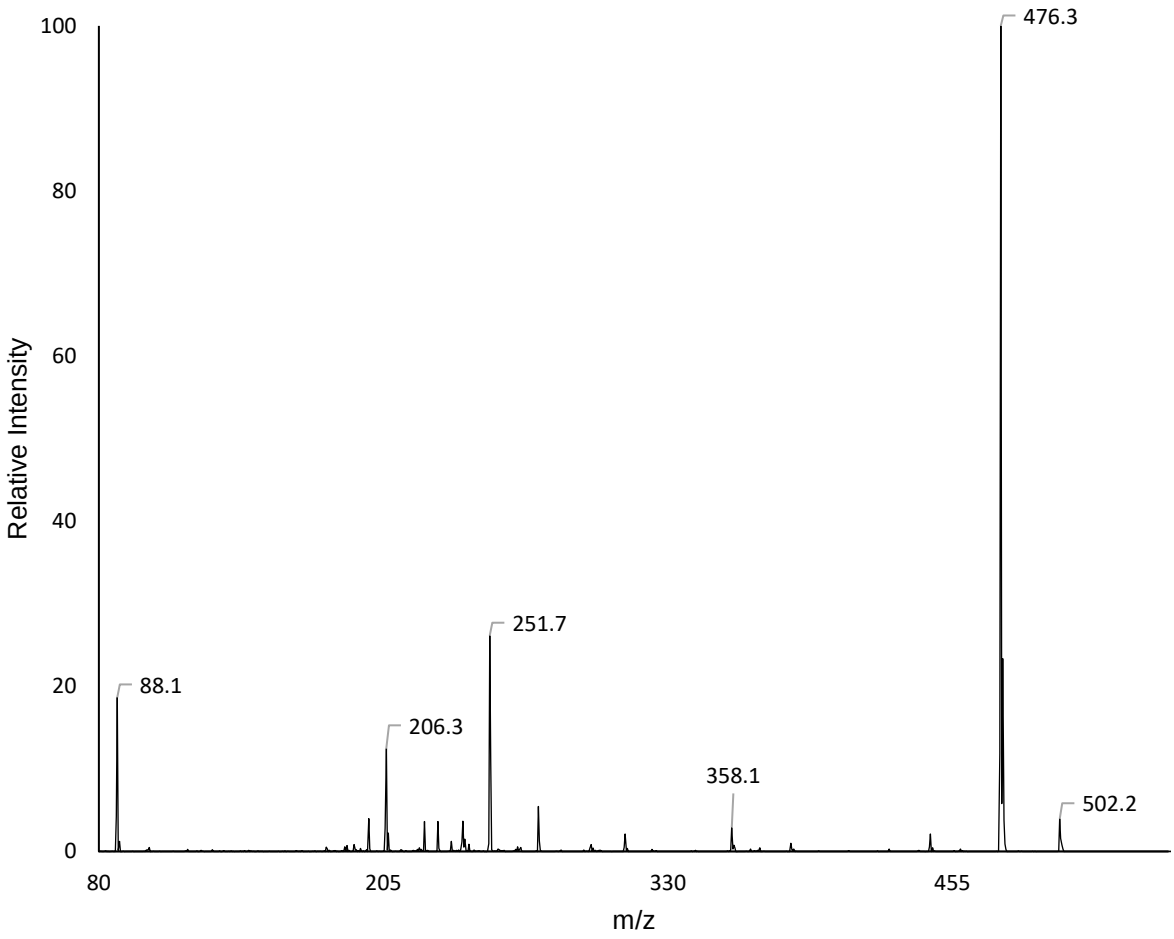

***m/z 282* selected ion ESI-MS^2 spectrum of the MTX-dR synthetic standard with CID fragmentation.**

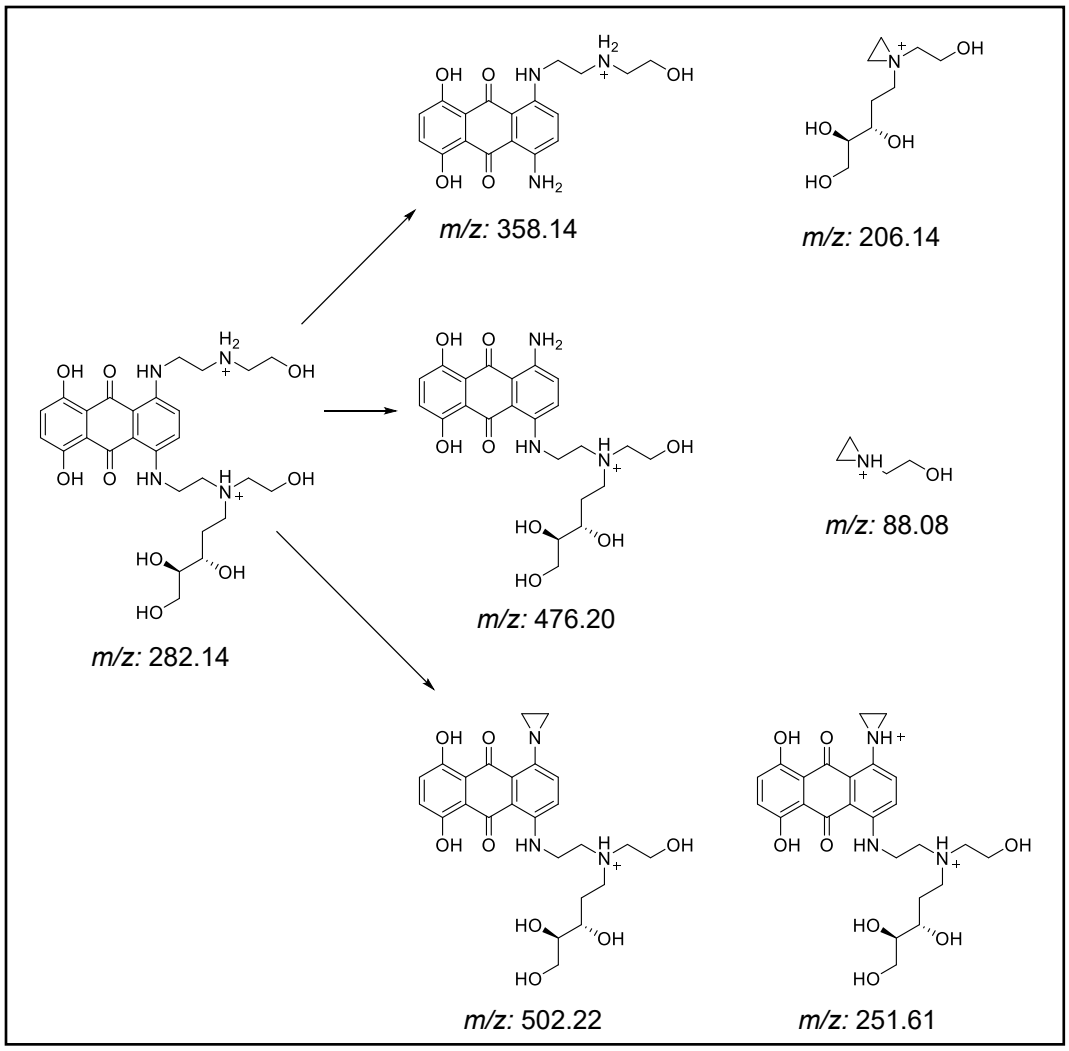

Assigned fragments for *m/z 282* selected ion ESI-MS^2 CID spectrum of the MTX-dR synthetic standard.

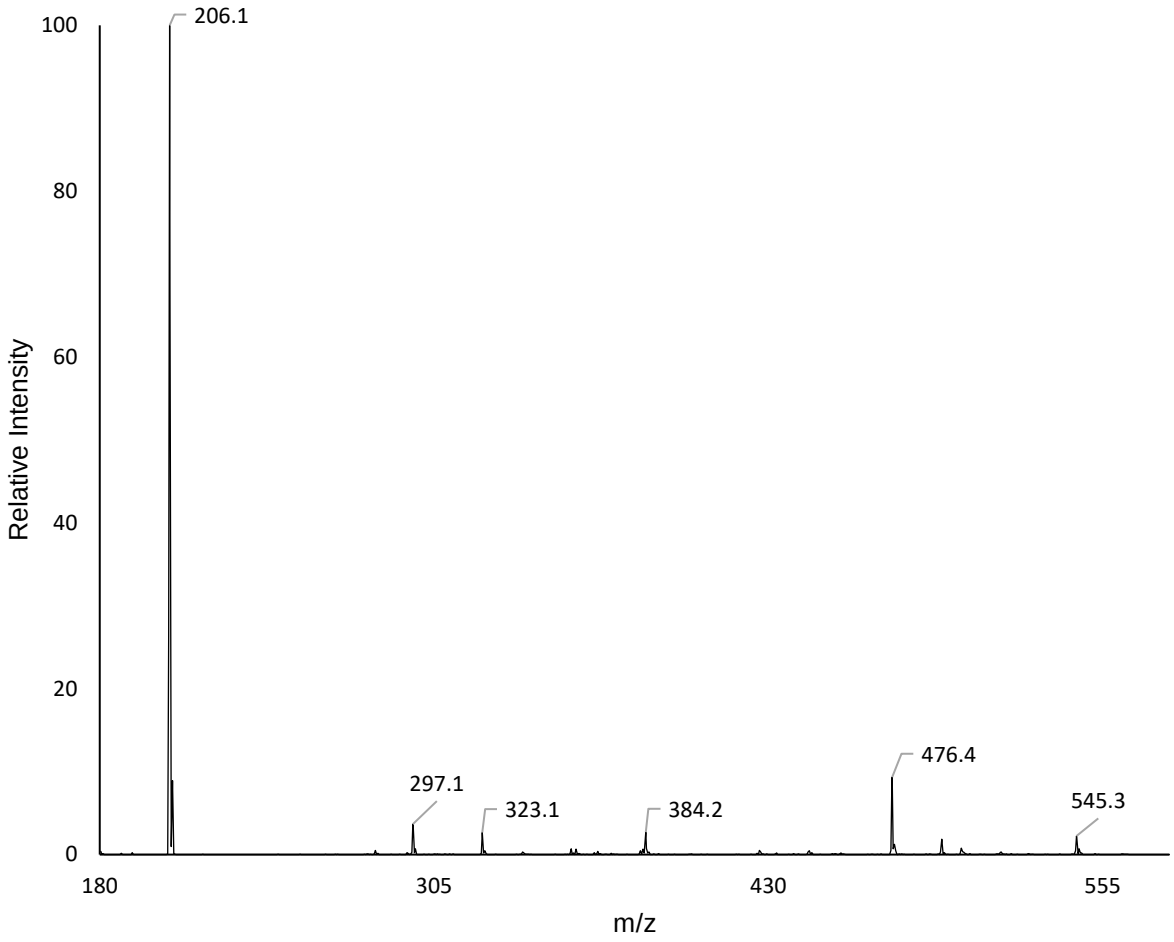

***m/z 563* selected ion ESI-MS^2 spectrum of the MTX-dR synthetic standard with CID fragmentation.**

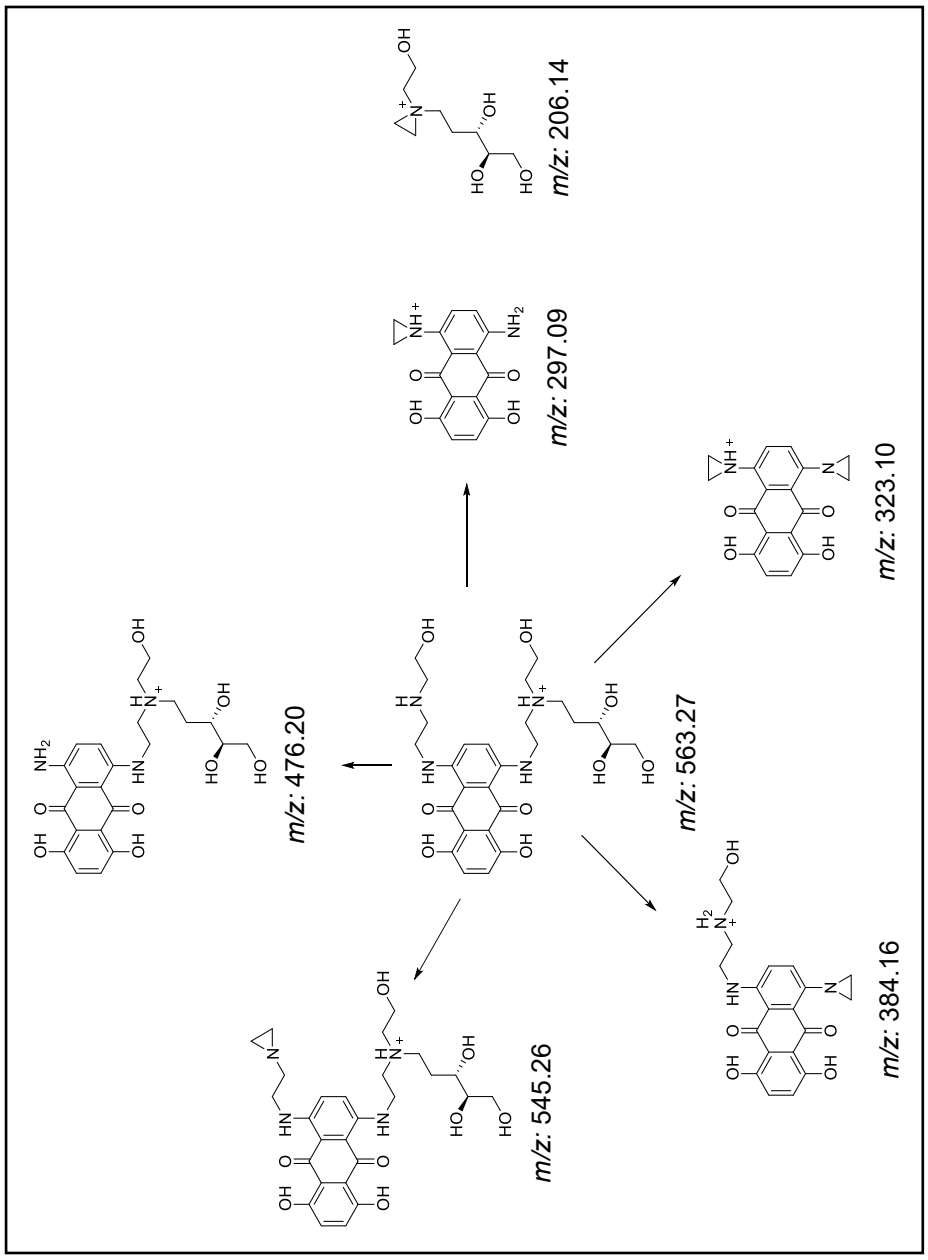

Assigned fragments for *m/z 563* CID ESI-MS^2 peaks of the MTX-dR synthetic standard.

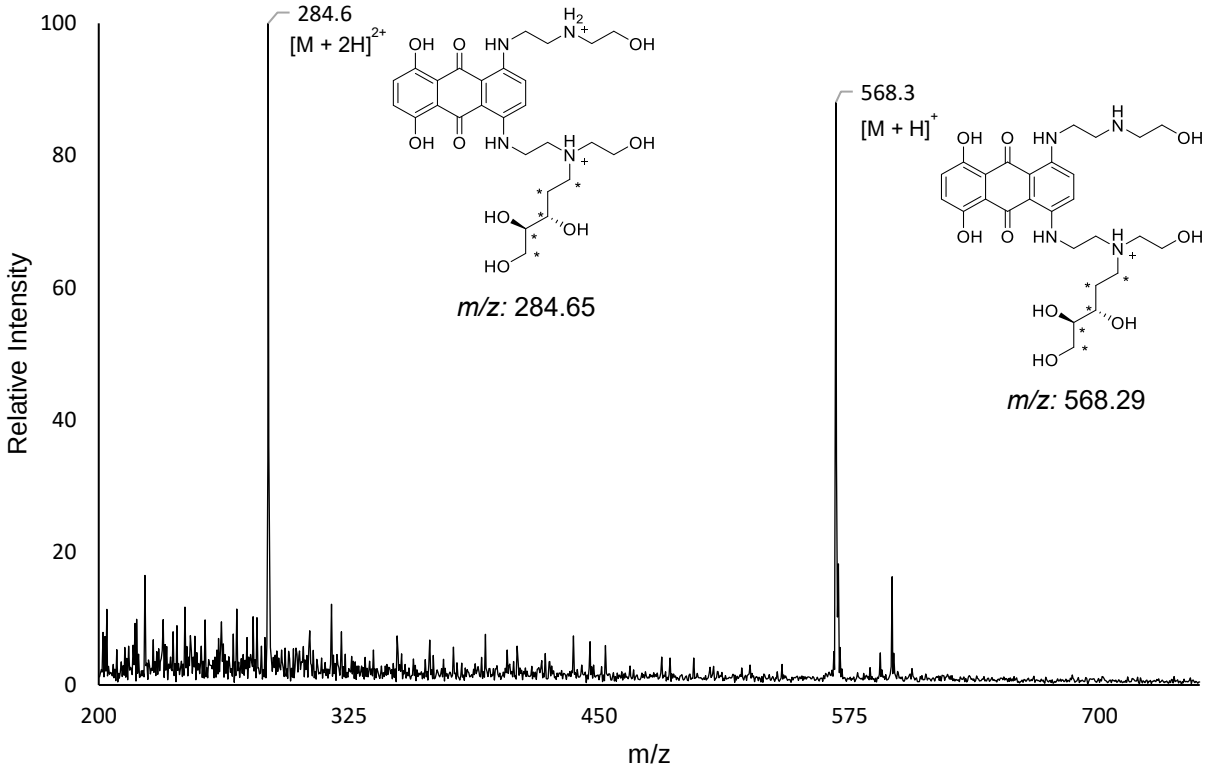

ESI-MS total ion mass spectrum of the MTX-($^{13}C_5$)dR isotopically labeled synthetic standard.

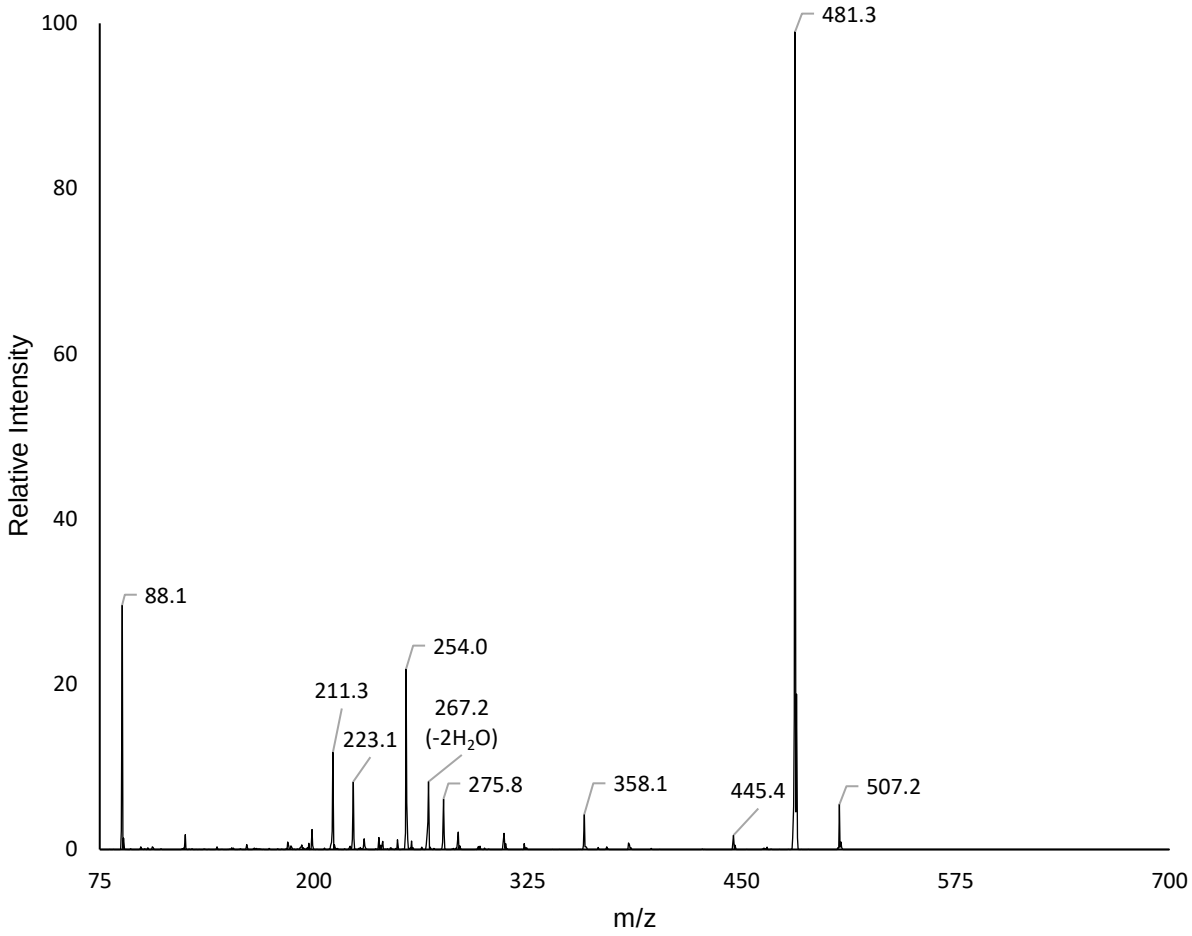

m/z 284 **selected ion ESI-MS^2 spectrum of the MTX-($^{13}C_5$)dR isotopically labeled synthetic standard with CID fragmentation.**

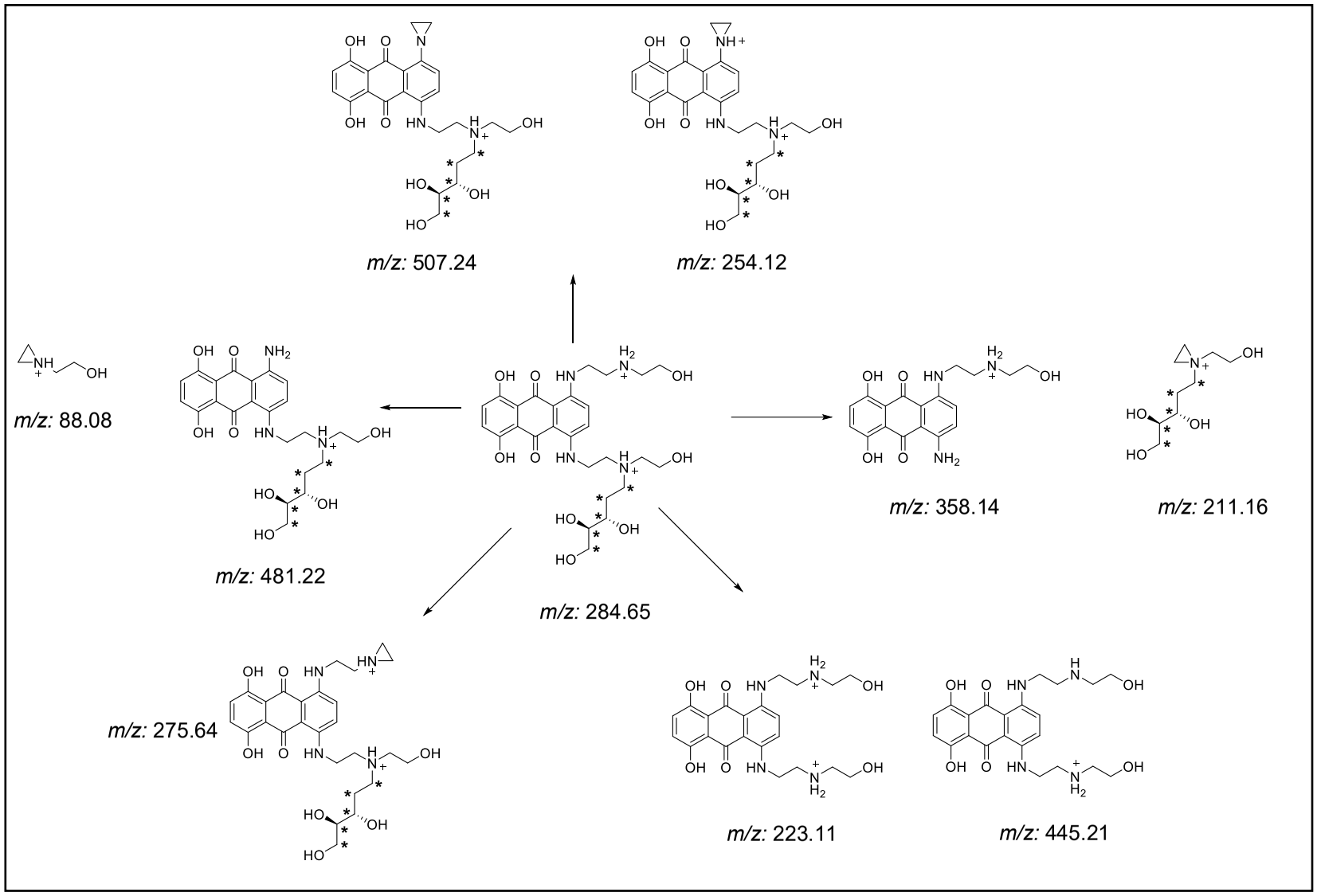

Assigned fragments for *m/z 284* selected ion ESI-MS^2 CID peaks of the MTX-($^{13}C_5$)dR isotopically labeled synthetic standard.

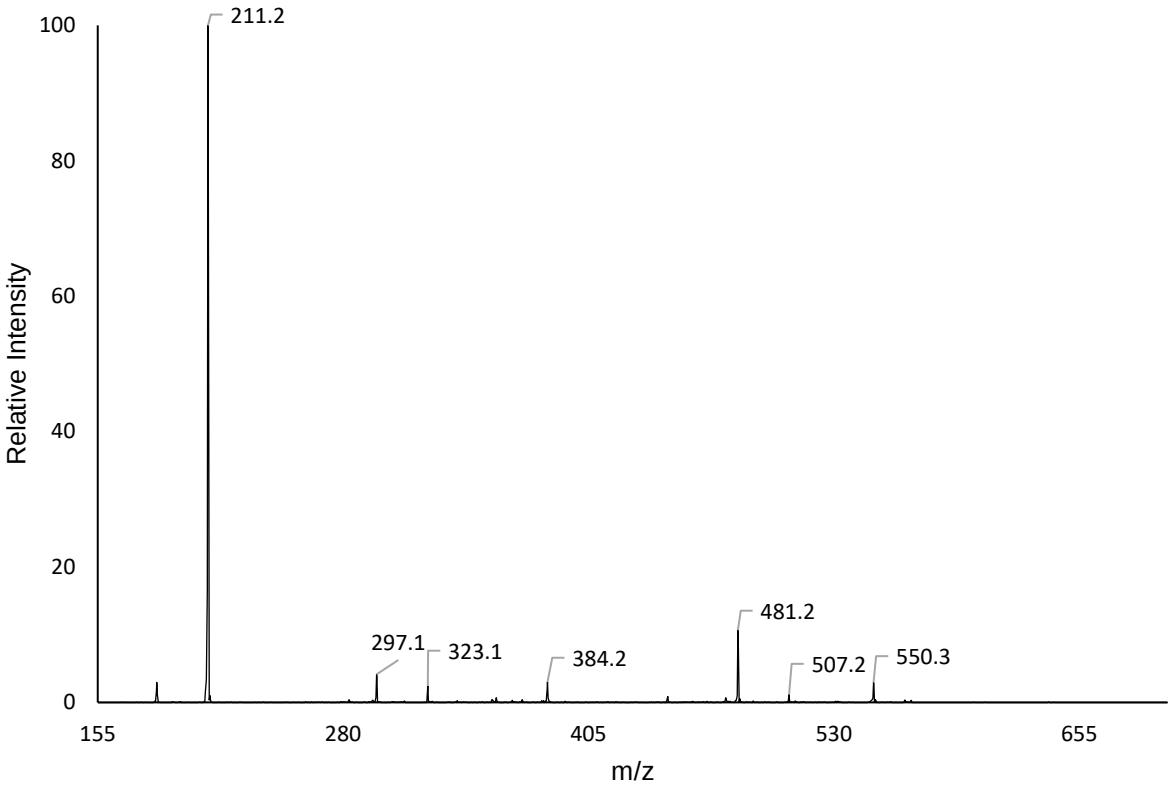

m/z 568 **selected ion ESI-MS^2 spectrum of the MTX-($^{13}C_5$)dR isotopically labeled synthetic standard with CID fragmentation.**

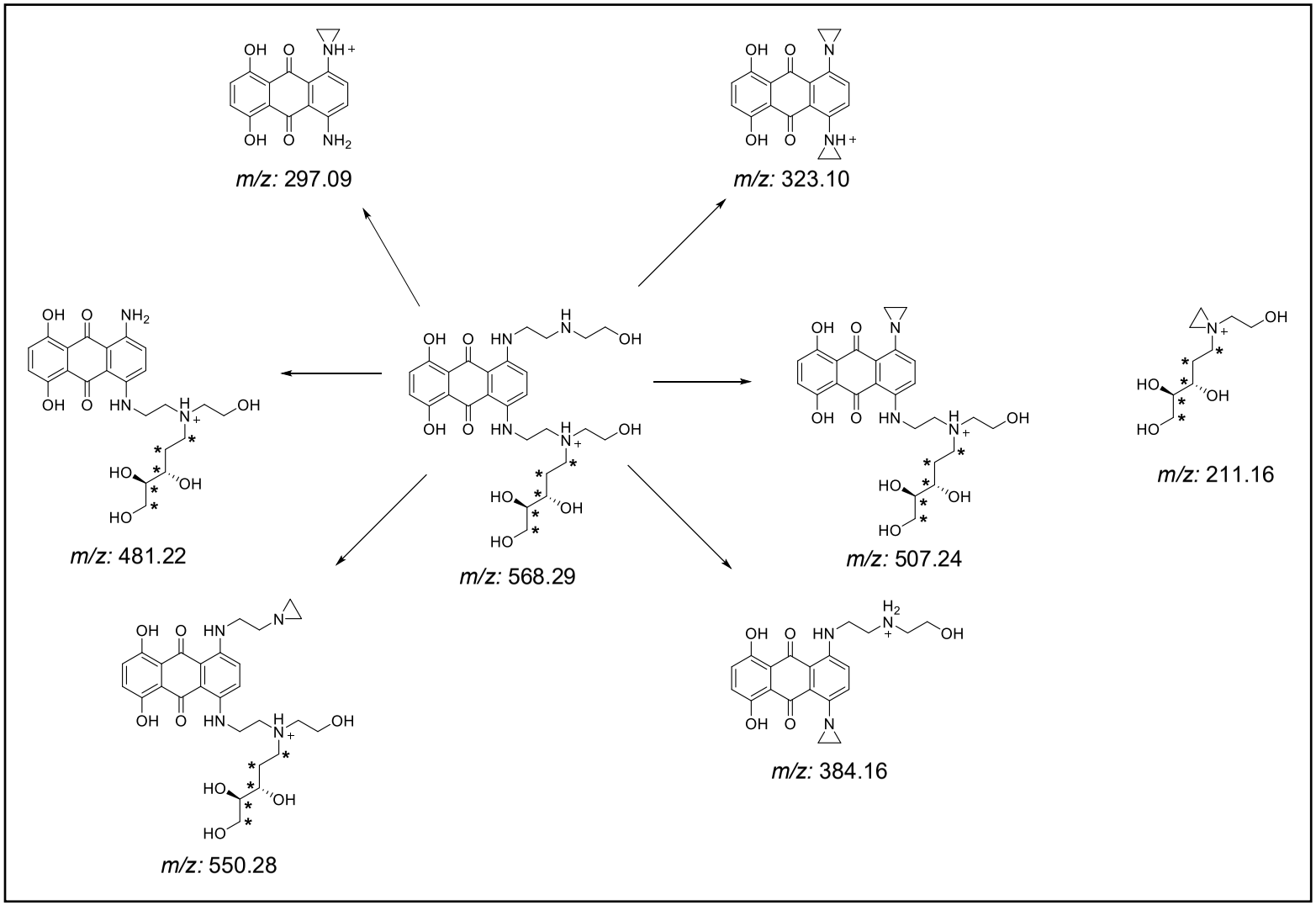

Assigned fragments for *m/z 568* selected ion ESI-MS^2 CID peaks of the MTX-($^{13}C_5$)dR isotopically labeled synthetic standard.

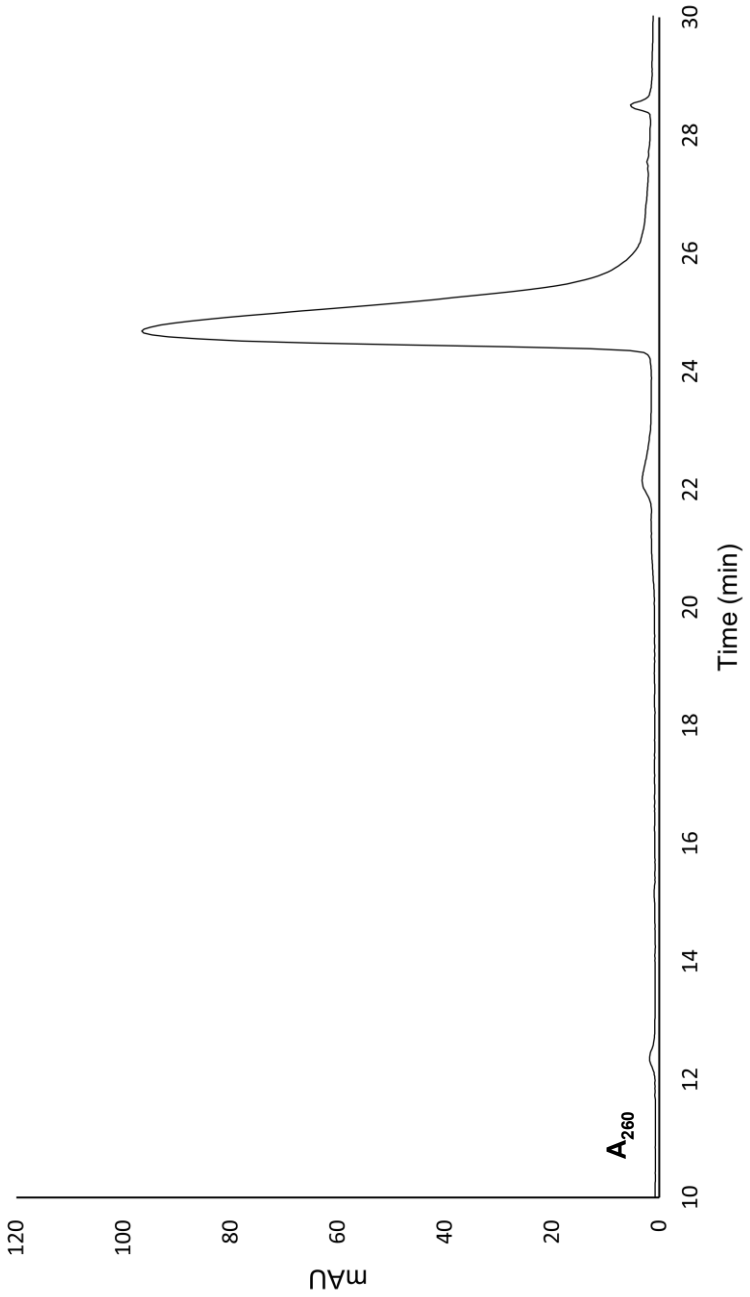

HPLC trace of the purified MTX-dR$_2$ synthetic standard.

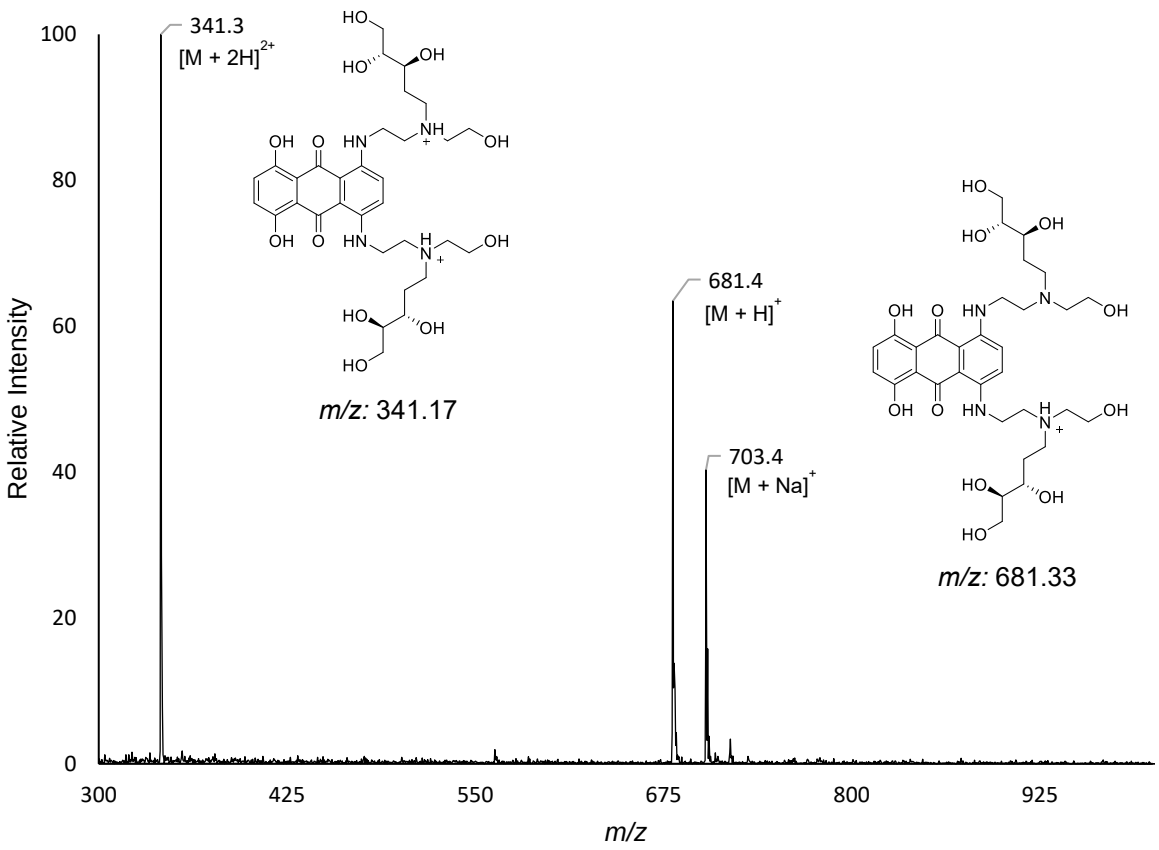

ESI-MS total ion mass spectrum of the MTX-dR$_2$ synthetic standard.

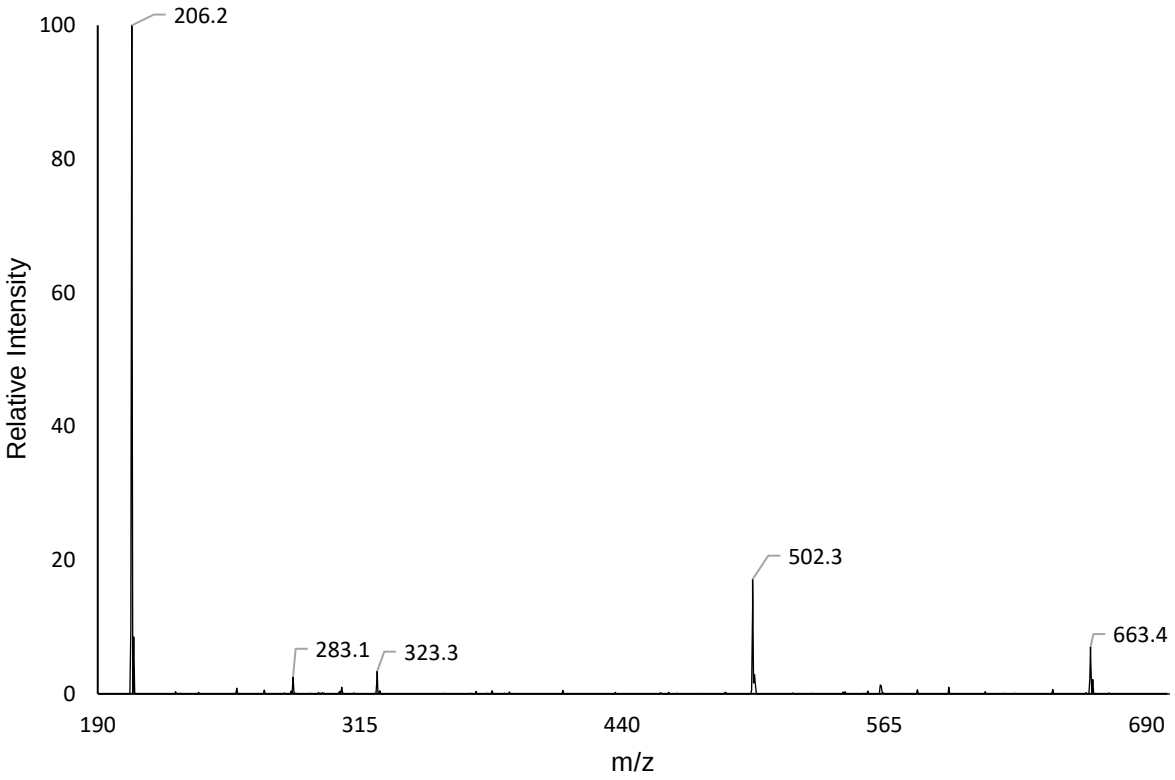

***m/z 681* selected ion ESI-MS^2 spectrum of the MTX-dR$_2$ synthetic standard with CID fragmentation.**

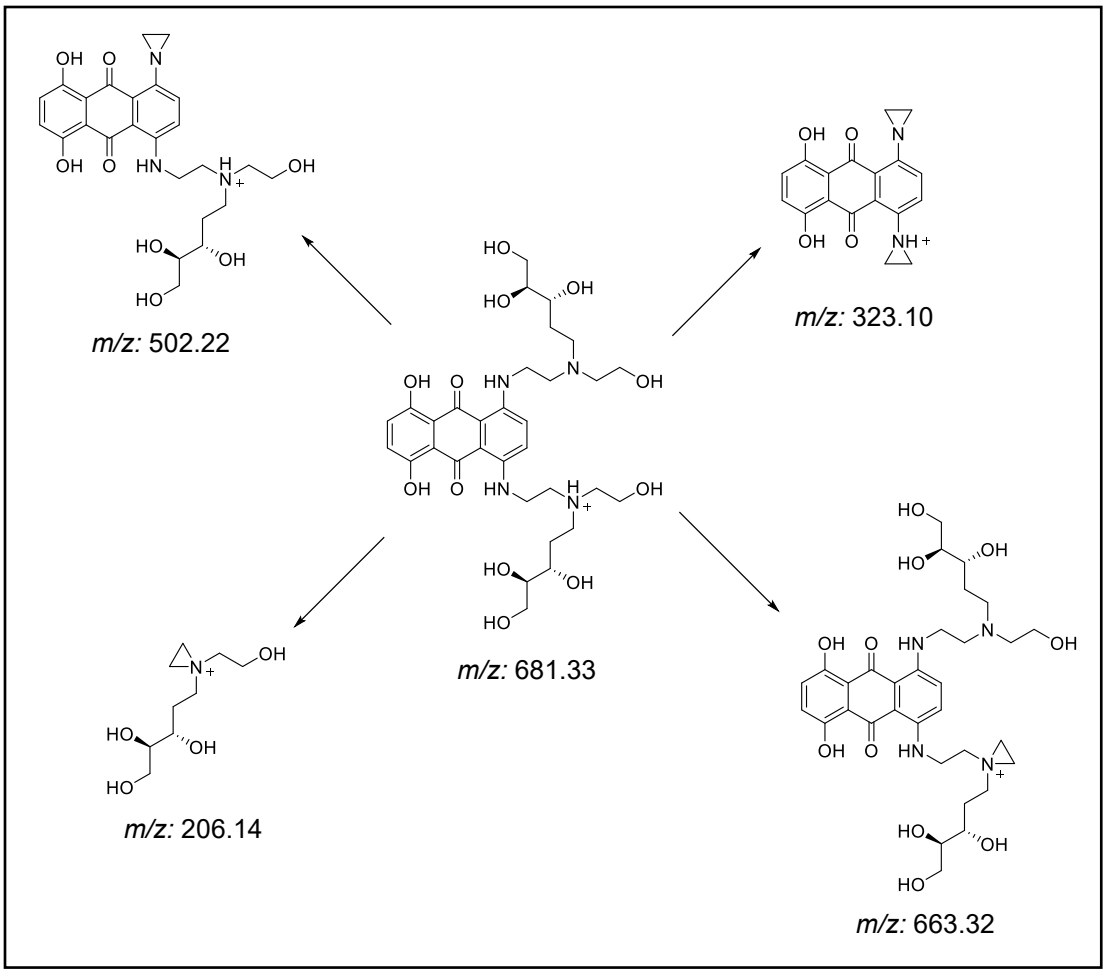

Assigned fragments for *m/z 681* selected ion ESI-MS^2 CID peaks of the MTX-dR$_2$ synthetic standard.

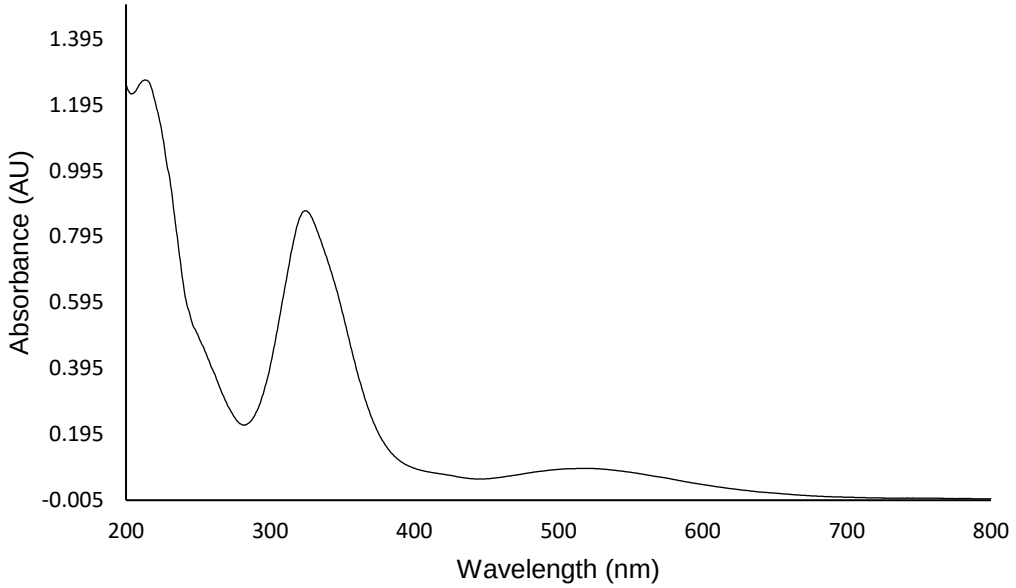

Representative UV spectrum of 40 µM PIX in water from 200-800 nm.

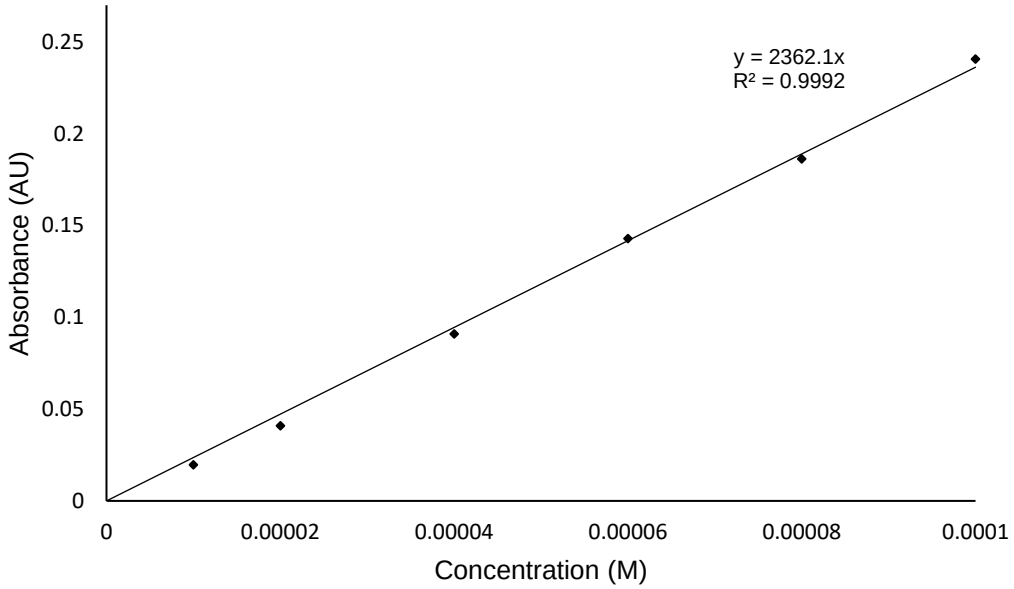

Calibration curve for PIX generated from UV absorbances at λ = 517 nm for 10-100 µM solutions in water with calculated extinction coefficient of ~2360 $M^{-1}cm^{-1}$.

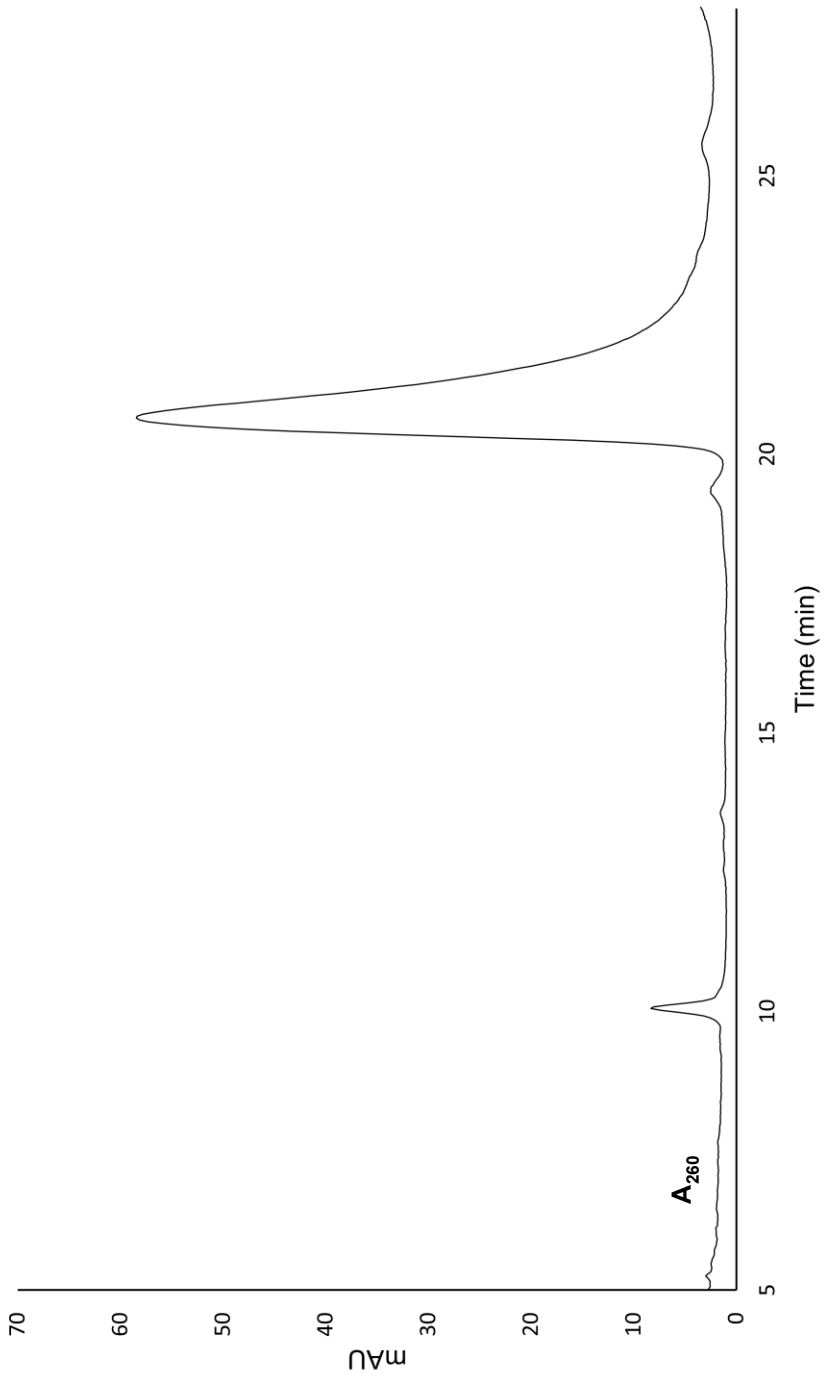

HPLC trace of the purified PIX-dR synthetic standard.

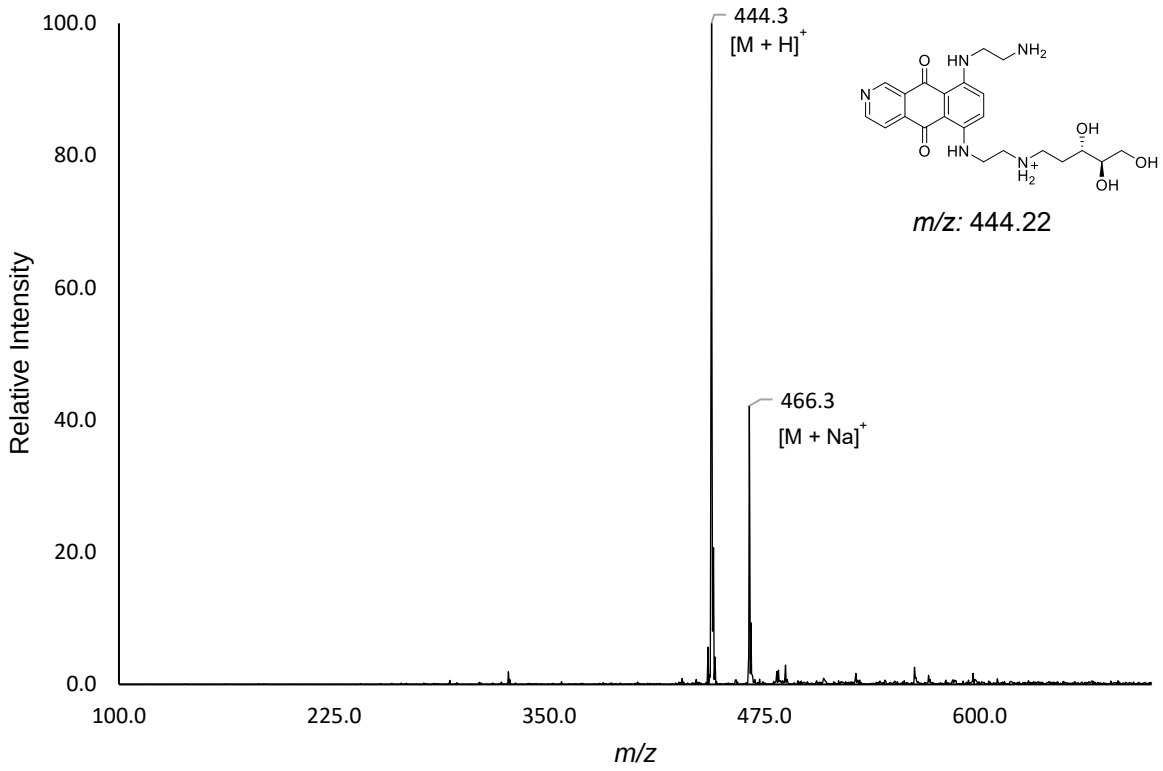

ESI-MS total ion mass spectrum of the PIX-dR synthetic standard.

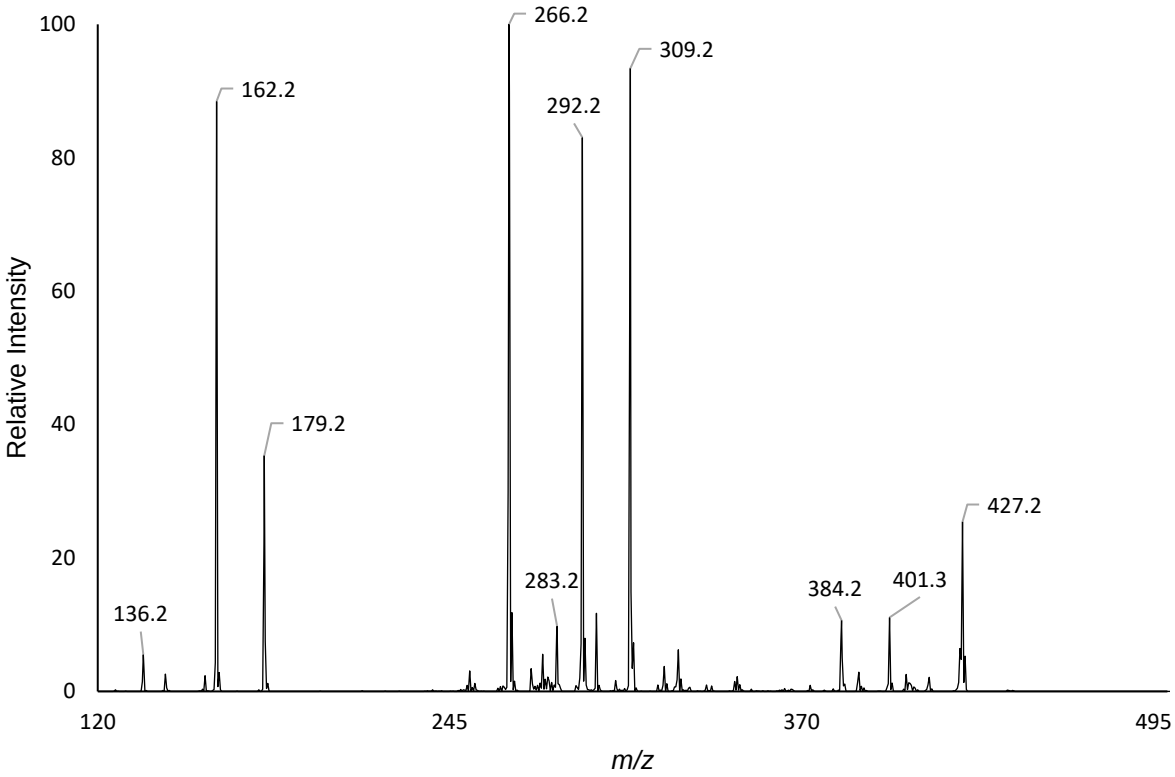

***m/z 444* selected ion ESI-MS^2 spectrum of the PIX-dR synthetic standard with CID fragmentation.**

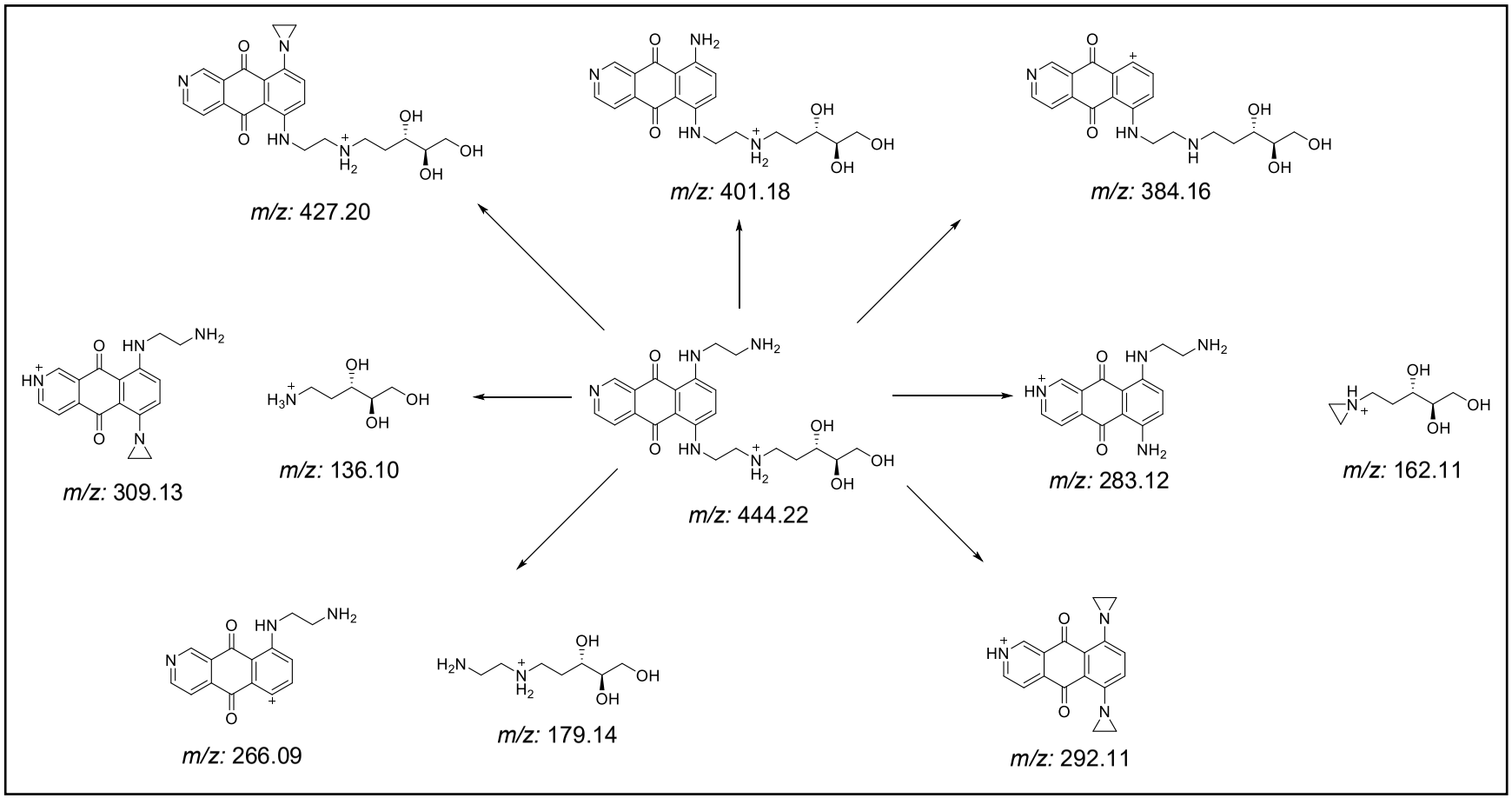

Assigned fragments for *m/z 444* selected ion ESI-MS^2 CID peaks of the PIX-dR synthetic standard.

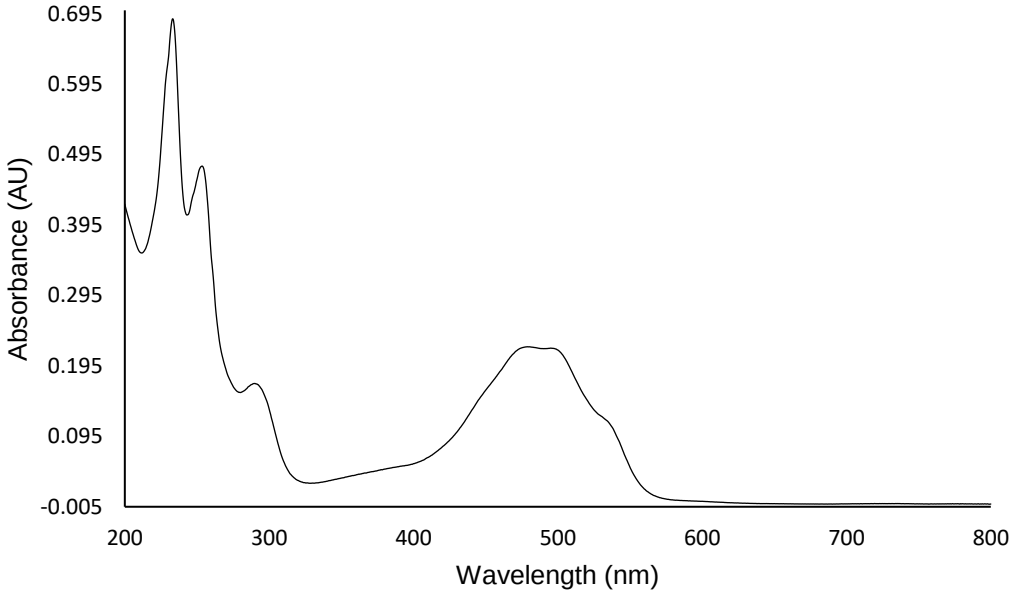

Representative UV spectrum of 20 μM DOX in water from 200-800 nm.

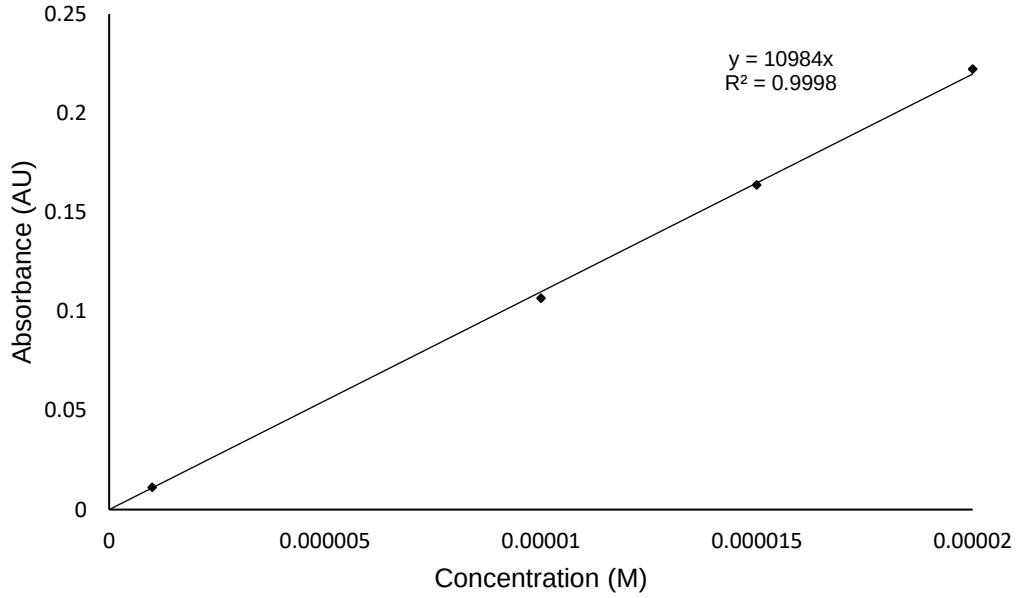

Calibration curve for DOX generated from UV absorbances at λ = 480 nm for 1-20 μM solutions in water with calculated extinction coefficient of ~11000 $M^{-1}cm^{-1}$.

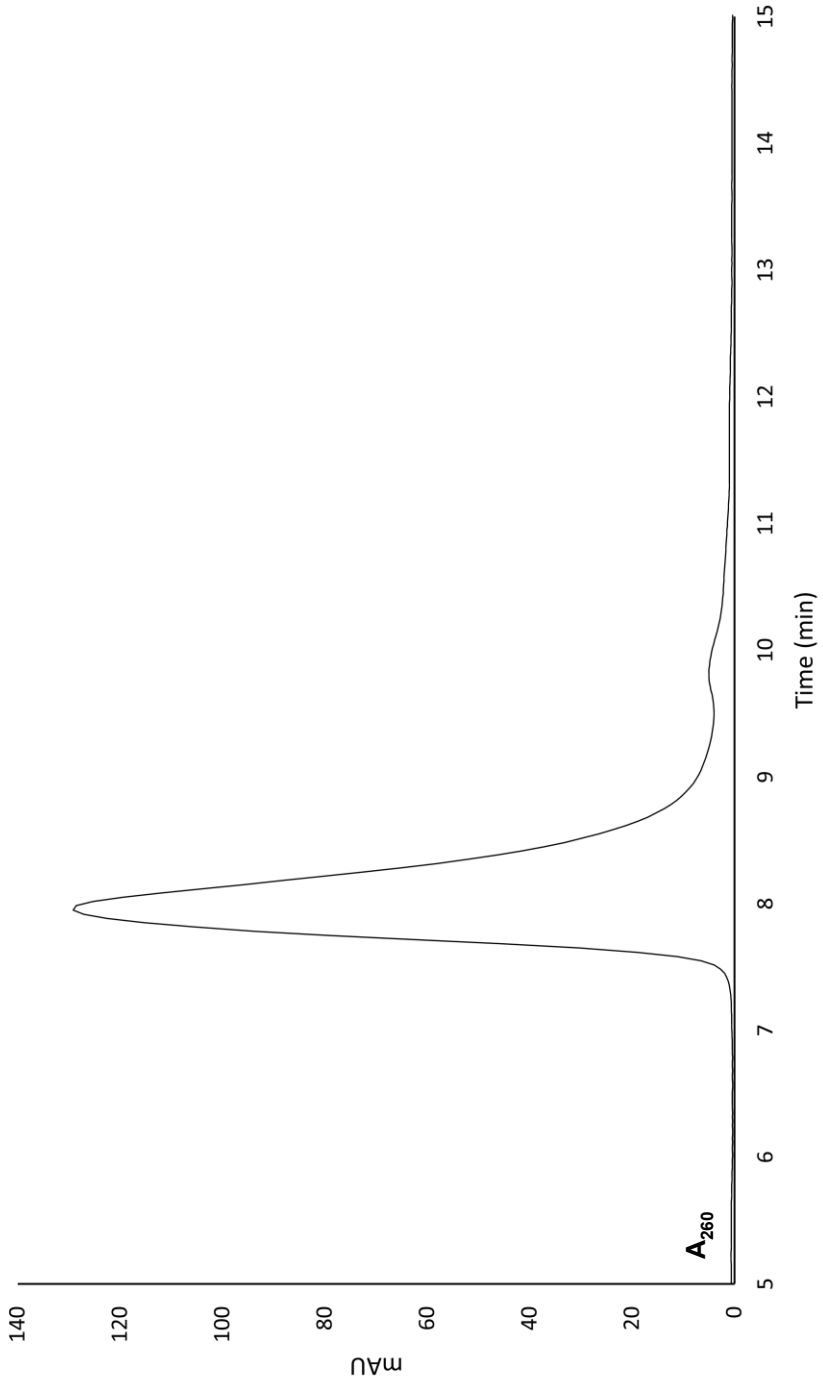

HPLC trace of the purified DOXol-dR synthetic standard.

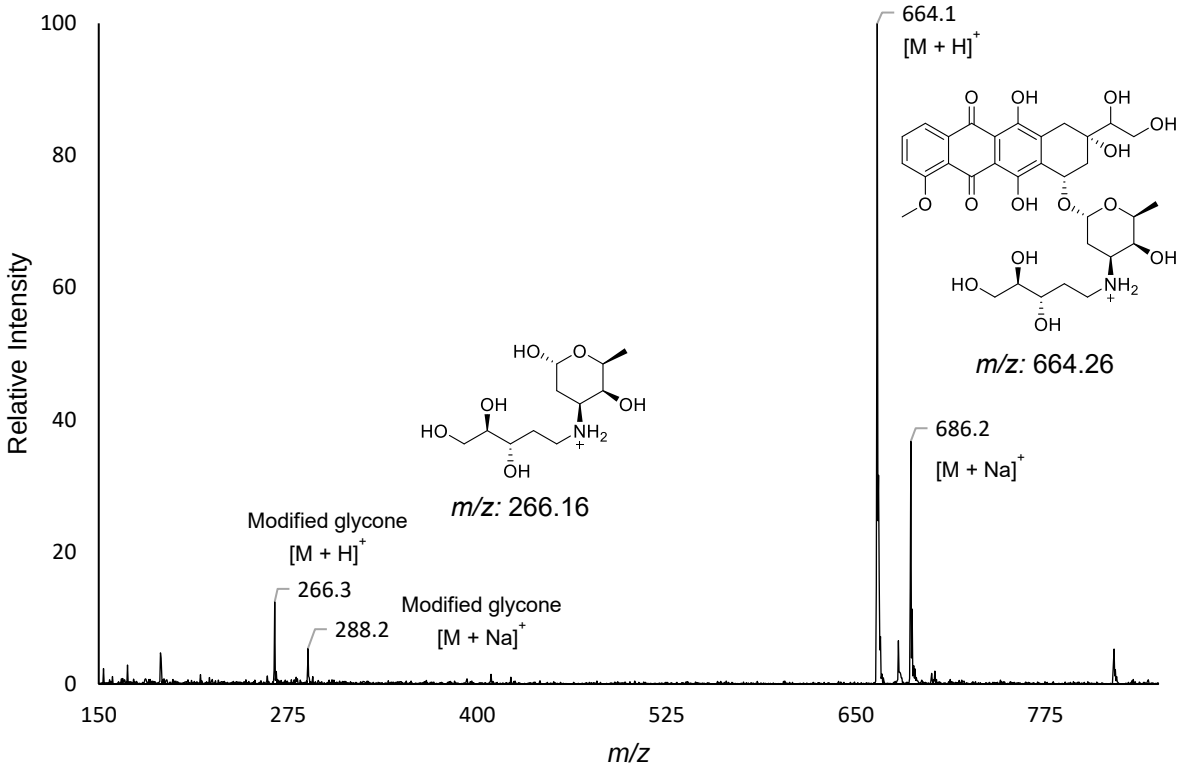

ESI-MS total ion mass spectrum of the DOXol-dR synthetic standard.

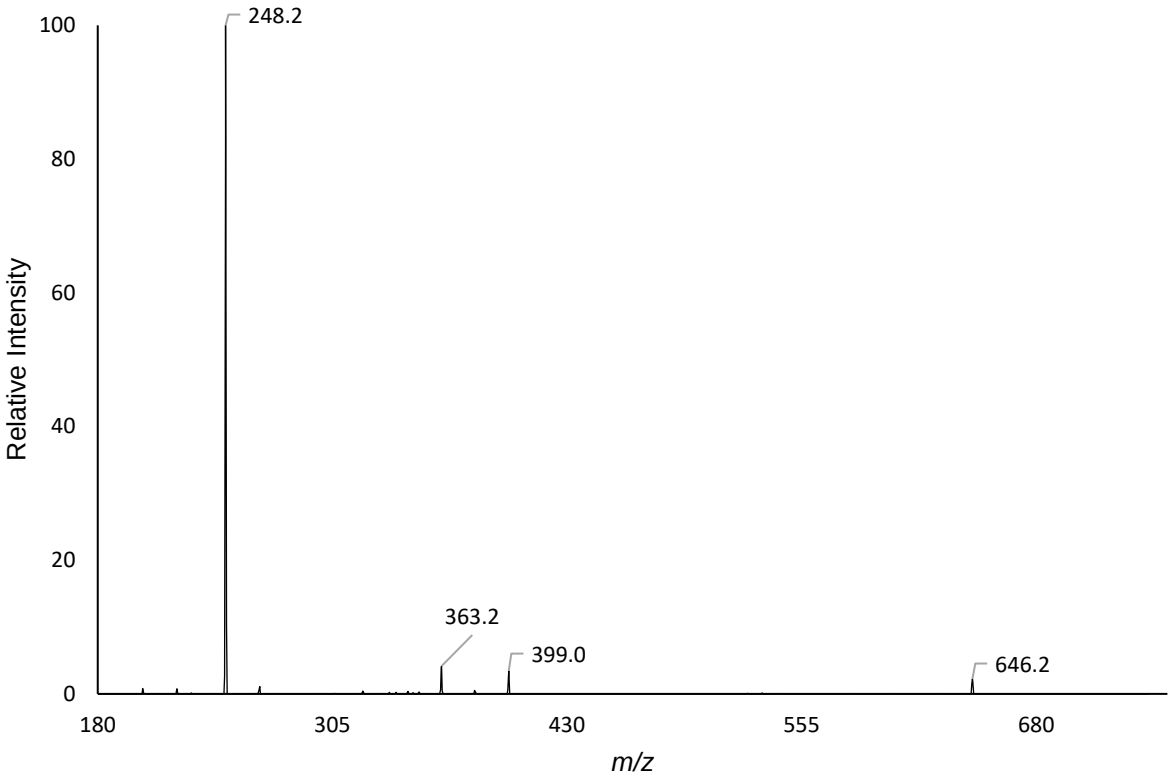

***m/z 664* selected ion ESI-MS^2 spectrum of the DOXol-dR synthetic standard with CID fragmentation.**

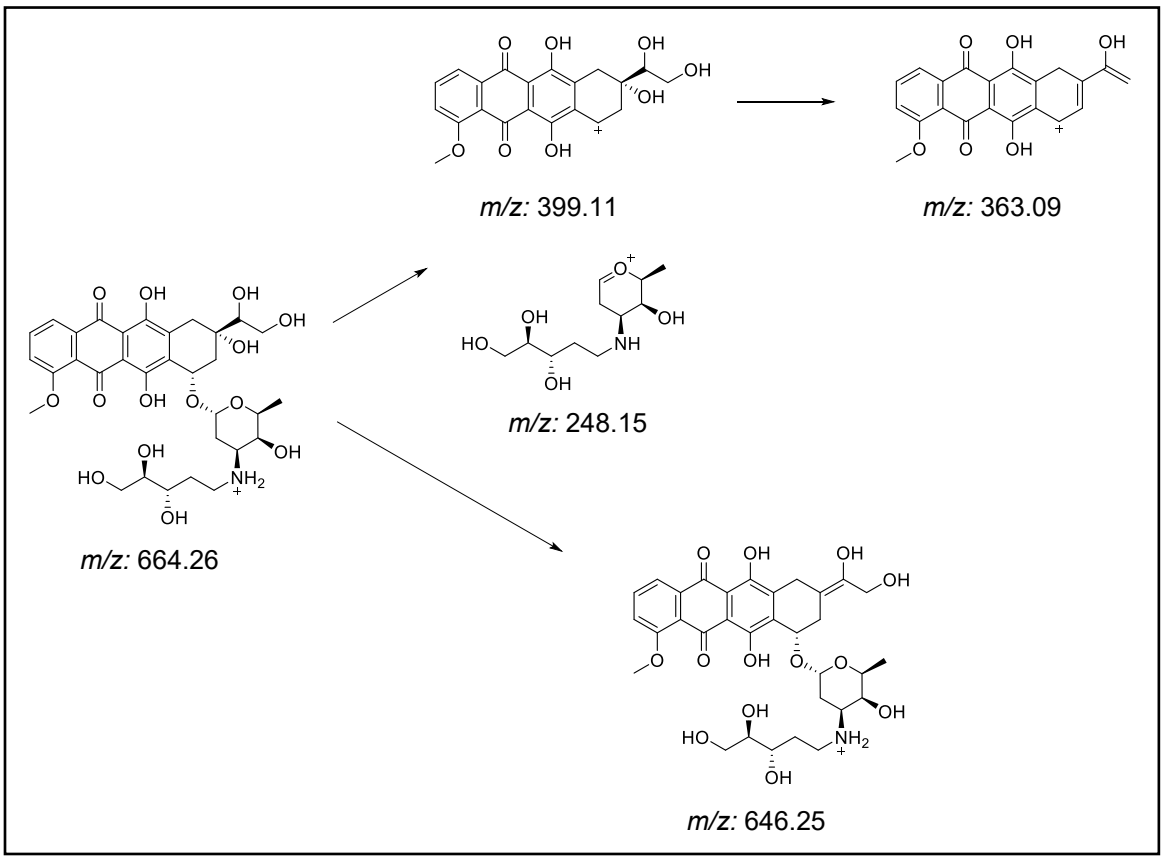

Assigned fragments for *m/z 664* selected ion ESI-MS^2 CID peaks of the DOXol-dR synthetic standard.

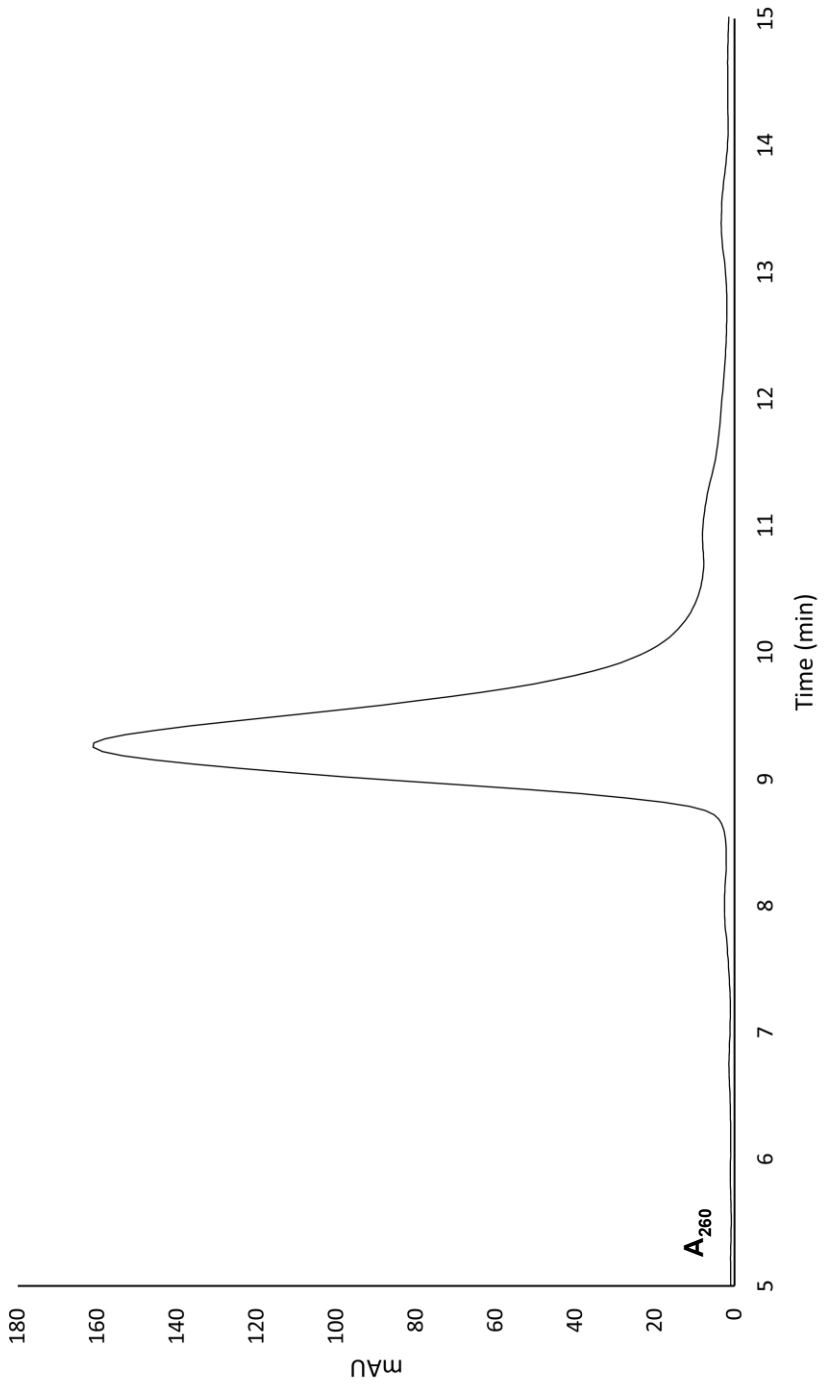

HPLC trace of the purified EPIol-dR synthetic standard.

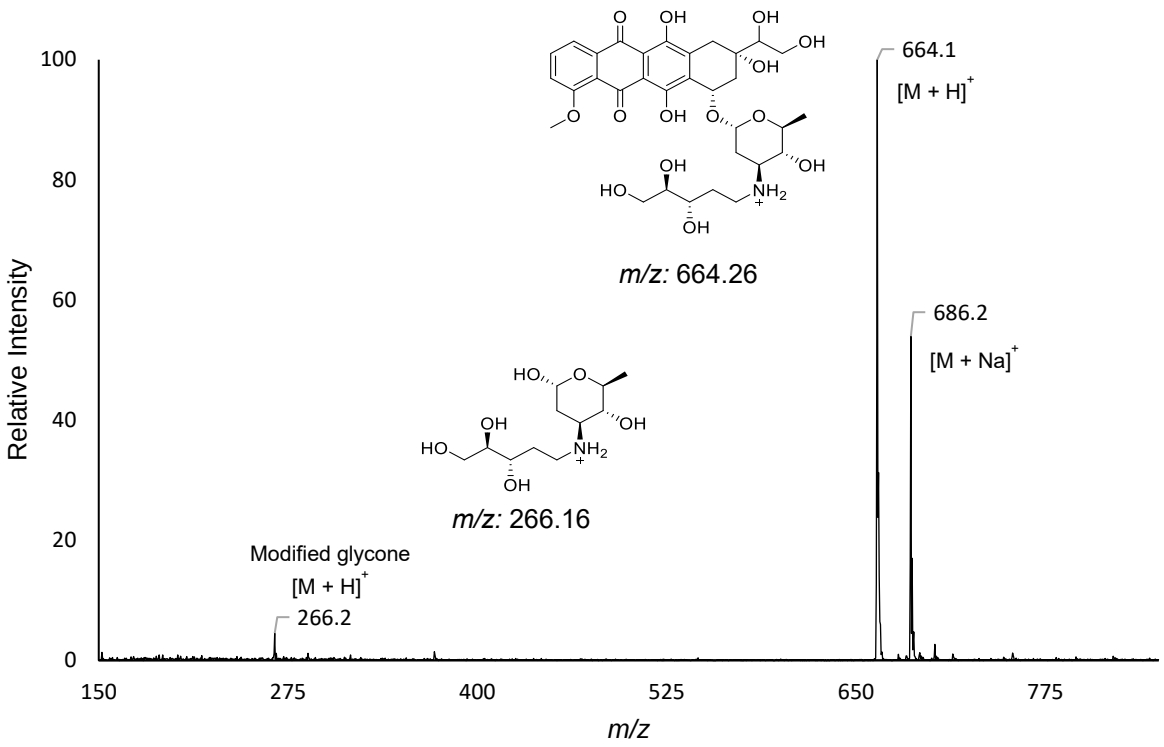

ESI-MS total ion mass spectrum of the EPIol-dR synthetic standard.

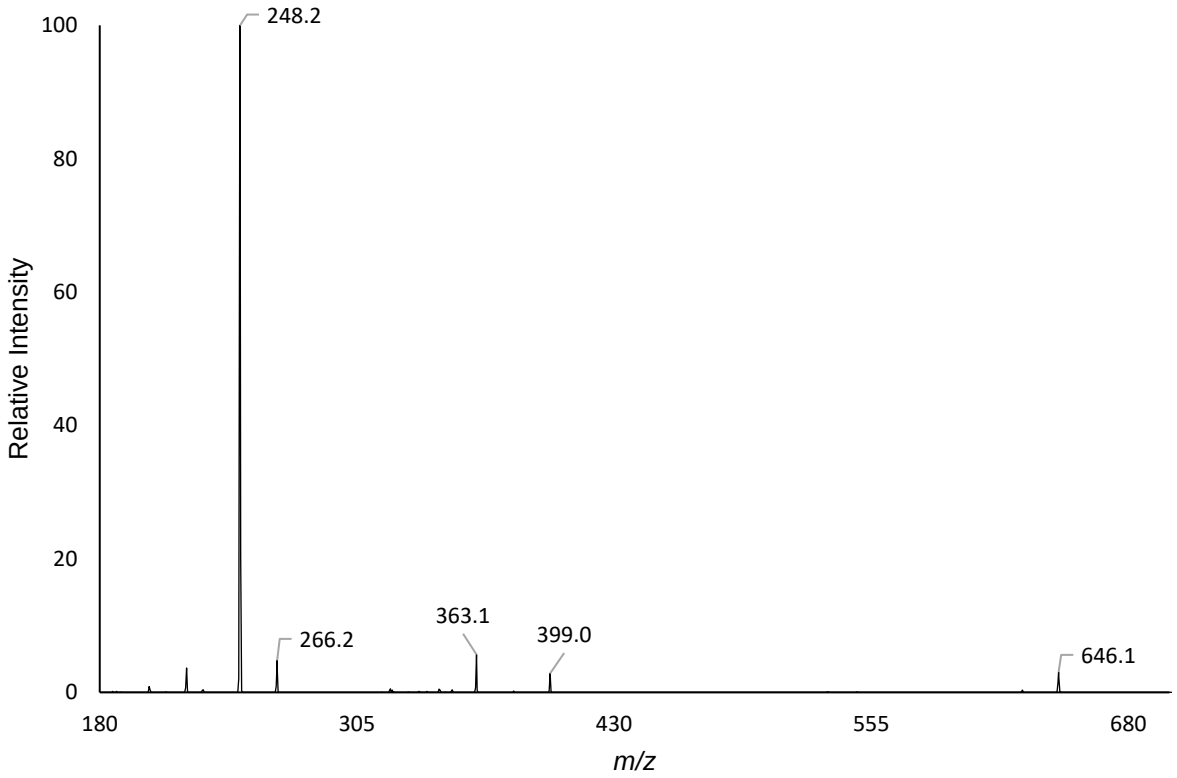

***m/z 664* selected ion ESI-MS^2 spectrum of the EPIol-dR synthetic standard with CID fragmentation.**

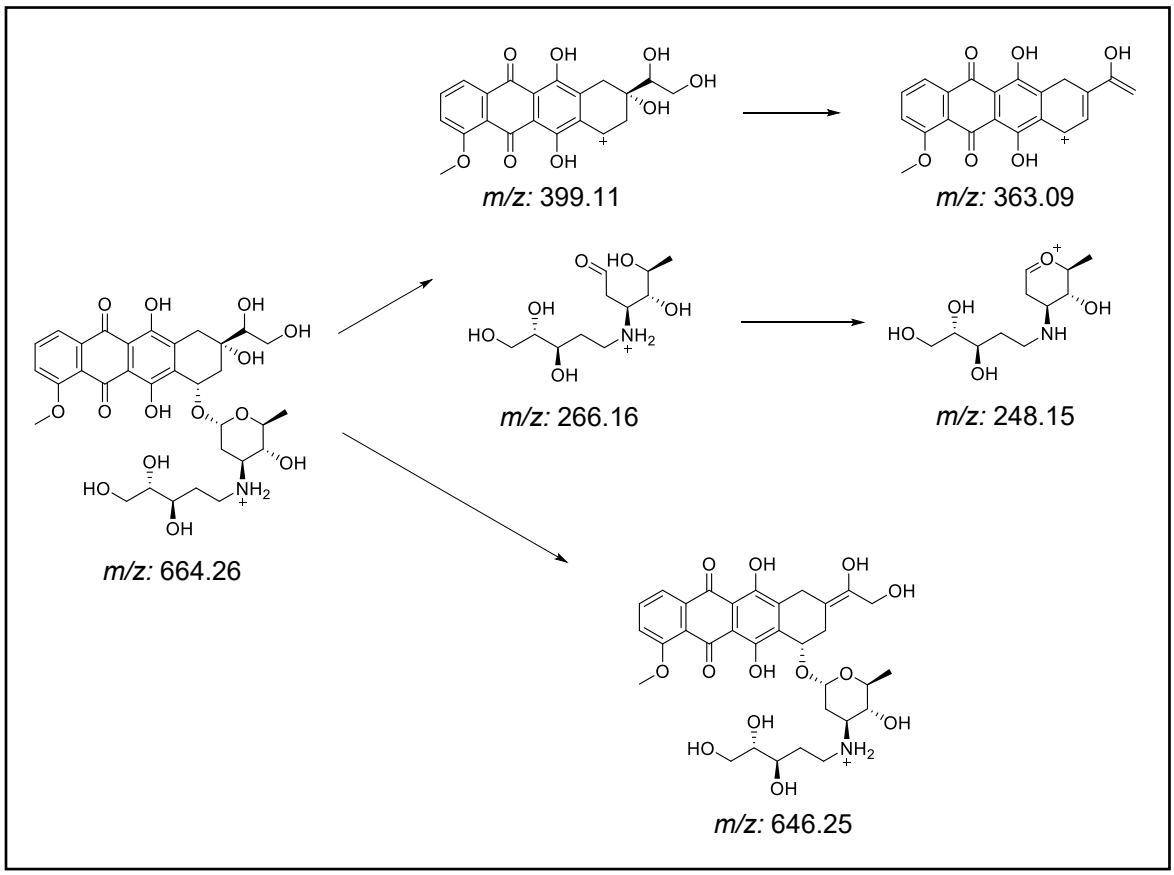

Assigned fragments for *m/z 664* selected ion ESI-MS^2 CID peaks of the EPIol-dR synthetic standard.

Appendix II:

HPLC and ESI-LC/MS^2 Characterization and Sequencing for Anthracycline-12mer Oligonucleotide Reduced Covalent Adducts in Chapter II

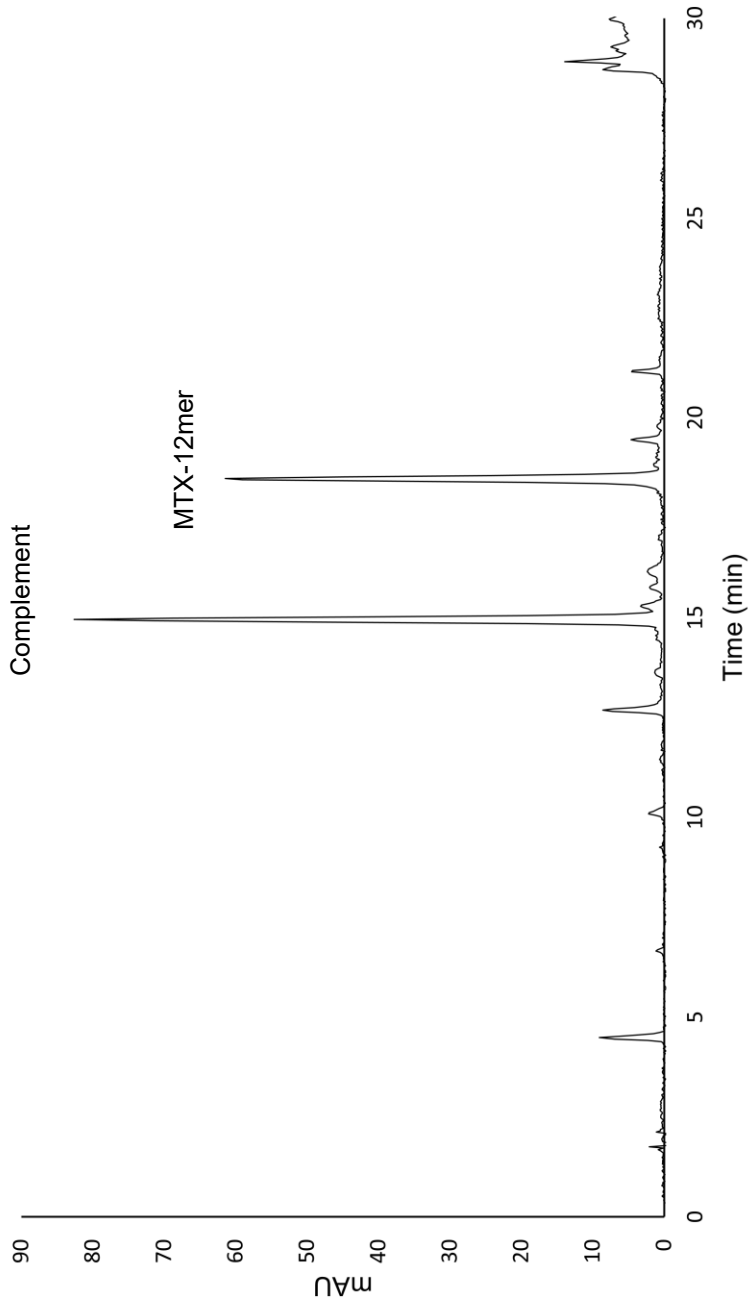

HPLC chromatogram of the dsMTX-12mer reduced conjugate crude reaction solution.

MTX-12mer: 5'-GTT GC[AP-MTX] CGT ATG-3'

Complement: 5'-CAT ACG CGC AAC-3'

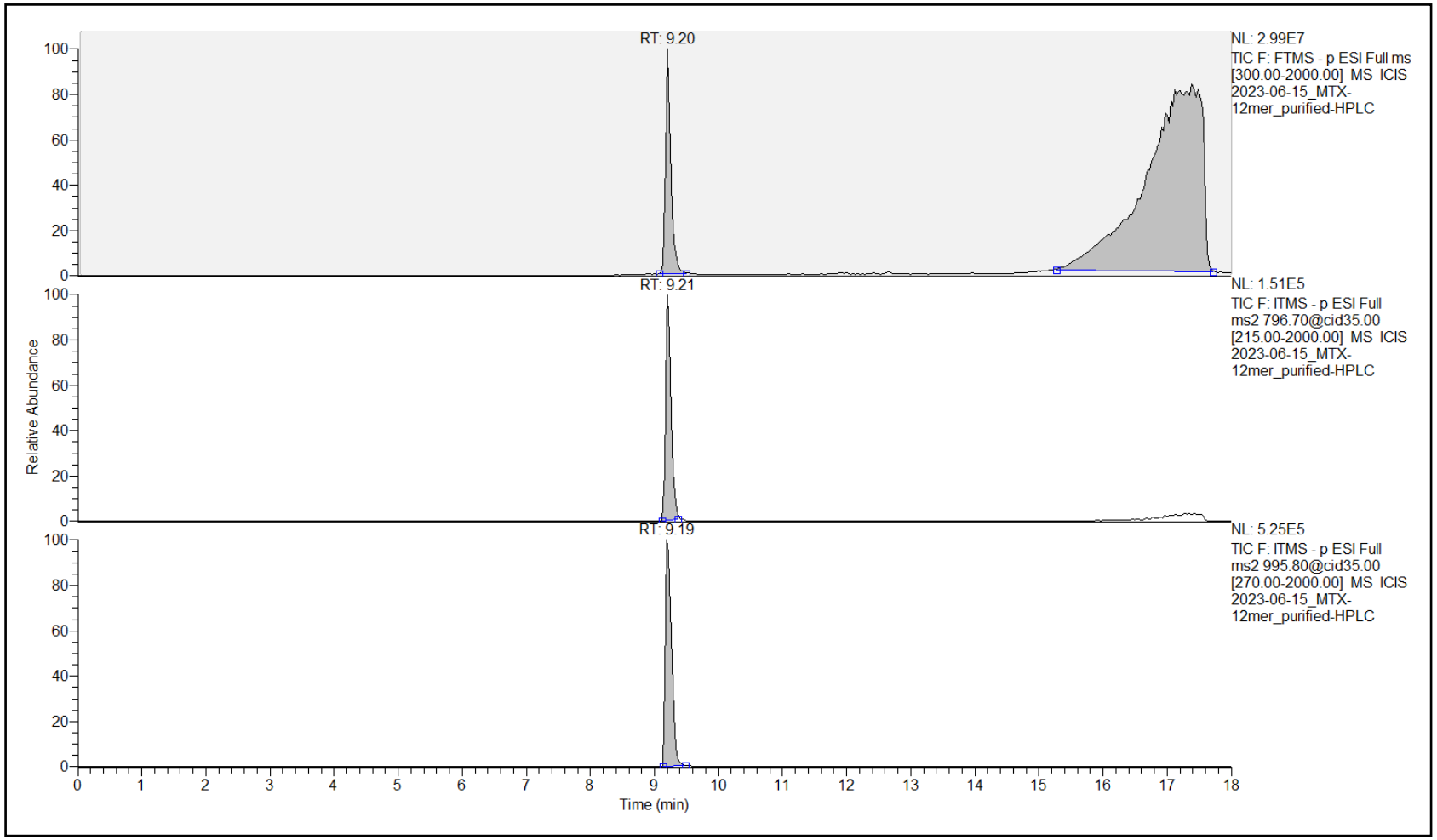

ESI-LC/MS chromatogram of the purified MTX-12mer reduced conjugate showing the total ion chromatogram (top) and selected ion chromatograms for *m/z 796* and *995*.

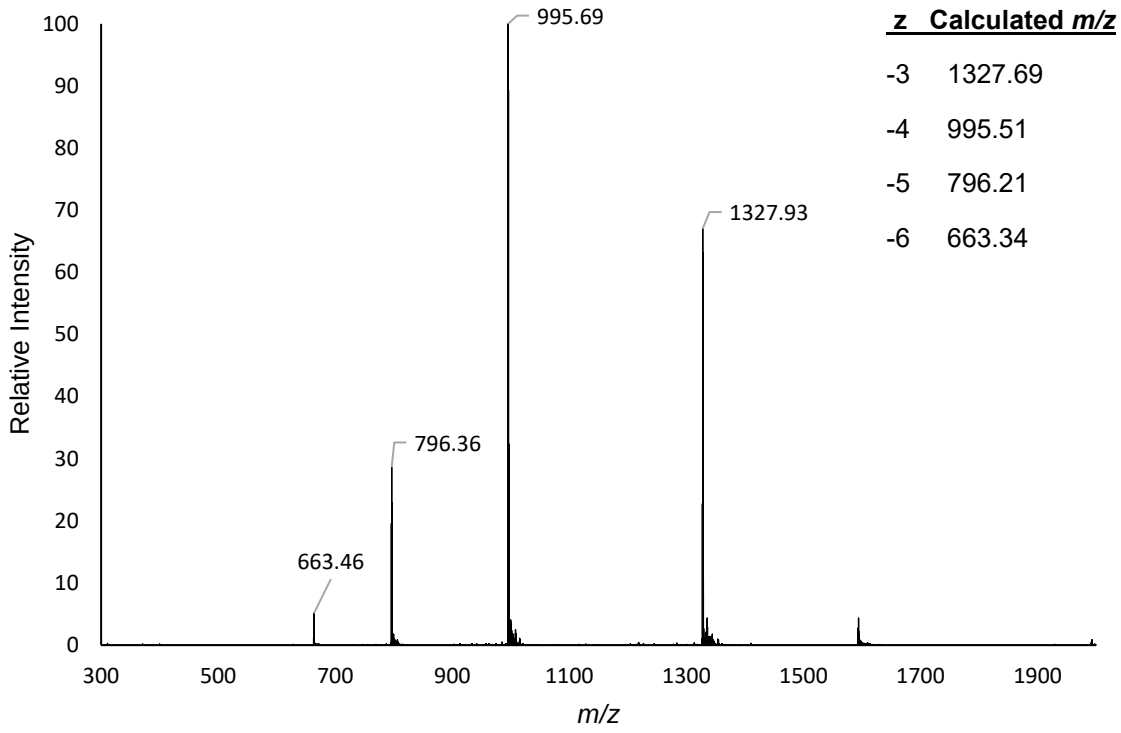

ESI-LC/MS total ion mass spectrum of the purified MTX-12mer reduced conjugate (5'-GTT GC[AP-MTX] CGT ATG-3') at retention time 9.20 minutes.

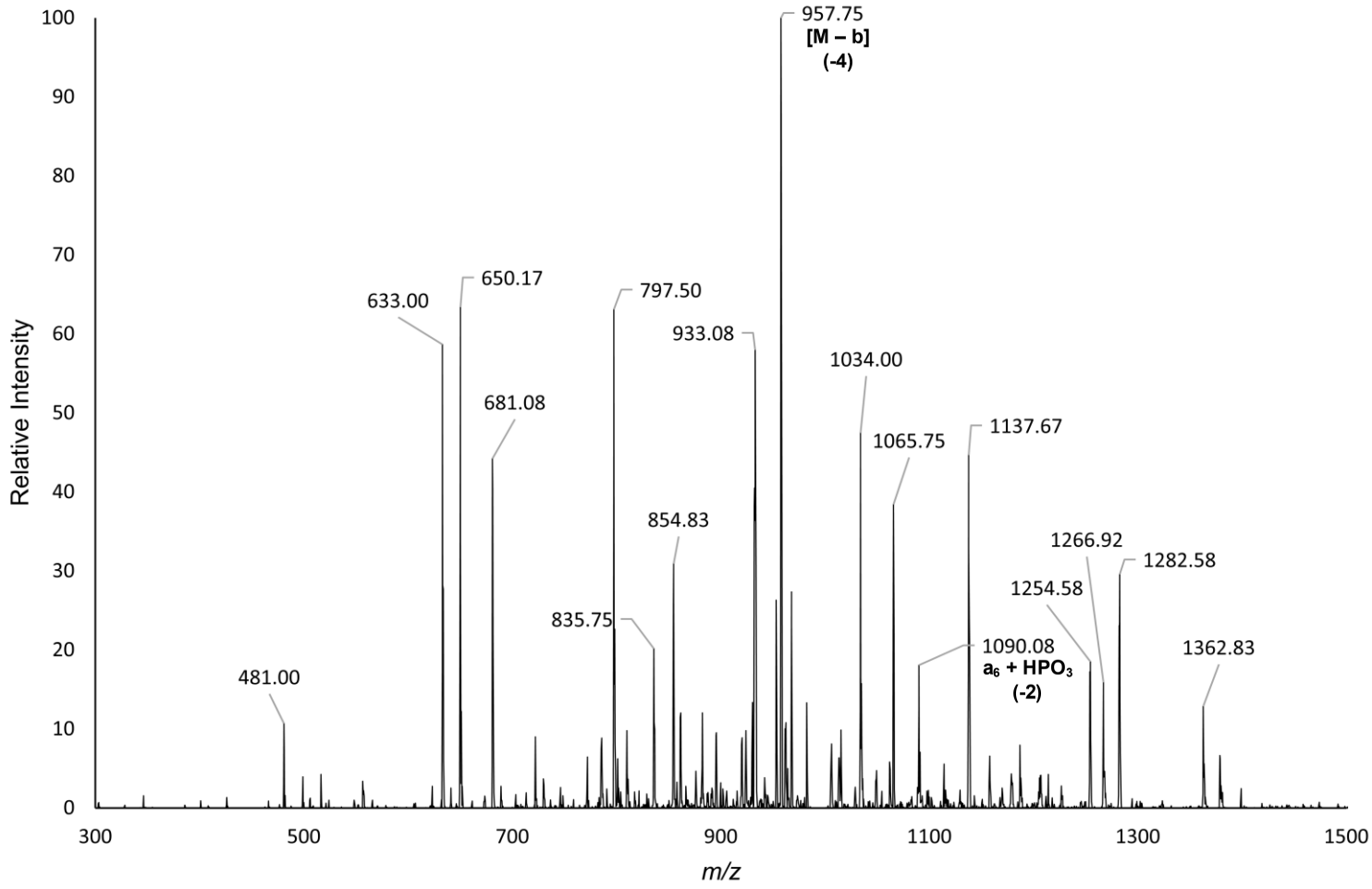

m/z 995 **selected ion ESI-LC/MS^2 mass spectrum with CID fragmentation of the purified MTX-12mer reduced conjugate (5'-GTT GC[AP-MTX] CGT ATG-3'). Peaks at *m/z 958* and *1090* not predicted by software; identity determined from ChemDraw structure.**

Calculated CID Fragments

n	z	a-B	w	y	d-H2O
1	-1		346.054	266.088	328.044
2	-1	426.080	650.100	570.134	632.090
	-2		324.546	284.563	315.541
3	-1	730.126	963.157	883.191	936.135
	-2	364.559	481.074	441.091	467.563
	-3		320.380	293.725	311.373
4	-1	1034.171	1267.203	1187.237	1265.187
	-2	516.582	633.097	593.114	632.090
	-3	344.052	421.729	395.073	421.057
	-4		316.044	296.053	315.541
5	-1	1363.224	1596.255	1516.289	1554.233
	-2	681.108	797.623	757.640	776.613
	-3	453.736	531.413	504.757	517.406
	-4	340.050	398.307	378.316	387.802
	-5		318.444	302.451	310.040
6	-1	2096.470	1885.301	1805.335	2177.444
	-2	1047.731	942.146	902.163	1088.218
	-3	698.151	627.761	601.106	725.142
	-4	523.361	470.569	450.577	543.605
	-5	418.487	376.254	360.260	434.682
	-6		313.377	300.049	362.067
7	-1	2275.480	2508.511	2428.545	2466.490
	-2	1137.236	1253.752	1213.769	1232.741
	-3	757.821	835.498	808.843	821.491
	-4	568.114	626.372	606.380	615.866
	-5	454.289	500.896	484.902	492.491
	-6	378.406	417.245	403.917	410.241
	-7		357.494	346.071	351.491
8	-1	2564.526	2797.557	2717.591	2795.542
	-2	1281.759	1398.275	1358.292	1397.267
	-3	854.170	931.847	905.192	931.175
	-4	640.375	698.633	678.642	698.129
	-5	512.099	558.705	542.712	558.302
	-6	426.581	465.419	452.092	465.083

	-7	365.497	398.787	387.363	398.499
	-8		348.812	338.817	348.561
9	-1	2893.578	3126.610	3046.644	3099.588
	-2	1446.285	1562.801	1522.818	1549.290
	-3	963.854	1041.531	1014.876	1032.524
	-4	722.638	780.896	760.905	774.141
	-5	577.909	624.515	608.522	619.111
	-6	481.423	520.261	506.934	515.758
	-7	412.504	445.794	434.371	441.934
	-8	360.815	389.944	379.948	386.566
	-9		346.505	337.620	343.502
10	-1	3197.624	3430.655	3350.689	3412.645
	-2	1598.308	1714.823	1674.840	1705.818
	-3	1065.203	1142.880	1116.224	1136.876
	-4	798.650	856.908	836.916	852.405
	-5	638.718	685.324	669.331	681.722
	-6	532.097	570.936	557.608	567.934
	-7	455.939	489.229	477.806	486.656
	-8	398.821	427.950	417.954	425.698
	-9	354.395	380.288	371.403	378.287
	-10		342.158	334.161	340.357
11	-1	3510.681	3734.701	3654.735	3716.691
	-2	1754.837	1866.846	1826.863	1857.841
	-3	1169.555	1244.228	1217.573	1238.225
	-4	876.914	932.919	912.928	928.417
	-5	701.330	746.134	730.140	742.532
	-6	584.273	621.610	608.282	618.608
	-7	500.662	532.664	521.241	530.092
	-8	437.953	465.955	455.960	463.704
	-9	389.179	414.070	405.185	412.069
	-10	350.161	372.563	364.566	370.762
	-11		338.602	331.332	336.964

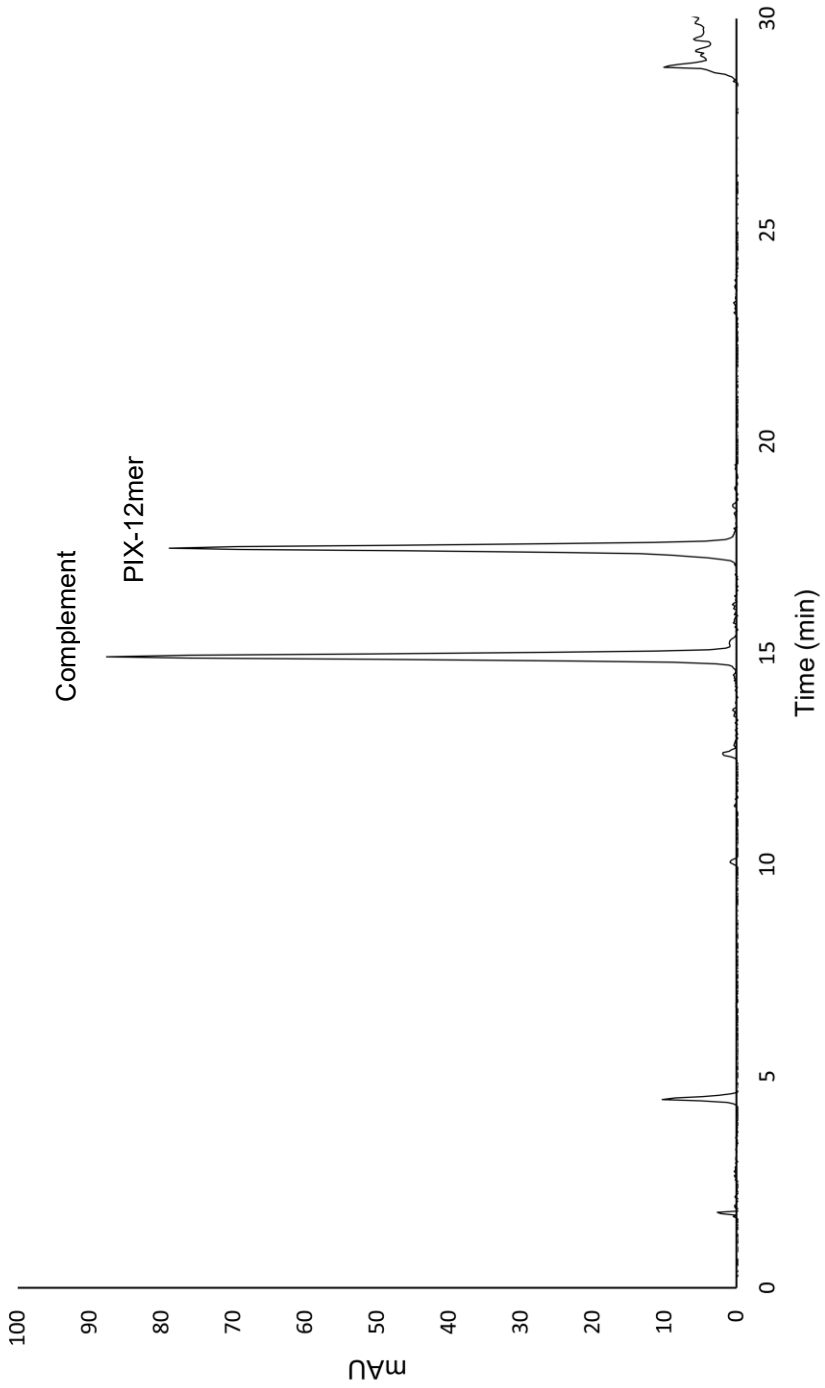

HPLC chromatogram of the dsPIX-12mer reduced conjugate crude reaction solution.

<u>PIX-12mer</u>: 5'-GTT GC[AP-PIX] CGT ATG-3'

<u>Complement</u>: 5'-CAT ACG CGC AAC-3'

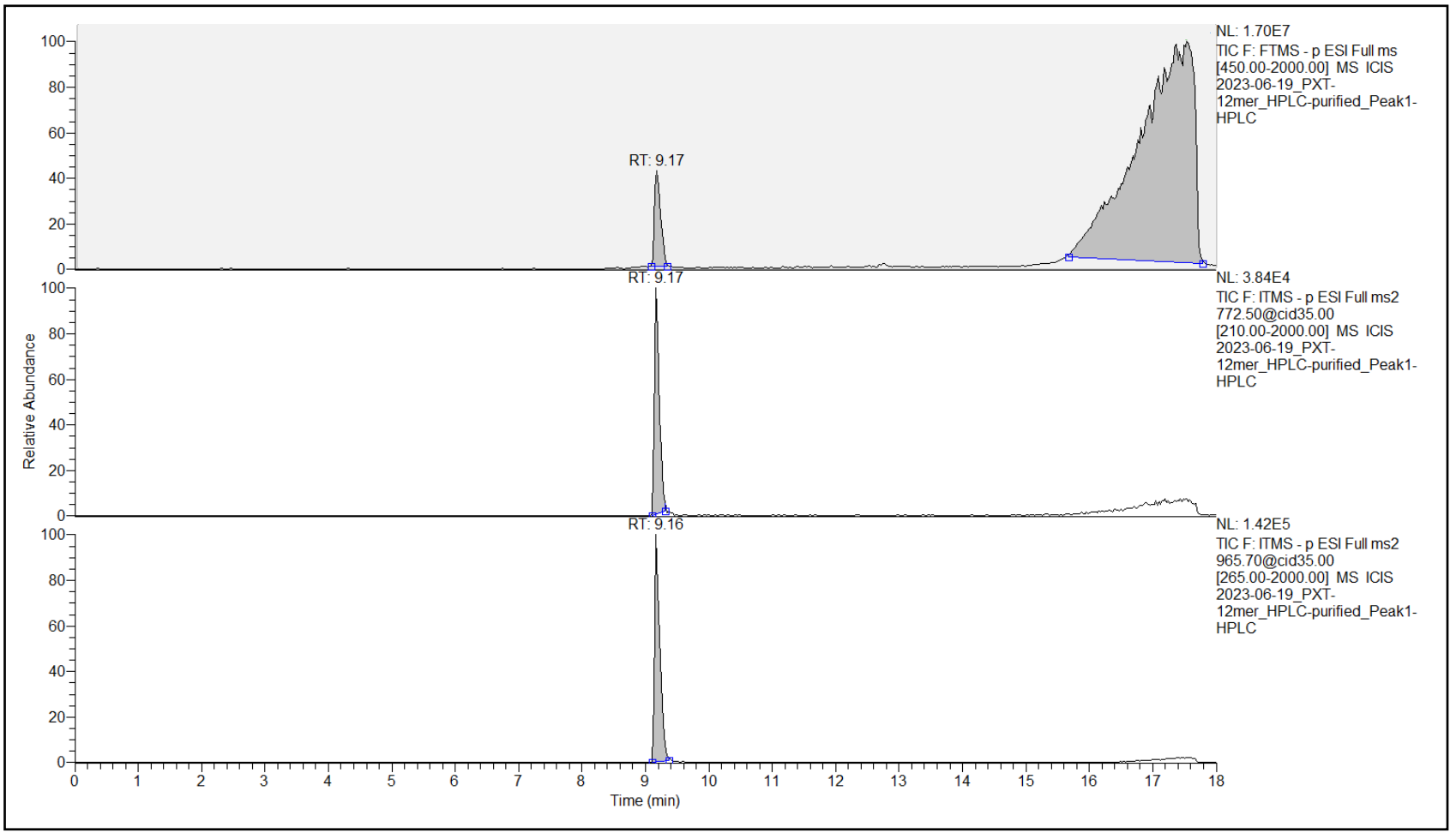

ESI-LC/MS chromatogram of the purified PIX-12mer reduced conjugate showing the total ion chromatogram (top) and selected ion chromatograms for *m/z 772* and *966*.

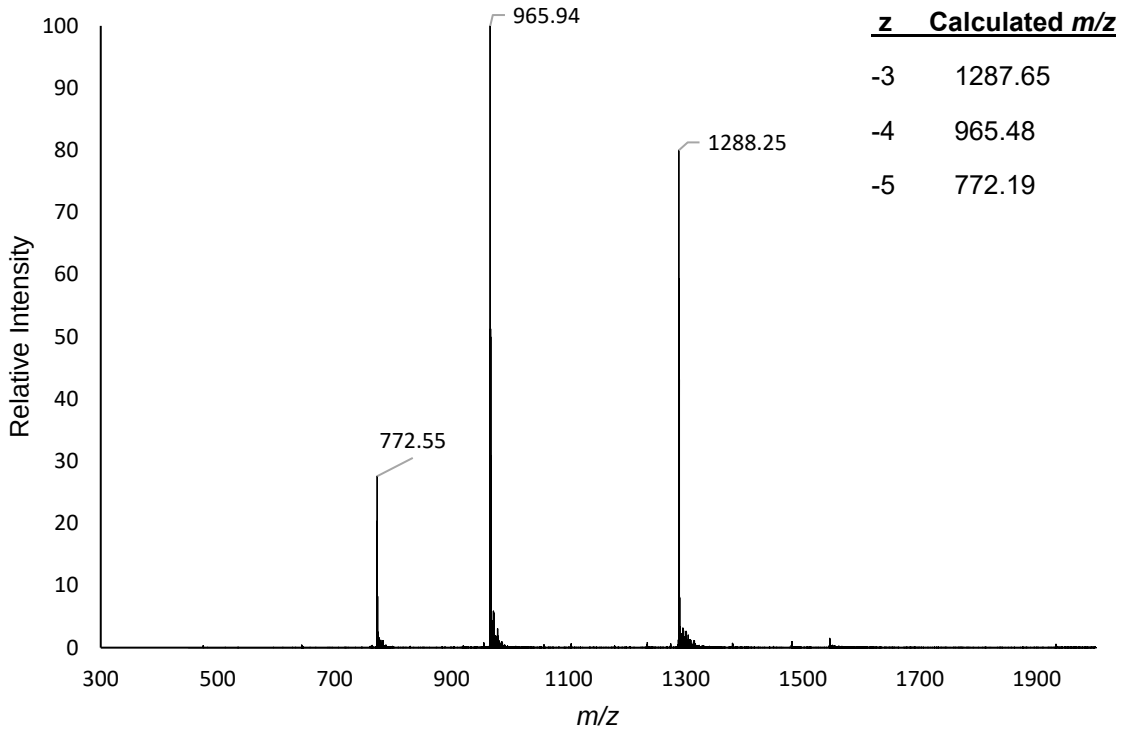

ESI-LC/MS total ion mass spectrum of the purified PIX-12mer reduced conjugate (5'-GTT GC[AP-PIX] CGT ATG-3') at retention time 9.17 minutes.

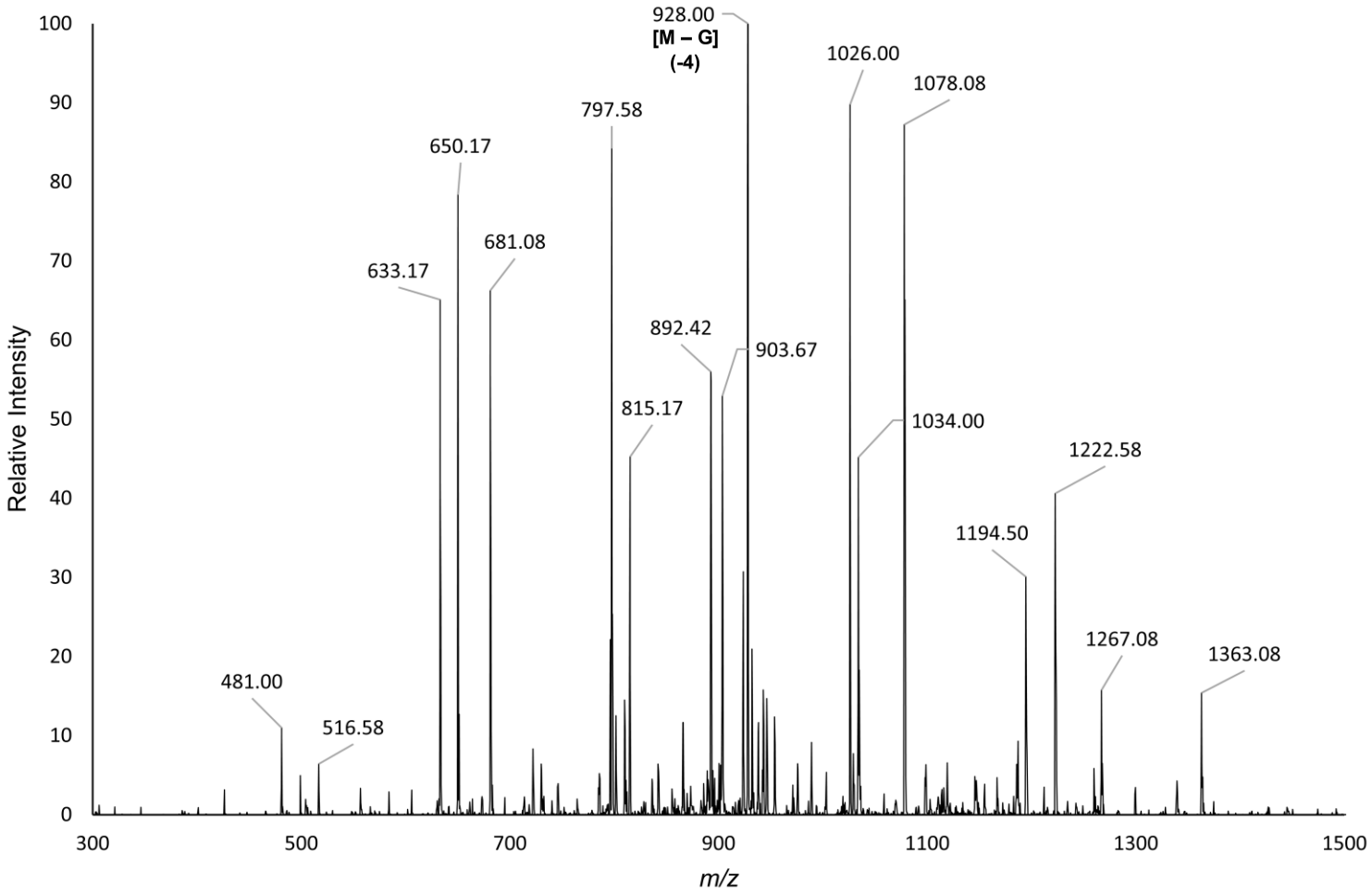

m/z 966 **selected ion ESI-LC/MS^2 mass spectrum with CID fragmentation of the purified PIX-12mer reduced conjugate (5'-GTT GC[AP-PIX] CGT ATG-3'). Peak at *m/z 928* not predicted by software; identity determined from ChemDraw structure.**

Calculated CID Fragments

n	z	a-B	w	y	d-H2O
1	-1		346.054	266.088	328.044
2	-1	426.080	650.100	570.134	632.090
	-2		324.546	284.563	315.541
3	-1	730.126	963.157	883.191	936.135
	-2	364.559	481.074	441.091	467.563
	-3		320.380	293.725	311.373
4	-1	1034.171	1267.203	1187.237	1265.187
	-2	516.582	633.097	593.114	632.090
	-3	344.052	421.729	395.073	421.057
	-4		316.044	296.053	315.541
5	-1	1363.224	1596.255	1516.289	1554.233
	-2	681.108	797.623	757.640	776.613
	-3	453.736	531.413	504.757	517.406
	-4	340.050	398.307	378.316	387.802
	-5		318.444	302.451	310.040
6	-1	1977.420	1885.301	1805.335	2058.394
	-2	988.206	942.146	902.163	1028.693
	-3	658.468	627.761	601.106	685.459
	-4	493.599	470.569	450.577	513.842
	-5	394.677	376.254	360.260	410.872
	-6		313.377	300.049	342.225
7	-1	2156.430	2389.461	2309.495	2347.440
	-2	1077.711	1194.227	1154.244	1173.216
	-3	718.138	795.815	769.160	781.808
	-4	538.351	596.609	576.618	586.104
	-5	430.479	477.086	461.092	468.681
	-6	358.565	397.403	384.076	390.400
	-7		340.487	329.064	334.484
8	-1	2445.476	2678.507	2598.541	2676.492
	-2	1222.234	1338.750	1298.767	1337.742
	-3	814.487	892.164	865.508	891.492
	-4	610.613	668.871	648.879	668.367
	-5	488.289	534.895	518.902	534.492
	-6	406.739	445.578	432.250	445.242
	-7	348.489	381.780	370.356	381.492

	-8		333.931	323.935	333.679
9	-1	2774.528	3007.560	2927.594	2980.538
	-2	1386.760	1503.276	1463.293	1489.765
	-3	924.171	1001.848	975.192	992.840
	-4	692.876	751.134	731.142	744.378
	-5	554.099	600.705	584.712	595.301
	-6	461.581	500.420	487.092	495.916
	-7	395.497	428.787	417.363	424.927
	-8	345.934	375.063	365.067	371.685
	-9		333.277	324.392	330.275
10	-1	3078.574	3311.605	3231.639	3293.595
	-2	1538.783	1655.298	1615.315	1646.293
	-3	1025.519	1103.196	1076.541	1097.193
	-4	768.887	827.145	807.154	822.643
	-5	614.908	661.514	645.521	657.912
	-6	512.255	551.094	537.766	548.092
	-7	438.932	472.222	460.798	469.649
	-8	383.939	413.068	403.073	410.817
	-9	341.168	367.060	358.175	365.059
	-10		330.253	322.256	328.452
11	-1	3391.631	3615.651	3535.685	3597.641
	-2	1695.312	1807.321	1767.338	1798.316
	-3	1129.872	1204.545	1177.889	1198.541
	-4	847.152	903.157	883.165	898.654
	-5	677.520	722.324	706.330	718.722
	-6	564.432	601.768	588.441	598.767
	-7	483.655	515.657	504.234	513.084
	-8	423.072	451.074	441.078	448.823
	-9	375.952	400.843	391.958	398.842
	-10	338.256	360.658	352.661	358.857
	-11		327.779	320.509	326.142

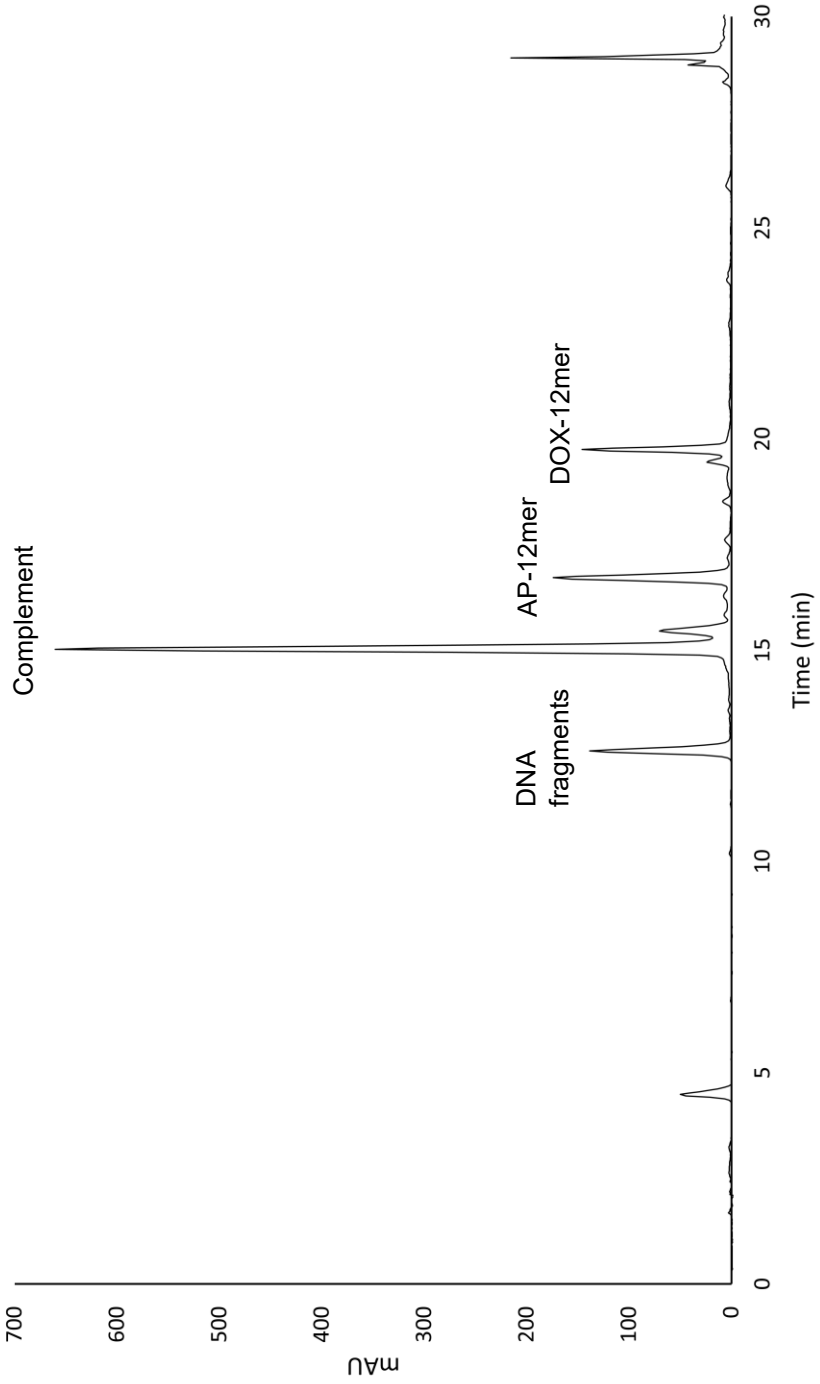

HPLC chromatogram of the DOX-12mer reduced conjugate crude reaction solution.

<u>DOX-12mer</u>: 5'-GTT GC[AP-DOX] CGT ATG-3'

<u>AP-12mer</u>: 5'-GTT GC[AP] CGT ATG-3'

<u>Complement</u>: 5'-CAT ACG CGC AAC-3'

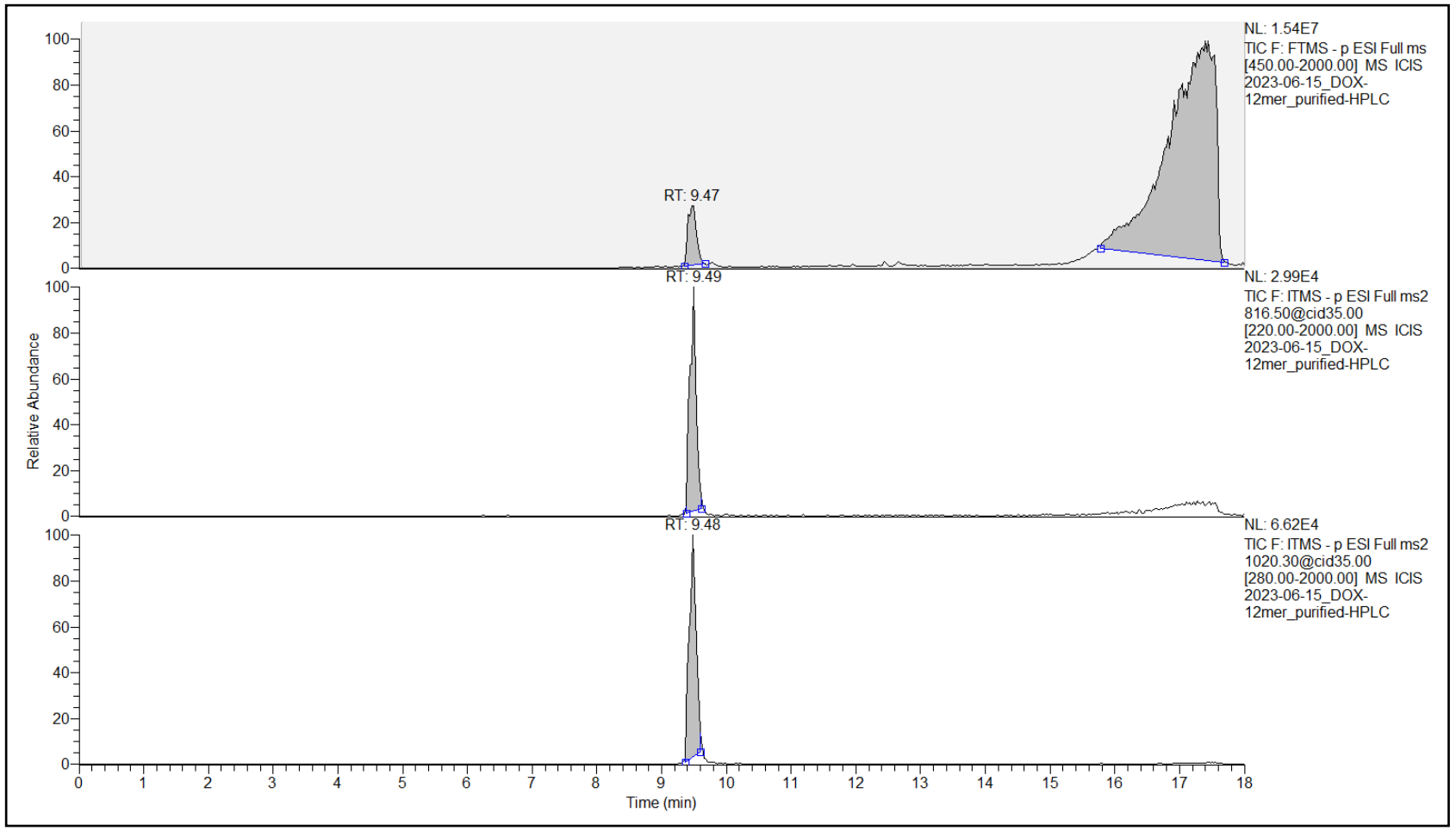

ESI-LC/MS chromatogram of the purified DOX-12mer reduced conjugate showing the total ion chromatogram (top) and selected ion chromatograms for *m/z 816* and *1020*.

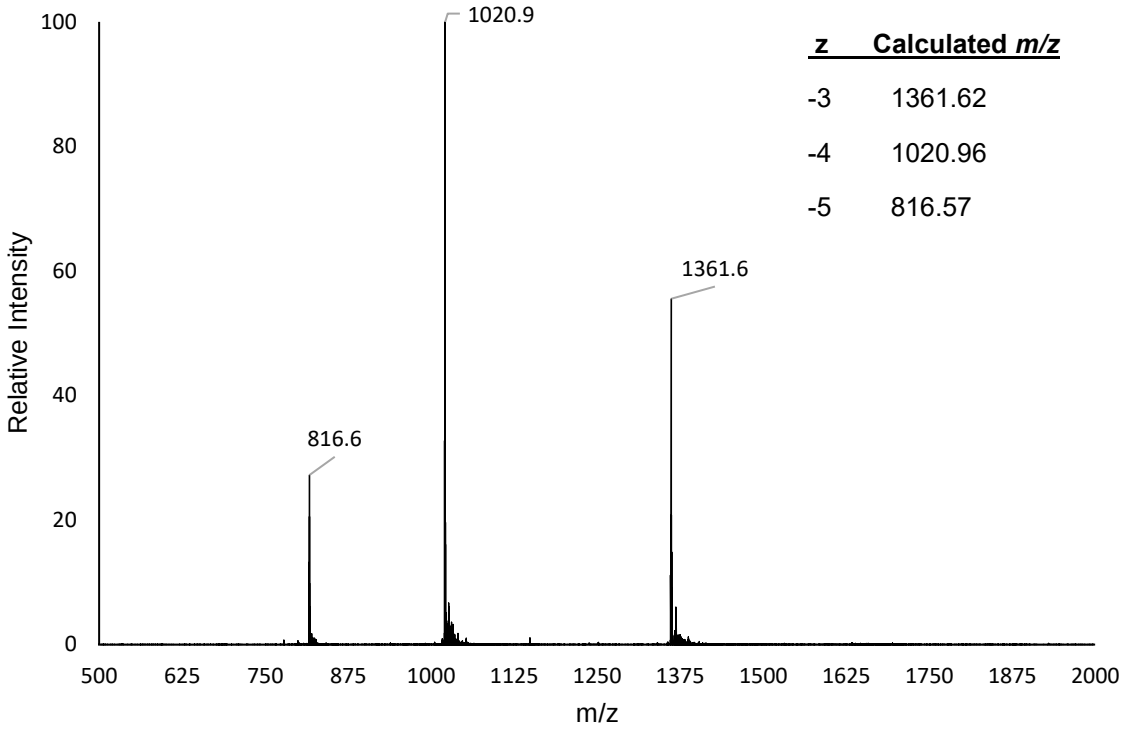

ESI-LC/MS total ion mass spectrum of the purified DOX-12mer reduced conjugate (5'-GTT GC[AP-DOX] CGT ATG-3') at retention time 9.49 minutes.

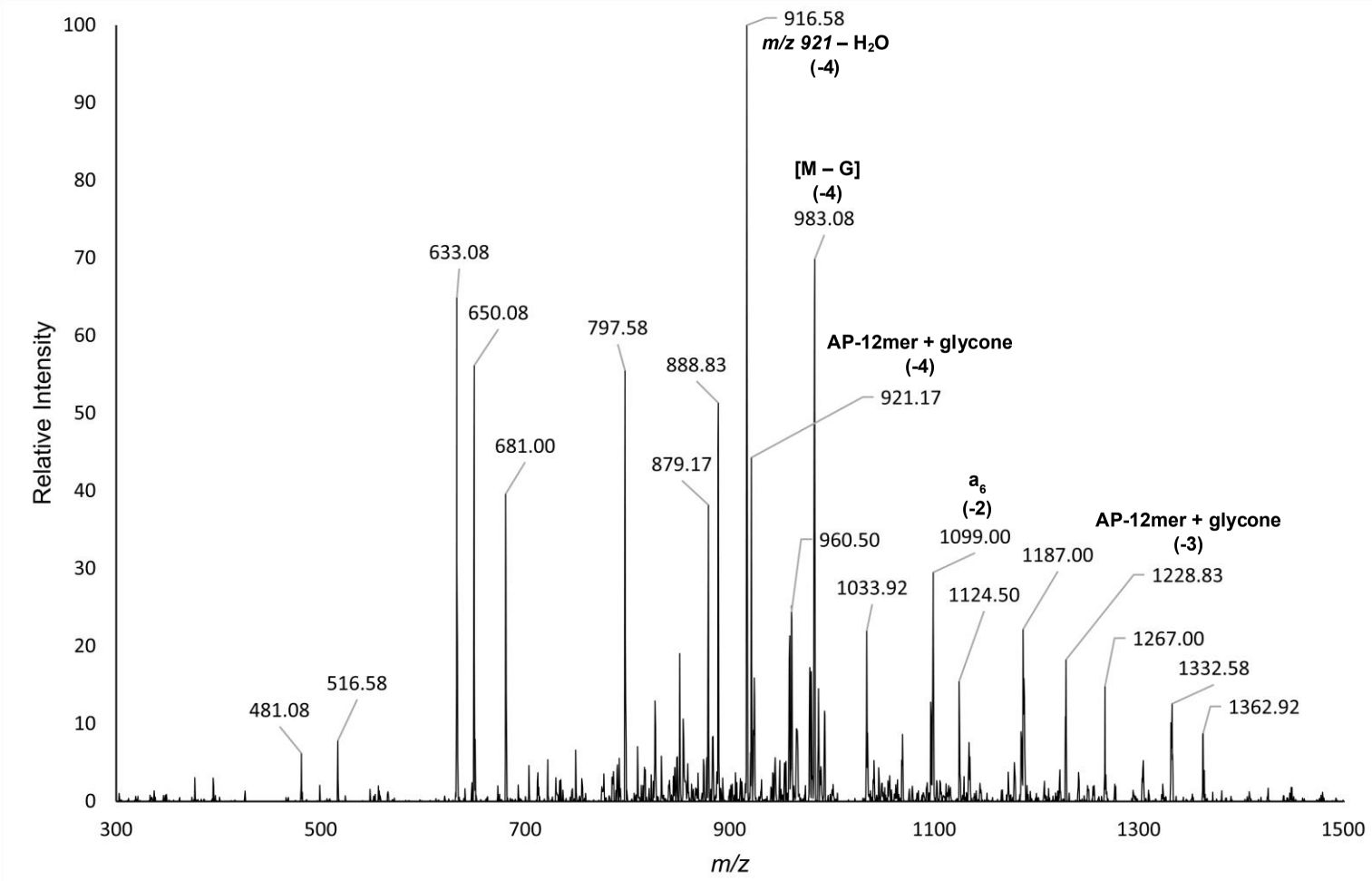

m/z 1020 **selected ion ESI-LC/MS^2 mass spectrum with CID fragmentation of the purified DOX-12mer reduced conjugate (5'-GTT GC[AP-DOX] CGT ATG-3'). Peaks at *m/z 1229*, *1099*, *921*, *983*, and *917* not predicted by software; identity determined from ChemDraw structure. See Appendix I for structure of glycone fragment from DOX.**

Calculated CID Fragments

n	z	a-B	w	y	d-H2O
1	-1		346.054	266.088	328.044
2	-1	426.080	650.100	570.134	632.090
	-2		324.546	284.563	315.541
3	-1	730.126	963.157	883.191	936.135
	-2	364.559	481.074	441.091	467.563
	-3		320.380	293.725	311.373
4	-1	1034.171	1267.203	1187.237	1265.187
	-2	516.582	633.097	593.114	632.090
	-3	344.052	421.729	395.073	421.057
	-4		316.044	296.053	315.541
5	-1	1363.224	1596.255	1516.289	1554.233
	-2	681.108	797.623	757.640	776.613
	-3	453.736	531.413	504.757	517.406
	-4	340.050	398.307	378.316	387.802
	-5		318.444	302.451	310.040
6	-1	2197.460	1885.301	1805.335	2278.434
	-2	1098.226	942.146	902.163	1138.713
	-3	731.814	627.761	601.106	758.806
	-4	548.609	470.569	450.577	568.852
	-5	438.685	376.254	360.260	454.880
	-6		313.377	300.049	378.899
7	-1	2376.470	2609.501	2529.535	2567.480
	-2	1187.731	1304.247	1264.264	1283.236
	-3	791.485	869.162	842.506	855.154
	-4	593.361	651.619	631.628	641.114
	-5	474.487	521.094	505.100	512.689
	-6	395.238	434.077	420.749	427.073
	-7		371.922	360.498	365.919
8	-1	2665.516	2898.547	2818.581	2896.532
	-2	1332.254	1448.770	1408.787	1447.762
	-3	887.833	965.510	938.855	964.839
	-4	665.623	723.881	703.889	723.377
	-5	532.297	578.903	562.910	578.500
	-6	443.412	482.251	468.923	481.915
	-7	379.924	413.214	401.790	412.926

	-8		361.436	351.440	361.184
9	-1	2994.568	3227.600	3147.634	3200.578
	-2	1496.780	1613.296	1573.313	1599.785
	-3	997.517	1075.194	1048.539	1066.187
	-4	747.886	806.144	786.152	799.388
	-5	598.107	644.713	628.720	639.309
	-6	498.254	537.093	523.765	532.589
	-7	426.931	460.221	448.798	456.361
	-8	373.439	402.568	392.572	399.190
	-9		357.726	348.841	354.723
10	-1	3298.614	3531.645	3451.679	3513.635
	-2	1648.803	1765.318	1725.335	1756.313
	-3	1098.866	1176.543	1149.888	1170.540
	-4	823.897	882.155	862.164	877.653
	-5	658.916	705.522	689.529	701.920
	-6	548.929	587.767	574.440	584.766
	-7	470.366	503.656	492.233	501.084
	-8	411.444	440.573	430.578	438.322
	-9	365.616	391.509	382.624	389.508
	-10		352.257	344.260	350.456
11	-1	3611.671	3835.691	3755.725	3817.681
	-2	1805.332	1917.341	1877.358	1908.336
	-3	1203.218	1277.891	1251.236	1271.888
	-4	902.162	958.167	938.175	953.664
	-5	721.528	766.332	750.338	762.730
	-6	601.105	638.442	625.114	635.440
	-7	515.089	547.092	535.668	544.519
	-8	450.577	478.579	468.583	476.328
	-9	400.401	425.292	416.406	423.290
	-10	360.260	382.662	374.665	380.861
	-11		347.783	340.513	346.145

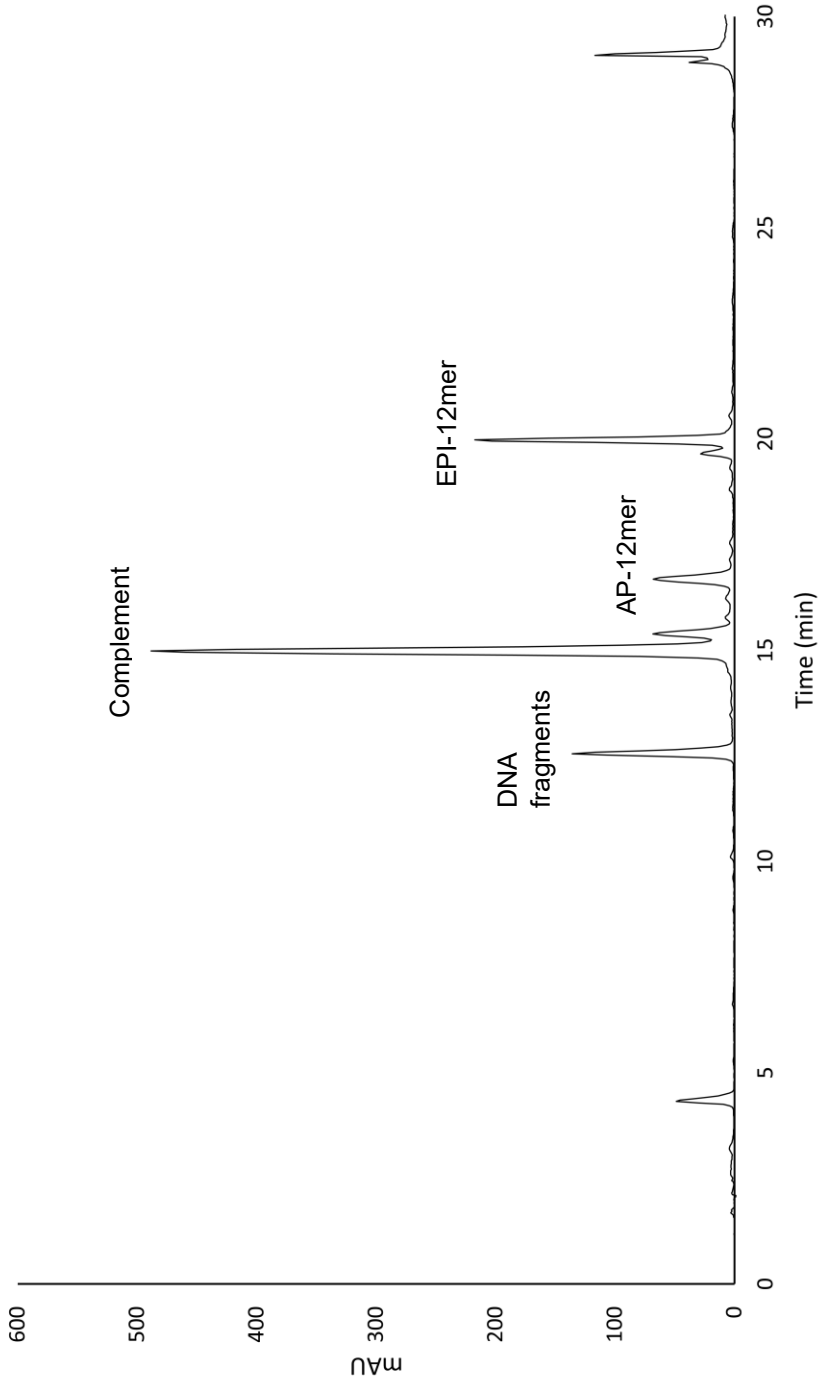

HPLC chromatogram of the EPI-12mer reduced conjugate crude reaction solution.

<u>EPI-12mer</u>: 5'-GTT GC[AP-EPI] CGT ATG-3'

<u>AP-12mer</u>: 5'-GTT GC[AP] CGT ATG-3'

<u>Complement</u>: 5'-CAT ACG CGC AAC-3'

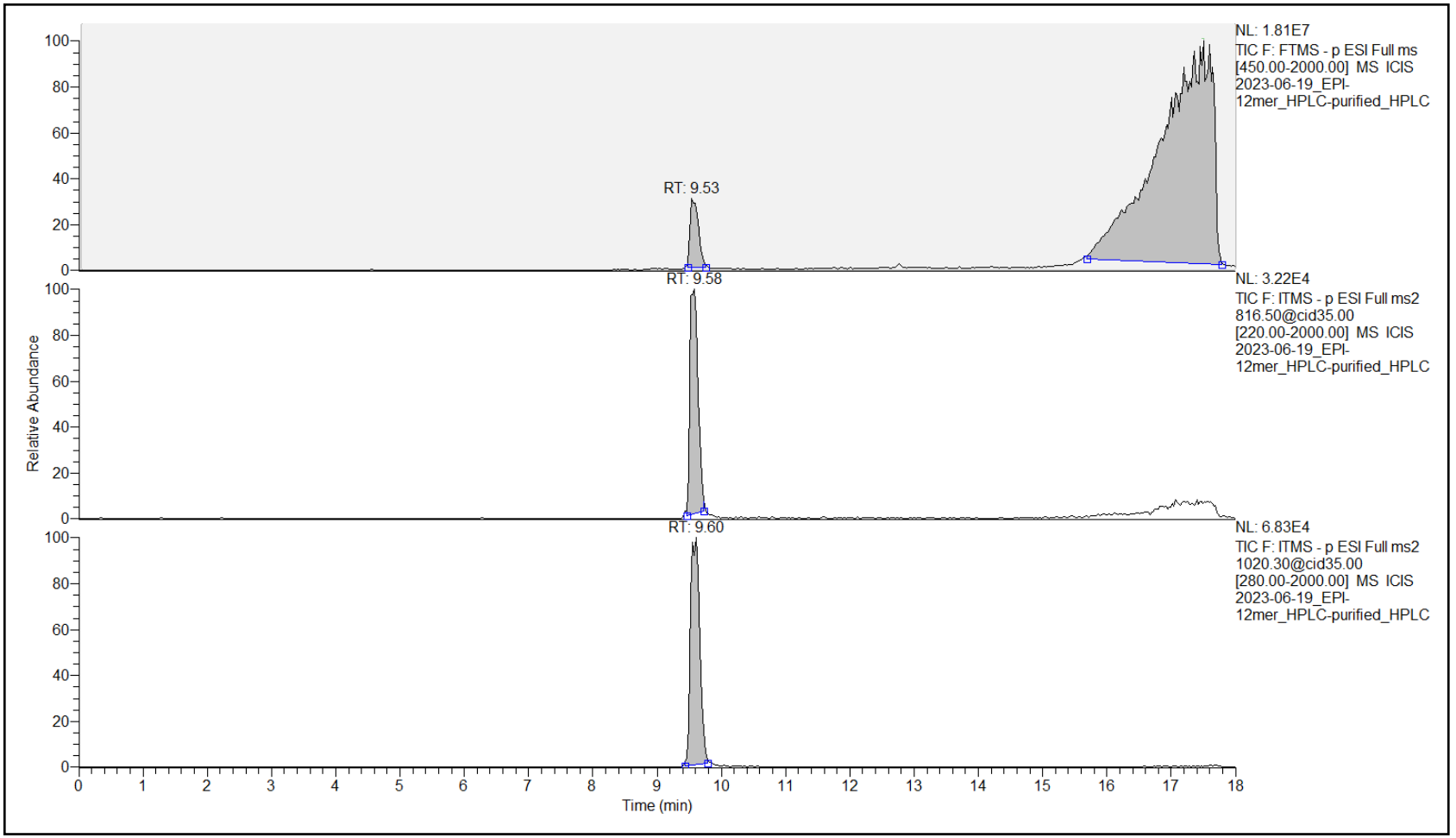

ESI-LC/MS chromatogram of the purified EPI-12mer reduced conjugate showing the total ion chromatogram (top) and selected ion chromatograms for *m/z 816* and *1020*.

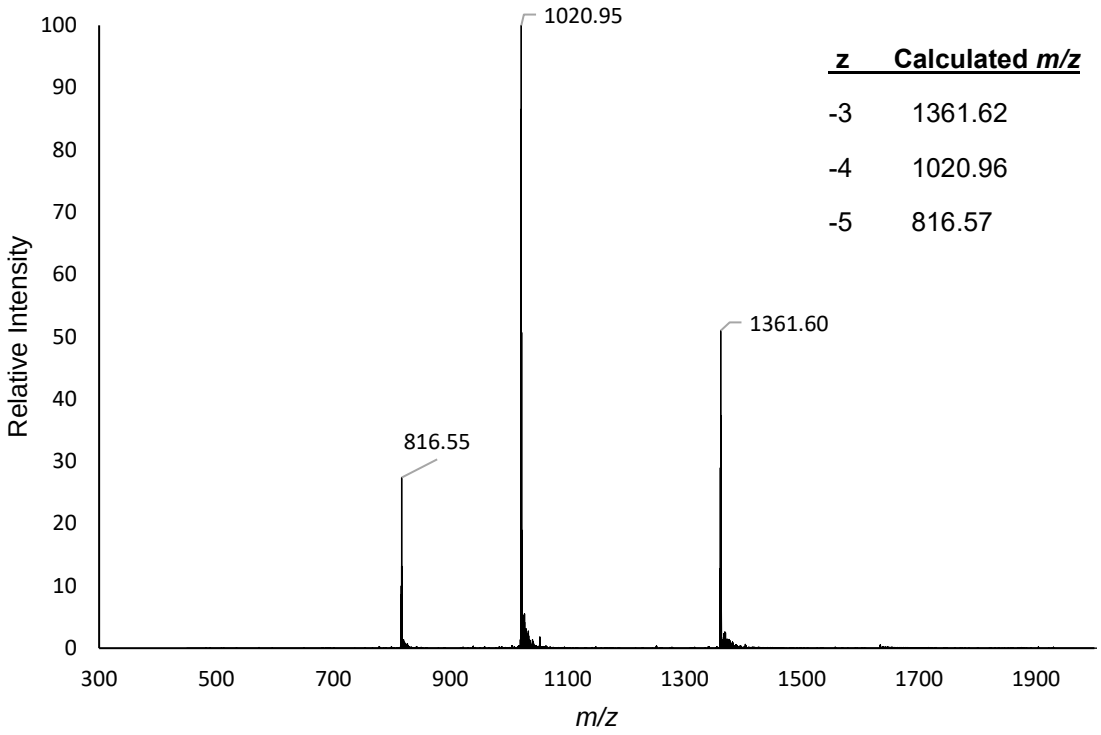

ESI-LC/MS total ion mass spectrum of the purified EPI-12mer reduced conjugate (5'-GTT GC[AP-EPI] CGT ATG-3') at retention time 9.58 minutes.

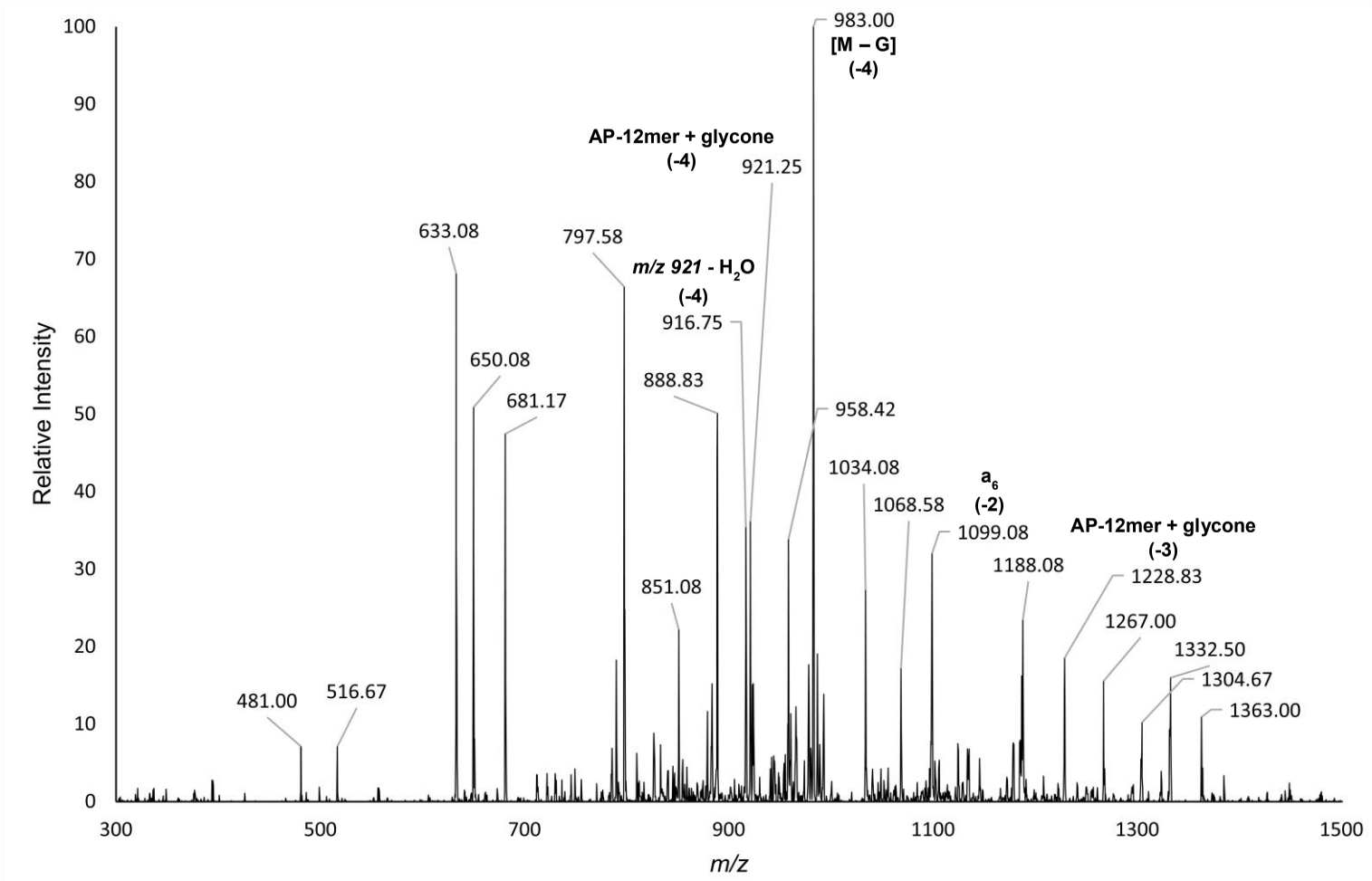

m/z 1020 **selected ion ESI-LC/MS^2 mass spectrum with CID fragmentation of the purified EPI-12mer reduced conjugate (5'-GTT GC[AP-EPI] CGT ATG-3'). Peaks at *m/z 1229*, *1099*, *983*, *921*, and *917* not predicted by software; identity determined from ChemDraw structure. See Appendix I for structure of glycone fragment from EPI.**

Calculated CID Fragments

n	z	a-B	w	y	d-H2O
1	-1		346.054	266.088	328.044
2	-1	426.080	650.100	570.134	632.090
	-2		324.546	284.563	315.541
3	-1	730.126	963.157	883.191	936.135
	-2	364.559	481.074	441.091	467.563
	-3		320.380	293.725	311.373
4	-1	1034.171	1267.203	1187.237	1265.187
	-2	516.582	633.097	593.114	632.090
	-3	344.052	421.729	395.073	421.057
	-4		316.044	296.053	315.541
5	-1	1363.224	1596.255	1516.289	1554.233
	-2	681.108	797.623	757.640	776.613
	-3	453.736	531.413	504.757	517.406
	-4	340.050	398.307	378.316	387.802
	-5		318.444	302.451	310.040
6	-1	2197.460	1885.301	1805.335	2278.434
	-2	1098.226	942.146	902.163	1138.713
	-3	731.814	627.761	601.106	758.806
	-4	548.609	470.569	450.577	568.852
	-5	438.685	376.254	360.260	454.880
	-6		313.377	300.049	378.899
7	-1	2376.470	2609.501	2529.535	2567.480
	-2	1187.731	1304.247	1264.264	1283.236
	-3	791.485	869.162	842.506	855.154
	-4	593.361	651.619	631.628	641.114
	-5	474.487	521.094	505.100	512.689
	-6	395.238	434.077	420.749	427.073
	-7		371.922	360.498	365.919
8	-1	2665.516	2898.547	2818.581	2896.532
	-2	1332.254	1448.770	1408.787	1447.762
	-3	887.833	965.510	938.855	964.839
	-4	665.623	723.881	703.889	723.377
	-5	532.297	578.903	562.910	578.500
	-6	443.412	482.251	468.923	481.915
	-7	379.924	413.214	401.790	412.926

	-8		361.436	351.440	361.184
9	-1	2994.568	3227.600	3147.634	3200.578
	-2	1496.780	1613.296	1573.313	1599.785
	-3	997.517	1075.194	1048.539	1066.187
	-4	747.886	806.144	786.152	799.388
	-5	598.107	644.713	628.720	639.309
	-6	498.254	537.093	523.765	532.589
	-7	426.931	460.221	448.798	456.361
	-8	373.439	402.568	392.572	399.190
	-9		357.726	348.841	354.723
10	-1	3298.614	3531.645	3451.679	3513.635
	-2	1648.803	1765.318	1725.335	1756.313
	-3	1098.866	1176.543	1149.888	1170.540
	-4	823.897	882.155	862.164	877.653
	-5	658.916	705.522	689.529	701.920
	-6	548.929	587.767	574.440	584.766
	-7	470.366	503.656	492.233	501.084
	-8	411.444	440.573	430.578	438.322
	-9	365.616	391.509	382.624	389.508
	-10		352.257	344.260	350.456
11	-1	3611.671	3835.691	3755.725	3817.681
	-2	1805.332	1917.341	1877.358	1908.336
	-3	1203.218	1277.891	1251.236	1271.888
	-4	902.162	958.167	938.175	953.664
	-5	721.528	766.332	750.338	762.730
	-6	601.105	638.442	625.114	635.440
	-7	515.089	547.092	535.668	544.519
	-8	450.577	478.579	468.583	476.328
	-9	400.401	425.292	416.406	423.290
	-10	360.260	382.662	374.665	380.861
	-11		347.783	340.513	346.145

Appendix III:

^{1}H NMR, COSY, and HSQC Spectra for the Reduced Covalent Anthracycline-dR Synthetic Standards in Chapter II

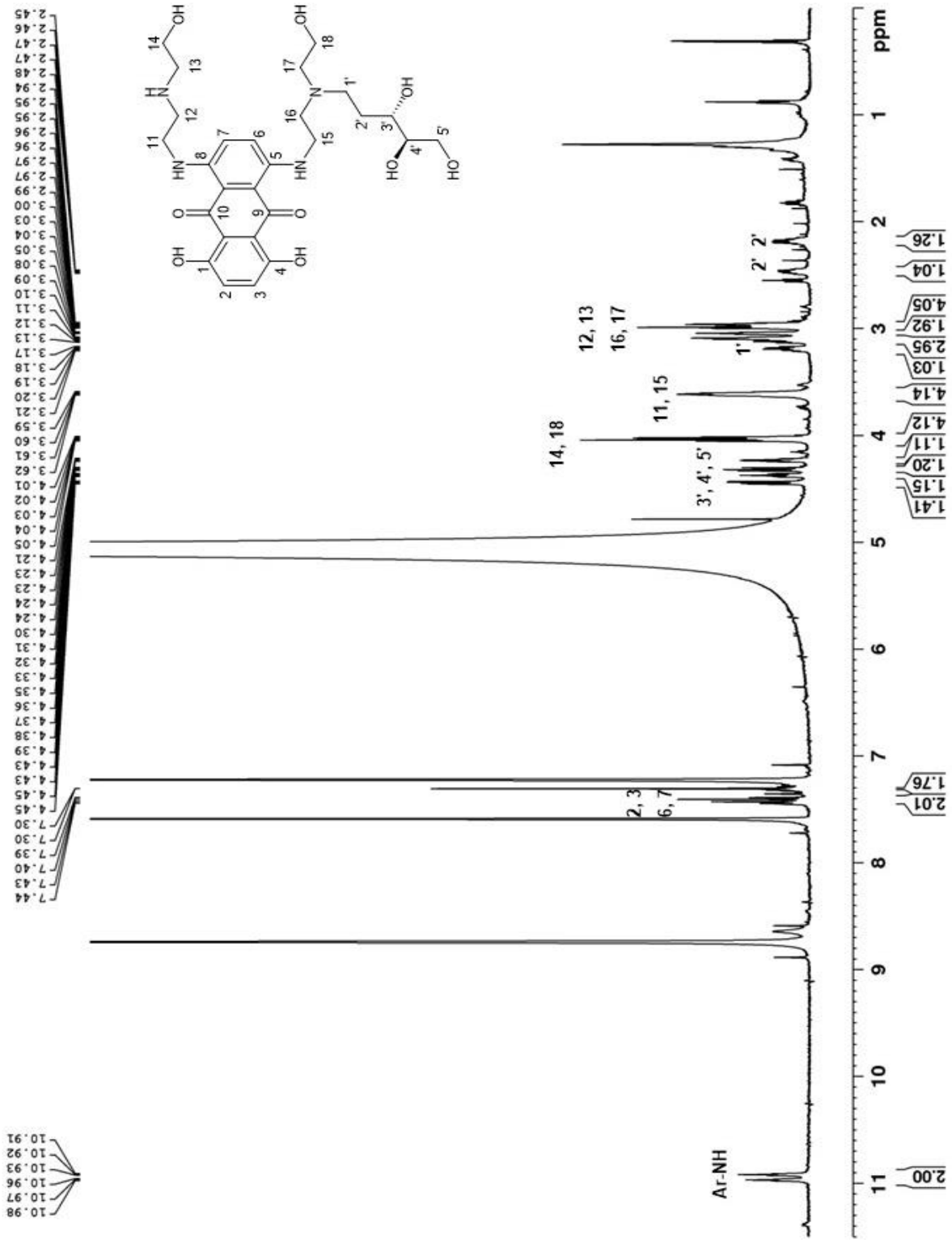

^{1}H NMR of the MTX-dR synthetic standard in pyridine-d_5

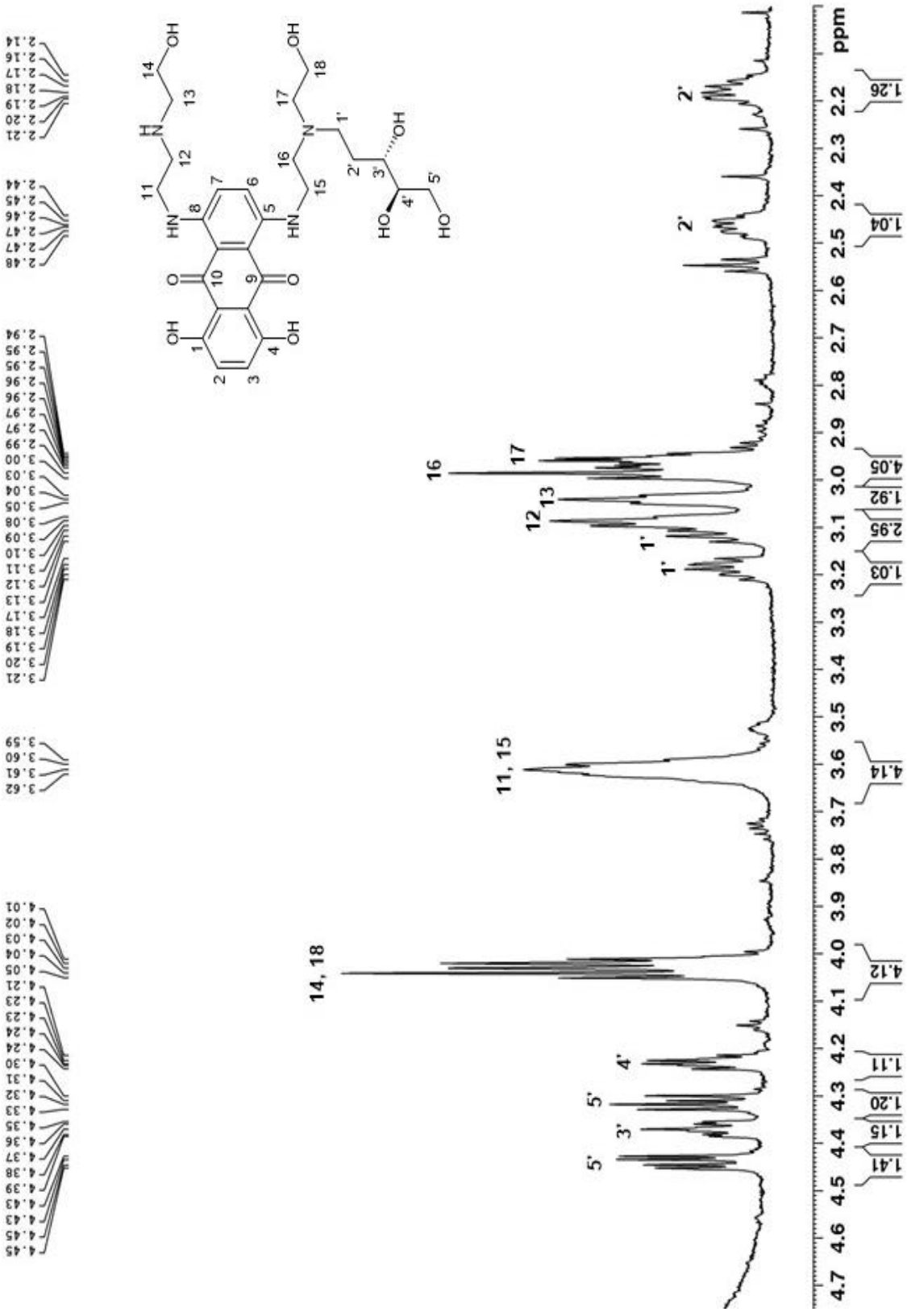

^{1}H NMR of the MTX-dR synthetic standard in pyridine-d_5 from 2-4.75 ppm

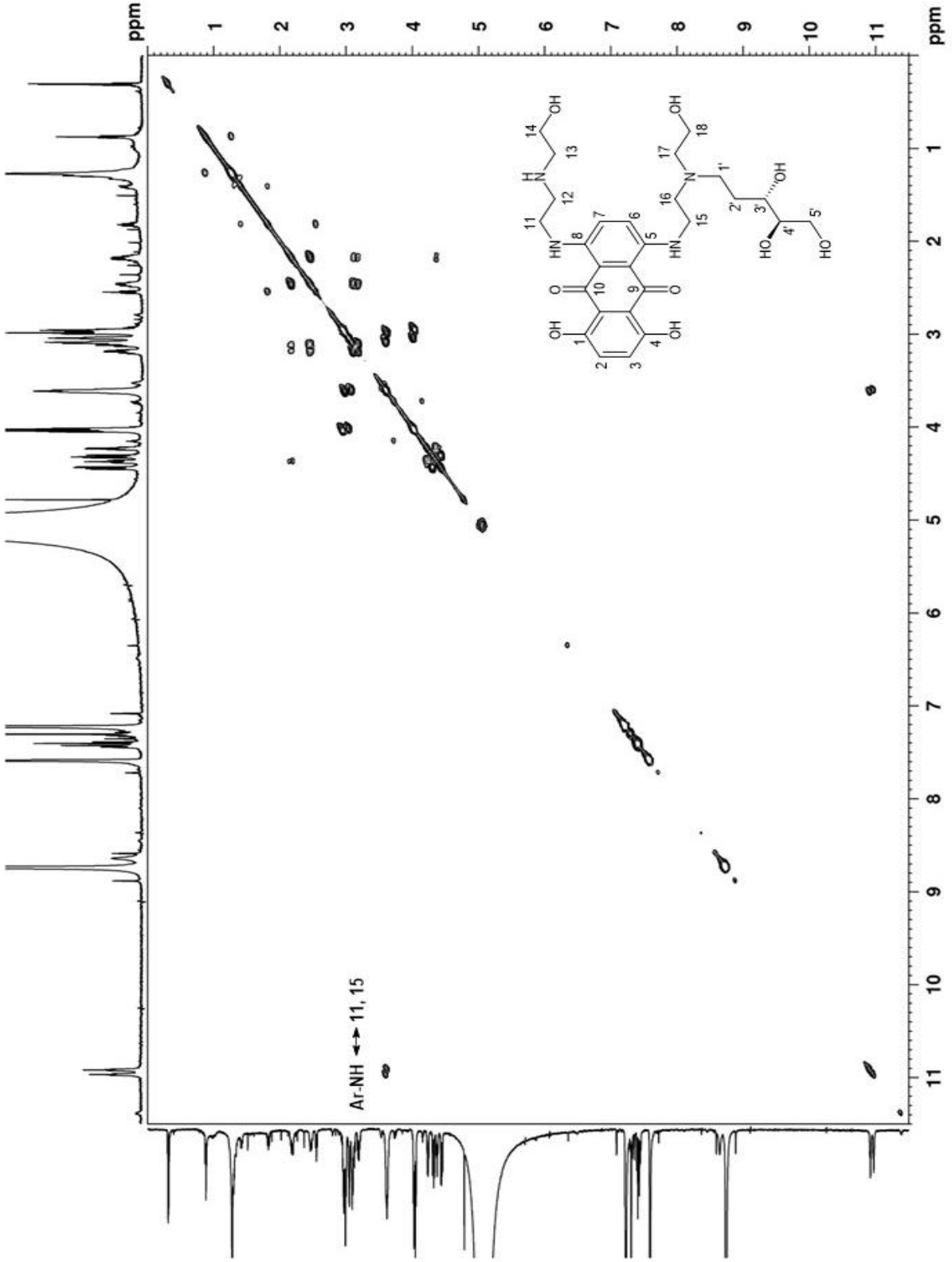

COSY spectrum of the MTX-dR synthetic standard in pyridine-d_5 with two-bond ^{1}H-^{1}H correlations labeled

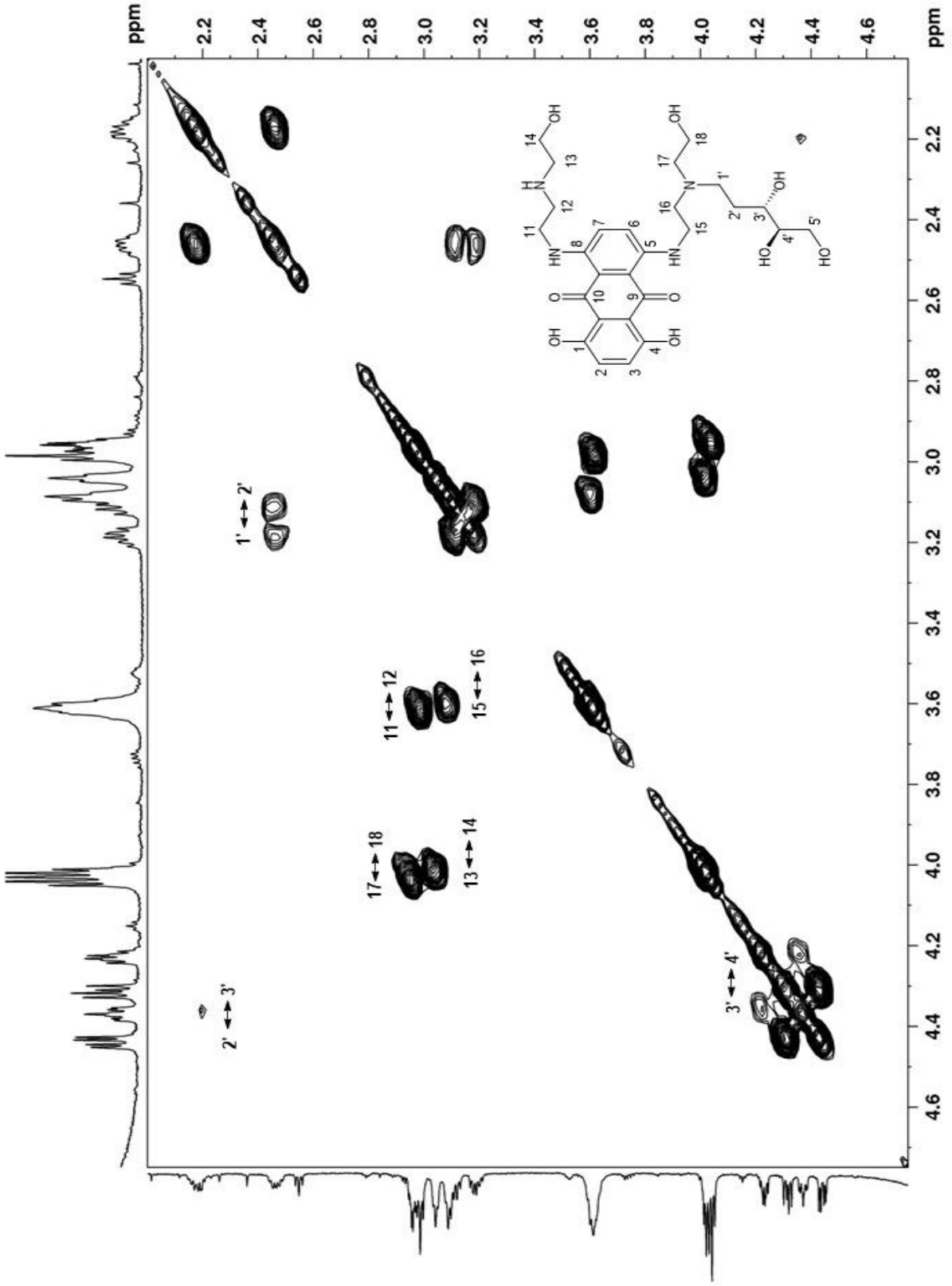

COSY spectrum of the MTX-dR synthetic standard in pyridine-d_5 from 2-4.75 ppm with two-bond ^{1}H-^{1}H correlations labeled

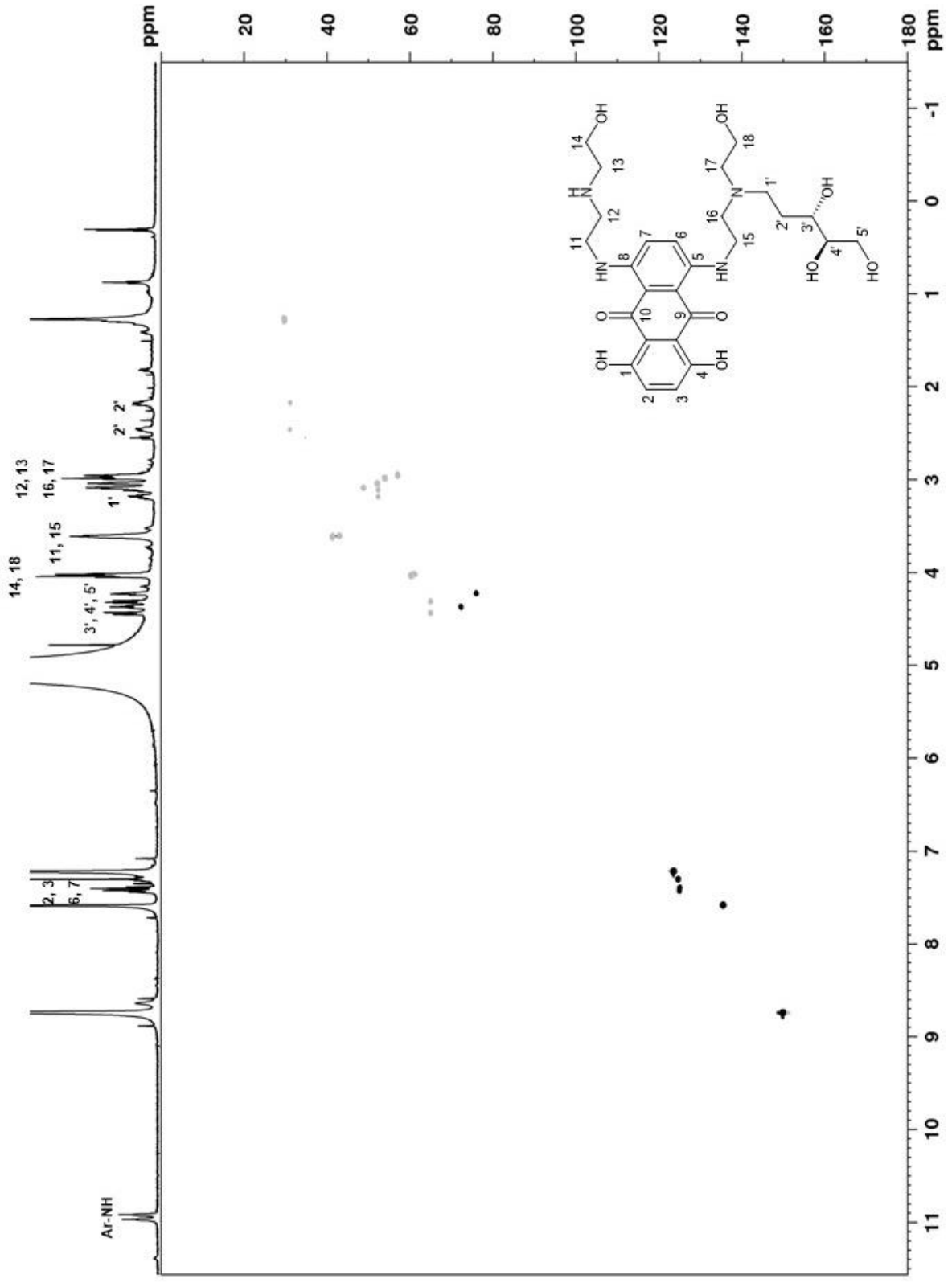

HSQC spectrum of the MTX-dR synthetic standard in pyridine-d_5.

Positive phasing in black; negative phasing in grey

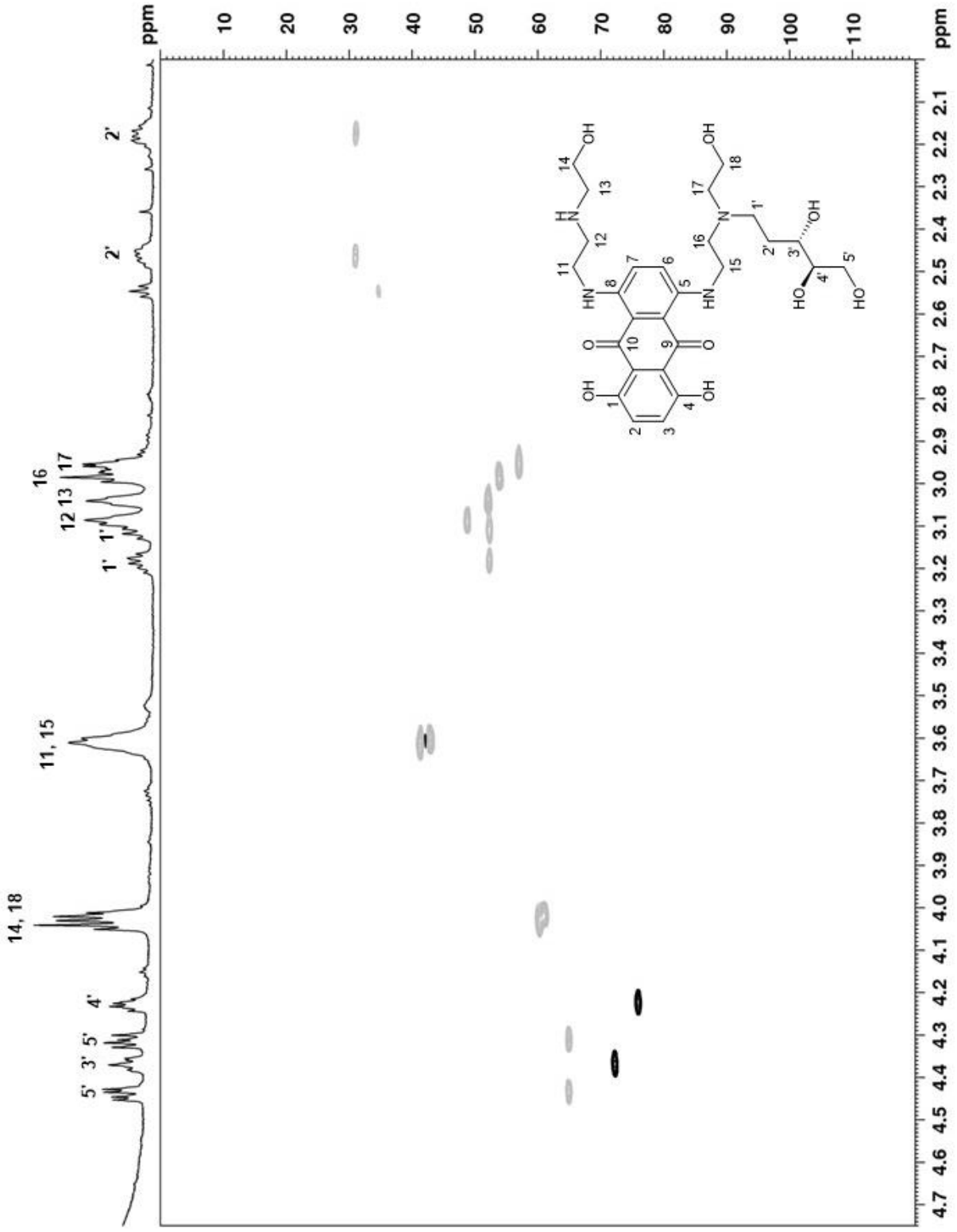

HSQC spectrum of the MTX-dR synthetic standard in pyridine-d_5 from 2-4.75 ppm. Positive phasing in black; negative phasing in grey

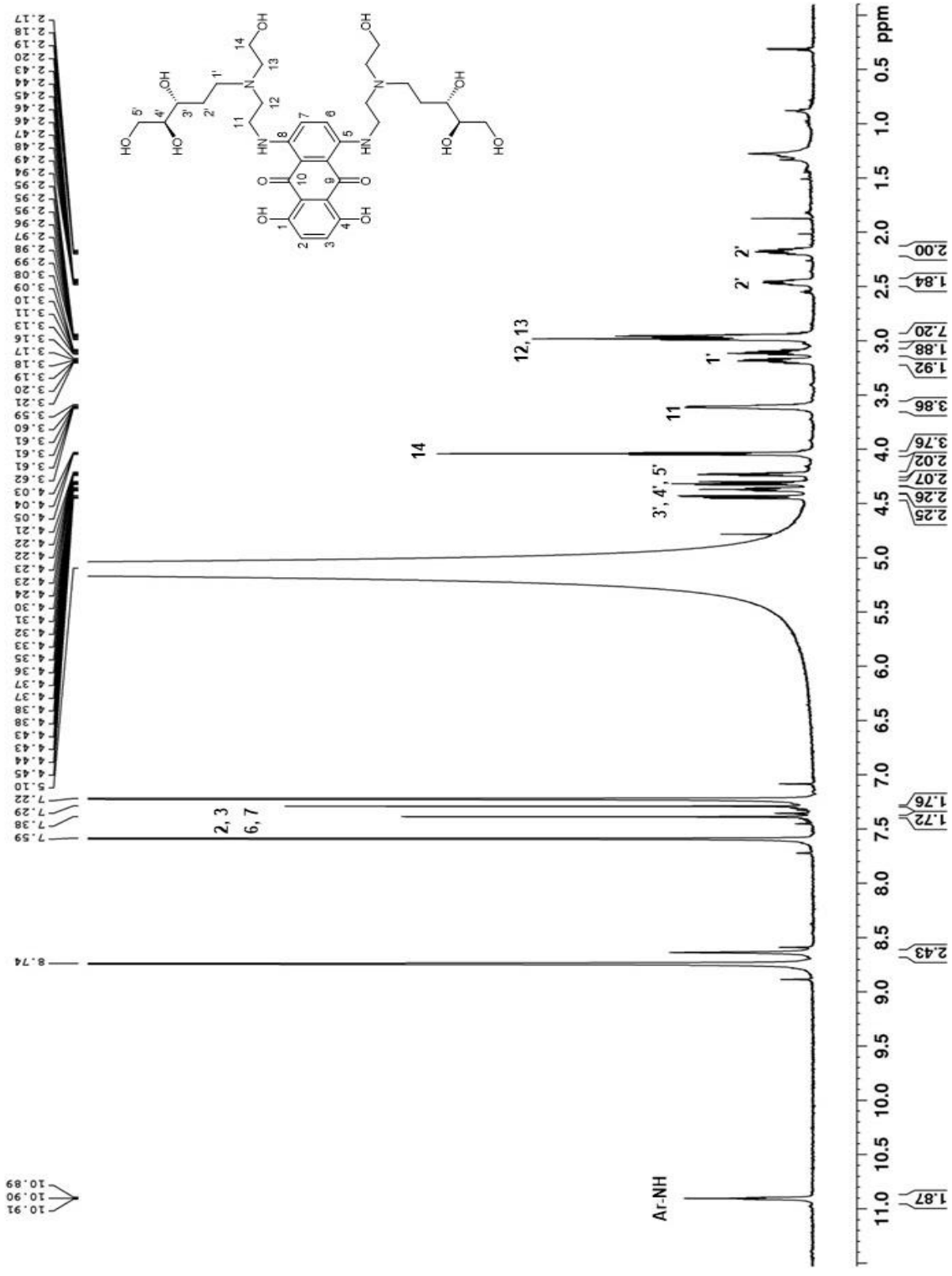

^{1}H NMR of the MTX-dR$_2$ synthetic standard in pyridine-*d*$_5$

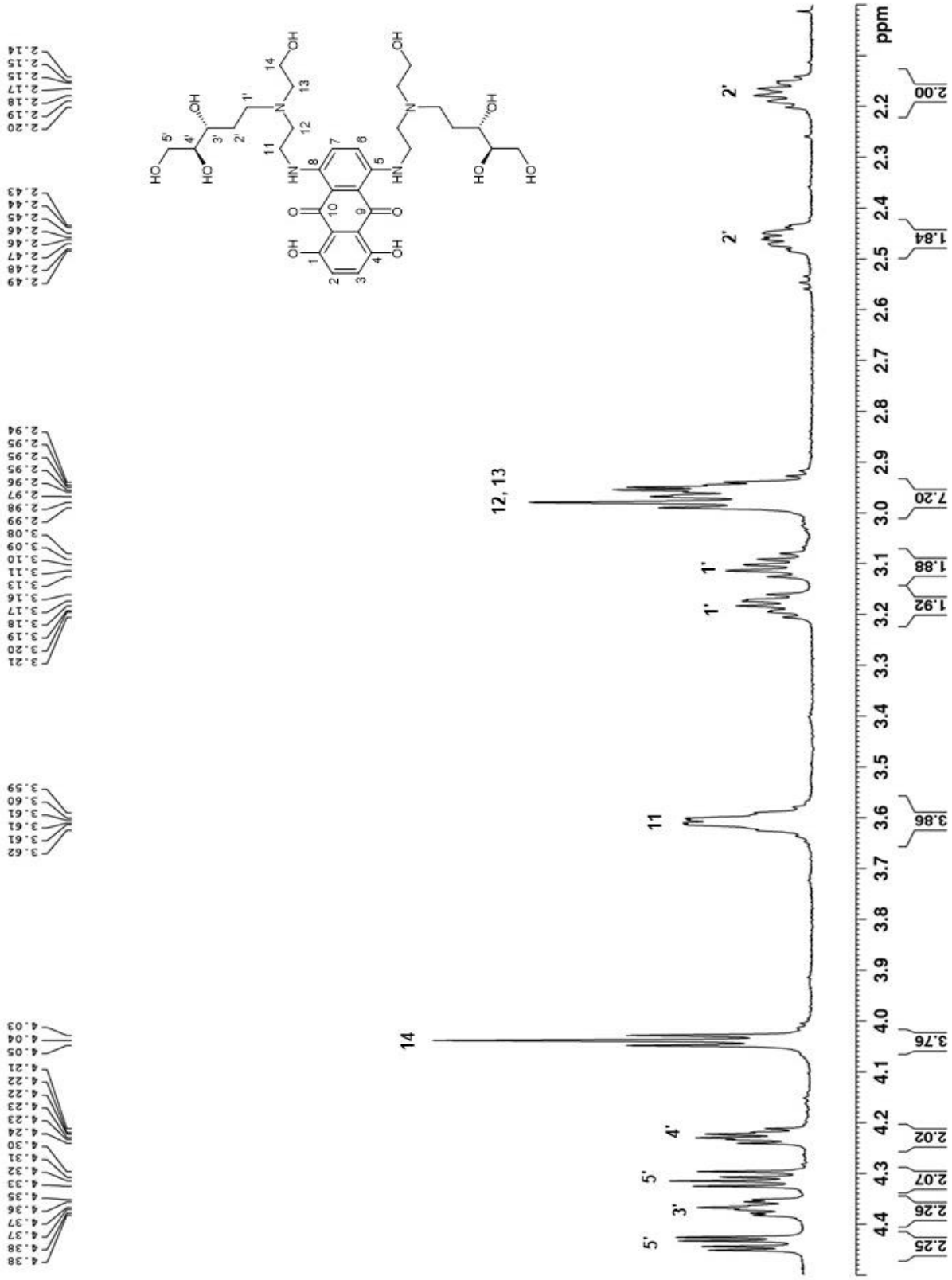

^{1}H NMR of the MTX-dR$_2$ synthetic standard in pyridine-*d*$_5$ from 2-4.5 ppm

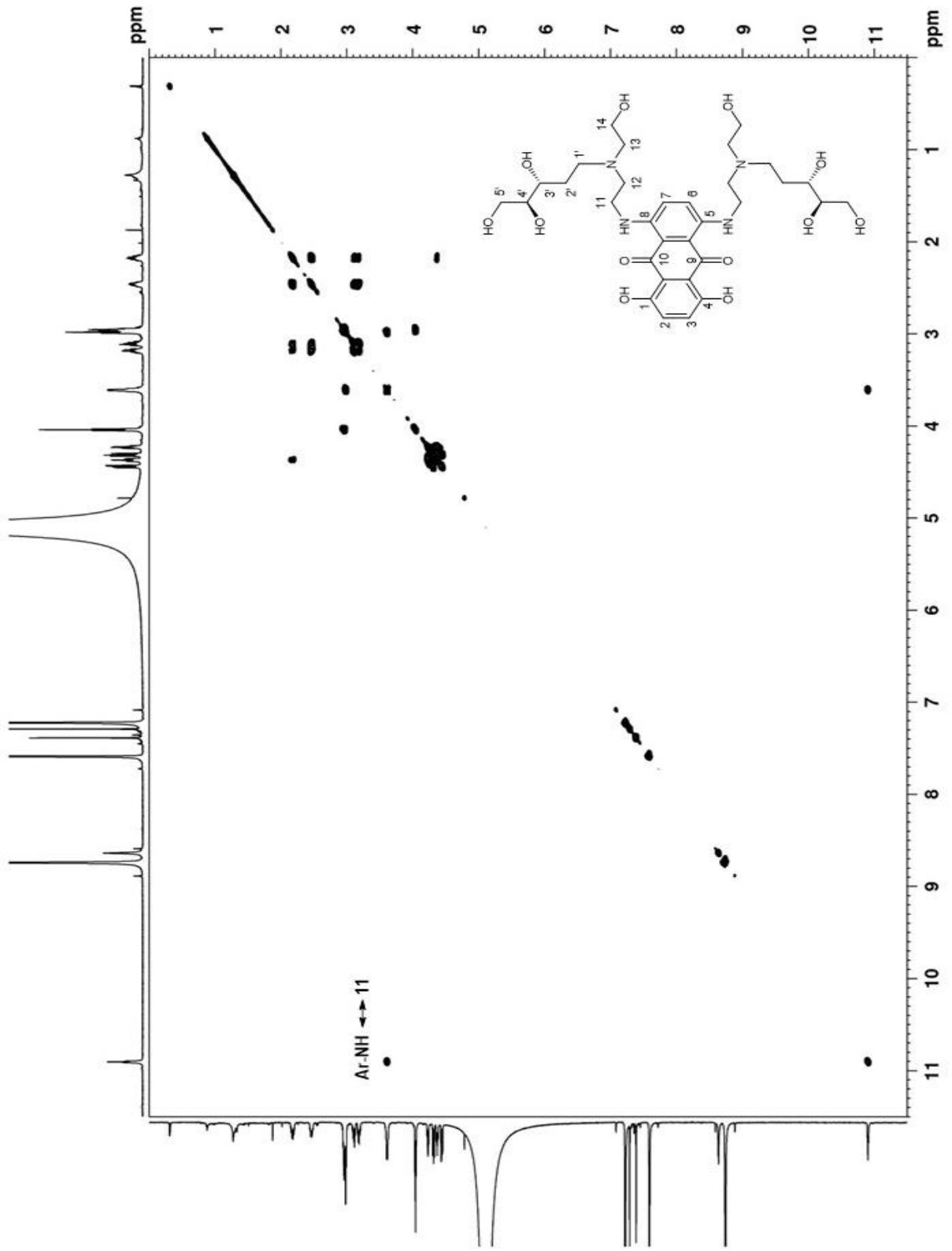

COSY spectrum of the MTX-dR$_2$ synthetic standard in pyridine-d_5 with two-bond ^{1}H-^{1}H correlations labeled

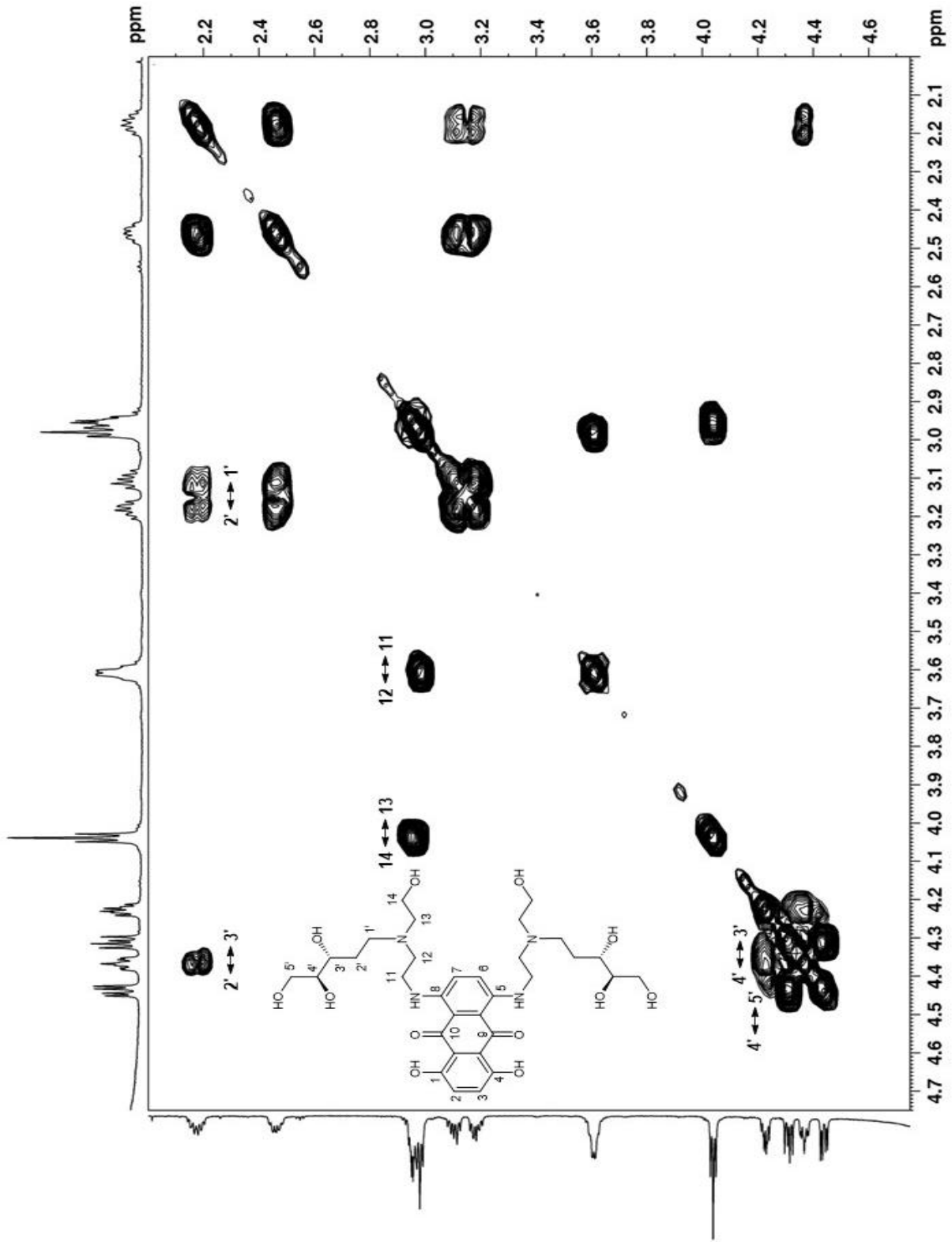

COSY spectrum of the MTX-dR$_2$ synthetic standard in pyridine-*d$_5$* from 2-4.75 ppm with two-bond ^{1}H-^{1}H correlations labeled

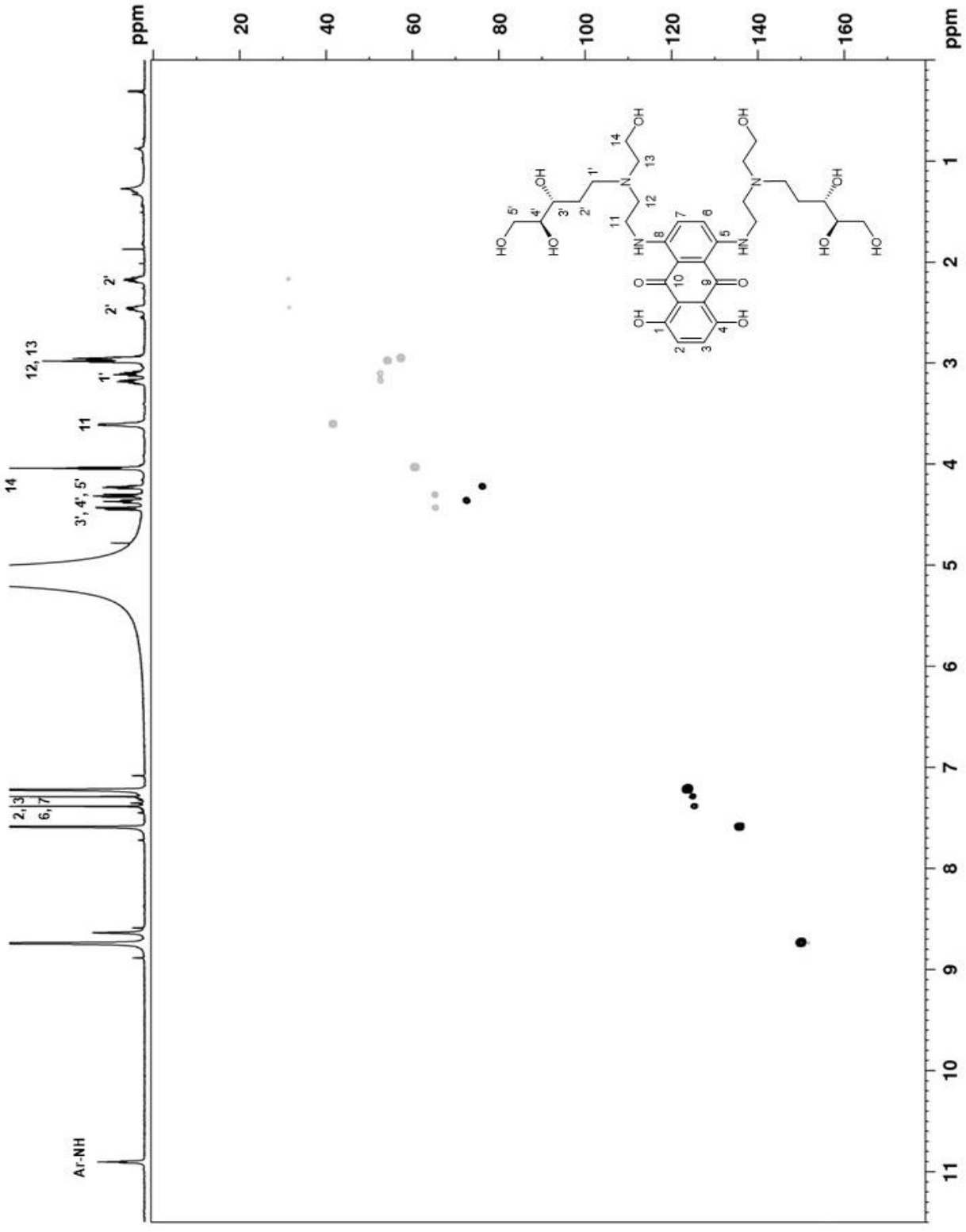

HSQC spectrum of the MTX-dR$_2$ synthetic standard in pyridine-*d*$_5$

Positive phasing in black; negative phasing in grey

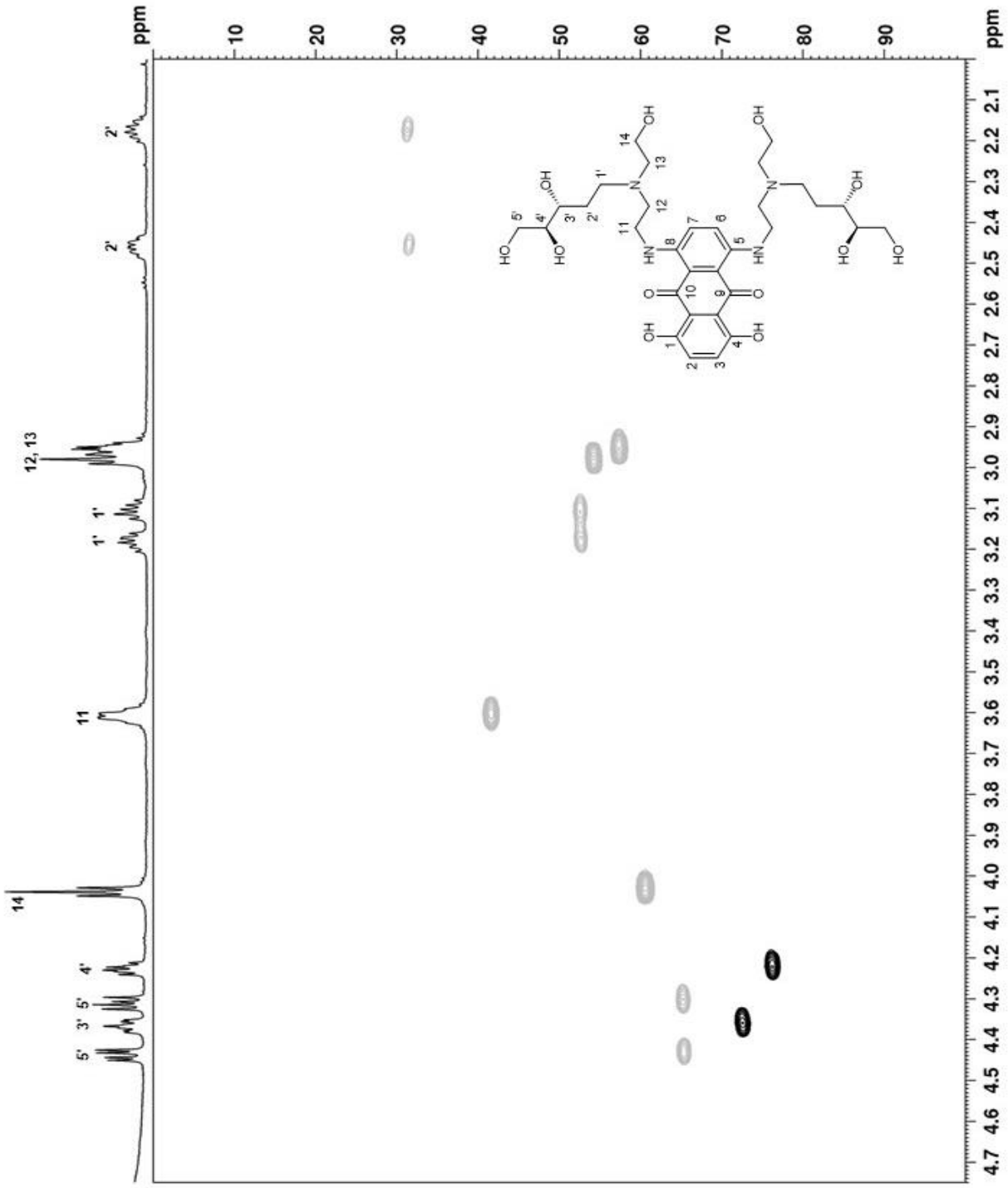

HSQC spectrum of the MTX-dR$_2$ synthetic standard in pyridine-d_5 from 2-4.75 ppm

Positive phasing in black; negative phasing in grey

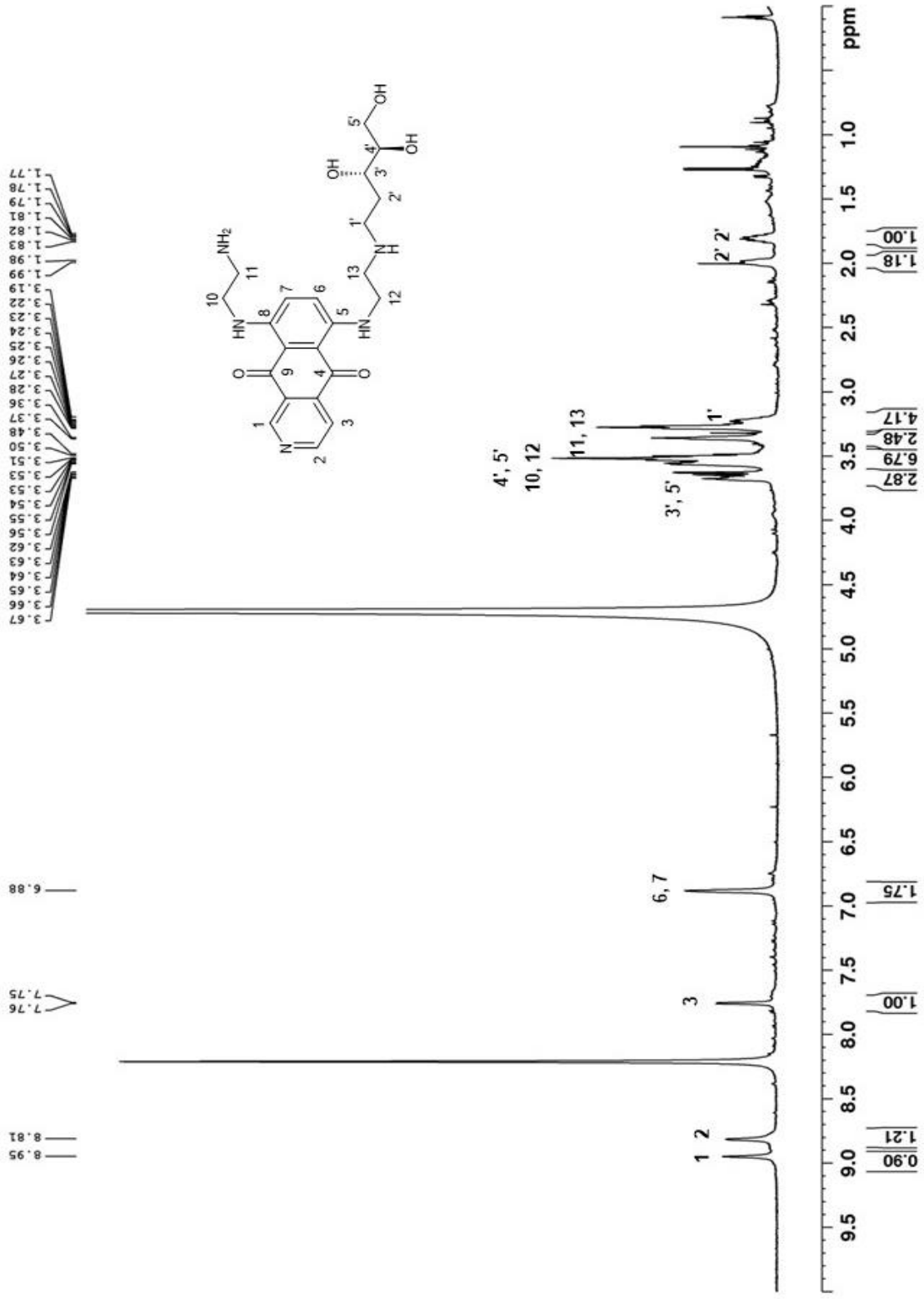

[1]H NMR of the PIX-dR synthetic standard in 0.1% deuterated formic acid

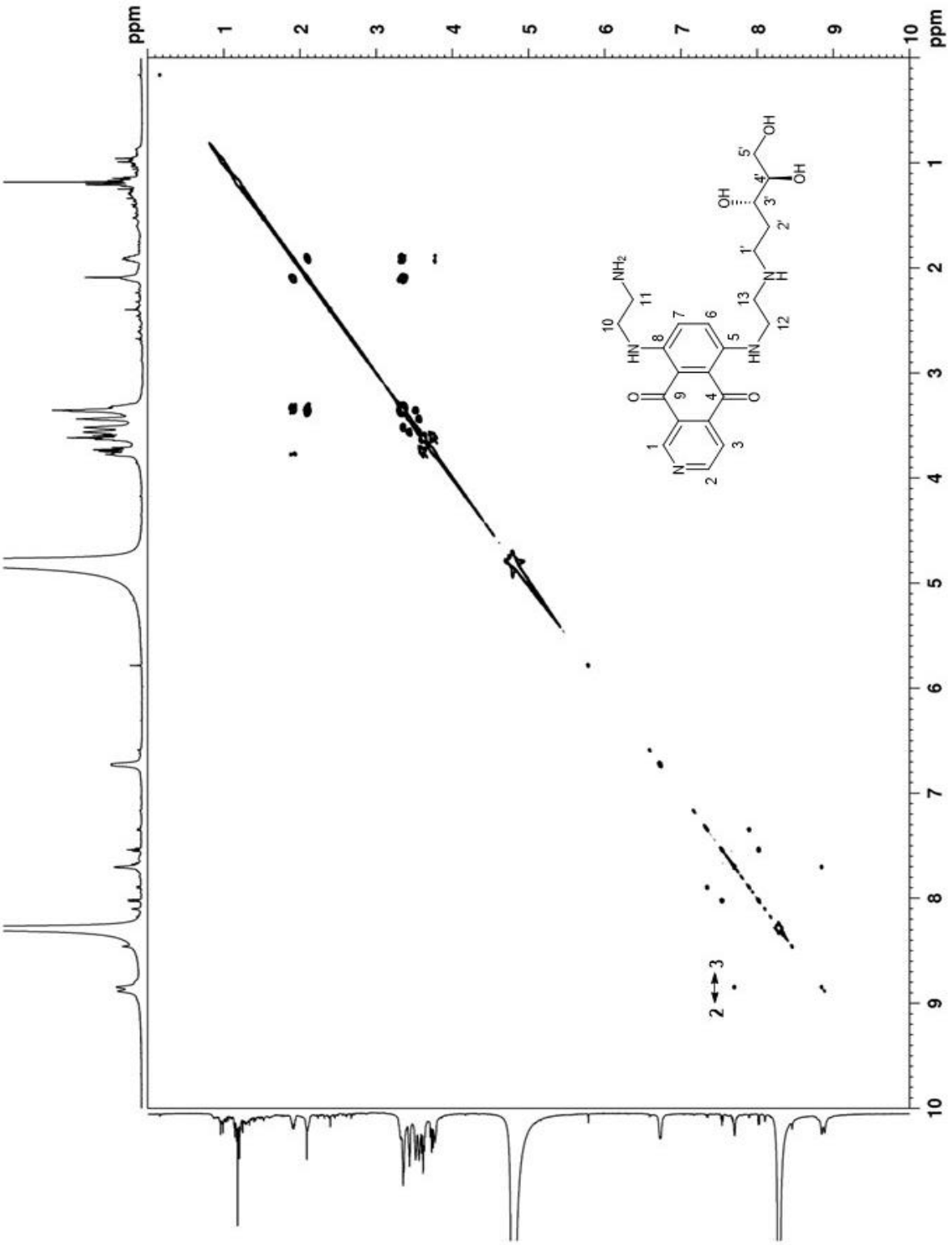

COSY spectrum of the PIX-dR synthetic standard in 0.1% deuterated formic acid with two-bond ^{1}H-^{1}H correlations labeled

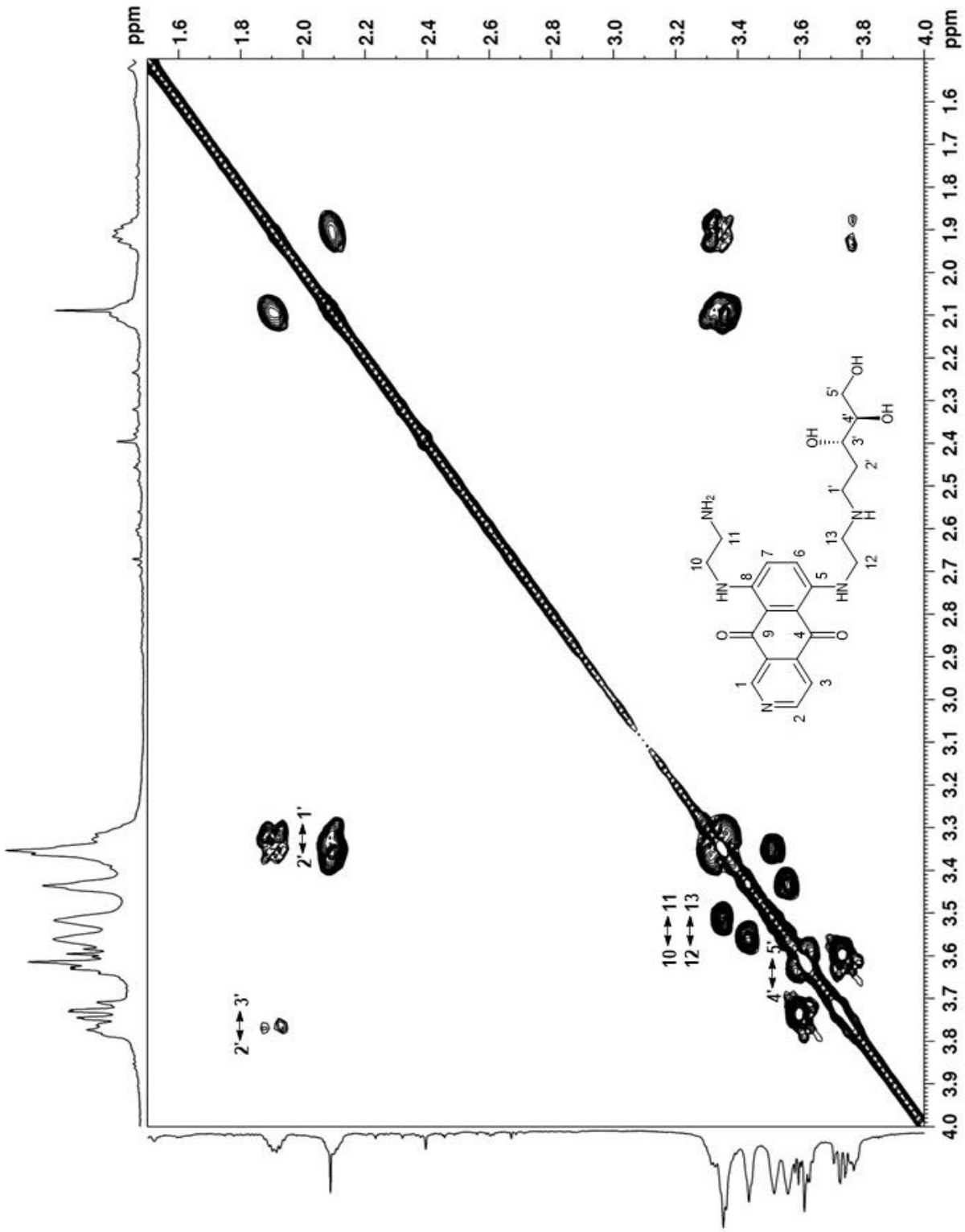

COSY spectrum of the PIX-dR synthetic standard in 0.1% deuterated formic acid from 1.5-4 ppm with two-bond ^{1}H-^{1}H correlations labeled

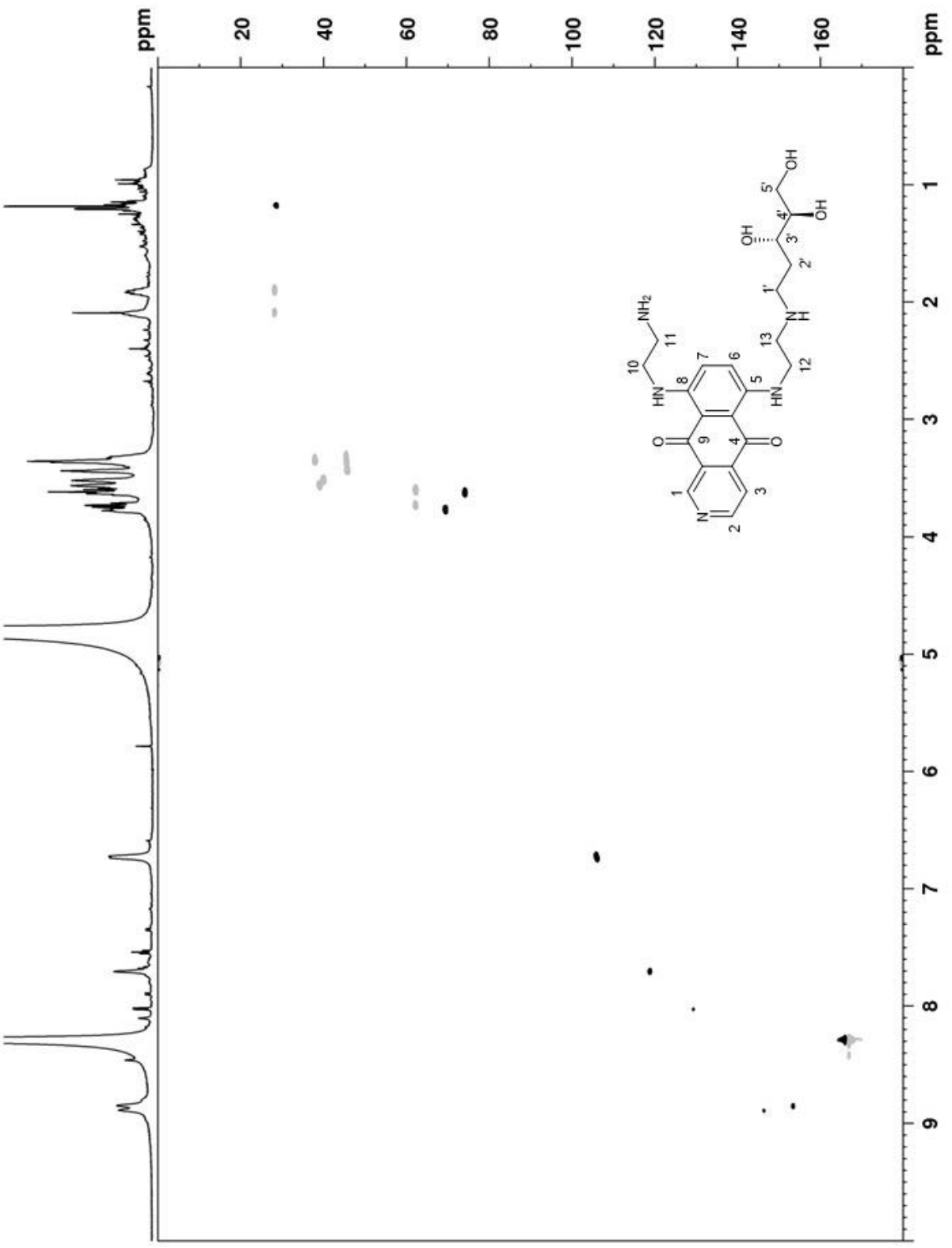

HSQC spectrum of the PIX-dR synthetic standard in 0.1% deuterated formic acid

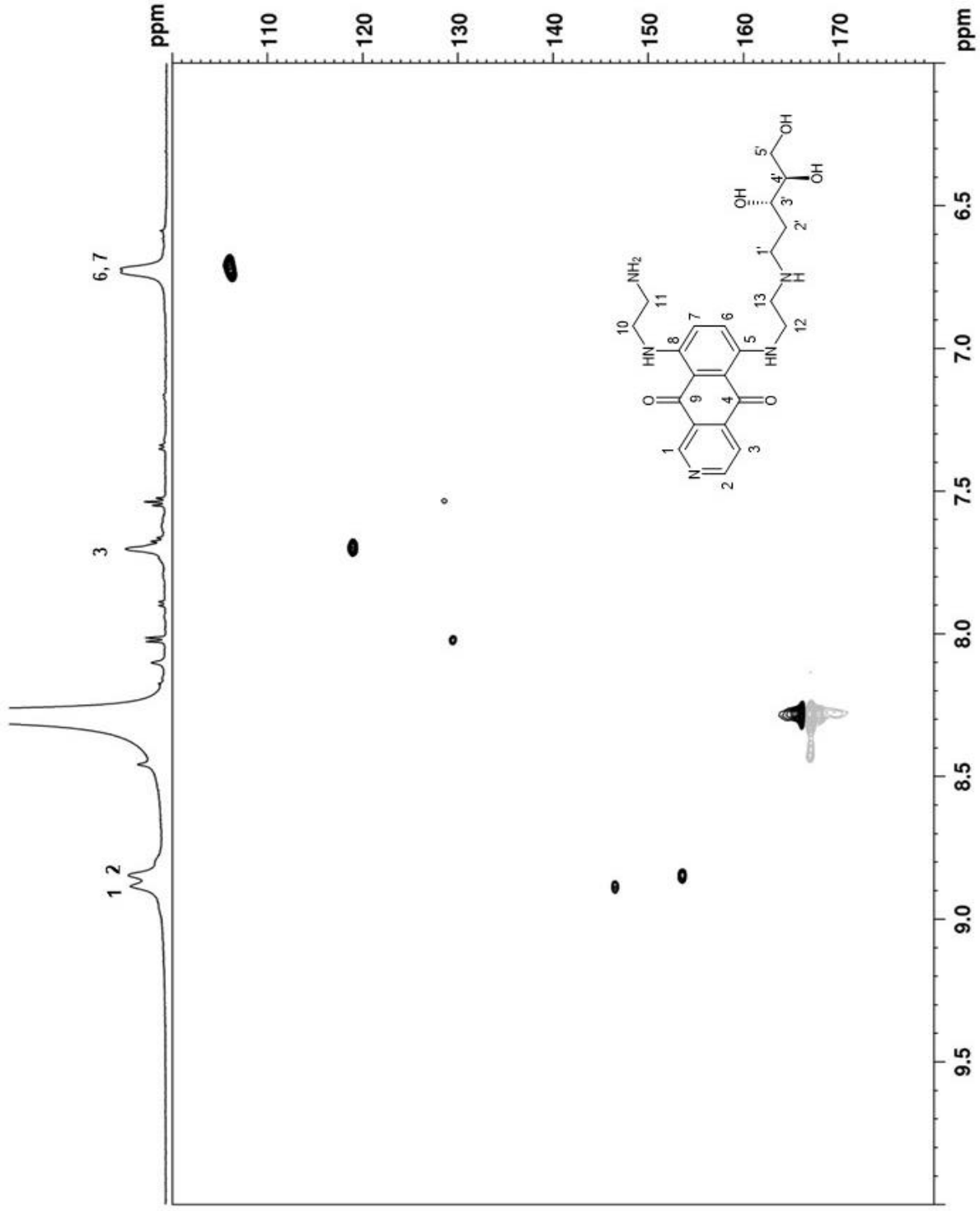

HSQC spectrum of the PIX-dR synthetic standard in 0.1% deuterated formic acid from 6-10 ppm

Positive phasing in black; negative phasing in grey

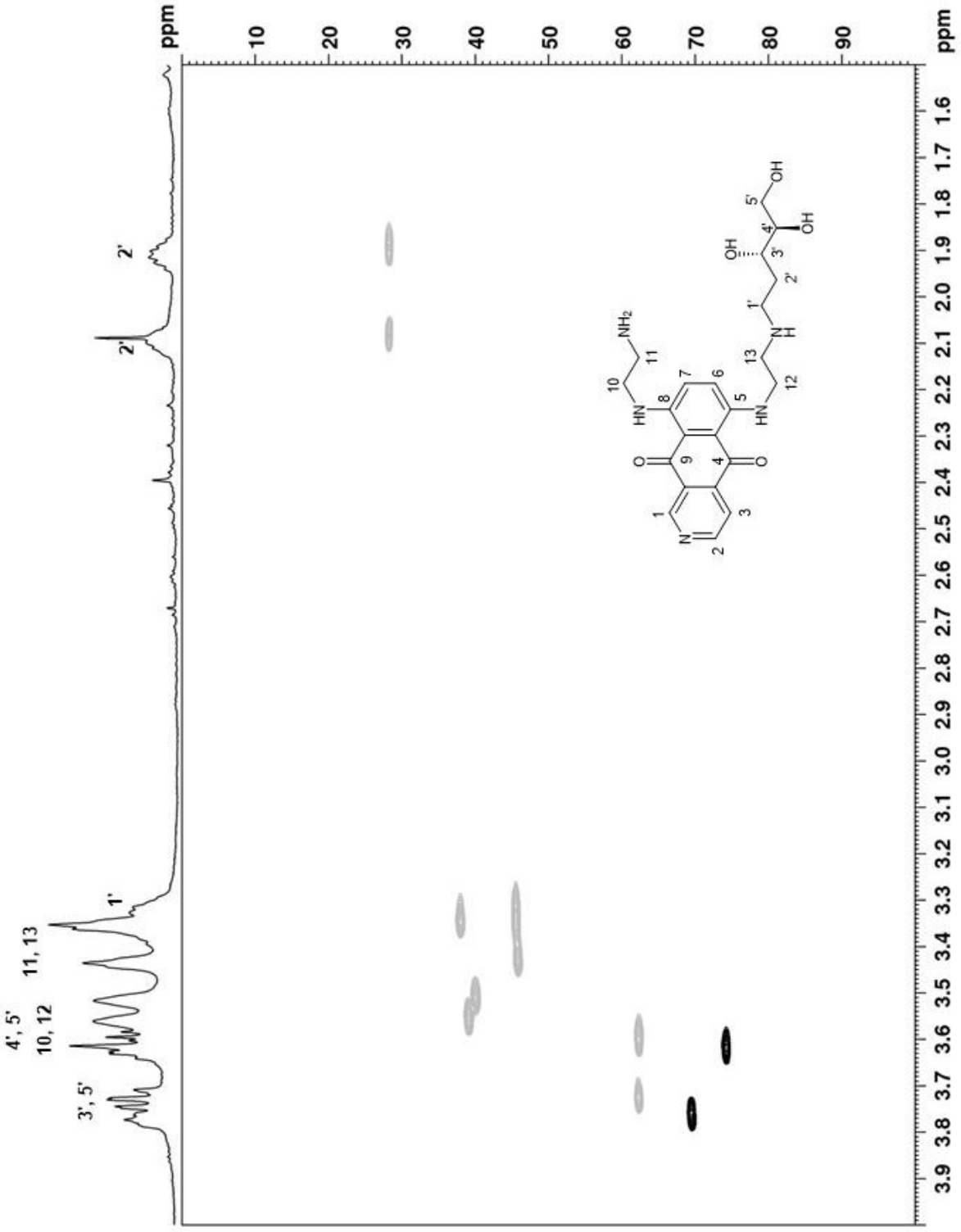

HSQC spectrum of the PIX-dR synthetic standard in 0.1% deuterated formic acid from 6-10 ppm

Positive phasing in black; negative phasing in grey

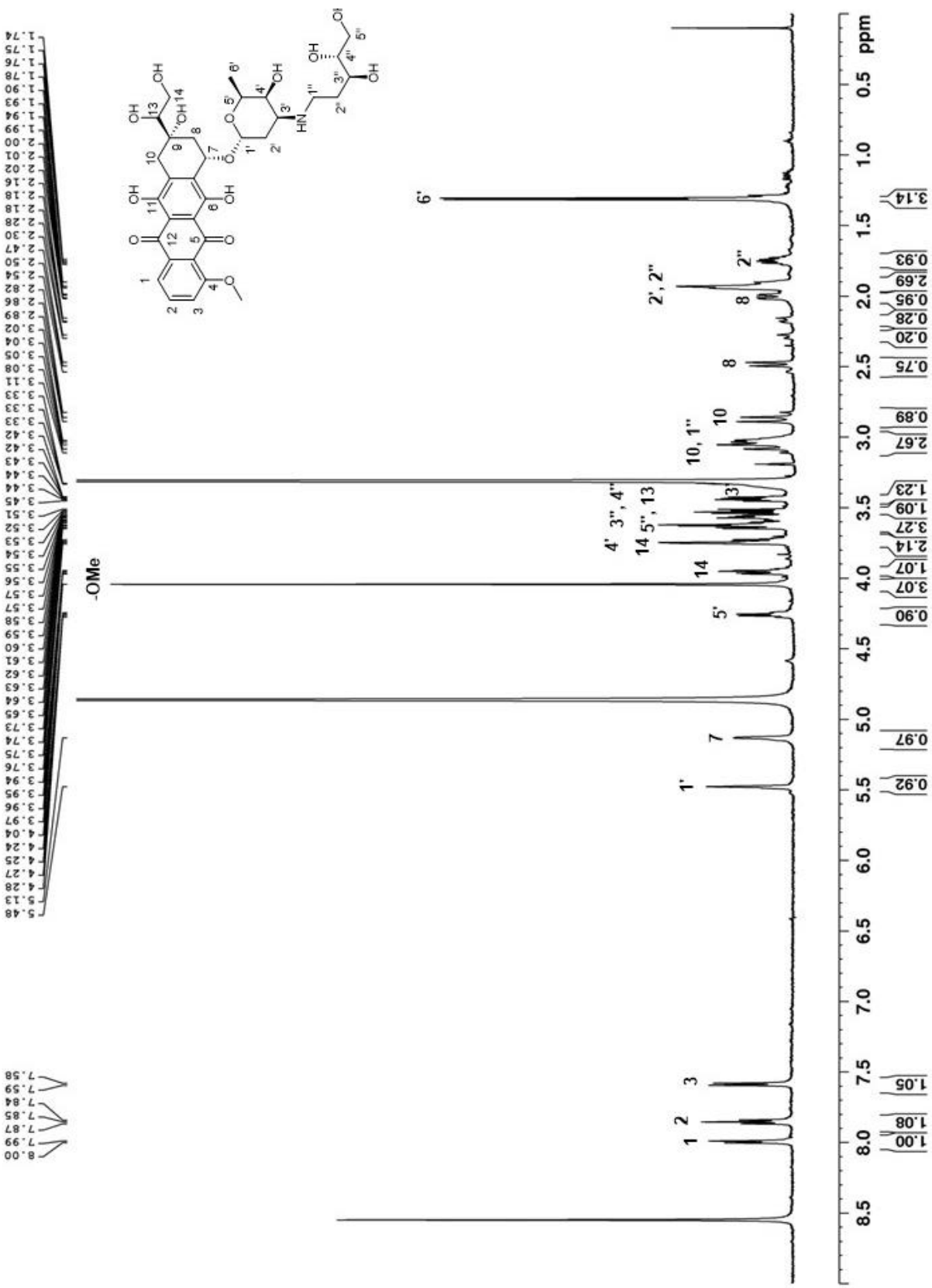

^{1}H NMR of the DOXol-dR synthetic standard in CD_3OD

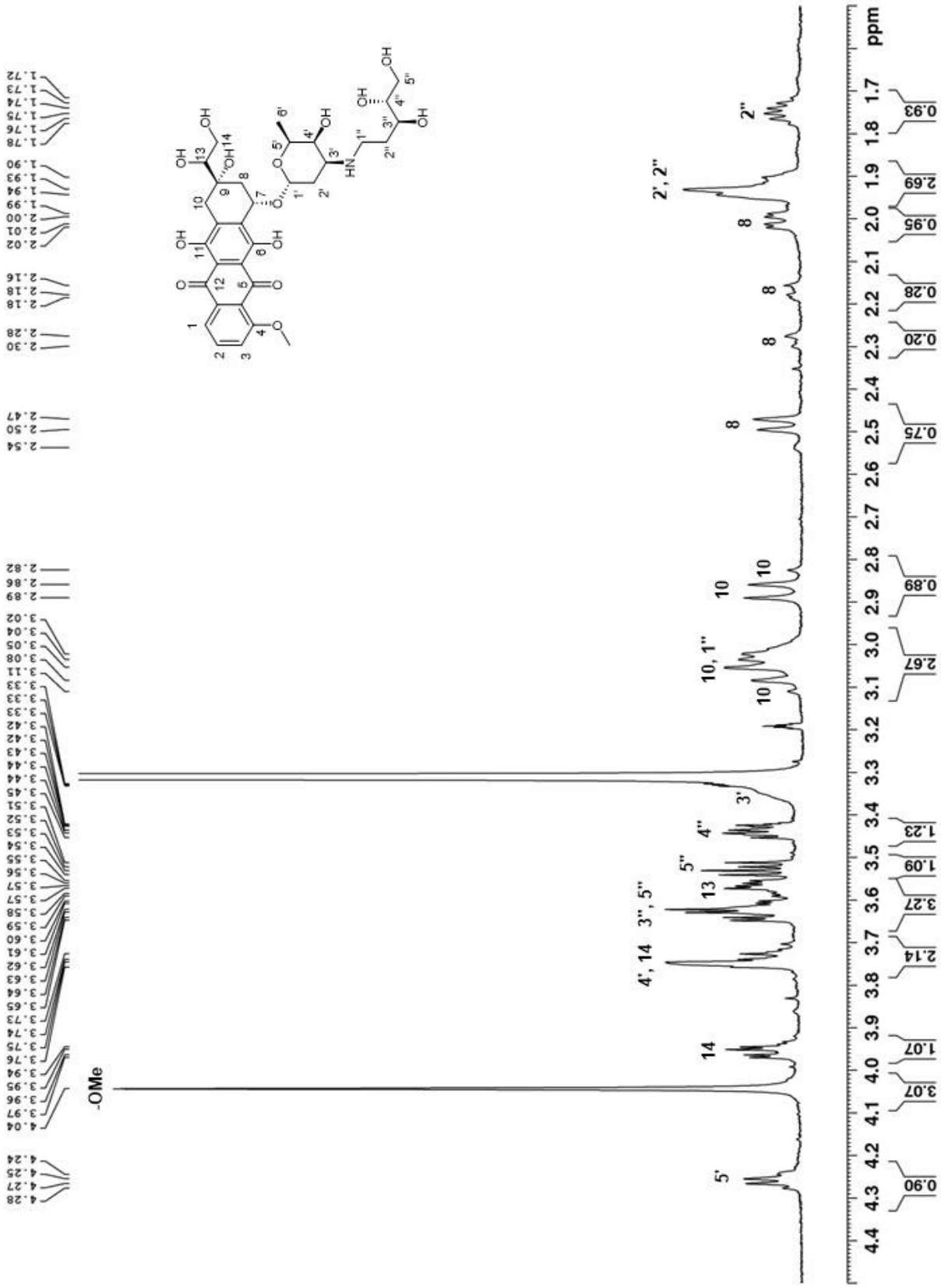

^{1}H NMR of the DOXol-dR synthetic standard in CD_3OD from 1.5-4.5 ppm

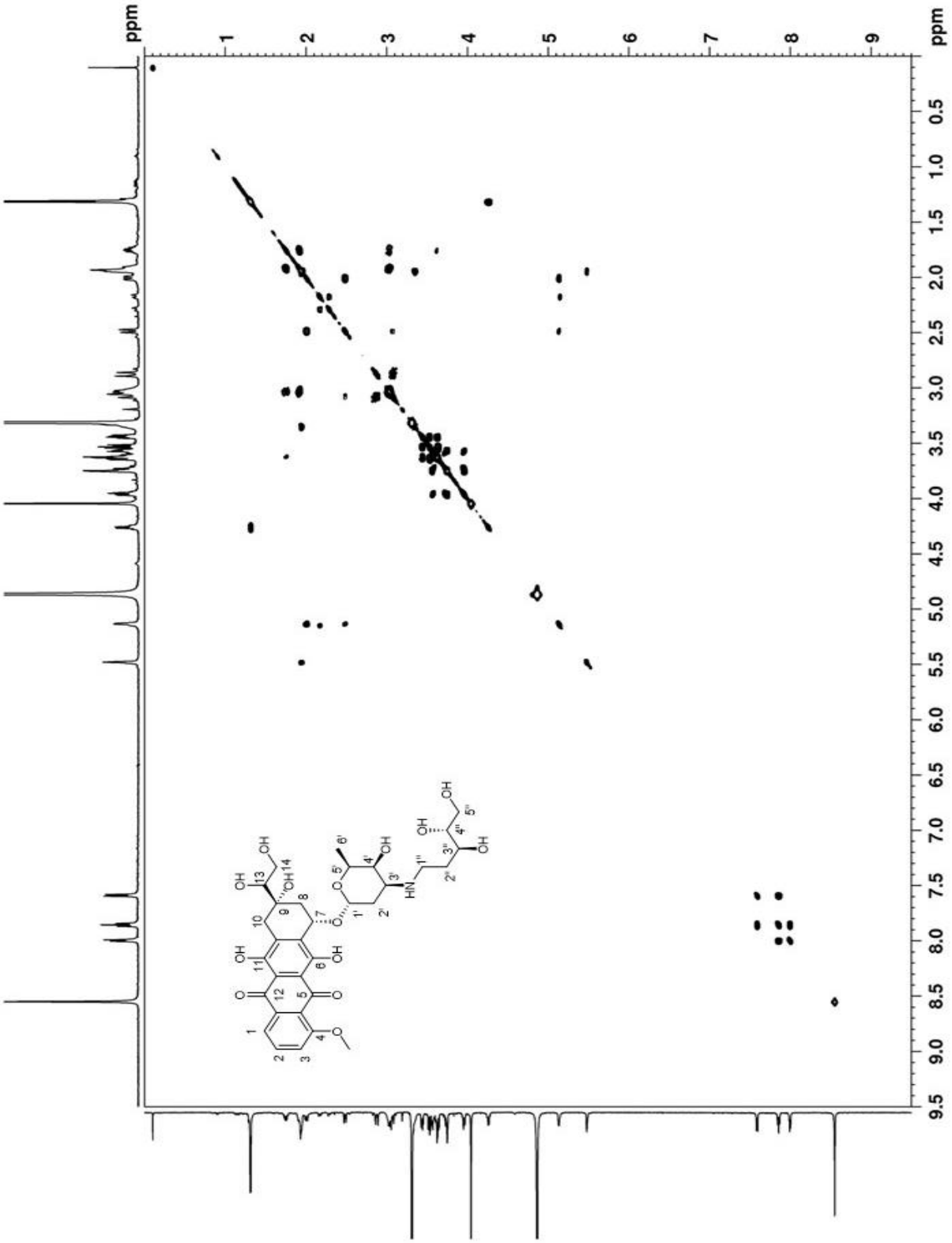

COSY spectrum of the DOXol-dR synthetic standard in CD_3OD with two-bond ^1H-^1H correlations labeled

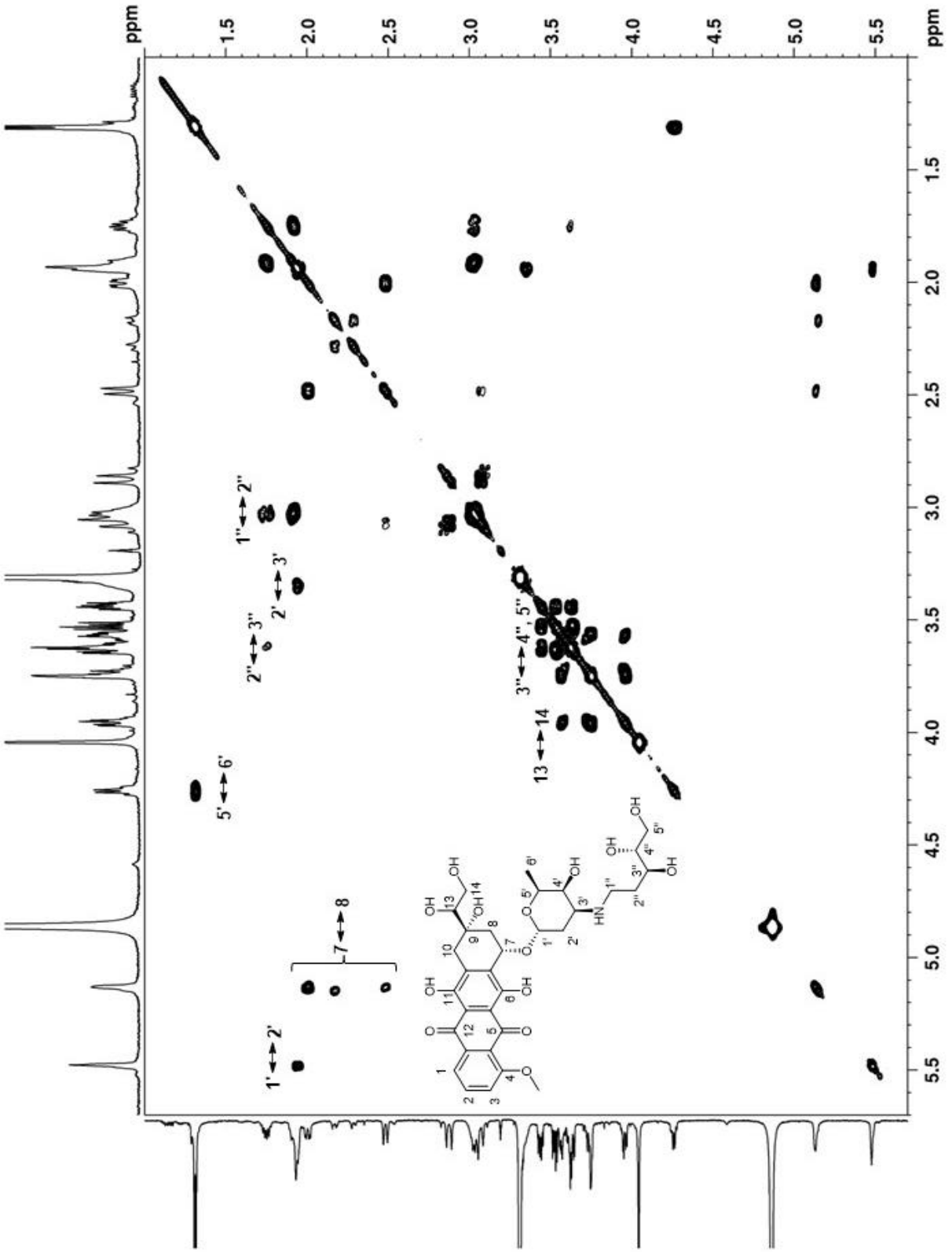

COSY spectrum of the DOXol-dR synthetic standard in CD_3OD from 1-5.6 ppm with two-bond ^1H-^1H correlations labeled

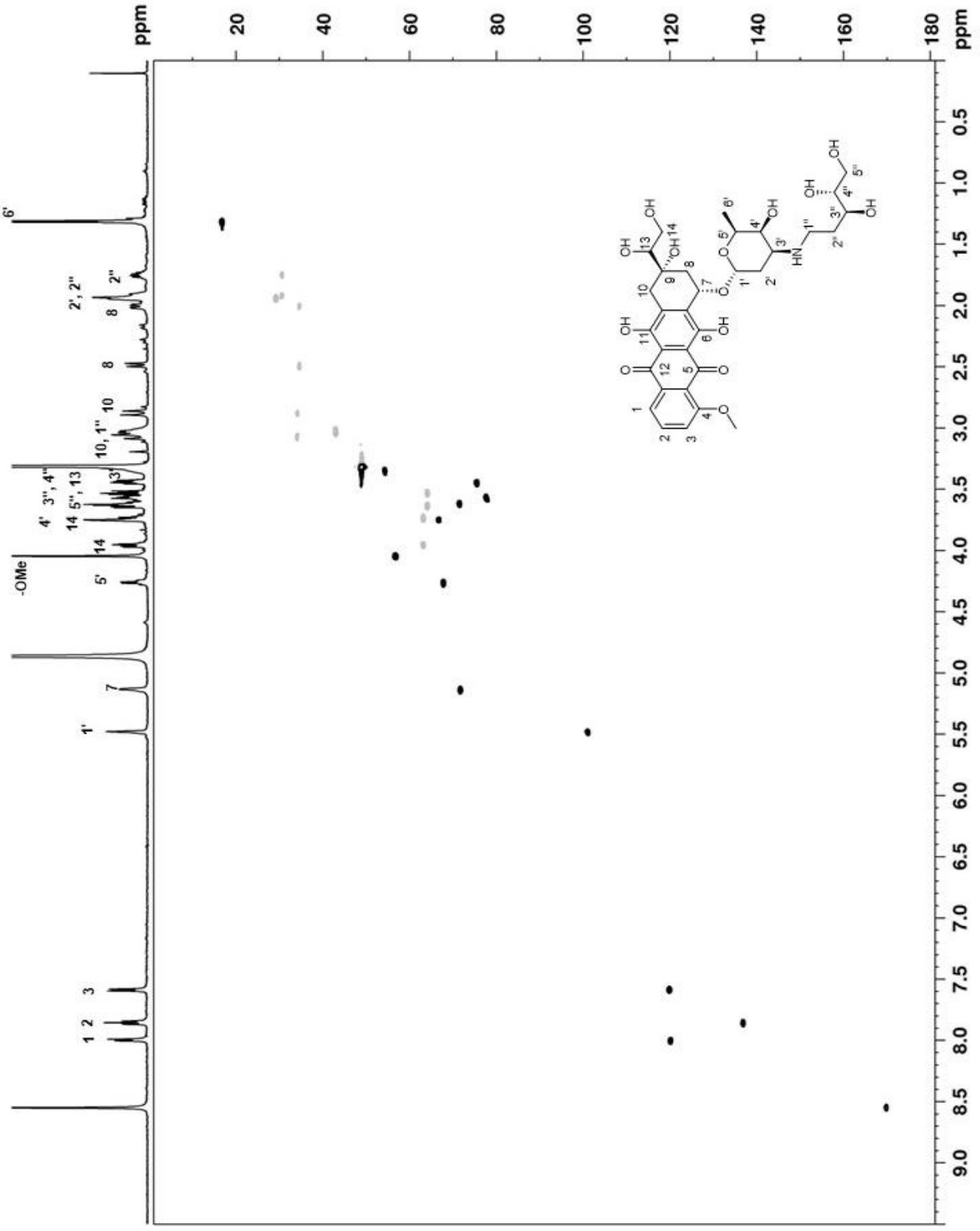

HSQC spectrum of the DOXol-dR synthetic standard in CD_3OD

Positive phasing in black; negative phasing in grey

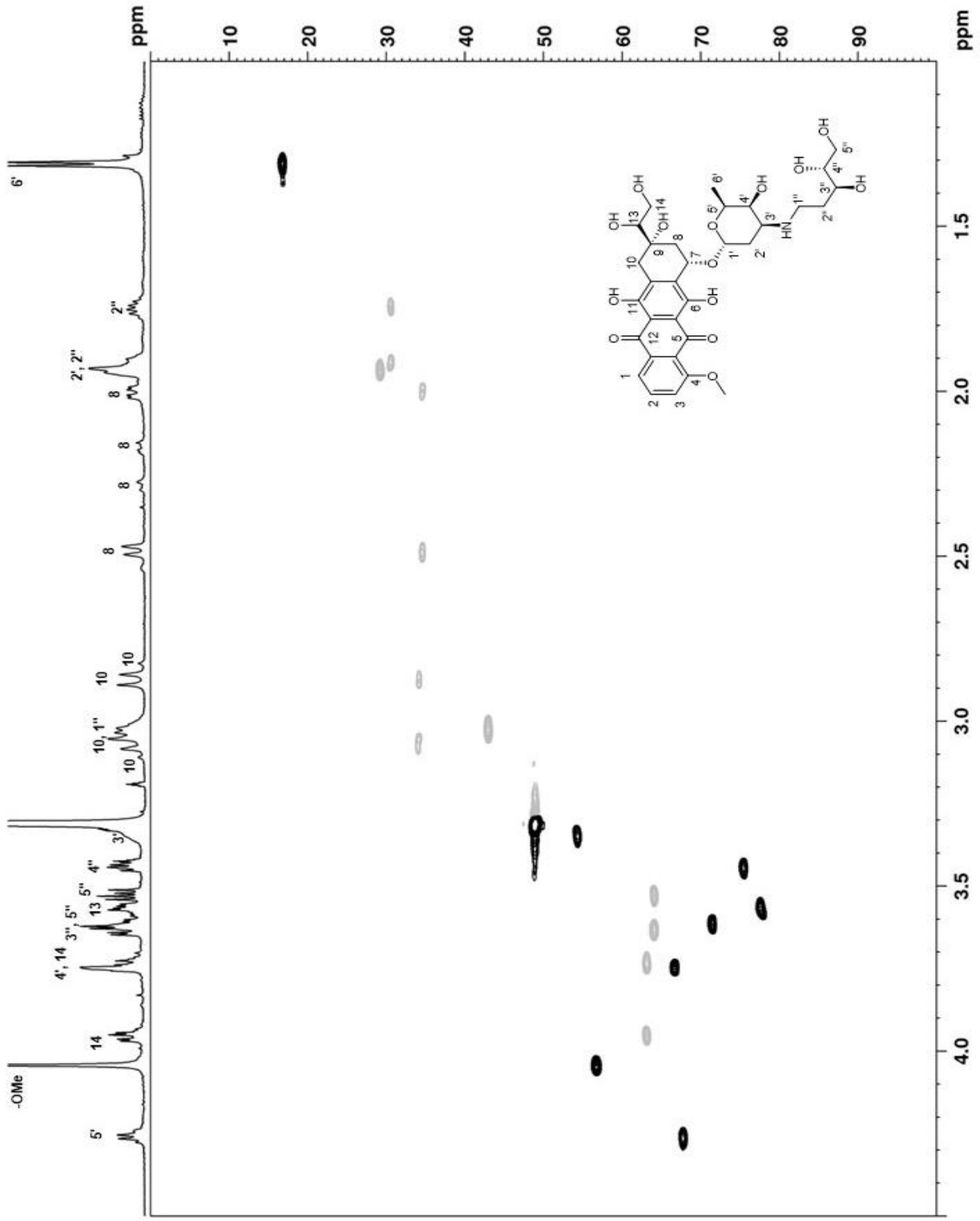

HSQC spectrum of the DOXol-dR synthetic standard in CD_3OD from 1-4.5 ppm

Positive phasing in black; negative phasing in grey

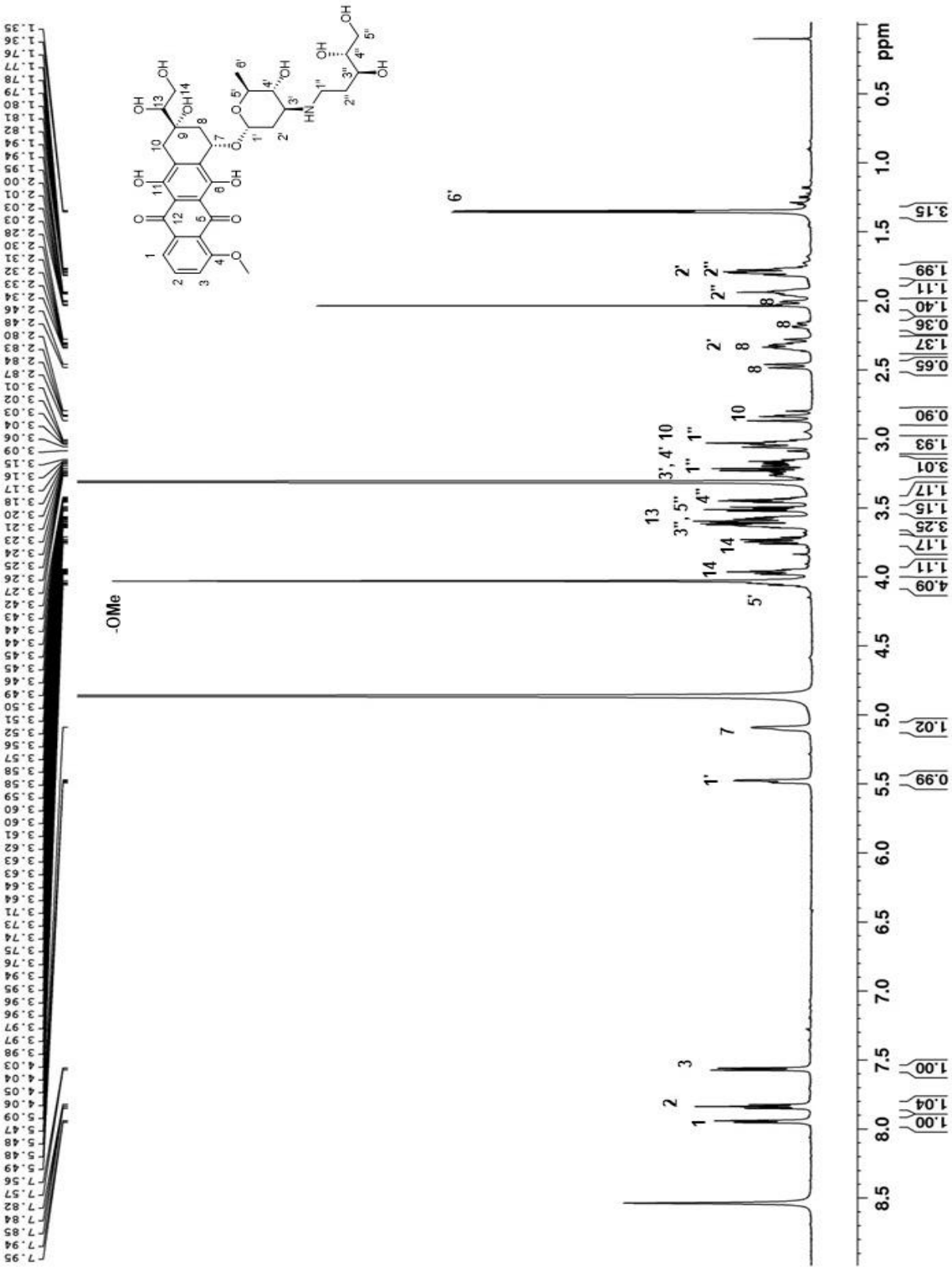

^{1}H NMR of the EPIol-dR synthetic standard in CD_3OD

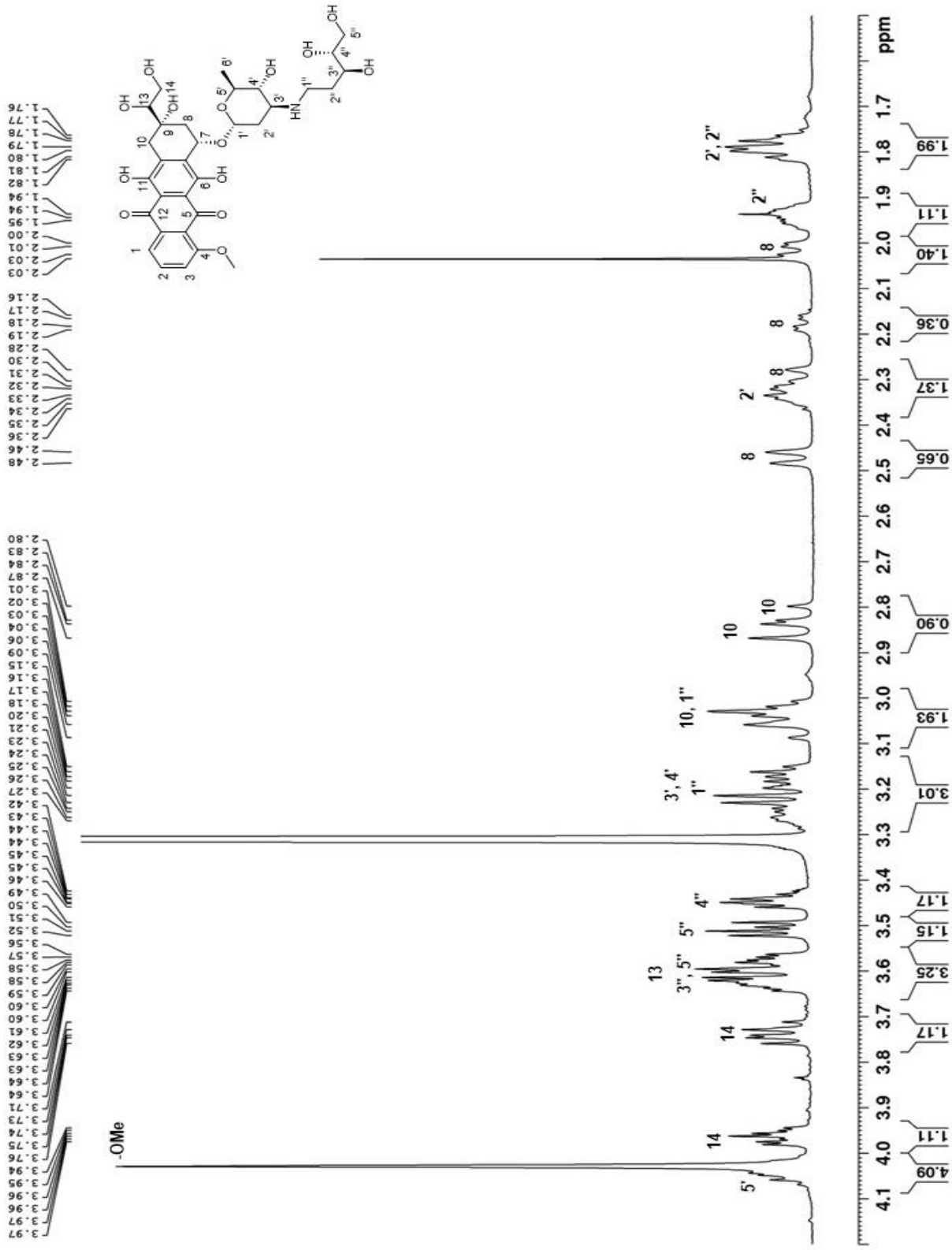

^{1}H NMR of the EPIol-dR synthetic standard in CD_3OD from 1.5-4.2 ppm

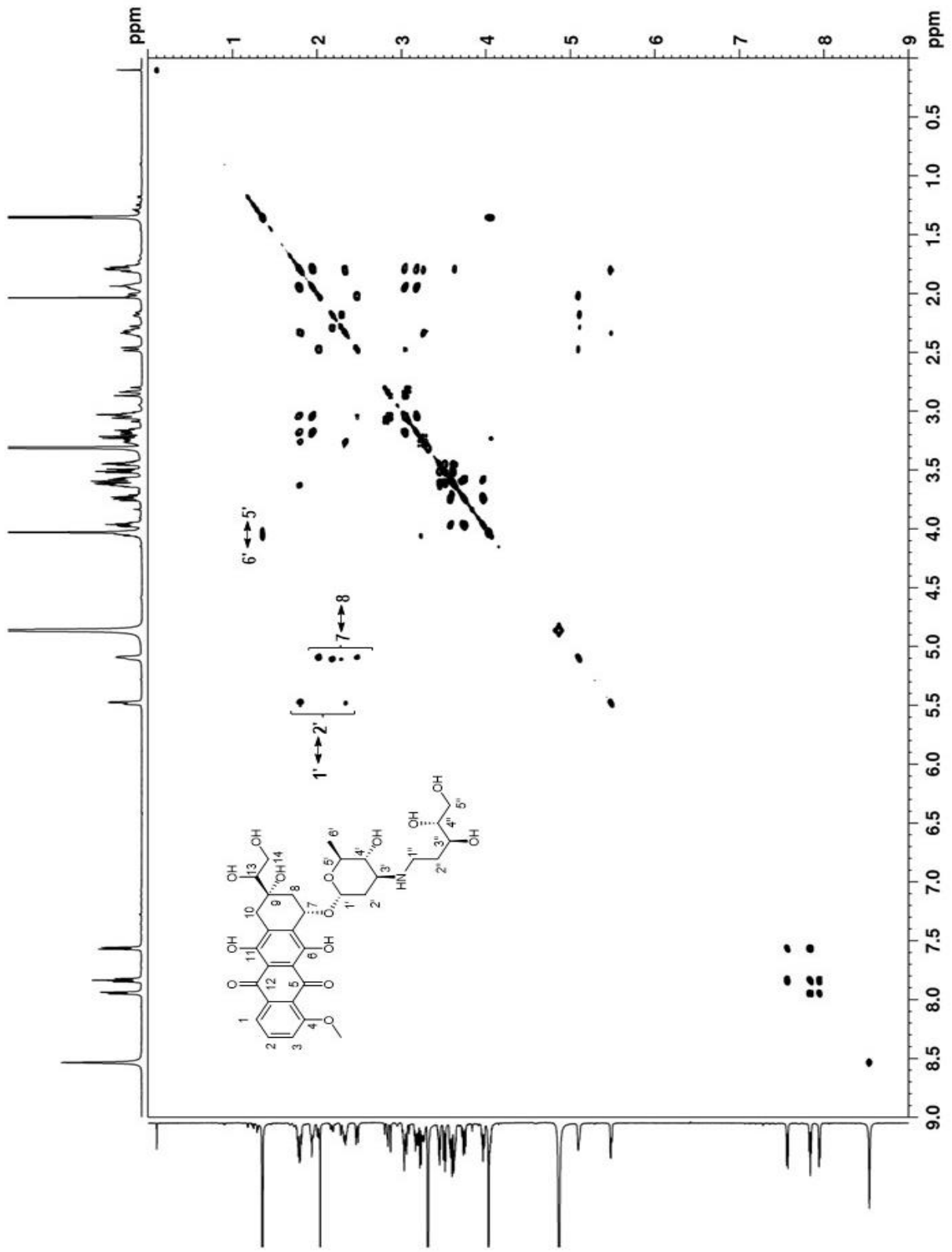

COSY spectrum of the EPIol-dR synthetic standard in CD_3OD with two-bond ^1H-^1H correlations labeled

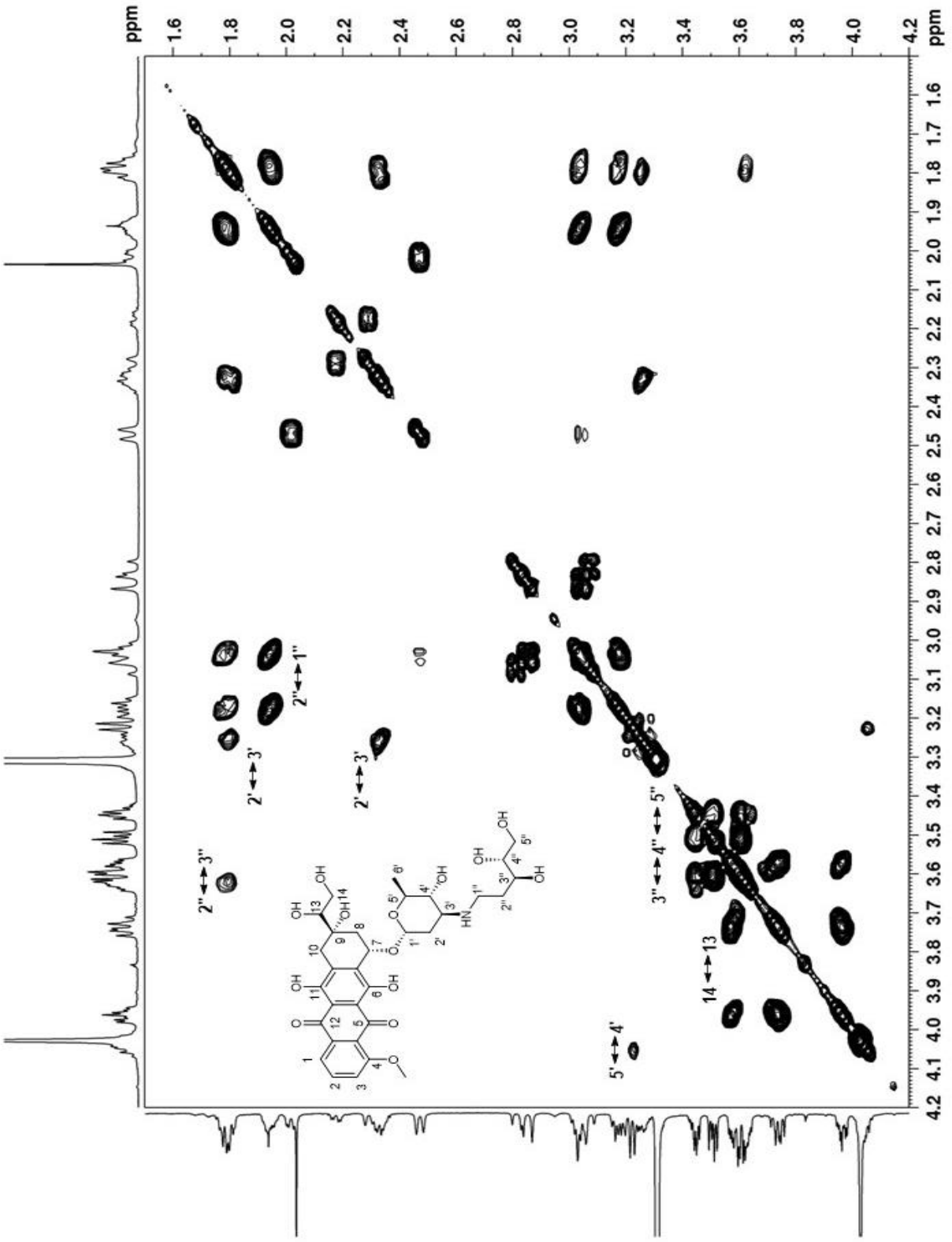

COSY spectrum of the EPIol-dR synthetic standard in CD_3OD from 1.5-4.2 ppm with two-bond ^1H-^1H correlations labeled

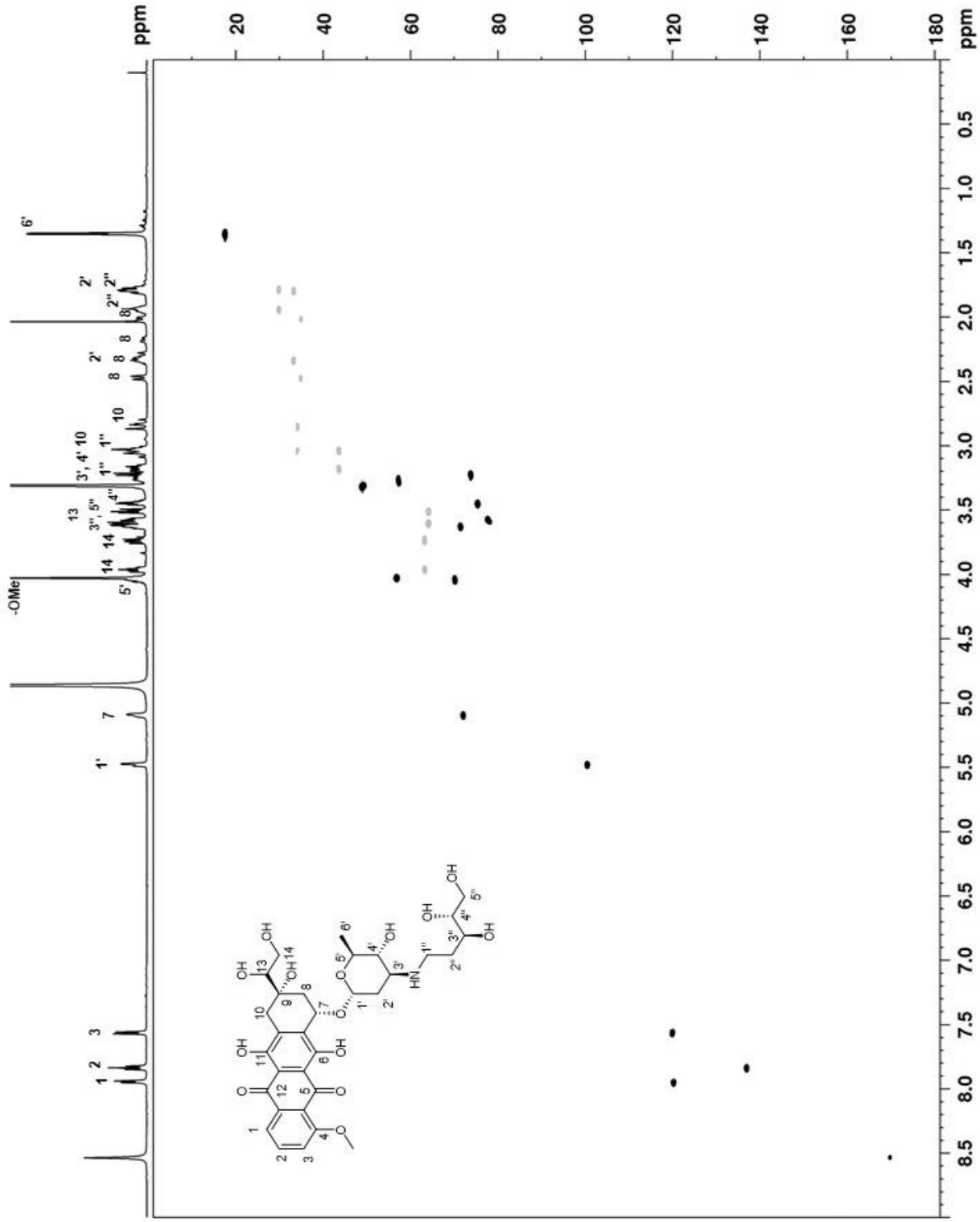

HSQC spectrum of the EPIol-dR synthetic standard in CD_3OD

Positive phasing in black; negative phasing in grey

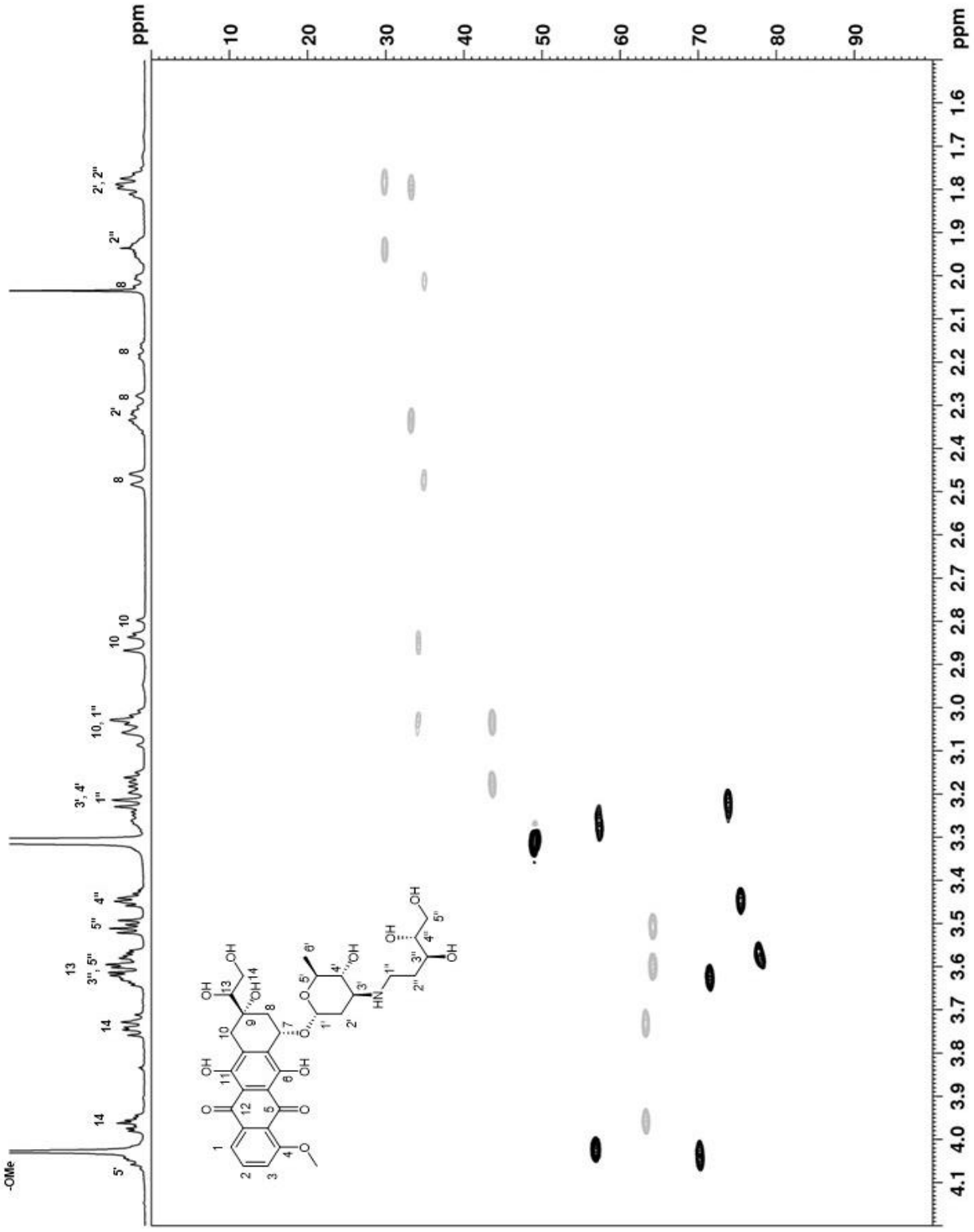

HSQC spectrum of the EPIol-dR synthetic standard in CD_3OD from 1.5-4.2 ppm

Positive phasing in black; negative phasing in grey

Appendix IV:

ESI-LC/MS^2 Characterization of Anthracycline-dR Reduced Covalent Adducts Isolated from Enzymatic Digestion of AP-modified 12mer Oligonucleotides in Chapter II

See Appendix I for Anthracycline-dR CID Fragmentation Product Identifications

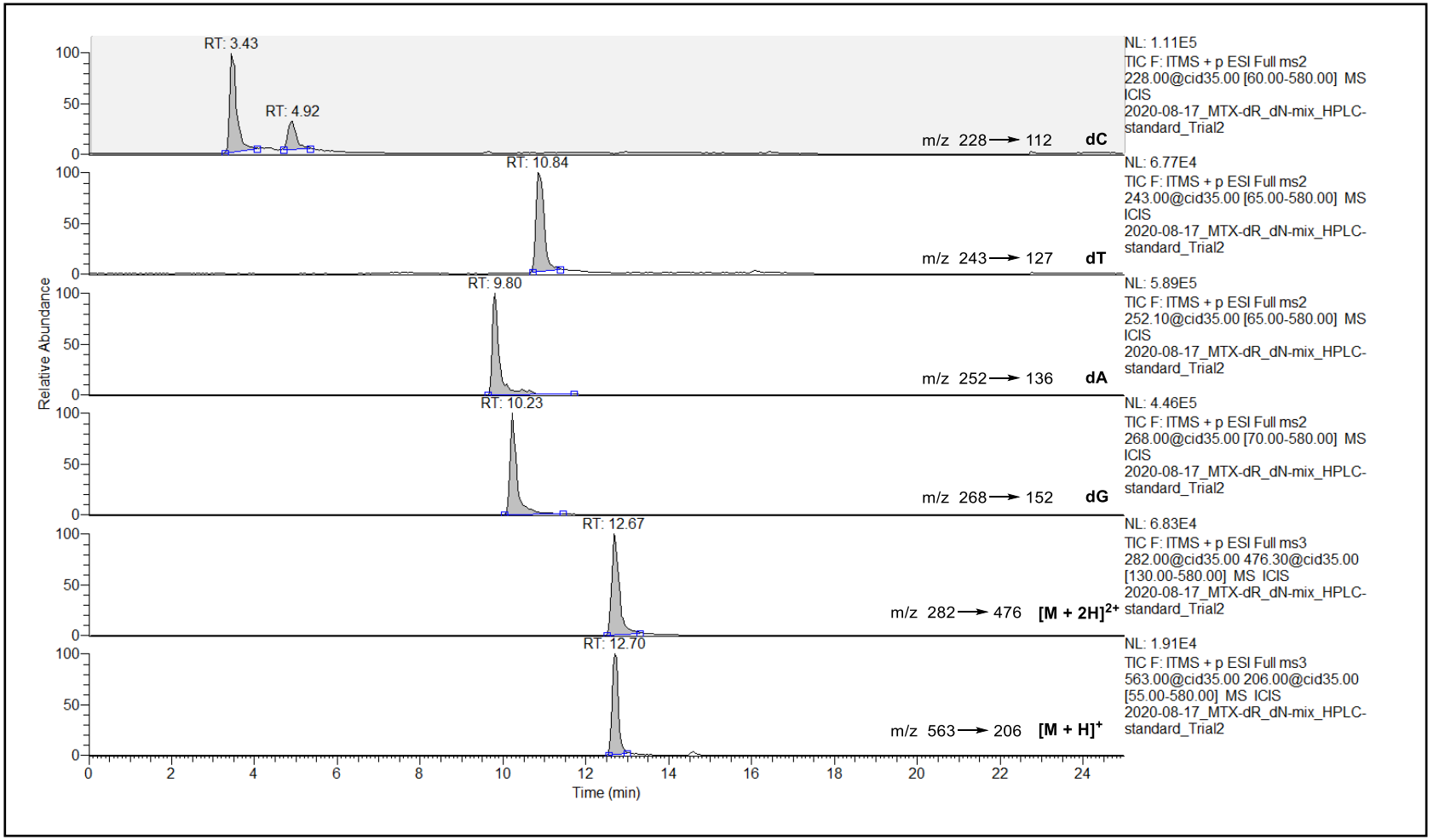

ESI-LC/MS chromatogram of a prepared solution of dC, dT, dA, dG, and the MTX-dR synthetic standard in equivalent ratios.

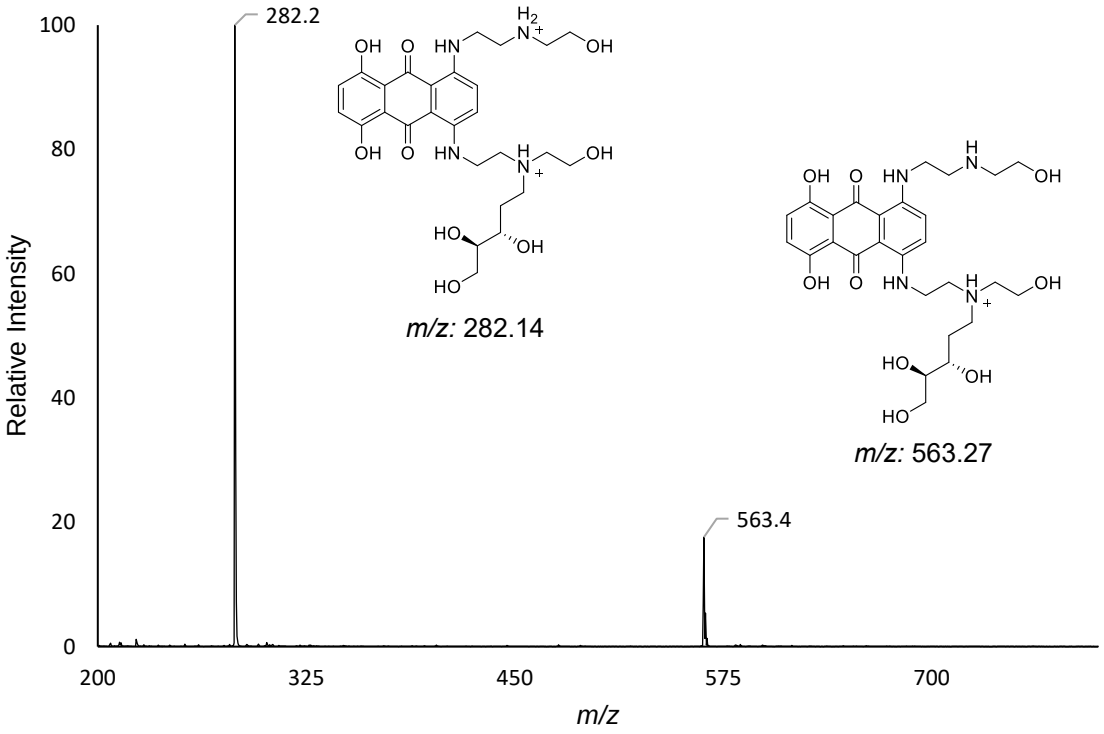

ESI-LC/MS total ion mass spectrum for retention time 12.7 minutes from analysis of the prepared solution of unmodified dNs + MTX-dR.

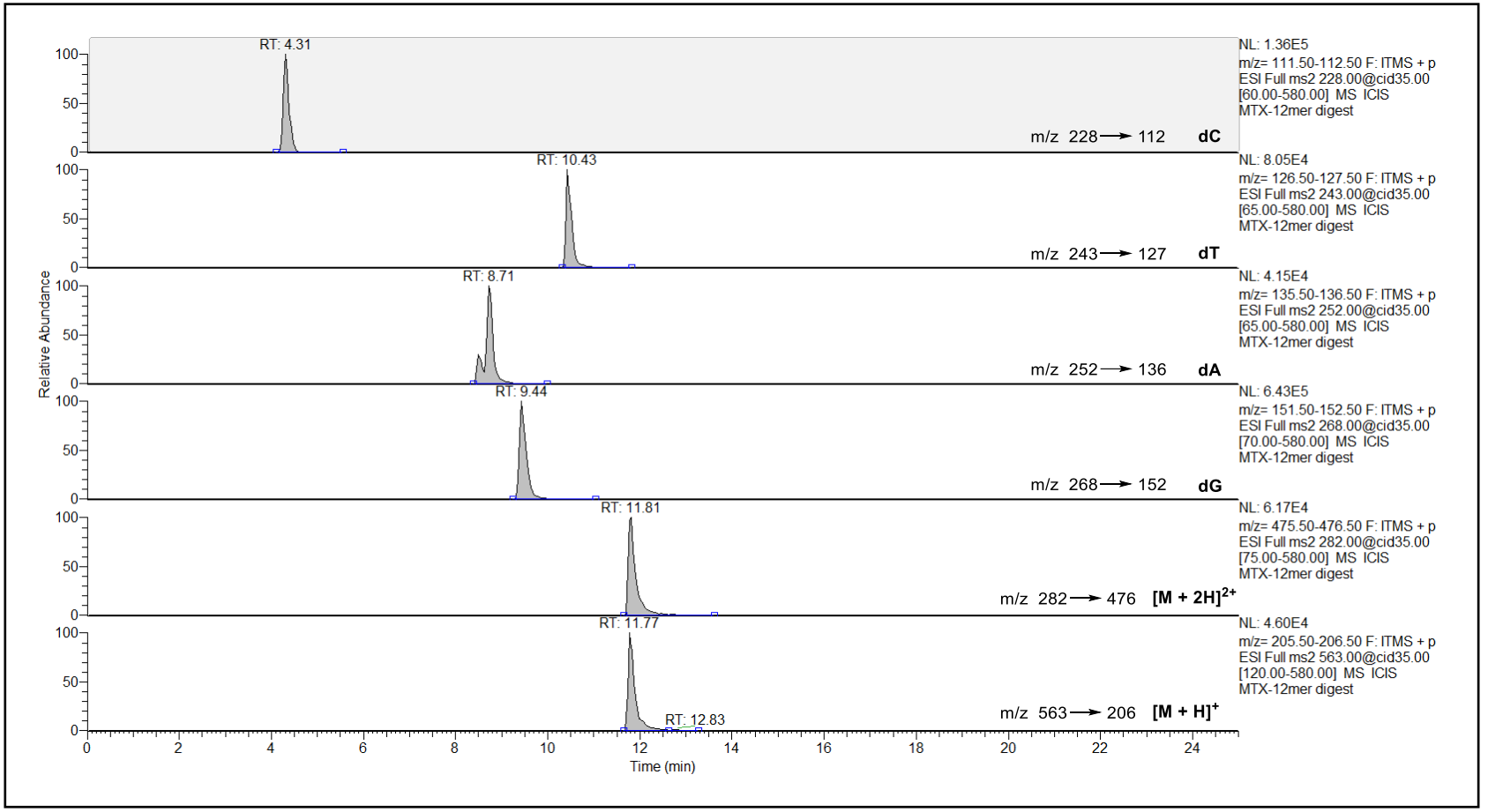

ESI-LC/MS chromatogram of the hydrolysate resulting from enzymatic digestion of the purified MTX-12mer reduced conjugate (5'-GTT GC[AP-MTX] CGT ATG-3').

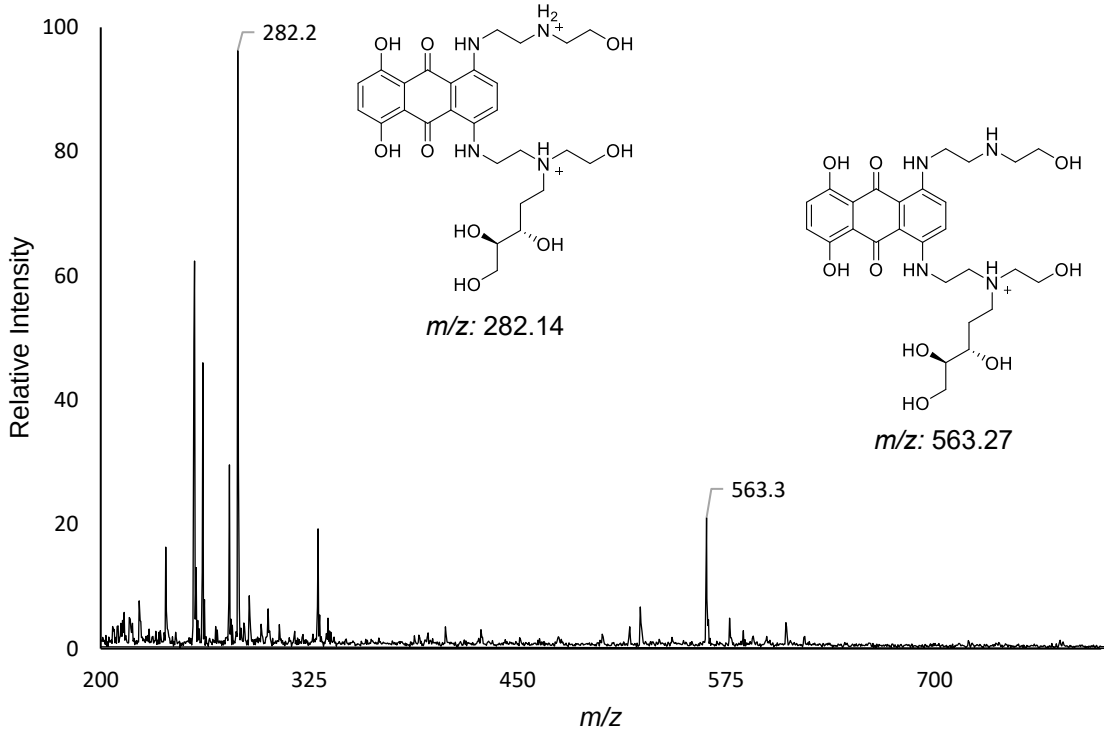

ESI-LC/MS total ion mass spectrum for retention time 11.8 minutes from the SPE-enriched MTX-12mer enzymatic digestion hydrolysate.

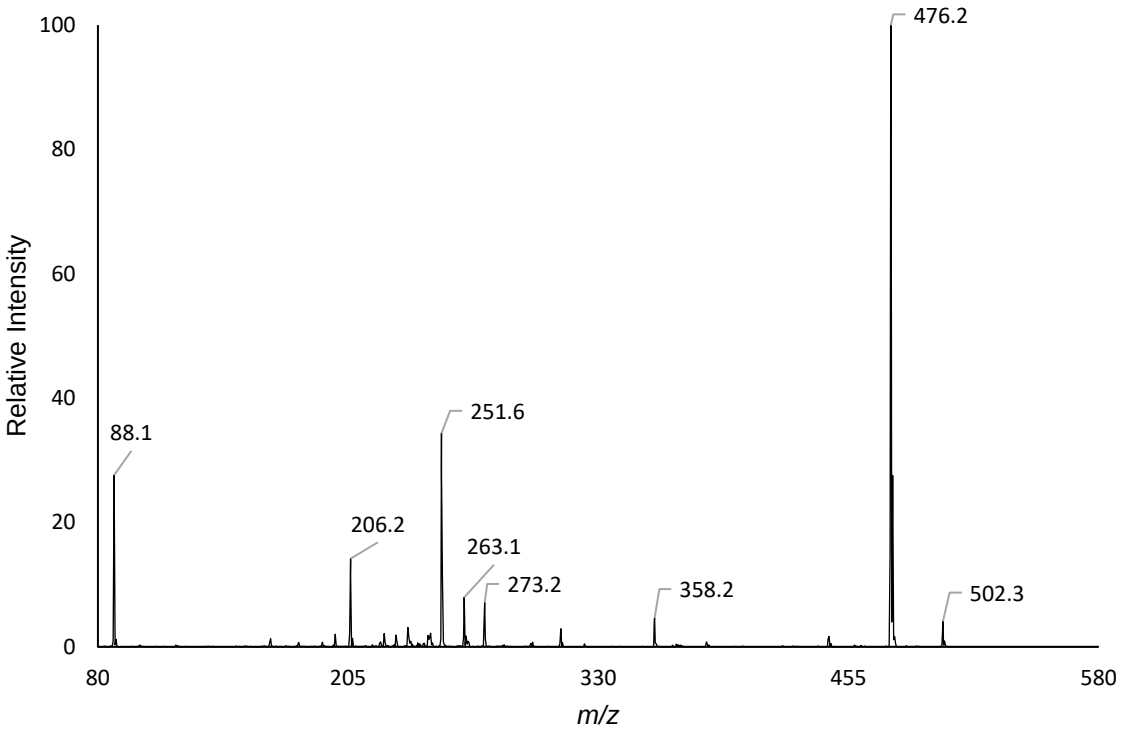

***m/z 282* selected ion ESI-LC/MS^2 mass spectrum with CID fragmentation of the SPE-enriched MTX-12mer enzymatic digestion hydrolysate.**

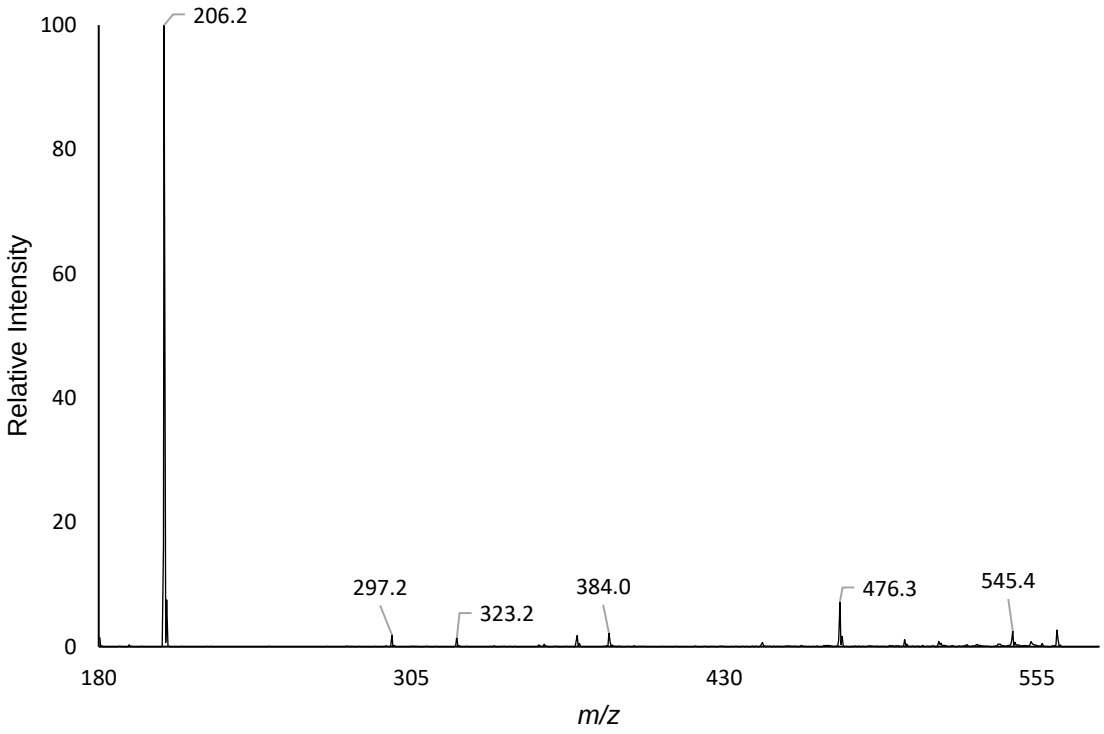

***m/z 563* selected ion ESI-LC/MS^2 mass spectrum with CID fragmentation of the SPE-enrichedMTX-12mer enzymatic digestion hydrolysate.**

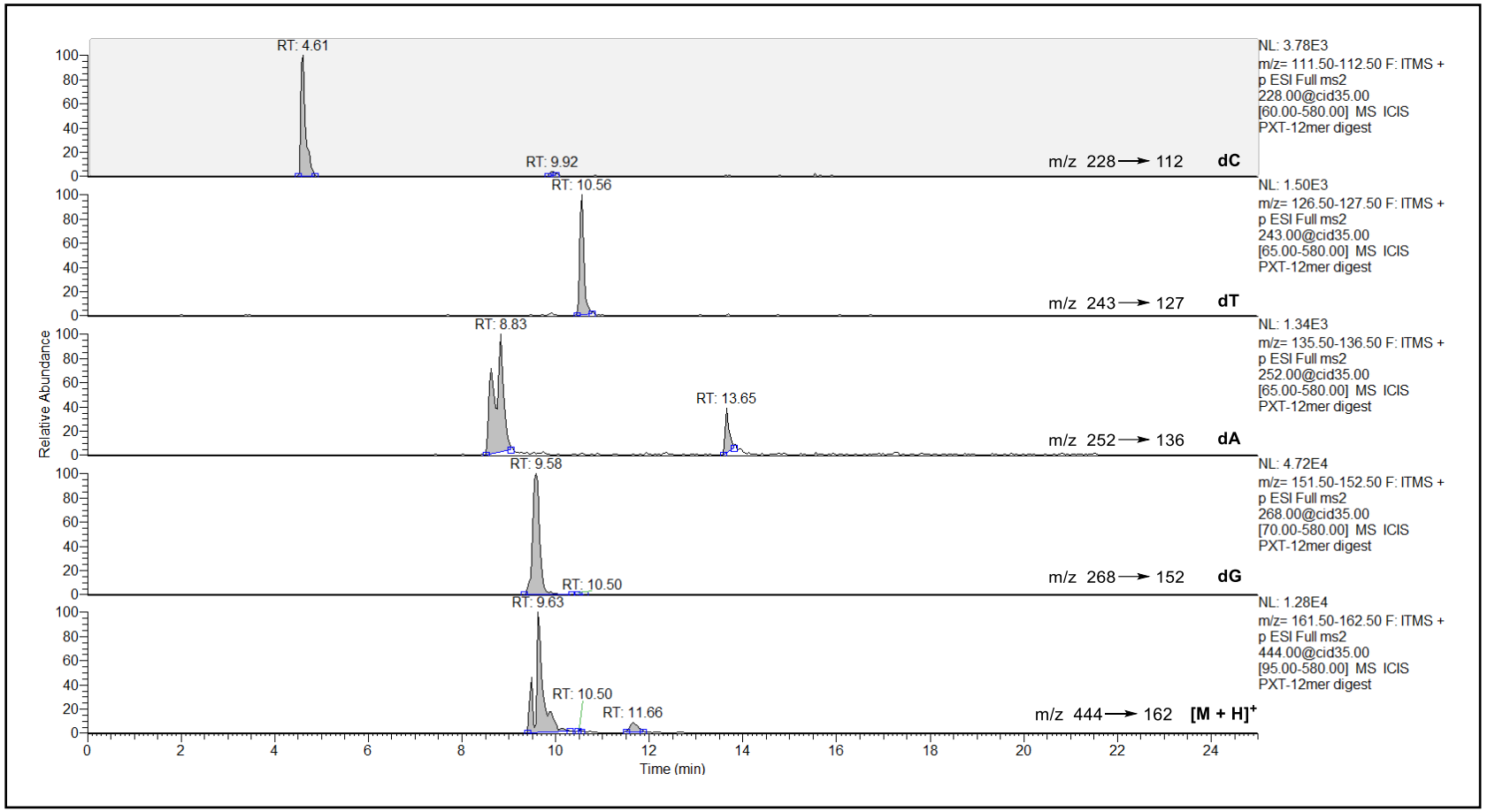

ESI-LC/MS chromatogram of the hydrolysate resulting from enzymatic digestion of the purified PIX-12mer reduced conjugate (5'-GTT GC[AP-PIX] CGT ATG-3').

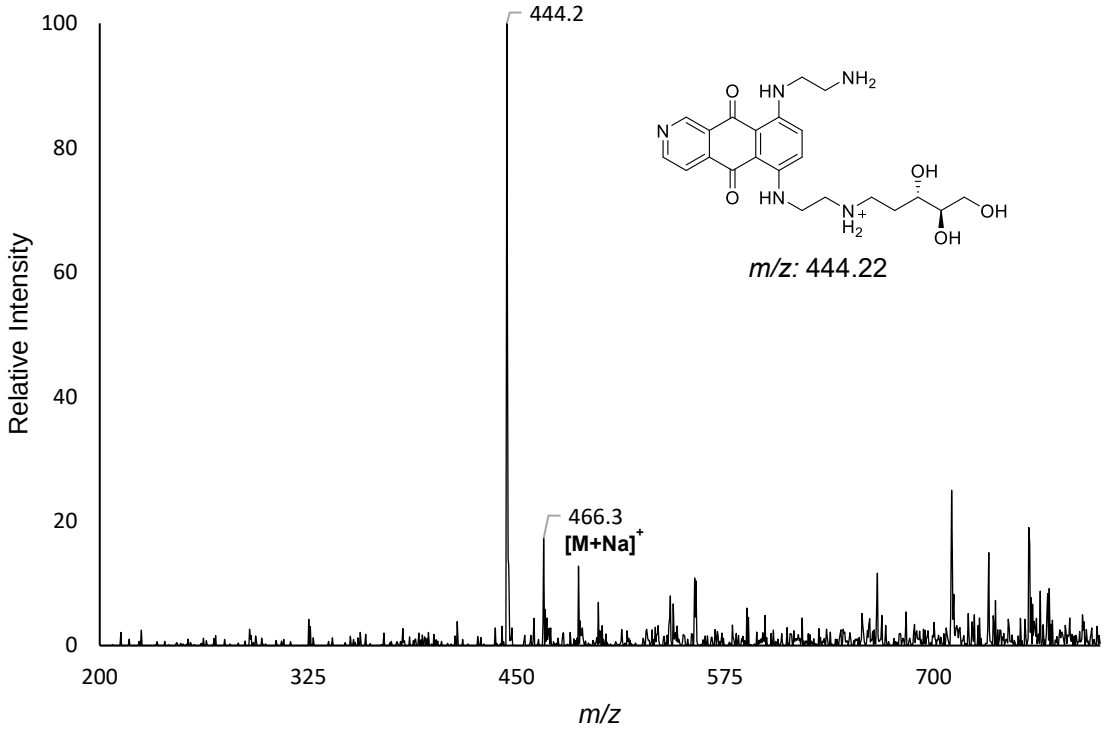

ESI-LC/MS total ion mass spectrum for retention time 9.6 minutes from the SPE-enriched PIX-12mer enzymatic digestion hydrolysate.

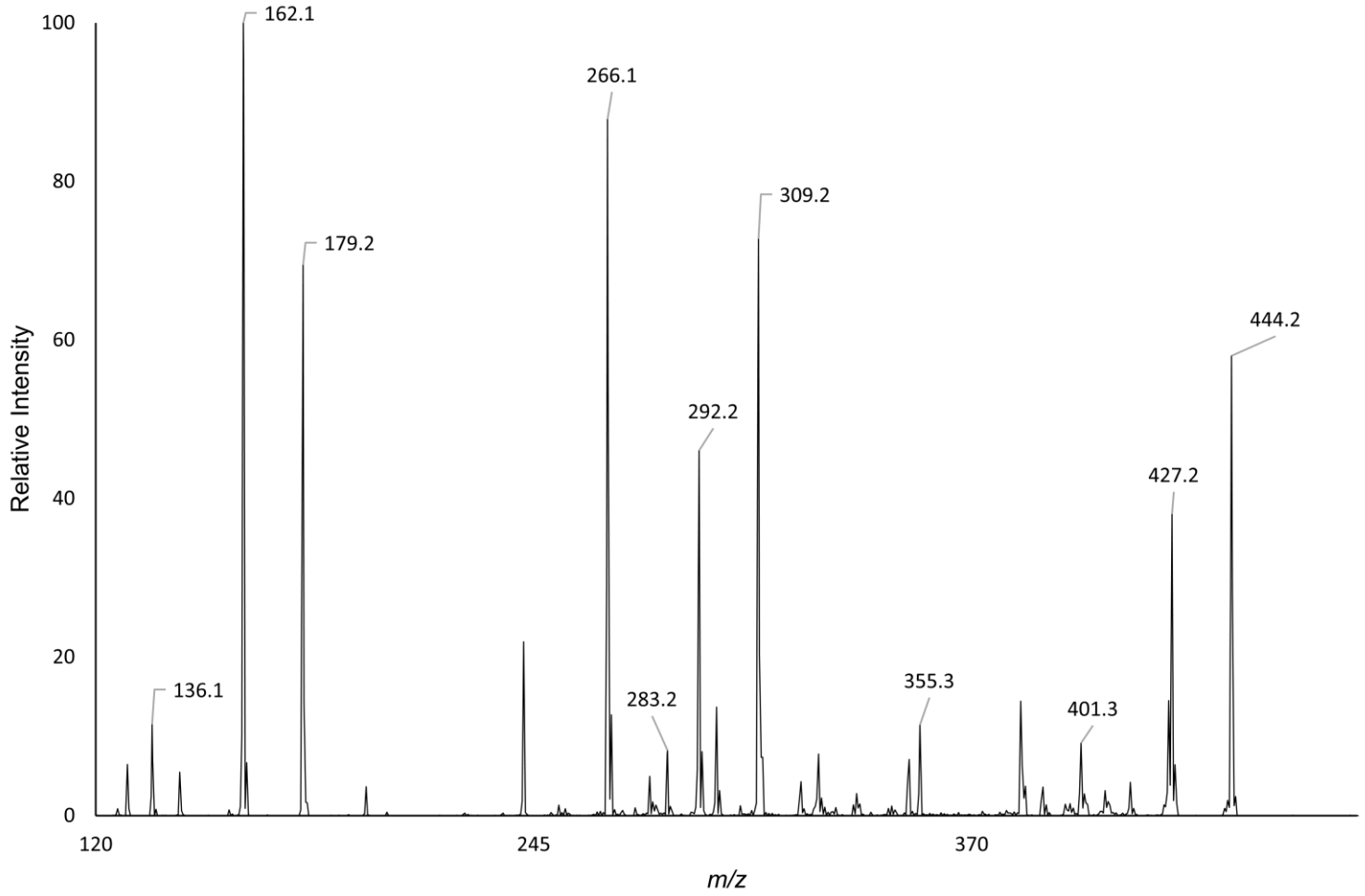

m/z 444 **selected ion ESI-LC/MS^2 mass spectrum with CID fragmentation of the SPE-enriched PIX-12mer enzymatic digestion hydrolysate.**

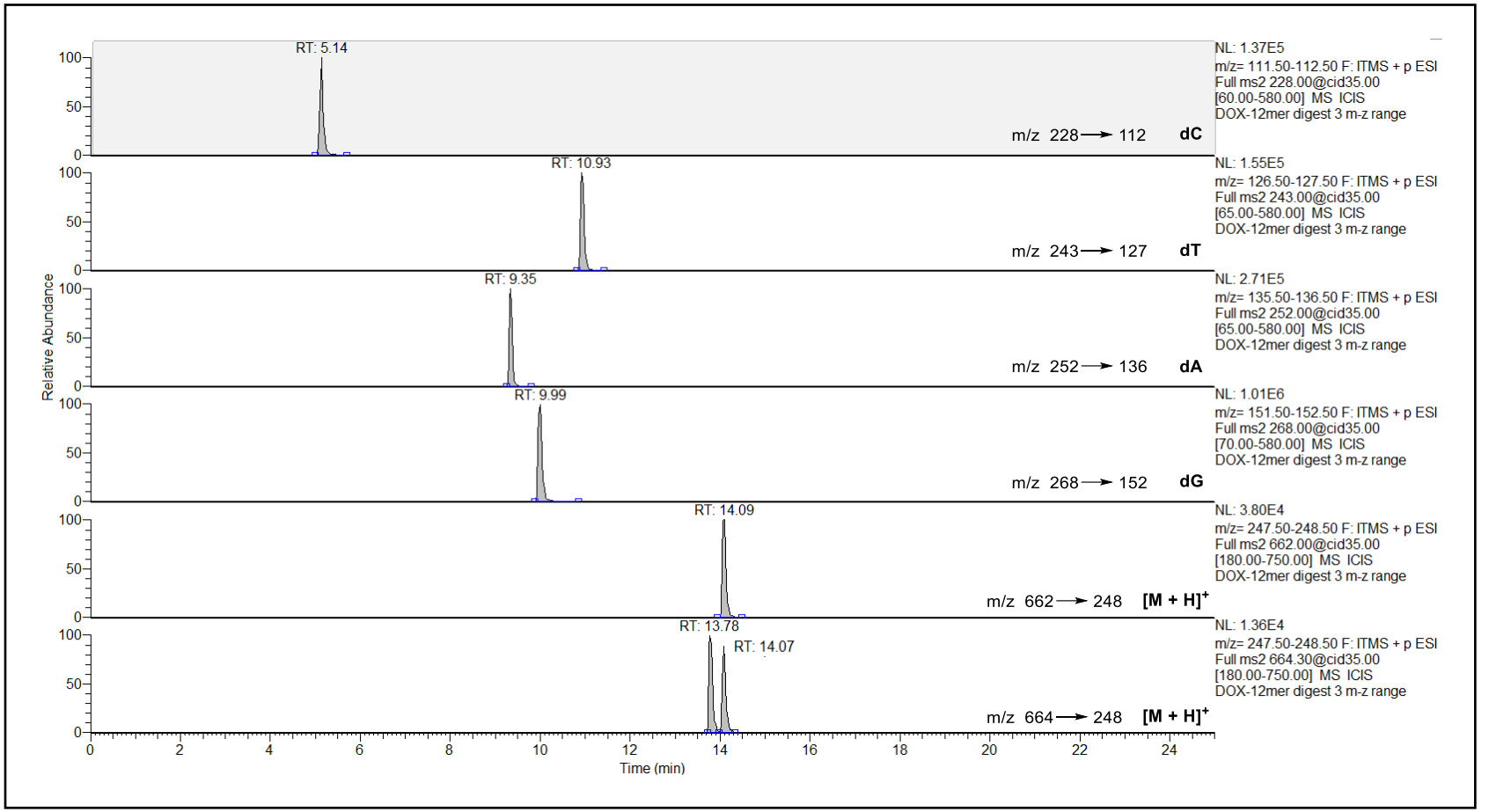

ESI-LC/MS chromatogram of the hydrolysate resulting from enzymatic digestion of the purified DOX-12mer reduced conjugate (5'-GTT GC[AP-DOX] CGT ATG-3').

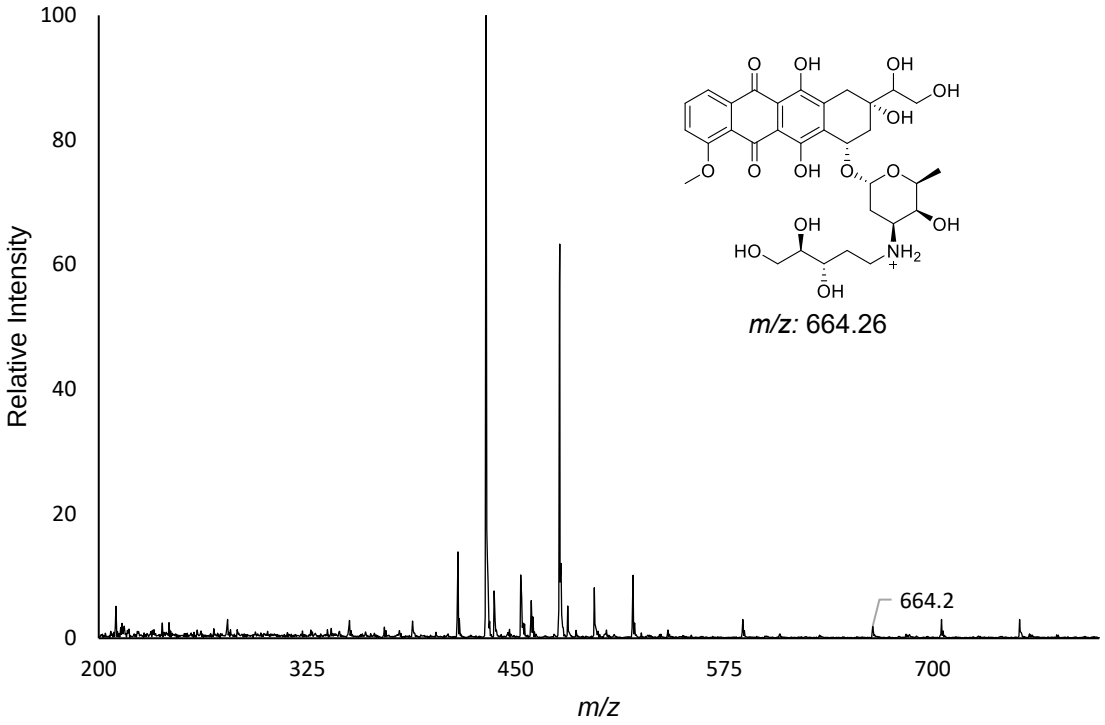

ESI-LC/MS total ion mass spectrum for retention time 13.8 minutes from the SPE-enriched DOX-12mer enzymatic digestion hydrolysate.

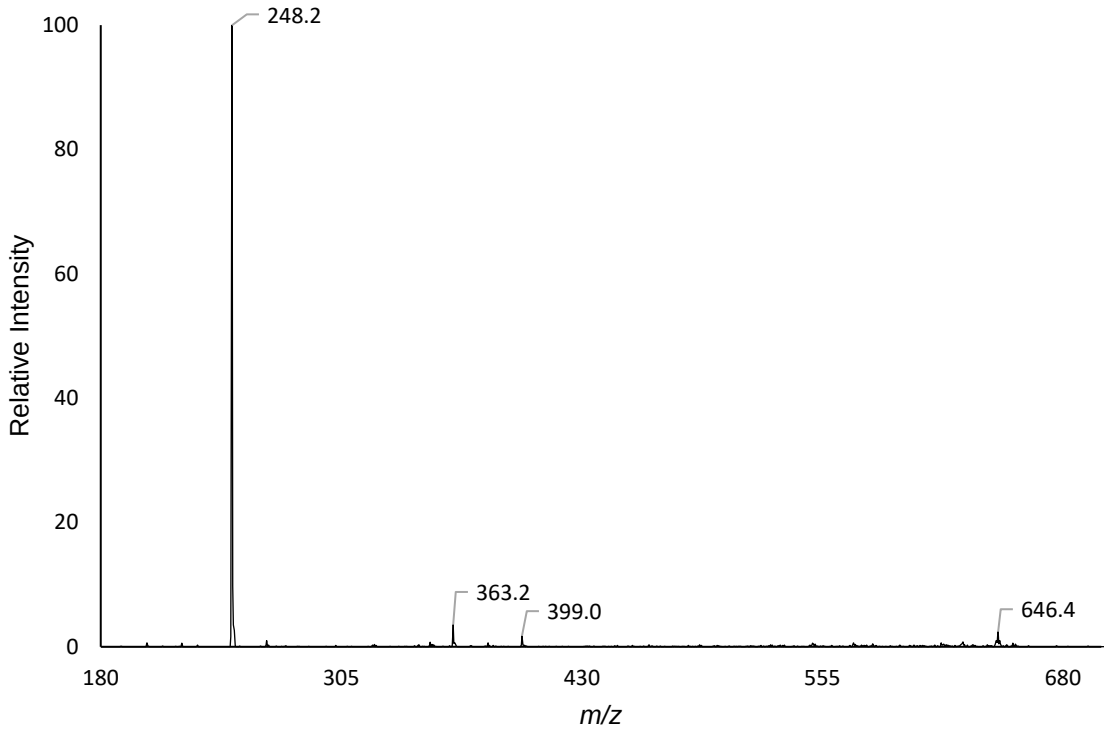

***m/z 664* selected ion ESI-LC/MS^2 mass spectrum with CID fragmentation of the SPE-enriched DOX-12mer enzymatic digestion hydrolysate.**

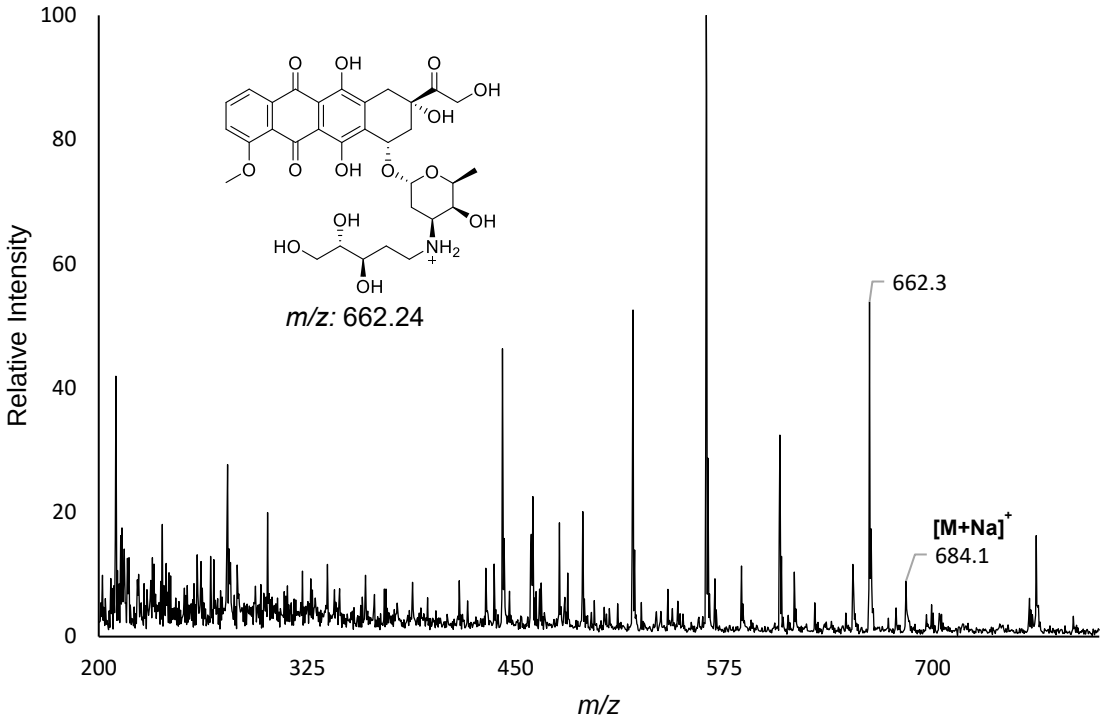

ESI-LC/MS total ion mass spectrum for retention time 14.1 minutes from the SPE-enriched DOX-12mer enzymatic digestion hydrolysate.

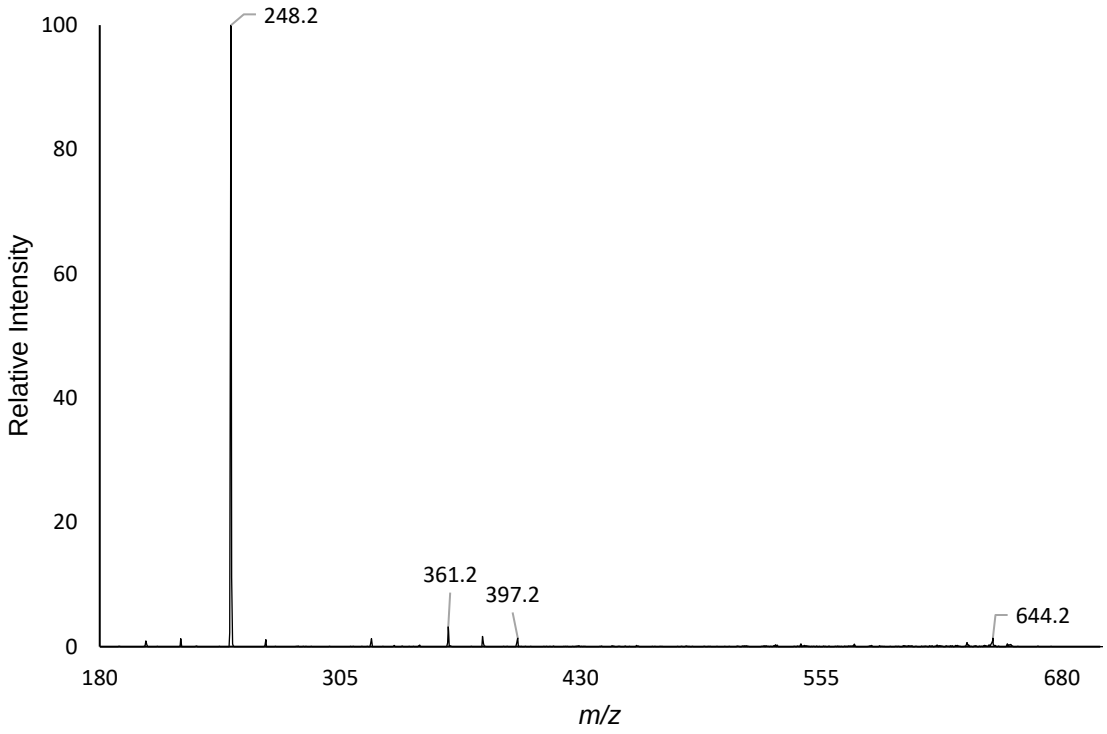

***m/z 662* selected ion ESI-LC/MS^2 mass spectrum with CID fragmentation of the SPE-enriched DOX-12mer enzymatic digestion hydrolysate.**

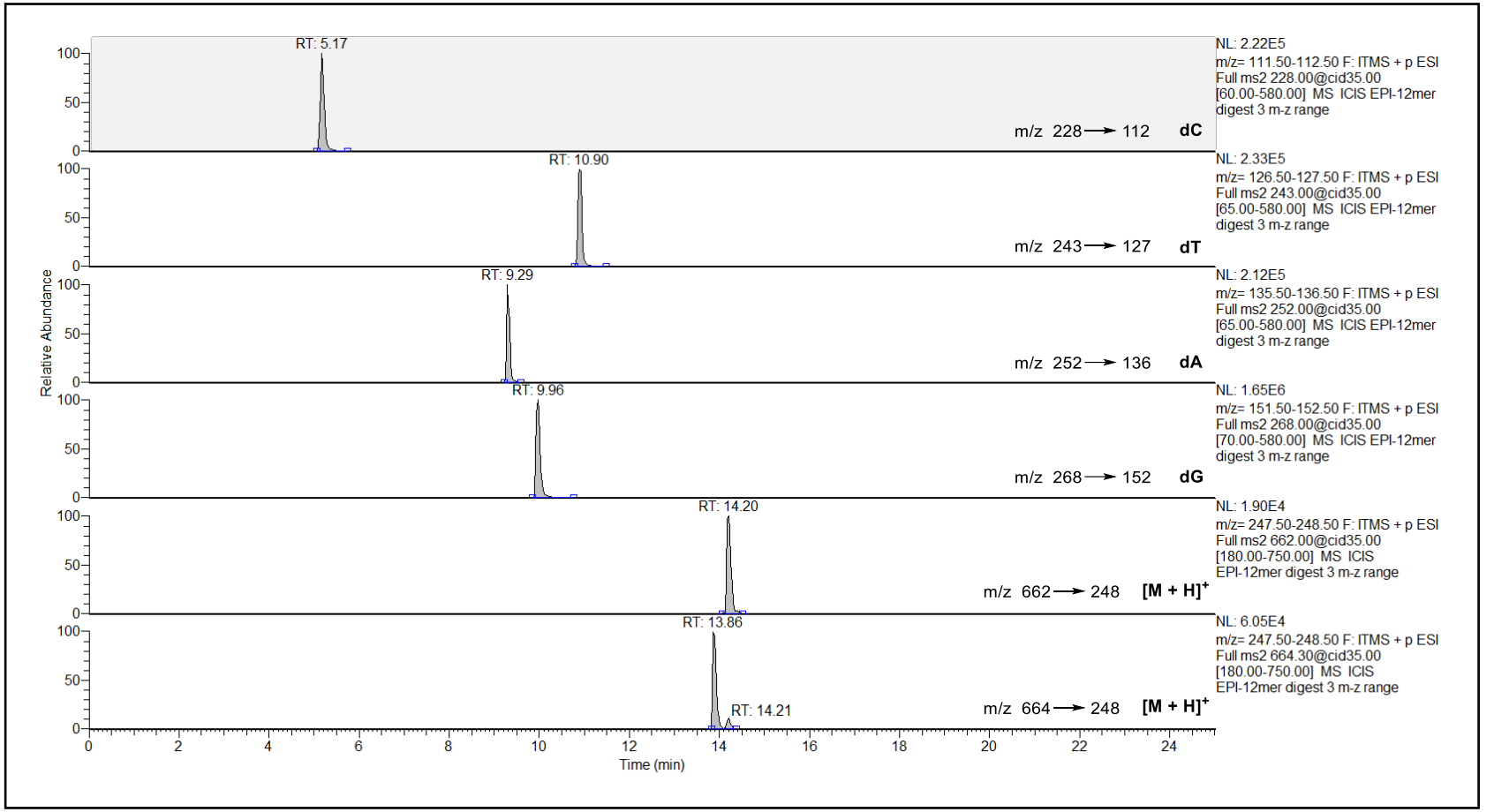

ESI-LC/MS chromatogram of the hydrolysate resulting from enzymatic digestion of the purified EPI-12mer reduced conjugate (5'-GTT GC[AP-EPI] CGT ATG-3').

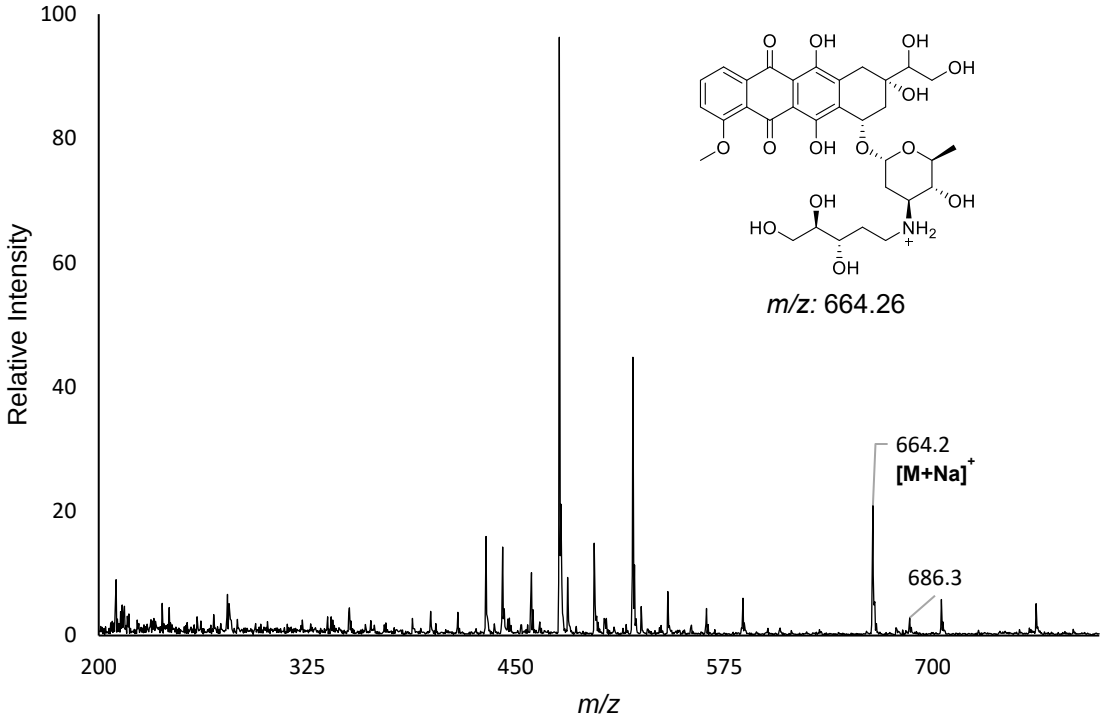

ESI-LC/MS total ion mass spectrum for retention time 13.9 minutes from the SPE-enriched EPI-12mer enzymatic digestion hydrolysate.

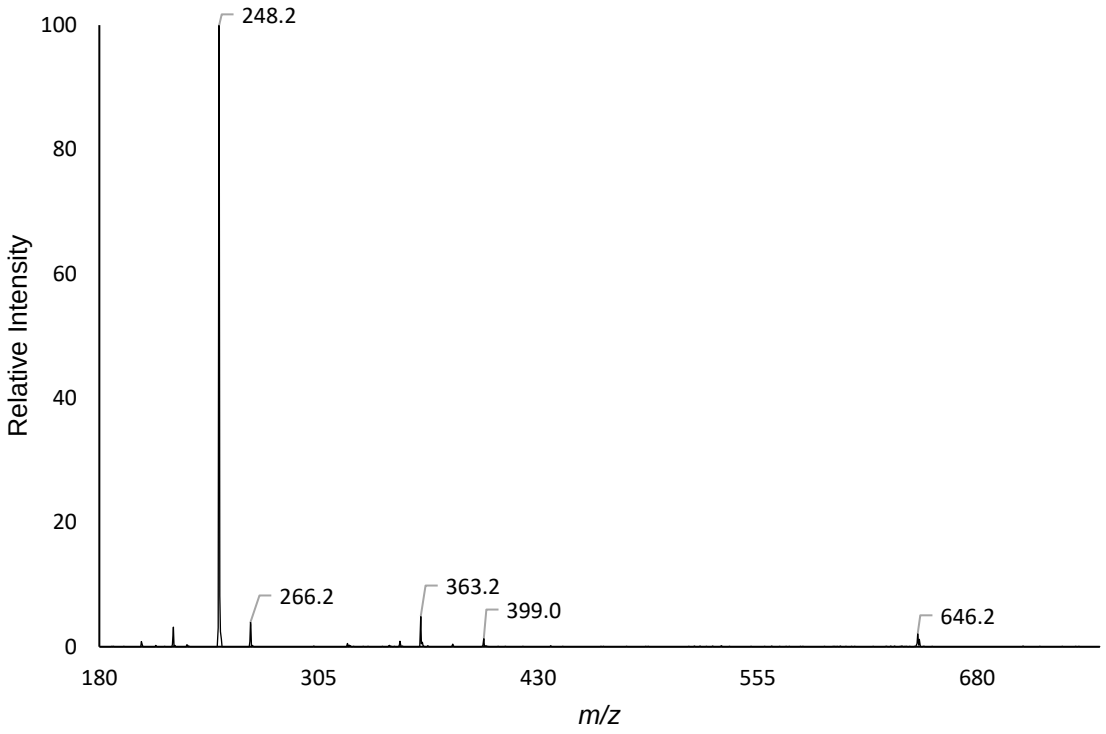

***m/z 664* selected ion ESI-LC/MS^2 mass spectrum with CID fragmentation of the SPE-enriched EPI-12mer enzymatic digestion hydrolysate.**

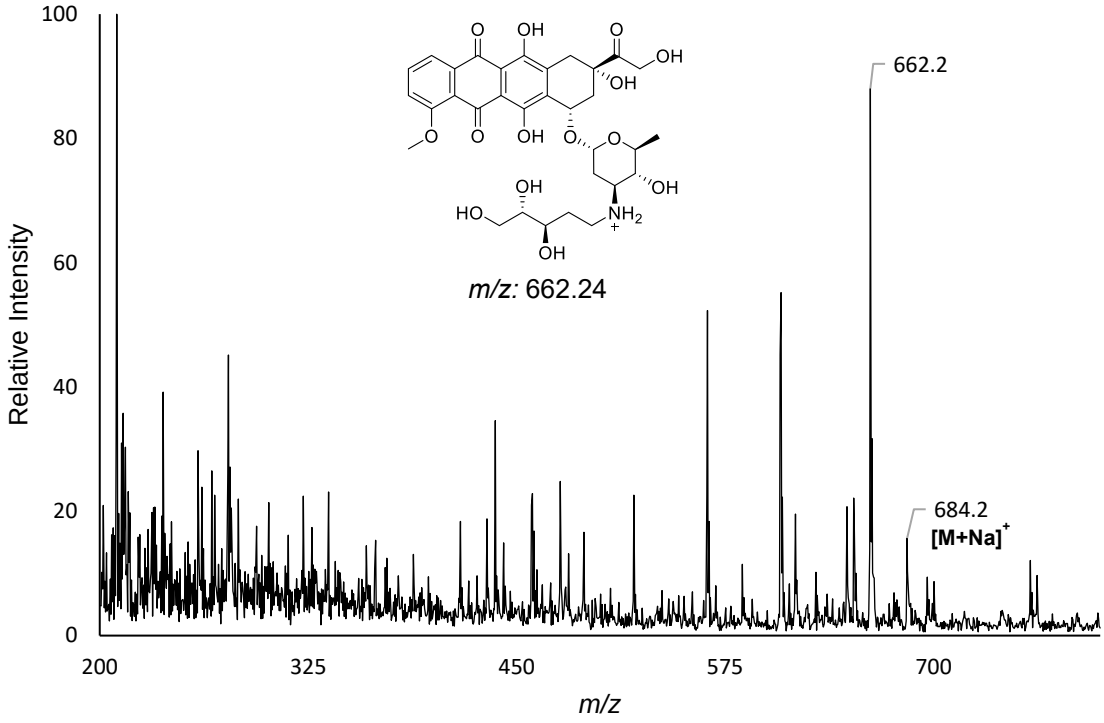

ESI-LC/MS total ion mass spectrum for retention time 14.2 minutes of the SPE-enriched EPI-12mer enzymatic digestion hydrolysate.

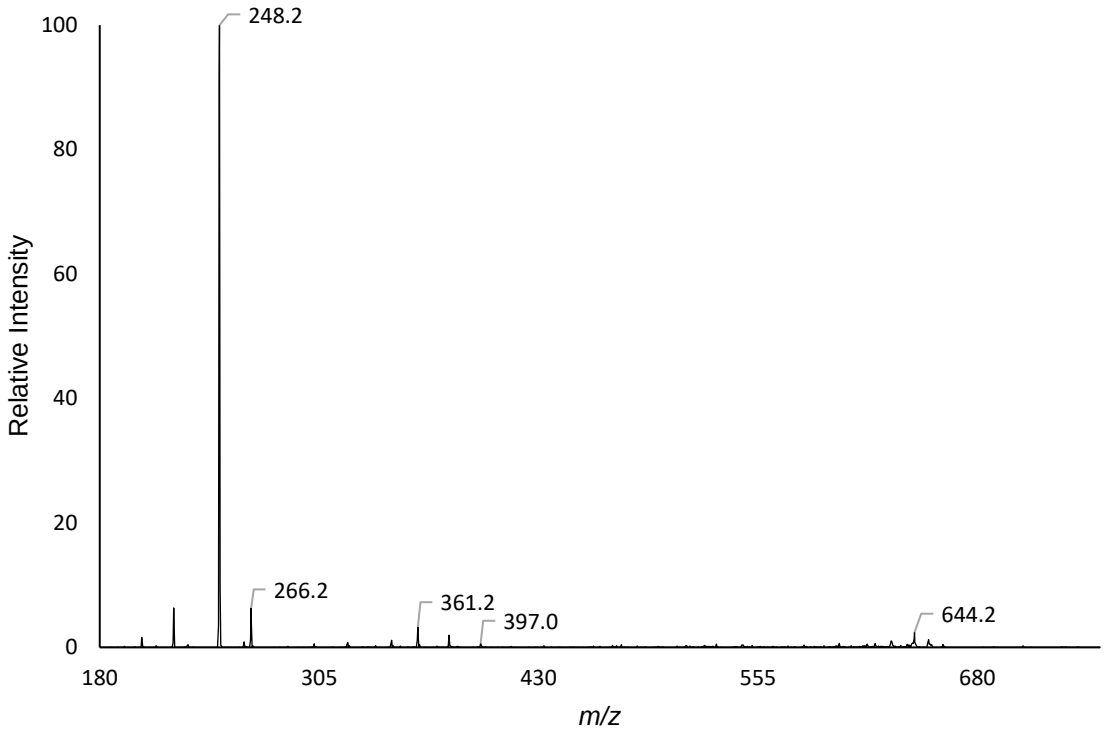

***m/z 662* selected ion ESI-LC/MS^2 mass spectrum with CID fragmentation of the SPE-enriched EPI-12mer enzymatic digestion hydrolysate.**

Appendix V:

HPLC and ESI-LC/MS^2 Characterization of the Purchased 12mer Oligonucleotide β-/δ-elimination Fragment Standards in Chapter III

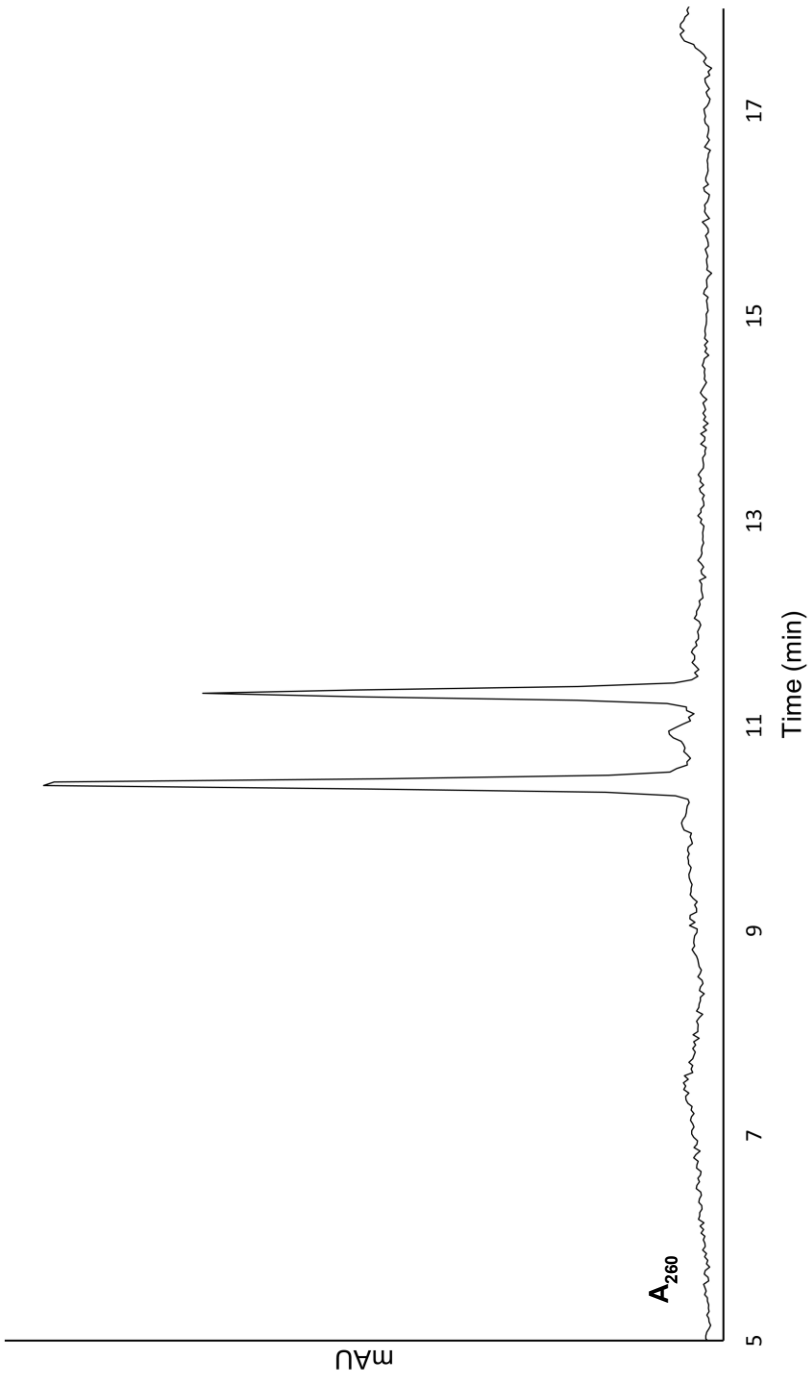

HPLC chromatogram of the purchased 5'-GTT GCp-3' oligonucleotide standard for the 5'-fragment resulting from β-/δ-elimination of the AP-12mer. Two peaks are a result of column-induced dephosphorylation to the 5'-GTT GC-3' oligo.

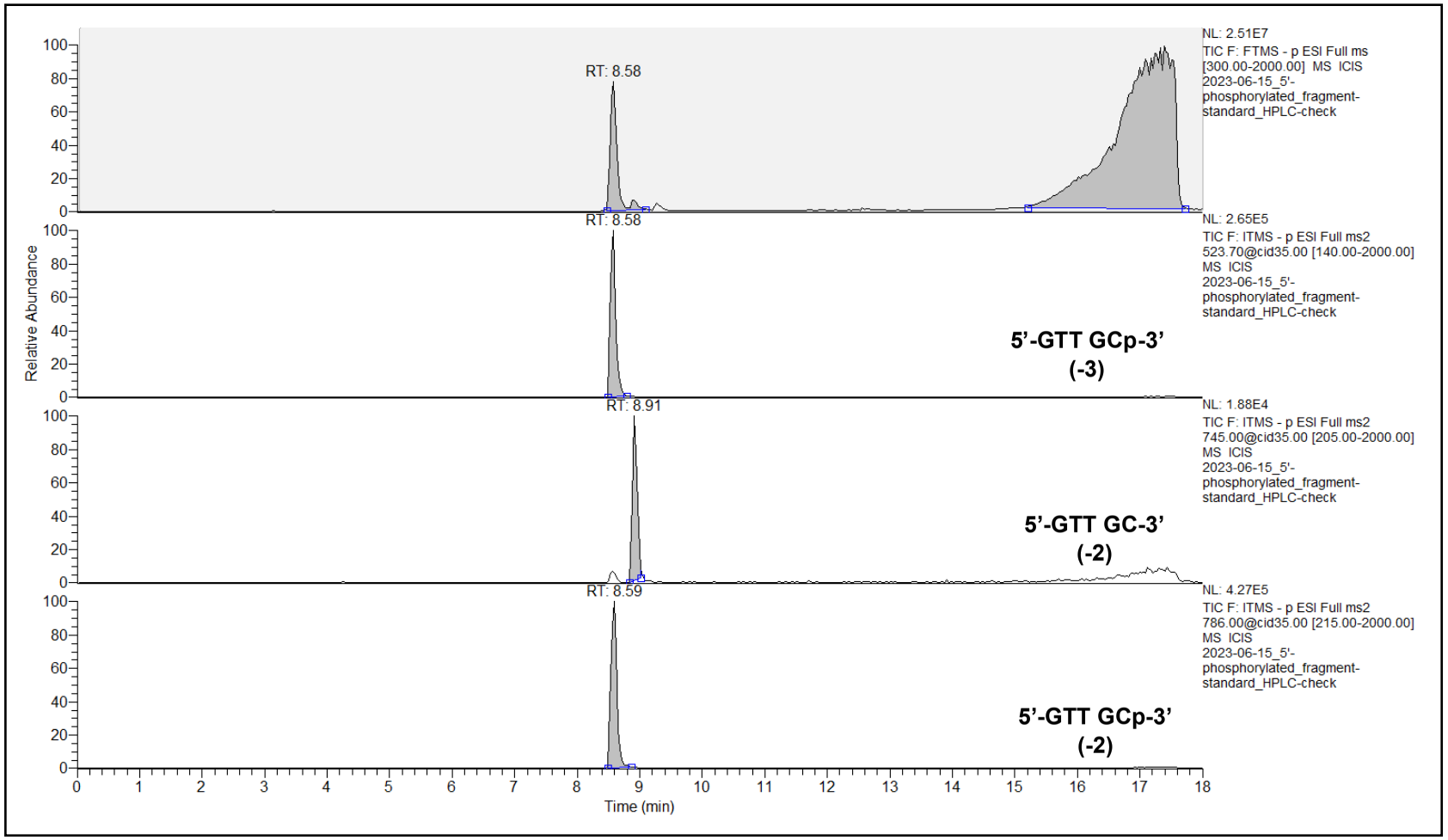

ESI-LC/MS chromatogram of the purchased 5'-GTT GCp-3' oligonucleotide standard for the 5'-fragment resulting from β-/δ-elimination of the AP-12mer. Two peaks are a result of column-induced dephosphorylation to the 5'-GTT GC-3' oligonucleotide.

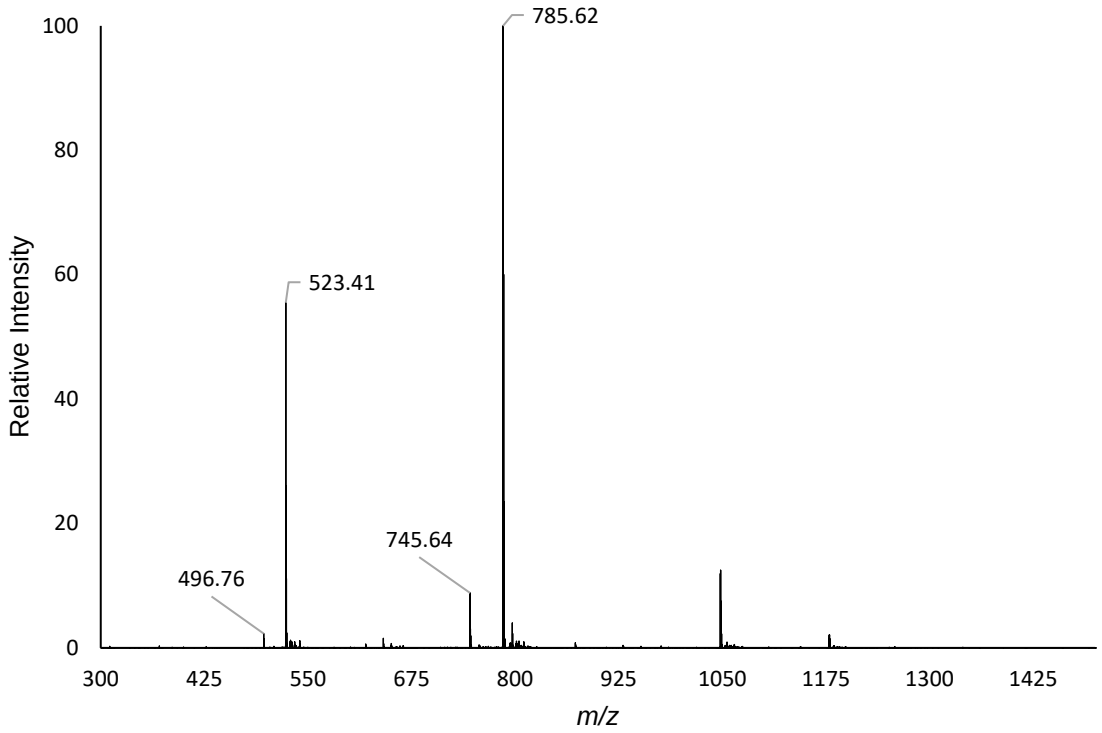

ESI-LC/MS total ion mass spectrum for retention time 8.5-9 minutes of the purchased 5'-GTT GCp-3' oligonucleotide standard for the 5'-fragment resulting from β-/δ-elimination of the AP-12mer.

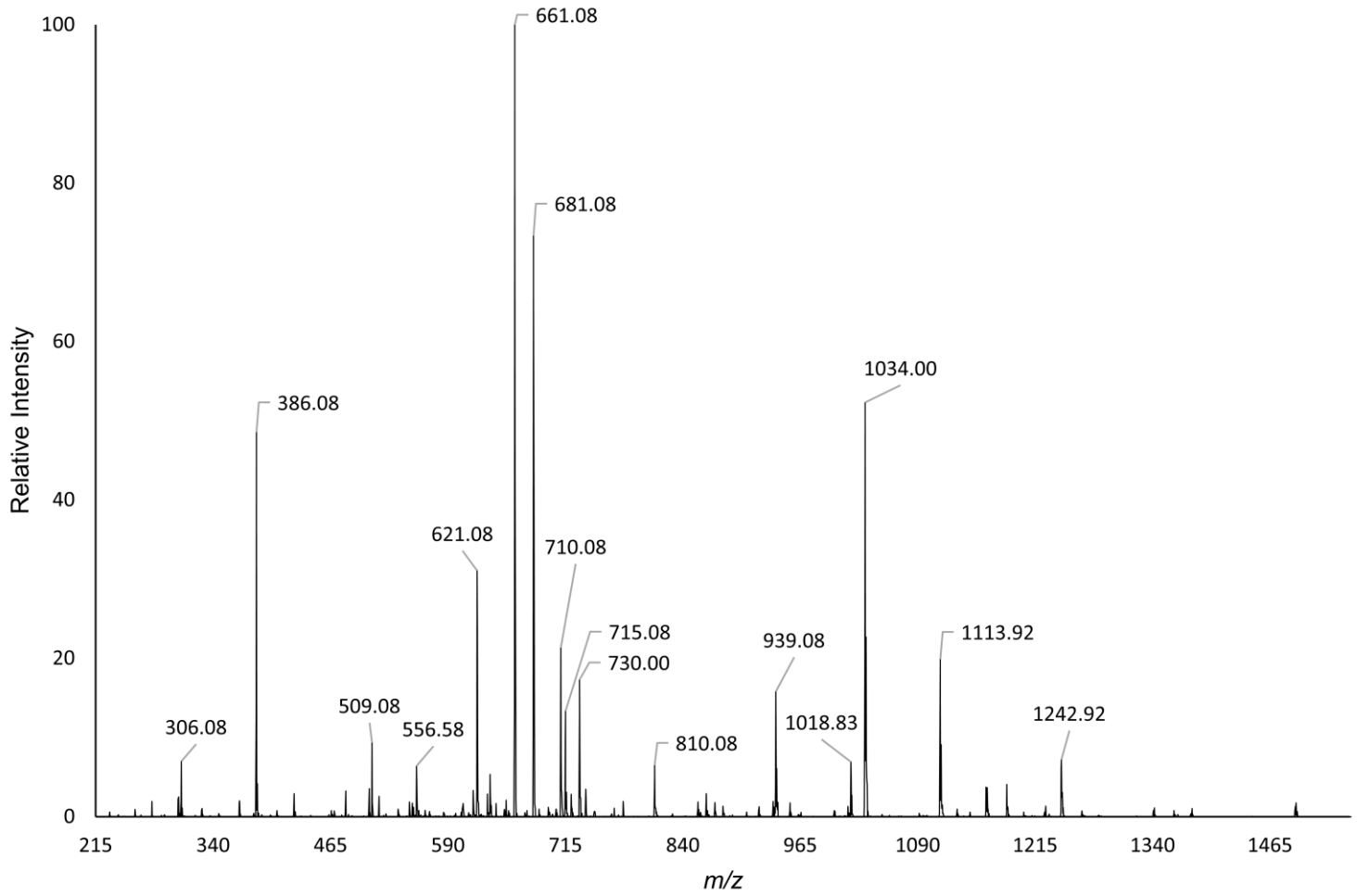

m/z 785 **selected ion ESI-LC/MS^2 mass spectrum with CID fragmentation of the purchased 5'-GTT GCp-3' oligonucleotide standard for the 5'-fragment resulting from β-/δ-elimination of the AP-12mer.**

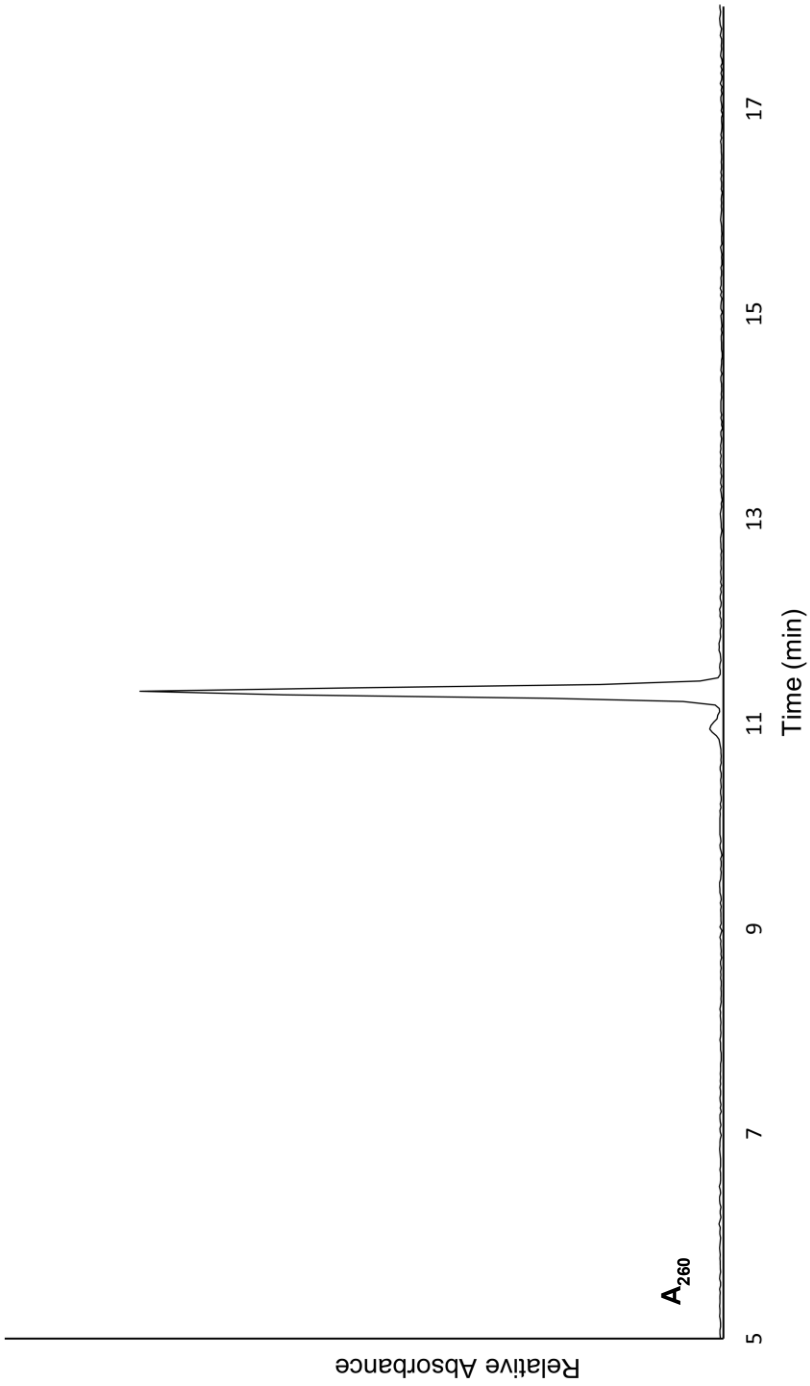

HPLC chromatogram of the purchased 5'-GTT GC-3' oligonucleotide standard for the 5'-fragment resulting from β-/δ-elimination of the AP-12mer.

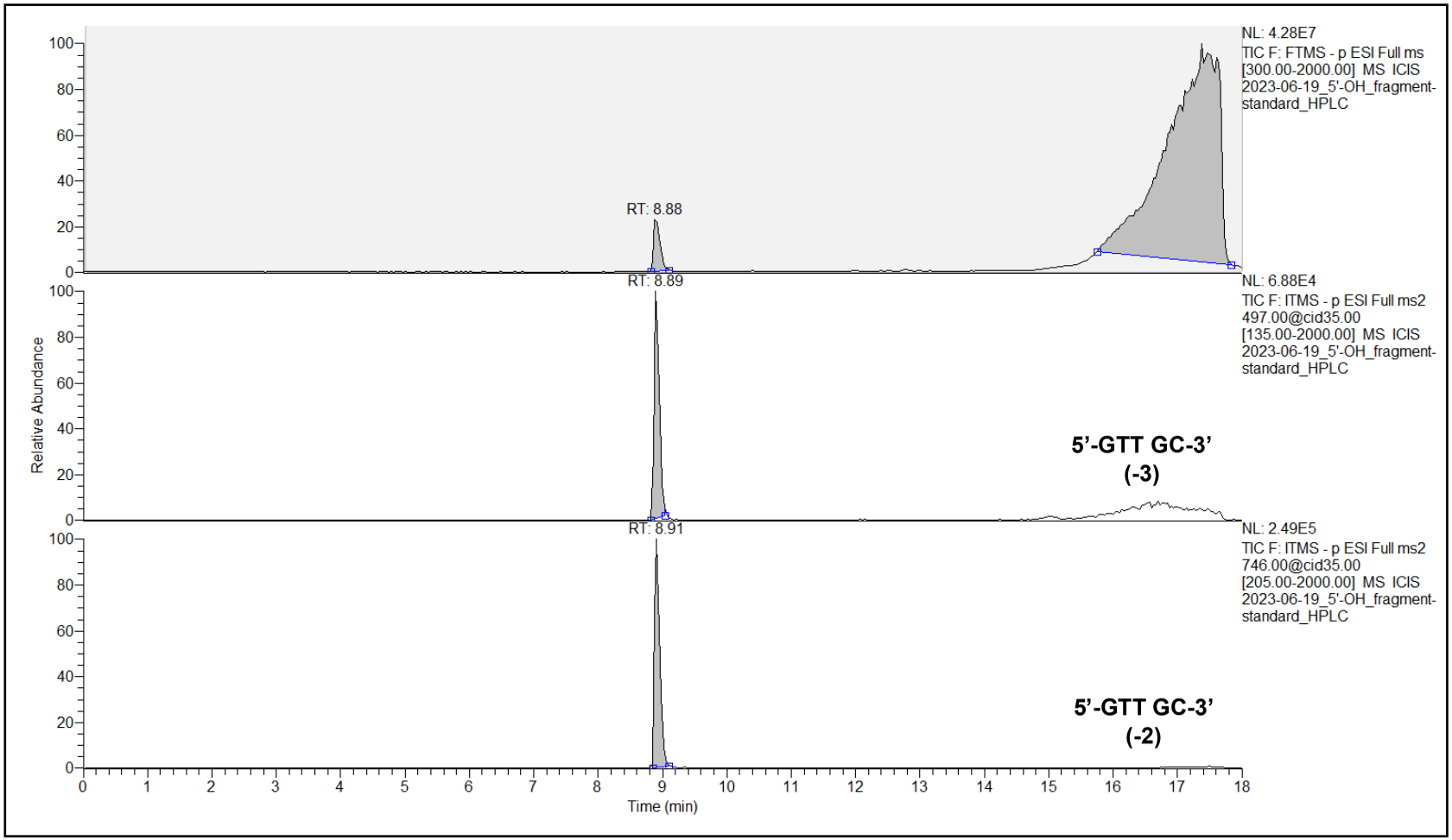

ESI-LC/MS chromatogram of the purchased 5'-GTT GC-3' oligonucleotide standard for the 5'-fragment resulting from β-/δ-elimination of the AP-12mer.

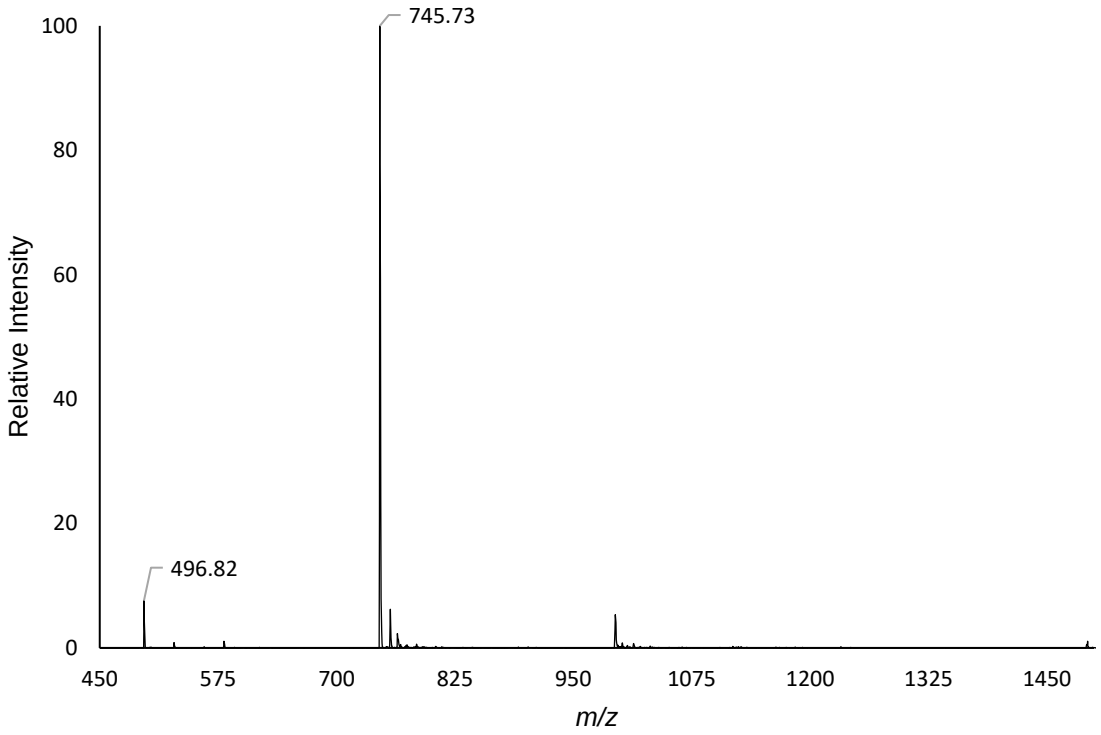

ESI-LC/MS total ion mass spectrum for retention time 8.9 minutes of the purchased 5'-GTT GC-3' oligonucleotide standard for the 5'-fragment resulting from β-/δ-elimination of the AP-12mer.

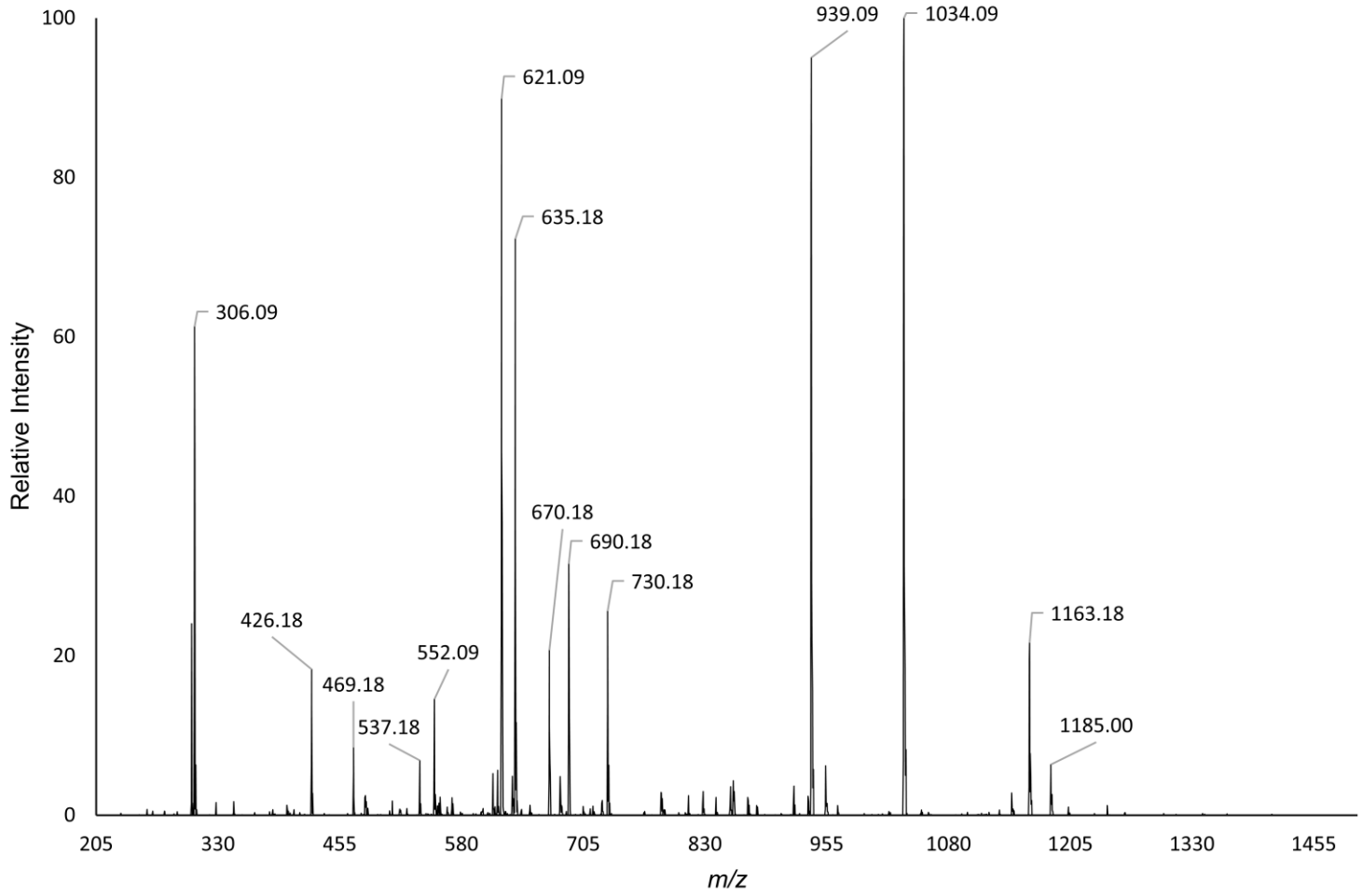

m/z 745 **ESI-LC/MS^2 mass spectrum with CID fragmentation of the purchased 5'-GTT GC-3' oligonucleotide standard for the 5'-fragment resulting from β-/δ-elimination of the AP-12mer.**

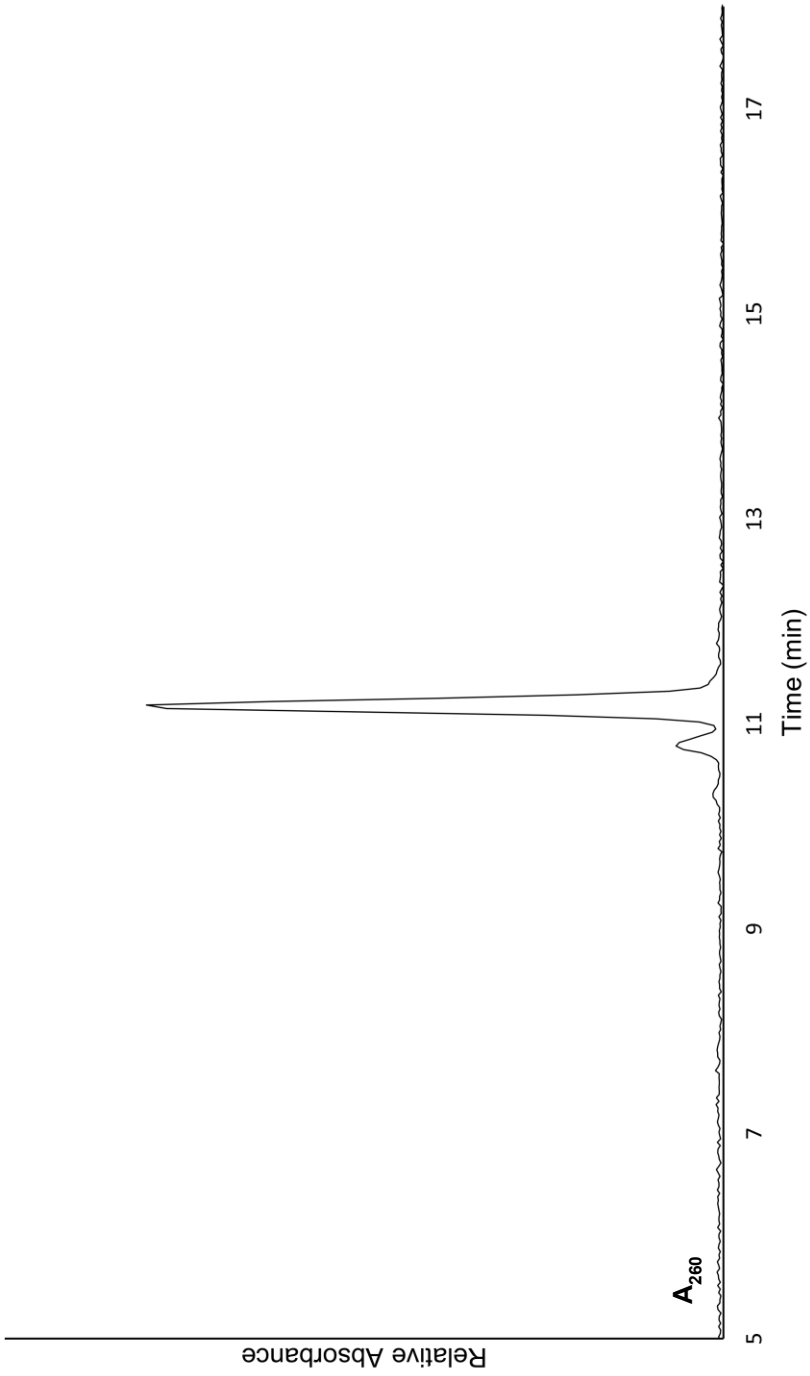

HPLC chromatogram of the purchased 5'-GTT GC(idSp)-3' oligonucleotide standard for the 5'-fragment resulting from β-elimination of the AP-12mer.

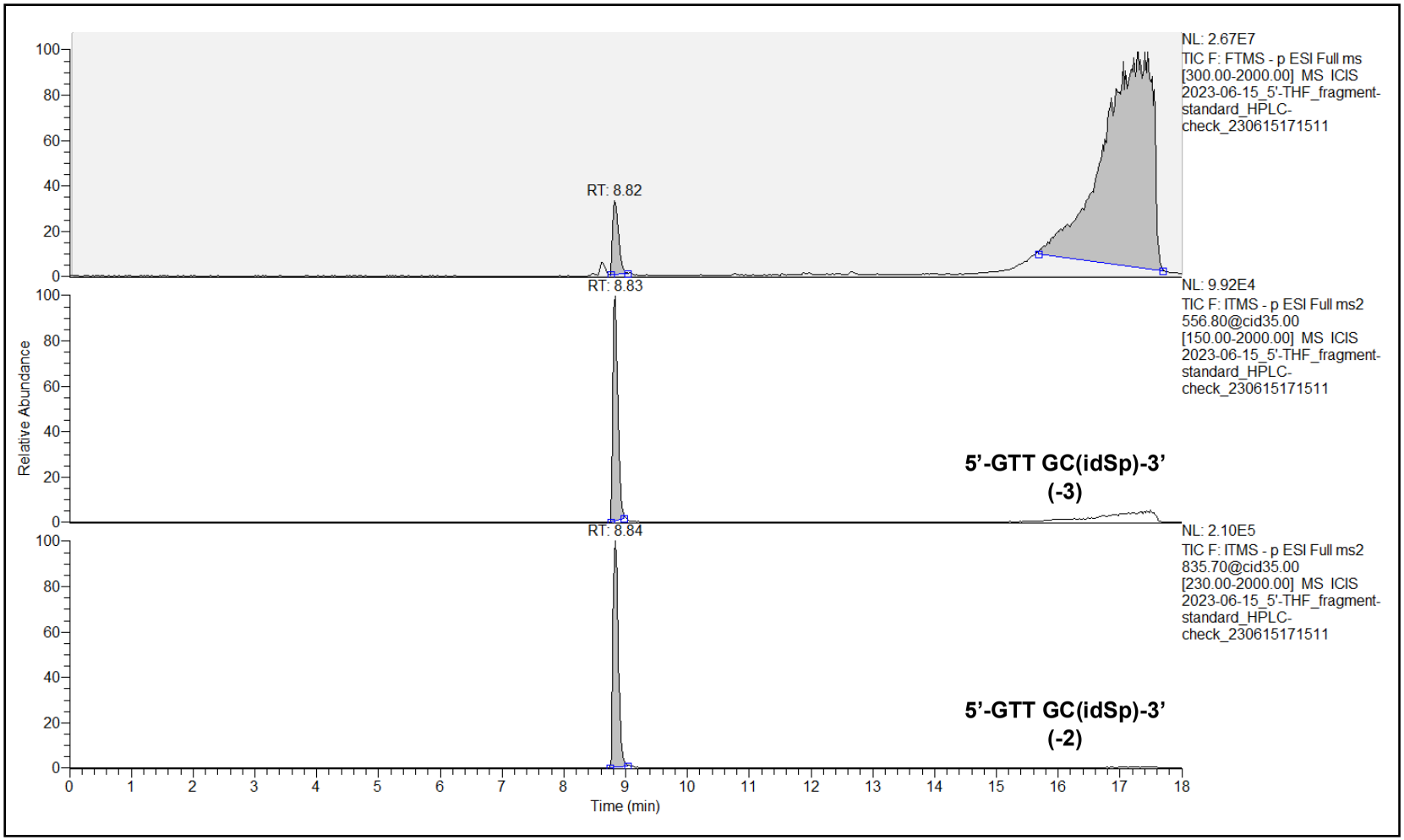

ESI-LC/MS chromatogram of the purchased 5'-GTT GC(idSp)-3' oligonucleotide standard for the 5'-fragment resulting from β-elimination of the AP-12mer.

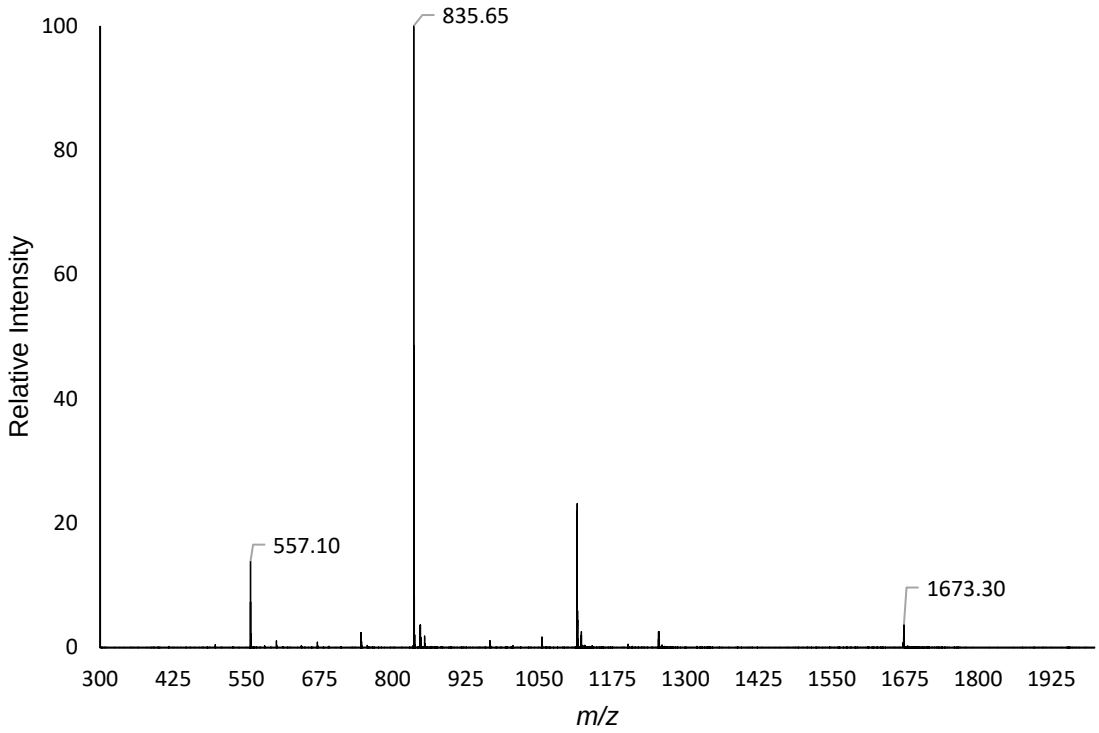

ESI-LC/MS total ion mass spectrum for retention time 8.8 minutes of the purchased 5’-GTT GC(idSp)-3’ oligonucleotide standard for the 5’-fragment resulting from β-elimination of the AP-12mer.

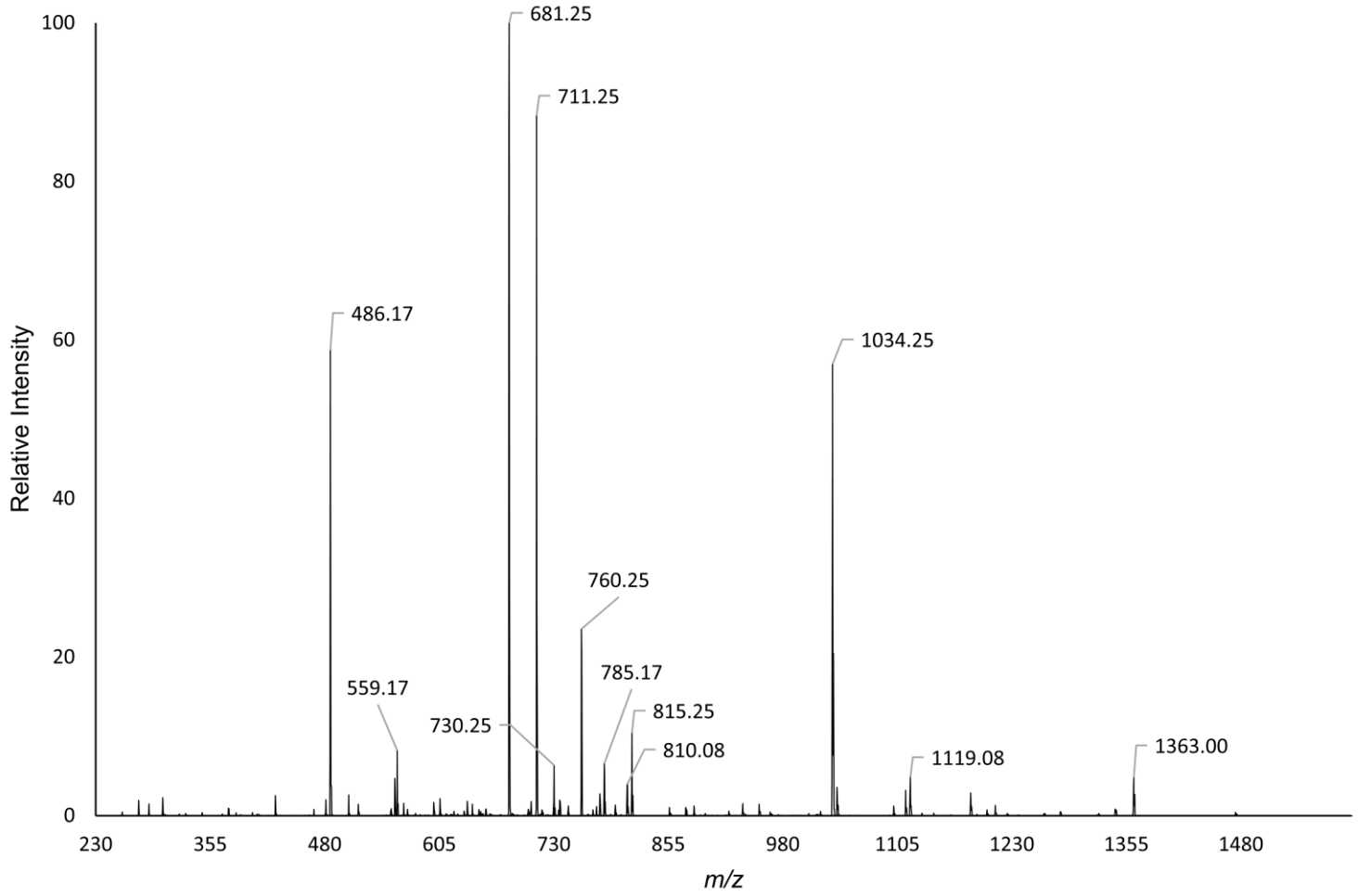

m/z 835 **ESI-LC/MS^2 mass spectrum with CID fragmentation of the purchased 5'-GTT GC(idSp)-3' oligonucleotide standard for the 5'-fragment resulting from β-elimination of the AP-12mer.**

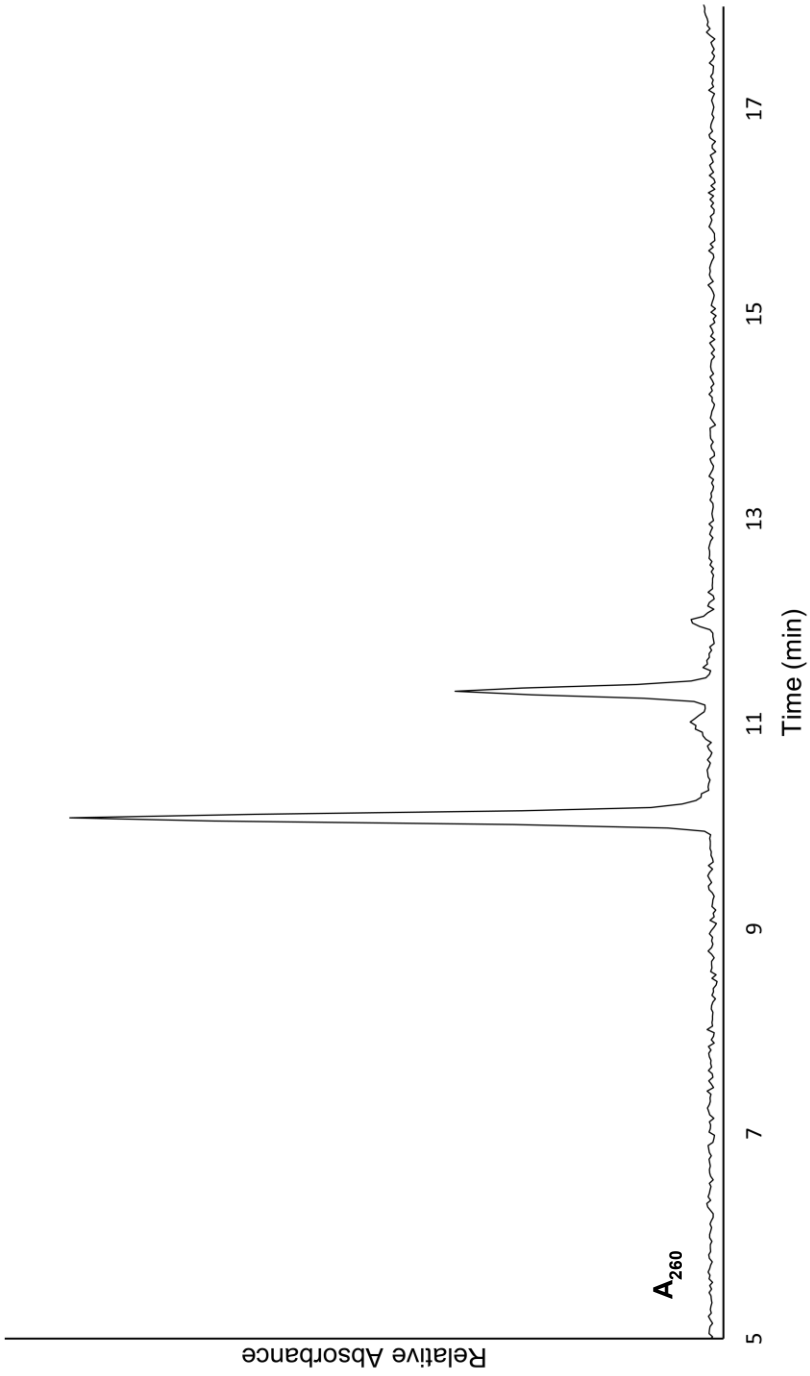

HPLC chromatogram of the purchased 5'-pCGT ATG-3' oligonucleotide standard for the 3'-fragment resulting from β-/δ-elimination of the AP-12mer. Two peaks are a result of column-induced dephosphorylation to the 5'-CGT ATG-3' oligonucleotide.

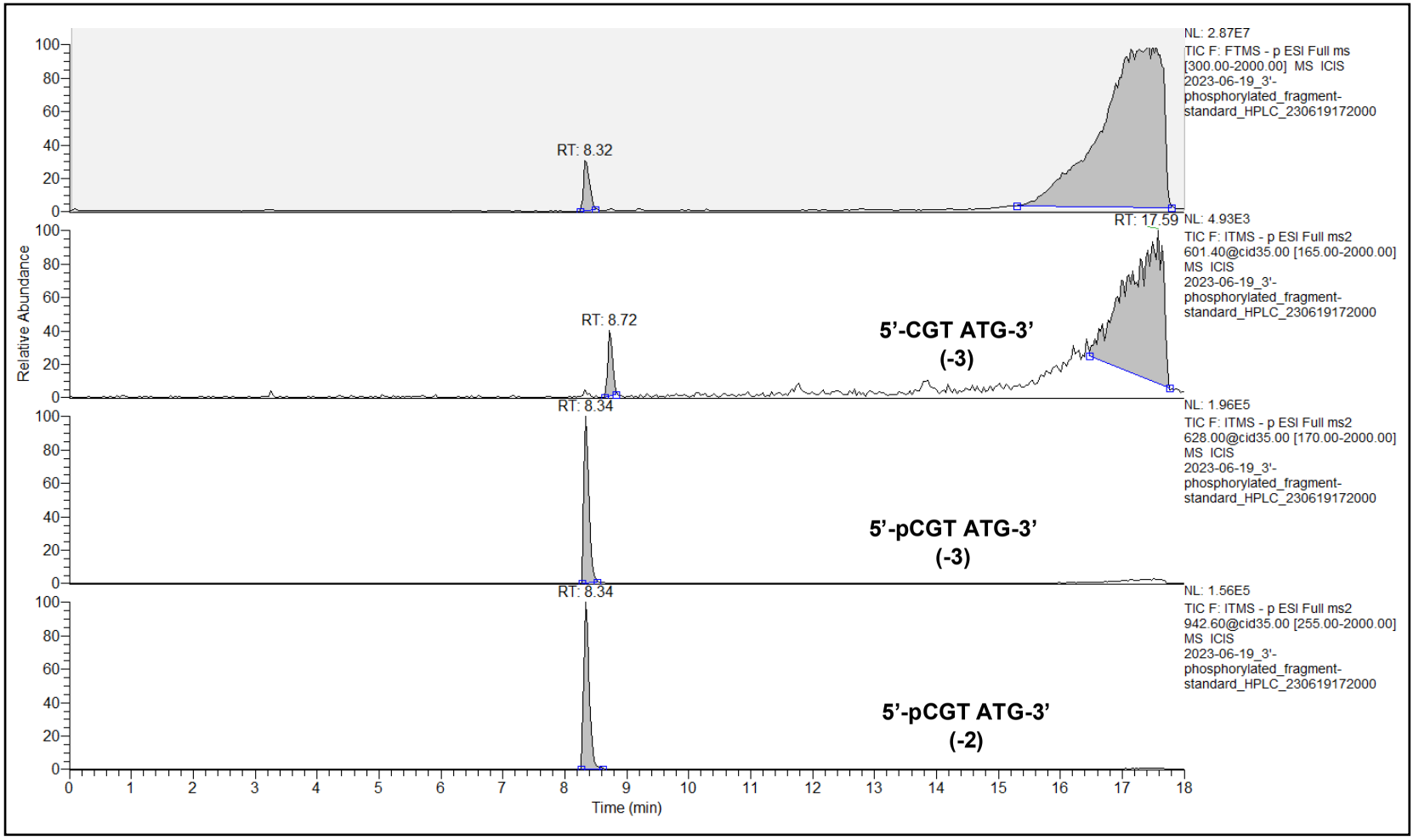

ESI-LC/MS chromatogram of the purchased 5'-pCGT ATG-3' oligonucleotide standard for the 3'-fragment resulting from β-/δ-elimination of the AP-12mer. Two peaks are a result of column-induced dephosphorylation to the 5'-pCGT ATG-3' oligonucleotide.

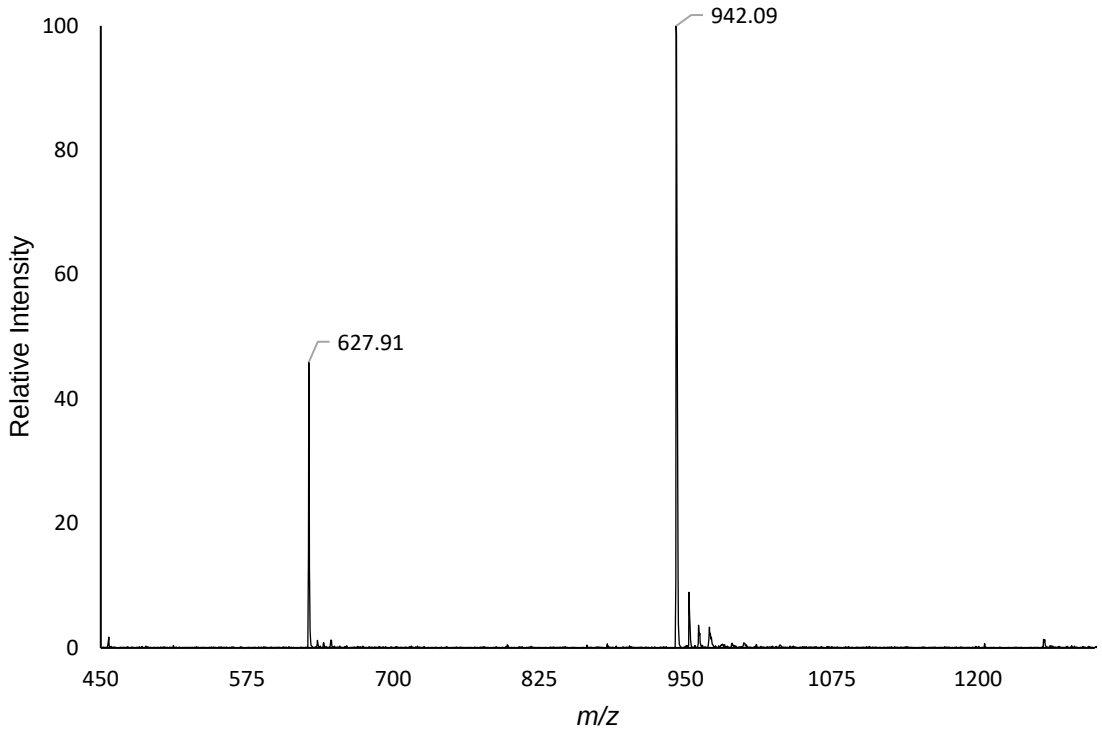

ESI-LC/MS total ion mass spectrum for retention time 8.3-8.8 minutes of the purchased 5'-pCGT ATG-3' oligonucleotide standard for the 3'-fragment resulting from β-/δ-elimination of the AP-12mer.

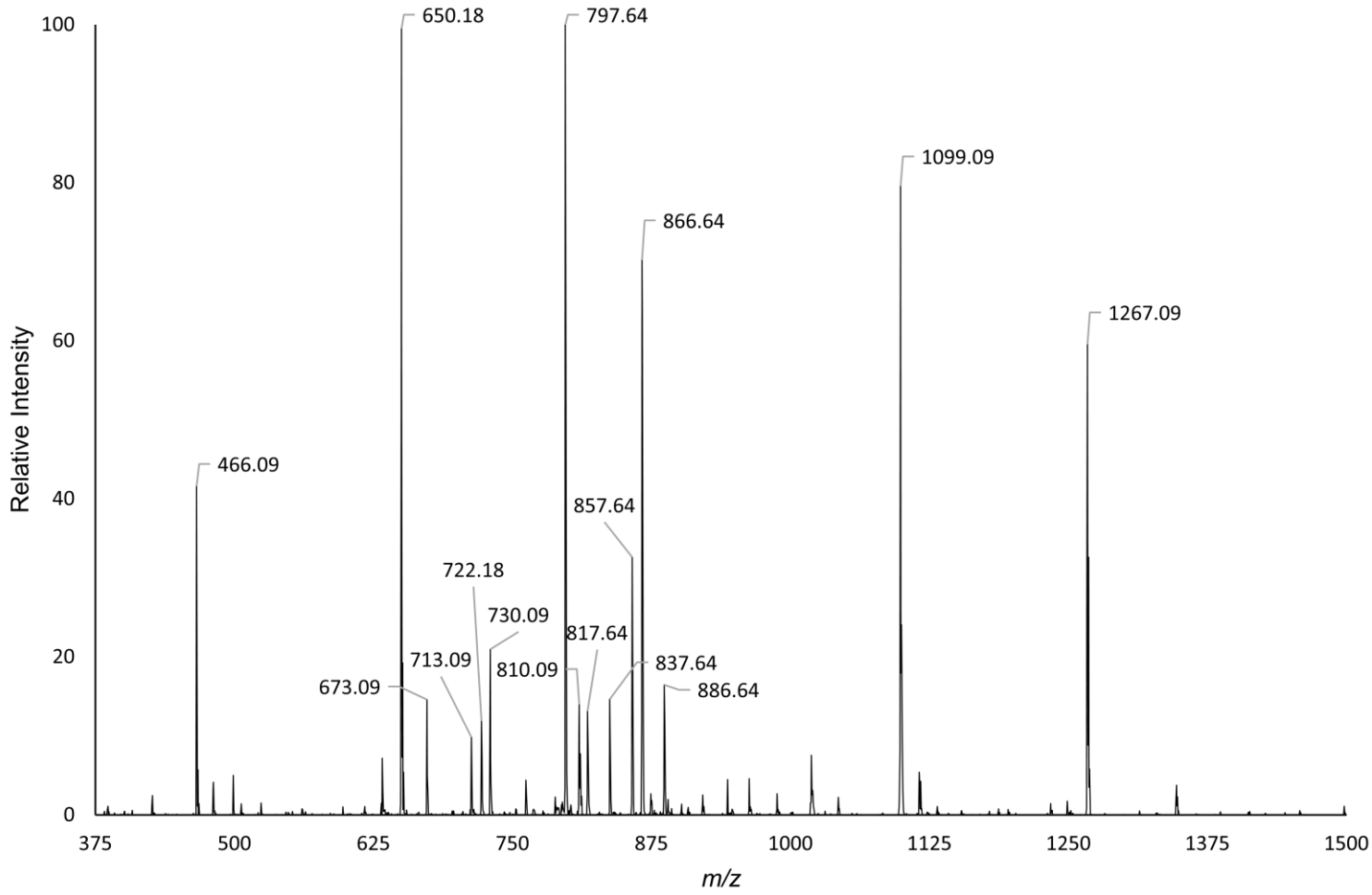

m/z 942 **ESI-LC/MS^2 mass spectrum with CID fragmentation of the purchased 5'-pCGT ATG-3' oligonucleotide standard for the 3'-fragment resulting from β-/δ-elimination of the AP-12mer.**

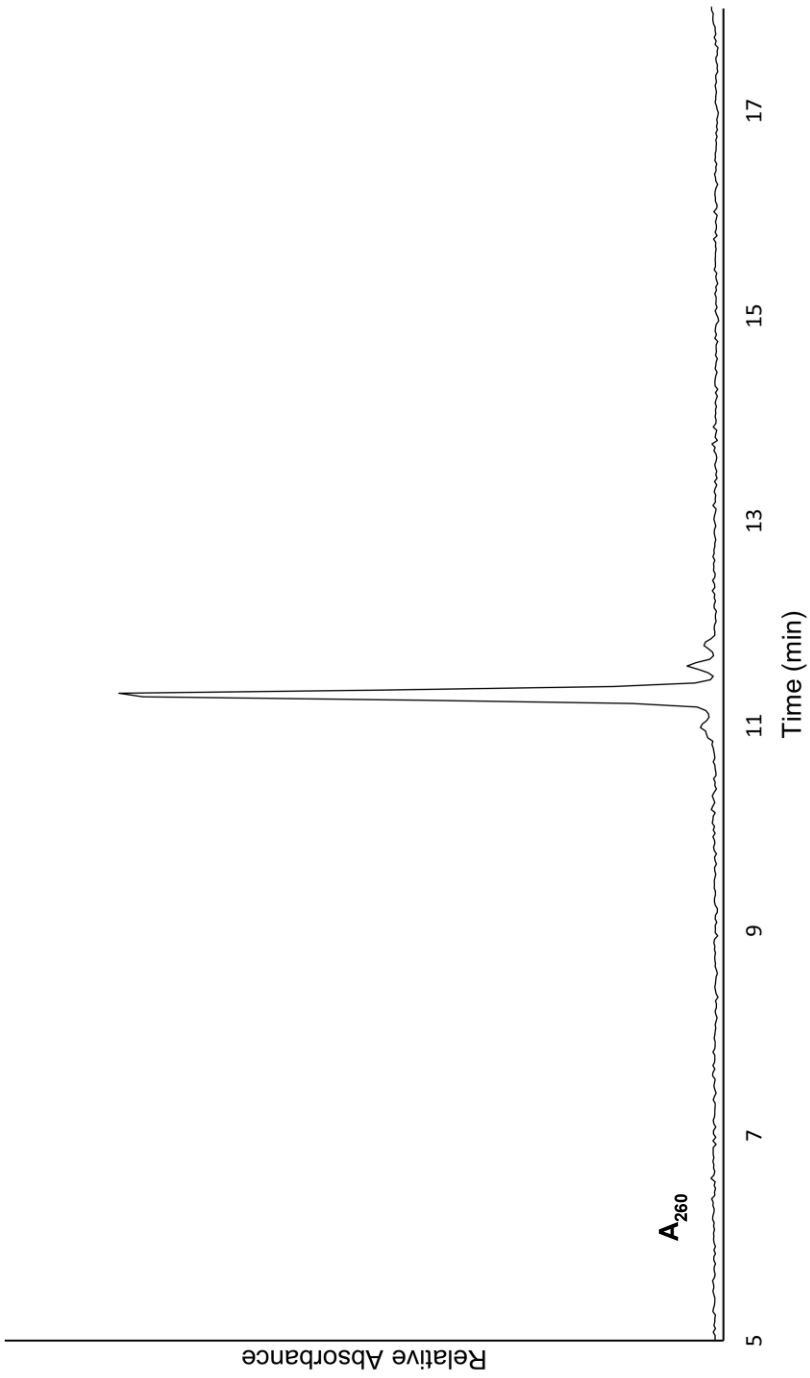

HPLC chromatogram of the purchased 5'-CGT ATG-3' oligonucleotide standard for the 3'-fragment resulting from β-/δ-elimination of the AP-12mer.

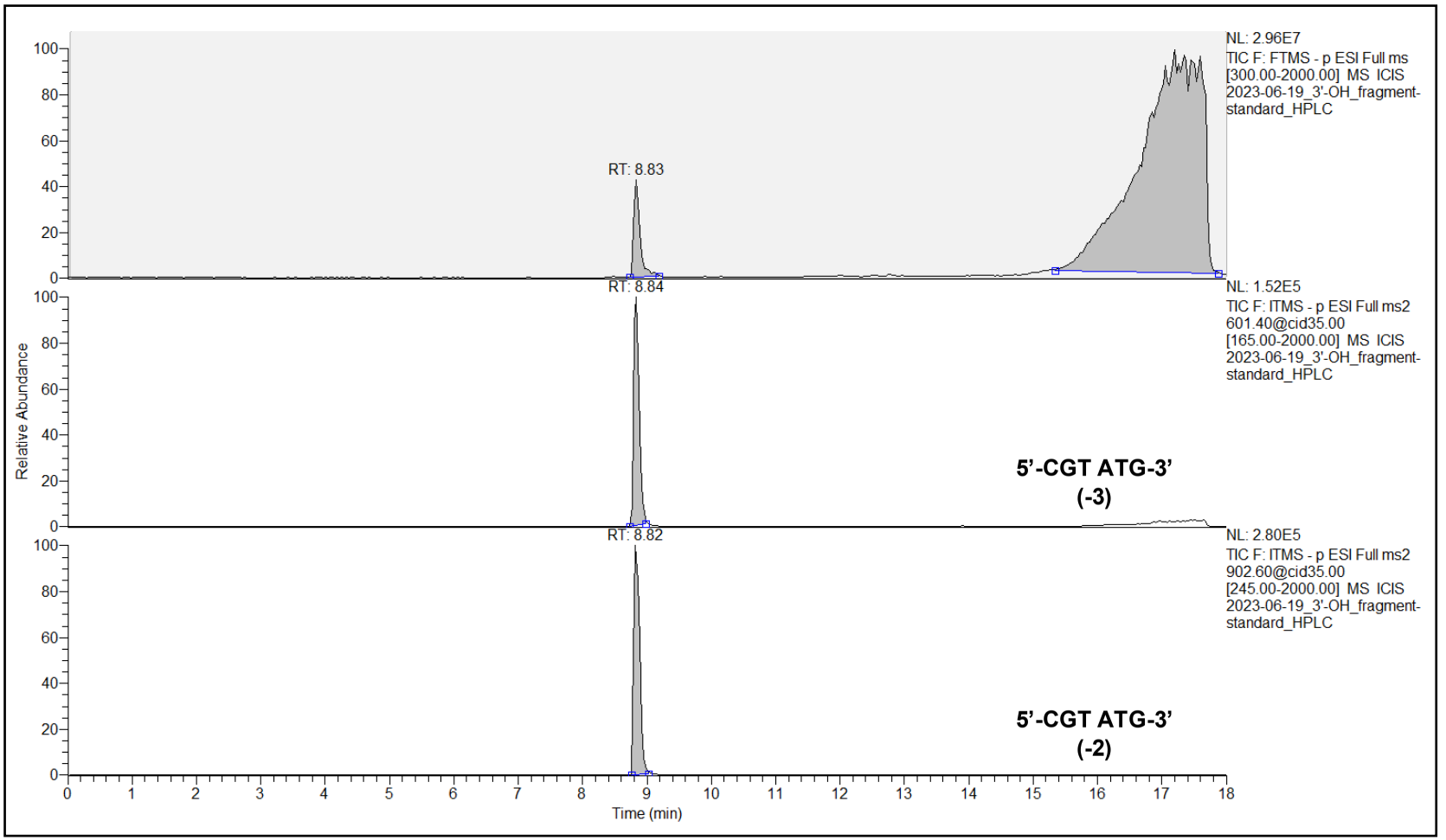

ESI-LC/MS chromatogram of the purchased 5'-CGT ATG-3' oligonucleotide standard for the 3'-fragment resulting from β-/δ-elimination of the AP-12mer.

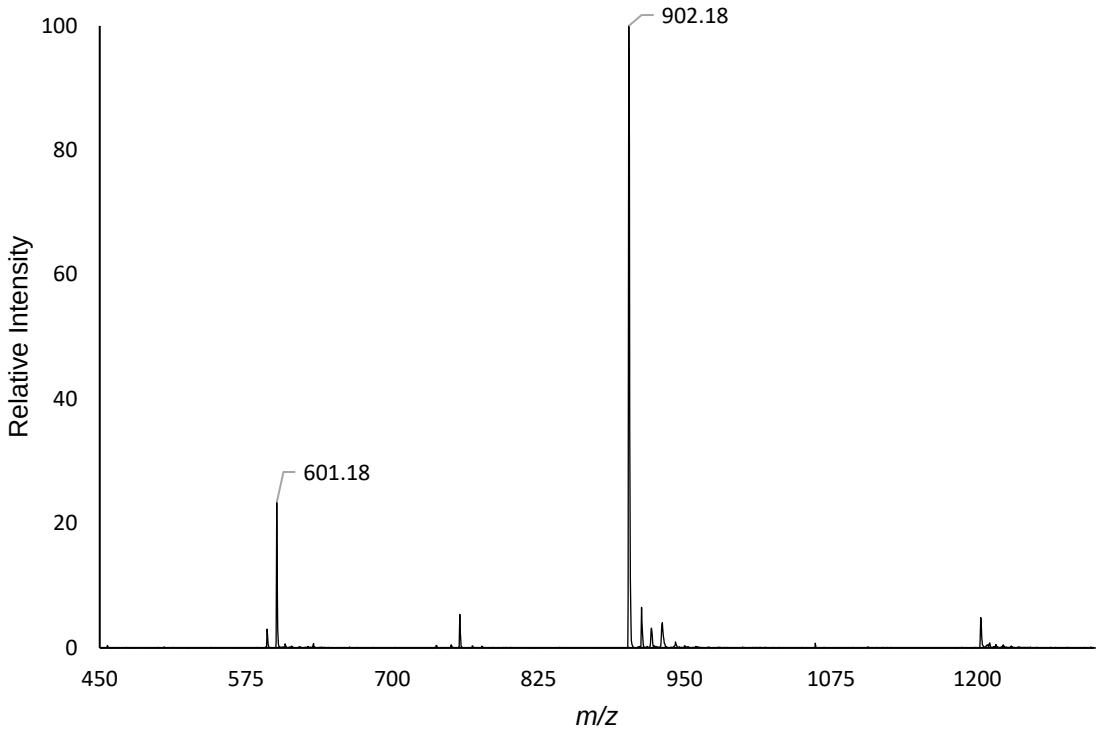

ESI-LC/MS total ion mass spectrum for retention time 8.8 minutes of the purchased 5'-CGT ATG-3' oligonucleotide standard for the 3'-fragment resulting from β-/δ-elimination of the AP-12mer.

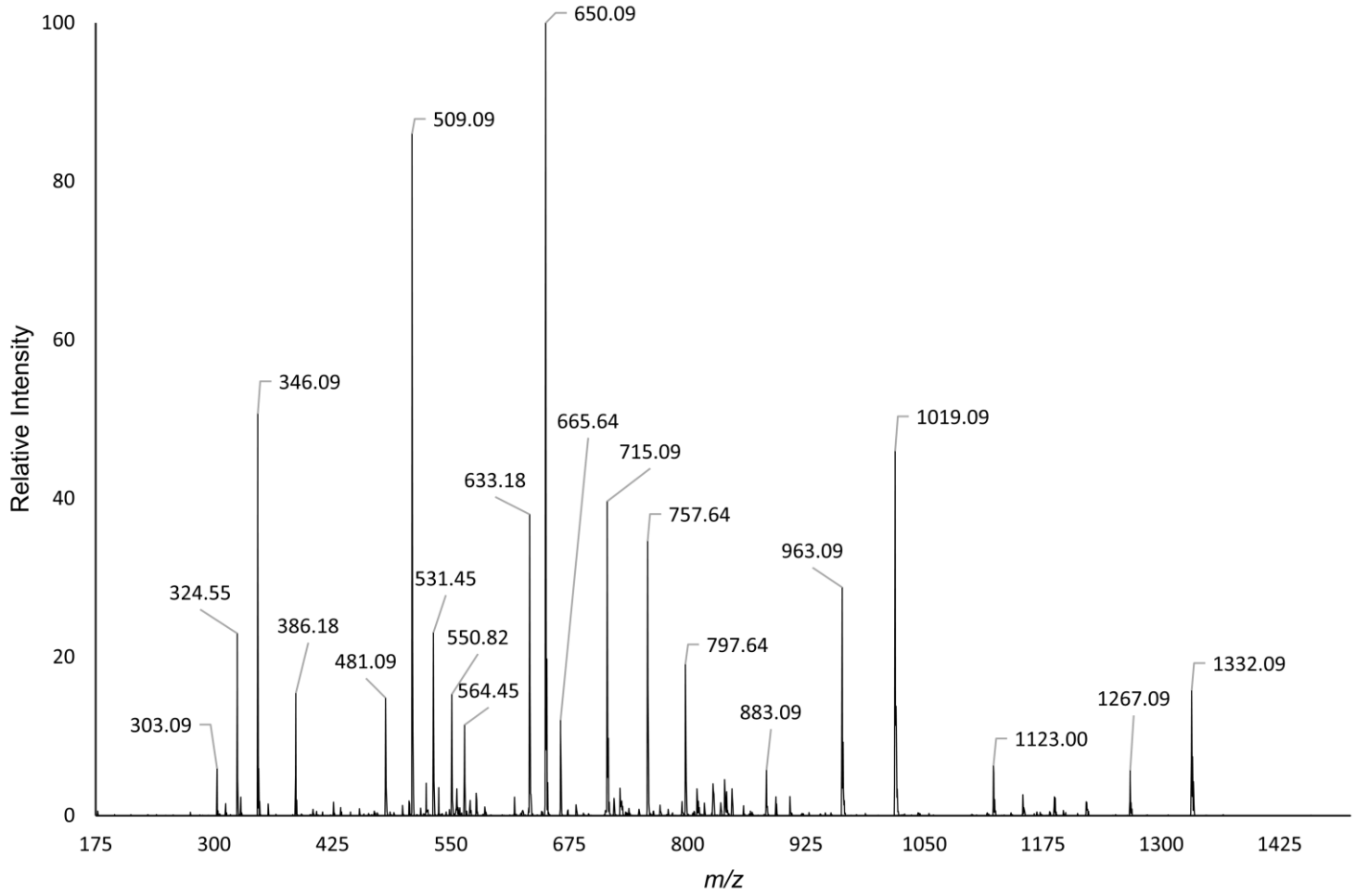

m/z 902 ESI-LC/MS^2 mass spectrum with CID fragmentation of the purchased 5'-GTT GC-3' oligonucleotide standard for the 3'-fragment resulting from β-/δ-elimination of the AP-12mer.

Appendix VI

HPLC and ESI-LC/MS^2/MS^3 Characterization of Anthracycline-induced 12mer Oligonucleotide Fragments in Chapter III

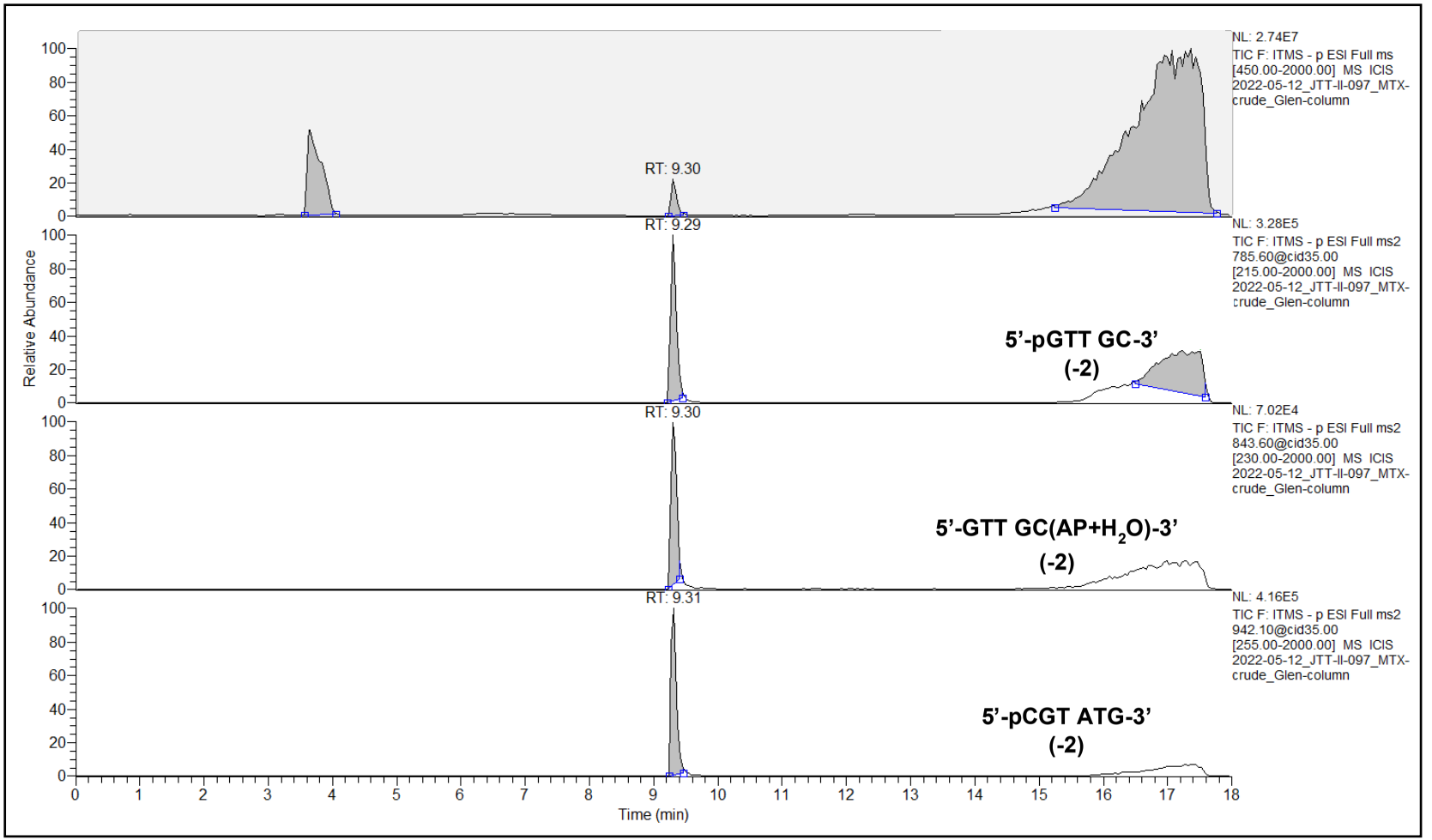

ESI-LC/MS chromatogram of the crude reaction solution from scission of the ssAP-12mer (10 µM) with MTX (0.15 mM, 37 °C, 10 min.) after passing twice through a Bio-Spin® desalting spin column.

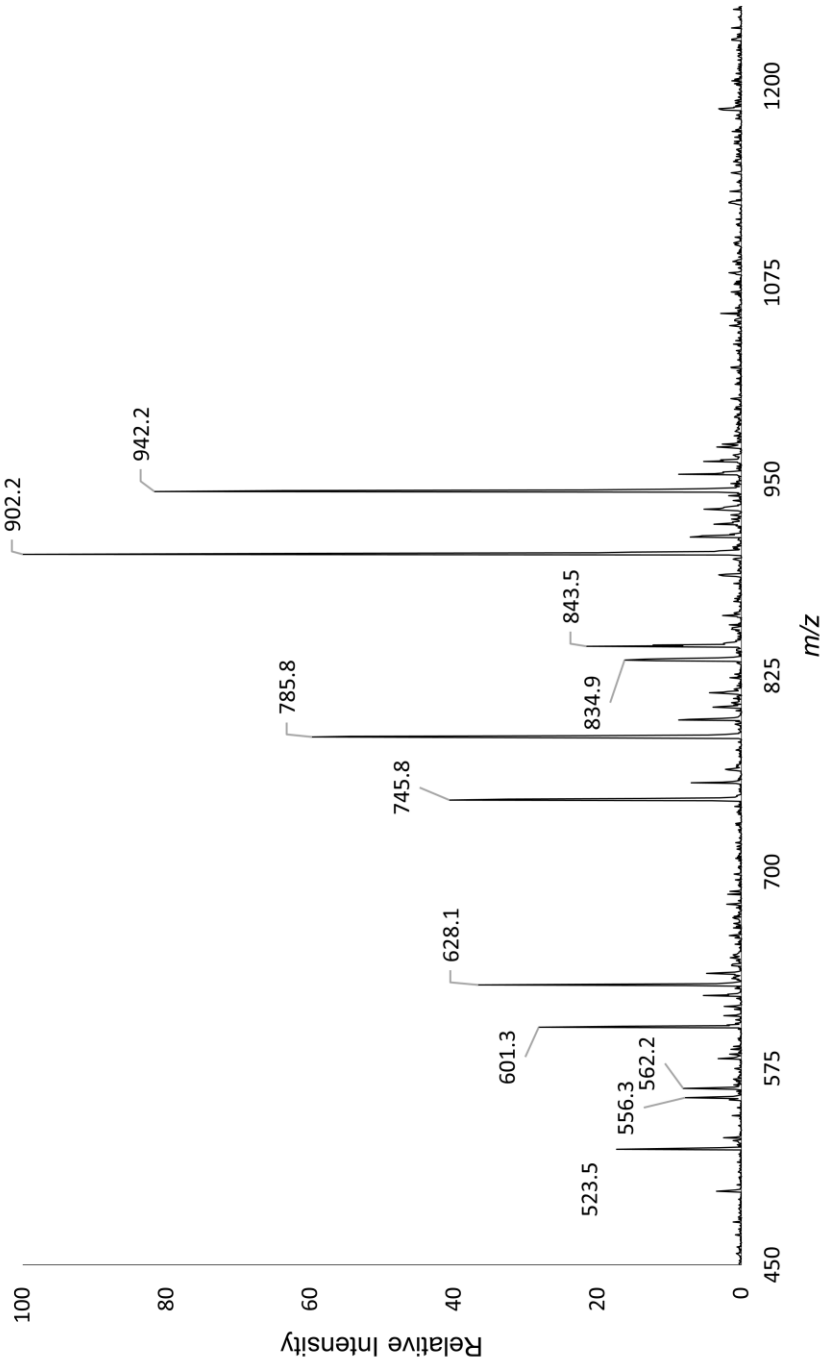

ESI-LC/MS total ion mass spectrum for retention time 9.3 minutes of the crude reaction solution from scission of the ssAP-12mer (10 μM) with MTX (0.15 mM, 37 °C, 10 min.) after passing twice through a Bio-Spin® desalting spin column.

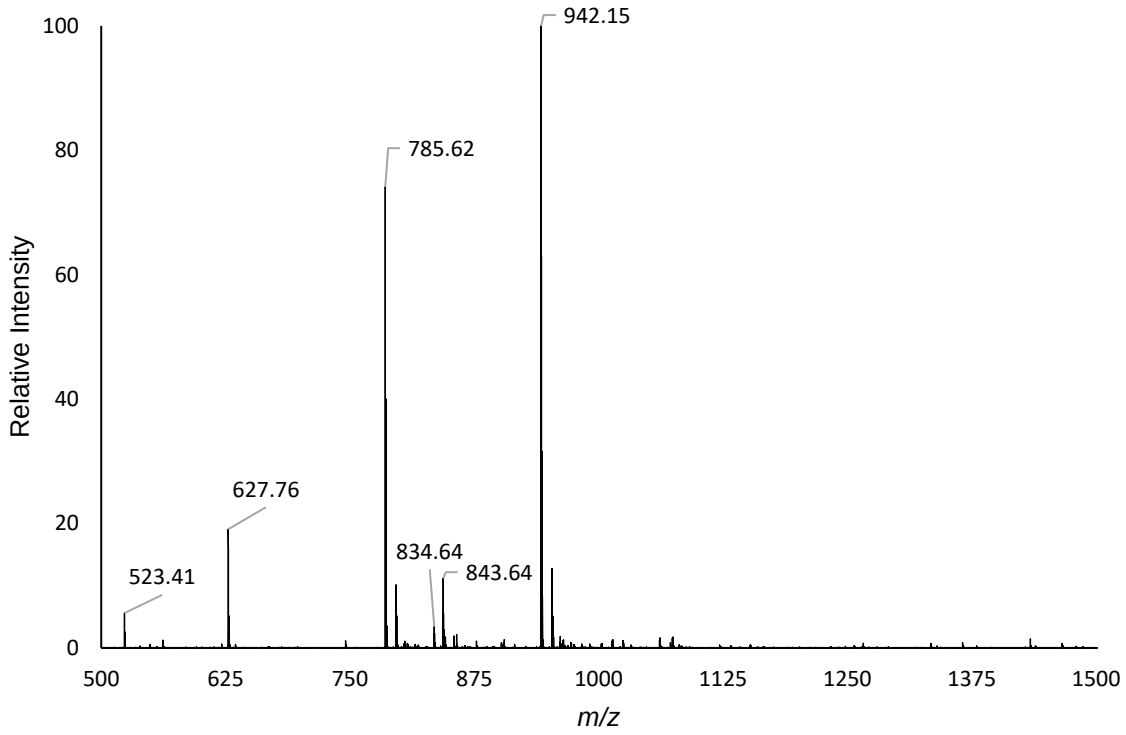

ESI-MS total ion mass spectrum of the crude reaction solution from scission of the ssAP-12mer (10 μM) with MTX (0.15 mM, 37 °C, 10 min.) after passing twice through a Bio-Spin® desalting spin column without LC separation.

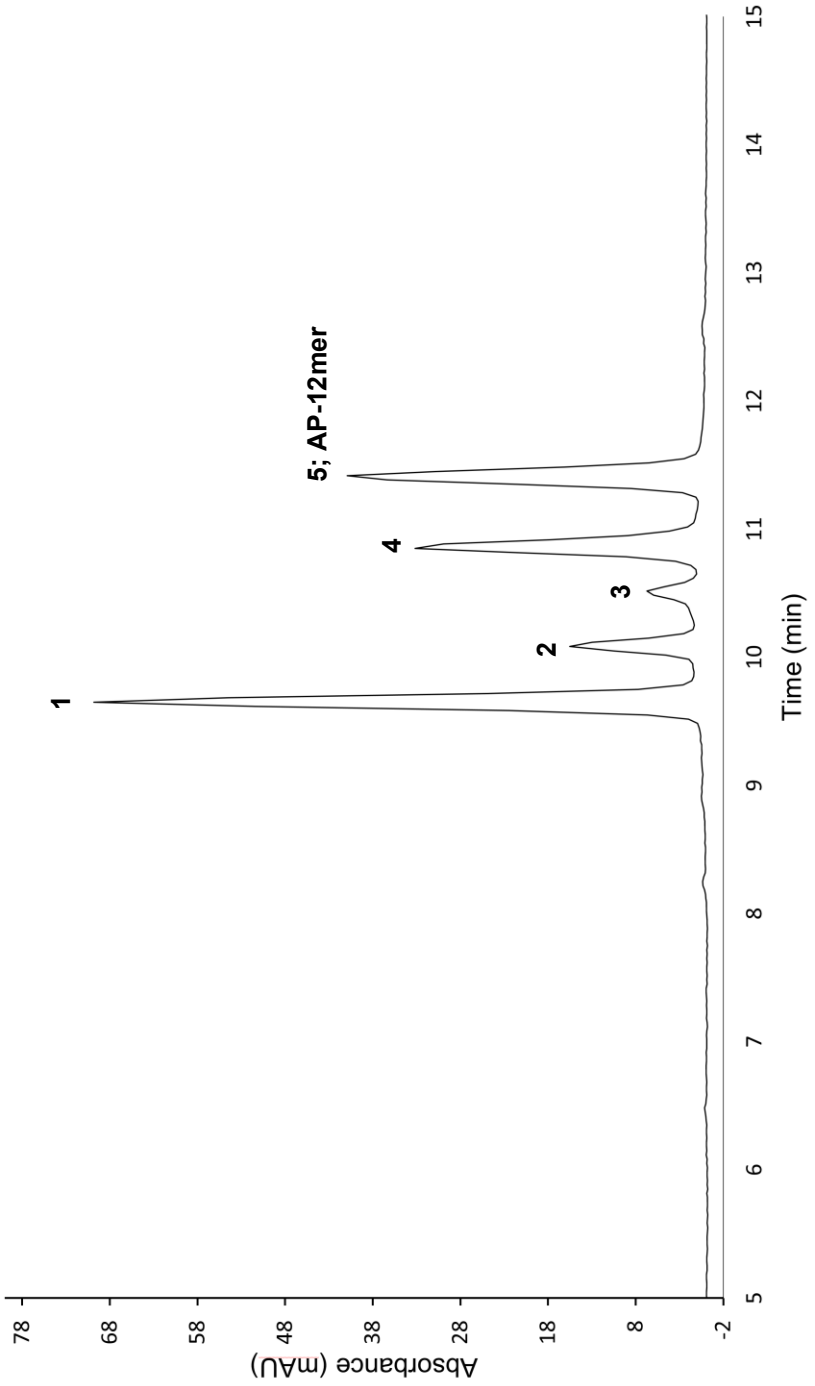

HPLC chromatogram of the crude reaction mixture from scission of the ssAP-12mer (10 μM) with MTX (0.04 mM, 37 °C, 10 min).

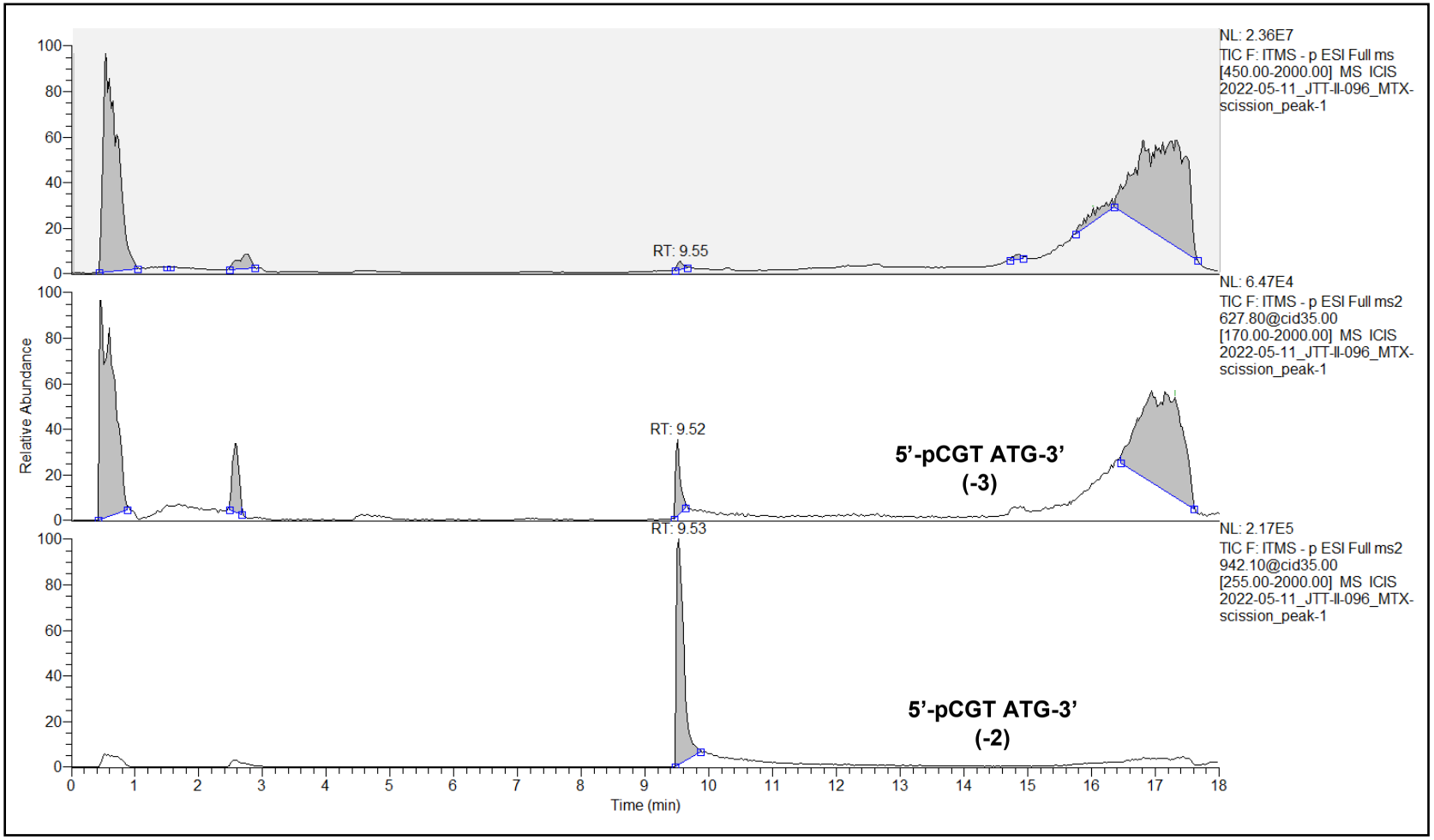

ESI-LC/MS chromatogram of the HPLC purified peak 1 from scission of the ssAP-12mer (10 μM) with MTX (0.04 mM, 37 °C, 10 min).

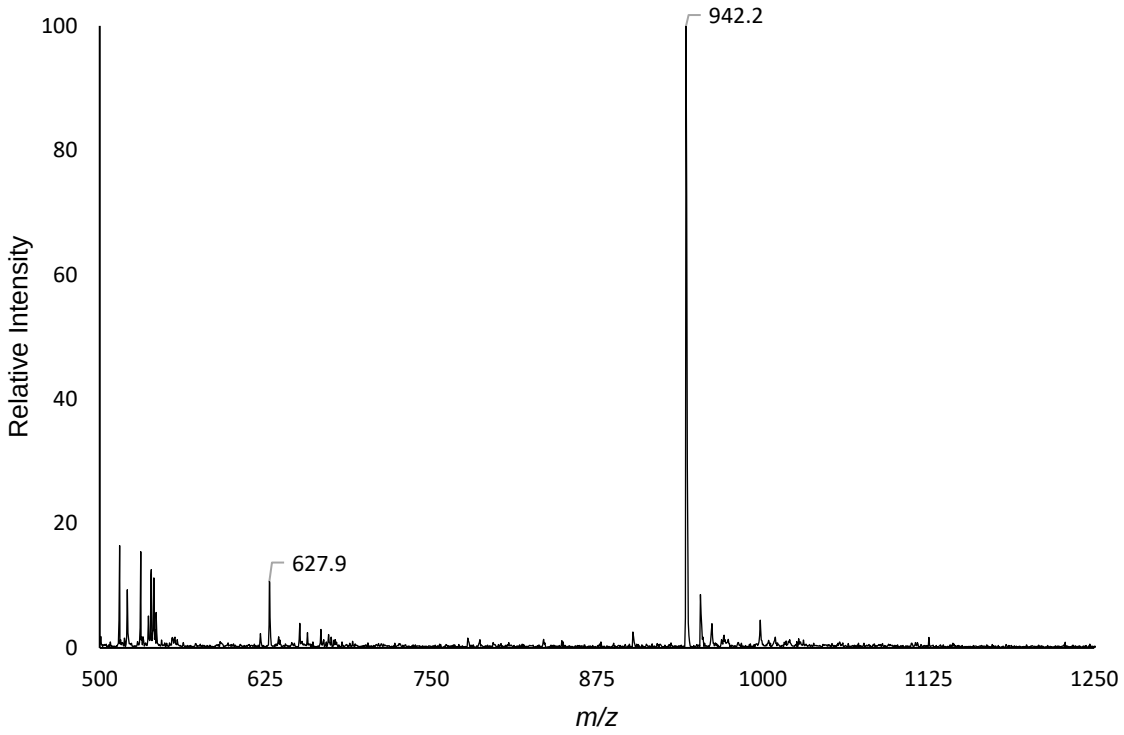

ESI-LC/MS total ion mass spectrum of the HPLC purified peak 1 from scission of the ssAP-12mer (10 μM) with MTX (0.04 mM, 37 °C, 10 min) at retention time 9.5 minutes.

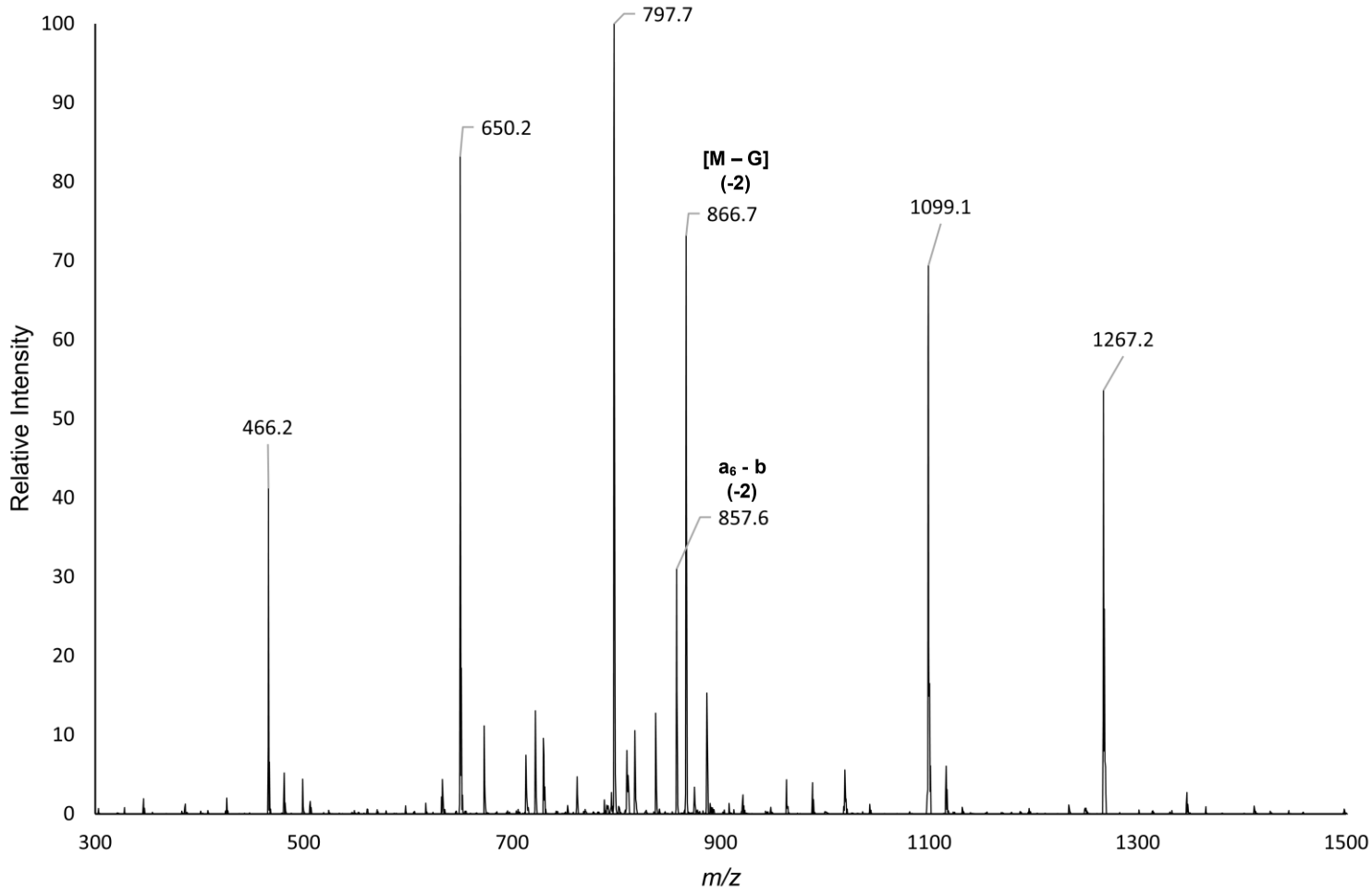

m/z 942 **selected ion ESI-LC/MS^2 spectrum with CID fragmentation of the HPLC purified peak 1 from scission of the ssAP-12mer (10 µM) with MTX (0.04 mM, 37 °C, 10 min) at retention time 9.5 minutes. Peaks at *m/z 867* and *858* not predicted by software; identity determined from ChemDraw structure.**

Calculated CID Fragments

n	z	a-B	w	y	d-H2O
1	-1		346.054	266.088	288.038
	-2				143.515
2	-1	466.040	650.100	570.134	617.090
	-2	232.516	324.546	284.563	308.041
	-3				205.024
3	-1	795.092	963.157	883.191	921.136
	-2	397.042	481.074	441.091	460.064
	-3	264.358	320.380	293.725	306.373
	-4				229.528
4	-1	1099.138	1267.203	1187.237	1234.193
	-2	549.065	633.097	593.114	616.592
	-3	365.707	421.729	395.073	410.725
	-4	274.028	316.044	296.053	307.792
	-5				246.032
5	-1	1412.195	1596.255	1516.289	1538.239
	-2	705.593	797.623	757.640	768.615
	-3	470.059	531.413	504.757	512.074
	-4	352.293	398.307	378.316	383.803
	-5	281.632	318.444	302.451	306.841
	-6				255.533

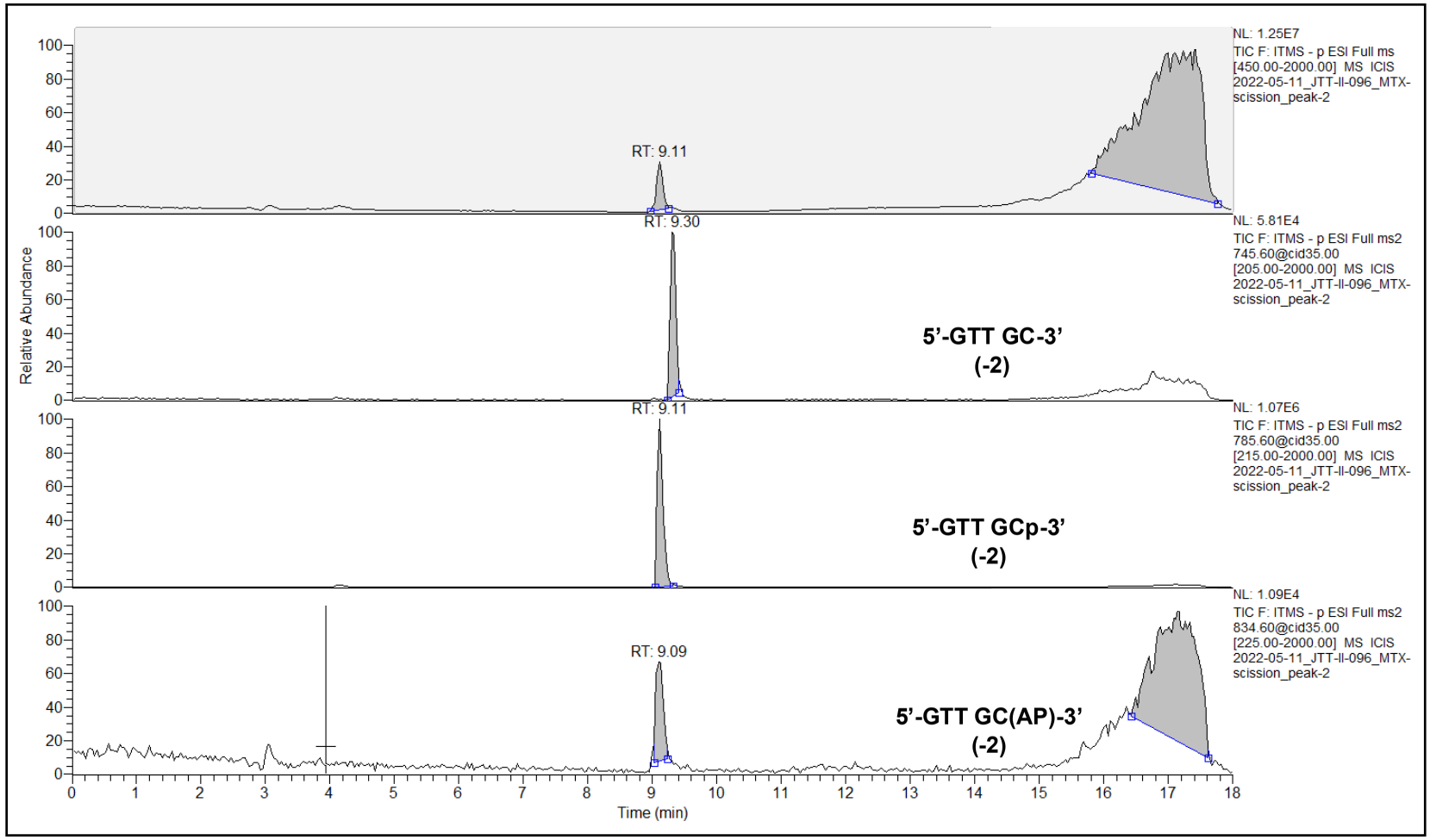

ESI-LC/MS chromatogram of the HPLC purified peak 2 from scission of the ssAP-12mer (10 μM) with MTX (0.04 mM, 37 °C, 10 min).

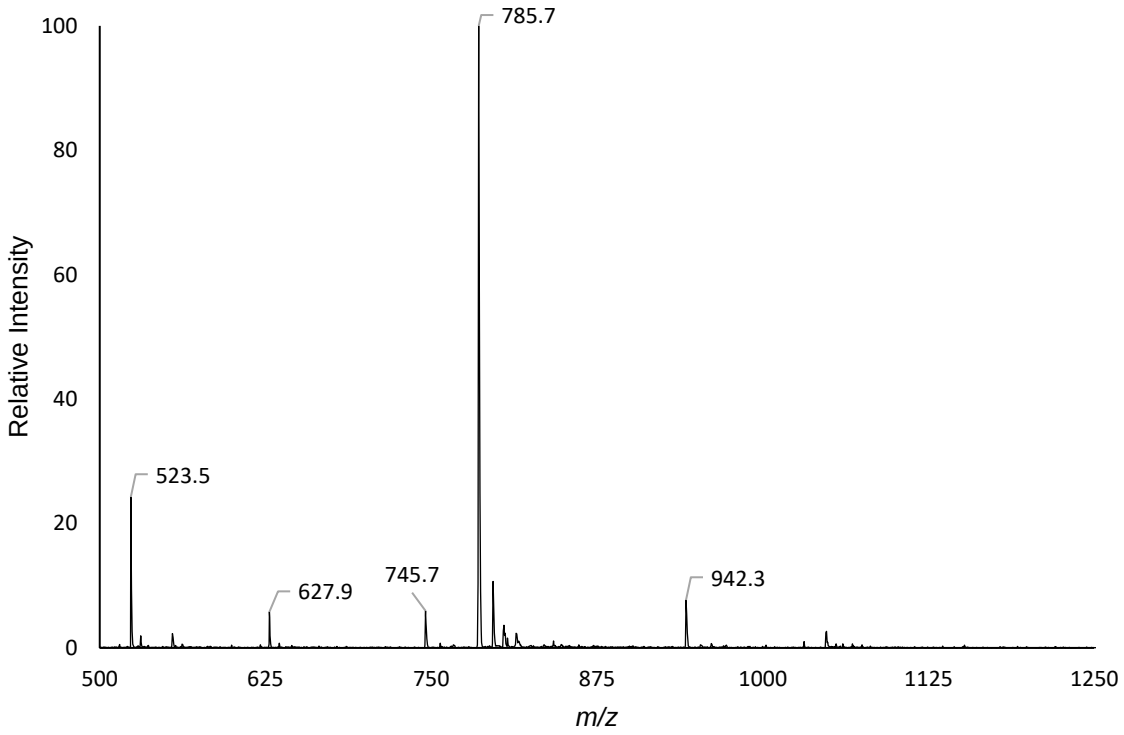

ESI-LC/MS total ion mass spectrum of the HPLC purified peak 2 from scission of the ssAP-12mer (10 μM) with MTX (0.04 mM, 37 °C, 10 min) at retention time 9-9.4 minutes.

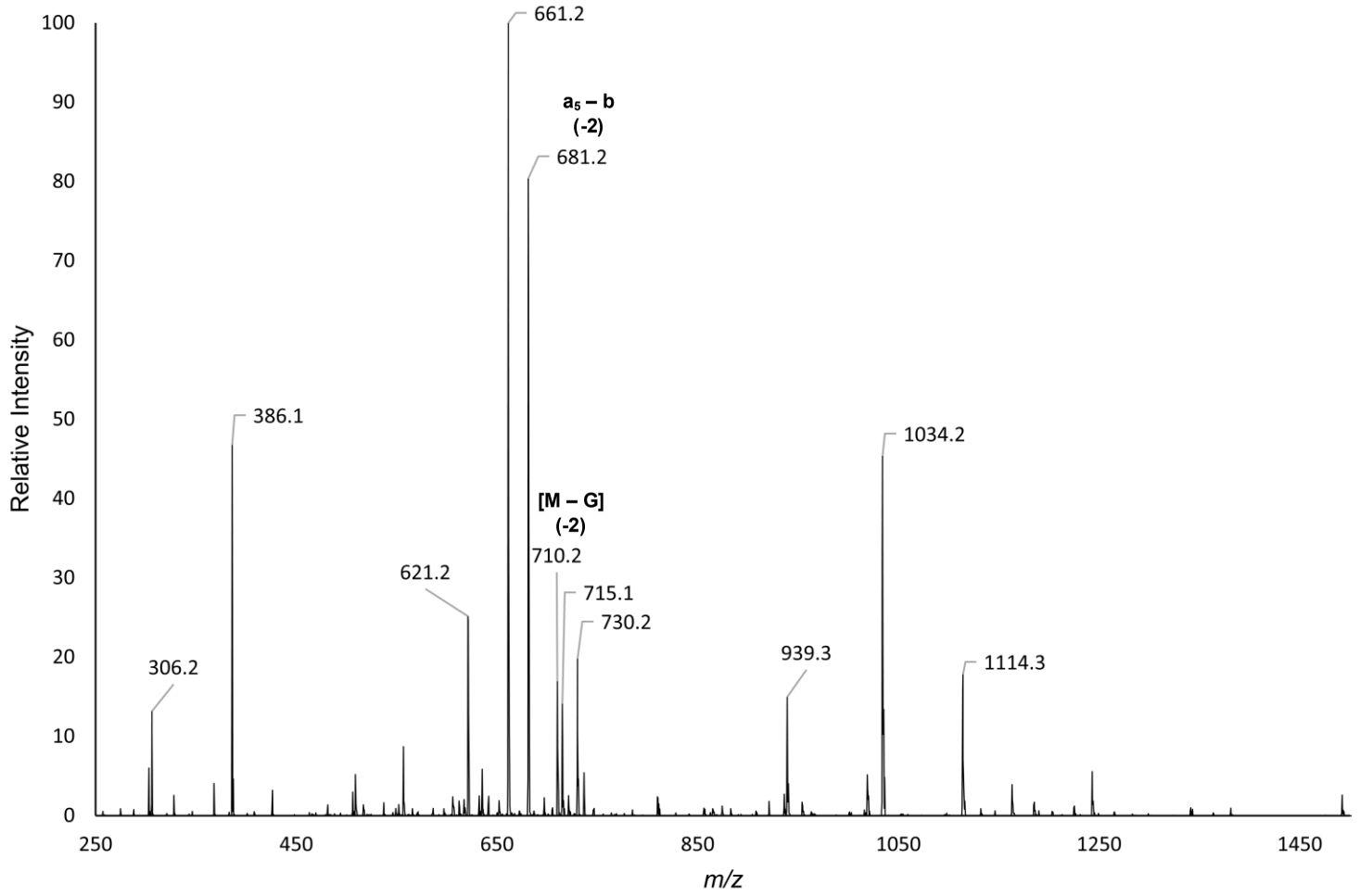

m/z 785 **selected ion ESI-LC/MS^2 spectrum with CID fragmentation of the HPLC purified peak 2 from scission of the ssAP-12mer (10 µM) with MTX (0.04 mM, 37 °C, 10 min) at retention time 9-9.4 minutes. Peaks at *m/z 681* and *710* not predicted by software; identity determined from ChemDraw structure.**

Calculated CID Fragments

n	z	a-B	w	y	d-H2O
1	-1		386.014	306.048	328.044
	-2		192.503	152.520	
2	-1	426.080	715.066	635.100	632.090
	-2		357.029	317.046	315.541
	-3		237.683	211.028	
3	-1	730.126	1019.112	939.146	936.135
	-2	364.559	509.052	469.069	467.563
	-3		339.032	312.376	311.373
	-4		254.022	234.030	
4	-1	1034.171	1323.157	1243.191	1265.187
	-2	516.582	661.074	621.091	632.090
	-3	344.052	440.380	413.725	421.057
	-4		330.033	310.042	315.541
	-5		263.825	247.832	

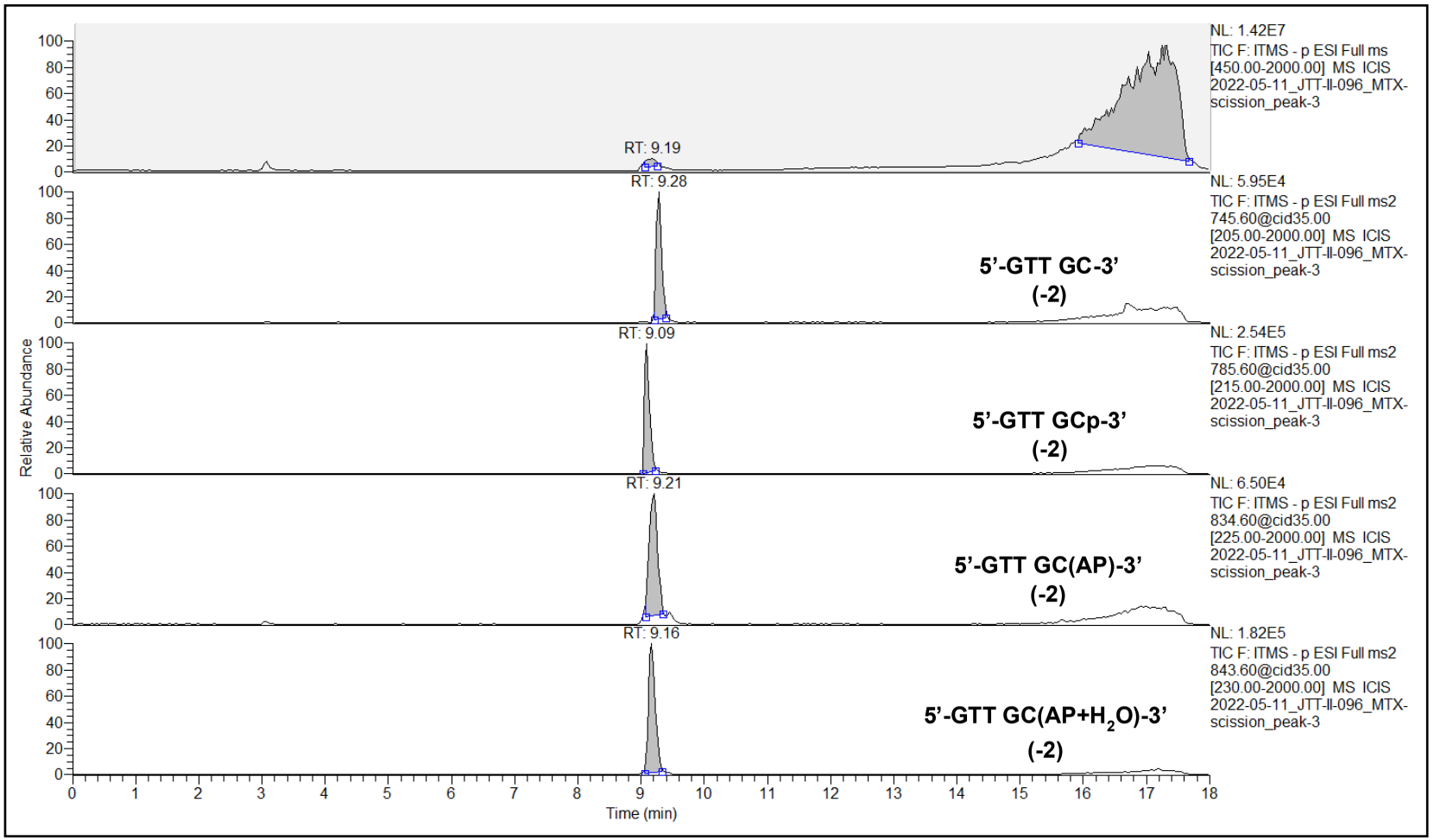

ESI-LC/MS chromatogram of the HPLC purified peak 3 from scission of the ssAP-12mer (10 μM) with MTX (0.04 mM, 37 °C, 10 min).

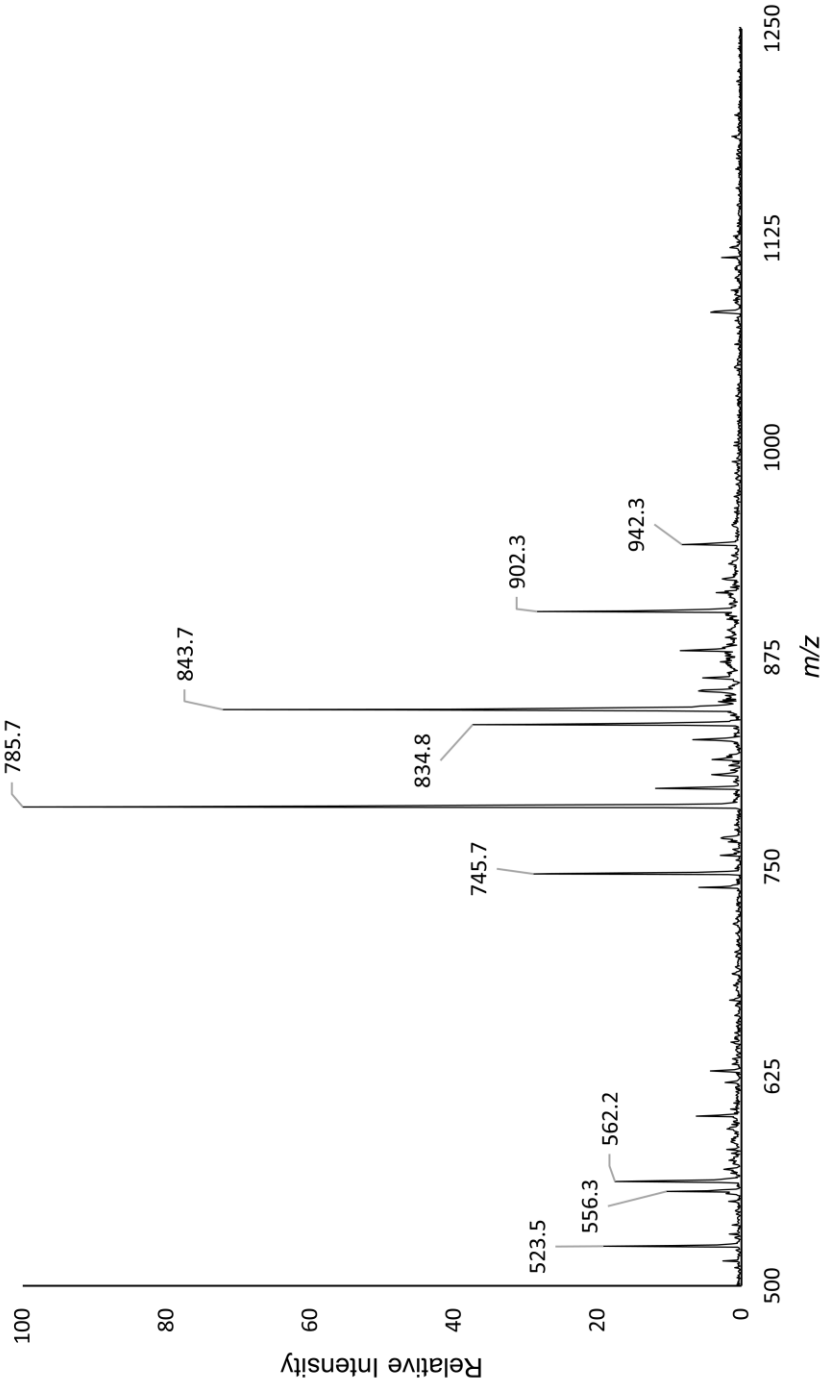

ESI-LC/MS total ion mass spectrum of the HPLC purified peak 3 from scission of the ssAP-12mer (10 μM) with MTX (0.04 mM, 37 °C, 10 min) at retention time 9-9.3 minutes.

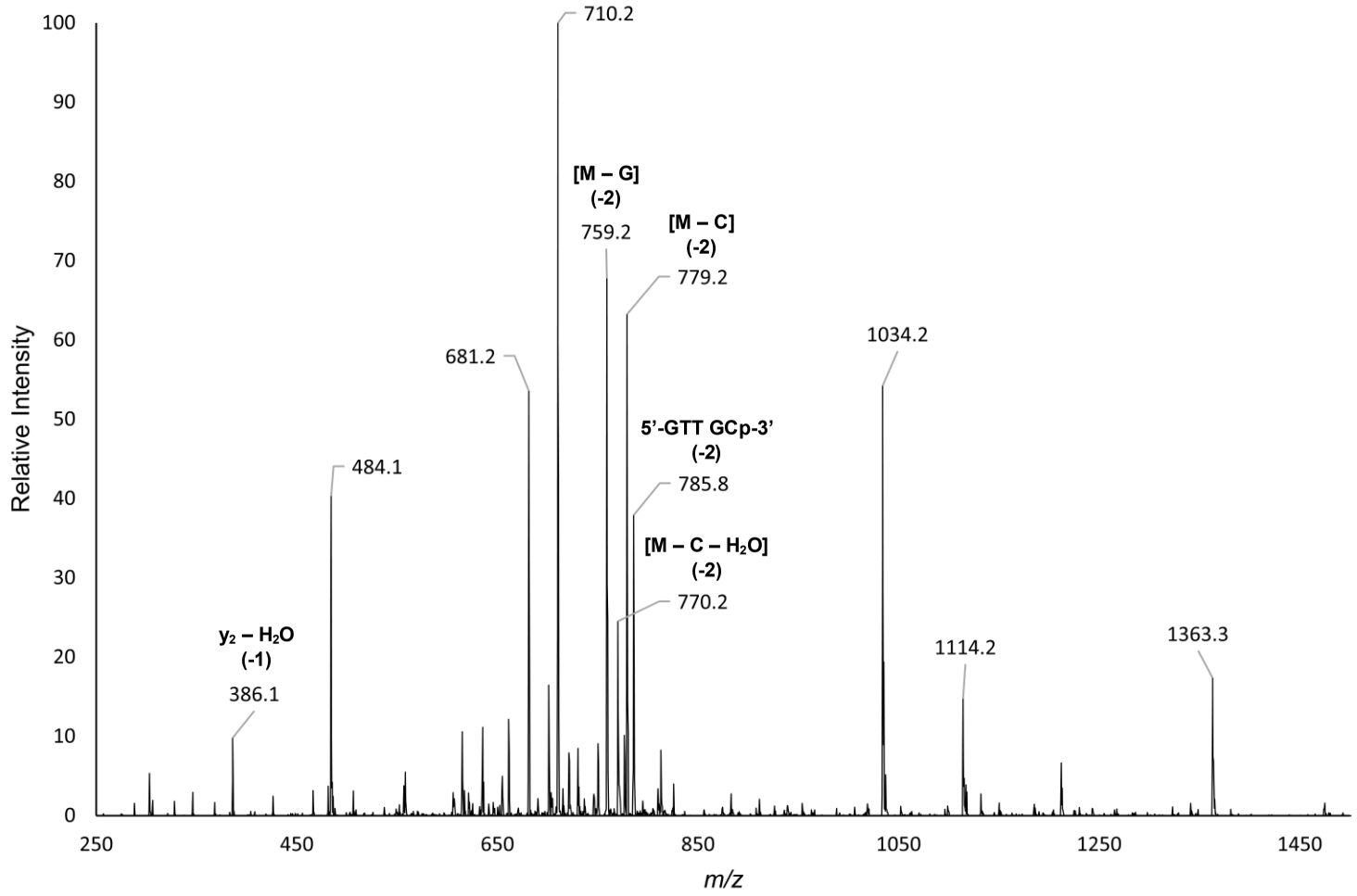

m/z 834 **selected ion ESI-LC/MS^2 spectrum with CID fragmentation of the HPLC purified peak 3 from scission of the ssAP-12mer (10 µM) with MTX (0.04 mM, 37 °C, 10 min) at retention time 9-9.3 minutes. Peaks at *m/z 786*, *779*, *770*, *759*, and *386* not predicted by software; identity determined from ChemDraw structure.**

Calculated CID Fragments

n	z	a-B	w	y	d-H2O
1	-1		195.002	115.036	328.044
2	-1	426.080	484.048	404.082	632.090
	-2		241.520	201.537	315.541
3	-1	730.126	813.100	733.134	936.135
	-2	364.559	406.046	366.063	467.563
	-3		270.361	243.706	311.373
4	-1	1034.171	1117.146	1037.180	1265.187
	-2	516.582	558.069	518.086	632.090
	-3	344.052	371.710	345.055	421.057
	-4		278.530	258.539	315.541
5	-1	1363.224	1421.192	1341.226	1554.233
	-2	681.108	710.092	670.109	776.613
	-3	453.736	473.058	446.403	517.406
	-4	340.050	354.542	334.550	387.802
	-5		283.432	267.439	310.040

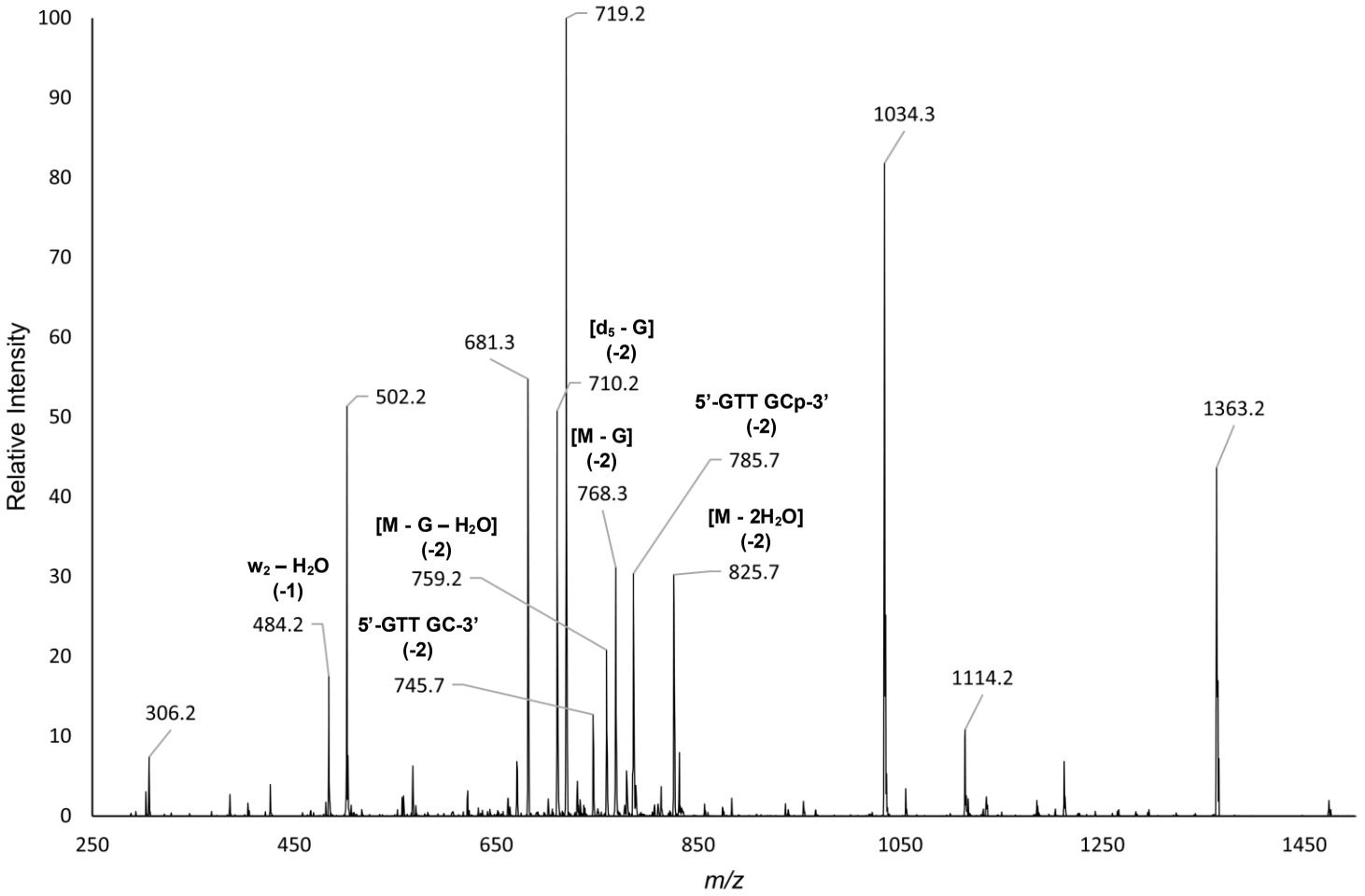

m/z 843 **selected ion ESI-LC/MS^2 spectrum with CID fragmentation of the HPLC purified peak 3 from scission of the ssAP-12mer (10 μM) with MTX (0.04 mM, 37 °C, 10 min) at retention time 9-9.3 minutes. Peaks at *m/z 826*, *786*, *768*, *759*, *746*, *710*, and *484* not predicted by software; identity determined from ChemDraw structure.**

Calculated CID Fragments

n	z	a-B	w	y	d-H2O
1	-1		213.022	133.056	328.044
2	-1	426.080	502.068	422.102	632.090
	-2		250.530	210.547	315.541
3	-1	730.126	831.120	751.154	936.135
	-2	364.559	415.056	375.073	467.563
	-3		276.368	249.713	311.373
4	-1	1034.171	1135.166	1055.200	1265.187
	-2	516.582	567.079	527.096	632.090
	-3	344.052	377.717	351.061	421.057
	-4		283.035	263.044	315.541
5	-1	1363.224	1439.212	1359.246	1554.233
	-2	681.108	719.102	679.119	776.613
	-3	453.736	479.065	452.410	517.406
	-4	340.050	359.047	339.055	387.802
	-5		287.036	271.043	310.040

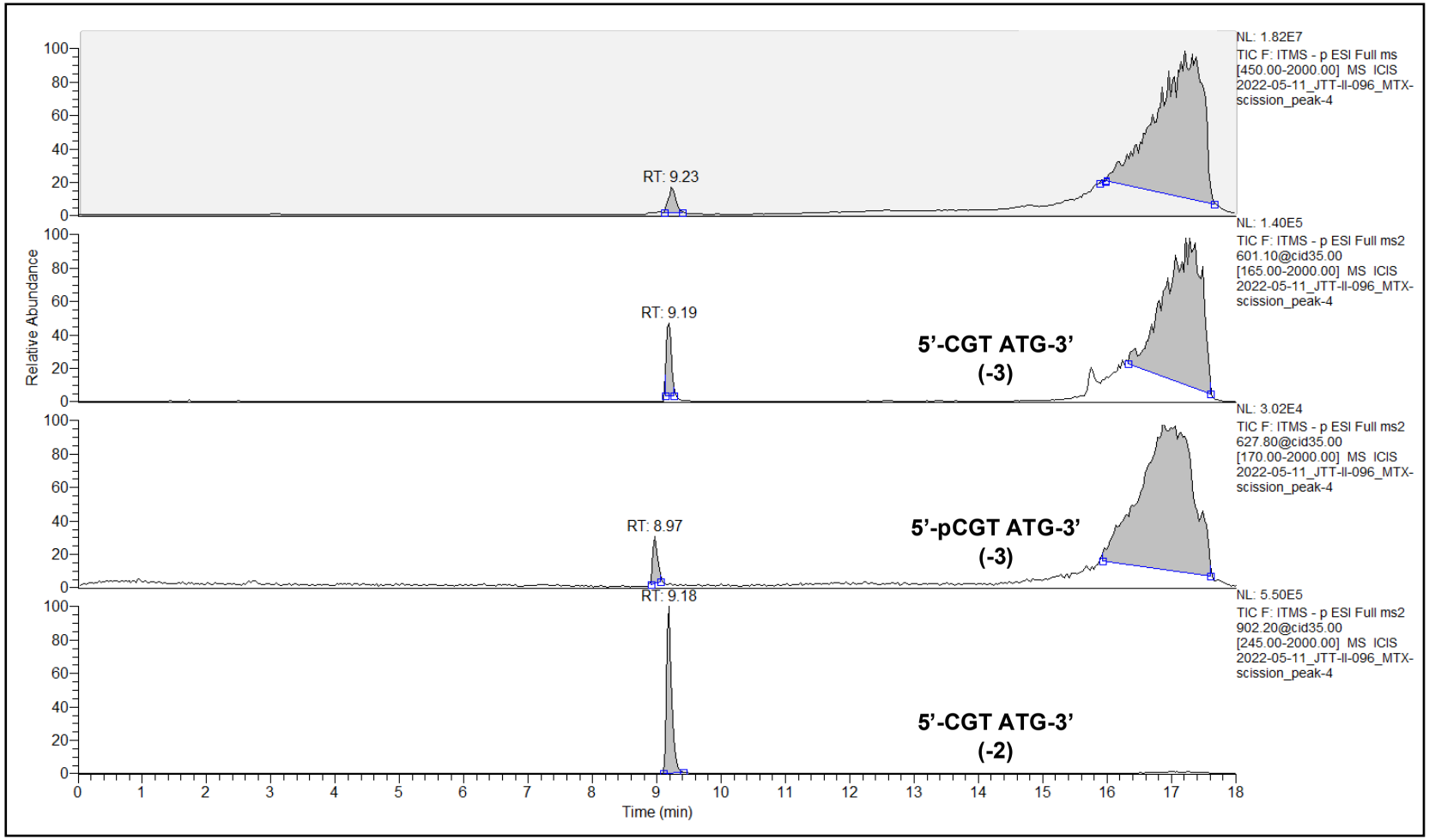

ESI-LC/MS chromatogram of the HPLC purified peak 4 from scission of the ssAP-12mer (10 μM) with MTX (0.04 mM, 37 °C, 10 min).

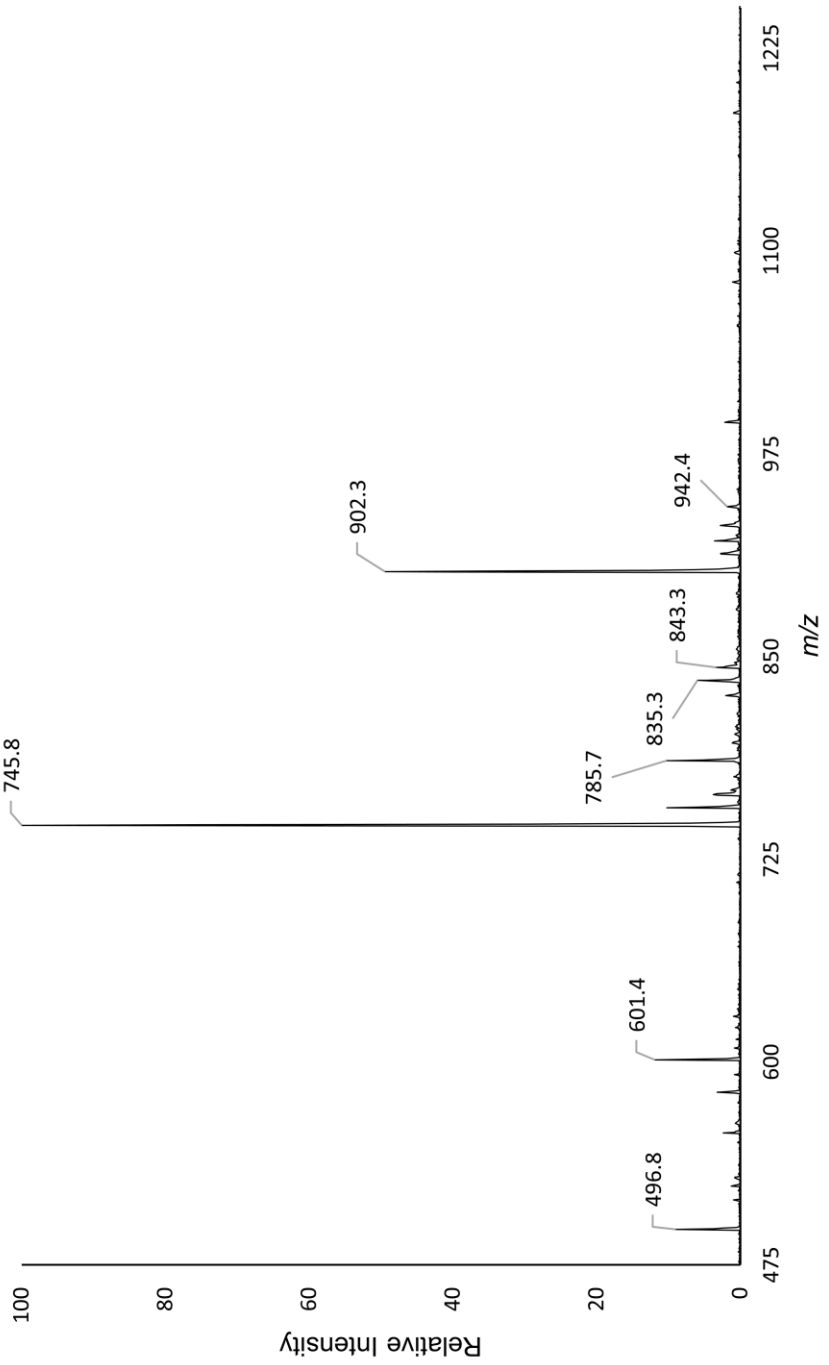

ESI-LC/MS total ion mass spectrum of the HPLC purified peak 4 from scission of the ssAP-12mer (10 μM) with MTX (0.04 mM, 37 °C, 10 min) at retention time 9-9.4 minutes.

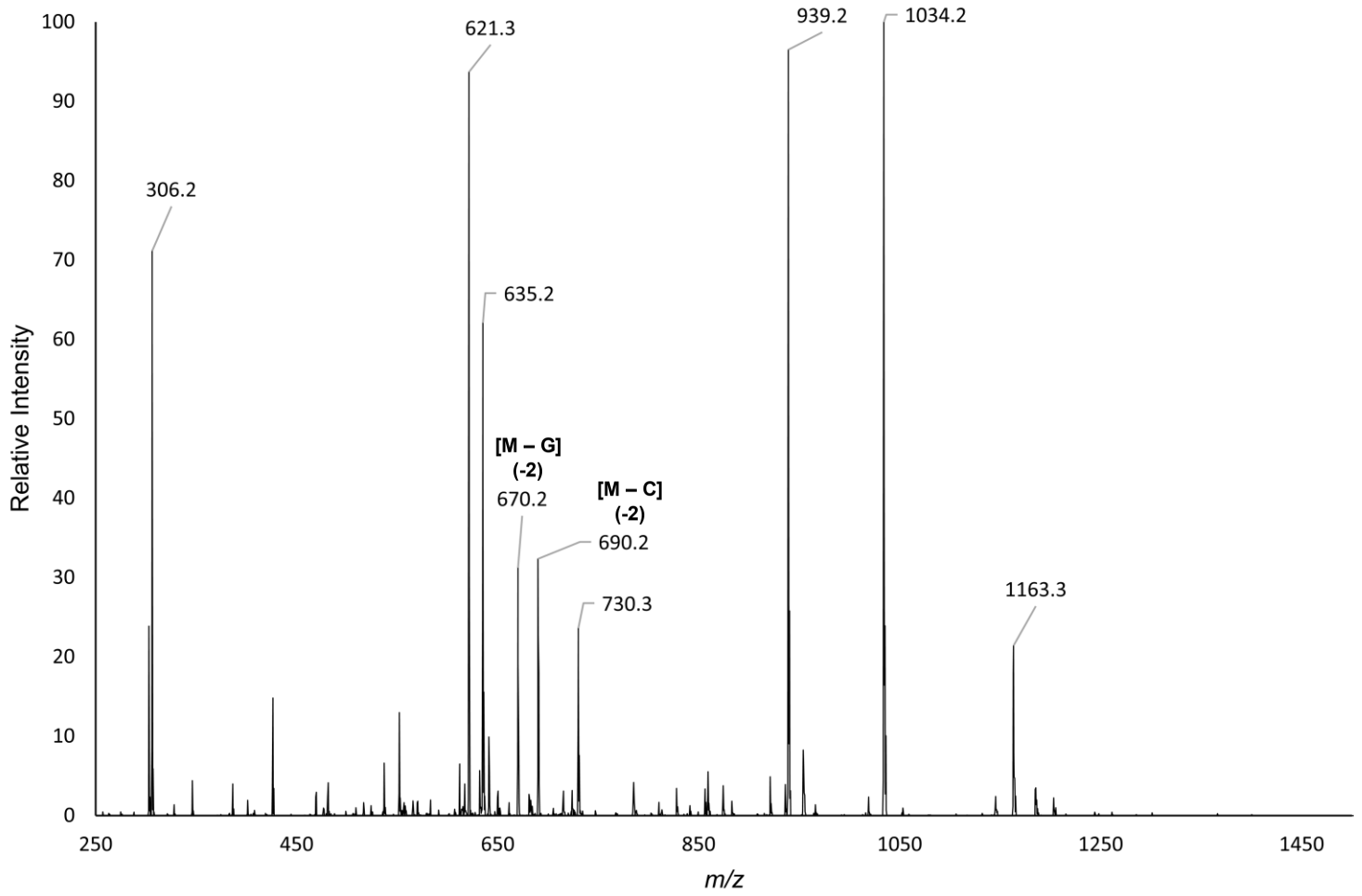

m/z 745 **selected ion ESI-LC/MS^2 spectrum with CID fragmentation of the HPLC purified peak 4 from scission of the ssAP-12mer (10 µM) with MTX (0.04 mM, 37 °C, 10 min) at retention time 9-9.4 minutes. Peaks at *m/z 690* and *670* not predicted by software; identity determined from ChemDraw structure.**

Calculated CID Fragments

n	z	a-B	w	y	d-H2O
1	-1		306.048	226.082	328.044
2	-1	426.080	635.100	555.134	632.090
	-2		317.046	277.063	315.541
3	-1	730.126	939.146	859.180	936.135
	-2	364.559	469.069	429.086	467.563
	-3		312.376	285.721	311.373
4	-1	1034.171	1243.191	1163.225	1265.187
	-2	516.582	621.091	581.108	632.090
	-3	344.052	413.725	387.070	421.057
	-4		310.042	290.050	315.541

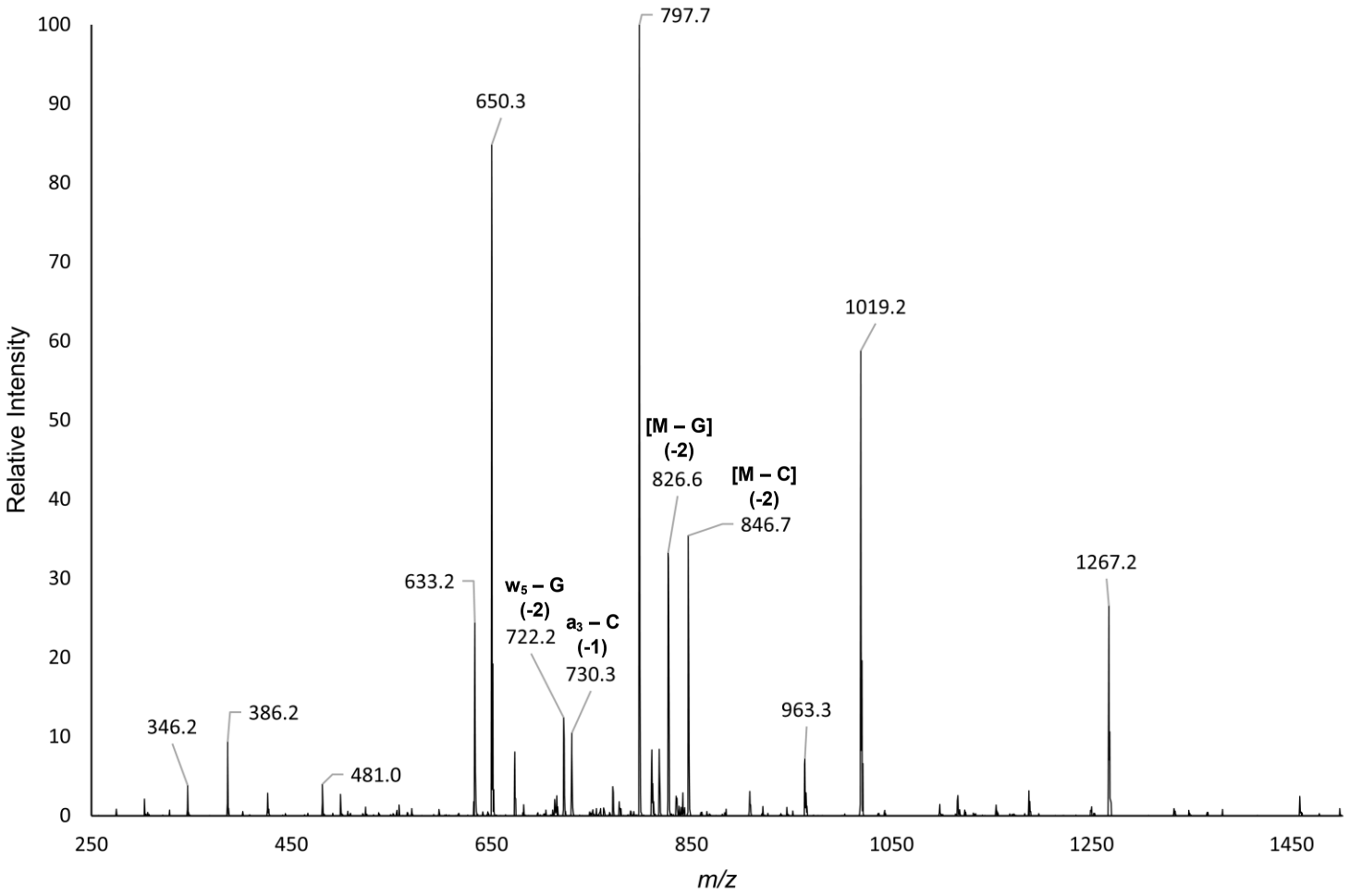

m/z 902 **selected ion ESI-LC/MS^2 spectrum with CID fragmentation of the HPLC purified peak 4 from scission of the ssAP-12mer (10 µM) with MTX (0.04 mM, 37 °C, 10 min) at retention time 9-9.4 minutes. Peaks at *m/z 847*, *827*, *730*, and *722* not predicted by software; identity determined from ChemDraw structure.**

Calculated CID Fragments

n	z	a-B	w	y	d-H2O
1	-1		346.054	266.088	288.038
2	-1	386.074	650.100	570.134	617.090
	-2		324.546	284.563	308.041
3	-1	715.126	963.157	883.191	921.136
	-2	357.059	481.074	441.091	460.064
	-3		320.380	293.725	306.373
4	-1	1019.172	1267.203	1187.237	1234.193
	-2	509.082	633.097	593.114	616.592
	-3	339.052	421.729	395.073	410.725
	-4		316.044	296.053	307.792
5	-1	1332.229	1596.255	1516.289	1538.239
	-2	665.610	797.623	757.640	768.615
	-3	443.404	531.413	504.757	512.074
	-4	332.301	398.307	378.316	383.803
	-5		318.444	302.451	306.841

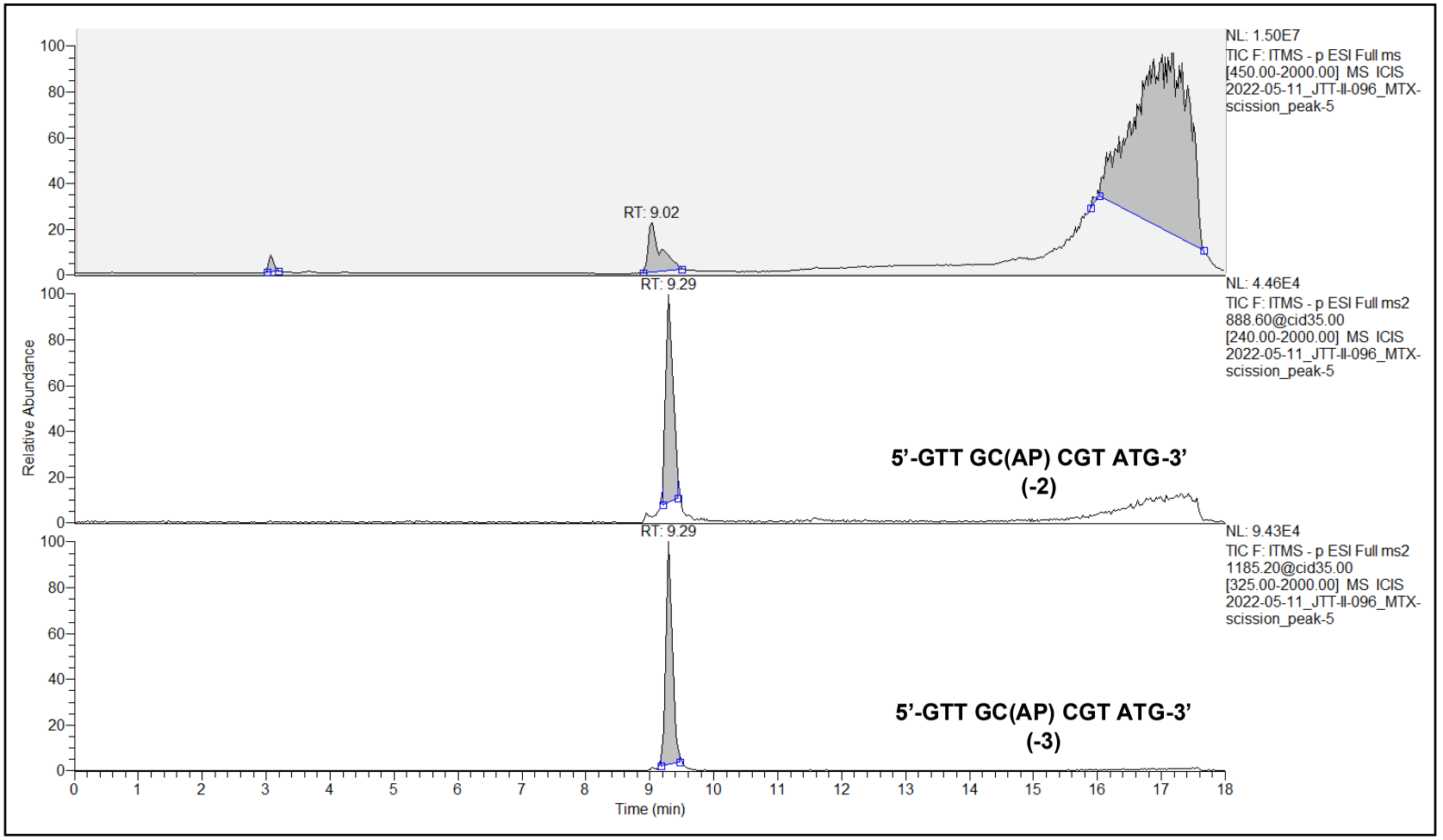

ESI-LC/MS chromatogram of the HPLC purified peak 5 from scission of the ssAP-12mer (10 μM) with MTX (0.04 mM, 37 °C, 10 min).

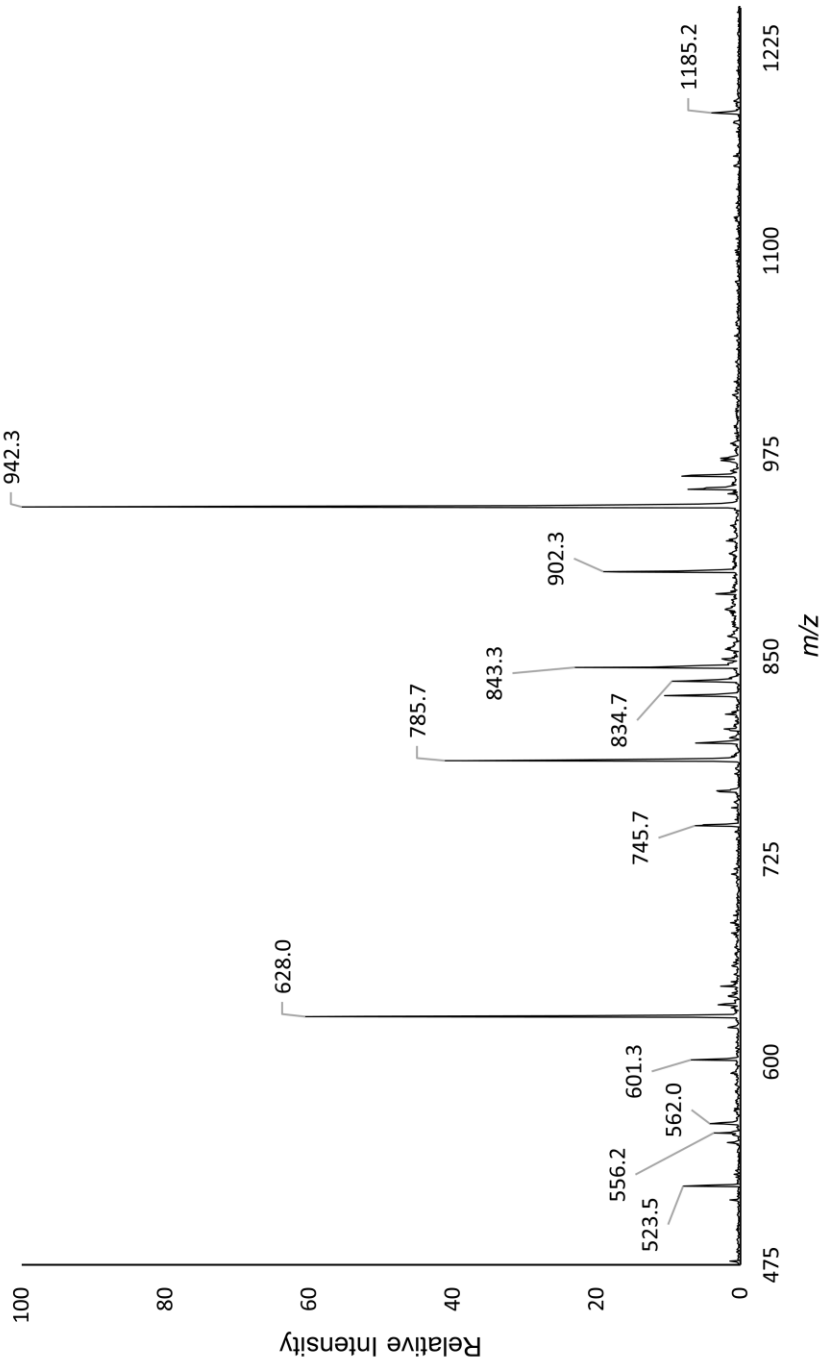

ESI-LC/MS total ion mass spectrum of the HPLC purified peak 5 from scission of the ssAP-12mer (10 μM) with MTX (0.04 mM, 37 °C, 10 min) at retention time 9-9.4 minutes. Instability of the AP-12mer leads to in-source fragmentation to the constituent β-/δ-elimination products.

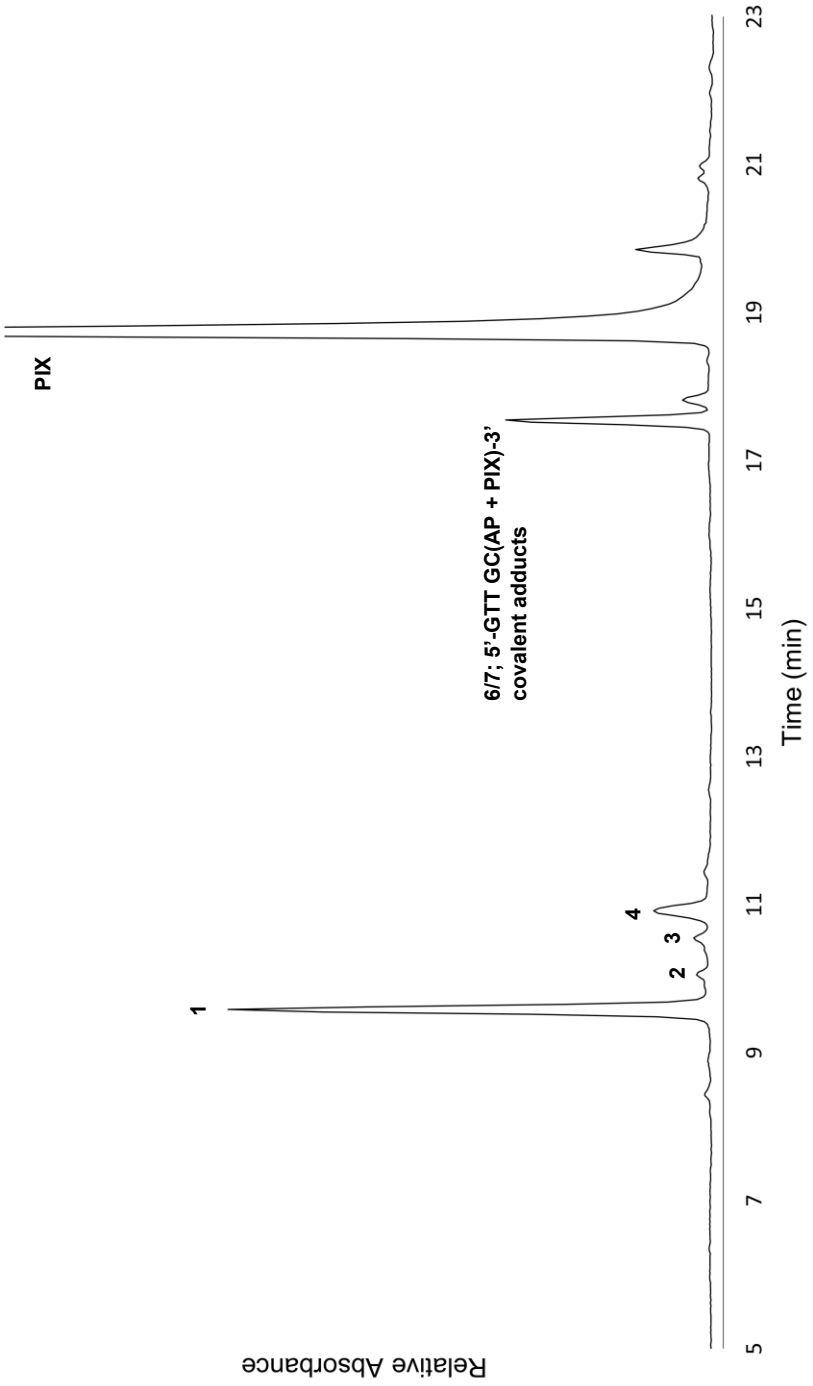

HPLC chromatogram of the crude reaction mixture from scission of the ssAP-12mer (10 μM) with PIX (0.25 mM, 25 °C, 90 min). Fragment labels match those for MTX-12mer scission.

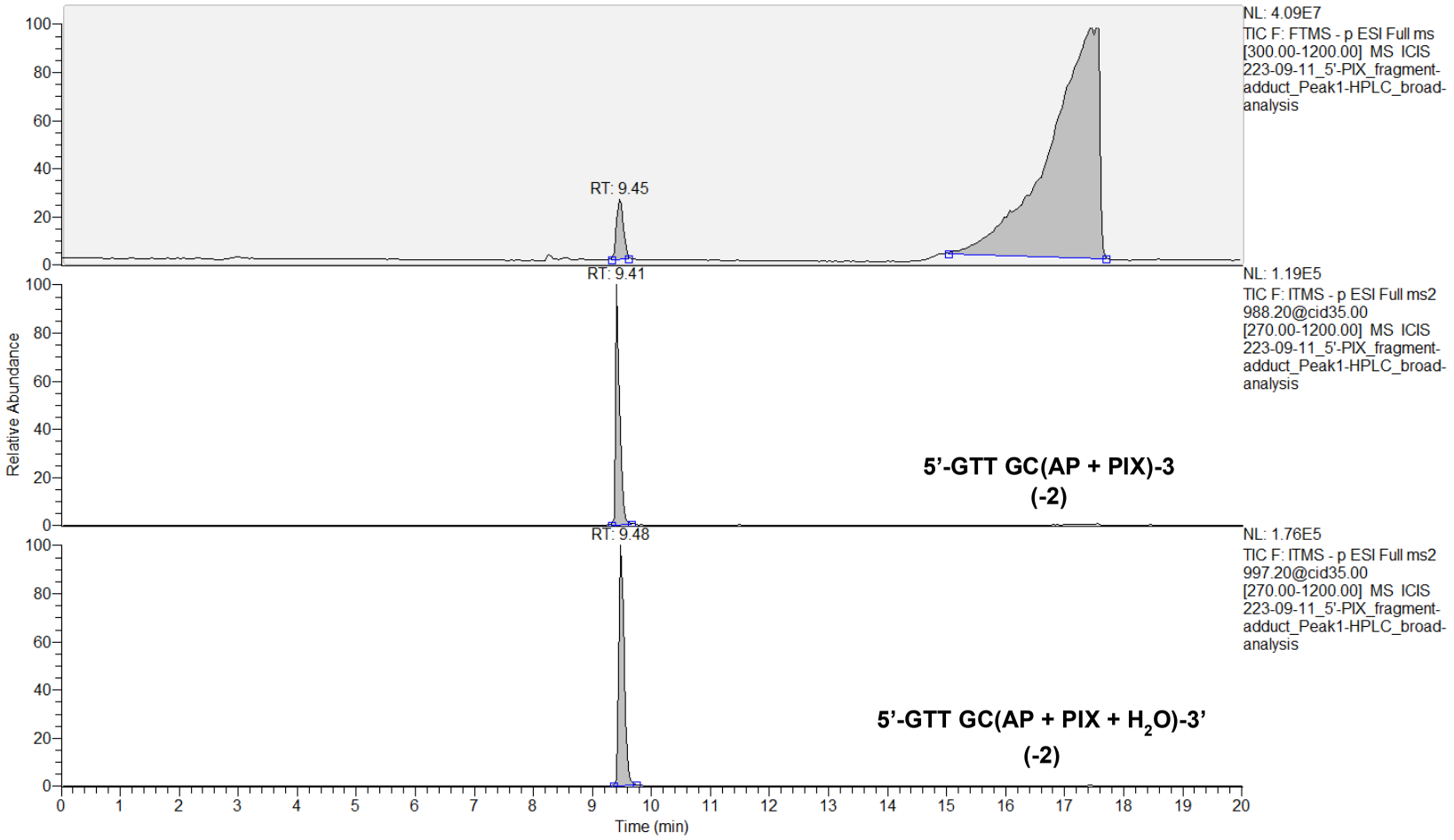

ESI-LC/MS chromatogram of the HPLC purified peak 6/7 from scission of the ssAP-12mer (10 µM) with PIX (0.25 mM, 25 °C, 90 min).

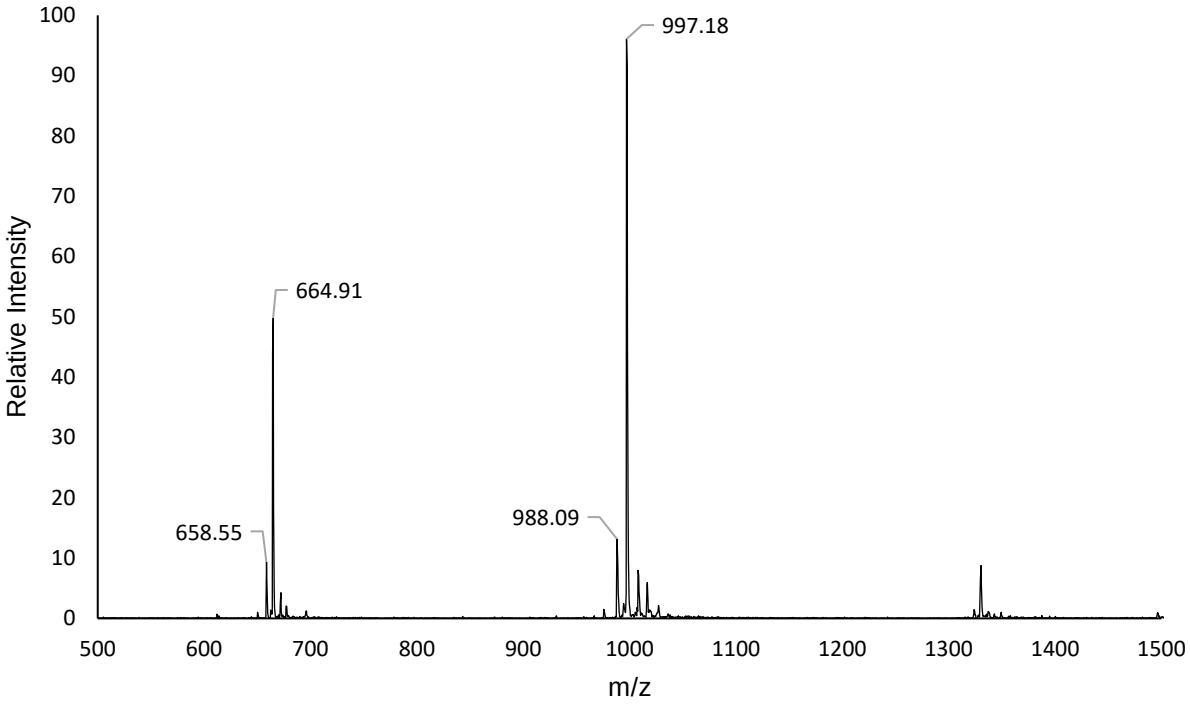

ESI-LC/MS total ion mass spectrum of the HPLC purified peak 6/7 from scission of the ssAP-12mer (10 μM) with PIX (0.25 mM, 25 °C, 90 min) at retention time 9.45 minutes.

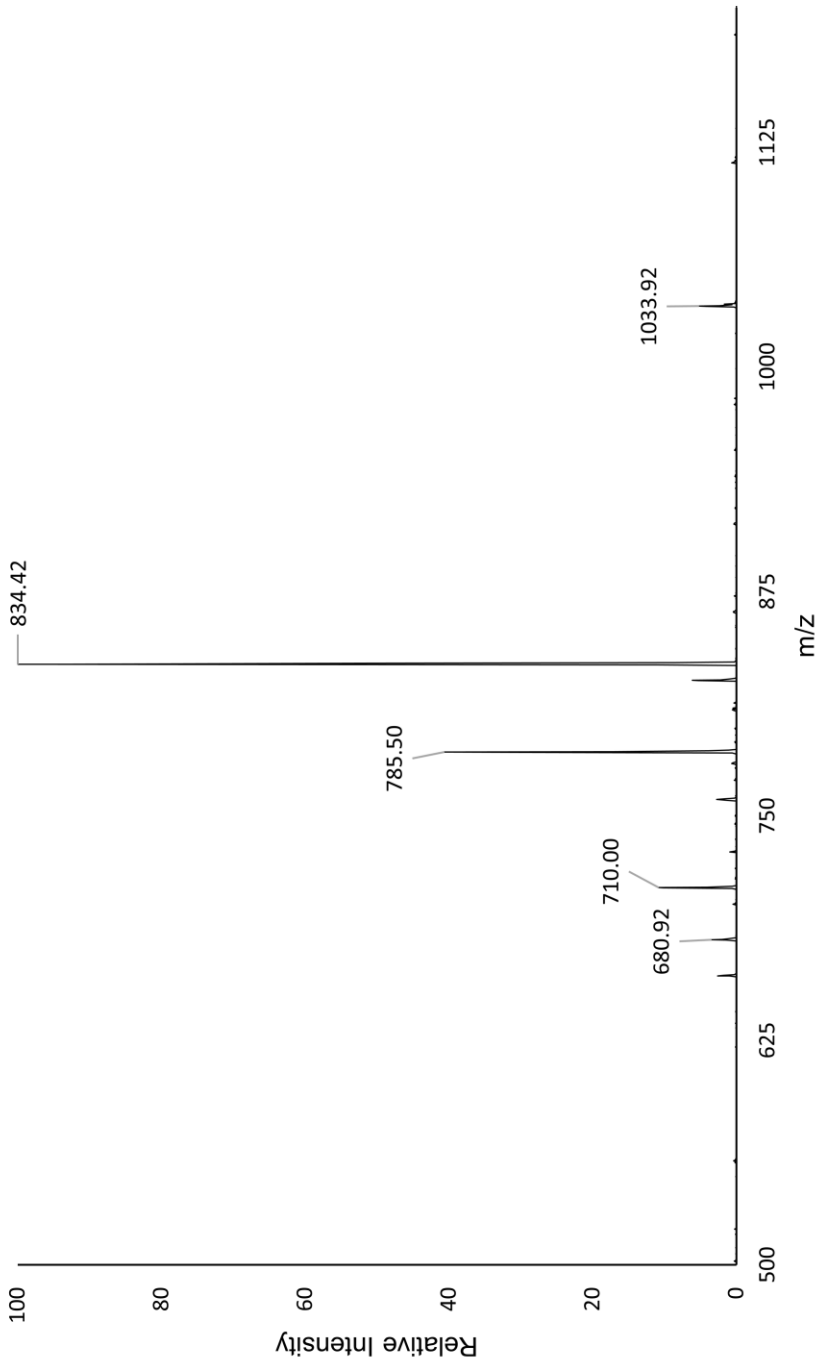

m/z 997 **selected ion ESI-LC/MS^2 spectrum with CID fragmentation of the HPLC purified peak 6/7 from scission of the ssAP-12mer (10 µM) with PIX (0.25 mM, 25 °C, 90 min) at retention time 9.5 minutes. Peaks at *m/z 1034*, *710*, and *681* result from secondary fragmentation of *m/z 785*.**

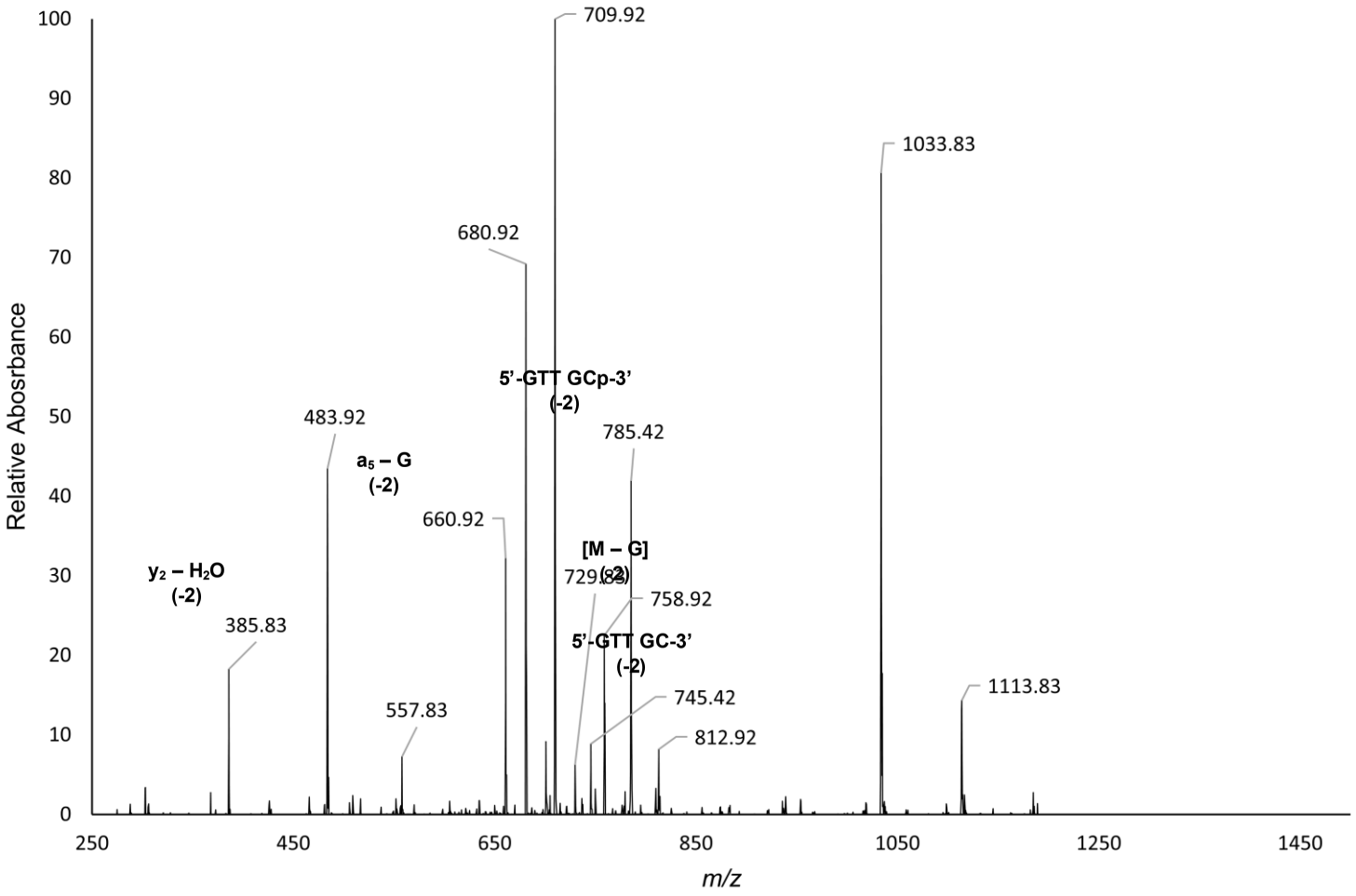

m/z 997 → 834 **selected ion ESI-LC/MS^3 spectrum with CID fragmentation of the HPLC purified peak 6/7 from scission of the ssAP-12mer (10 µM) with PIX (0.25 mM, 25 °C, 90 min) at retention time 9.5 minutes. Peaks at *m/z 785*, *759*, *745*, and *386* not predicted by software; identity determined from ChemDraw structure.**

Calculated CID Fragments

n	z	a-B	w	y	d-H2O
1	-1		195.002	115.036	328.044
2	-1	426.080	484.048	404.082	632.090
	-2		241.520	201.537	315.541
3	-1	730.126	813.100	733.134	936.135
	-2	364.559	406.046	366.063	467.563
	-3		270.361	243.706	311.373
4	-1	1034.171	1117.146	1037.180	1265.187
	-2	516.582	558.069	518.086	632.090
	-3	344.052	371.710	345.055	421.057
	-4		278.530	258.539	315.541
5	-1	1363.224	1421.192	1341.226	1554.233
	-2	681.108	710.092	670.109	776.613
	-3	453.736	473.058	446.403	517.406
	-4	340.050	354.542	334.550	387.802
	-5		283.432	267.439	310.040

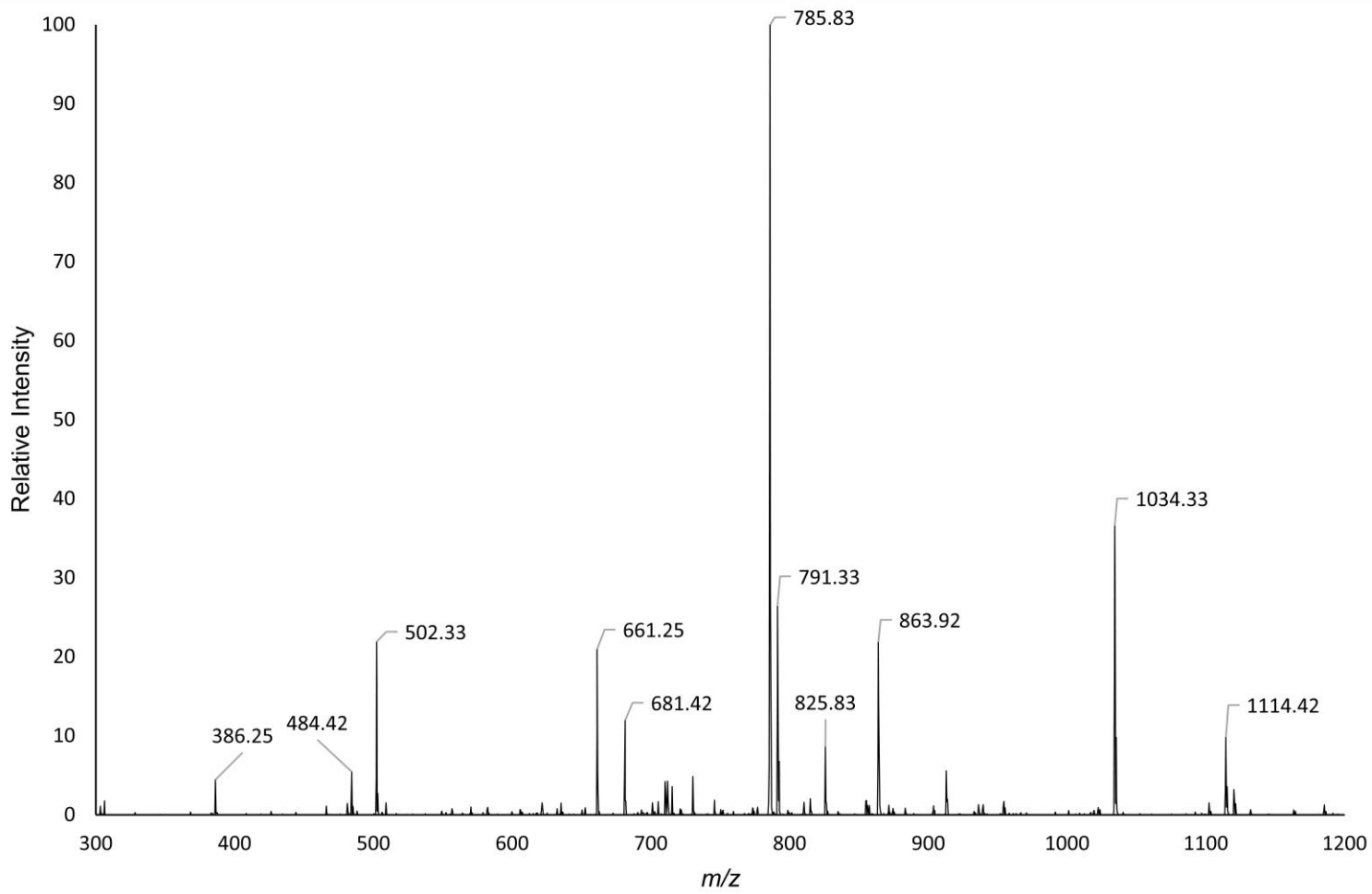

m/z 988 **selected ion ESI-LC/MS^2 spectrum with CID fragmentation of the HPLC purified peak 6/7 from scission of the ssAP-12mer (10 µM) with PIX (0.25 mM, 25 °C, 90 min) at retention time 9.4 minutes.**

Calculated CID Fragments

n	z	a-B	w	y	d-H2O
1	-1		502.132	422.166	328.044
2	-1	426.080	791.178	711.212	632.090
	-2		395.085	355.102	315.541
3	-1	730.126	1120.230	1040.264	936.135
	-2	364.559	559.611	519.628	467.563
	-3		372.738	346.083	311.373
4	-1	1034.171	1424.276	1344.310	1265.187
	-2	516.582	711.634	671.651	632.090
	-3	344.052	474.087	447.431	421.057
	-4		355.313	335.321	315.541
5	-1	1363.224	1728.322	1648.356	1554.233
	-2	681.108	863.657	823.674	776.613
	-3	453.736	575.435	548.780	517.406
	-4	340.050	431.324	411.333	387.802
	-5		344.858	328.865	310.040

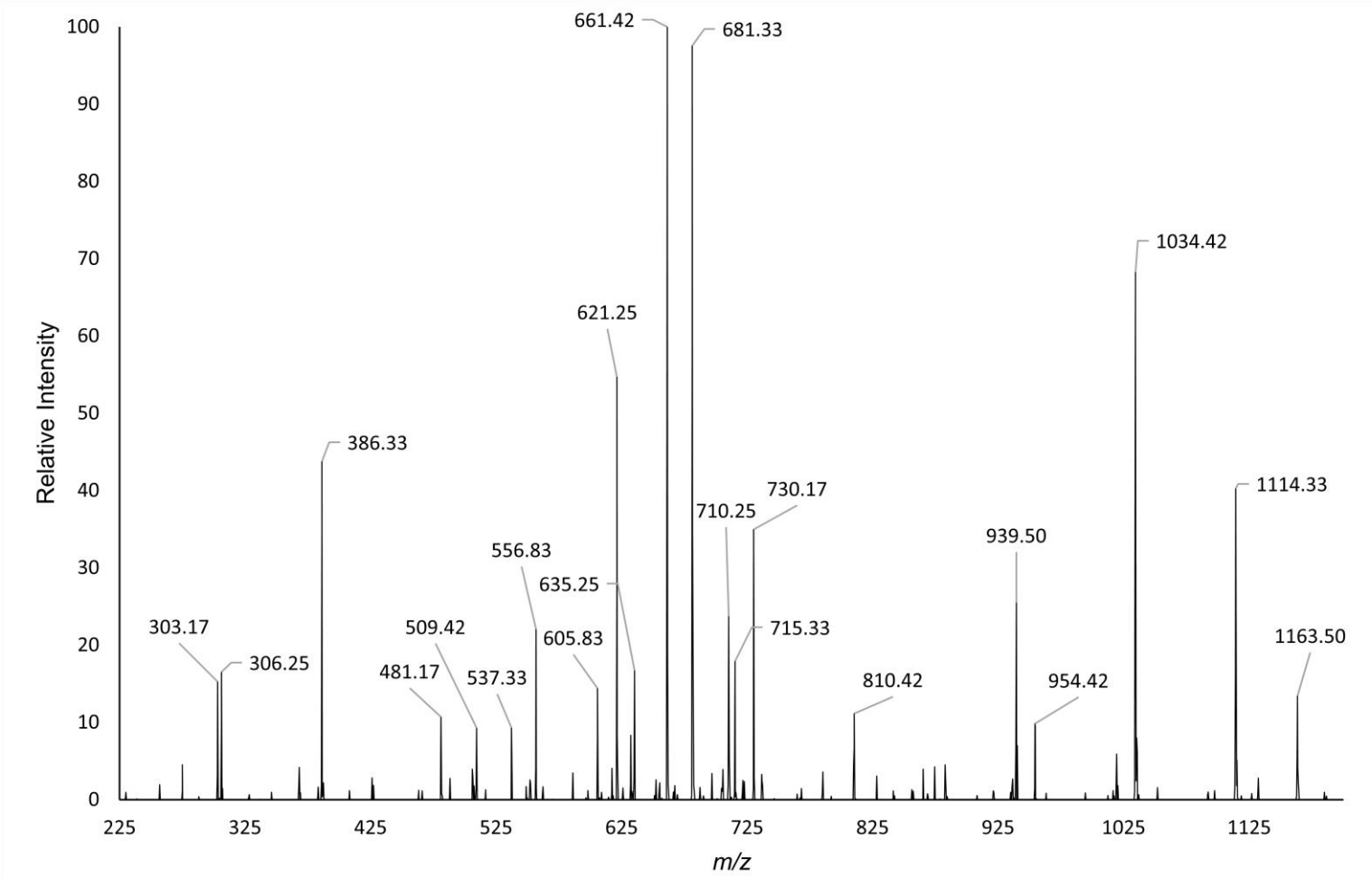

m/z 988 → 785 **selected ion ESI-LC/MS^3 spectrum with CID fragmentation of the HPLC purified peak 6/7 from scission of the ssAP-12mer (10 µM) with PIX (0.25 mM, 25 °C, 90 min) at retention time 9.4 minutes. Peaks are a significant mix of those seen previously for *m/z 745* and *785*.**

Appendix VII

Anthracycline-induced Scission Efficiency Plots for Reactions of MTX, PIX, and DOX with the 12mer Oligonucleotide in Chapter III

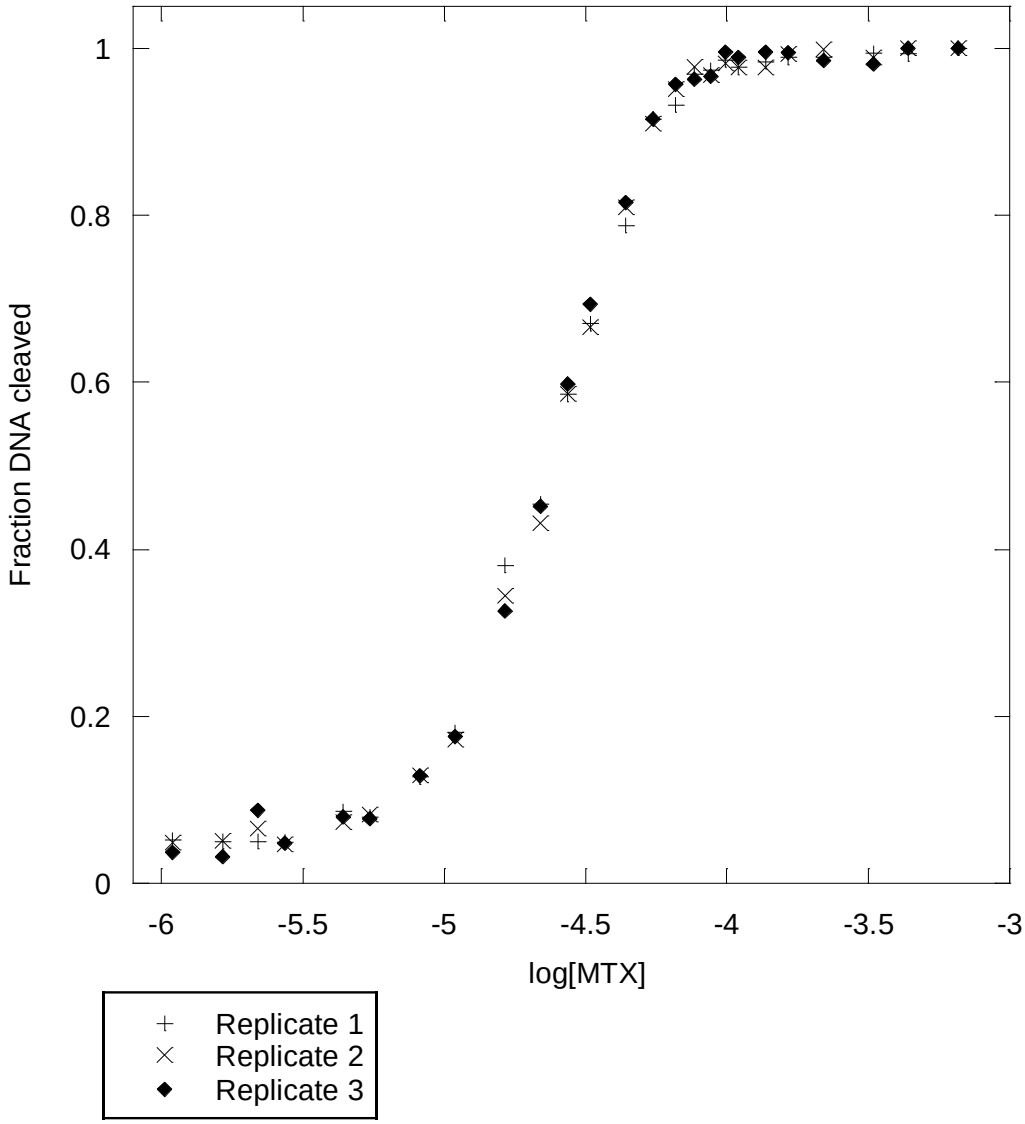

Plot of log[Drug] vs fraction of DNA cleaved for the reaction of the ssAP-12mer (0.001 mM) with MTX (0.001-0.65 mM) at 37 °C for 10 minutes.

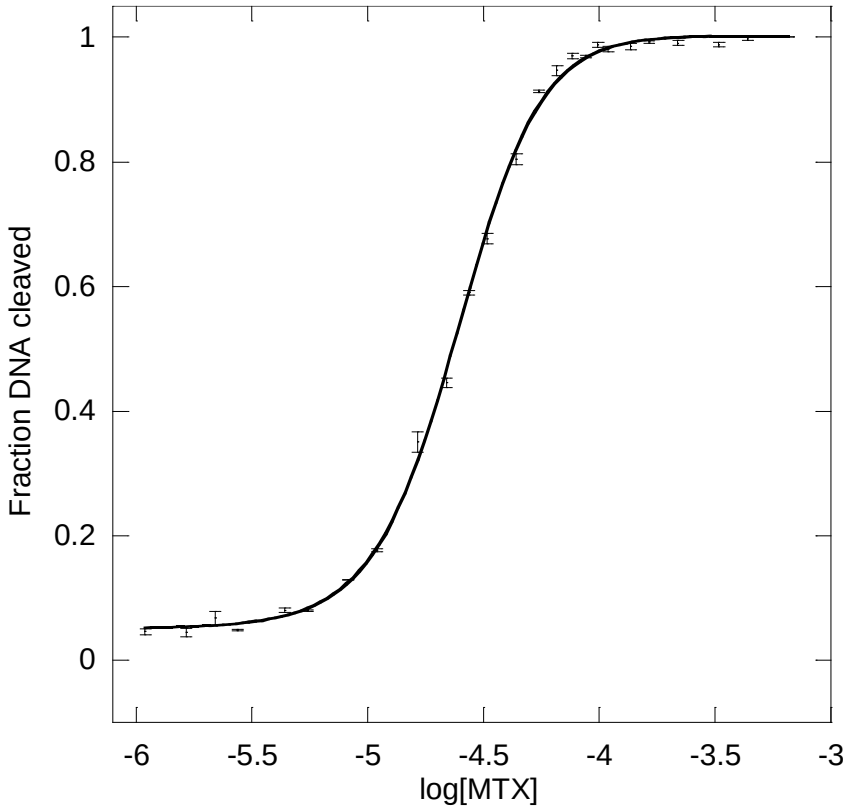

y = m1+(m2-m1)/(1+(x/m3)^m4)		
	Value	Error
m1	0.050896	0.0062181
m2	1.0024	0.005094
m3	-4.6117	0.0064822
m4	25.443	0.84305
Chisq	0.003935	NA
R	0.99951	NA

EC_{50} curve for the reaction of the ssAP-12mer (0.01 mM) with MTX (0.001-0.65 mM) at 37 °C for 10 minutes.

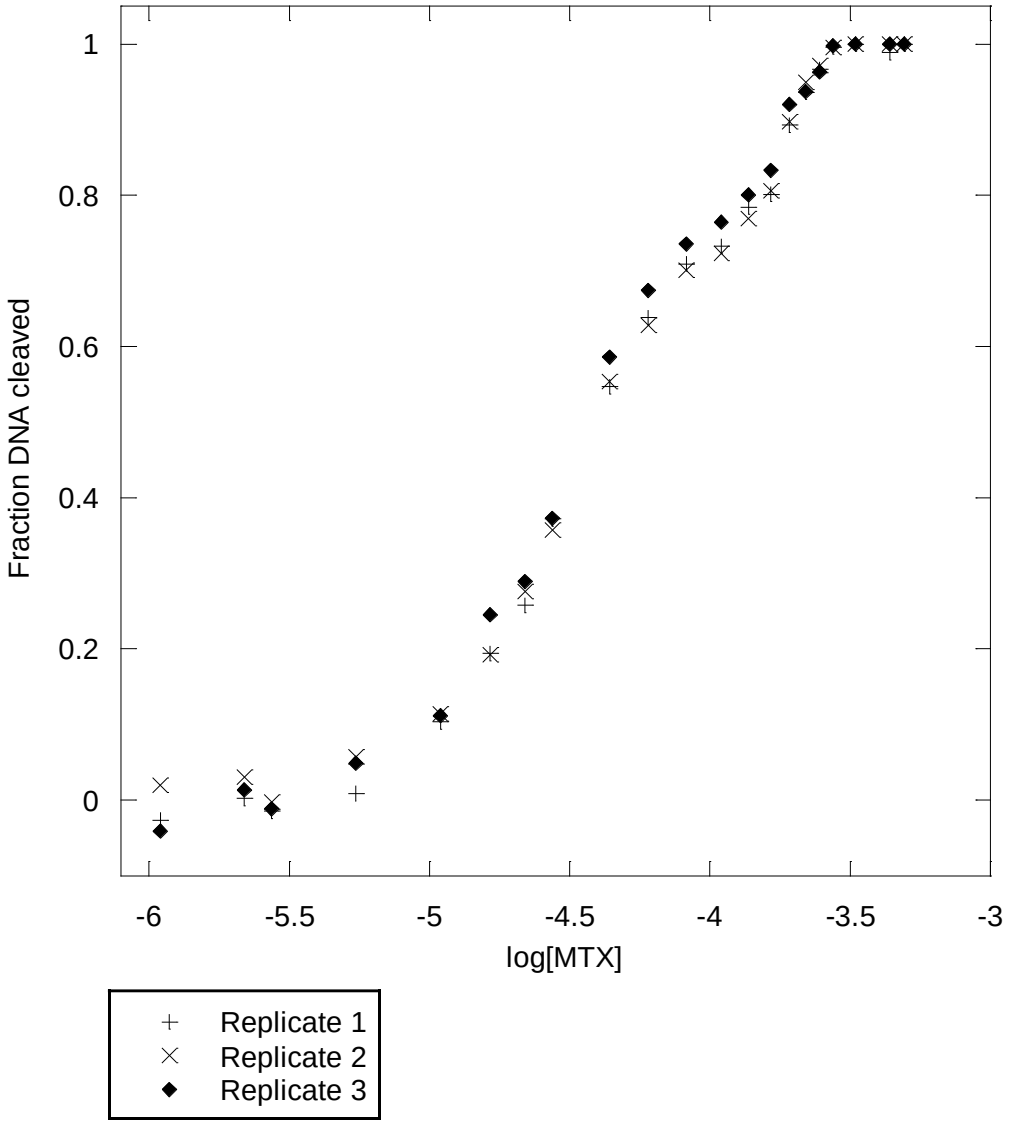

Plot of log[Drug] vs fraction of DNA cleaved for the reaction of the dsAP-12mer (0.01 mM) with MTX (0.001-0.5 mM) at 37 °C for 30 minutes.

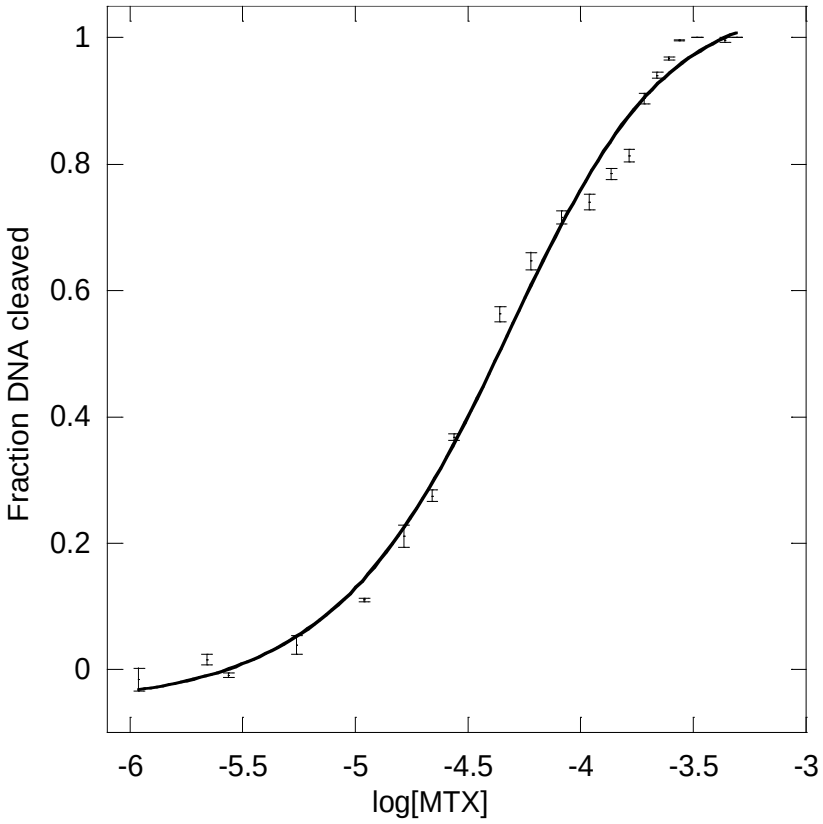

y = m1+(m2-m1)/(1+(x/m3)^m4)		
	Value	Error
m1	-0.060635	0.030169
m2	1.0484	0.03133
m3	-4.3705	0.034241
m4	11.757	1.1642
Chisq	0.019954	NA
R	0.99671	NA

EC_{50} curve for the reaction of the dsAP-12mer (0.01 mM) with MTX (0.001-0.5 mM) at 37 °C for 30 minutes.

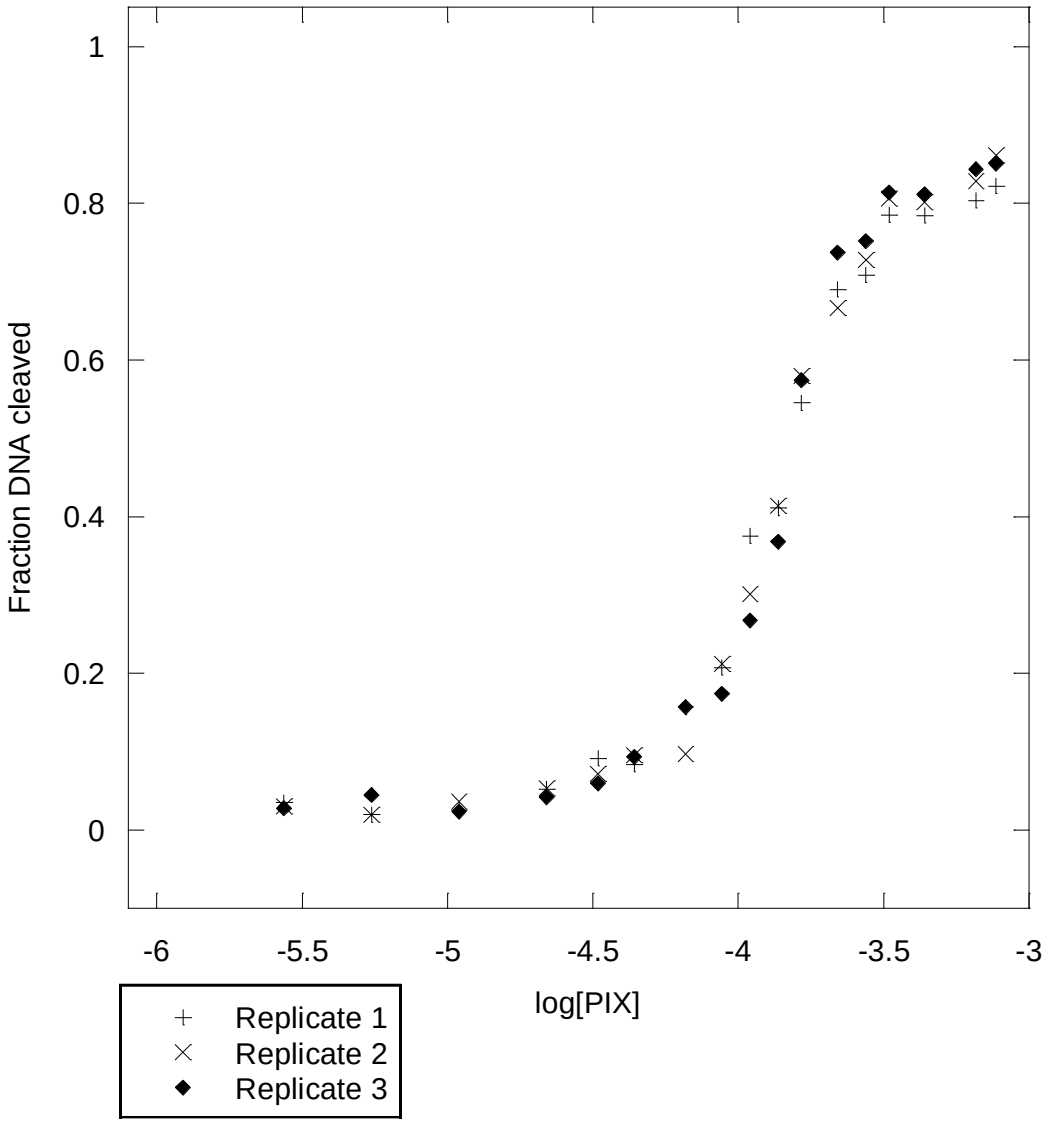

Plot of log[Drug] vs fraction of DNA cleaved for the reaction of the ssAP-12mer (0.01 mM) with PIX (0.0025-0.75 mM) at 37 °C for 10 minutes.

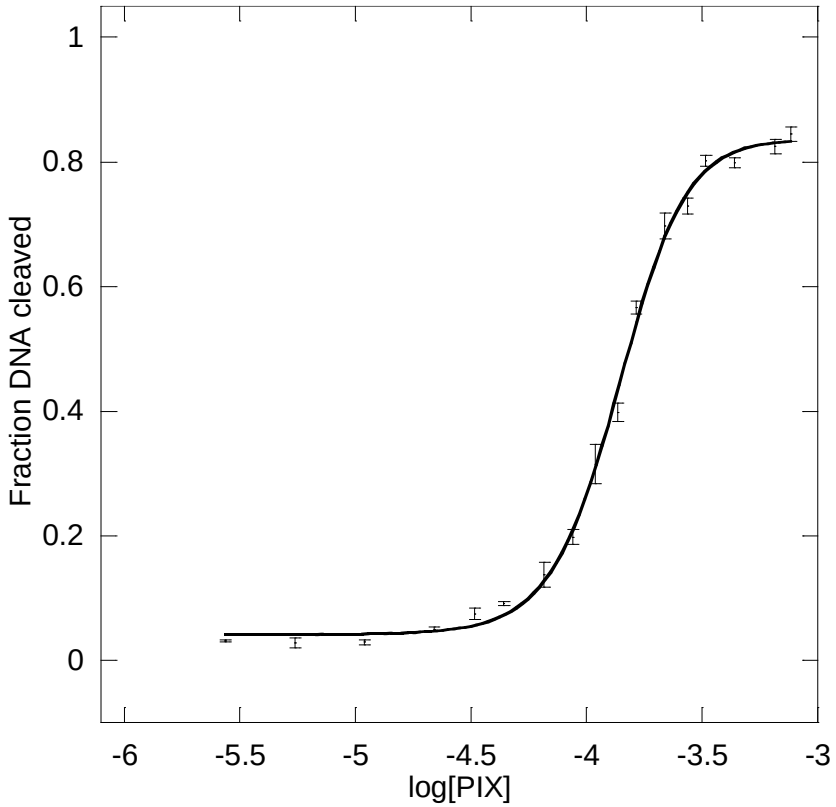

y = m1+(m2-m1)/(1+(x/m3)^m4)		
	Value	Error
m1	0.041182	0.0087387
m2	0.83558	0.011849
m3	-3.8599	0.010099
m4	26.375	1.6756
Chisq	0.0049018	NA
R	0.99862	NA

EC_{50} curve for the reaction of the ssAP-12mer (0.01 mM) with PIX (0.0025-0.75 mM) at 37 °C for 10 minutes.

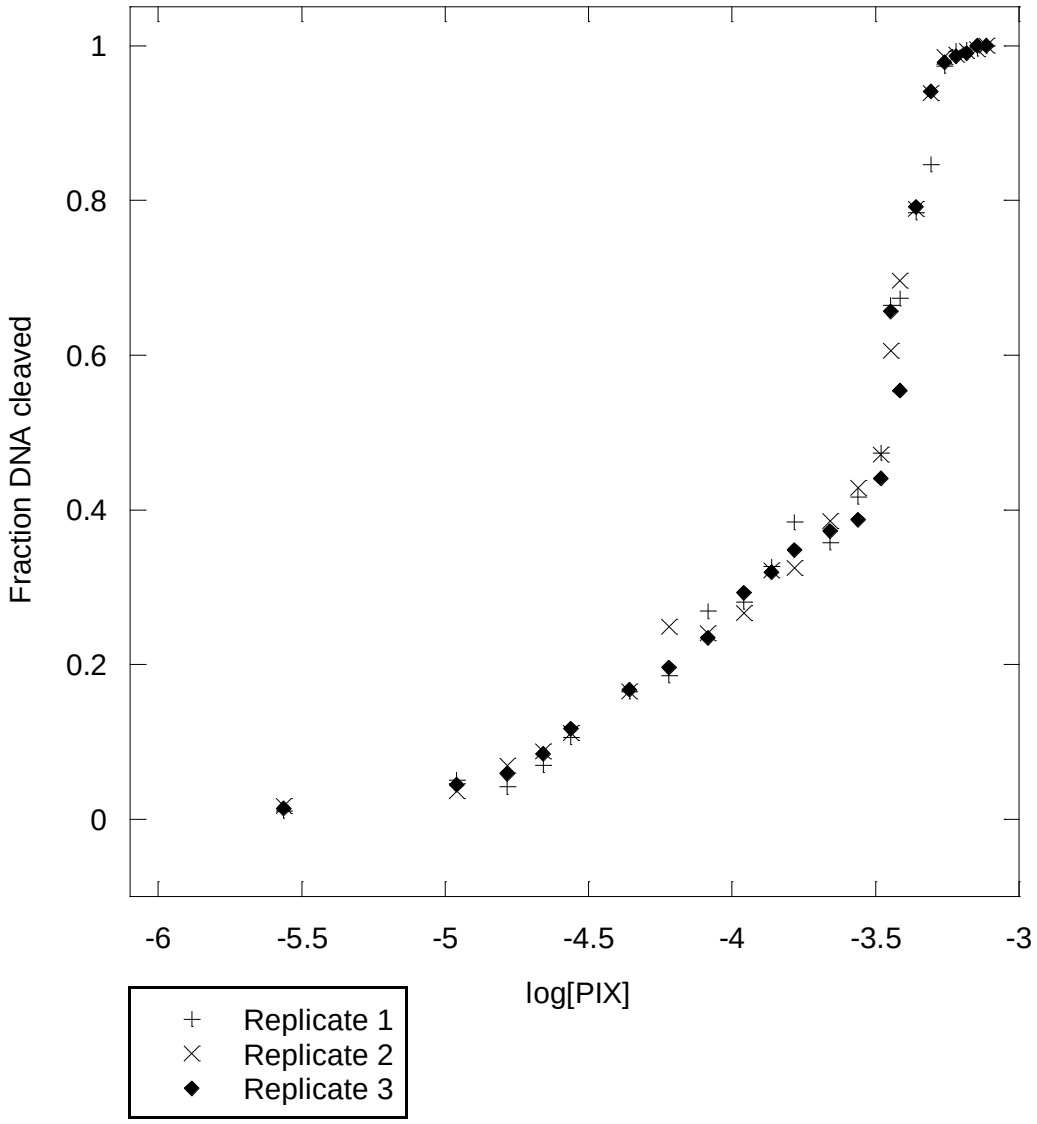

Plot of log[Drug] vs fraction of DNA cleaved for the reaction of the dsAP-12mer (0.01 mM) with PIX (0.0025-0.75 mM) at 37 °C for 30 minutes.

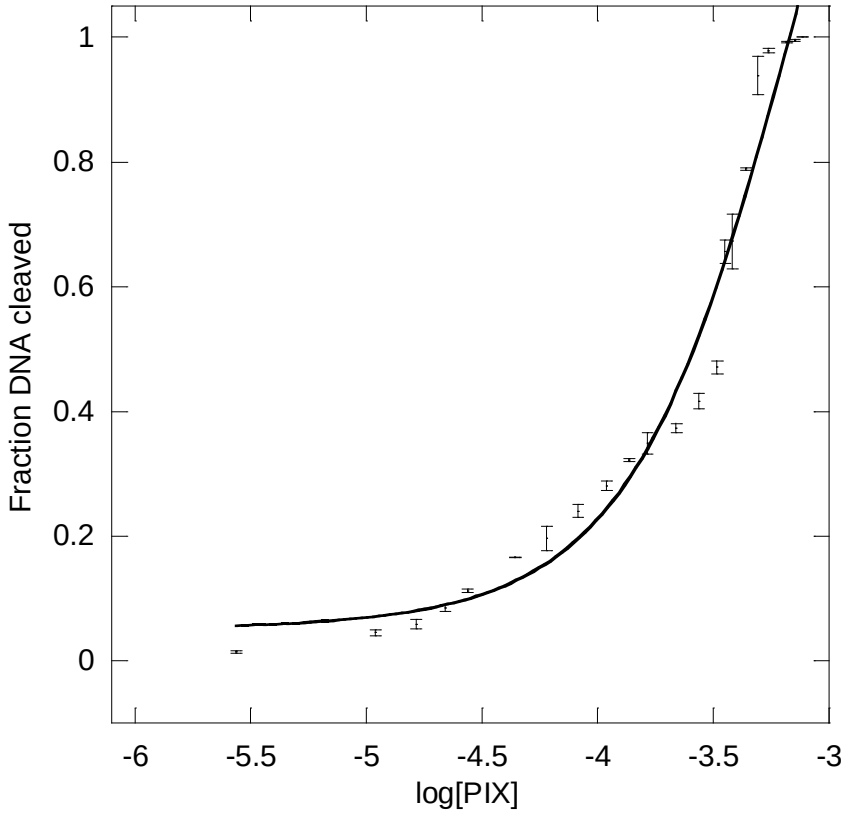

y = m1+(m2-m1)/(1+(x/m3)^m4)		
	Value	Error
m1	0.049749	0.045097
m2	1.7278	0.62705
m3	-3.2514	0.23127
m4	10.324	3.0015
Chisq	0.075964	NA
R	0.98542	NA

EC_{50} curve for the reaction of the dsAP-12mer (0.01 mM) with PIX (0.0025-0.75 mM) at 37 °C for 30 minutes.

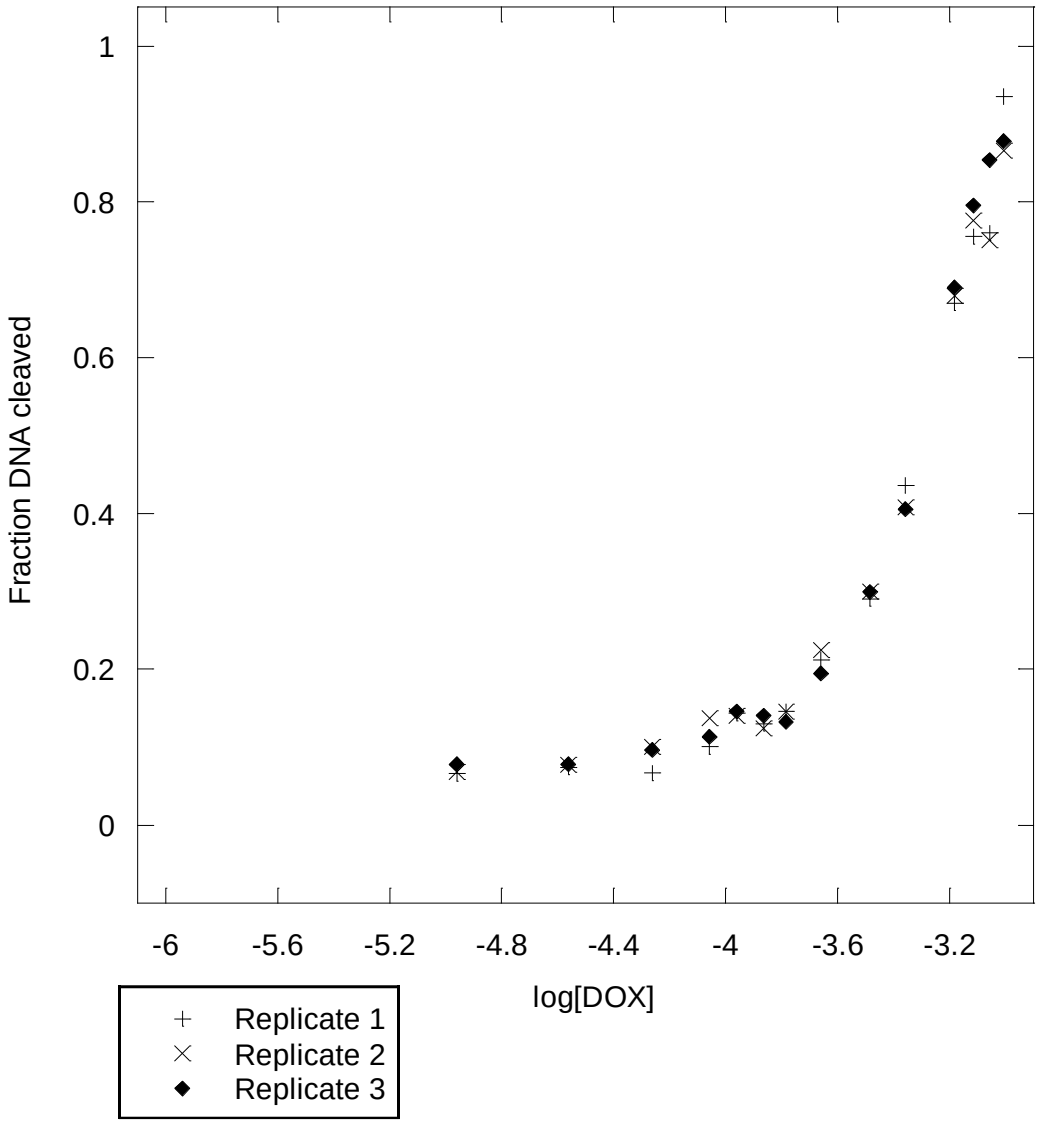

Plot of log[Drug] vs fraction of DNA cleaved for the reaction of the ssAP-12mer (0.01 mM) with DOX (0.01-1 mM) at 37 °C for 10 minutes.

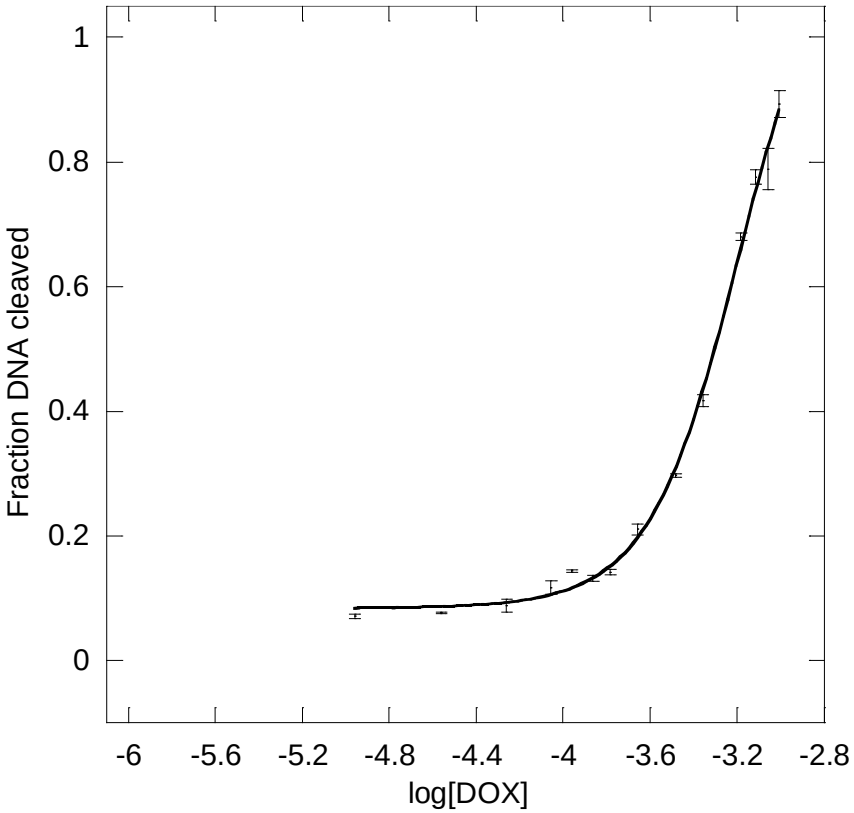

y = m1+(m2-m1)/(1+(x/m3)^m4)		
	Value	Error
m1	0.083158	0.011775
m2	1.143	0.11
m3	-3.2178	0.046288
m4	16.524	1.9349
Chisq	0.0041845	NA
R	0.99827	NA

EC_{50} curve for the reaction of the ssAP-12mer (0.01 mM) with DOX (0.01-1 mM) at 37 °C for 10 minutes.

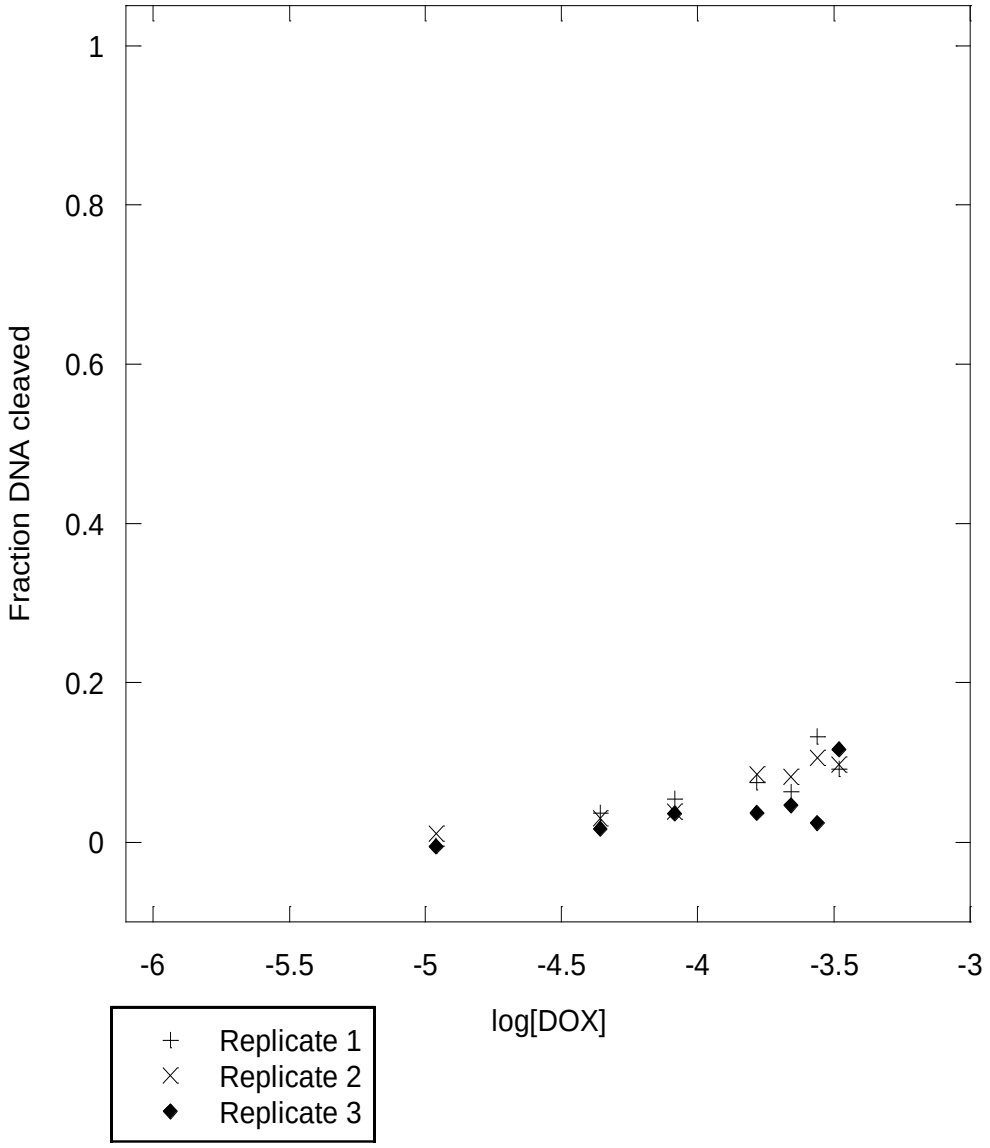

Plot of log[Drug] vs fraction of DNA cleaved for the reaction of the dsAP-12mer (0.01 mM) with DOX (0.01-0.325 mM) at 37 °C for 30 minutes.

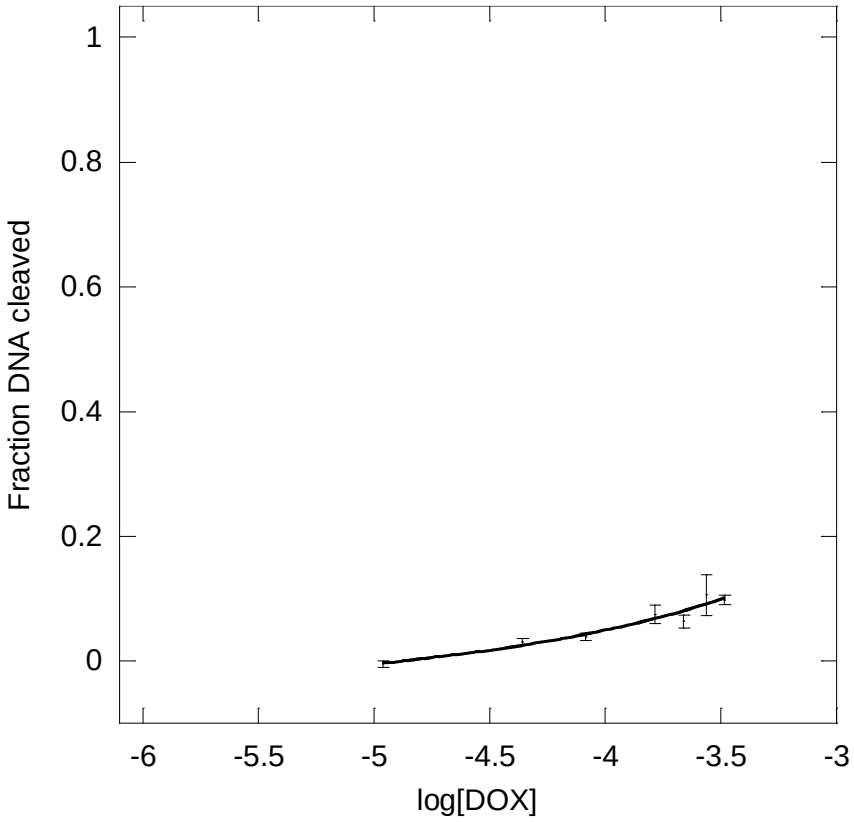

y = m1+(m2-m1)/(1+(x/m3)^m4)		
	Value	Error
m1	-0.072025	0.80638
m2	1.5646	145.38
m3	-1.6264	71.716
m4	2.8054	38.306
Chisq	0.00062285	NA
R	0.96582	NA

EC_{50} curve for the reaction of the dsAP-12mer (0.01 mM) with DOX (0.01-0.325 mM) at 37 °C for 30 minutes.

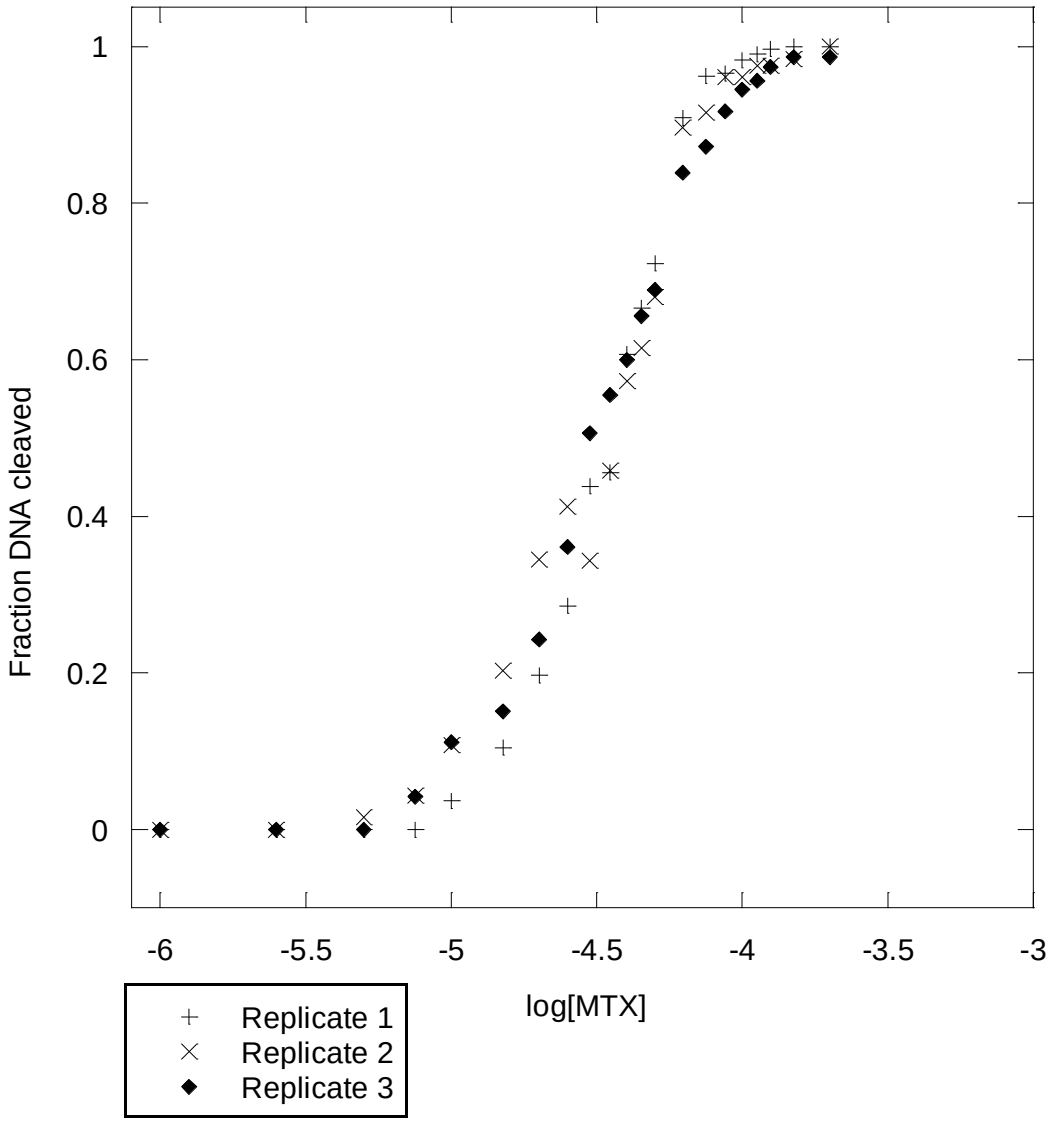

Plot of log[Drug] vs fraction of DNA cleaved for the reaction of the ssAP-12mer (0.01 mM) with MTX (0.001-0.2 mM) at 25 °C for 20 minutes.

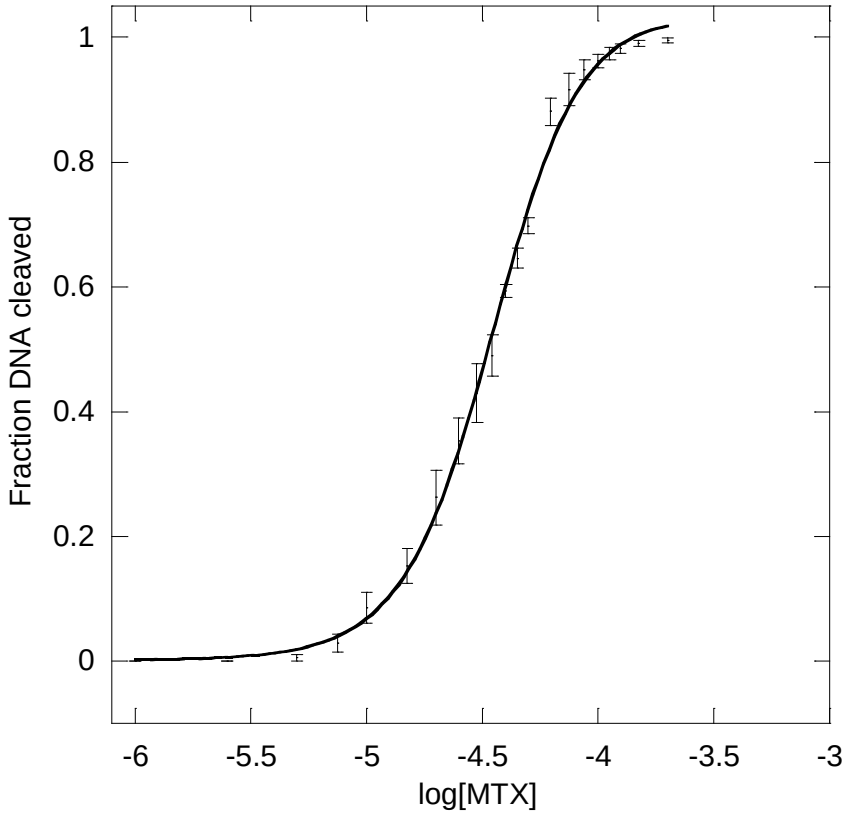

y = m1+(m2-m1)/(1+(x/m3)^m4)		
	Value	Error
m1	0.00094988	0.012791
m2	1.0311	0.015355
m3	-4.4615	0.010559
m4	23.412	1.3433
Chisq	0.0089563	NA
R	0.99853	NA

EC_{50} curve for the reaction of the ssAP-12mer (0.01 mM) with MTX (0.001-0.2 mM) at 25 °C for 20 minutes.

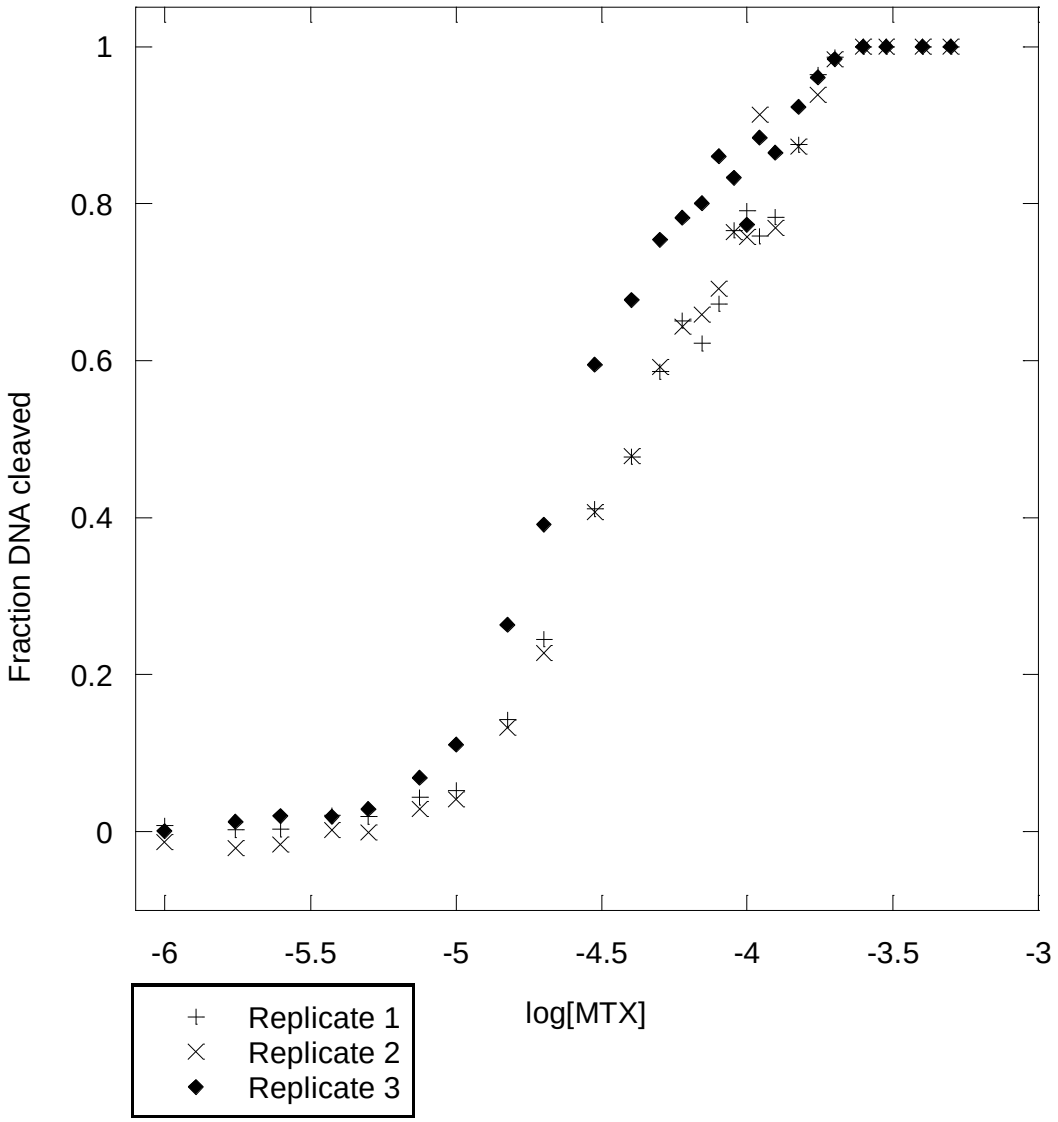

Plot of log[Drug] vs fraction of DNA cleaved for the reaction of the dsAP-12mer (0.01 mM) with MTX (0.001-05 mM) at 25 °C for 240 minutes.

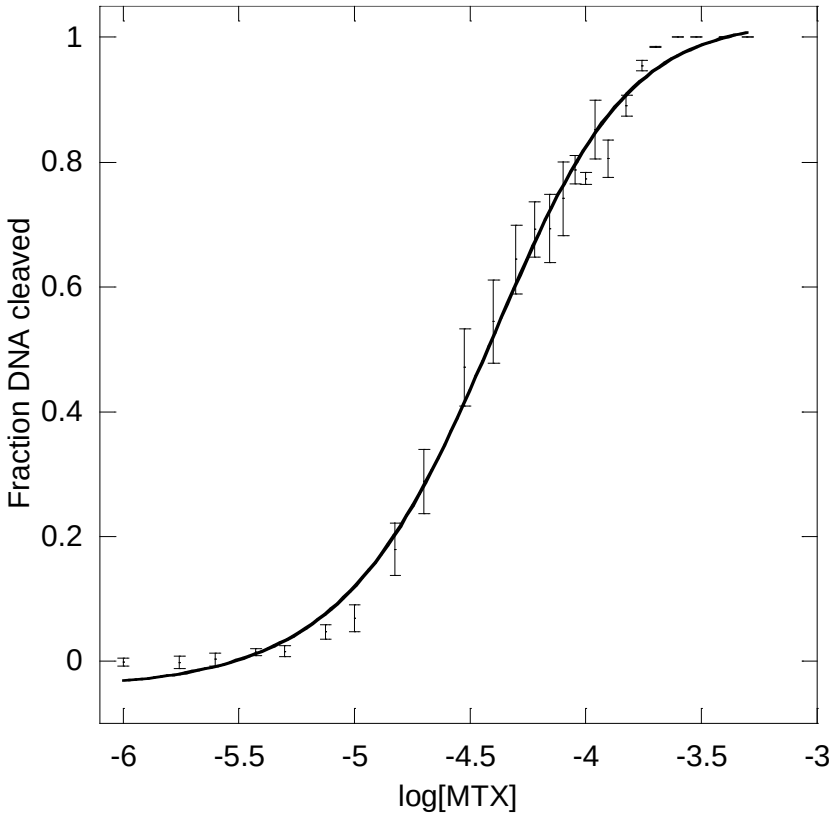

y = m1+(m2-m1)/(1+(x/m3)^m4)		
	Value	Error
m1	-0.046053	0.021589
m2	1.0231	0.020934
m3	-4.4364	0.024109
m4	14.216	1.0652
Chisq	0.023145	NA
R	0.99695	NA

EC_{50} curve for the reaction of the dsAP-12mer (0.01 mM) with MTX (0.001-0.5 mM) at 25 °C for 240 minutes.

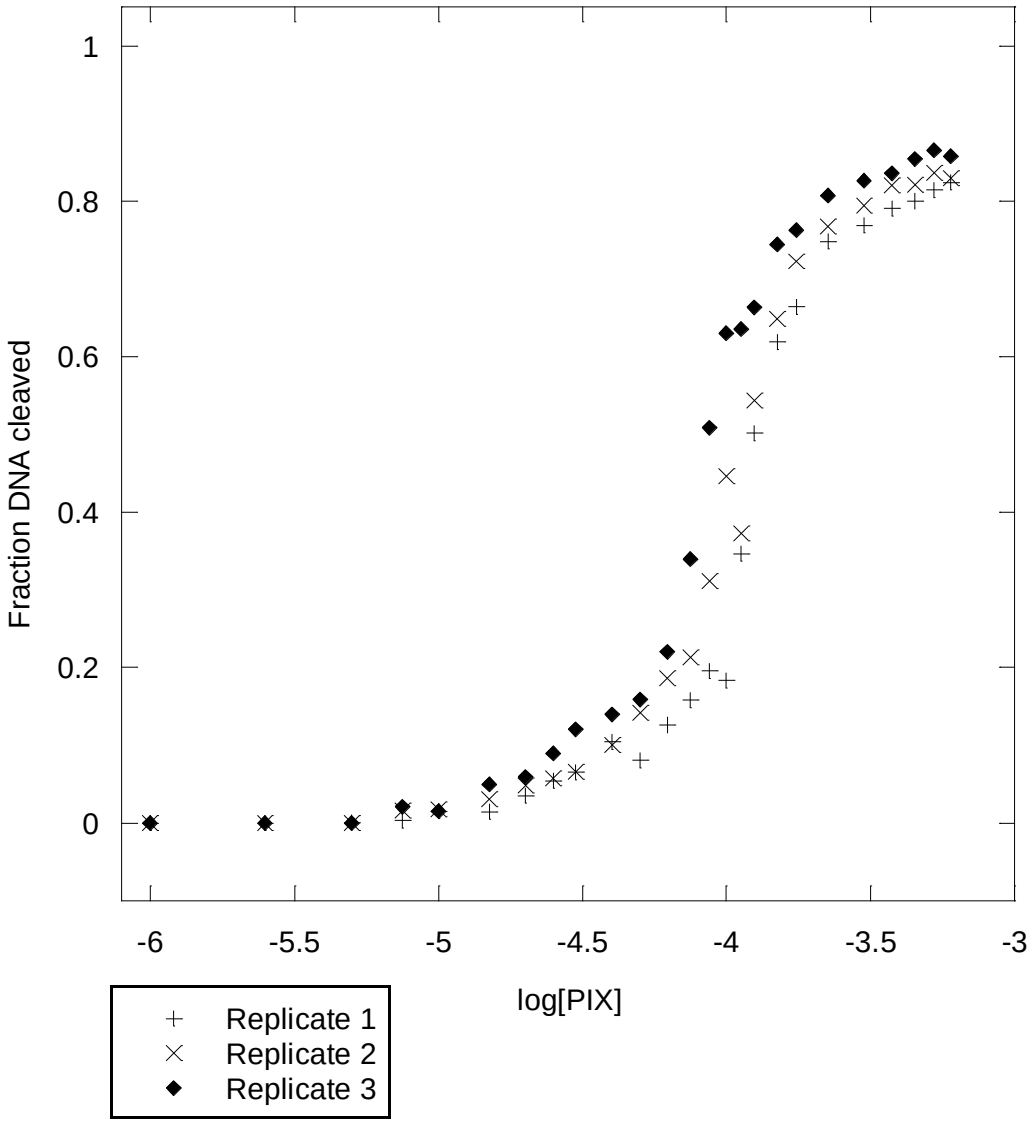

Plot of log[Drug] vs fraction of DNA cleaved for the reaction of the ssAP-12mer (0.01 mM) with PIX (0.001-0.6 mM) at 25 °C for 20 minutes.

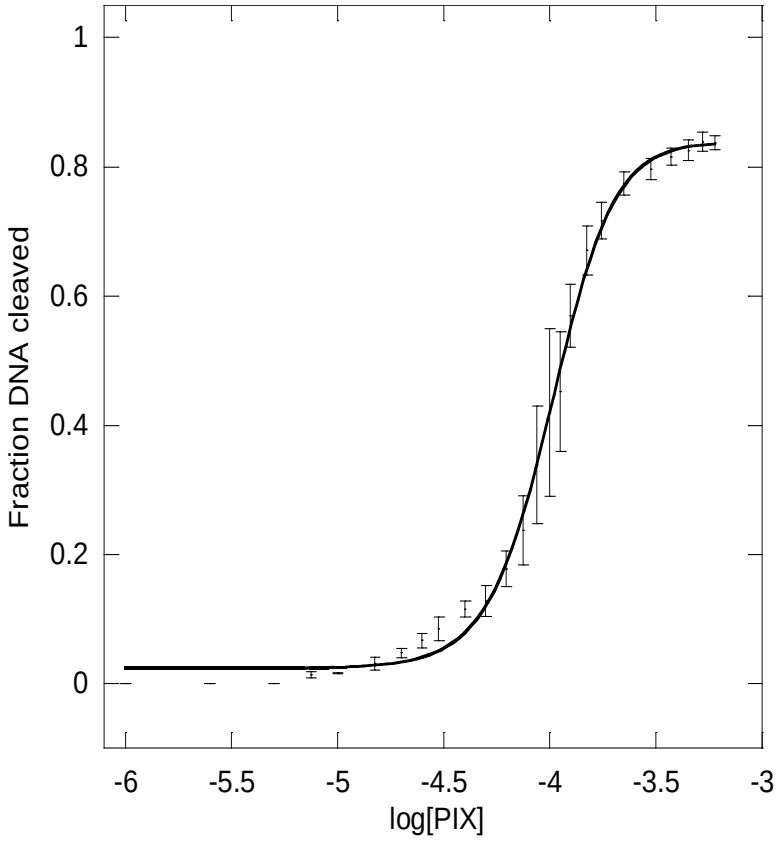

y = m1+(m2-m1)/(1+(x/m3)^m4)		
	Value	Error
m1	0.023191	0.0074003
m2	0.83831	0.01025
m3	-3.9913	0.0083983
m4	26.827	1.4749
Chisq	0.0089217	NA
R	0.99833	NA

EC_{50} curve for the reaction of the ssAP-12mer (0.01 mM) with PIX (0.001-0.6 mM) at 25 °C for 20 minutes.

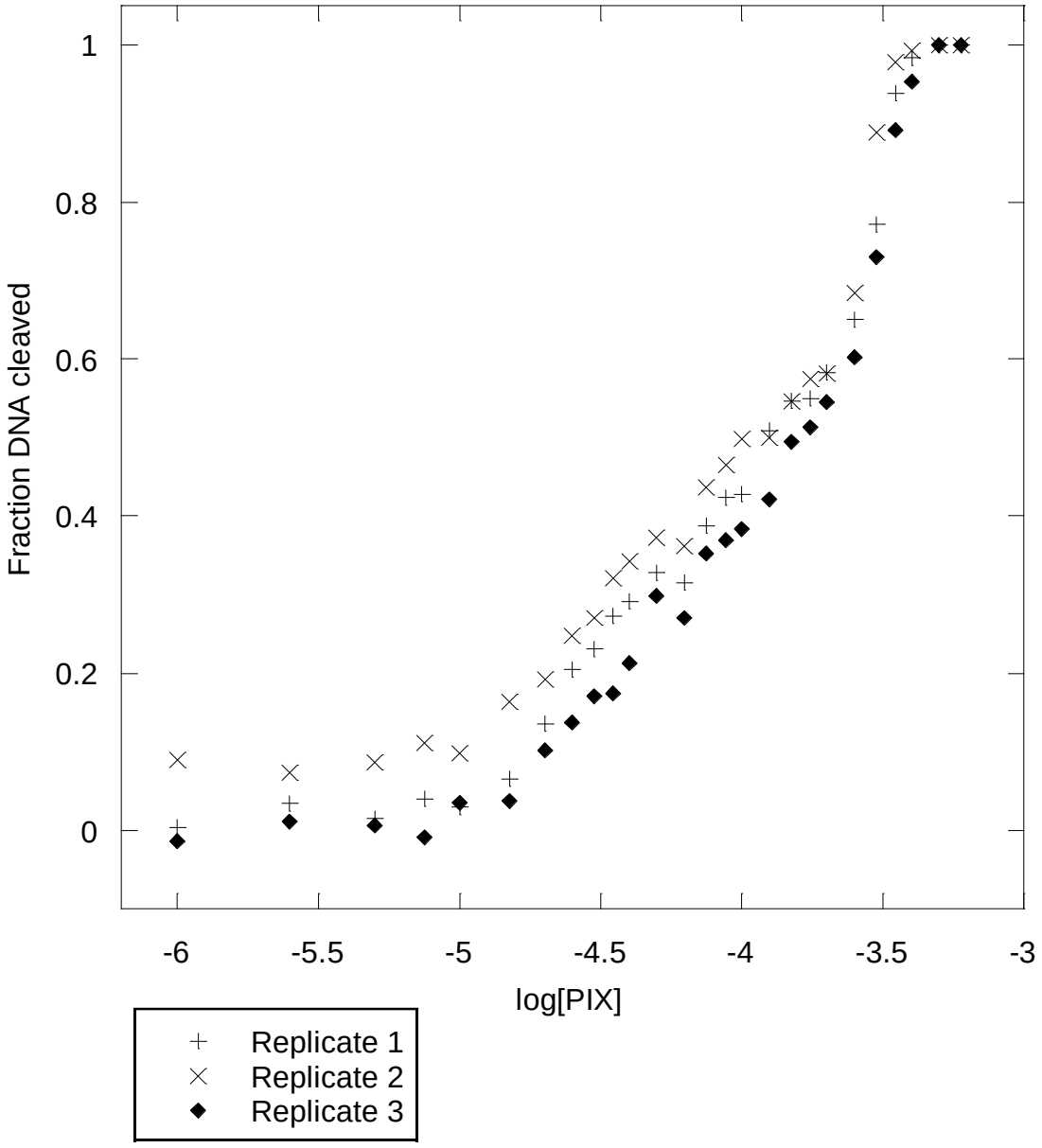

Plot of log[Drug] vs fraction of DNA cleaved for the reaction of the dsAP-12mer (0.01 mM) with PIX (0.001-0.6 mM) at 25 °C for 240 minutes.

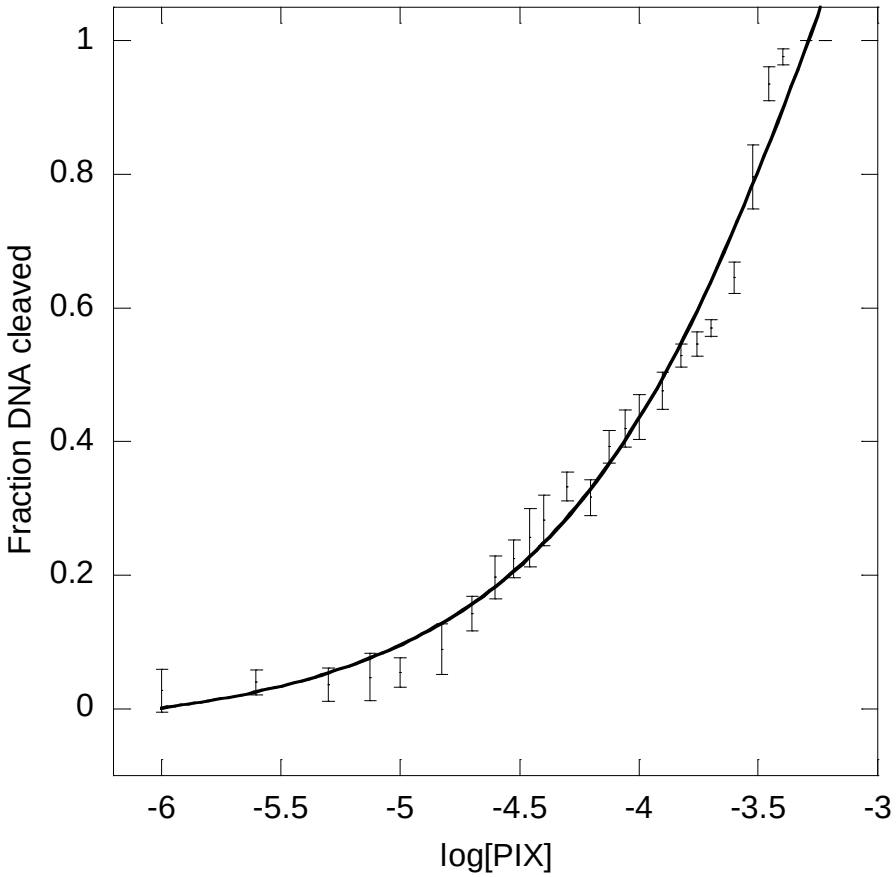

y = m1+(m2-m1)/(1+(x/m3)^m4)		
	Value	Error
m1	-0.044536	0.056094
m2	1.9123	0.64753
m3	-3.3581	0.31936
m4	6.458	1.5626
Chisq	0.043363	NA
R	0.99147	NA

EC_{50} curve for the reaction of the dsAP-12mer (0.01 mM) with PIX (0.001-0.6 mM) at 25 °C for 240 minutes.

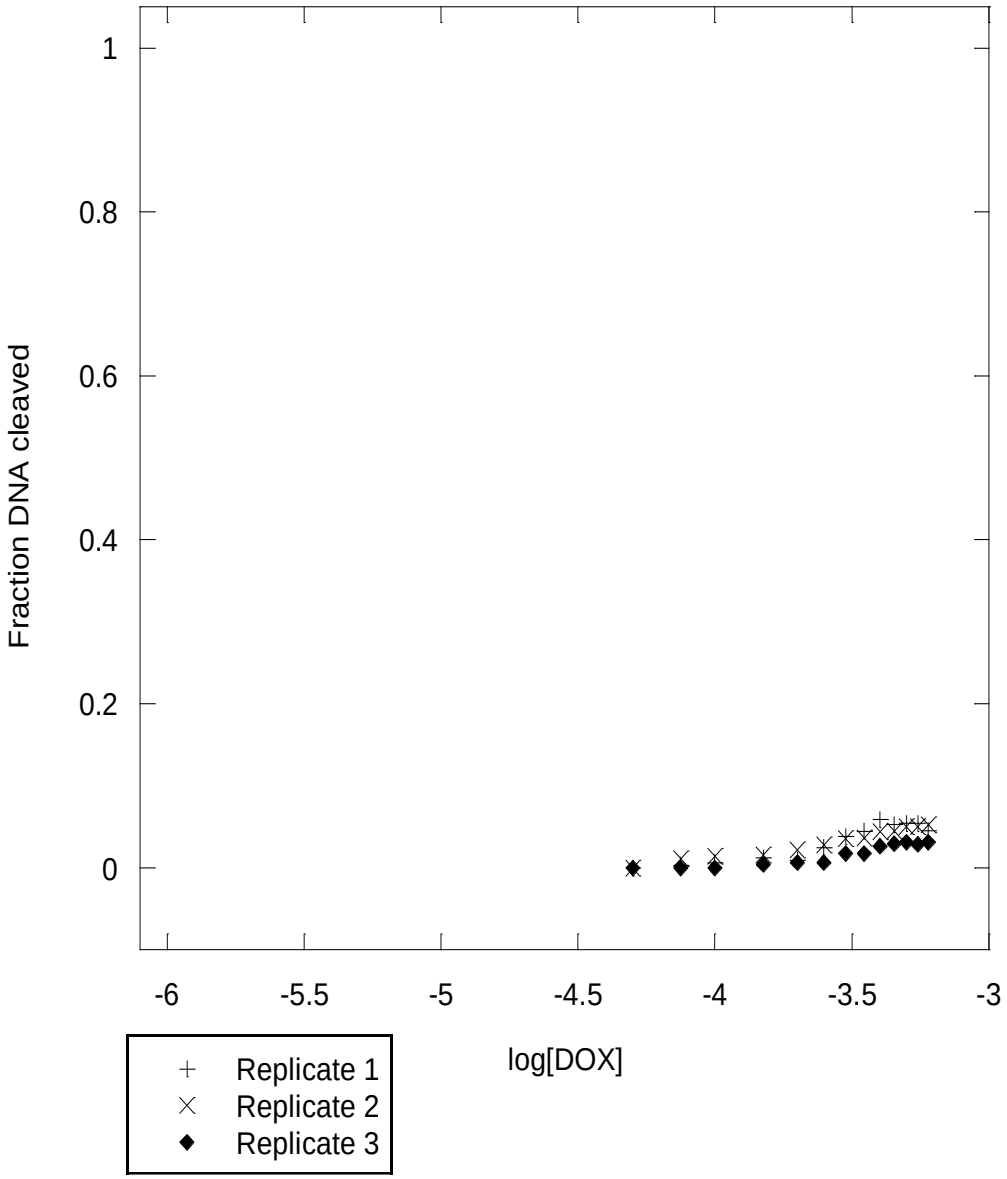

Plot of log[Drug] vs fraction of DNA cleaved for the reaction of the ssAP-12mer (0.01 mM) with DOX (0.05-0.6 mM) at 25 °C for 20 minutes.

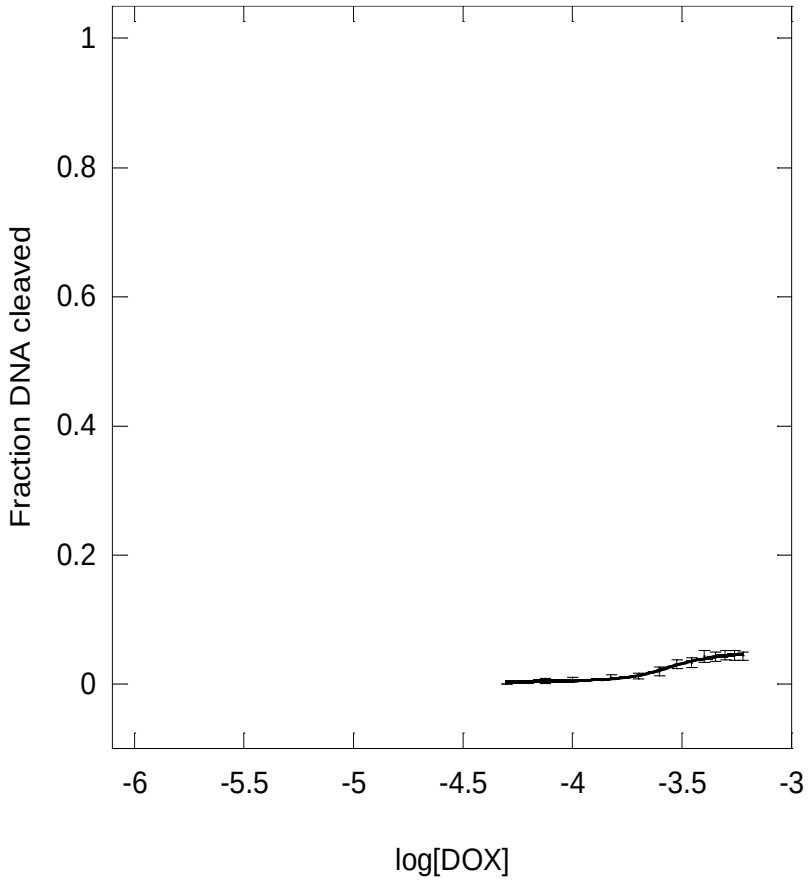

y = m1+(m2-m1)/(1+(x/m3)^m4)		
	Value	Error
m1	0.0039823	0.0016087
m2	0.046811	0.0025119
m3	-3.5621	0.022152
m4	33.717	6.8938
Chisq	5.8295e-5	NA
R	0.9918	NA

EC_{50} curve for the reaction of the ssAP-12mer (0.01 mM) with DOX (0.05-0.6 mM) at 25 °C for 20 minutes.

Appendix VIII

Thermal Melting Curves for Interactions of the Double-stranded AP-12mer, THF-12mer, and G-12mer Oligonucleotides with MTX, PIX, and DOX in Chapter III

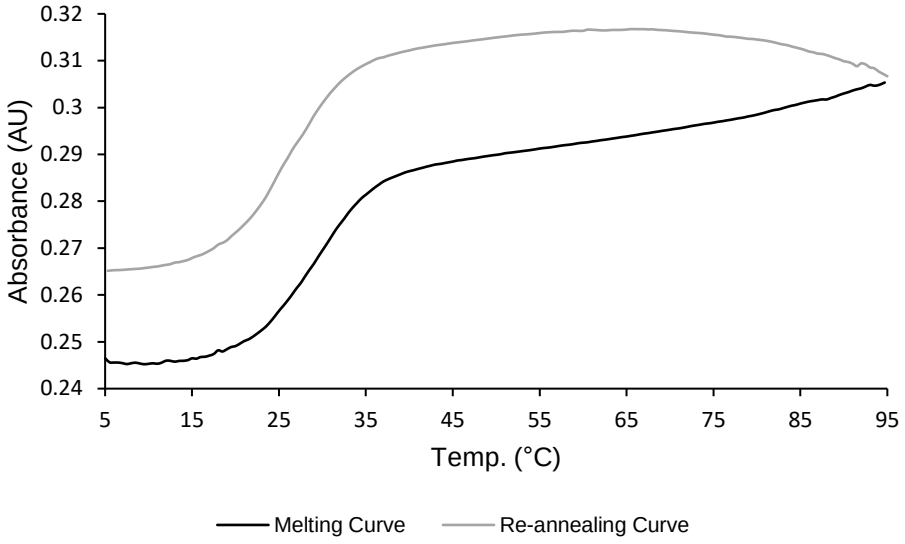

5'-GTT GC(idSp) CGT ATG-3' (THF-12mer) thermal melting stability from 5-95 °C with absorbance measured at 260 nm.

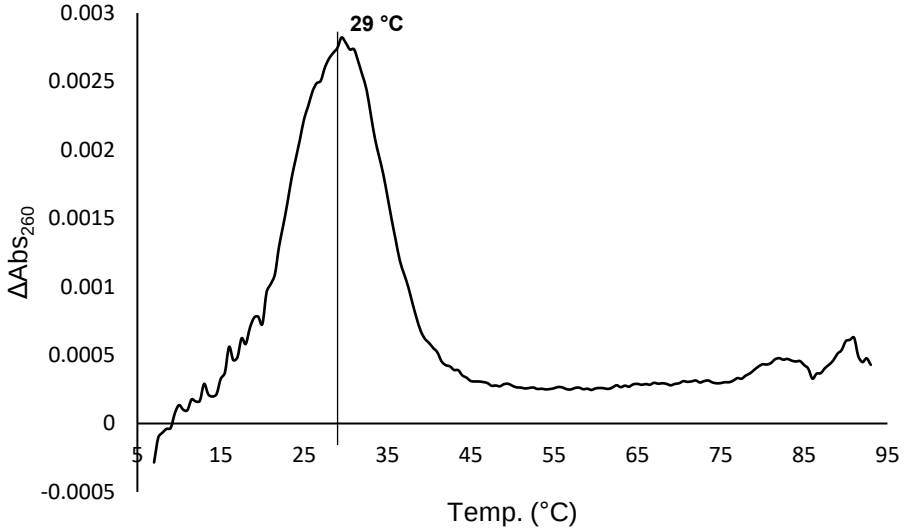

5'-GTT GC(idSp) CGT ATG-3' (THF-12mer) first derivative of the melting curve from 5-95 °C with absorbance measured at 260 nm.

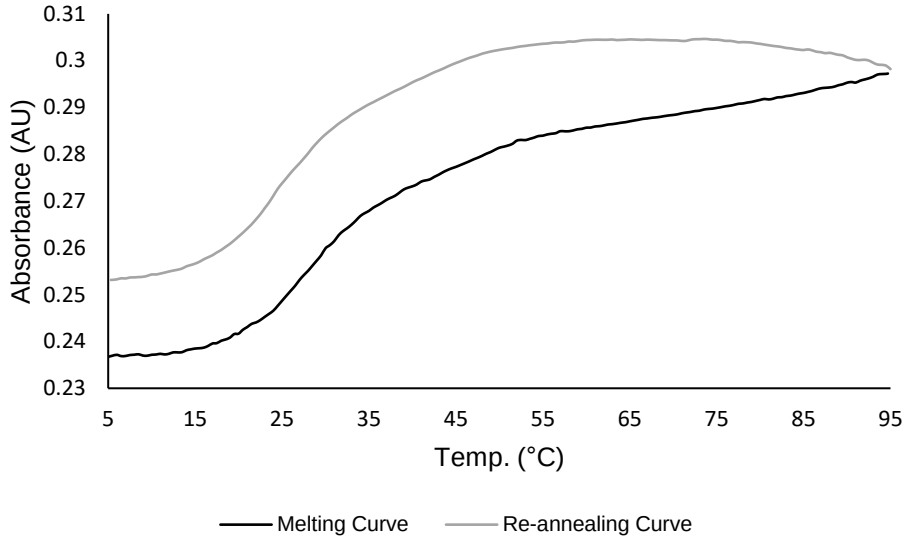

5'-GTT GC(idSp) CGT ATG-3' (THF-12mer) thermal melting stability with 0.25 equivalents MTX added from 5-95 °C with absorbance measured at 260 nm.

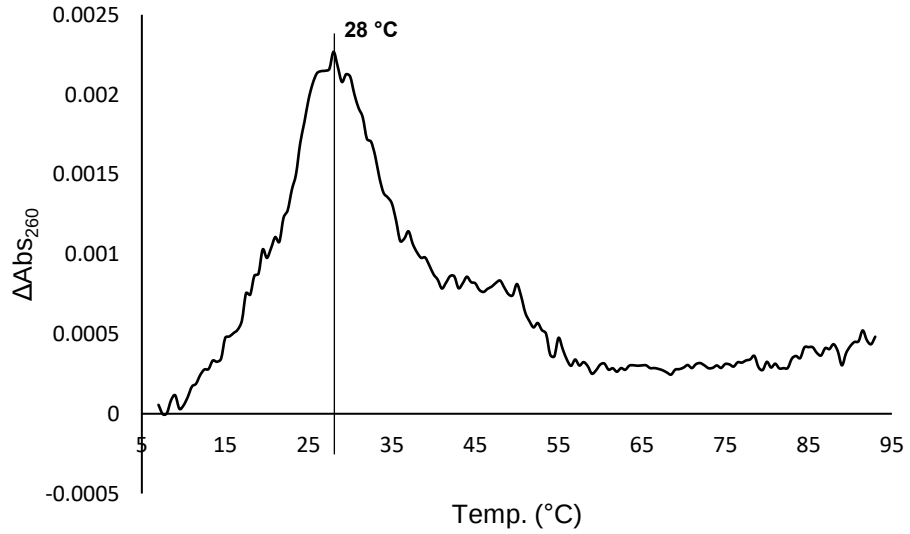

5'-GTT GC(idSp) CGT ATG-3' (THF-12mer) first derivative of the melting curve with 0.25 equivalents MTX added from 5-95 °C with absorbance measured at 260 nm.

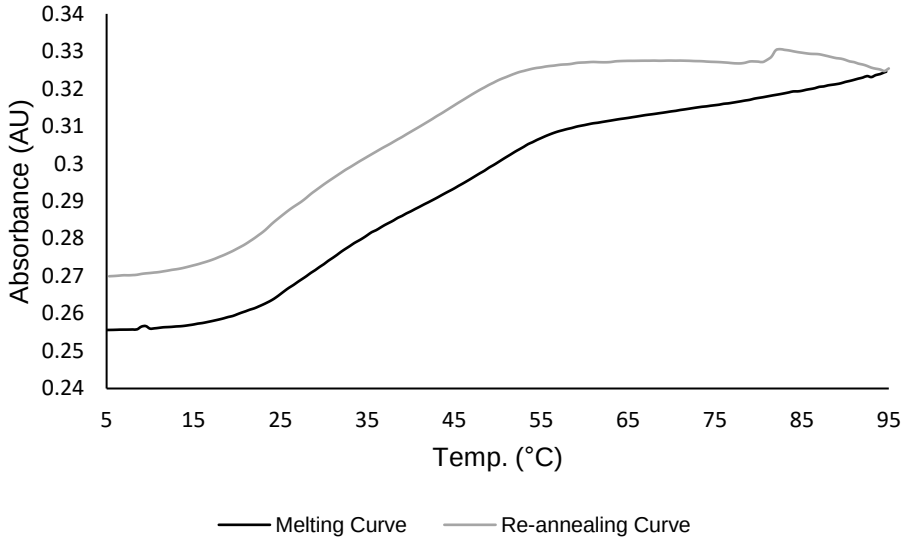

5'-GTT GC(idSp) CGT ATG-3' (THF-12mer) thermal melting stability with 0.5 equivalents MTX added from 5-95 °C with absorbance measured at 260 nm.

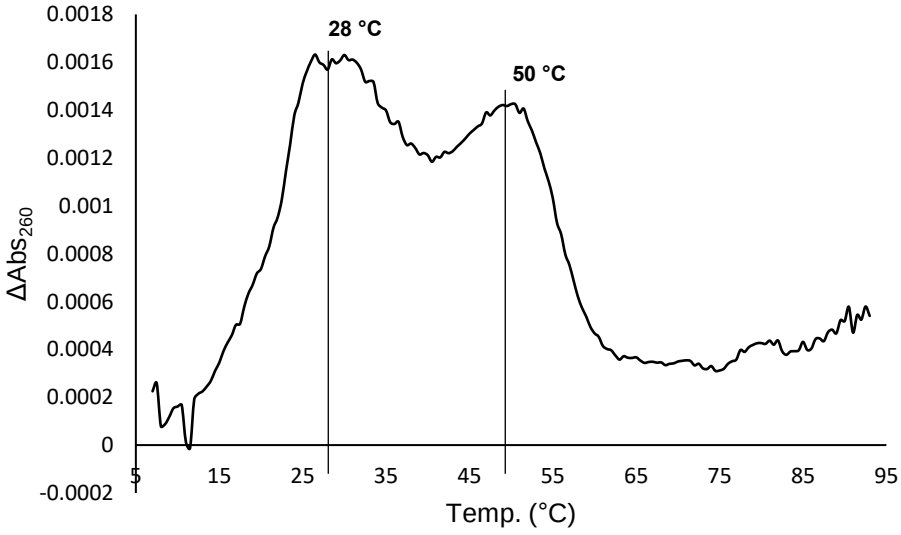

5'-GTT GC(idSp) CGT ATG-3' (THF-12mer) first derivative of the melting curve with 0.5 equivalents MTX added from 5-95 °C with absorbance measured at 260 nm.

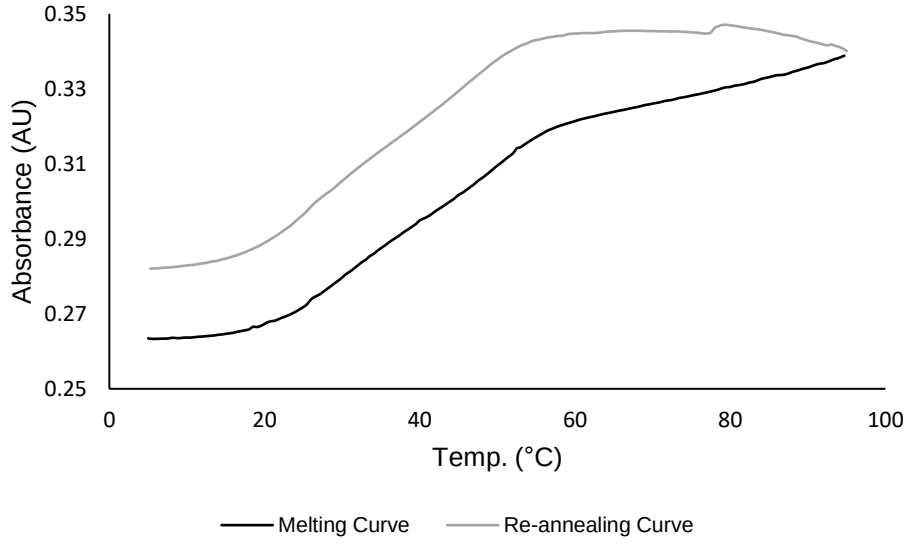

5'-GTT GC(idSp) CGT ATG-3' (THF-12mer) thermal melting stability with 0.75 equivalents MTX added from 5-95 °C with absorbance measured at 260 nm.

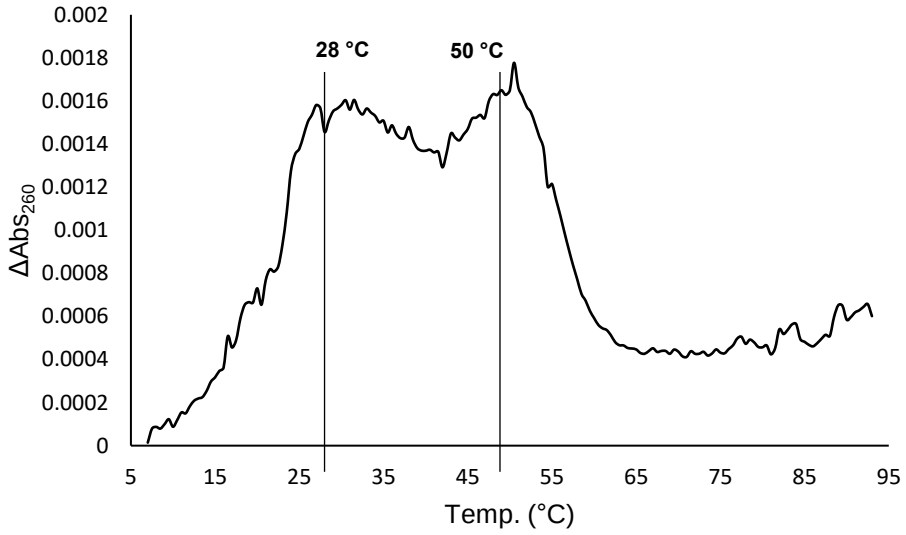

5'-GTT GC(idSp) CGT ATG-3' (THF-12mer) first derivative of the melting curve with 0.75 equivalents MTX added from 5-95 °C with absorbance measured at 260 nm.

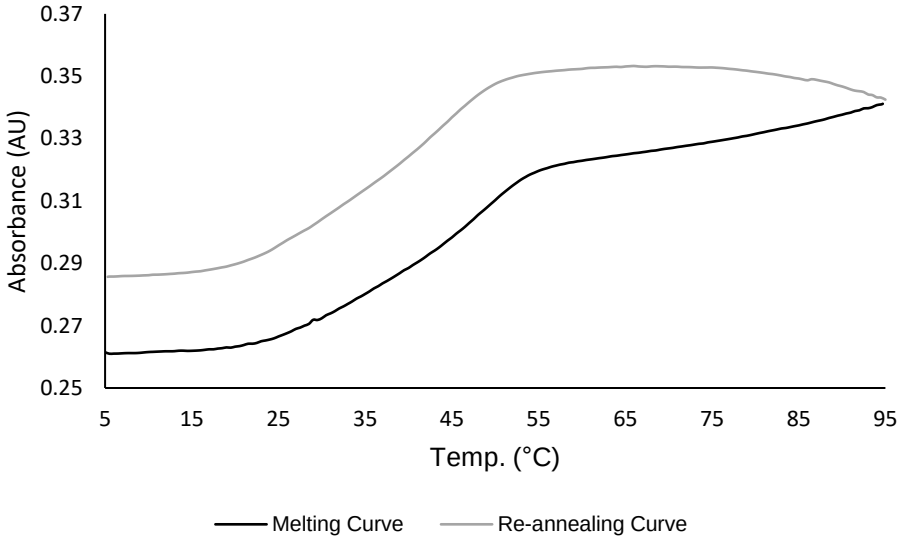

5'-GTT GC(idSp) CGT ATG-3' (THF-12mer) thermal melting stability with 1 equivalent MTX added from 5-95 °C with absorbance measured at 260 nm.

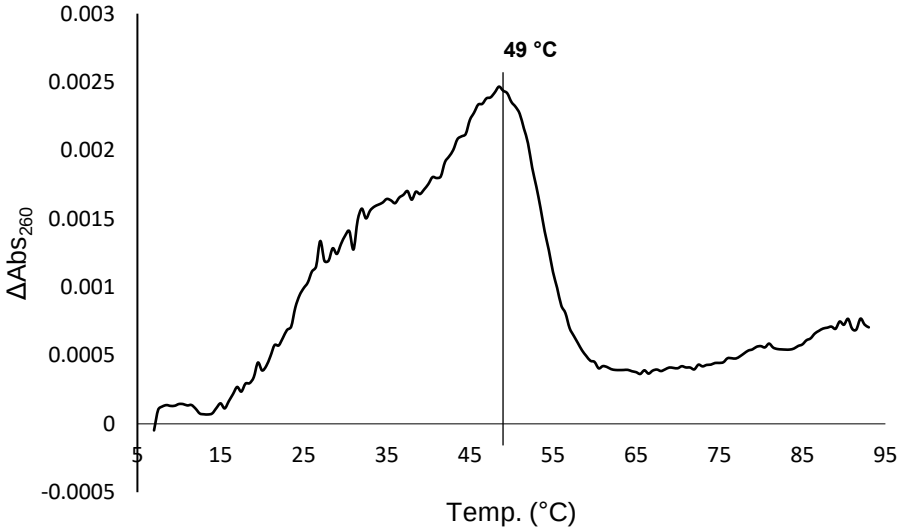

5'-GTT GC(idSp) CGT ATG-3' (THF-12mer) first derivative of the melting curve with 1 equivalent MTX added from 5-95 °C with absorbance measured at 260 nm.

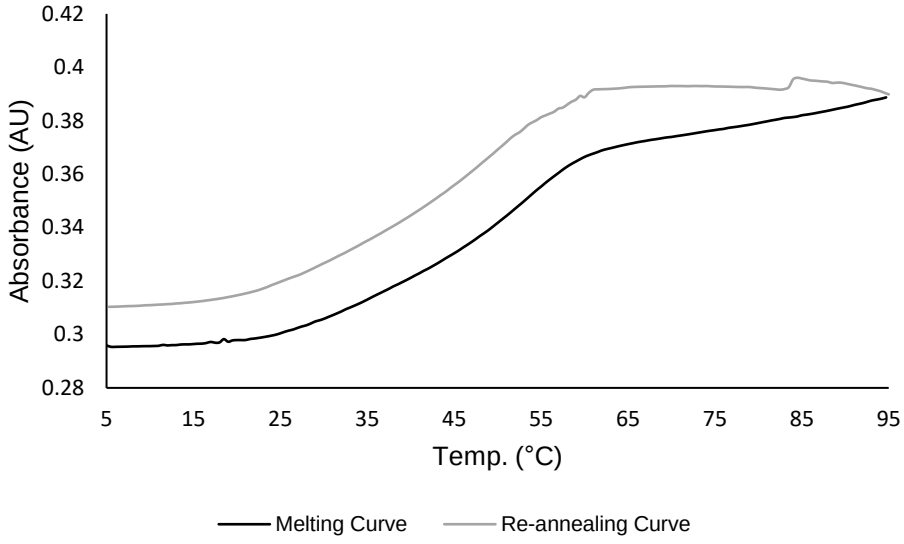

5'-GTT GC(idSp) CGT ATG-3' (THF-12mer) thermal melting stability with 1.6 equivalents MTX added from 5-95 °C with absorbance measured at 260 nm.

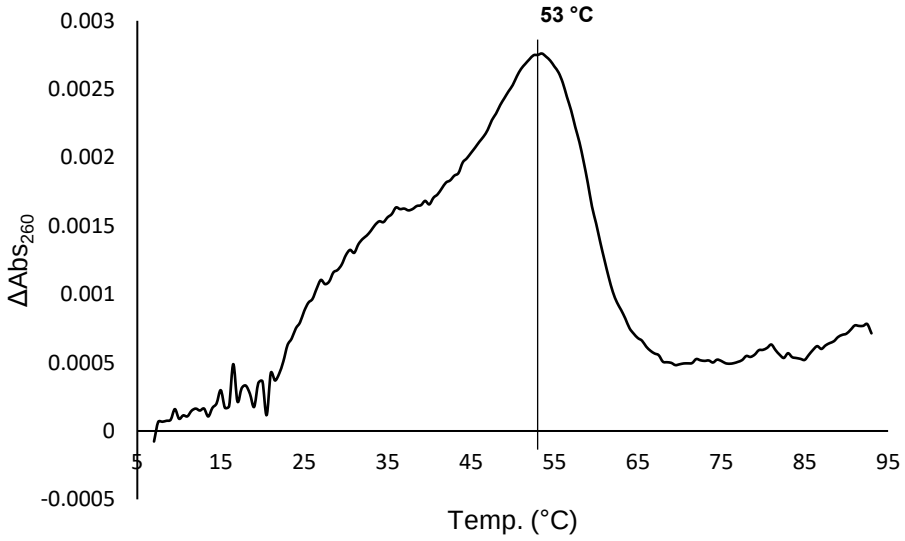

5'-GTT GC(idSp) CGT ATG-3' (THF-12mer) first derivative of the melting curve with 1.6 equivalents MTX added from 5-95 °C with absorbance measured at 260 nm.

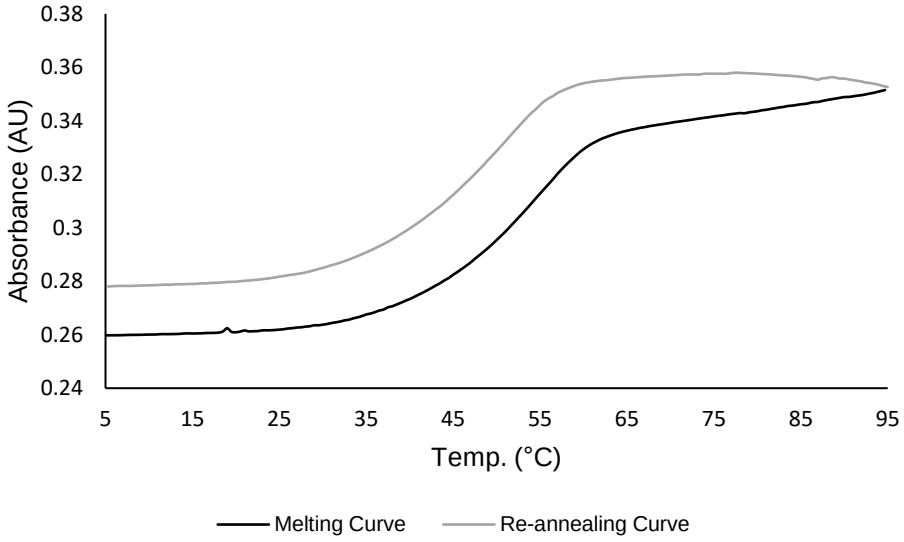

5'-GTT GC(idSp) CGT ATG-3' (THF-12mer) thermal melting stability with 2.5 equivalents MTX added from 5-95 °C with absorbance measured at 260 nm.

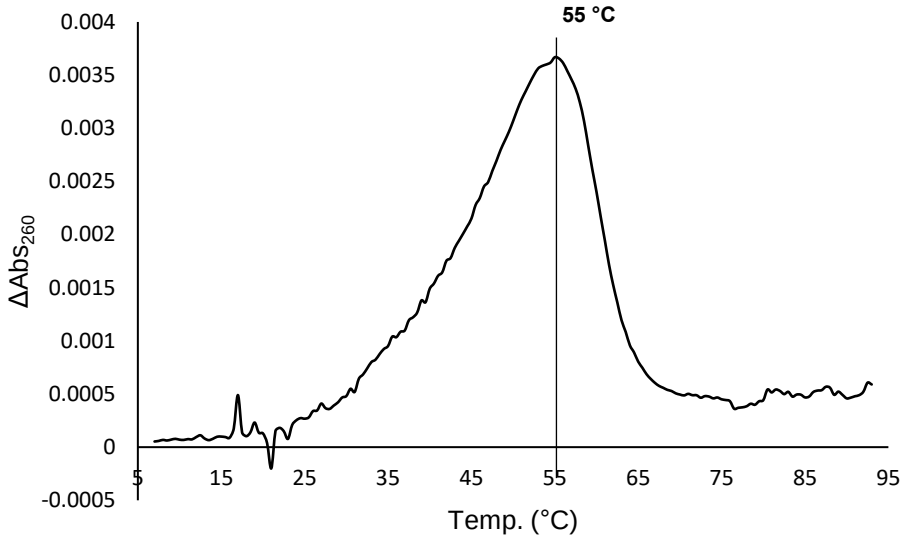

5'-GTT GC(idSp) CGT ATG-3' (THF-12mer) first derivative of the melting curve with 2.5 equivalents MTX added from 5-95 °C with absorbance measured at 260 nm.

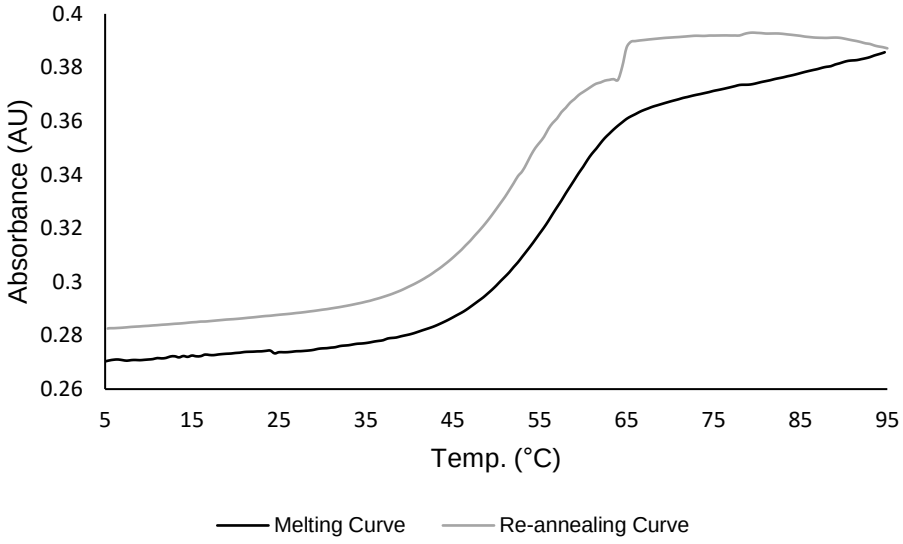

5'-GTT GC(idSp) CGT ATG-3' (THF-12mer) thermal melting stability with 5 equivalents MTX added from 5-95 °C with absorbance measured at 260 nm.

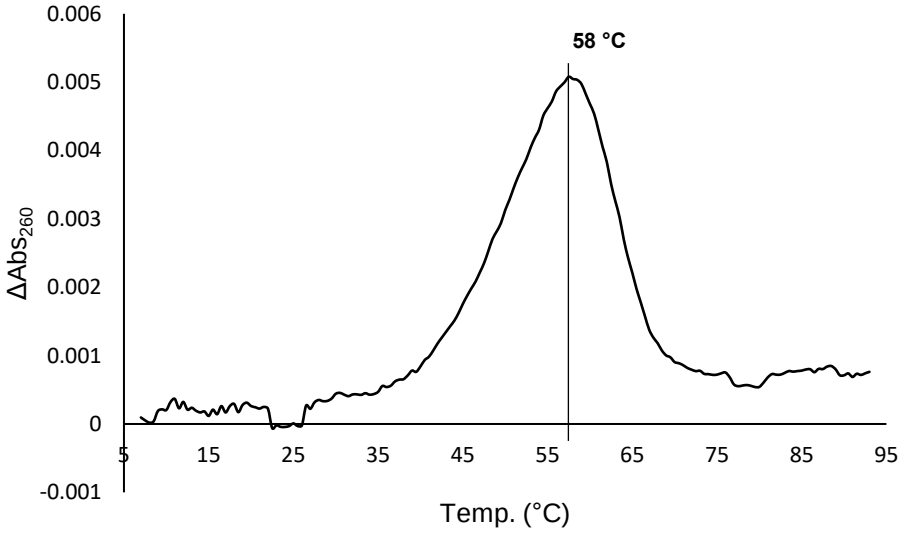

5'-GTT GC(idSp) CGT ATG-3' (THF-12mer) first derivative of the melting curve with 5 equivalents MTX added from 5-95 °C with absorbance measured at 260 nm.

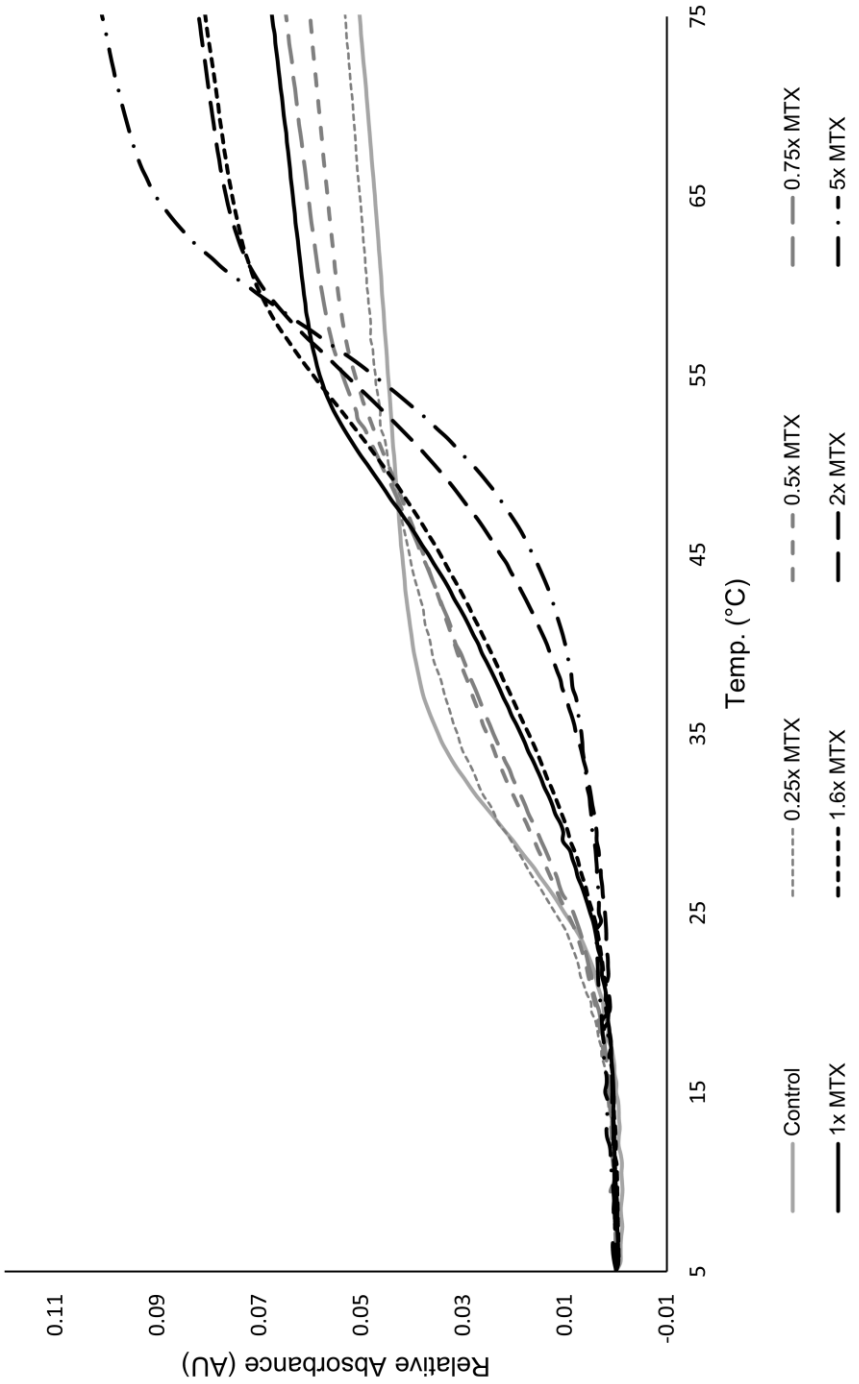

5’-GTT GC(idSp) CGT ATG-3’ (THF-12mer) thermal melting stability comparison with increasing MTX concentration from 5-95 °C with absorbance measured at 260 nm.

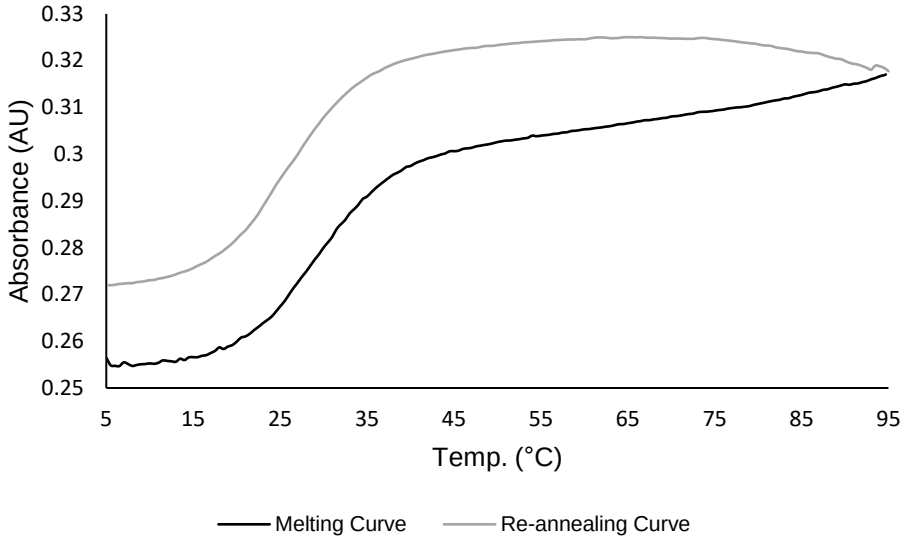

5'-GTT GC(idSp) CGT ATG-3' (THF-12mer) thermal melting stability with 0.25 equivalents PIX added from 5-95 °C with absorbance measured at 260 nm.

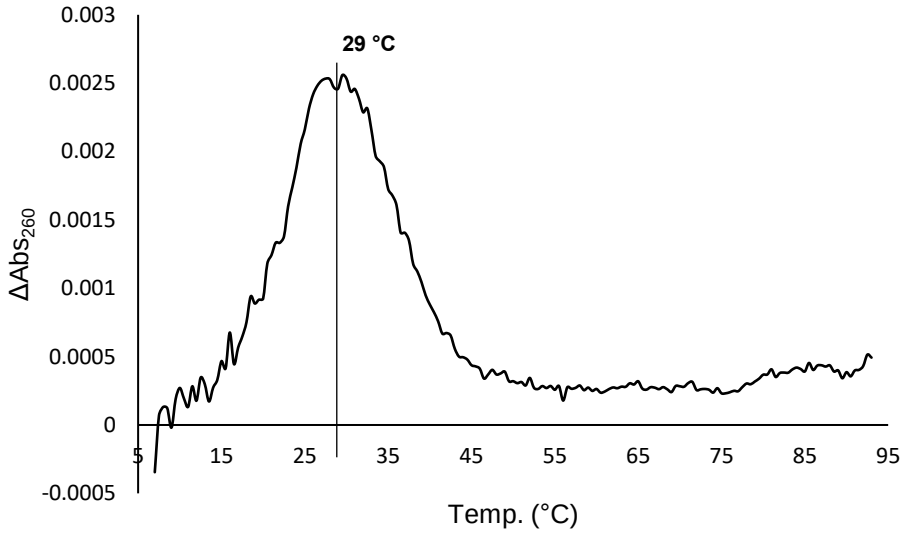

5'-GTT GC(idSp) CGT ATG-3' (THF-12mer) first derivative of the melting curve with 0.25 equivalents PIX added from 5-95 °C with absorbance measured at 260 nm.

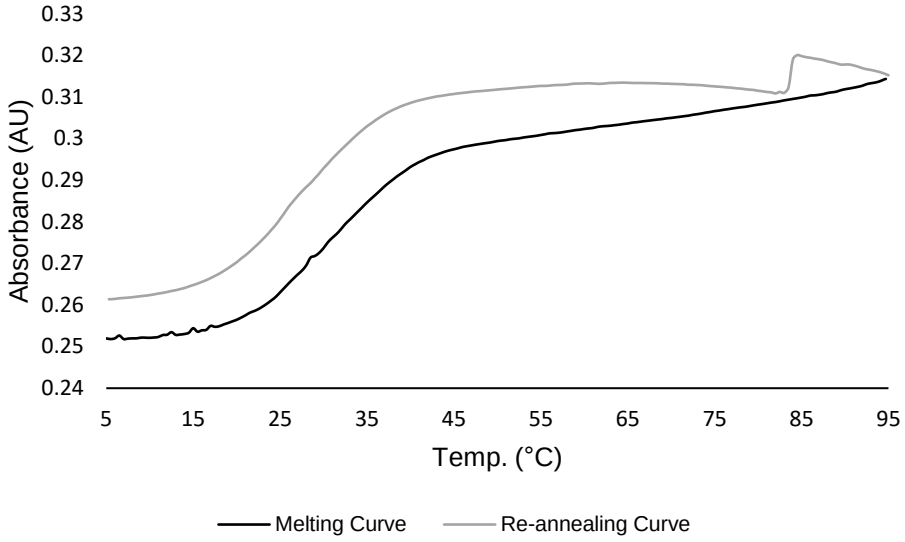

5'-GTT GC(idSp) CGT ATG-3' (THF-12mer) thermal melting stability with 0.5 equivalents PIX added from 5-95 °C with absorbance measured at 260 nm.

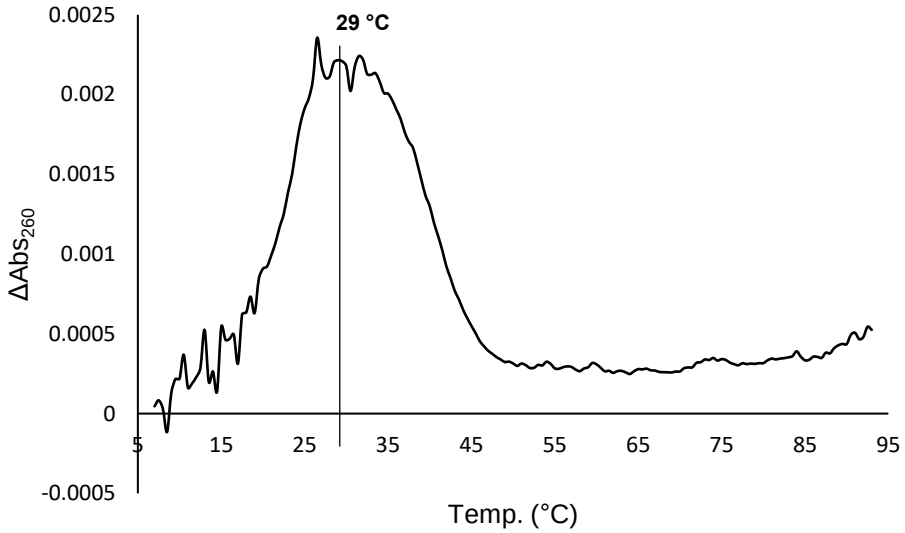

5'-GTT GC(idSp) CGT ATG-3' (THF-12mer) first derivative of the melting curve with 0.5 equivalents PIX added from 5-95 °C with absorbance measured at 260 nm.

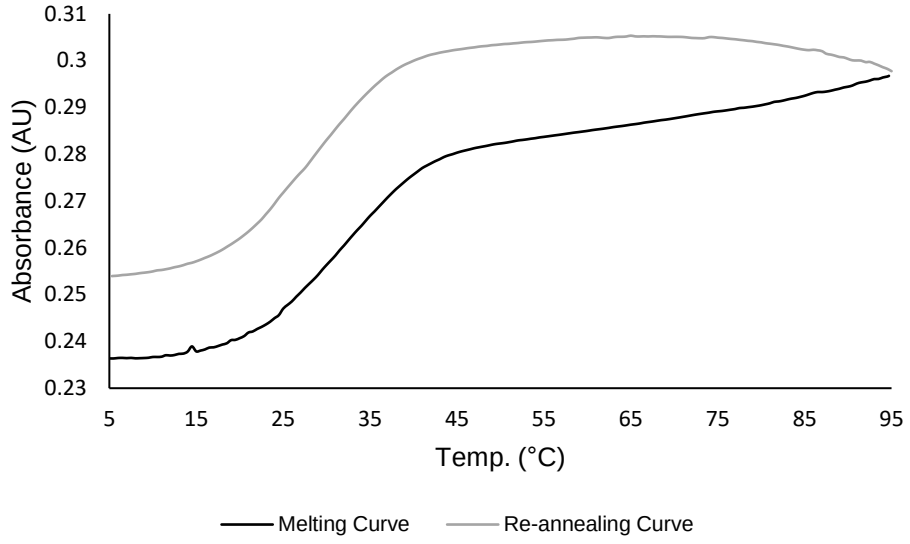

5'-GTT GC(idSp) CGT ATG-3' (THF-12mer) thermal melting stability with 0.8 equivalents PIX added from 5-95 °C with absorbance measured at 260 nm.

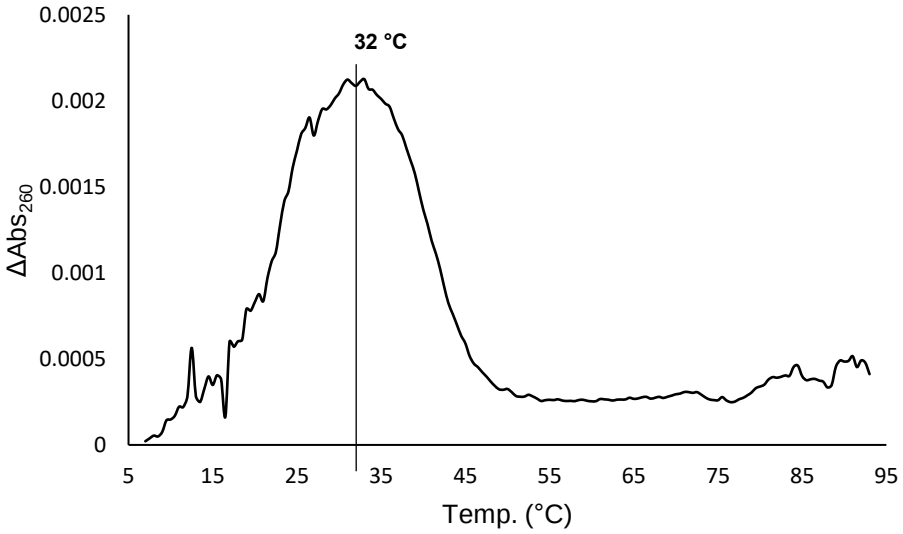

5'-GTT GC(idSp) CGT ATG-3' (THF-12mer) first derivative of the melting curve with 0.8 equivalents PIX added from 5-95 °C with absorbance measured at 260 nm.

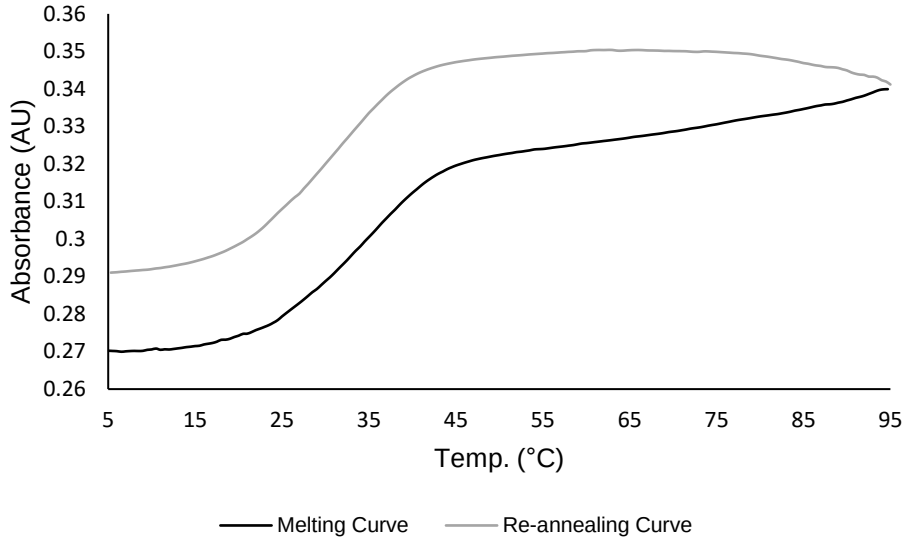

5'-GTT GC(idSp) CGT ATG-3' (THF-12mer) thermal melting stability with 1 equivalent PIX added from 5-95 °C with absorbance measured at 260 nm.

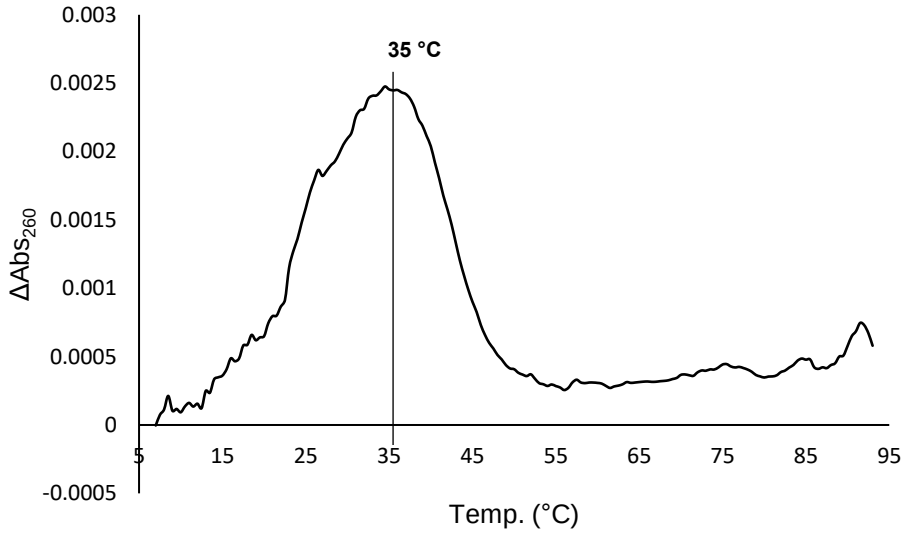

5'-GTT GC(idSp) CGT ATG-3' (THF-12mer) first derivative of the melting curve with 1 equivalent PIX added from 5-95 °C with absorbance measured at 260 nm.

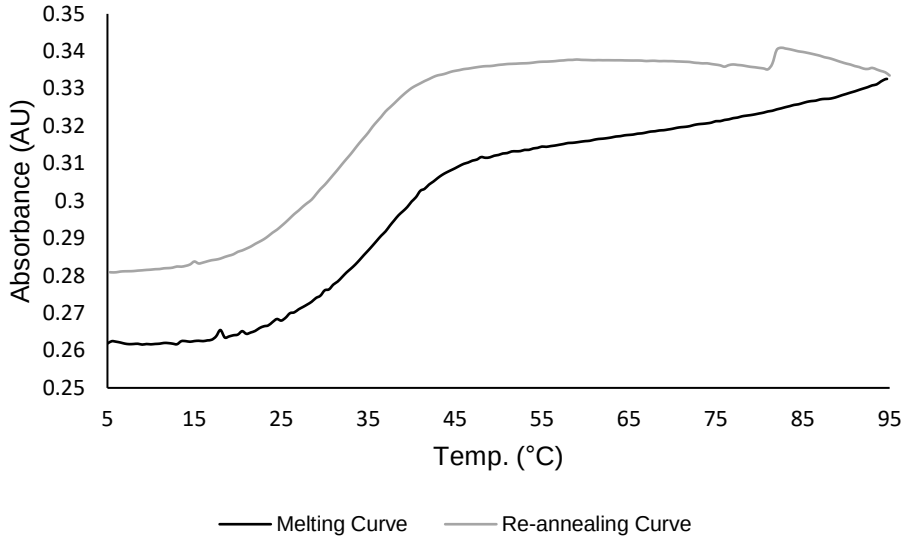

5'-GTT GC(idSp) CGT ATG-3' (THF-12mer) thermal melting stability with 1.6 equivalents PIX added from 5-95 °C with absorbance measured at 260 nm.

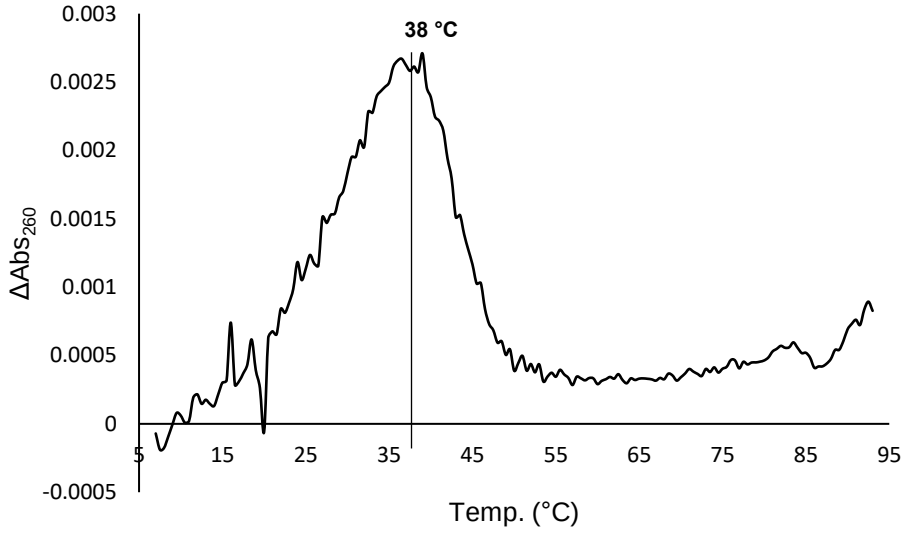

5'-GTT GC(idSp) CGT ATG-3' (THF-12mer) first derivative of the melting curve with 1.6 equivalents PIX added from 5-95 °C with absorbance measured at 260 nm.

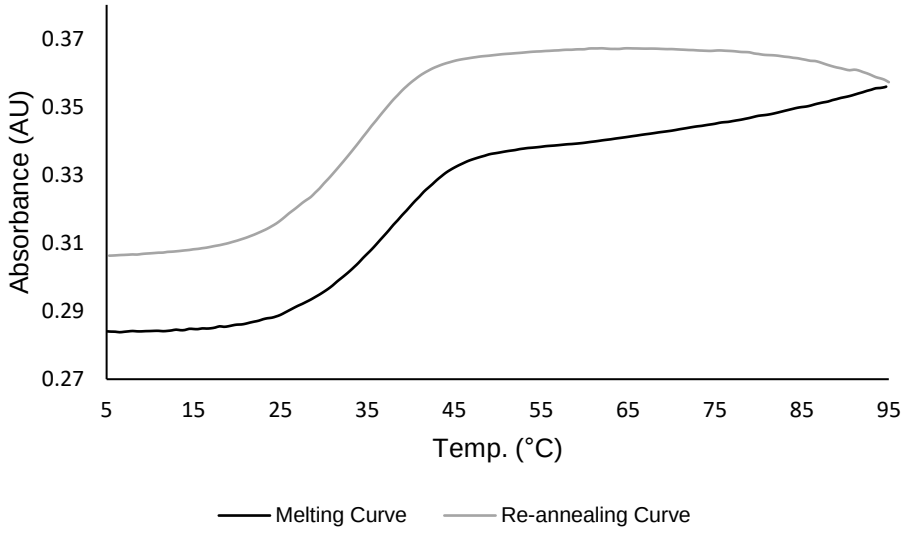

5'-GTT GC(idSp) CGT ATG-3' (THF-12mer) thermal melting stability with 2 equivalents PIX added from 5-95 °C with absorbance measured at 260 nm.

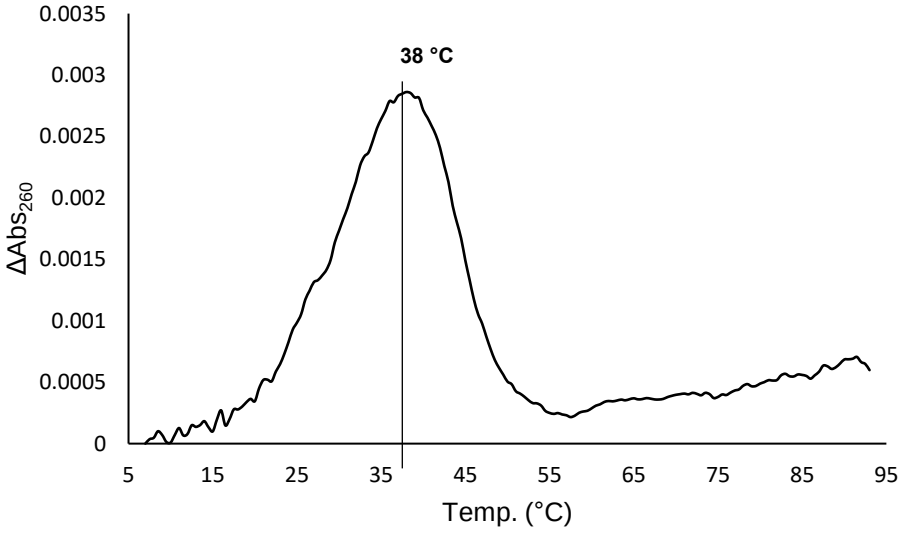

5'-GTT GC(idSp) CGT ATG-3' (THF-12mer) first derivative of the melting curve with 2 equivalents PIX added from 5-95 °C with absorbance measured at 260 nm.

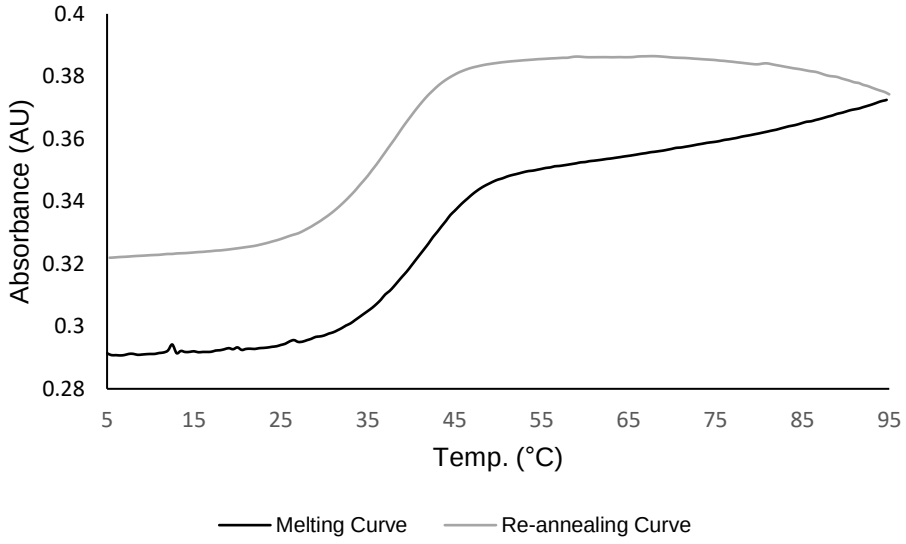

5'-GTT GC(idSp) CGT ATG-3' (THF-12mer) thermal melting stability with 5 equivalents PIX added from 5-95 °C with absorbance measured at 260 nm.

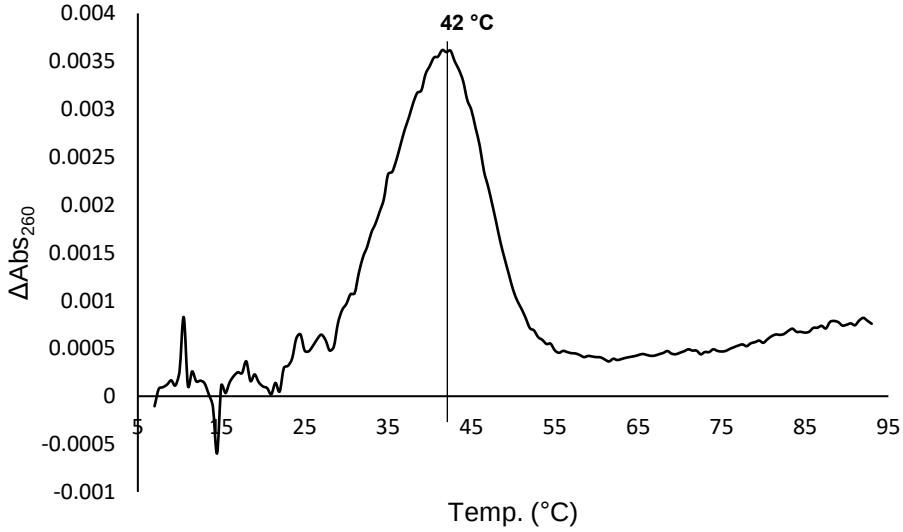

5'-GTT GC(idSp) CGT ATG-3' (THF-12mer) first derivative of the melting curve with 5 equivalents PIX added from 5-95 °C with absorbance measured at 260 nm.

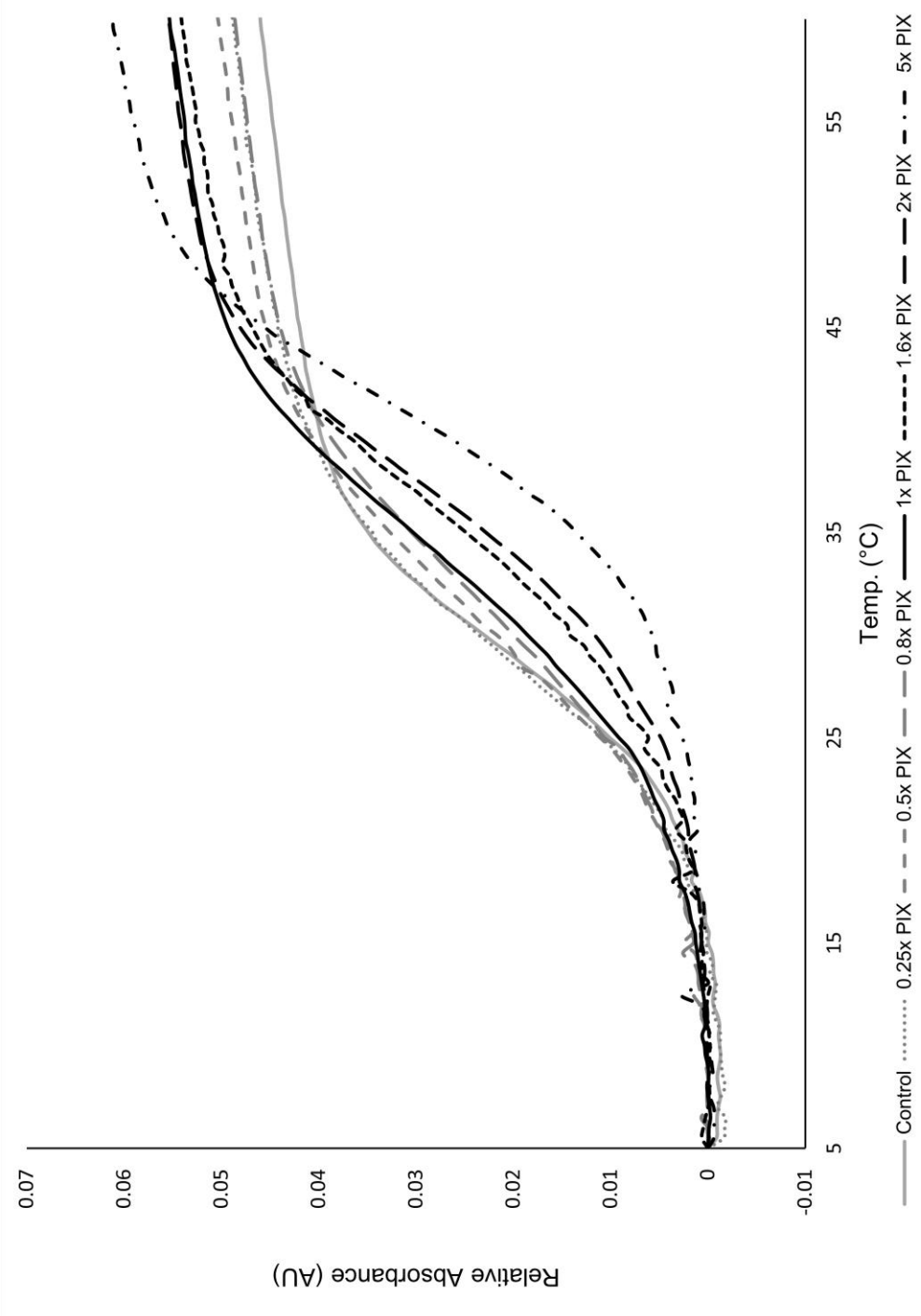

5’-GTT GC(idSp) CGT ATG-3’ (THF-12mer) thermal melting stability comparison with increasing PIX concentration from 5-95 °C with absorbance measured at 260 nm.

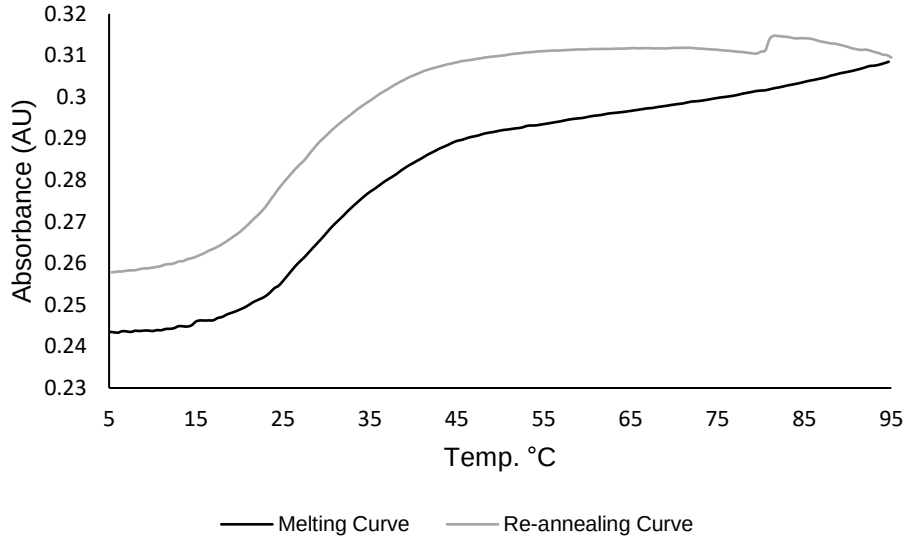

5'-GTT GC(idSp) CGT ATG-3' (THF-12mer) thermal melting stability with 0.25 equivalents DOX added from 5-95 °C with absorbance measured at 260 nm.

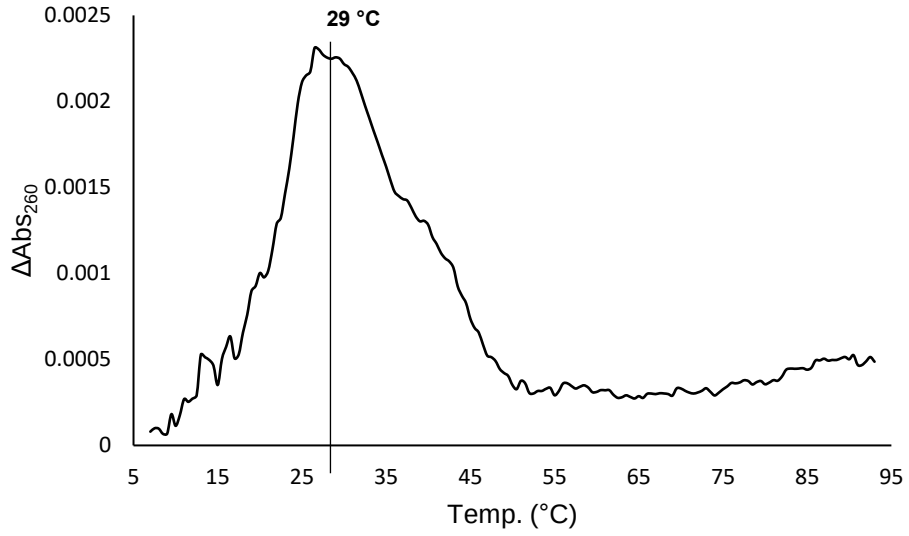

5'-GTT GC(idSp) CGT ATG-3' (THF-12mer) first derivative of the melting curve with 0.25 equivalents DOX added from 5-95 °C with absorbance measured at 260 nm.

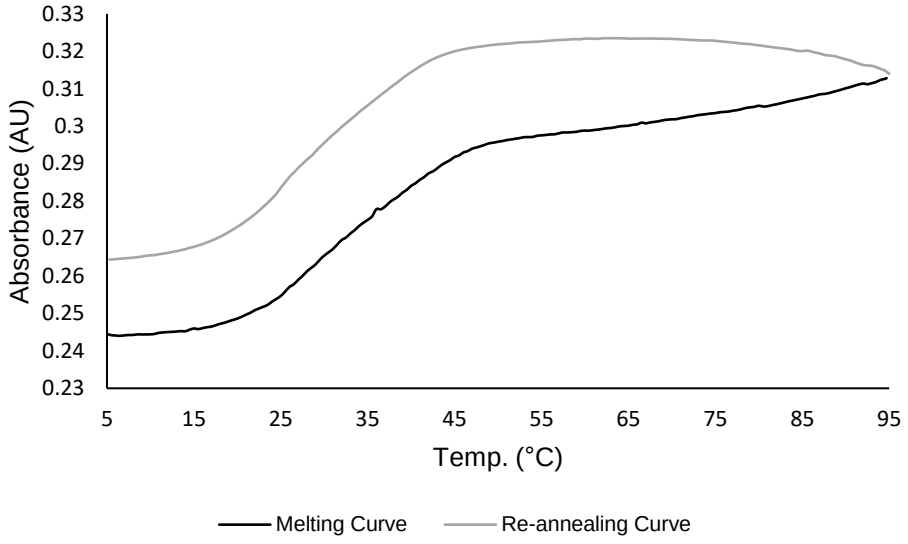

5'-GTT GC(idSp) CGT ATG-3' (THF-12mer) thermal melting stability with 0.5 equivalents DOX added from 5-95 °C with absorbance measured at 260 nm.

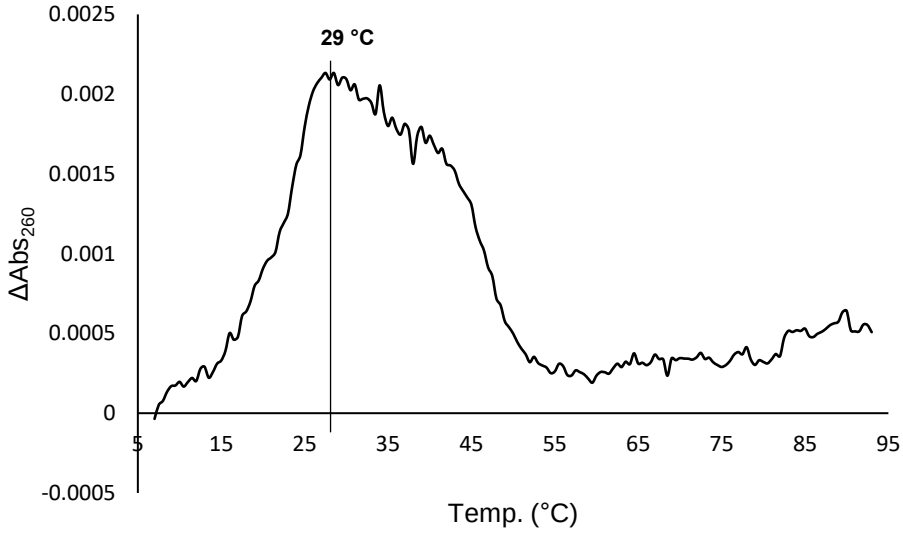

5'-GTT GC(idSp) CGT ATG-3' (THF-12mer) first derivative of the melting curve with 0.5 equivalents DOX added from 5-95 °C with absorbance measured at 260 nm.

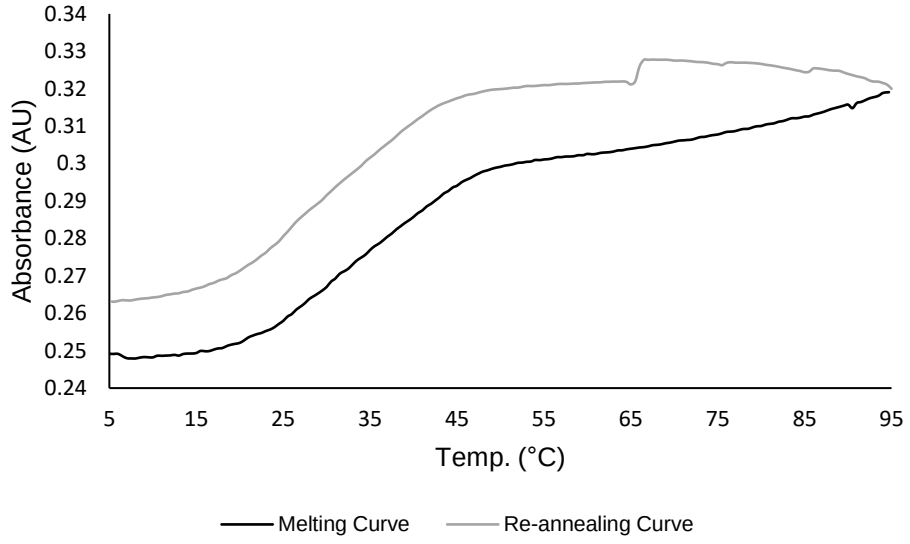

5'-GTT GC(idSp) CGT ATG-3' (THF-12mer) thermal melting stability with 0.75 equivalents DOX added from 5-95 °C with absorbance measured at 260 nm.

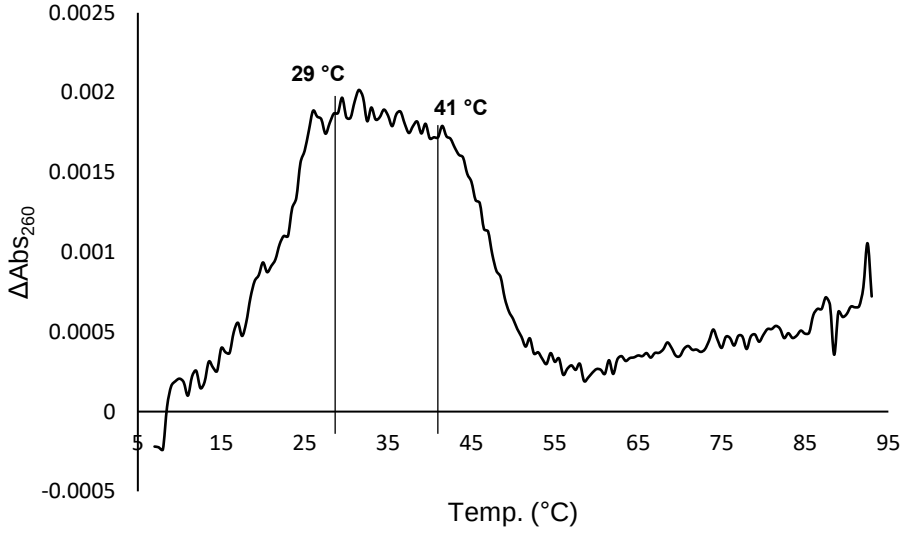

5'-GTT GC(idSp) CGT ATG-3' (THF-12mer) first derivative of the melting curve with 0.75 equivalents DOX added from 5-95 °C with absorbance measured at 260 nm.

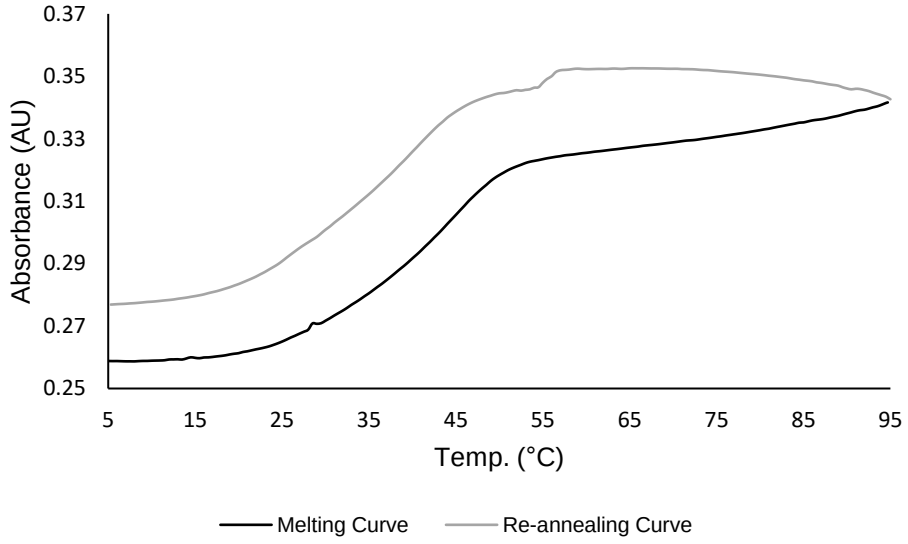

5'-GTT GC(idSp) CGT ATG-3' (THF-12mer) thermal melting stability with 1 equivalent DOX added from 5-95 °C with absorbance measured at 260 nm.

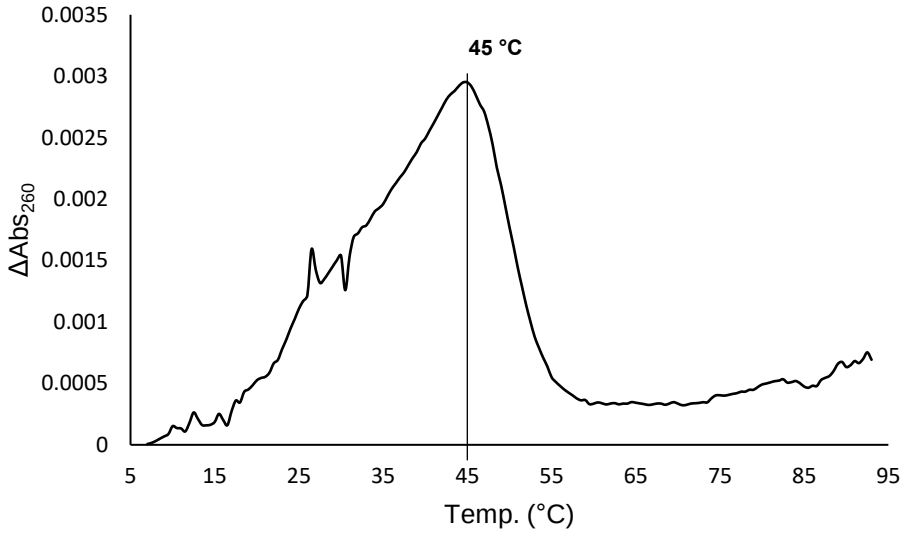

5'-GTT GC(idSp) CGT ATG-3' (THF-12mer) first derivative of the melting curve with 1 equivalent DOX added from 5-95 °C with absorbance measured at 260 nm.

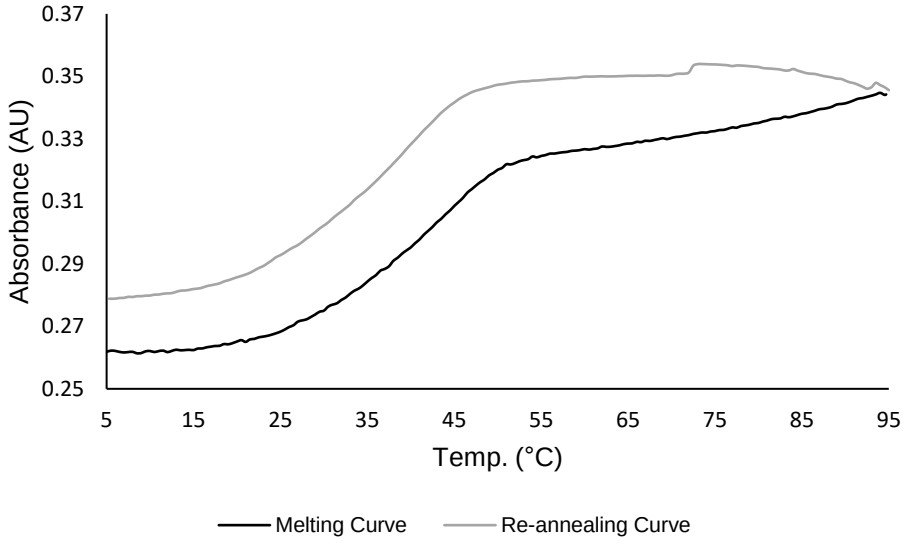

5'-GTT GC(idSp) CGT ATG-3' (THF-12mer) thermal melting stability with 1.6 equivalents DOX added from 5-95 °C with absorbance measured at 260 nm.

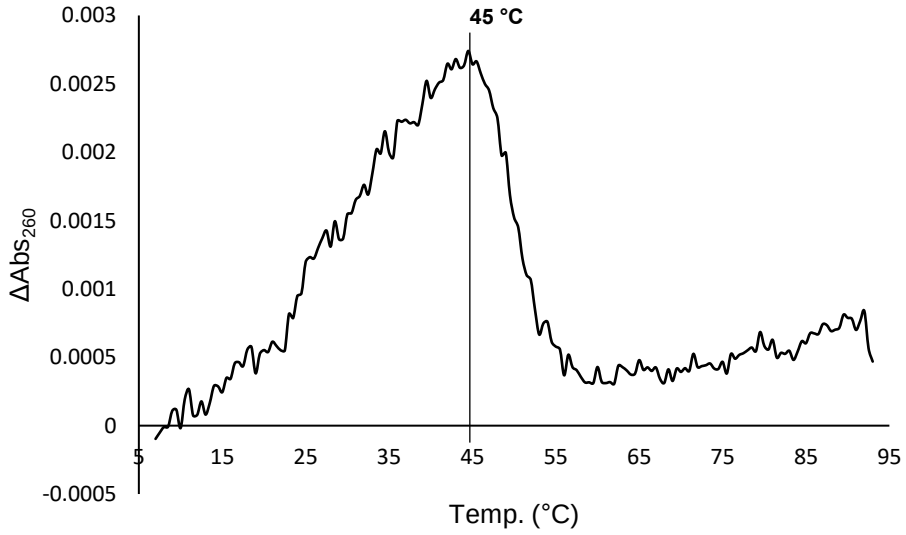

5'-GTT GC(idSp) CGT ATG-3' (THF-12mer) first derivative of the melting curve with 1.6 equivalents DOX added from 5-95 °C with absorbance measured at 260 nm.

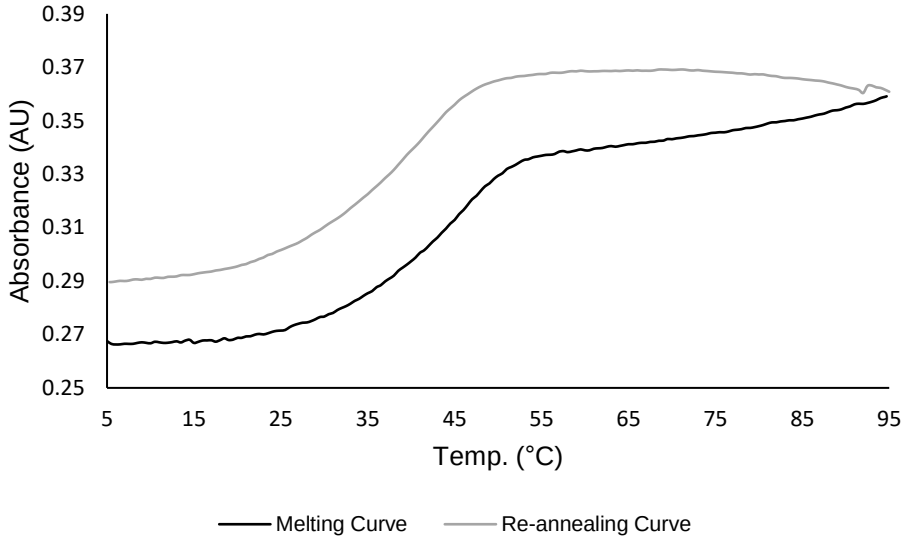

5'-GTT GC(idSp) CGT ATG-3' (THF-12mer) thermal melting stability with 2 equivalents DOX added from 5-95 °C with absorbance measured at 260 nm.

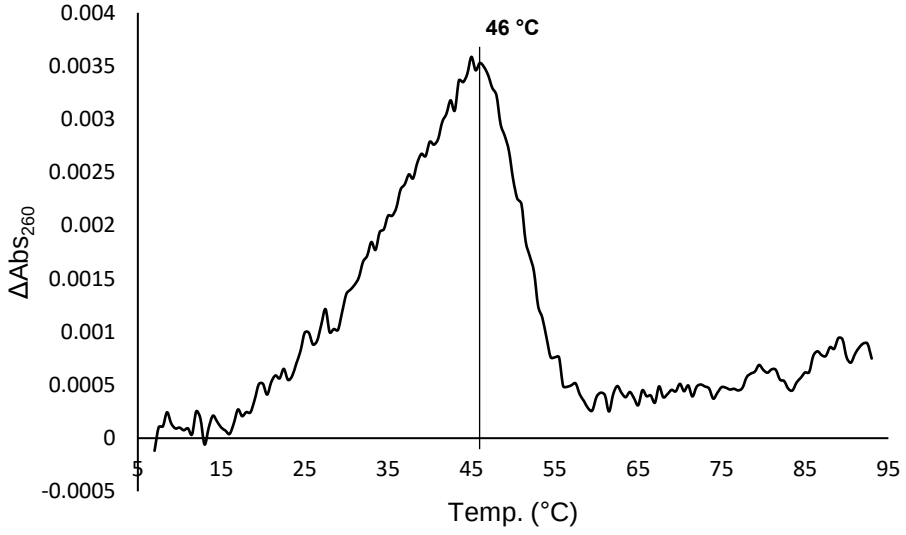

5'-GTT GC(idSp) CGT ATG-3' (THF-12mer) first derivative of the melting curve with 2 equivalents DOX added from 5-95 °C with absorbance measured at 260 nm.

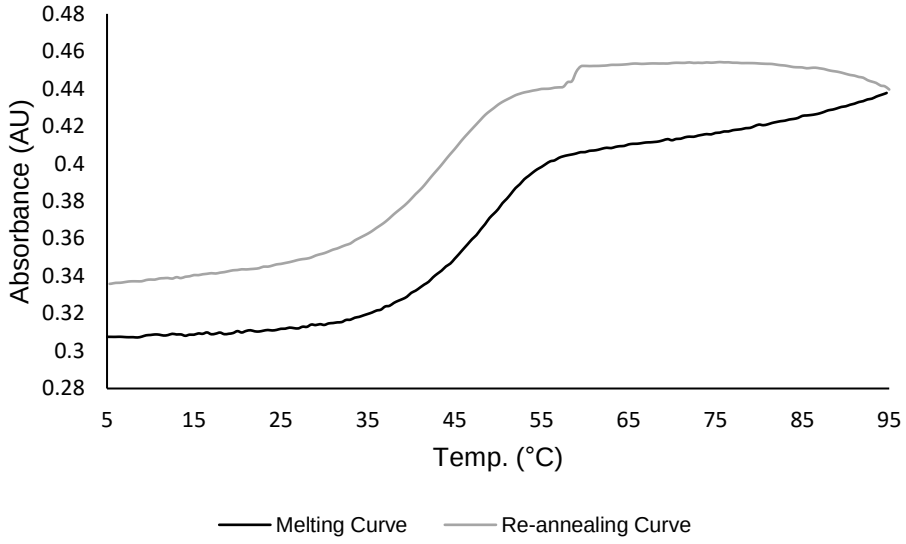

5'-GTT GC(idSp) CGT ATG-3' (THF-12mer) thermal melting stability with 5 equivalents DOX added from 5-95 °C with absorbance measured at 260 nm.

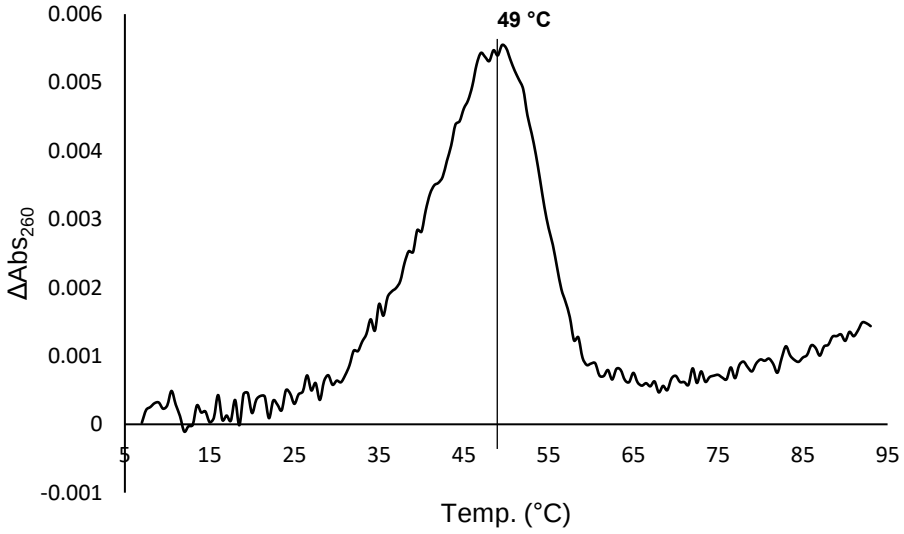

5'-GTT GC(idSp) CGT ATG-3' (THF-12mer) first derivative of the melting curve with 5 equivalents DOX added from 5-95 °C with absorbance measured at 260 nm.

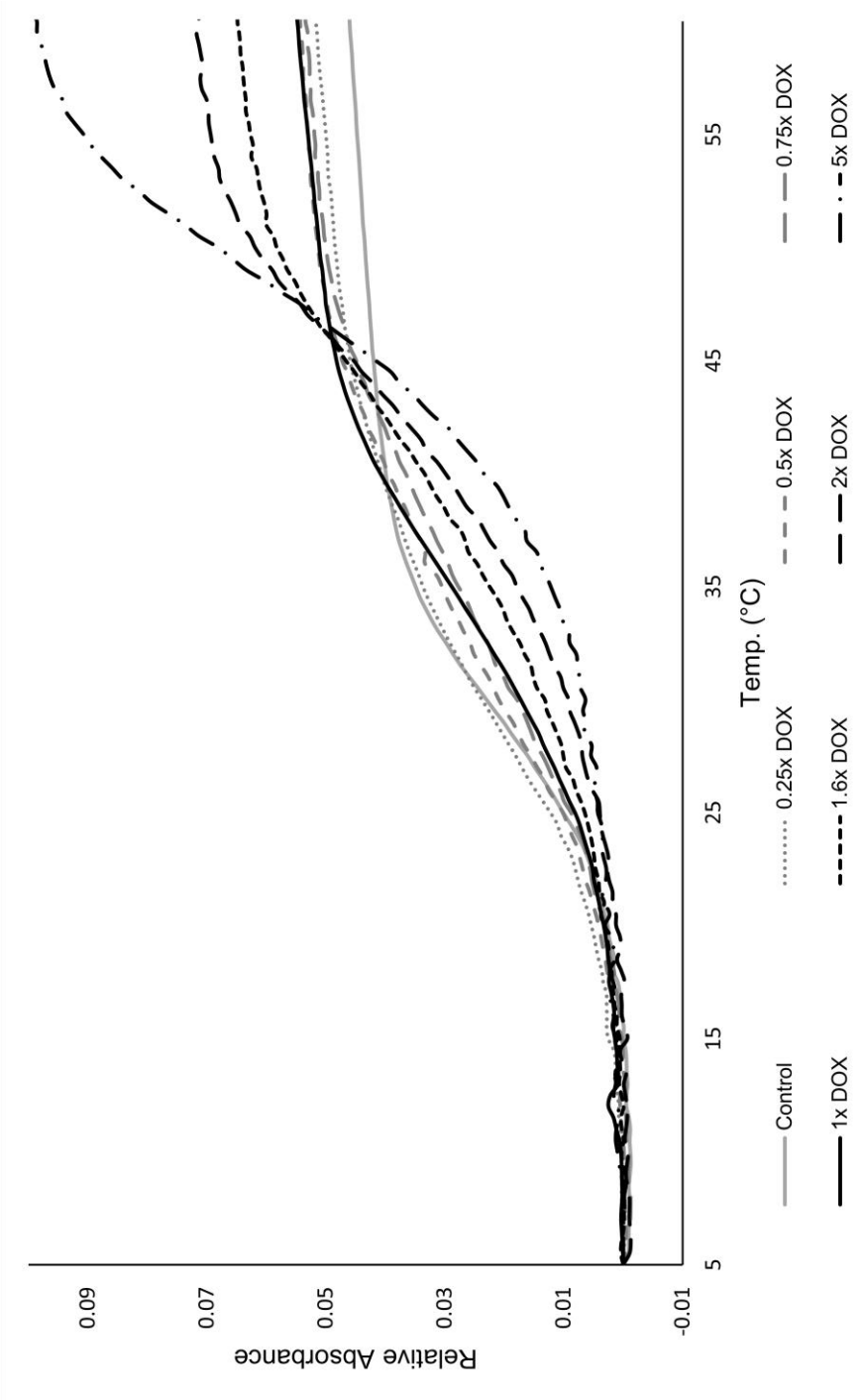

5’-GTT GC(idSp) CGT ATG-3’ (THF-12mer) thermal melting stability comparison with increasing DOX concentration from 5-95 °C with absorbance measured at 260 nm.

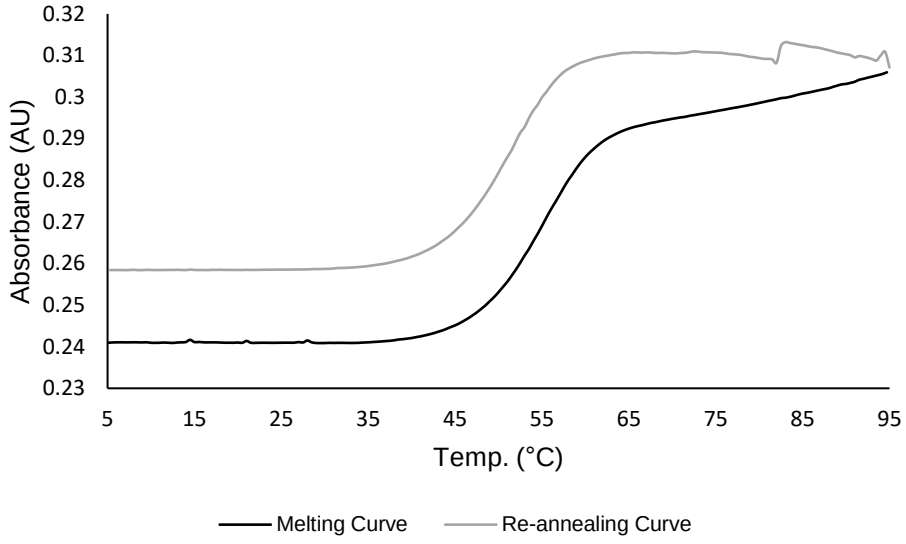

5'-GTT GCG CGT ATG-3' (G-12mer) thermal melting stability from 5-95 °C with absorbance measured at 260 nm.

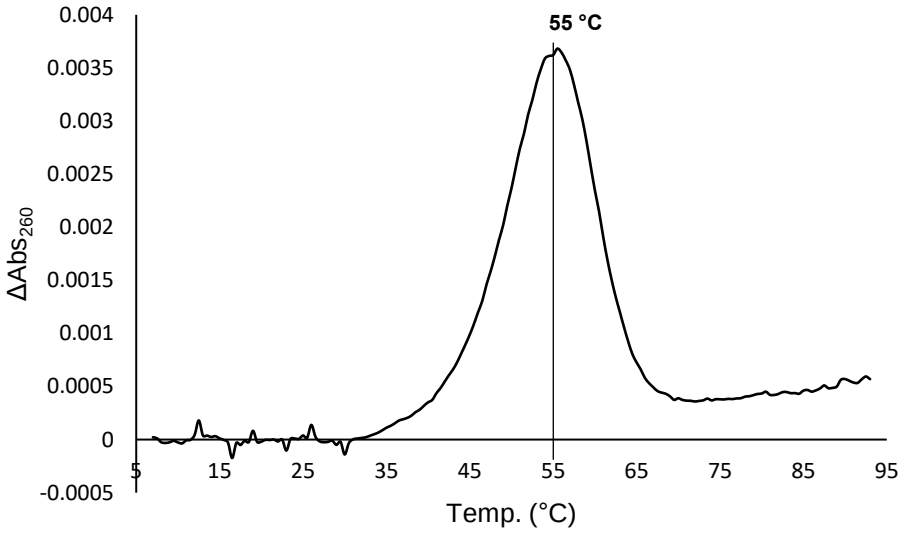

5'-GTT GCG CGT ATG-3' (G-12mer) first derivative of the melting curve from 5-95 °C with absorbance measured at 260 nm.

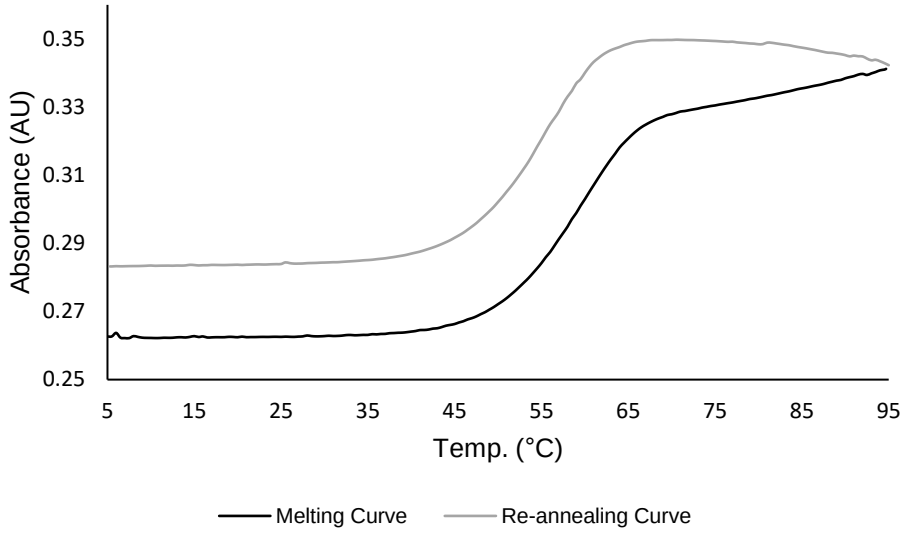

5'-GTT GCG CGT ATG-3' (G-12mer) thermal melting stability with 1 equivalent MTX added from 5-95 °C with absorbance measured at 260 nm.

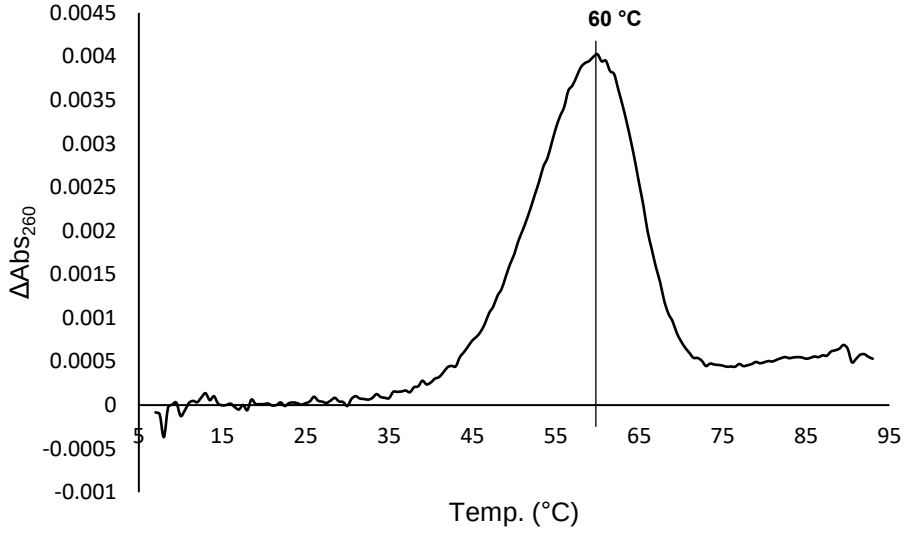

5'-GTT GCG CGT ATG-3' (G-12mer) first derivative of the melting curve with 1 equivalent MTX added from 5-95 °C with absorbance measured at 260 nm.

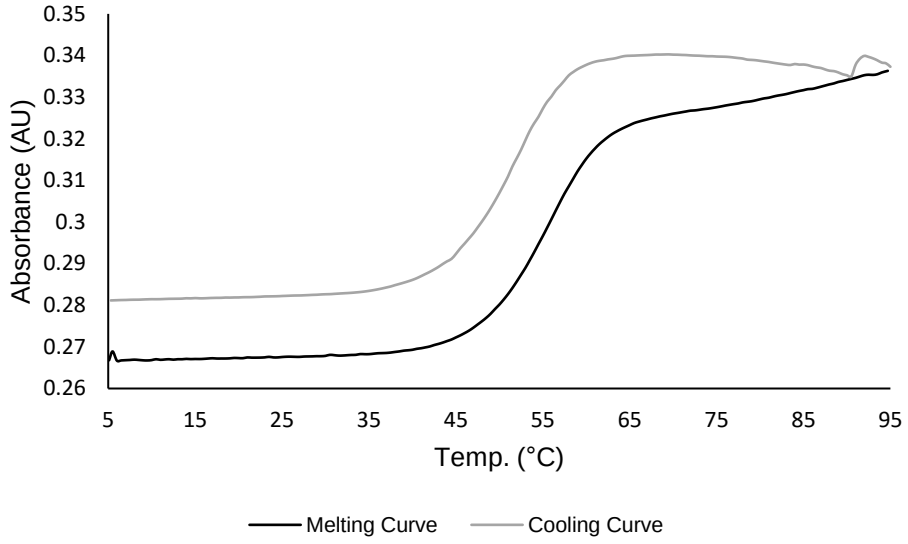

5'-GTT GCGCGT ATG-3' (G-12mer) thermal melting stability with 1 equivalent PIX added from 5-95 °C with absorbance measured at 260 nm.

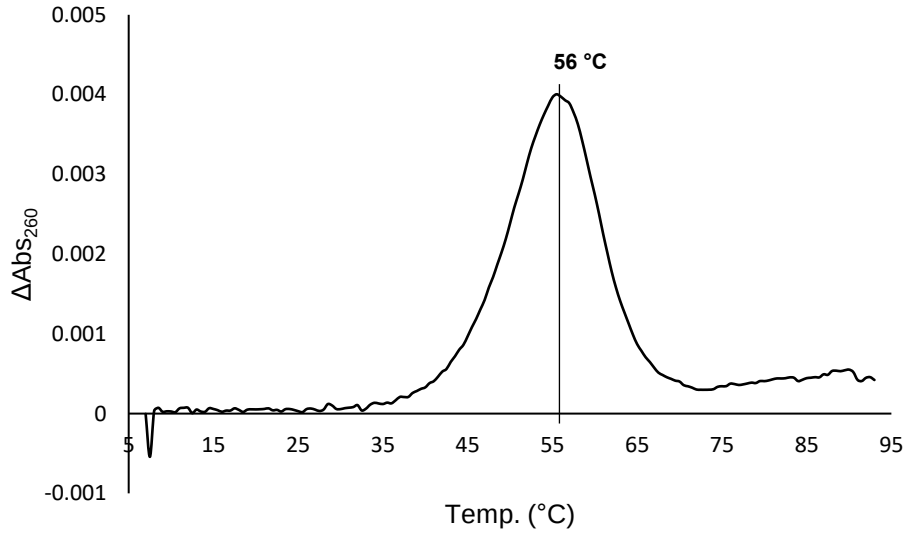

5'-GTT GCG CGT ATG-3' (G-12mer) first derivative of the melting curve with 1 equivalent PIX added from 5-95 °C with absorbance measured at 260 nm.

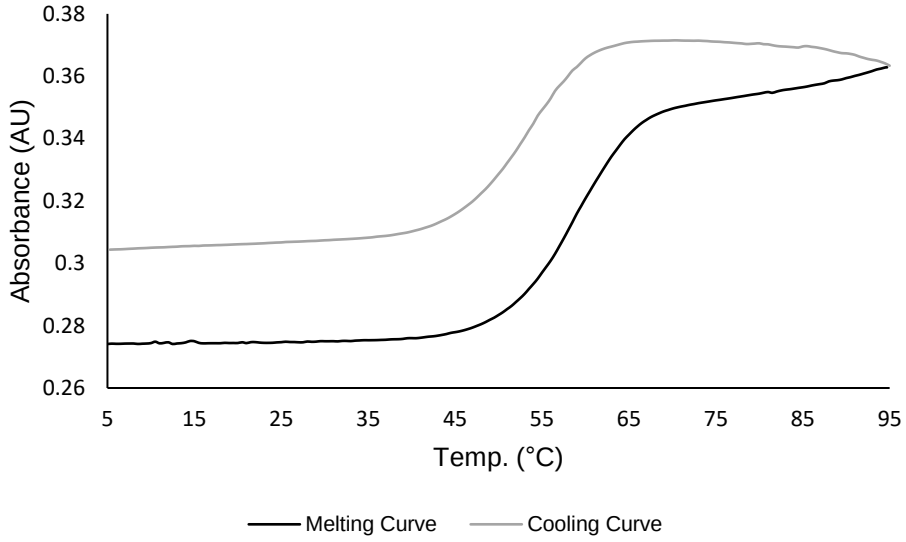

5'-GTT GCG CGT ATG-3' (G-12mer) thermal melting stability with 1 equivalent DOX added from 5-95 °C with absorbance measured at 260 nm.

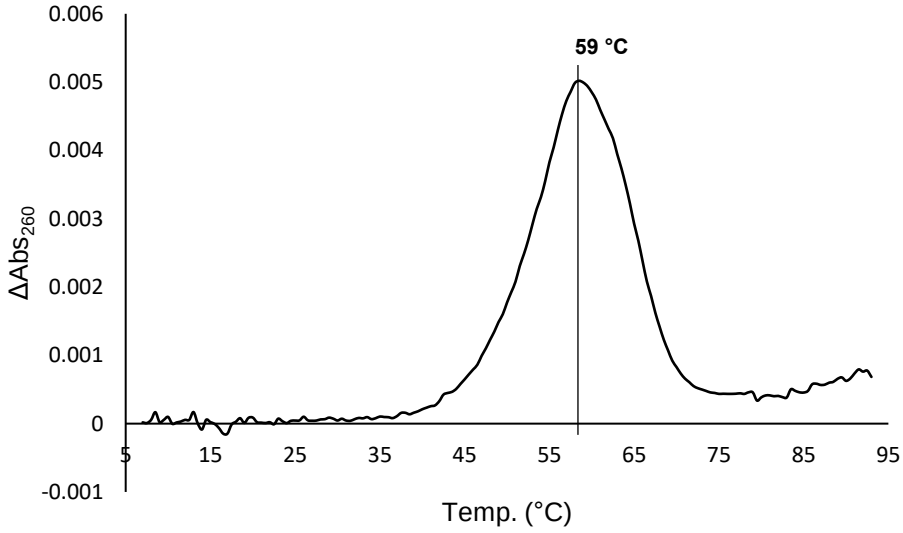

5'-GTT GCG CGT ATG-3' (G-12mer) first derivative of the melting curve with 1 equivalent DOX added from 5-95 °C with absorbance measured at 260 nm.

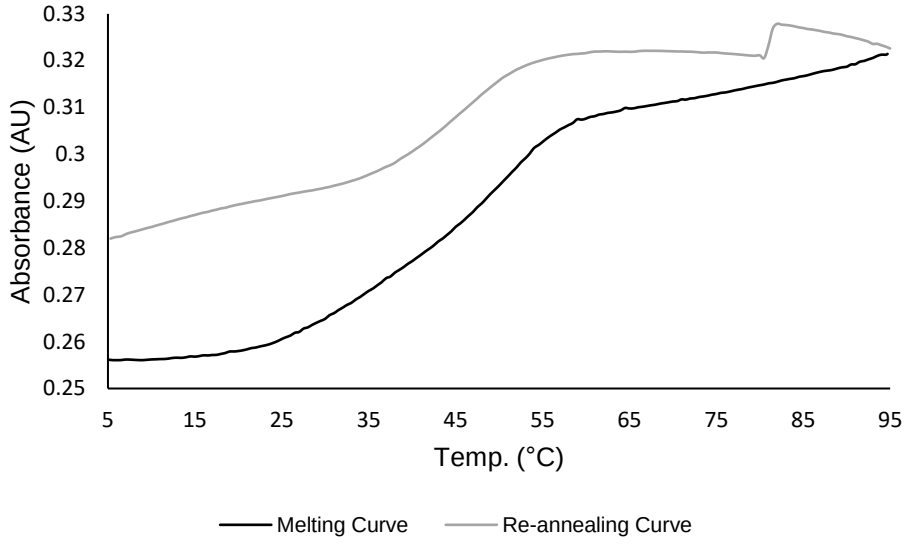

5'-GTT GC(AP) CGT ATG-3' (AP-12mer) thermal melting stability with 1 equivalent MTX added (t_0-3h) from 5-95 °C with absorbance measured at 260 nm.

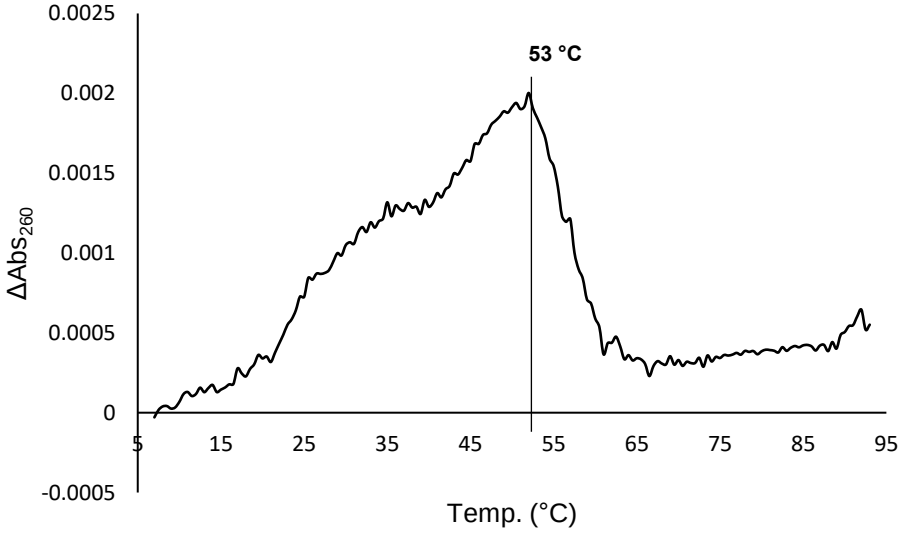

5'-GTT GC(AP) CGT ATG-3' (AP-12mer) first derivative of the melting curve with 1 equivalent MTX added (t_0-3h) from 5-95 °C with absorbance measured at 260 nm.

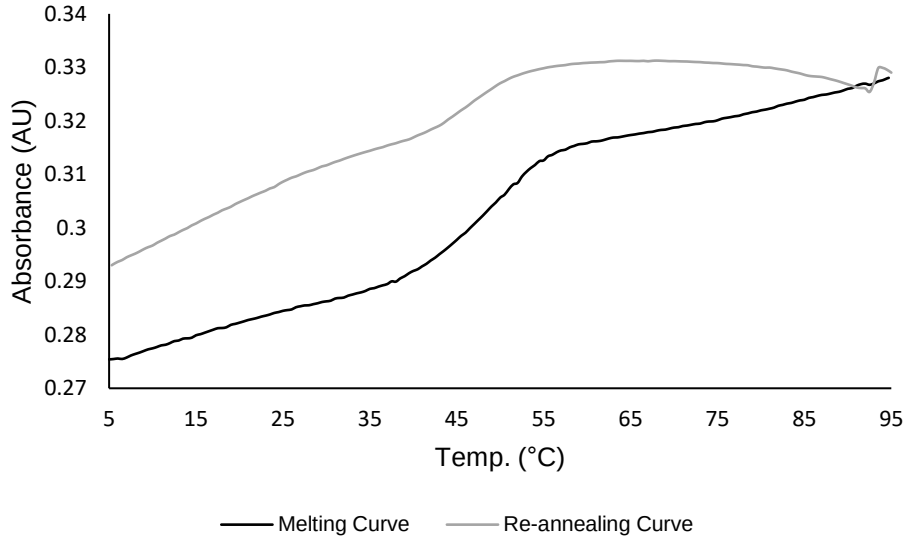

5'-GTT GC(AP) CGT ATG-3' (AP-12mer) thermal melting stability with 1 equivalent MTX added (3-6h) from 5-95 °C with absorbance measured at 260 nm.

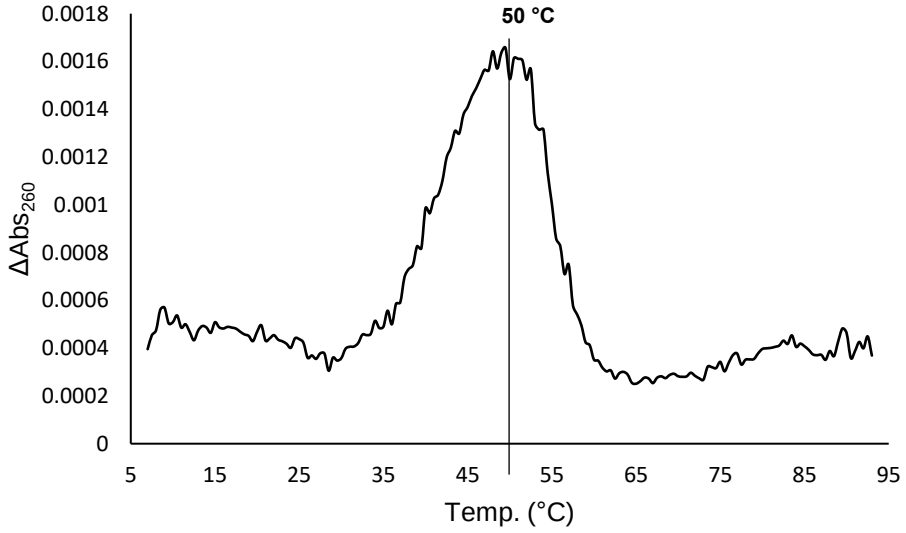

5'-GTT GC(AP) CGT ATG-3' (AP-12mer) first derivative of the melting curve with 1 equivalent MTX added (3-6h) from 5-95 °C with absorbance measured at 260 nm.

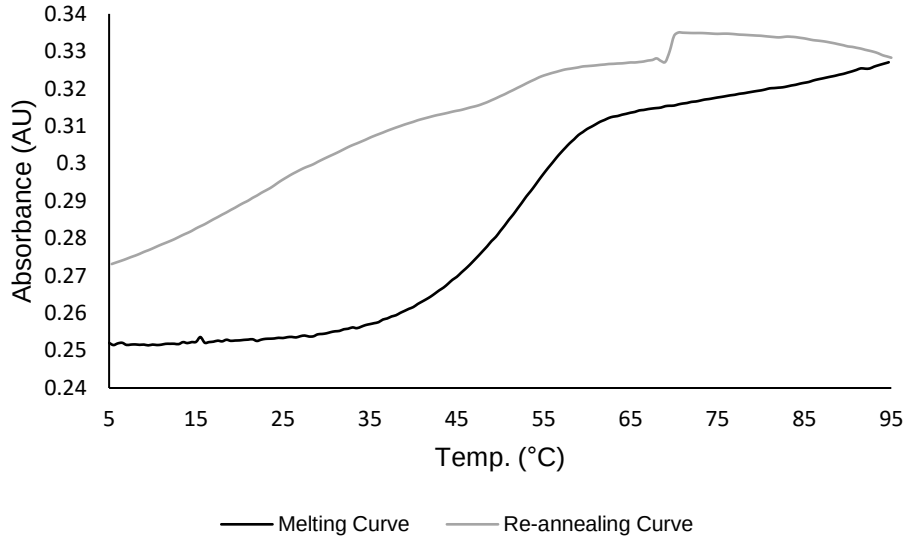

5'-GTT GC(AP) CGT ATG-3' (AP-12mer) thermal melting stability with 2.5 equivalents MTX added (t_0-3h) from 5-95 °C with absorbance measured at 260 nm.

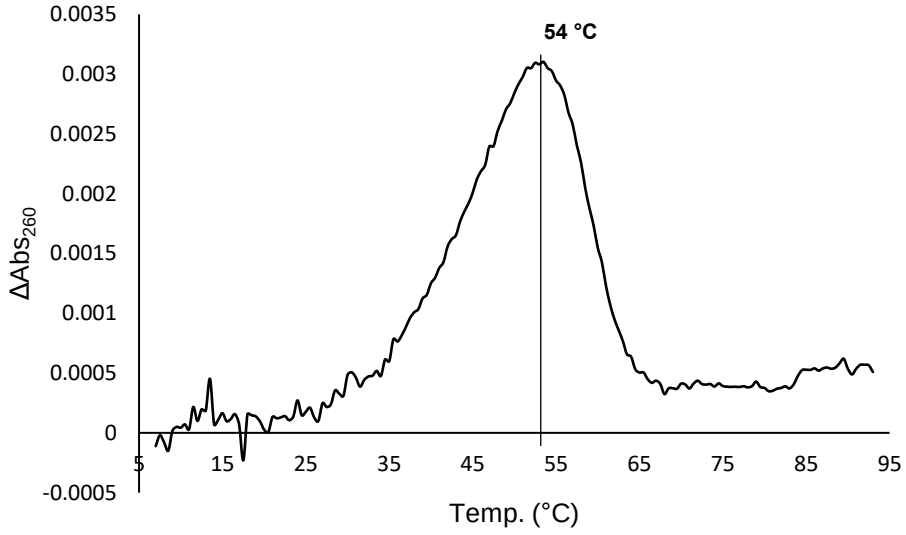

5'-GTT GC(AP) CGT ATG-3' (AP-12mer) first derivative of the melting curve with 2.5 equivalents MTX added (t_0-3h) from 5-95 °C with absorbance measured at 260 nm.

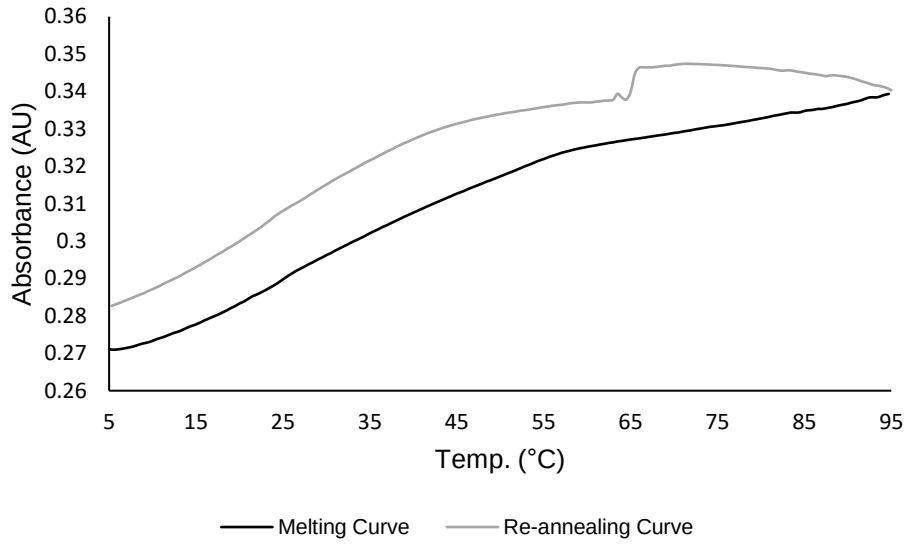

5'-GTT GC(AP) CGT ATG-3' (AP-12mer) thermal melting stability with 2.5 equivalents MTX added (3-6h) from 5-95 °C with absorbance measured at 260 nm.

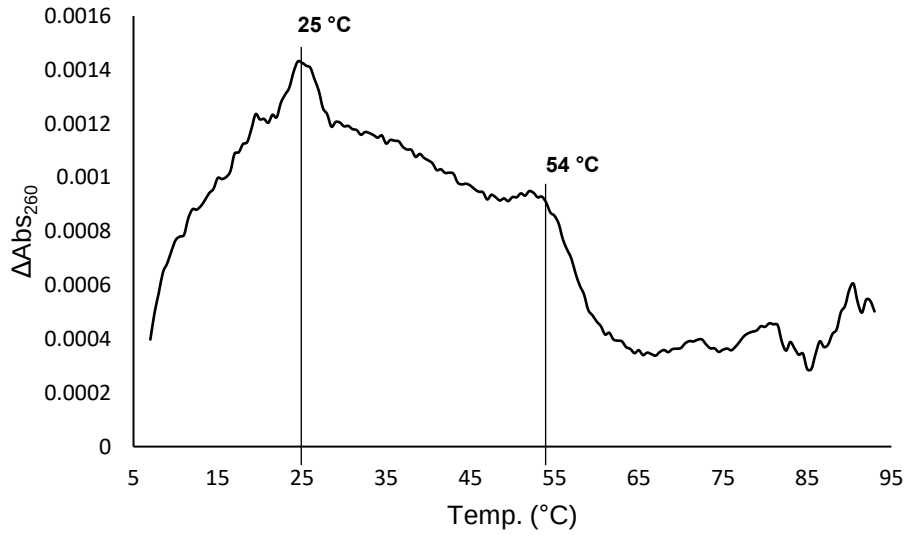

5'-GTT GC(AP) CGT ATG-3' (AP-12mer) first derivative of the melting curve with 2.5 equivalents MTX added (3-6h) from 5-95 °C with absorbance measured at 260 nm.